



Watson, David Stewart (2006) *Modelling aspects of the influence of edge effects on expansion anchors*. PhD thesis.

<http://theses.gla.ac.uk/8049/>

Copyright and moral rights for this thesis are retained by the author

A copy can be downloaded for personal non-commercial research or study, without prior permission or charge

This thesis cannot be reproduced or quoted extensively from without first obtaining permission in writing from the Author

The content must not be changed in any way or sold commercially in any format or medium without the formal permission of the Author

When referring to this work, full bibliographic details including the author, title, awarding institution and date of the thesis must be given

# **MODELLING ASPECTS OF THE INFLUENCE OF EDGE EFFECTS ON EXPANSION ANCHORS**

**By  
David Stewart Watson  
Department of Civil Engineering  
Faculty of Engineering  
University of Glasgow  
May 2006**

**A Thesis Submitted to the University of Glasgow in Fulfilment of the Degree of  
Doctor of Philosophy**

**© *David Stewart Watson* 2006.**



## Acknowledgements

*“We choose to go to the moon ... and do the other things, not because they are easy, but because they are hard”*

- John F. Kennedy

JFK may have had loftier goals in mind than a PhD (quite literally) however he elegantly defined the nature of a challenge. His words have been an inspiration to me when I found myself questioning why I’d chosen to follow this path. For me this PhD research has been a personal challenge. One which has brought a great many highs and lows but also brought many rewards. Although I said that this has been a personal challenge it is not one I could have met alone. I would like to acknowledge the help and support given to me by the following people.

I give special thanks to my supervisor, Professor Nenad Bićanić, for his continual support and encouragement throughout this research. Thank you to Dr Chris Pearce who assisted with supervision and who provided an alternative perspective on things. Thanks also to my colleagues in the Department of Civil Engineering, both staff and students.

Thanks to my friends for their moral support and for listening to my PhD rants. In particular Brendon Glass (for his programme of stress management via hill walking and beer drinking) and Michael Dales (for his software consultancy and regular excursions to Little Italy). Also Chris Stirling and Colin Davie, my partners in crime in the Department, for helping me with technical issues and putting up with me in an enclosed space. Thanks to the DCS lunch bunch, in particular Jonathan Paisley, for their welcome and regular distraction. And thank you to Nidhi Sharma for believing in me and helping me see beyond the PhD.

I wish to give special thanks to my family who have supported me 100% during not only this PhD but throughout my university career and my life as a whole. It is to them that this work is dedicated.

## **Abstract**

The principal aim of this work was to investigate and develop modelling techniques capable of accurately and robustly analysing expansion anchor bolts in concrete under tensile loading. Of special interest was the influence of low edge distances on such devices.

Since the 20<sup>th</sup> century increased demands for flexibility, safety and cost have lead to significant development of new anchor products. Modern design methods for new products follow a scientific approach but still rely on substantial and expensive programs of experimental testing. Current design methods for structural designers using anchors are based on semi-empirical approaches derived from extensive experimental testing. It is proposed that much of this experimental work can be replaced with numerical modelling.

A number of suitable finite element constitutive models are considered. Initially a Multi-surface Plasticity Model and a Traditional Crack Model using a Multiple Fixed Crack (MFC) formulation are considered. Both are shown to give satisfactory results when used to analyse a common, plane-stress benchmark problem. However, although the Plasticity Model gave a better post peak response a 3D implementation was not available within the chosen FE framework. Spurious stress accumulation was identified as the cause of the problems with the MFC Model and its various causes are investigated in detail. A Total Strain Based Rotating Crack Model was chosen as an alternative constitutive model and together with suitable modelling parameters was able to reduce these spurious stress accumulation effects to an acceptable level.

3D modelling of a non-expanding, fully bonded anchor at various distances to the free edge accurately predicted the expected reduction in strength and compared well with reduction factors supplied by anchor manufacturers. The study was extended to include the effect of two free edges and results allowed the strength reduction to be calculated for

any arbitrary position rather than for just the single edge approach given in the anchor design guides.

Modelling of anchor expansion was tackled on two fronts. Firstly anchor-concrete interfacial behaviour was considered. A Coulomb Friction Model applied to zero thickness structural interface elements to simulate the pressure dependant frictional bond. The role of FE model geometry and material properties in producing a realistic interfacial stress profile was studied in detail. For the kinematics of the expansion modelling of the expander mechanism as a contact problem was found to be the most accurate approach. However, limitations of the modelling framework required that the contact analysis be performed separately and resulting contact stress profile be applied to the existing, non-contact problem. This approach, although somewhat inflexible, provided a useful insight into the important factors pertaining to both the geometric and constitutive models. Results showed realistic crack patterns and demonstrated the effect of varying expansion pressures on the structural response of the anchor bolt.

The modelling approach used in this study was highly complex in terms of the multiple non-linear material models and the associated solution process. This resulted in problems with robustness and stability. As an alternative and inherently stable modelling framework a Sequentially Linear (SL) Model was developed. In its isotropic form it proved fast, accurate and reliable for plane-stress anchor problems. Orthotropic fracturing and 3D analysis capabilities were introduced to the model and a number of rules for crack initiation and orientation were tested. Although limitations in the possible crack orientations produced significant mesh bias to the crack pattern, the model was able to capture the changes in anchor behaviour associated with reduced edge distance. The overall assessment is that that SL Model has great potential especially for highly non-linear problems where stability and robustness are issues.

# Table of Contents

ACKNOWLEDGEMENTS.....	II
ABSTRACT.....	III
TABLE OF CONTENTS.....	V
<b>CHAPTER 1 INTRODUCTION.....</b>	<b>1</b>
1.1 ANCHOR TYPES .....	3
1.2 FAILURE MECHANISMS.....	7
1.3 CURRENT DESIGN PRACTICES.....	11
1.4 PROJECT AIMS AND OBJECTIVES .....	12
<b>CHAPTER 2 REVIEW OF ANCHOR RESEARCH.....</b>	<b>13</b>
2.1 ANCHOR DESIGN PROCESS .....	14
2.2 COMPUTATIONAL ANALYSIS OF CONCRETE .....	24
2.3 NUMERICAL MODELLING OF ANCHOR BOLTS .....	35
2.3.1 RILEM Round Robin Problem .....	35
2.3.2 Wider World of Anchor Modelling.....	38
2.4 CONCLUSIONS .....	52
<b>CHAPTER 3 NON-LINEAR MATERIAL MODELS .....</b>	<b>53</b>
3.1 PLASTICITY MODEL .....	53
3.2 TRADITIONAL FIXED CRACK MODEL.....	67
3.2.1 Basics .....	67
3.2.2 Constitutive Equations .....	73
3.2.3 Softening Models.....	75
3.2.4 Shear Stiffness Reduction.....	79
3.3 SUMMARY .....	81
<b>CHAPTER 4 2D AND PRELIMINARY 3D MODELLING .....</b>	<b>82</b>
4.1 RILEM BENCHMARK PROBLEM .....	82
4.1.1 Problem Details .....	82
4.1.2 RILEM Analysis Results.....	85
4.2 EXPANSION ANCHOR MODELLING IN 2D.....	89
4.2.1 Plane Stress Modelling of Anchor Bolt .....	91

4.2.2	<i>Axisymmetric Modelling of Anchor Bolt</i> .....	102
4.3	ANCHOR MODELLING IN 3D .....	112
4.3.1	<i>Complexities Introduced by 3D Modelling</i> .....	112
4.4	PRELIMINARY 3D ANCHOR MODELLING .....	117
4.5	SUMMARY .....	125
<b>CHAPTER 5 TOTAL STRAIN BASED CRACK MODEL</b> .....		<b>126</b>
5.1	INTRODUCTION .....	126
5.2	THEORY .....	127
5.2.1	<i>Basics</i> .....	127
5.2.2	<i>Loading and Unloading</i> .....	131
5.2.3	<i>Stiffness Matrices</i> .....	134
5.2.4	<i>Poisson's Effects</i> .....	141
5.2.5	<i>Tensile and Compressive Behaviour</i> .....	144
5.2.6	<i>Lateral Confinement Effects</i> .....	146
5.2.7	<i>Compression Softening Effects</i> .....	147
5.2.8	<i>Shear Behaviour</i> .....	149
5.2.9	<i>Post-processing</i> .....	150
5.3	BENCHMARKING OF MODEL .....	152
5.3.1	<i>Biaxial Loading-Unloading Response</i> .....	153
5.3.2	<i>Ghavamian Uniaxial Load Reversal Test</i> .....	160
5.3.3	<i>Willam Anisotropy Test</i> .....	164
5.4	SUMMARY .....	170
<b>CHAPTER 6 INVESTIGATION OF THE CAUSES AND EFFECTS OF STRESS LOCKING</b> .....		<b>171</b>
6.1	TRADITIONAL STRESS LOCKING .....	172
6.2	STRESS LOCKING DUE TO LOCAL CRACK MISALIGNMENT .....	175
6.2.1	<i>1D Bar Problem</i> .....	183
6.2.2	<i>Three Point Notched Beam Bending Problem</i> .....	186
6.3	STRESS LOCKING DUE TO POOR KINEMATIC REPRESENTATION OF CRACK DISCONTINUITY ....	197
6.4	STRESS LOCKING DUE TO FINITE ELEMENT DISPLACEMENT COMPATIBILITY .....	207
6.5	SUMMARY AND CHOICE OF MODEL AND PARAMETERS .....	208
<b>CHAPTER 7 INFLUENCE OF EDGE EFFECTS</b> .....		<b>209</b>
7.1	EXPANSION ANCHOR FAILURE MODES .....	209
7.2	MIDDLE/EDGE/CORNER MODELS REVISITED .....	211
7.3	DETAILED EDGE EFFECT STUDY .....	219
7.4	INVESTIGATION INTO MESH SENSITIVITY .....	228

7.5	SUMMARY .....	232
<b>CHAPTER 8</b>	<b>MODELLING OF ANCHOR EXPANSION EFFECTS .....</b>	<b>233</b>
8.1	MATERIAL BEHAVIOUR ASSOCIATED WITH ANCHOR EXPANSION .....	233
8.2	STRUCTURAL INTERFACE ELEMENTS.....	236
8.3	SENSITIVITY STUDIES ON COULOMB FRICTION INTERFACE .....	240
8.4	2D MODELLING OF ANCHOR BOLT WITH FRICTIONAL INTERFACE .....	246
8.5	3D MODELLING OF ANCHOR BOLT WITH FRICTIONAL INTERFACE.....	256
8.6	3D OCTAGONAL ANCHOR BOLT GEOMETRY .....	273
8.7	KINEMATIC MODEL FOR ANCHOR EXPANSION.....	285
8.8	CONTACT MODELLING OF ANCHOR MECHANISM.....	290
8.9	EDGE EFFECT STUDY WITH EXPANDING ANCHOR MODEL .....	303
8.10	SUMMARY .....	306
<b>CHAPTER 9</b>	<b>SEQUENTIALLY LINEAR ORTHOTROPIC FRACTURE MODEL.....</b>	<b>308</b>
9.1	BACKGROUND .....	310
9.2	IMPLEMENTATION OF SEQUENTIALLY LINEAR MODEL .....	314
9.2.1	<i>Initialise &amp; Read Input Data.....</i>	<i>315</i>
9.2.2	<i>Perform Linear-Elastic Analysis.....</i>	<i>316</i>
9.2.3	<i>Identify Critical Element.....</i>	<i>317</i>
9.2.4	<i>Calculate Global Load and Displacement.....</i>	<i>319</i>
9.2.5	<i>Update DIANA Input Data.....</i>	<i>319</i>
9.3	2D ANCHOR MODELLING – COARSE MESH .....	321
9.4	2D ANCHOR MODELLING – FINE MESH .....	328
9.5	3D ANCHOR MODELLING .....	333
9.6	3D ANCHOR MODELLING – REGULAR MESH.....	346
9.7	EDGE EFFECT STUDY.....	349
9.8	SUMMARY AND CONCLUSIONS .....	360
<b>CHAPTER 10</b>	<b>SUMMARY AND RECOMMENDATION FOR FUTURE WORK .....</b>	<b>362</b>
10.1	SUMMARY .....	362
10.2	RECOMMENDATIONS FOR FUTURE WORK.....	367
<b>APPENDIX A</b>	<b>SOURCE CODE FOR SEQUENTIALLY LINEAR WRAPPER PROGRAM..</b>	<b>370</b>
<b>APPENDIX B</b>	<b>SEQUENTIALLY LINEAR ANALYSIS DIAGRAMS.....</b>	<b>380</b>
<b>APPENDIX C</b>	<b>REFERENCES AND BIBLIOGRAPHY .....</b>	<b>400</b>

# CHAPTER 1

## Introduction

Fastener technology dates back to the 1<sup>st</sup> century B.C. In his ten books on architecture and building design, “De Architectura”, Vitruvius described techniques for the use of grouted or cast in place anchorage systems. It is believed that such technologies played an important role in the construction of the Colosseum in Rome as evidenced by the ruins (Figure 1-1).

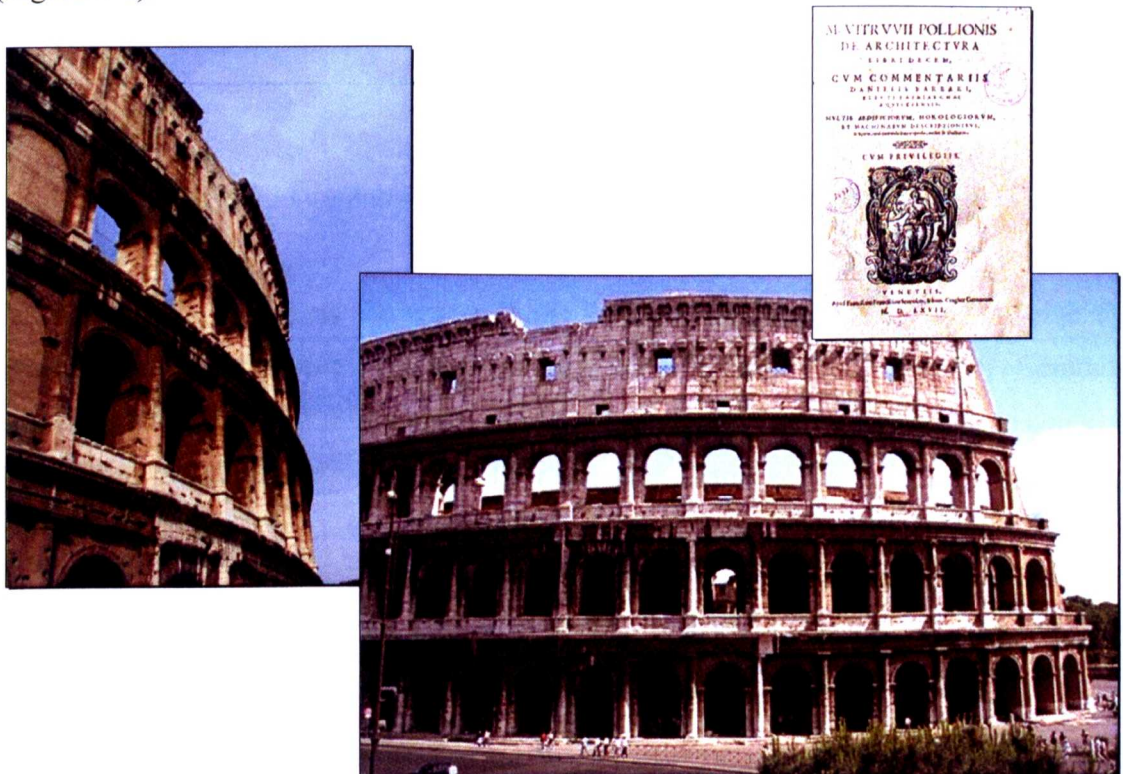
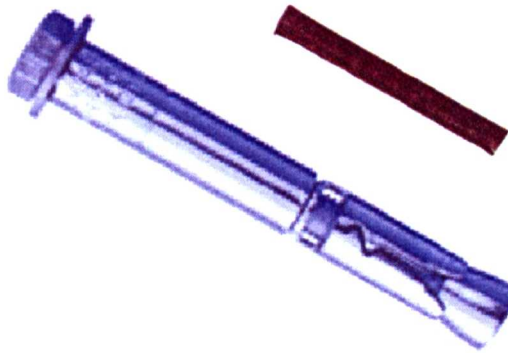


Figure 1-1 - Colosseum in Rome. Built around 50 A.D.

Evolution of fastener technology was slow as designers preferred to stick to tried and tested methods and development was a trial and error process. However, increased demands for flexibility and safety at the start of the 20<sup>th</sup> century lead to the development of new, more advanced products [Fuchs, 2001]. In the 1920s John Rawlings developed the first expansion anchors (Figure 1-2). These consisted of a small brass tube with four

threaded strips at the end. A screw was placed in the tube and the action of turning it caused the strips to expand [Rawlplug (2005)]. Although popular for small-scale applications it wasn't until the advent of the compact, electric hammer drill in the 1960s that post-installed anchors gained public favour for structural applications. Since then there has been rapid development of anchor bolts and fasteners as a whole.



**Figure 1-2 - First Expanding Anchor and Modern Expansion Anchor Bolt**

The range of applications for anchor bolts is huge. In general they are suitable for situations where items need to be fixed to concrete structures, rock or masonry. Common uses include the fixing of utility conduits to walls, fixing of column baseplates to concrete foundations, façade retention schemes, fixing of safety barriers, etc.



## 1.1 Anchor Types

Anchor technology is predominantly driven by the desire to combine steel and concrete structures. The structural designer may consider such factors as reliability, safety, aesthetics and satisfaction of the design provisions when designing an anchorage system. Because of these different demands a number of different anchor types have been developed. These divide into two main categories; cast in place and post-installed.

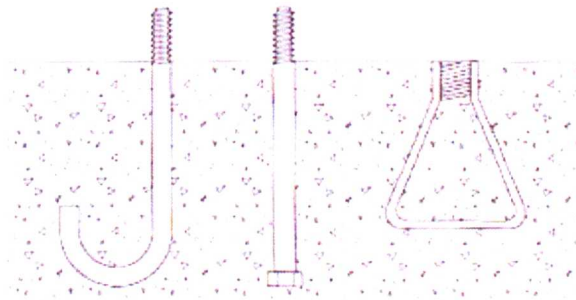


**Figure 1-3 - Examples of Cast In Place Anchors**

As the name suggests, cast in place anchors are positioned before the concrete is poured. These may simply be headed studs or perhaps a formed metal bar, usually with a thread on the exposed end to allow a nut to be attached (Figure 1-3). When the concrete sets, pullout of the anchor is resisted via mechanical interlock. This is the simplest form of anchor but the least flexible as its position needs to be known in advance of construction. For applications such as the fixing of pipework to walls it is usually necessary to have some leeway to allow for unforeseen, on-site factors.

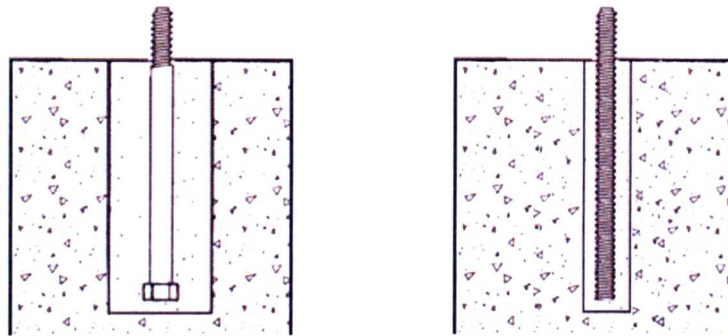


**Figure 1-4 – a) Grouted and b) Resin Bonded Anchors**

Post-installed anchors provide this freedom and are usually located in drilled holes. Of these there are three main types; bonded anchors, expansion anchors and undercut anchors. Bonded anchors are usually threaded rods that are fixed to the surrounding concrete either with a resin adhesive or a cementitious grout (Figure 1-4). The resin is usually contained in a glass capsule that is placed in the drilled hole first, then the rod is driven into it with a hammer. For grouted anchors the rod is positioned first and the hole in-filled with grout. Load transfer between anchor and concrete is therefore via the bond material.

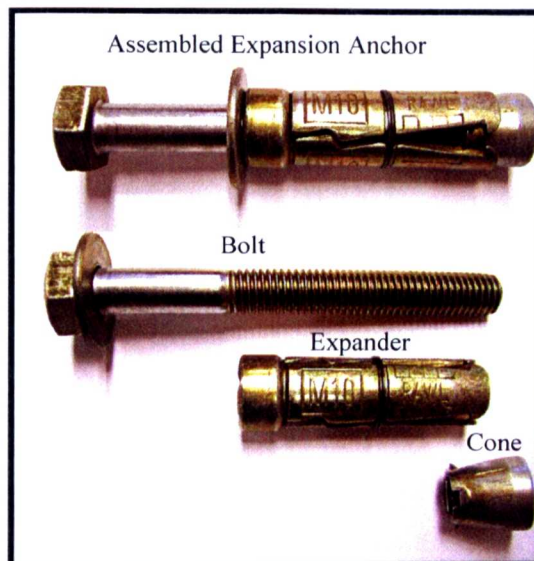


**Figure 1-5 - Components of an Expansion Anchor**

Expansion anchors are rather more sophisticated in their design (Figure 1-5). At the centre of the anchor is a standard bolt over which the expander is placed. The expander typically consists of a number of leaves that are able to rotate about their top end. A threaded cone is then screwed onto the end of the bolt.

For installation, the drilled hole is the same diameter as the anchor itself (Figure 1-6). This requires the anchor to be driven into the hole by lightly tapping it with a mallet. The bolt head is then turned until a specified torque is achieved. This causes the cone to be drawn upwards and cause an expansion of the leaves. It also ensures that the anchor exerts a high enough normal force on the concrete such that the frictional resistance to tensile forces acting to pull the anchor out of the concrete is sufficiently high to prevent slipping of the anchor. Application of tensile forces on the anchor also causes further expansion and thus higher resistance to pullout.

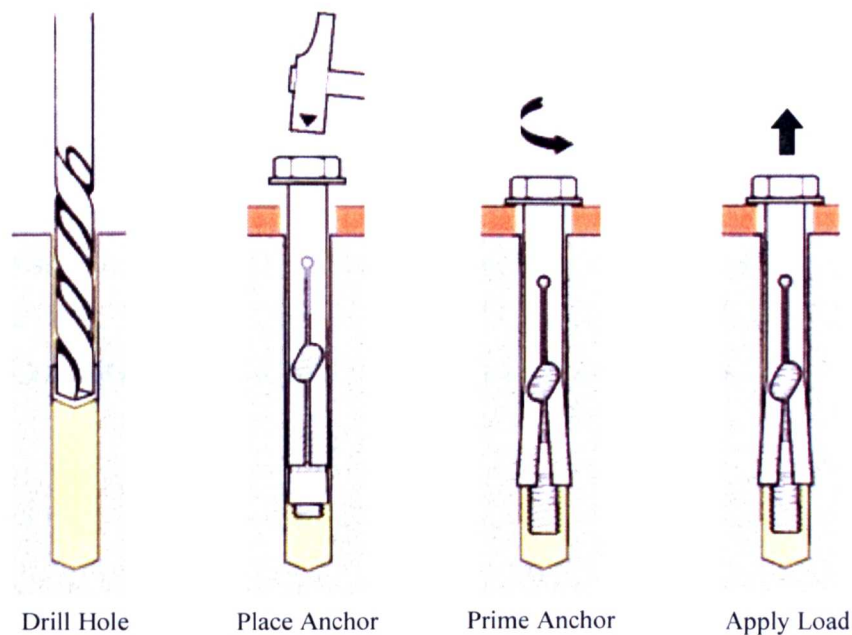


**Figure 1-6 - Installation of Expansion Anchor**

Expansion of the anchor may also lead to some localised crushing around the tips of the leaves. Thus a degree of mechanical interlock is present when resisting pullout. This

effect is called keying and is very much secondary to friction as the means by which expansion anchors resist tensile loading.

Undercut anchors exploit the benefits of keying more fully (Figure 1-7). The undercut into which the anchor expands is either created by a special drill bit or by the anchor itself [Cook, et al (1992)]. In all other respects the undercut anchor is the same as a standard expansion anchor.

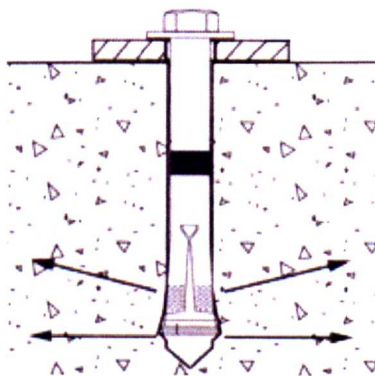


**Figure 1-7 - Undercut Anchor Bolt**

The focus of this work is on the modelling of expansion anchors since their complex nature presents an interesting challenge and because current expansion anchor research is lacking in detail. However, many of the modelling aspects considered in the course of this investigation are applicable to other types of anchors and fasteners.



## 1.2 Failure Mechanisms

Expansion anchors may fail in shear, tension or a combination of both. This work concentrates on tensile failure only as this provided sufficient scope for the purposes of this research. However it is noted that much of the work presented here is applicable to other failure types. For expansion anchors subjected to tensile, pull-out loading a number of different failure modes are possible. Which of these becomes dominant in a particular situation depends on a number of different factors [Rawlplug (1999b)].

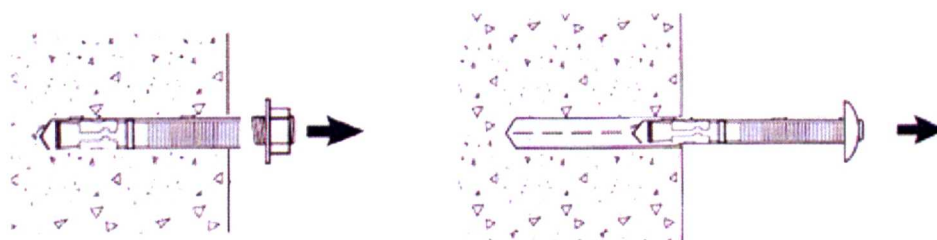


**Figure 1-8 – a) Anchor Body Failure, b) Pullout Failure**

In cases where the applied load exceeds the tensile capacity of the steel of the anchor a body failure will occur (Figure 1-8a). This situation occurs when an expanding anchor is placed at a large embedment depth. The frictional load transfer mechanism between expander and concrete remains effective up until failure and the large depth provides a larger body of concrete over which these forces may be resisted. This will be a ductile failure as the failure is in the steel rather than in the concrete and as such is often desirable for safety critical installations.

A pullout failure occurs when the frictional load transfer mechanism is not sufficiently effective (Figure 1-8b). This type of failure is most commonly caused by incorrect installation of the anchor. For example, the hole may not have been cleaned properly before the anchor was inserted or the correct torque was not applied during the setting stage. Another possibility is that cracking of the concrete in the region of the anchor relieves some of the initial expansion force thus reducing the frictional resistance to the point where the frictional resistance is less than the applied load.

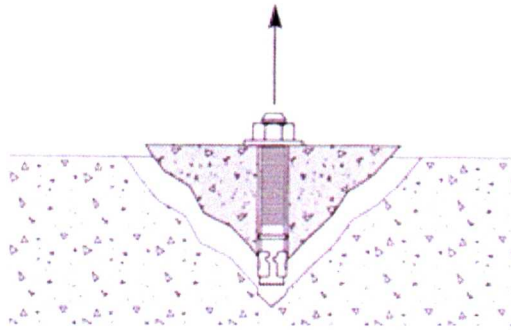


**Figure 1-9 - Concrete Cone Failure**

For shallower embedment depths the most common failure mode is via the pullout of a concrete cone (Figure 1-9). Tensile cracks initiate around the expander and radiate outwards and towards the free surface. The angle of these cracks is dependent on such factors as embedment depth, anchor type and support conditions. However a typical cone forms at an angle of between  $35^{\circ}$  and  $45^{\circ}$ . In the photographs below an actual concrete cone is shown (Figure 1-10). Also of note is the presence of vertical radial cracks that extend from the anchor position outwards through the cone.

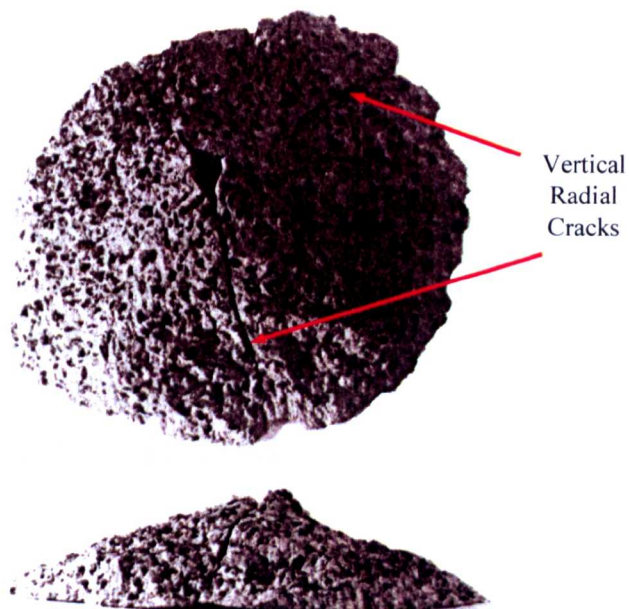


**Figure 1-10 - Concrete Cone Resulting From Failure of Expansion Anchor Subject to Tensile Pullout (Plan and Elevation) [Ohlsson, Elfgrén (1993)]**

The above failure modes are common for anchors that are distant from the free edge of the concrete block in which they are installed. However, when the anchor is situated at a distance less than 1.5 times the embedment depth from the free edge, so-called ‘edge effects’ become important and a variety of other failure modes are possible (Figure 1-11).

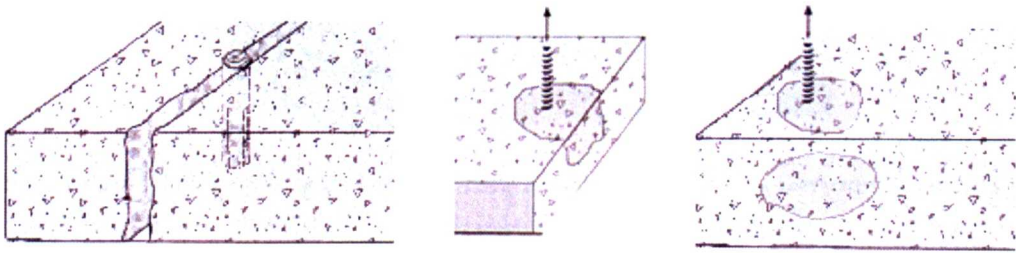


**Figure 1-11 - a) Splitting Failure, b) Edge Failure, c) Breakout Failure**

Splitting failures are produced as a result of radial expansion forces. Narrow concrete blocks and those of small thickness are particularly susceptible. For blocks of larger dimension a low edge distance can result in the concrete cone being truncated by the free edge and therefore result in a lower anchor capacity. At very low edge distances breakout failures can occur. These happen because there is not enough material between the expander and the free face to provide sufficient confinement to resist expansion.

Edge effects can still cause a reduction in anchor capacity even when the failure mode is via concrete cone. The figure below (Figure 1-12) shows an anchor with an embedment depth of 120mm in the centre of a concrete block of plan dimensions 600x600mm and a depth of 300mm. The zone of high tensile stress extends well away from the anchor itself. This zone is often called a ‘stress bulb’ because of its initial bulbous shape. Obviously any reduction in size of this stress bulb caused by the proximity of a free edge will result in a reduction of anchor capacity. Indeed a similar reduction in strength occurs when two or more anchors are close enough for their stress bulbs to touch. This is the so-called ‘group-effect’.

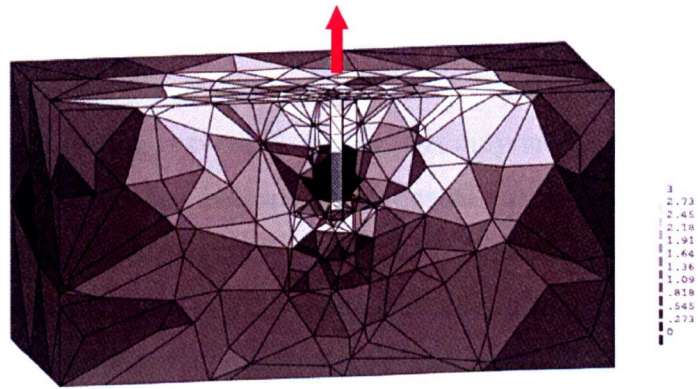


**Figure 1-12 – Maximum Principal Stress Cross-Sectional Contour Plot Showing Stress Bulb. Large Volume of Base Material Resisting Pullout Load**



### **1.3 Current Design Practices**

The design of new anchor products is based on numerical modelling backed up with a very extensive program of experimental testing [Fuchs (2001)]. The reason for this large amount of experimental testing is twofold. Firstly it is only more recently that numerical modelling of concrete fracture has become sophisticated enough to tackle such complex problems with an acceptable degree of accuracy. Therefore experimental testing represents the historical, tried and tested method and is used to validate the results of the numerical analyses. Secondly, for a product to gain acceptance on the market it must gain the relevant technical approvals. In Europe, the European Organisation for Technical Approvals (EOTA) sets out the requirements for approval for “Metal Anchors for Use In Concrete” [EOTA (1997)]. To obtain this approval a product must pass a series of stringent tests. This includes testing under a variety of tensile, shear and combined loadings, testing at various edge distances and testing in concrete of various strengths. It is therefore important from a cost perspective to have confidence that a new product will meet these requirements before submitting it for approval. Currently this aim is best achieved by extensively testing the product in-house first. Such a process is still expensive and it would be advantageous to reduce the amount of testing required by instead using reliable numerical modelling. This would also allow for more rapid product development, allow a greater number of factors and loading conditions to be examined and give a clearer insight into the behaviour and failure mechanisms of the new product.

In industry the design of anchorage systems currently relies on semi-empirical methods [Eligehausen (2001)]. Although these are generally safe they can be overly conservative. However, in rare cases they can give non-conservative results. Work continues on developing better design methods that cater for an increased number of anchor types and include provision for a greater range of design situations. However a suitably accurate and robust numerical model for anchorage systems would provide a more flexible tool for design. This would be especially true of complex systems involving numerous anchors in close proximity and/or low edge distances.

#### **1.4 Project Aims and Objectives**

The focus of the work carried out for this thesis was the behaviour of expansion anchor bolts in concrete when subjected to tensile pullout loading. Of particular interest was the influence of low edge distances on such devices. The primary aim of this work was to develop modelling techniques capable of accurately and robustly analysing anchor bolts under these conditions.

The objectives of the work were:

- To investigate and evaluate a number of FE frameworks and constitutive models for the analysis of expansion anchors in concrete. These models were required to simulate accurately and robustly the fracturing of concrete under constantly evolving non-linear stress conditions.
- To model the effects of low edge distance on anchors under tensile loading. This includes the reduction of anchor strength and the change in failure mode. The results of this modelling were verified by comparing against design data provided by anchor bolt manufacturers.
- To model the effects of anchor expansion on the failure mode and pull-out load-displacement response of an expansion anchor. This required the development and evaluation of a number of different modelling approaches to capture both the effects of the kinematics of expansion and the interfacial effects between anchor and concrete.

## **CHAPTER 2**

### **Review of Anchor Research**

Numerical modelling of anchor bolts plays an increasingly important part in anchor research. The key feature of this modelling is that it provides a unique insight into the behaviour of anchors from installation, through loading to ultimate failure. At its most detailed level it is used as a tool by anchor designers in developing new products. There is also scope for its use by structural designers. Compared with current design methods, numerical modelling provides a much more flexible and informative solution.

Numerical modelling of anchor bolts sits at a crossroad of two different fields of research. The first of these is research and development of anchorage technologies. Experimental work forms the largest part of this. It serves to determine the behaviour of existing and emerging anchorage systems. Under laboratory conditions, sensitivity studies into a wide range of parameters associated with both the installation of anchor itself and the material in which it is fixed are performed. Anchor bolt manufacturers use such studies in the development of new anchor products [Eligehausen, Hofacker, Lettow (2001)]. However, this work remains unpublished due to its commercially sensitive nature. Experimental testing is often carried out by independent research bodies as well with a view to developing an understanding of different anchor types without being concerned with the specifics of a given manufacturer's product. The aim of this is to produce data suitable for the development of design methods and standards.

The second area of research associated with numerical modelling of anchors is the development and testing of constitutive models of concrete. Loading of anchors sets up a complex, triaxial stress state whilst the failure process requires the accurate simulation of the fracturing of concrete. Presently headed-stud anchors have received the most attention as their load transfer mechanism is via mechanical interlock. It is usually assumed that failure of the anchor body is unlikely hence only a suitable material model for concrete is

required. However, more research on complex anchor types is required where anchor-concrete interfaces and internal anchor mechanics need to be considered.

## **2.1 Anchor Design Process**

Historically advancements in anchoring systems were made through a trial and error approach. Designers generally preferred to be conservative, rely on techniques that had worked in the past and pushed the boundaries of anchor knowledge infrequently. Indeed, some of these techniques using grouted or cast in place anchorage systems date back to the 1<sup>st</sup> century A.D. and are described by Vitruvius in his books on building design, “De Architectura”. As such, progress remained slow until the 20<sup>th</sup> century brought new demands for higher performance, greater flexibility and increased reliability, especially in safety critical applications. These are the driving forces behind current research into anchorage systems.

Although anchors have been in existence for almost two-thousand years only over the past three decades have significant advances been made both in the understanding of anchor systems and in the development of associated design codes [Fuchs, 2001]. As such the bodies responsible for these codes have been playing a game of ‘catch up’ with developments from anchor manufacturers (Figure 2-1).

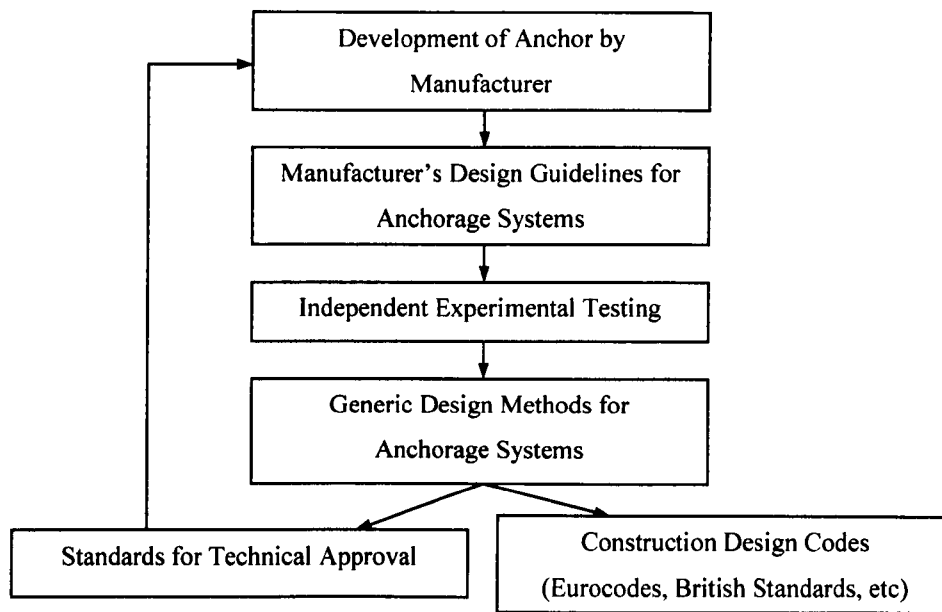


**Figure 2-1 - Development Process for Anchor Design Codes and Technical Approvals**

Traditionally anchor manufacturers have provided design guidelines and data for their products based on their own experimental testing. This resulted in a bewildering array of differing design approaches [Klingner, 2001]. As well as complicating the design process it was difficult to compare products and assess their relative merits for a given application. This situation remained until around 1970. Therefore there was a clear demand for independent experimental testing to allow the development of generic anchor design methods and also structural design codes.

In 1972 an expert committee was set up in Germany to research and hence gain an understanding of the behaviour of channel bar and dowels. Investigations lead to testing guidelines and also showed that the load-bearing capacity of the fasteners followed a normal Gaussian distribution. This second result allowed the use of statistical evaluation techniques to assess anchor reliability and hence a reduction in the necessary factor of safety. Previously manufacturers had suggested a factor of safety for mean ultimate load in the range of 4 to 5. This could now be reduced to 3 for concrete failure and 1.75 for steel failure [Fuchs, 2001].

The first technical approvals for post-installed bonded and expansion anchors appeared in 1975. These initially covered only single anchors at large edge-distances in uncracked concrete but were extended in 1978 to include double anchors and then again in 1979 for the assessment of single anchors in cracked concrete. The inclusion of cracked concrete is important for situations where anchors are fitted to existing structures. If the anchor is placed in a zone of concrete that is in tension, minor cracking may be present.

In the USA during the same period there was a drive to produce a design method for use with headed studs. The resulting method was adopted by the American Concrete Institute in its “Code Requirements for Nuclear Safety Related Concrete Structures” (ACI 349-76). This method assumes that under tensile loading the capacity of the concrete around an anchor is calculated considering a constant tensile stress distributed equally on the surface of an ideal truncated cone. This cone is representative of the concrete cone failure surface and has sides inclined at an angle of  $45^\circ$  (Figure 2-2). A similar approach was taken when considering the shear capacity of an anchor [Fuchs, Eligehausen, Breen, (1995)].

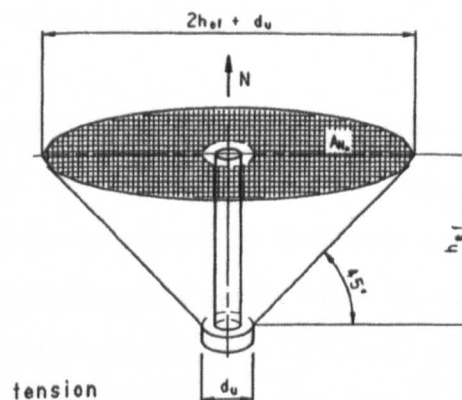


**Figure 2-2 - ACI349 Idealisation of Concrete Cone Failure [Fuchs, et al (1995)]**

In the early 1980s a similar design method was developed in Germany. Known as the  $\kappa$ -Method, its advantage over other design methods of the time was that it dealt with arrangements of multiple fasteners, with anchor spacings and with low edge distances. Its formulation took into account the mechanics of both interlock and expansion of the anchors. Key parameters were the embedment depth and diameter of the anchor as well as

the concrete strength. No product specific data was required. The  $\kappa$ -method was adopted into the German technical approvals firstly for the assessment of cast-in place studs and later post-installed anchors.

During this period the ACI design method was also expanded to cater for multiple anchors, anchor spacing and edge distance and to allow the assessment of post-installed anchors (ACI 349-85).

In other countries where appropriate technical approvals were not available designers still had to rely upon information provided by anchor manufacturers. Also, many manufacturers were of the opinion that the proposed theoretical design methods were insufficient in that they did not consider many variables which they deemed important (material strength, friction coefficients, etc). For this reason the manufacturer Hilti developed its own design method based on similar concepts to the  $\kappa$ -method but incorporating product specific data. Melcher and Karmazinova report their use of experimental testing and linear regression analysis to attain product specific strength factors for an expansion anchor [Melcher, Karmazinova (2001)].

The early 1990s saw greater co-operation between American and European researchers. Databases of test data from both groups were merged to create a much more comprehensive set of data. Advances were also made in giving the  $\kappa$ -method the same transparency and user-friendliness of the ACI method. The result was the CC-Method (sometimes known as the Concrete Capacity Design (CCD) method) [Fuchs, et al, 1995]. On first inspection the CC-method appears quite similar to the ACI349 approach (Figure 2-3). However, instead of using a cone for the approximation of the failure surface a pyramid is used. This greatly simplifies the calculation of the area of the failure surface especially in situations where anchor spacing or edge distance reduces the surface area for an individual anchor. The other immediate difference is in the angle of the failure surface. The CC-Method proposes an angle of approximately  $35^\circ$  in line with observations from experiments that the radius of the failure surface is one and a half times the embedment depth.

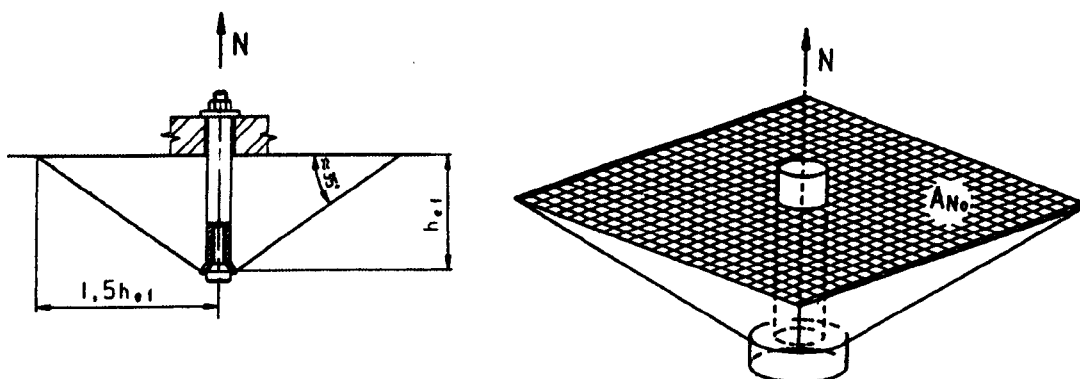


Figure 2-3 - CC-Method Idealisation of Concrete Cone Failure [Fuchs, et al (1995)]

Supporters of the ACI349 method argue that this angle is not valid for deeper embedment depths as the effects of increased confinement on the anchor at such depths increases the angle of the failure cone [Cannon, 1995a]. Also related is the issue of size effect. This states that as member size increases the rate of increase of the associated failure load will be less than the rate of increase of the failure surface (i.e. nominal stress at failure ('peak load' / 'failure area') decreases) [Bazant (1984)]. European researchers have shown this phenomenon to be present in anchors [Ozbolt, Eligehausen, Reinhardt (1999), Eligehausen, Ozbolt (1990)] and it is accounted for in the CC-Method. However there is reportedly nothing in the US test data for headed studs or undercut anchors that show size effect [Cannon, 1995a]. Therefore its influence is omitted from the ACI349 method. A later statistical analysis of the two methods using an existing public domain database of test results was carried out for the US Nuclear Regulation Commission [Shirvani, Klingner, Graves, 2001]. This showed that, for a wide variety of conditions, the CC-Method had a lower probability of failure than the ACI349 method. That is to say that the CC-Method produced fewer unconservative results. This advantage was more apparent for higher embedment depths.

It would seem that at least some of the differences between the US and European approaches to design come from the differing use of anchor bolts. In America there is a lot of use of anchors within nuclear power facilities. Applications include the fixing of



pipework and equipment supports [Czarnecki, Manrique, Sammaddar (1993)]. In these cases it is deemed important that structural failure be ductile in nature. Therefore the recommendation is for anchors to be placed at greater embedment depths in order to ensure steel failure of the anchor. In Europe there is a greater emphasis on lower embedment depths and hence concrete failure is the most likely failure mechanism. These differing aims result in slightly different approaches to testing of anchors therefore differences in the results are to be expected.

Despite the continued discussion of the pros and cons of the CC-Method, it has received wide acceptance internationally and has been adopted in several design guides in Europe (DIBt (1993), EOTA (1997), CUR (2000) and SIA (1998)), in the USA (IBC (2000) and ACI 318 (2001)) and is has provoked interest in China [Stark, Hordijk (2001)].

More recent work has been on expanding both the CC-Method and the ACI349 Method (present revision, at the time of writing this thesis, is dated 2001) to incorporate more anchor types. In particular, bonded anchors were not well represented by these models due to their complex failure modes [Obata, Inoue, Goto (1997)]. The usual failure is via a mixed bond-cone failure (Figure 2-4).

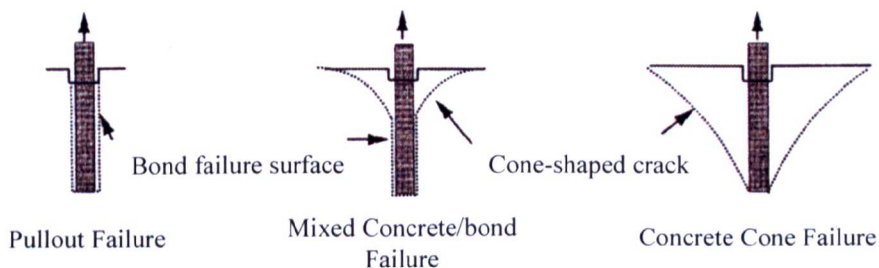


**Figure 2-4 - Common Modes of Failure for Bonded Anchors [Obata, et al (1998)]**

Another area receiving increased attention is the behaviour of expansion anchors in cracked concrete [Czarnecki, et al (1993)]. This is especially of interest if cyclic loading is present either due to vibrations from machinery or from seismic events [Kim, Yu, Yoon (2003)]. Both the expansion action of the anchor and the drilled hole in which it is

installed act as crack initiators so it is likely that, if an anchor is installed in the tension region of a member, it will be located in a crack. Experimental research shows up to a 25% decrease in tensile strength of an anchor due to cracking and a 10% decrease in shear strength. These reductions are lower than those suggested by ACI349-01. Results of fatigue tests due to cyclic loading actually revealed an increase in strength because of a build up of anchoring force caused by the expansion mechanism. This occurred when the expansion forces resulting from the application of tensile load remained in part even upon the release of the tensile load. Moreover, subsequent cycles lead to further expansion and hence an increased anchoring force.

The first Eurocode for anchors called “Design of Fastenings for Use in Concrete” is due to be published in January of 2006. This covers a wide range of cast-in-place and post-installed anchors and includes the issue of cracking. It is certain that experimental research will continue to improve existing design codes and to cater for new applications and products. For instance, although the capacity of cast-in-place has proven to be predictable by calculation, post installed anchors must be tested to derive product specific data due to their more complex nature.

Predictability is a quality sought after by engineers and it is in the deeper understanding of a problem that the governing influences can be identified and quantified. Experimental research is certainly vital in this goal however the use of numerical modelling can provide a more detailed insight into the failure process. In 1989 the technical committee of RILEM (Réunion Internationale des Laboratoires d’Essais et de Recherches sur le Matériaux et les Constructions) proposed a round robin analysis of an anchor bolt problem [Elfgren (1998)] (Figure 2-5). Researchers were invited to submit both experimental and numerical modelling results. The object of the study was to compare the results to give an indication of the possible applications and suitability of fracture mechanics models in the analysis and design of concrete structures. The final report for the study included results from 27 groups of researchers with more than 300 results.



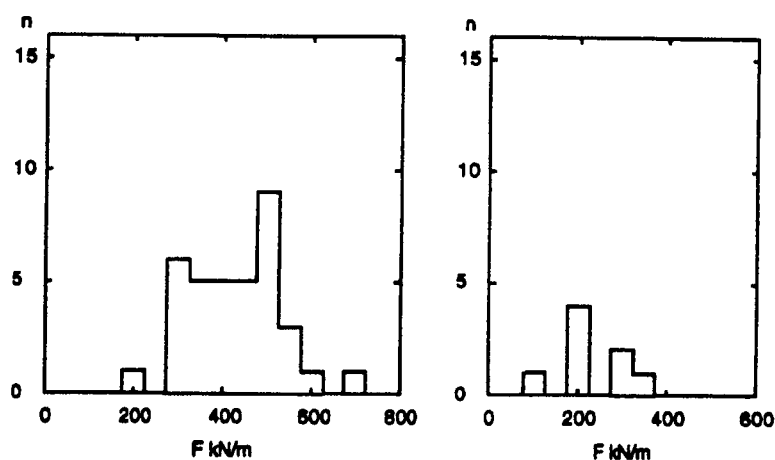


**Figure 2-6 - Distribution of RILEM Results for Peak Load Attained via Numerical Analysis for a) Plane Stress Case, and b) Axisymmetric Case. ( $d=150\text{mm}$ ,  $a=2d$ )**

However these results must be viewed in context. For the same problem experimental testing produced a variation percentage of 20% for the plane stress model and a value of 13% for the axisymmetric one (Figure 2-7). In both computational and experimental testing it must be noted that the sample group is much smaller for the axisymmetric problem than for the plane stress one, thirty-five results versus eight for the numerical analyses and twenty-six versus five for the experimental tests.

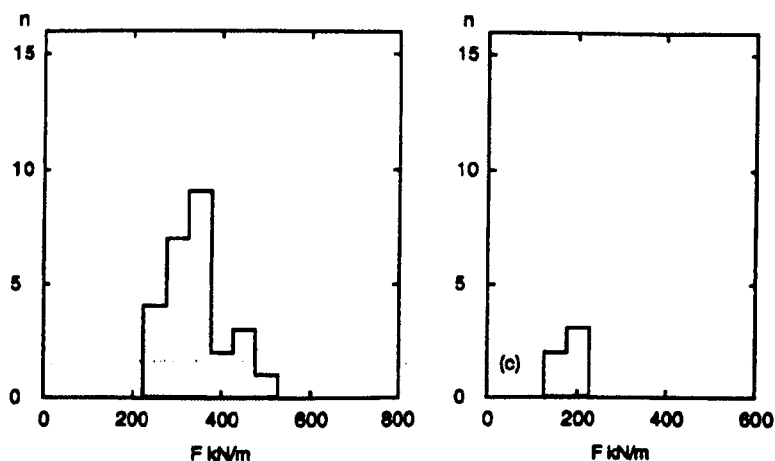


**Figure 2-7 - Distribution of RILEM Results for Peak Load Attained via Experimental Testing for a) Plane Stress Case, and b) Axisymmetric Case. ( $d=150\text{mm}$ ,  $a=2d$ )**

In relation to the experimental testing the scatter in the results was mainly attributed to differences in the boundary conditions both at the supports and at the outer surface of the specimens. This was due to the differing testing set-ups at the various labs and highlights the reason for the strict specification of test apparatus and procedure as defined in the guidelines for technical approval [EOTA, (1997)]. For the numerical analyses two main causes for the scatter were identified - mesh geometry and the constitutive model [di Tommaso and Manfronti (1993)]. Mesh geometry includes aspects such as element type, orientation of the mesh and level of mesh discretisation. However, more significant in this case is the choice of constitutive model as the description of the material characteristics has a very strong influence on the outcome of the analysis.

## 2.2 Computational Analysis of Concrete

Currently there is a wide range of constitutive models for concrete that have the potential for use in anchor bolt modelling. These models are classified in a number of different ways. For instance, concrete is generally studied at one of three scales – macro, meso or micro [van Mier (1995)] (Figure 2-8). The various characteristics concrete exhibits (cohesion, friction, aggregate interlock, formation and interaction of cracks, etc) come from the properties of its constituent elements. At the macro scale concrete is generally considered to be a homogeneous material and the individual material properties of the aggregate, mortar, etc are represented by an equivalent average set of properties. The constitutive model must also describe the behaviours mentioned above at this level. At the meso level three distinct phases are modelled explicitly; coarse aggregate, sand-cement matrix and the aggregate-matrix interface. Finally, at the micro scale the crystalline structure of the cement matrix, and other constituents, are considered.

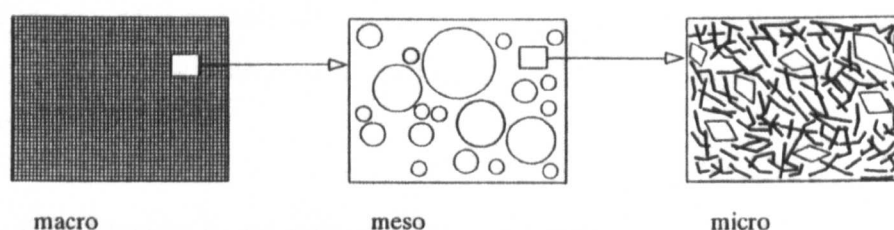


**Figure 2-8 – Definition of Modelling Scales for Concrete Analysis [van Meir (1995)]**

Micro scale modelling remains impractical for the analysis of real world structures due to the computational demands required. However, meso scale shows more promise in this respect. For example, Tran, Dorfmann and Rhie used an assemblage of discrete elements bonded together by springs to represent coarse aggregate and cement matrix [Tran, et al (1998)] (Figure 2-9). Wang, Navi and Huet also used a meso-scale model to tackle the RILEM benchmark and produced some realistic crack patterns [Wang, et al (1993)]. With this they were able to model simple tension, compression and shear benchmarks. However, more commonly meso scale models are used in the investigation of the micro-mechanical behaviour of concrete [Mark (1998), Wang, Navi, Huet (1993)].

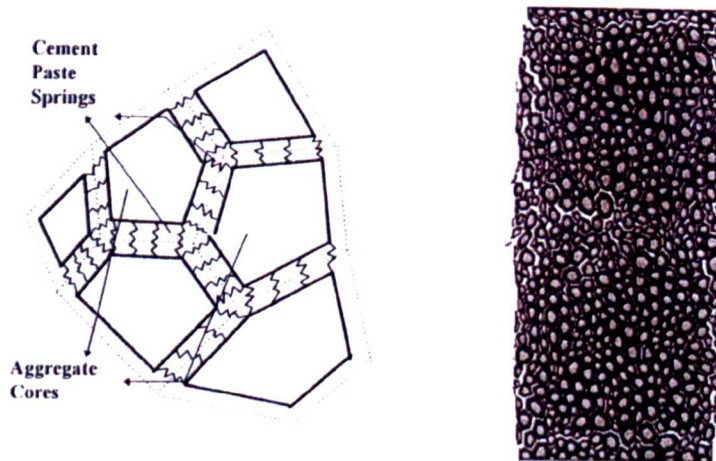


**Figure 2-9 - a) Discrete Element Representation of Cement-Aggregate Interaction, b) Crack Propagation in Direct Tension Benchmark [Tran, et al (1998)]**

Because macro level models are required to simulate micro-mechanical behaviour the formulation of their constitutive equations is complex and many different approaches have been developed.

Within a finite element framework cracking and damage is either modelled via discrete or continuum based methods. For discrete crack methods the crack opening is modelled by a separation between element edges [Hillerborg, Moder, Petersson (1976), Rots, Blaauwendraad (1989)]. Because of this either the crack follows the predefined element boundaries as set by the FE mesh or a remeshing approach is required to make available element boundaries dependent on the crack trajectory. The first restriction is not a significant issue when the crack pattern is known *a priori*. For example, in the case of debonding of reinforcement, three-point bending tests or other well understood cases. If the crack path is unknown before the analysis then remeshing can be used. It is a rather complex and computationally expensive procedure but it does have the advantage that results are not dependent on the original mesh. A more recent method produces a discrete crack by introducing a displacement discontinuity embedded in the displacement field for the finite element itself [Jirasek (1998), Alfaiate, Wells, Sluys, de Borst (2001)]. This means that arbitrary crack directions are possible without remeshing and the added



computational expense is significantly less than for remeshing procedures (Figure 2-10). Methods including an embedded displacement discontinuity are recent advancements and work is continuing on introducing three-dimensionality [Wells, Sluys (2001)] and multiple cracks per element.

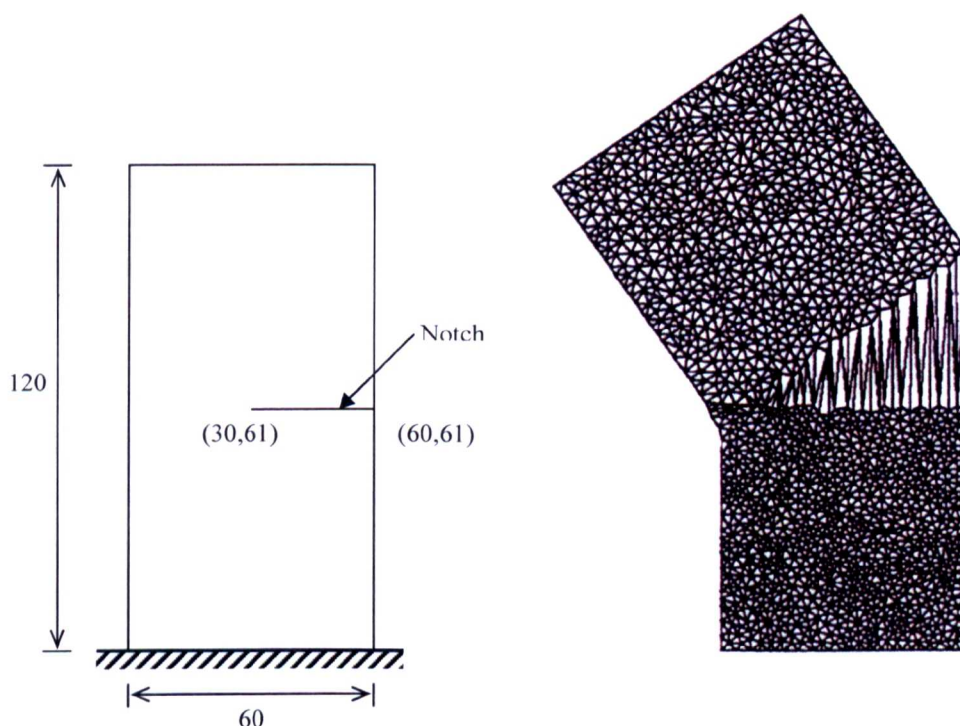


**Figure 2-10 – a) Biaxial Specimen With Initial Discontinuity, b) Deformed Mesh at an Average Top Boundary Displacement of 3mm When Distributed Tensile Load Is Applied To Specimen and Analysed Using Finite Elements with Embedded Discontinuities [Wells, Sluys and de Borst (2001)]**

The continuum crack approach spreads (or smears) the effects of the crack over some tributary area within the finite element. Typically the strain components for the element are decomposed into an inelastic part, representing the relative displacements caused by crack opening, and an elastic part representing the strain behaviour of the intact material (Figure 2-11). Alternative approaches are available whereby the constitutive equations are formulated in terms of total strain throughout without this decomposition. By handling cracking in this way the smeared approach fits into the existing continuum FE framework as it only requires the augmentation of the existing constitutive stress-strain relationship.



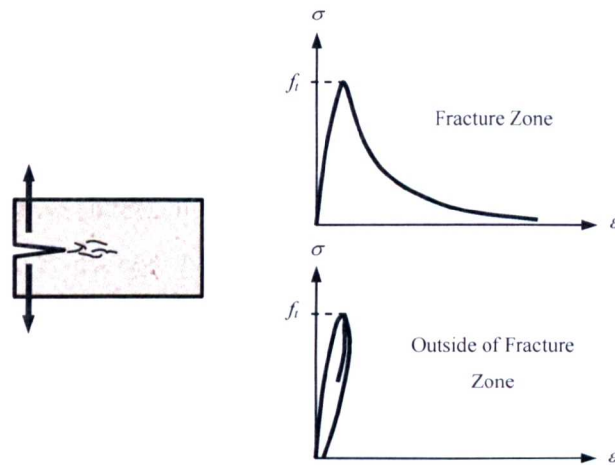


**Figure 2-11 – Stress-Strain Material Behaviour of Fracture and Intact Zones in Fracturing Concrete**

Computational Plasticity, Continuum Damage and Crack models all use this continuum representation of cracking and damage although the fundamentals of each approach are quite different. Within Plasticity modelling the material yield criterion is defined as a function and is commonly represented as a surface in three-dimensional principal stress space. The current stress state may be represented as a point in this space. This stress point may not move outside the bounds of the yield surface and changes in stress state which potentially violate this condition result in plastic straining, the rate and direction of which is defined by a so-called ‘flow rule’. Full details of the formulation of the Plasticity Model, as used in this research, are given in Chapter 3 and other texts [e.g. Chakrabarty (1987), Waszczyszyn (1989)]. However, the important aspects in terms of concrete modelling are the definition of the yield function and of the flow rule as they govern the criterion for crack initiation and the subsequent change in material behaviour due to cracking or crushing. One feature that is common amongst Plasticity Models is that the strain is decomposed into elastic and plastic (inelastic) components. The elastic component is recoverable upon unloading whereas the plastic component is not.

Initially Plasticity was used in the modelling of materials such as metals where the tensile and compressive response was the same. This allowed for the formulation of relatively simple yield functions (e.g. Von Mises). However, since the behaviour of concrete is very

different in tension and compression more complex functions are needed. Hsieh, Ting and Chen developed a four-parameter model that may be thought of as an amalgamation of some simpler models [Hsieh, Ting, Chen (1982)] (Figure 2-12). Indeed, with the appropriate values for these four parameters the Von-Mises, Drucker-Prager or Coulomb yield criterion may be obtained. The strength of this model is that when compared against experimental data, it accurately represents the tensile and compressive behaviours of concrete as well as its response to hydrostatic confinement and does so in a single function. A so-called ‘crushing coefficient’ is used to determine the failure mode (cracking, crushing or mixed). For post-cracking failure the four-parameter model performs linear, anisotropic softening. Post-crushing failure is modelled as perfectly plastic and mixed cases are modelled as a linear interpolation of the other two cases.

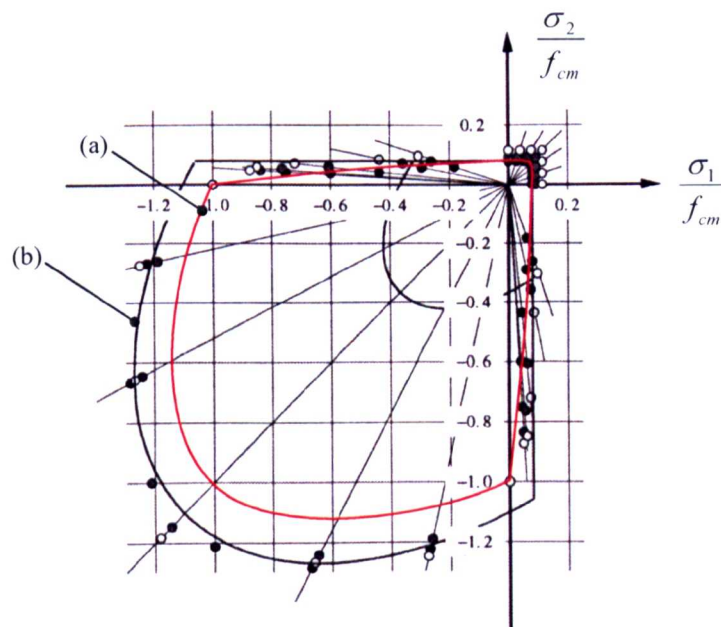


**Figure 2-12 - a) Hsieh-Ting-Chen 4 Parameter, and b) Feenstra-De Borst Composite Plasticity Models. Yield Surfaces Shown with Experimental Data of Kupfer and Gerstle (1974). Axes are (principal stress / failure stress).**

An alternative approach is multi-surface plasticity. This differs from the four-parameter model above in that instead of having a single function that defines the yield surface, multiple, individual functions are used to define it. Feenstra and de Borst used a Rankine

criterion to control the tensile behaviour of concrete and a Drucker-Prager criterion for the compressive stresses [Feenstra, de Borst (1995)]. The composite yield surface was found to fit experimental data for concrete loaded in biaxial loading conditions very well (Figure 2-12). Despite the use of two separate yield functions there are reportedly no convergence problems associated with the ‘corner’ regime where the two contours intersect. For this model, because of the two distinct yield conditions, mixed cracking and crushing failure is not considered. Instead an exponential softening behaviour is followed for the Rankine criterion and a parabolic stress-equivalent strain relationship for the Drucker-Prager criterion. It is unclear as to whether or not anisotropy is considered for one or either of these.

In comparison to Plasticity, Continuum Damage theory is generally much less complex. In its simplest, isotropic, scalar damage form the constitutive equation reads:

$$\boldsymbol{\sigma} = (1 - d)\mathbf{D}_0 : \boldsymbol{\varepsilon} \quad \text{Equation 2-1}$$

where  $\boldsymbol{\sigma}$  and  $\boldsymbol{\varepsilon}$  are the stress and strain tensors,  $\mathbf{D}_0$  is the undamaged stiffness tensor and  $d$  is the so-called ‘damage’ variable. This damage variable takes the value in the range of 0, for virgin material, and 1, for material that has failed completely. The criterion for damage is defined by the loading-unloading function. Its formulation is dependent on the chosen initial yield conditions and is history dependent via the damage evolution law. The isotropic formulation of Damage is sufficient in many cases but not so in analyses where compressive strut action is present. Anchor pullout is one example of this. However, it is also possible to produce an anisotropic formulation of Continuum Damage by degrading the material stiffness in a preferential direction. Further details on the Damage-based model approaches can be found in the following references: [Mazars, Pijaudier-Cabot (1989), Oliver, Cervera, Oller, Lubliner (1990), de Borst (2002)]. Unlike the Plasticity Model, unloading and reloading follows the secant path therefore inelastic strains are fully recoverable upon load removal. Many researchers report Continuum Damage models perform well in the simulation of concrete behaviour and cited in particular their computational efficiency with regards to modelling large problems [Mazars et al (1989),

Oliver et al (1990)]. Its simplicity has also allowed it to be combined with other fracture models. For example, composite Damage-Plasticity models have been developed to introduce unrecoverable inelastic strain [Simo, Ju (1987)]. Also a Rotating Crack Model with transition to Scalar Damage was developed to tackle the effects of spurious stress transfer [Jirasek, Zimmermann (1998)] (discussed further in Chapter 6).

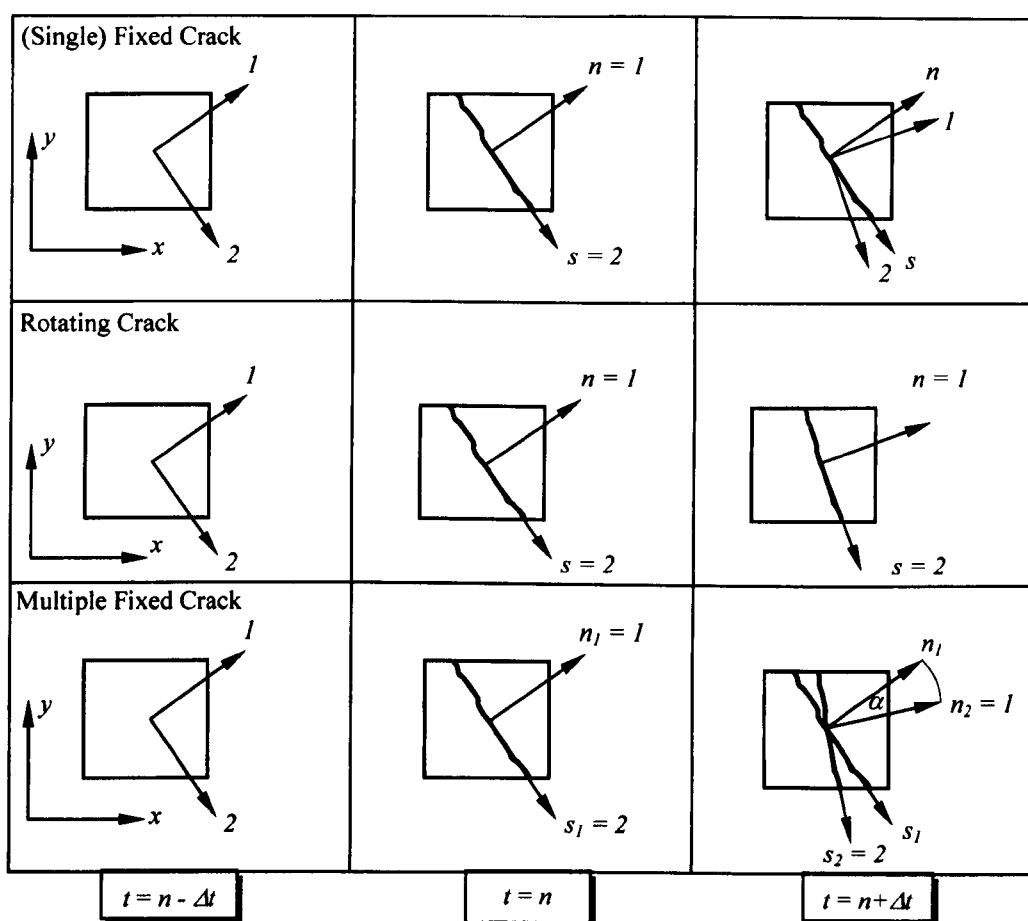


**Figure 2-13 - Crack Formation and Evolution Procedures for Crack Models**

Crack Models come in many different forms. The basic feature that they have in common is that the stress state and material degradation is assessed and performed on a finite number of planes. The number of planes considered and the manner in which their orientation is determined are the features that classify Crack Models (Figure 2-13). For (Single) Fixed Crack Models (FC) the principal stress is monitored. A so-called ‘crack

plane' is created co-planar with the principal plane if the principal stress exceeds the uniaxial tensile strength of the material (Rankine criterion). This crack plane remains fixed in this orientation for the remainder of the analysis and no additional planes may be formed. Rotating Crack Models (RC) follow the same approach with the exception that the crack plane continues to rotate with the principal plane after its formation. The Multiple Fixed Crack Model (MFC) also follows the same approach as the Fixed Crack Model but allows additional crack plane formation if the uniaxial strength is again exceeded and the principal plane is some predefined 'threshold angle' away from existing planes. In all cases tensile strain softening associated with crack opening is modelled by reducing the stiffness moduli for the crack plane(s). This is performed according to a predefined tension softening function.

The differences between these Crack Models are apparent when considering non-proportional loading (i.e. cases where the direction of the resultant load vector changes during the analysis). In the case of the FC Model the lack of alignment of the crack plane and the current principal plane can lead to principal stresses in excess of the material strength and also large shear stresses across the crack plane. Rots and Blaauwendraad also showed that non-proportional loading of an element can occur due to cracking, and hence stress redistribution, in surrounding elements [Rots, Blaauwendraad (1989)]. To some extent the shear stresses may be relaxed by means of the 'shear reduction factor'. This factor modifies the shear modulus to account for the reduction in shear stiffness due to crack formation. However, although specifying a large (or complete) reduction in shear stiffness does improve the response in such situations the presence of an overly large principal stress still results in an overly stiff response. It is also worth considering the physical meaning of zero shear retention. It implies that for elements subject to proportional (or near proportional) loading there is a complete loss of shear stiffness upon cracking. This does not fit with reality where friction and aggregate interlock play a significant part in stress transfer.

The strength of the RC Model is that continuously keeping the crack and principal planes coplanar prevents the problems mentioned above. However, this does also imply that no

shear stresses are generated across the crack plane and so an overly soft response can be produced in problems where shear effects are important (as shown by Li and Zimmermann [Li, Zimmermann (1993)]). Once again there is also the consideration of the physical meaning of a rotating crack. Certainly, in reality, cracks do not rotate. However, Ohmenhauser, Weihe and Kroplin note that the trajectory of microcracks are observed to curve therefore in the context of a finite element the crack rotation can be seen as following this trajectory change before the crack fully develops [Ohmenhauser, et al (1998)].

The MFC Model also seeks to avoid the spurious stress accumulation and overly stiff response of the FC Model by allowing additional cracks to form whilst still allowing for shear stress transfer across cracks. However, Weihe, Kroplin and de Borst noted that the computational results of a Multiple Fixed Crack analysis were strongly dependent on the choice of threshold angle [Weihe, Kroplin, de Borst (1998)]. This fact is shown by tests performed by Rots and Blaauwendraad in which a single element was subject to non-proportional loading such as to cause a smooth rotation of principal stress [Rots, Blaauwendraad (1989)]. Weihe, et al (1998) also note that there is no physical basis by which an appropriate threshold angle may be determined from material properties nor by calibration. Instead the analyst must choose an appropriate, possibly arbitrary, value. A similar observation can also be made of the shear retention factor, especially in the case of the MFC Model.

These Crack Models most often consider that total strain is decomposed, in a similar way to Plasticity Theory, into elastic and crack components. As such it is easy to conceptually consider the crack and the intact material to be separate entities. From a mathematical standpoint it is also easier to add further sources of strain from additional cracks or creep [Rots, et al (1985)]. In subsequent chapters these models are referred to as 'Traditional Crack Models'. An alternative model proposed by Feenstra et al is formulated in terms of total strain throughout [Feenstra, Rots, Arnesen, Teigen, Hoiseth (1998), Feenstra (1999)]. This model also differs from Traditional Crack Models by considering crushing

behaviour via a uniaxial compressive failure criterion derived from the Hsieh-Ting-Chen Plasticity Model mentioned above. Full details of this model are given in Chapter 5.

The Microplane Model can also be considered to be a Crack Model. Again material behaviour is described on a finite number of planes. Unlike the other Crack Models, the orientation and number of so-called ‘microplanes’ are specified *a priori*. It is assumed that the strains on each microplane are the resolved components of the macroscopic stress tensor (i.e. the stress tensor at the intersection of the microplanes) and, conversely, the macroscopic behaviour is derived by summing the contributions from each microplane. Physically these microplanes may be considered to represent weak planes in the microstructure of the material (e.g. cement-aggregate bond layer) [Ozbolt (2001)]. Rather like the MFC Model’s sensitivity to the value of the threshold angle, the accuracy of the Microplane Model is dependent on the number of microplanes [Weihe, et al (1998)]. This necessitates compromises between accuracy and efficiency, especially for three-dimensional problems [Ohmenhauser, et al (1998), Ozbolt (2001)].

There are other, less commonly used, models available for the simulation of concrete fracture and damage. For instance, Rots et al propose a finite element based model that models concrete fracture by means of series of linear-elastic analyses (Sequentially Linear Analysis) [Rots (2001), Rots, Invernizzi (2003)]. After each linear step the stress state of the model is assessed according to an appropriate failure criterion (e.g. Rankine) and the most critical element has its material properties updated so as to simulate softening. This model is explored in more detail in Chapter 9. It has a number of key advantages over current non-linear models. First of these is its numerical stability. Because it is based on a sequence of linear analyses there is no need for iterations and non-linear solution schemes. It follows that problems of divergence, lack of convergence and many sources of spurious behaviour are completely avoided. It has also been shown that for simple crack patterns the Sequentially Linear Model is computationally much less expensive than current non-linear models (see Chapter 9).



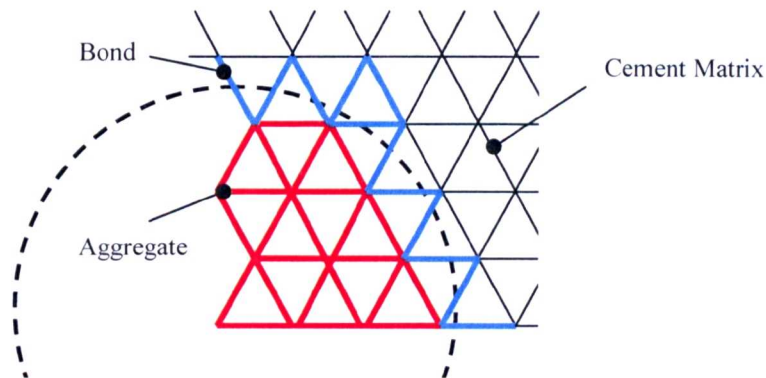


**Figure 2-14 - Assignment of Material Properties to Lattice According to Underlying Material Makeup**

Inspiration for the Sequentially Linear Model above was drawn from Lattice Modelling [Schlangen, Vervuurt, van Vliet, van Mier (1999)]. This also makes use of a series of linear analyses but, instead of using the continuum framework, a DEM (Discrete Element Method) approach is used and the structure is represented by a network of brittle breaking linear elements (Figure 2-14). These elements may be springs, bars or beams depending on the behaviour required and particular implementation. It must be noted that although the element behaviour is brittle, at a structural level a softening behaviour can be expected for structures that exhibit a progressive failure (especially if a finer discretisation is used) [Vervuurt, van Mier, Schlangen (1993)]. Lattice modelling is generally aimed at modelling concrete at a meso-level where the properties of the lattice elements are derived from the underlying structure of the concrete. However, this implies that for the modelling of realistic engineering structures a large number of elements are necessary. However, by concentrating the fine lattice around the cracking zone and having a coarse lattice elsewhere, problems such as anchor pullout have been analysed [van Mier, Lilliu (2001)]. More recently the computational power to make three-dimensional analyses possible has become available on desktop PCs.

There is no doubt that there are many more suitable modelling approaches that are applicable for concrete modelling, and anchor analysis in particular, however the models described above represent those most commonly used in this field.



## **2.3 Numerical Modelling Of Anchor Bolts**

The RILEM round robin invitation in 1989 appears to have been the catalyst to promote increased interest in anchor modelling. This perhaps coincided with a time when suitable constitutive models and necessary computing power became available to allow such analyses to be performed. In the following paragraphs some of the key aspects and findings from this round robin study are presented. The information was mainly sourced from the final RILEM report [Elfgren (1998)] and related papers.

### **2.3.1 RILEM Round Robin Problem**

Because of the strict specification of the problem geometry and boundary conditions there was practically no variation in the geometrical models created by the analysts of this problem. Almost all analysts chose to model a symmetric half of the problem for computational efficiency and to model the anchor-concrete contact on the upper surface of the anchor head as fully bonded whilst having no contacts elsewhere. However, the finite element discretisations of the problem did vary significantly. As already mentioned, di Tommaso and Manfronti stated that this variation was one of the key reasons for the scatter in results [di Tommaso, Manfronti (1993)]. However, it must be noted that their observations were largely based on results of their own analyses using an unspecified smeared crack model. Furthermore they then go on to state that choice of constitutive model also has a significant influence over the results. The point about mesh bias remains valid though. The results of Uchida, Rokugo and Koyanagi show a significant mesh bias for both fixed and rotating formulations of the Crack Model [Uchida, et al (1993)]. In particular it was shown that the crack pattern has a tendency to align itself with the element boundaries. In contrast, the Microplane Model in its non-local formulation exhibited no mesh bias [Ozbolt, Eligehausen (1993)]. The ‘non-local’ feature means that variables such as the stress state are assessed over a representative area rather than at a single point. The size of this area is controlled by the so-called ‘characteristic length parameter’,  $l_c$  and is not constrained by the finite element boundaries [Ozbolt (2001)]. This improved behaviour for the Non-Local Microplane Model is to be expected since the basic model is relatively mesh insensitive itself and the non-local formulation improves upon this.

Another observation made of the submissions is that in a great many cases the peak load is defined as the maximum load reached before the analysis terminated rather than the true peak before softening occurred. Determining the reason for the analyses not progressing further is impossible without more detailed information. For instance, Merabet, Fleury and Reynouard use a multi-surface Plasticity Model based on a modified Drucker-Prager criterion for compressive behaviour and a Rankine-type criterion for tension [Elfgren (1998)]. Although softening behaviour is seen in the load-displacement responses produced, the analysis appears to fail to converge prior to the peak load being found. Stork and Mazars used a combined Rankine-Von Mises Model and although they reached the peak the analyses produced a brittle unloading response rather than the expected softening. In contrast, Palm and Gylltoft were able to transition the peak and map the softening response using a Mohr-Coulomb Plasticity Model and a relatively coarse mesh.

The Discrete Crack analyses of Hassanzadeh and also Ohlsson and Elfgren produce excellent load-displacement responses but, due to the nature of the Discrete Crack Model, the crack direction is set *a priori* rather than evolving due to the changing stress state in the concrete. As such the influence of anchor depth or support span on the crack pattern cannot be determined.

The submissions using Crack Models generally showed good load-displacement responses. Analysts using Fixed Crack formulations either chose very small shear retention factors or modified the retention factor automatically during the analysis according to the magnitude of the crack strain. The Multiple Fixed Crack Model used by Leonard, Rots, de Borst and Feenstra performed well for plane-stress conditions and gave good load-displacement responses and realistic crack patterns [Elfgren (1998)]. However, for axisymmetric problems the analyses failed before a peak load was found. Both Rotating and Fixed Crack Models used by Cervenka, Pukl and Eligehausen and also by Uchida, et al, both performed well with the Rotating Model generally giving better post-peak softening behaviour [Elfgren (1998), Uchida, et al (1993)].

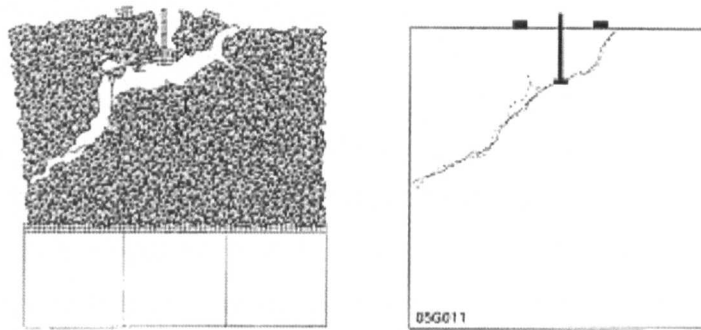


**Figure 2-15 - Displaced Shape and Crack Pattern Produced By Lattice Modelling of RILEM Problem**  
[Adri, et al (1998)]

Finally it is worth paying attention to the Lattice Model submission by Adri, Vervuurt, Schlangen and van Mier [Elfgren (1998)]. Because the failure of the lattice elements is via brittle breaking rather than a softening behaviour dependent on Fracture Energy (the energy required to open a crack), the results were very dependent on the element size. However the load-displacement diagrams showed a global softening behaviour. Also of note is that, instead of modelling just a symmetric half of the problem geometry, the full geometry was represented. The failure pattern that was produced for the plane-stress analyses was a non-symmetric crack (Figure 2-15). Only one other group of researchers who also modelled the whole specimen caught this lack of symmetry. The crack patterns closely match those produced by many of the experimental submissions. Since the geometry, boundary conditions and loading are all symmetric this asymmetry in the results must be due to some other factor. For experimental work this is most likely due to small variations in the strength of the concrete throughout its volume. For numerical work asymmetry in the mesh (or lattice) structure can produce a slight bias that will lead to an asymmetric failure.

Conclusions to be drawn from this round robin study are that the choice of both mesh discretisation and material model for concrete are very influential in the anchor simulation. The robustness of the material model is also important if the peak load is to be

determined. And modelling of the whole problem geometry must be considered when there is a possibility of a non-symmetric failure.

### **2.3.2 Wider World of Anchor Modelling**

Analysis of anchor bolts has progressed a great deal from the early 1990's. In particular the work of Ozbolt, Eligehausen, et al at the University of Stuttgart have examined and modelled a range of anchor types and situations. Initially studies were on headed studs as their load transfer mechanism is by simple mechanical interlock and no bond or frictional interfaces need be considered. The RILEM problem was used as the basis for a comprehensive set of sensitivity studies [Ozbolt, Eligehausen (1993), Ozbolt, Eligehausen, Reinhardt (1999)]. The problem was analysed using the non-local Microplane Model and discretised by 4-noded axisymmetric elements. Meshes were rather fine with increased density around the anchor head. The anchor itself was treated as a linear elastic material and was fully bonded to the concrete along the upper face of the head. Also the restraining effects of the stud are modelled by restraining the concrete in the radial direction in the vicinity of the head. Results from the analyses were good with realistic fracture patterns produced following the expected  $35^\circ$  angle concrete cone. Although the peak loads found matched those of experimental tests well the reported displacements were rather low. This was attributed to errors in modelling the compression softening in the zone of concrete above the anchor head. The sensitivity study showed the headed stud to be relatively insensitive to tensile and compressive failure stress ( $f_t$  and  $f_c$ ) and there was also a strong size effect reported. Obviously results such as these are important not only in the development and testing of numerical frameworks for the analysis of anchorage systems but also in the development of empirical design methods.

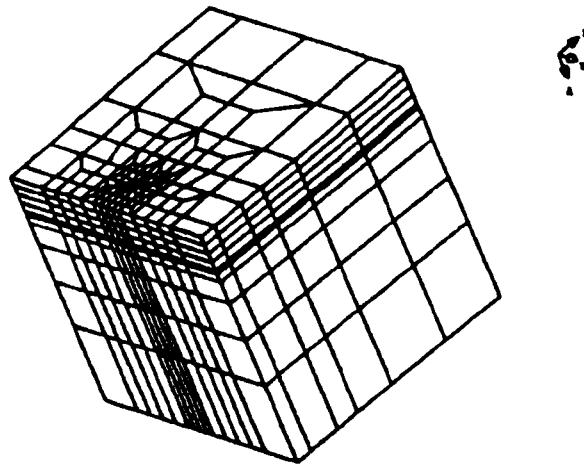


**Figure 2-16 - Finite Element Mesh for 3D Edge Effect Study [Ozbolt, Eligehausen (1993)]**

The influence of edge effects on the tensile capacity of headed studs was also studied [Ozbolt, Eligehausen (1993)]. For this a three-dimensional geometry was considered and discretised by 8-noded, 8-integration point elements (Figure 2-16). Edge distances with a edge-distance:embedment-depth ratio of 0.44 to 2.22 were examined. In these analyses the characteristic length parameter ( $l_c$ ) for the non-local continuum was adjusted so that, for large edge distances (no edge effect), the results fitted with those of an empirical formula. This parameter controls the volume over which the other non-local parameters are calculated. In particular it has an influence on the Fracture Energy ( $G_f$ ) and hence the peak strength and softening behaviour of the analysis. Because the characteristic length is not a material property, in cases where no empirical or test data exists the analyst has to rely on their experience and judgement to evaluate this important parameter. Reduction in peak strength due to lower edge distance followed a parabolic curve that approximately followed the trend defined by the empirical method.

By 2001 more demanding problems were being considered. Headed studs under tensile or shear loading were analysed with a edge-distance:embedment-depth ratio of 0.01875 [Hofmann, Eligehausen, Ozbolt (2001), Hofmann, Ozbolt, Eligehausen (2001)]. For these tests contact elements were included to better model the stud-concrete interface. With these elements compressive forces were allowed to be transferred but tensile forces were not permitted. The tensile analyses were compared with experimental test results and in

all cases failure was due to so-called 'break-out', where the face of the concrete block closest to the anchor head ruptures laterally. Hofmann, et al, found a good match between the failure loads of experimental and numerical tests however vertical displacements were underestimated in the numerical models. No indication was given as to why this may be the case. Shear analyses also produced realistic failure patterns and loads in the majority of cases.

Some more 'real-life' problems have also been considered such as the case of a column base, fixed by headed studs, subject to bending stresses [Bruckner, Eligehausen, Ozbolt (2001)]. In particular this study examined the effects of the compression zone, formed in the concrete by the bending stresses, on the anchor capacity. This study is an excellent example of the union of experimental testing, numerical modelling and empirical methods in improving the design approaches for anchor bolts. For different spacings of headed stud the failure loads were compared between all three. The results showed that the existing CC-Method under-predicted in cases of lower spacing because it failed to take into account the beneficial effects of the compressive zone. A proposed modification to the CC-Method was examined and found to give predictions that followed the results of the numerical analyses.

The group in Stuttgart also began analysing bonded anchors via finite element modelling in 1997. The behaviour of bonded anchors is much more complex to model as load is transferred between the anchor and concrete via layer of grout or adhesive that bonds the two together. Failure may be in the concrete, bonding agent, steel or a combination thereof [Obata, Inoue, Goto (1997)]. As with headed studs the aim was to better understand the influences of various parameters on the behaviour of bonded anchors and therefore develop the CC design method further. Initial analyses were tension test performed on single bonded anchors, free from edge effects [Pukl, Ozbolt, Eligehausen (1998)]. The Microplane Model was again used both in axisymmetric and three-dimensional analyses to model the concrete and grout (Figure 2-17). The steel anchor was modelled as linear-elastic. Over 400 numerical tests were performed in sensitivity studies on the effects of embedment depth, anchor diameter, span of supports, shear strength of

grout, tensile strength of concrete and the thickness of the grout layer. The trends in the failure modes followed those of experimental work. For example, the progression from bond failure, through mixed bond/cone failure and into concrete cone failure with increasing embedment depth was recreated. Crack patterns were also realistic.

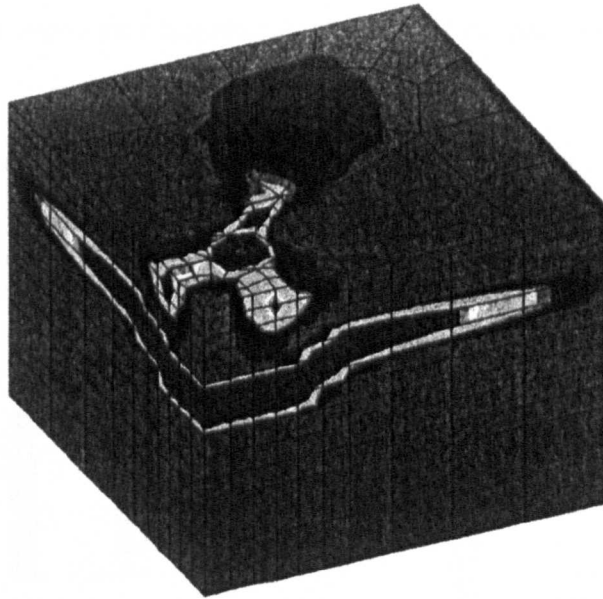


**Figure 2-17 - Maximum Principal Strain Contour Plot for Analysis of a Group of 4 Bonded Anchors (Symmetrical Quarter Shown) [Pukl, Ozbolt, Eligehausen (1998)]**

A special interface model was developed as a variation of the standard Microplane Model. In this only the shear stress components are considered. This was necessary to correctly model the bond behaviour present in the mortar [Li, Eligehausen, Ozbolt, Lehr (1999)]. This was then used in the analysis of more complex bonded anchor problems including those of low edge distance and anchor groups [Li, Eligehausen (2001), Li, Eligehausen, Lehr, Ozbolt (2001)]. In particular for groups of quadruple anchors the influence of bond strength and the so-called ‘group effect’ were examined. Group Effect refers to the reduction in overall failure load observed when the spacing between adjacent anchors is decreased. These analyses were performed three-dimensionally and only a symmetric quarter of the overall problem was modelled. Results showed the bond strength to have a strong influence on the failure mode, lower bond strengths being likely

to fail via pullout whereas higher bond strengths lead to concrete cone failures (when group effects were not present). The influence group effect also produced a number of different failure modes (Figure 2-18). These were also reproduced in the simulations. As with the modelling of headed studs, peak loads produced by the analyses compared well against those from experimental work. However the stiffness of the numerical analyses were sometimes too high leading to incorrect prediction of the anchor displacements. This was attributed to an overly stiff response from the bond interface model [Li, et al (1999)].

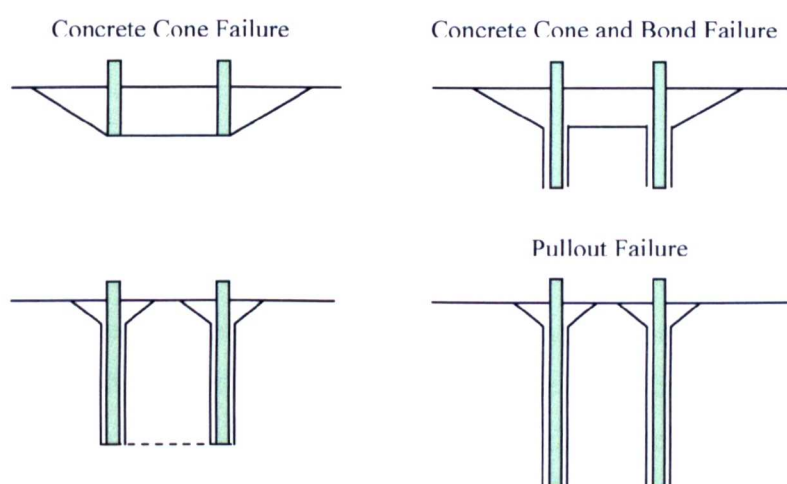


**Figure 2-18 - Failure Modes Observed for Anchor Groups**

The bond model also caused the failure of the anchor to be incorrectly predicted as a shear failure in the bond when the bond strength was set to be high instead of the concrete cone failure seen in reality. In order to avoid this problem the bond layer thickness was increased from 1mm to 6mm. For the 16mm diameter anchor analysed this would result in a rather large hole. For grouted anchors the concrete hole is generally 1.5 times the anchor diameter. Adhesive anchors are installed in holes 10-25% larger than the anchor [Cook, Konz (2001)]. However, there may be further modelling aspects that make this choice applicable.

Results of the analyses also showed the interaction between bond strength and group effect. In cases where the bond strength was low the anchor failure was confined more to



the bond material and therefore the concrete cones produced (if any) were smaller and did not influence each other.

The most demanding type of anchor to model is the expanding type. As with the bonded anchor, load transfer is via shear force however the shear strength of the anchor-concrete interface is generated mechanically expanding the anchor and it bearing against the concrete. In general, this expansion pressure can increase during loading as a function of the tensile force applied to the anchor bolt head. Depending on the modelling approach used these characteristics require the analytical model to cater for frictional interface behaviour and solid body contacts in addition to modelling of fracturing and crushing concrete.

Ozbolt, Eligehausen et al tackled the problem of splitting failure caused by expanding anchors [Pukl, Ozbolt, Schlottke, Eligehausen (1994), Asmus, Ozbolt (2001)]. This type of failure is associated with anchors placed either in narrow concrete members or at low edge distances. Neither paper gives much detail on the specifics of how the anchor was modelled. It is worth noting that the methods of modelling anchor expansion are poorly reported in all of the papers found in the course of this investigation. In this case it seems that instead of modelling the anchor specifically it was instead represented by suitable boundary constraints. The loading was applied via prescribed displacements in two stages. Firstly the expansion phase and secondly a combined expansion and axial pullout displacement. Once again the non-local Microplane Model was used to model the concrete and the characteristic length parameter calibrated to match analytical with experimental results. Analyses were performed both axisymmetrically and also three-dimensionally.

Ozbolt, et al, discretised the axisymmetric problem with between 450 and 1400 linear, quadrilateral elements. A range of edge distances were analysed (although it must be noted that for axisymmetric analyses the edge distance is the same in every direction whereas typically the term 'edge distance' refers to the shortest distance to a single free edge). A shortcoming that was observed in the analyses was that no transition from

splitting failure at small edge distances to concrete cone failure at larger distances was produced. The reason for this was found to be that the high radial compressive stresses developed induced large tensile stresses and hence cracking in the tangential direction. In reality there would be a finite number of these cracks with largely intact material in between. In the axisymmetric approximation this cracked state is 'smeared' around the whole loading zone thus resulting in a localised failure around the anchor expander.

To avoid the problems mentioned above Ozbolt, et al, also performed the analyses in 3D. A symmetrical quarter of the whole problem was analysed in order to save on computation time. Between 1800 and 3000 8-noded brick elements were used in the FE meshes. These analyses correctly predicted the transition from splitting to concrete cone failure for increasing edge distance. The influence of member depth was also examined and shown to only be important for depths less than twice the effective depth of the anchor embedment.

This work was revisited in 2001 [Asmus, Ozbolt (2001)] where greater computing power allowed for a finer discretisation of the 3D problem and hence provided more detailed results on the influence of edge distance, member depth, embedment depth and bearing area. The aim was to better understand these parameters and how they affected splitting failure. The numerical results compared well with experimental ones.

The above work by Ozbolt, et al, represents a rather simplistic approach to the modelling of expanding anchors. Although the results were good they lack the detail that a more complex model can provide. The simplistic approach also required *a priori* knowledge of the anchor expansion behaviour. This is difficult to obtain given it is dependant on such factors as confinement level, crack evolution and anchor-concrete interface behaviour. In contrast Pivonka, Lackner and Mang decided to model each component of an undercut anchor explicitly and also model each stage of the anchor life from installation to failure [Pivonka, et al (2004)]. Two different material models for concrete were compared in the analyses. Firstly the Extended Leon Model [Etse (1998)] which is a complex, single surface softening plasticity model. Secondly a combined Rankine-Drucker Prager, multi-

surface, plasticity model. Modelling of the steel components of the anchor were performed using a Von Mises plasticity model. Although contacts between the different bodies are considered there is no information given on the particular approach used. The problem is modelled axisymmetrically with an exceptionally fine finite element mesh around the loading zone and more so around the contact surfaces (Figure 2-19).

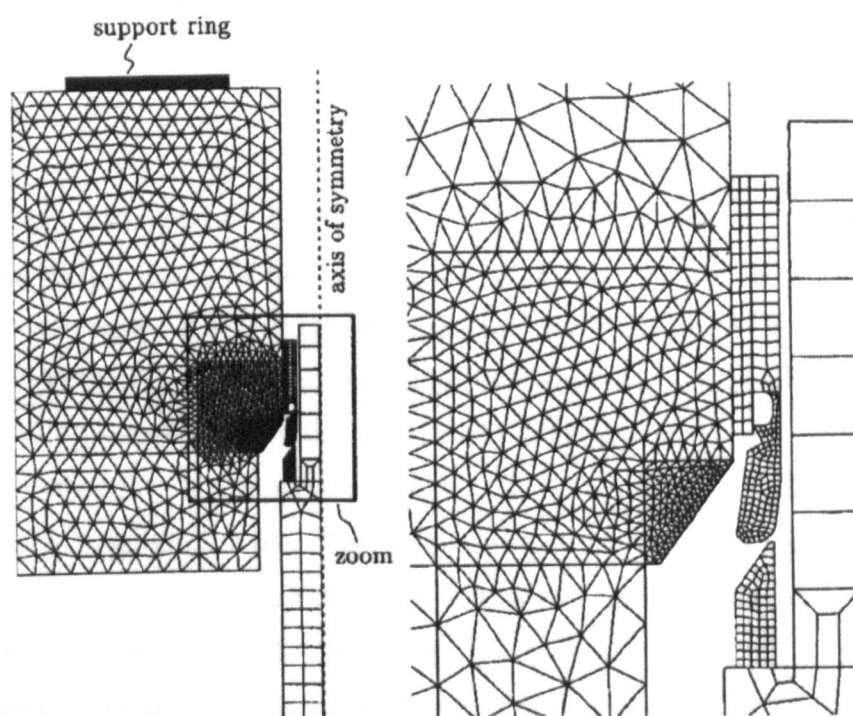


**Figure 2-19 - Finite Element Mesh Used for Complex Modelling of an Undercut Anchor**  
[Pivonka, et al (2004)]

The analyses were performed in four stages. In the first stage the anchor is primed. By prescribing a downward displacement of the expander its leaves are forced to expand as it contacts the cone. The parameters of the Von Mises Plasticity Model for the expander were set to produce elastic-perfectly plastic behaviour. Also, since the individual leaves of the expander cannot be modelled in the axisymmetric approximation the material properties of these were defined as an orthotropic material with zero circumferential stiffness. When performing this stage of the analysis plastic hinges formed at the top of the leaves allowing them to rotate as expected. The end of the stage was recognised by a

sharp increase in the resistance to the displacement as the leaves reached the limit of their movement.

The second stage of the analysis was a rigid body displacement of the anchor so that the leaves were in contact with the concrete. The end of this stage was also signalled by a sharp increase in resistance when the concrete surface was contacted. For the third stage the prescribed displacements that produced the anchor expansion were released. This was associated with a slight relaxation in the stresses as the expander found a new equilibrium state.

The final stage of the analysis was the pullout of the anchor via prescribed displacements. The ultimate failure load determined using the Extended Leon Model was in very good agreement with experimental results whereas the Multi-Surface Model under predicted the load by 33%. The error from the Multi-Surface Model was attributed to it over predicting the lateral deformations. As such deformations were constrained high compressive stresses were induced which lead to a premature failure of the anchor. However, it is important to note that both constitutive models produced a failure by localised crushing of the concrete above the expander. In reality the mode of failure was via a concrete cone pullout. Therefore it would be inappropriate to put too much trust in the peak strength alone as a guide to the accuracy of a model.

Researchers working for the anchor manufacturer Hilti have published the most comprehensive modelling of expanding anchors to date. Not only do Hilti use numerical modelling of anchors as a means to better understand the processes and factors affecting their behaviour they also mention the idea of testing anchors by computer simulation as part of the qualification and approval process [Boussa, Mounajed, Mesureur, Heck (2001)]. They suggest that such 'virtual testing' would give a fuller understanding of anchor behaviour and consider an increased number of parameters influencing this behaviour. Testing in this way could reduce the number of experimental tests required and also the time and cost.

As early as 1994 Hilti had developed an FE code in-house to model anchor bolts [Jussel, Wall, Bourgund (1994)]. Unfortunately owing to the commercially sensitive nature of the code and its capabilities not a great deal of information is available on it. What is known is that concrete is modelled using a Rotating Crack Model with a Rankine failure criterion and bilinear softening based on  $G_f$  for tension and a non-linear hardening/softening model in compression. It is also apparent in many of the results that a contact model has been used for the interaction of the anchor components and their interaction with the concrete. However no details are given.

Earlier papers detail the axisymmetric analysis of bonded, deformation-controlled expanding anchors (driven anchor) and load-controlled expanding anchors [Jussel, et al (1994), Nienstedt, Dietrich (1995)]. The difference between the last two is as follows: the deformation-controlled anchor requires the anchor cone to be driven into the expansion sleeve by means of hammering. In contrast, the expansion mechanism of a load-controlled is activated initially by turning the bolt head to draw the expansion cone into the expander and then tensile forces applied to the bolt may induce additional expansion. The bonded anchor is the simplest bolt modelled in terms of geometry but the geometry modelled included, in addition to the bolt and concrete block, the nut, washer, fastened plate and possibly a bond layer. It is expected that the nut, washer and plate were modelled in order to produce the required boundary conditions at the top surface of the concrete accurately. Both the pre-stressing and pullout phases were analysed with realistic looking stress distributions and crack patterns (Figure 2-20).

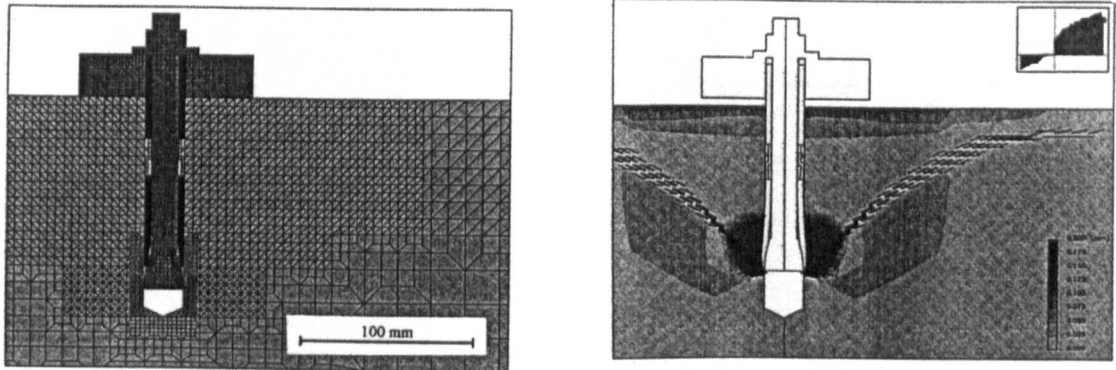


**Figure 2-20 - FE Mesh and Crack Pattern for an Axisymmetrically Modelled Expansion Anchor**  
[Jussel, et al (1994), Nienstedt and Dietrich (1995)]

The finite element mesh for the driven anchor is very fine, especially around the contact surfaces between cone and sleeve. Once again the stress distributions and crack patterns are believable. For the load-controlled expansion anchor the discretisation level is higher again. The high compressive stresses around the tips of the expansion leaves are correctly produced during the priming stage and a classic cone failure is producing during the pullout phase.

In 1999 three-dimensional modelling of a driven anchor was presented briefly [Nienstedt, Mattner, Wiesbaum (1999)]. Modelling of edge and group effects are stated as the reasons for the need for 3D analyses. The results presented are little more than pictorial.

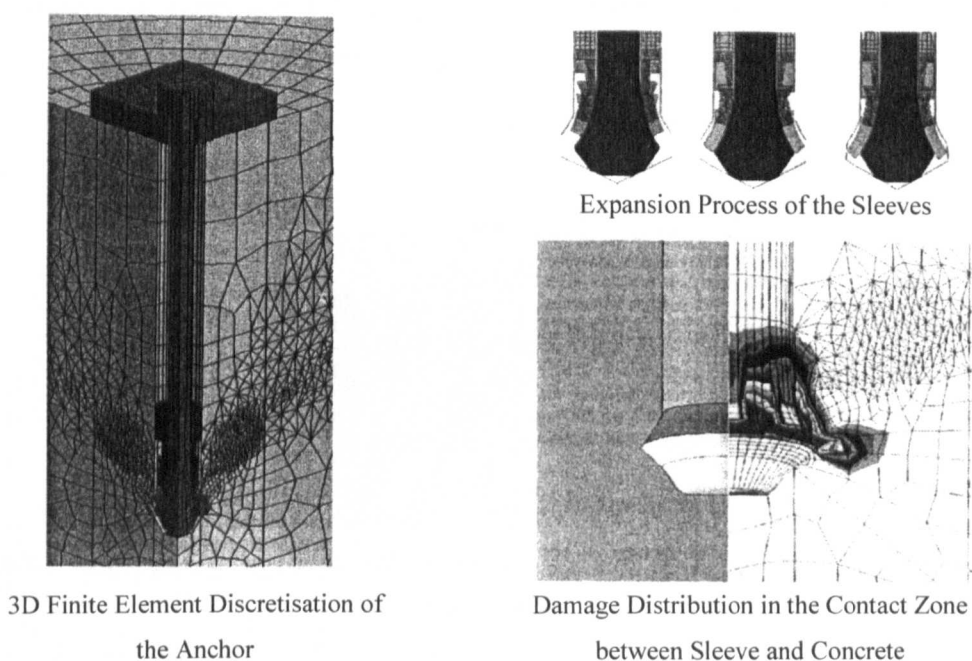


**Figure 2-21 - 3D FE Analysis of Undercut Anchor [Nienstedt, Mattner (2001)]**

Simulation of an undercut anchor in cracked concrete was presented in 2001 [Nienstedt, Mattner (2001)]. In many ways the geometry of the problem followed that of the problem tackled by Pivonka, et al, however, in this case three-dimensional modelling was used (Figure 2-21). A symmetric quarter of the whole problem was modelled but the symmetry boundary condition on one of the planes was removed in order to represent a crack opening on that plane. Once again the discretisation of the anchor and concrete around the contact zone was very fine. In particular the location of the leaf hinges used an exceptionally fine mesh. Both the setting/priming stage and the axial pullout were modelled.

Comparisons of the load-displacement graphs for cracked and uncracked concrete verified that the performance of undercut anchors is relatively insensitive to cracking. For both the failures were via yielding of the anchor rods showing that the anchor transferred the pullout force effectively, even when the concrete was damaged. Stress contour plots give an insight into the different stress distributions for cracked and uncracked concrete. The level of detail present also allowed the localised damage of the concrete around the

contact zone to be examined. It is stated in the paper that this type of analysis allows the development of new products to be sped up.

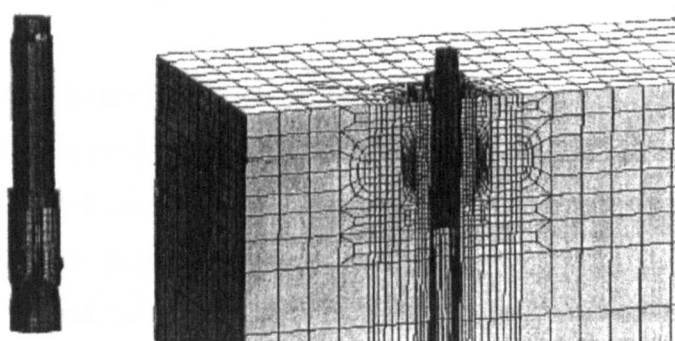


**Figure 2-22 - 3D FE Mesh for the Modelling of an Expansion Anchor [Nienstedt, Mattner, Nestler, Song (2001)]**

Similarly good results were produced when analysing the effects of shear and pullout loads on adhesive and expansion anchors close to a free edge [Nienstedt, Mattner, Nestler, Song (2001)]. Owing to the geometry of the problem one half of the full domain was analysed (Figure 2-22). It was noted that the failure load for the shear test of the expansion anchor was within the range of experimental results and very close to the mean value.

Finally, a group that is part of the CSTB (Centre Scientifique et Technique du Bâtiment) analysed undercut anchors in co-operation with Hilti [Boussa, Mounajed, Mesureur, Heck (2001)]. Their choice of constitutive models was slightly different. For the concrete a Single Fixed Crack Model was adopted. In this case the term ‘Single Crack’ means that in each of the mutually perpendicular axes set upon the initiation of a crack (the so-called ‘crack axes’) a crack may form. Therefore up to three mutually perpendicular cracks may form at each point. A shear retention factor of zero was chosen to avoid the stress-locking phenomenon mentioned above. It is stated that because the failure of concrete when an anchor is placed close to a free edge is very brittle the plasticity of concrete was not modelled. This suggests a brittle behaviour is assumed post-peak rather than a softening one. However it is also stated that mesh objectivity of the model is ensured by setting the



crack band width,  $h$ , according to the element dimensions and crack direction. However, such an approach is associated with a post-peak softening behaviour for the material so the specifics of the assumed post-peak behaviour remain unclear. Steel was modelled using a Von Mises Plasticity Model.

As with the Hilti modelling, each component of the fixing was modelled explicitly. Contact analysis was performed using the 'Constraint Method' although no further details are given. Both steel-steel and steel-concrete contacts were considered and treated as frictionless. This is perhaps appropriate for an undercut anchor as much of its performance is gained from mechanical interlock between the expander and the concrete.

The main part of the FE mesh was made up of over 8,500, 8-noded, iso-parametric brick elements. The non-linear material models were applied to these. The larger domain of concrete outside of the fracturing zone was modelled using almost 17,000, 4-noded tetrahedra and were considered to be linear elastic. Thus savings could be made in computational time. Unlike the Hilti analyses discussed above, no symmetry conditions were used to reduce the analysis domain. Indeed modelling only a symmetric portion of the problem would have obscured the corner failure produced under shear loading.

Shear tests were performed on the model for a range of different edge distances. The failure modes shown in the results accurately match those produced for the corresponding experimental tests. Peak loads and associated displacements were also reproduced very well by the numerical analyses. It is noted that the initial stiffness of the load-displacement responses was a little soft. Incorrect identification of the concrete properties used in the experimental study (e.g. fracture energy or tensile strength) was cited as one possibility for this. The other was the lack of plasticity in the modelling of the concrete.

## **2.4 Conclusions**

It can be seen that due to the demands for higher performance, greater reliability and more flexibility, numerical modelling of anchor bolts has become an essential part of the development process. This includes areas such as the development of new products, the testing of existing types and in the development of increasingly accurate design approaches for industry. The strength of numerical modelling is its ability to provide a unique insight into the processes involved in transfer of forces from anchor to concrete from the initial installation phase right up to ultimate failure. It is also relatively easy and inexpensive to run series of sensitivity studies to discover the important factors that dictate anchor behaviour. Recent advances in constitutive modelling of concrete have enabled more accurate analyses to be performed. The increases in computer capacity and performance have allowed for higher resolution and detail. It is envisaged that as numerical analysis tools become more accessible and designers become more skilled that numerical modelling of anchorage systems won't just be confined to research, it will also become part of the design process of structures in practice.

## CHAPTER 3

### Non-linear Material Models

This chapter describes in detail the two non-linear material models used in the subsequent 2D analysis of anchor-type problems. The first of these is the Plasticity Model. As mentioned in the previous chapter, the initial failure criterion is defined as a surface residing in principal stress space or any other stress invariant space. If a load increment induces a failure an inelastic strain will be produced and the initial failure surface will be updated via the so-called evolution law. The Crack Model is the second material model presented. In contrast to plasticity, material behaviour is assessed on a finite number of planes that correspond to individual cracks, the formation of which is controlled by the Rankine failure criterion and separation angle from existing cracks. Inelastic behaviour is governed by uniaxial material softening functions.

The vast majority of the analysis work performed as part of this project was carried out within the framework of the finite element package, DIANA v7.2 [TNO (1999)]. The theories below refer to plasticity and crack modelling in general but highlight specifics relating to the particular implementations within DIANA where appropriate.

#### 3.1 Plasticity Model<sup>1</sup>

Within plasticity the initial yield condition that defines the stress state at which plastic flow is initiated is given by:

$$F(\sigma_{ij}) = 0 \quad \text{Equation 3-1}$$

The initial yield function,  $F$ , is a scalar valued function of the stress tensor,  $\sigma_{ij}$ . The stress tensor can be represented as a point in principal stress space (or similar stress invariant space) and the yield function defines a surface in this space. A fundamental condition of

---

<sup>1</sup> The description of the Plasticity Model follows that of the NAFEMS Introduction To Non-Linear Finite Element Analysis [Hinton (1992)].

computational plasticity is that the stress point may not lie outside of the yield surface. If the stress point is on the failure surface (Figure 3-1) subsequent loading of the structure may cause the stress point to:

- Unload elastically - move to a position within the surface
- Remain in a neutral state - moves on the failure surface without exceeding the yield criterion
- Load and induce plastic straining - attempt to move beyond the bounds of the surface therefore causing the yield surface to evolve.

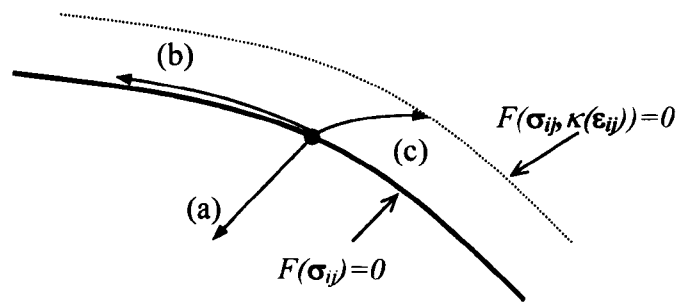


**Figure 3-1 – Possibilities for Movement of Stress Point Due to Loading of Structure**

Rate and direction of plastic straining is defined by the flow rule and is given by the following expression:

$$\dot{\epsilon}_{ij}^p = \dot{\lambda} \frac{\partial Q}{\partial \sigma_{ij}} = \dot{\lambda} \mathbf{b} \quad \text{Equation 3-2}$$

where  $\dot{\epsilon}_{ij}^p$  is the plastic strain rate tensor,  $Q(\sigma_{ij})$  is the plastic potential function and  $\dot{\lambda}$  is the plastic strain-rate multiplier.  $Q$  takes a similar form to  $F$  in that it too is a scalar valued function of the stress tensor and may be represented in stress invariant space as a surface.

As shown in Figure 3-2, plastic flow takes place in the direction orthogonal to the plastic potential surface.

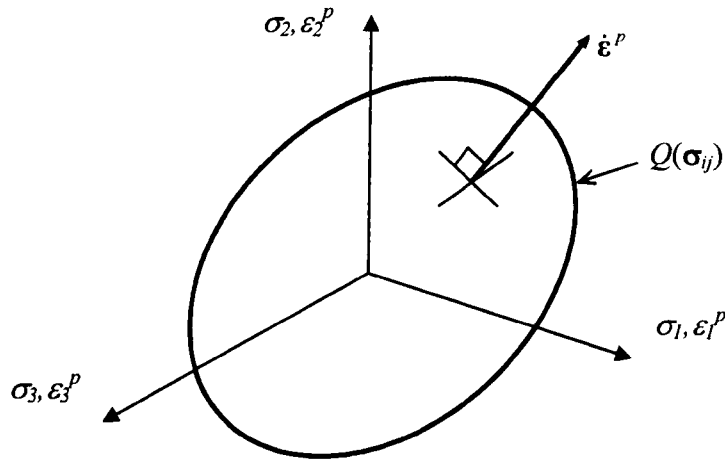


Figure 3-2 - Plastic Strain Rate Vector

The implementation of the Plasticity Model in DIANA offers both associative ( $Q=F$ ) and non-associative ( $Q \neq F$ ) flow rules. Following derivations are presented for the associative rule but are equally valid for the non-associative rule if the appropriate substitutions are performed.

The evolution of the yield surface caused by plastic straining is defined by the hardening rule such that the subsequent yield function is given by:

$$F(\boldsymbol{\sigma}_{ij}, \kappa(\boldsymbol{\varepsilon}_{ij}^p)) = 0 \quad \text{Equation 3-3}$$

where  $\kappa$  is the so-called hardening parameter and is a function of the plastic strain,  $\boldsymbol{\varepsilon}_{ij}^p$ . Similarly, the subsequent plastic potential function is also a function of the hardening parameter,  $Q(\boldsymbol{\sigma}_{ij}, \kappa(\boldsymbol{\varepsilon}_{ij}^p))$ .

It is important to note that the updated yield and plastic potential functions define the condition for and nature of further plastic straining. In the context of the modelling of

concrete this process of transitioning from initial state to the subsequent one can be interpreted as initial cracking or crushing of the material resulting in the development of permanent, in-elastic strains and a change in the material behaviour.

Models for material behaviour are often derived from the results of uniaxial experimental testing. In order to relate these results to multiaxial computational models the hardening/softening rules are commonly defined in terms of either strain or work hardening. The von Mises Model is adopted in the following descriptions of strain and work hardening. Although this model is more suitable for the modelling of metals rather than concrete (e.g. no pressure dependence, identical material behaviour in tension and compression) the concepts discussed are common for other models.

The von Mises yield condition is defined such that yielding will initiate when a critical value of deformational energy,  $k^2$ , is reached which causes a change in the shape of a body with no associated volumetric change. In the deviatoric plane it is described as a circle:

$$F_{VM} = (\sigma_1 - \sigma_2)^2 + (\sigma_2 - \sigma_3)^2 + (\sigma_3 - \sigma_1)^2 - k^2 = 0 \quad \text{Equation 3-4}$$

In 3-dimensional principal stress space the von Mises yield surface is interpreted as a cylinder co-axial with the line  $\sigma_1 = \sigma_2 = \sigma_3$  and with a radius of  $k$ .

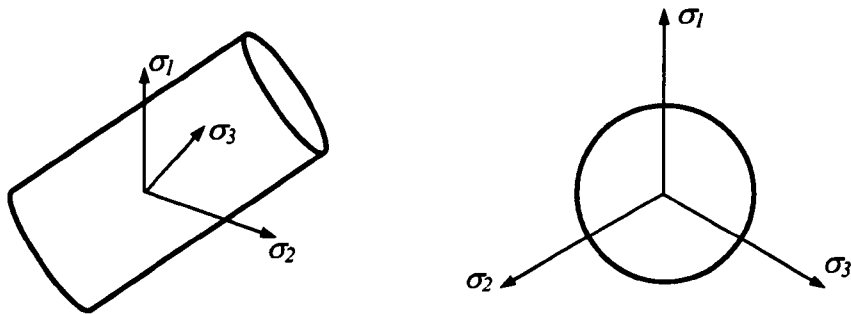


**Figure 3-3 - Von Mises Yield Surface shown in a) 3D Principal Stress Space, b)  $\pi$ -plane**

In uniaxial tension testing  $\sigma_2 = \sigma_3 = 0$  and so  $\sigma_I = \sigma_0$ , where  $\sigma_0$  is the yield stress level. Therefore:

$$k = \sqrt{2}\sigma_0 \quad \text{Equation 3-5}$$

The yield criterion may also be rewritten in terms of the second invariant of deviatoric stress,  $J_2$ , as follows:

$$J_2 = \frac{1}{6} [(\sigma_2 - \sigma_3)^2 + (\sigma_3 - \sigma_1)^2 + (\sigma_1 - \sigma_2)^2] \quad \text{Equation 3-6}$$

Therefore combining Equation 3-4 and Equation 3-6 gives:

$$F_{VM} = 6J_2 - k^2 \quad \text{Equation 3-7}$$

Or

$$F_{VM} = J_2 - 3\sigma_0^2 \quad \text{Equation 3-8}$$

For this reason the von Mises criterion is often referred to as  $J_2$  plasticity.

In strain hardening effective stress,  $\sigma_{eff}$ , provides a scalar measure of the current stress state. It is defined as:

$$\sigma_{eff} = \sqrt{3J_2} \quad \text{Equation 3-9}$$

By comparing with Equation 3-8 it can be seen for unconfined, uniaxial conditions the equation for effective stress reduces to the uniaxial stress,  $\sigma_0$ . Effective plastic strain,  $\epsilon_{eff}^p$ , is used as a guide to the history of the deformation process by giving a measure of the plastic strain path length. An increment of plastic strain is defined as:

$$d\epsilon_{eff}^p = \left[ \frac{2}{3} d\epsilon_{ij}^p d\epsilon_{ij}^p \right]^{1/2} \quad \text{Equation 3-10}$$



The total path length can then be calculated.

$$\varepsilon_{eff}^p = \int d\varepsilon_{eff}^p = \int_0^t \dot{\varepsilon}_{eff}^p dt = \int_0^{\varepsilon_{ij}^p} \left( \frac{2}{3} d\varepsilon_{ij}^p d\varepsilon_{ij}^p \right)^{1/2} \quad \text{Equation 3-11}$$

The equivalence of this multiaxial formulation to the uniaxial one may be illustrated by considering an unconfined tension test in which no plastic flow occurs. Hence:

$$\varepsilon_1^p + \varepsilon_2^p + \varepsilon_3^p = 0 \quad \text{Equation 3-12}$$

In this form of test transverse strains are equal. Therefore:

$$\varepsilon_2^p = \varepsilon_3^p = -0.5\varepsilon_1^p \quad \text{Equation 3-13}$$

The effective plastic strain consequently reduces to the uniaxial plastic strain length as follows:

$$\varepsilon_{eff}^p = \left[ \frac{2}{3} \left( (\varepsilon_1^p)^2 + (\varepsilon_2^p)^2 + (\varepsilon_3^p)^2 \right) \right]^{1/2} = \varepsilon_1^p \quad \text{Equation 3-14}$$

Hardening can be introduced to the yield criterion, Equation 3-8, by expressing the yield stress as a function of effective plastic strain.

$$F_{VM} = J_2 - 3\sigma_0^2 (\varepsilon_{eff}^p)^2 = 0 \quad \text{Equation 3-15}$$

For linear hardening this is written as:

$$F_{VM} = J_2 - 3(\sigma_0 + H_s \varepsilon_{eff}^p)^2 = 0 \quad \text{Equation 3-16}$$

where  $H_s$  is the strain hardening modulus. Defined as:

$$H_s = \frac{\partial \sigma_0}{\partial \varepsilon_{eff}^p} \quad \text{Equation 3-17}$$

And may be derived from the linear hardening diagram.

For work hardening the subsequent yield stress is expressed as a function of accumulated plastic work,  $W_p$ .

$$W_p = \int \boldsymbol{\sigma}_{ij} \boldsymbol{\varepsilon}_{ij}^p dt = \int \boldsymbol{\sigma}_{ij} d\boldsymbol{\varepsilon}_{ij}^p \quad \text{Equation 3-18}$$

The subsequent yield function is written as:

$$F = J_2 - 3(\sigma_0 + H_w W_p)^2 = 0 \quad \text{Equation 3-19}$$

where  $H_w$  is the work hardening modulus and is defined as:

$$H_w = \frac{\partial \sigma_0(W_p)}{\partial W_p} \quad \text{Equation 3-20}$$

The tangential material law relates stress rate to strain rate and is written in tensor form as:

$$\dot{\boldsymbol{\sigma}}_{ij} = \mathbf{D}_{ijkl} \dot{\boldsymbol{\varepsilon}}_{kl} \quad \text{Equation 3-21}$$

Or in vector form as:

$$\dot{\boldsymbol{\sigma}} = \mathbf{D}_t \dot{\boldsymbol{\varepsilon}} \quad \text{Equation 3-22}$$

where  $\mathbf{D}_t$  is the tangential matrix. Derivation of this matrix starts by firstly expressing the yield function (Equation 3-3) in rate form:

$$\dot{F} = \frac{\partial F}{\partial \boldsymbol{\sigma}}^T \dot{\boldsymbol{\sigma}} + \frac{\partial F}{\partial \kappa} \dot{\kappa} = 0 \quad \text{Equation 3-23}$$

If we define:

$$\mathbf{a} = \frac{\partial F}{\partial \boldsymbol{\sigma}} \quad \text{and} \quad A = -\frac{1}{\dot{\lambda}} \frac{\partial F}{\partial \kappa} \dot{\kappa} \quad \text{Equation 3-24}$$

We can then write:

$$\mathbf{a}^T \dot{\boldsymbol{\sigma}} - A \dot{\lambda} = 0 \quad \text{or} \quad \mathbf{a}^T \dot{\boldsymbol{\sigma}} = A \dot{\lambda} \quad \text{Equation 3-25}$$

Total strain may be decomposed into elastic (recoverable) and plastic (irrecoverable) components. In rate form this is expressed as:

$$\dot{\boldsymbol{\epsilon}} = \dot{\boldsymbol{\epsilon}}_e + \dot{\boldsymbol{\epsilon}}_p \quad \text{Equation 3-26}$$

Plastic strain rate has been previously defined in Equation 3-2 and elastic strain rate is given by Hooke's Law:

$$\dot{\boldsymbol{\epsilon}}_e = \mathbf{D}^{-1} \dot{\boldsymbol{\sigma}} \quad \text{Equation 3-27}$$

Hence Equation 3-26 may be rewritten as:

$$\dot{\boldsymbol{\epsilon}} = \mathbf{D}^{-1} \dot{\boldsymbol{\sigma}} + \lambda \mathbf{b} \quad \text{Equation 3-28}$$

Multiplying both sides by  $\mathbf{a}^T \mathbf{D}$  gives:

$$\mathbf{a}^T \mathbf{D} \dot{\boldsymbol{\epsilon}} = \mathbf{a}^T \mathbf{D} \mathbf{D}^{-1} \dot{\boldsymbol{\sigma}} + \mathbf{a}^T \lambda \mathbf{D} \mathbf{b} \quad \text{Equation 3-29}$$

Simplifying, making the substitution given by Equation 3-25 and rearranging produces the following expression for  $\dot{\lambda}$ :

$$\dot{\lambda} = \frac{\mathbf{a}^T \mathbf{D} \dot{\boldsymbol{\epsilon}}}{A + \mathbf{a}^T \mathbf{D} \mathbf{b}} \quad \text{Equation 3-30}$$

This is then substituted back into the equation for strain rate decomposition (Equation 3-28):

$$\dot{\boldsymbol{\epsilon}} = \mathbf{D}^{-1} \dot{\boldsymbol{\sigma}} + \mathbf{b} \frac{\mathbf{a}^T \mathbf{D} \dot{\boldsymbol{\epsilon}}}{A + \mathbf{a}^T \mathbf{D} \mathbf{b}} \quad \text{Equation 3-31}$$

Multiplying through by  $\mathbf{D}$  gives:

$$\mathbf{D}\dot{\boldsymbol{\varepsilon}} = \mathbf{D}\mathbf{D}^{-1}\dot{\boldsymbol{\sigma}} + \frac{\mathbf{D}\mathbf{b}\mathbf{a}^T\mathbf{D}\dot{\boldsymbol{\varepsilon}}}{A + \mathbf{a}^T\mathbf{D}\mathbf{b}} \quad \text{Equation 3-32}$$

Simplifying and rearranging gives:

$$\dot{\boldsymbol{\sigma}} = \left[ \mathbf{D} - \frac{\mathbf{D}\mathbf{b}\mathbf{a}^T\mathbf{D}}{A + \mathbf{a}^T\mathbf{D}\mathbf{b}} \right] \dot{\boldsymbol{\varepsilon}} \quad \text{Equation 3-33}$$

Hence the tangent modulus is:

$$\mathbf{D}_t = \mathbf{D} \left[ I - \frac{\mathbf{b}\mathbf{a}^T\mathbf{D}}{A + \mathbf{a}^T\mathbf{D}\mathbf{b}} \right] \quad \text{Equation 3-34}$$

For non-associative plasticity ( $F \neq Q$ , hence  $\mathbf{a} \neq \mathbf{b}$ ) the tangent modulus matrix is non-symmetric. However an associative flow rule results in a symmetric matrix.

In common with other non-linear material models, plasticity uses a stepwise incremental approach to carry out the analysis. The initial approximation made is to assume that the tangent modulus derived previously to relate stress rate to strain rate is also valid in relating incremental stress to incremental strain as follows:

$$\Delta\boldsymbol{\sigma} = \mathbf{D}_t\Delta\boldsymbol{\varepsilon} \quad \text{Equation 3-35}$$

Furthermore it is assumed to be valid in the calculation of the FE tangent stiffness matrix.

$$\mathbf{K}_t = \int_V \mathbf{B}^T \mathbf{D}_t \mathbf{B} dV \quad \text{Equation 3-36}$$

From the start state or previously converged stress state, each analysis step is initiated by applying a prescribed load increment,  $\Delta\mathbf{f}$ . The problem is then linearised in order to obtain the associated displacement increment,  $\Delta\mathbf{u}$ , via the tangent stiffness matrix.

$$\Delta \mathbf{u} = \mathbf{K}_T^{-1} \Delta \mathbf{f} \quad \text{Equation 3-37}$$

From this incremental displacement the total strain increment,  $\Delta \boldsymbol{\varepsilon}$  is calculated via the FE strain displacement matrix,  $\mathbf{B}$ .

$$\Delta \boldsymbol{\varepsilon} = \mathbf{B} \Delta \mathbf{u} \quad \text{Equation 3-38}$$

However although the total strain is known the relative contributions from elastic and plastic strain are unknown. Hence it is not possible to calculate the stress increment  $\Delta \boldsymbol{\sigma}$ . The strategy adopted to overcome this problem is to assume the step to be purely elastic and so the stress increment is given via Hooke's law:

$$\Delta \boldsymbol{\sigma} = \mathbf{D} \Delta \boldsymbol{\varepsilon} \quad \text{Equation 3-39}$$

The total stress is then calculated to produce what is known as the elastic predictor stress. The yield condition is assessed and if it has not been violated then the assumption that the increment was purely elastic is valid and the analysis may proceed to the next increment. If the yield criterion has been violated then a plastic correction must be made to return the stress to the yield surface. This process is illustrated in Figure 3-4.

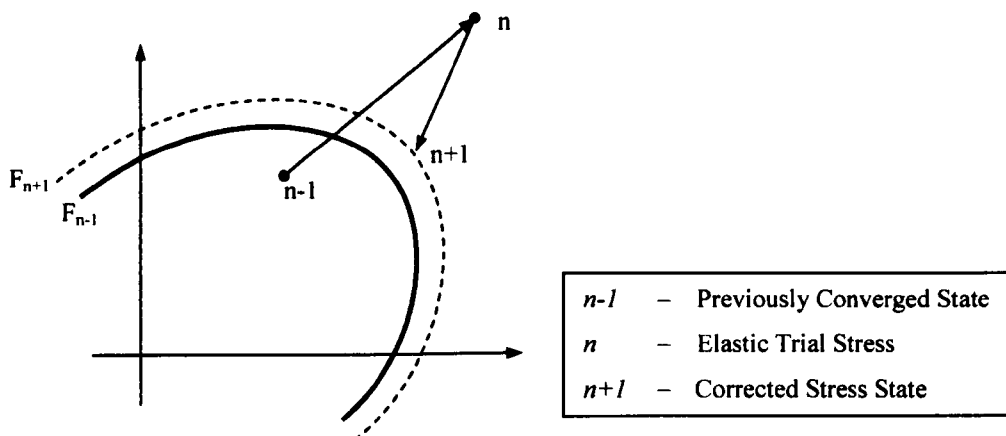


**Figure 3-4 - Elastic Predictor - Plastic Corrector Stress Return**

Calculation of the correct  $\Delta\sigma$  requires the integration of the constitutive equation below (Equation 3-40) hence the integration of  $d\epsilon_p$ .

$$d\sigma = \mathbf{D}(d\epsilon - d\epsilon_p) \quad \text{Equation 3-40}$$

Integration is performed over an increment of pseudo-time. This should not be confused with real-time as plastic flow is assumed to occur instantaneously.

$$\Delta\sigma = \int_{\Delta} d\sigma = \int_{\Delta} \mathbf{D}(d\epsilon) - \int_{\Delta} \mathbf{D}(d\epsilon_p) \quad \text{Equation 3-41}$$

From Equation 3-2  $d\epsilon_p$  may be expressed as:

$$d\epsilon_p = d\lambda \mathbf{b} \quad \text{Equation 3-42}$$

Therefore:

$$\Delta\sigma = \int_{\Delta} \mathbf{D}(d\epsilon) - \int_{\Delta} \mathbf{D}d\lambda \mathbf{b} \quad \text{Equation 3-43}$$

and

$$\Delta\epsilon_p = \int_{\Delta} d\epsilon_p = \int_{\Delta} d\lambda \mathbf{b} \quad \text{Equation 3-44}$$

It must be noted that during this integration step  $\Delta$  the values of  $\lambda$ ,  $\mathbf{a}$  and  $\mathbf{A}$  will be continuously changing. To overcome this complexity the integration scheme used assumes a linear strain path.

The Backward Euler algorithm is a commonly used integration scheme. This method is implicit and unconditionally stable. From Equation 3-40 the stress at the end of the increment is defined by:

$$\sigma_{n+1} = \sigma_n + \Delta\sigma_{n+1} \quad \text{Equation 3-45}$$

where  $\Delta\sigma_{n+1}$  is given by:

$$\Delta\sigma_{n+1} = \Delta\sigma_n - \Delta\sigma_{n+1}^p \quad \text{Equation 3-46}$$

An estimate for  $\Delta \boldsymbol{\varepsilon}_{n+1}^p$  is obtained via the mid-point rule with the weighting value,  $\beta$ , set to 1:

$$\Delta \boldsymbol{\varepsilon}_{n+1}^p = \Delta \lambda [(1 - \beta) \mathbf{b}_n + \beta \mathbf{b}_{n+1}] \quad \text{Equation 3-47}$$

Hence:

$$\Delta \boldsymbol{\sigma}_{n+1} = \Delta \boldsymbol{\sigma}_n - \Delta \lambda \mathbf{D} \mathbf{b}_{n+1} \quad \text{Equation 3-48}$$

Performing a first order Taylor expansion on the plastic consistency equation (Equation 3-1) for the end state gives:

$$F_{n+1} = F_n + \left( \frac{\partial F}{\partial \boldsymbol{\sigma}} \right)_{n+1}^T \Delta \boldsymbol{\sigma} + \left( \frac{\partial F}{\partial \kappa} \right) \Delta \kappa = 0 \quad \text{Equation 3-49}$$

$$F_n - \Delta \lambda \mathbf{a}_n^T \mathbf{D} \mathbf{b}_n - A_{n-1} \Delta \lambda = 0 \quad \text{Equation 3-50}$$

Rearranging for  $\Delta \lambda$  produces:

$$\Delta \lambda = \frac{F_n}{\mathbf{a}_n^T \mathbf{D} \mathbf{b}_n + A_{n-1}} \quad \text{Equation 3-51}$$

Hence the new stress state  $\boldsymbol{\sigma}_{n+1}$  is calculated using Equation 3-52. Similarly, the new plastic strain can be calculated via Equation 3-53:

$$\boldsymbol{\sigma}_{n+1} = \boldsymbol{\sigma}_n + \mathbf{D}(\boldsymbol{\varepsilon}_{n+1} - \Delta \lambda \mathbf{b}_{n+1}) \quad \text{Equation 3-52}$$

$$\boldsymbol{\varepsilon}_{n+1}^p = \boldsymbol{\varepsilon}_n^p + \Delta \lambda \mathbf{D} \mathbf{b}_n \quad \text{Equation 3-53}$$

At this stage the yield condition is checked for the newly calculated stress state. If satisfied, the FE analysis proceeds to global equilibrium checks. If not satisfied, the calculated stress state at  $n+1$  is set as the new trial state,  $n$ , and the procedure to calculate the end stress state is repeated as before.



A significant increase in both the performance and robustness of the iterative process can be made by ensuring the consistent linearisation of the non-linear incremental equations. In particular the tangent stiffness matrix must be obtained by consistent linearisation of the stress resulting from the return-mapping algorithm. This objective is obtained by deriving the consistent tangent matrix from the updated stress at the end of iteration  $n+1$ .

The equation for calculating the finite stress increment (Equation 3-48) can be written in the form:

$$\Delta \boldsymbol{\sigma}_n = \mathbf{D}(\Delta \boldsymbol{\varepsilon} - \Delta \lambda \mathbf{b}_n) \quad \text{Equation 3-54}$$

Differentiating gives:

$$d\Delta \boldsymbol{\sigma}_n = \mathbf{D} \left( d\Delta \boldsymbol{\varepsilon}_n - d\Delta \lambda \mathbf{b}_n - \Delta \lambda \left( \frac{\partial \mathbf{b}}{\partial \boldsymbol{\sigma}} \right)_n d\Delta \boldsymbol{\sigma}_n \right) \quad \text{Equation 3-55}$$

Rearranging produces:

$$d\Delta \boldsymbol{\sigma}_n = \mathbf{H}_n (d\Delta \boldsymbol{\varepsilon}_n - d\Delta \lambda \mathbf{b}_n) \quad \text{Equation 3-56}$$

where

$$\mathbf{H}_n = \mathbf{D} \left[ \mathbf{I} + \Delta \lambda \mathbf{D} \left( \frac{\partial \mathbf{b}}{\partial \boldsymbol{\sigma}} \right)_n \right]^{-1} \quad \text{Equation 3-57}$$

Differentiating the consistence equation gives:

$$dF_n = \mathbf{a}_n^T d\Delta \boldsymbol{\sigma}_n - d\Delta \lambda A_n = 0 \quad \text{Equation 3-58}$$

Substituting Equation 3-56 into Equation 3-58 and rearranging yields an expression for the plastic multiplier:

$$d\Delta \lambda = \frac{\mathbf{a}_n^T \mathbf{D}_n d\Delta \boldsymbol{\varepsilon}_n}{A_n + \mathbf{a}_n^T \mathbf{D}_n \mathbf{b}_n} \quad \text{Equation 3-59}$$

Substitution into Equation 3-56 results in the consistent tangent stiffness relationship after some algebraic manipulation.

$$d\boldsymbol{\sigma}_n = \hat{\mathbf{D}}_n d\Delta\boldsymbol{\varepsilon}_n \quad \text{Equation 3-60}$$

where  $\hat{\mathbf{D}}$  is the consistent tangent modulus and is defined as:

$$\hat{\mathbf{D}}_n = \mathbf{H}_n \left[ \mathbf{I} - \frac{\mathbf{b}_n \mathbf{a}_n^T \mathbf{H}_n}{A_n + \mathbf{a}_n^T \mathbf{H}_n \mathbf{b}_n} \right] \quad \text{Equation 3-61}$$

Comparison of the consistent tangent modulus and the continuum tangent modulus (Equation 3-35) shows that they are identical save for the use of the modified elastic stiffness,  $\mathbf{H}$ , instead of the original elastic stiffness,  $\mathbf{D}$ . Examination of Equation 3-57 shows that if  $\Delta\lambda=0$  (i.e. rate of plastic strain is zero) the modified elastic stiffness reduces to the original elastic stiffness. A non-zero value for the plastic strain multiplier activates the second term which is a second derivative of the scalar yield function with respect to the stress tensor. Therefore the change in the yield function gradient during an integration increment is taken into account in the calculation of the consistent tangent material matrix. This consistency ensures quadratic convergence is achieved when the Newton-Raphson scheme is used for the overall equilibrium iterations whereas use of the original material modulus results in only linear convergence. Such a consistent tangent modulus is used in DIANA's plasticity models.

### 3.2 Traditional Fixed Crack Model<sup>2</sup>

Since its introduction in 1968 [Rashid (1968)] the concept of smeared cracking has been approached and formulated in many different ways. The particular formulation presented here is representative of the modern smeared crack models in its use of strain decomposition and choice of orthotropic material law. It is referred to in this text as the ‘Traditional Fixed Crack Model’ in order to differentiate it from the Total Strain Based Crack Model that is investigated later in this thesis. The model is of the Multiple Fixed Crack (MFC) type with a choice of tension cut-off failure criterion. A variety of tension-softening models are available and choice of full, constant or variable shear retention for the post peak behaviour. The formulation of this model within DIANA supports both plane-stress and plane-strain as well as axisymmetric and fully three-dimensional modelling.

#### 3.2.1 Basics

The fundamental assumption of this model is that the total strain,  $\varepsilon$ , may be decomposed into contributions from the elastic strain in the uncracked concrete,  $\varepsilon^e$ , and strains arising from the crack opening smeared over the tributary area,  $\varepsilon^{cr}$ .

$$\varepsilon = \varepsilon^e + \varepsilon^{cr} \quad \text{Equation 3-62}$$

This decomposition is comparable to the strain decomposition employed in plasticity theory. However, unlike plasticity, a secant path is assumed during unloading. Therefore, on the removal of the loading the crack will close completely and the inelastic strain component is completely recovered (Figure 3-5).

---

<sup>2</sup> The term ‘Traditional’ refers to the commonly used formulation of the Crack Model, employing strain decomposition, as proposed by Rots, *et al.* The description of the Traditional Crack Model follows that of the DIANA manual [TNO (1999)] and HERON report on ‘Smeared Crack Approach and Fracture Localisation in Concrete’ [Rots, Nauta, Kusters, Blaauwendraad (1985)].

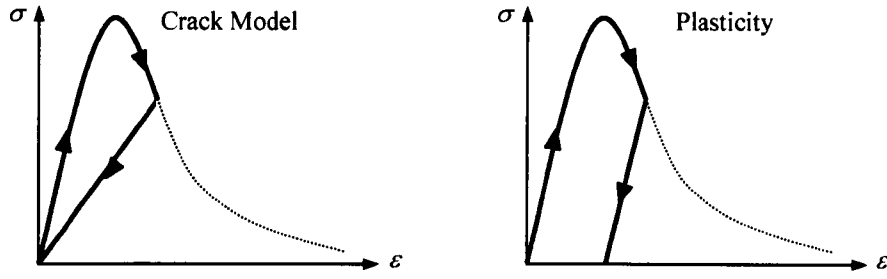


**Figure 3-5 – Comparison of Unloading Behaviours**

The aim of this decomposition is to separate the behaviour of the crack and the intact concrete. This is partly done for conceptual reasons; the crack may be considered as a separate entity. Thus the Crack Model appears more similar to the discrete crack model. A further consequence of the decomposition it is that possible to further decompose the crack strain into separate contributions from a number of individual cracks thus leading to a Multiple Fixed Crack formulation.

$$\boldsymbol{\varepsilon}^{cr} = \mathbf{N} \mathbf{e}^{cr} \quad \text{Equation 3-63}$$

where  $\mathbf{e}^{cr}$  is the vector assembled from the individual crack strains,  $\mathbf{e}_n^{cr}$ , and  $\mathbf{N}$  is the vector assembled from the corresponding transformations matrices,  $\mathbf{N}_n$ .

$$\mathbf{e}^{cr} = [\mathbf{e}_1^{cr} \quad \mathbf{e}_2^{cr} \quad \dots \quad \mathbf{e}_n^{cr}]^T \quad \text{Equation 3-64}$$

$$\mathbf{N} = [\mathbf{N}_1 \quad \mathbf{N}_2 \quad \dots \quad \mathbf{N}_n] \quad \text{Equation 3-65}$$

On the formation of each crack a corresponding local coordinate system,  $nst$ , is set-up as shown in Figure 3-6.

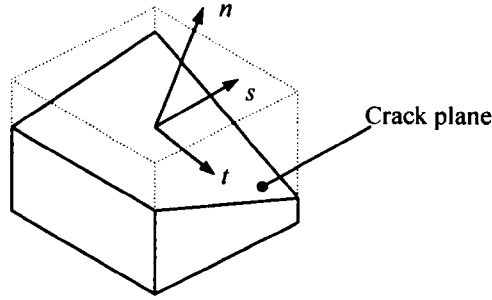


Figure 3-6 - Crack Coordinate System

The strain for crack  $i$  can then be expressed as follows:

$$\mathbf{e}_i^{cr} = [\varepsilon_{nn,i}^{cr} \quad \varepsilon_{ns,i}^{cr} \quad \varepsilon_{in,i}^{cr}]^T \quad \text{Equation 3-66}$$

where  $\varepsilon_{nn}^{cr}$  is the mode I crack strain (tension) and  $\varepsilon_{ns}^{cr}$  and  $\varepsilon_{in}^{cr}$  are the mode II and III crack strains respectively (shear). Rotation from the crack coordinate system to the global system is performed via the associated transformation matrix  $\mathbf{N}$ .

$$\mathbf{N} = \begin{bmatrix} c_{xn}^2 & c_{xn}c_{xs} & c_{xt}c_{xn} \\ c_{yn}^2 & c_{yn}c_{ys} & c_{yt}c_{yn} \\ c_{zn}^2 & c_{zn}c_{zs} & c_{zt}c_{zn} \\ 2c_{xn}c_{yn} & c_{xc}c_{ys} + c_{xs}c_{yn} & c_{xt}c_{yn} + c_{xn}c_{yt} \\ 2c_{yn}c_{zn} & c_{yc}c_{zs} + c_{ys}c_{zn} & c_{yt}c_{zn} + c_{yn}c_{zt} \\ 2c_{zn}c_{xn} & c_{zc}c_{xs} + c_{zs}c_{xn} & c_{zt}c_{xn} + c_{zn}c_{xt} \end{bmatrix} \quad \text{Equation 3-67}$$

where  $c_{xn} = \cos \theta_{xn}$ , the cosine between the  $x$  &  $n$  axes, etc (Figure 3-7).

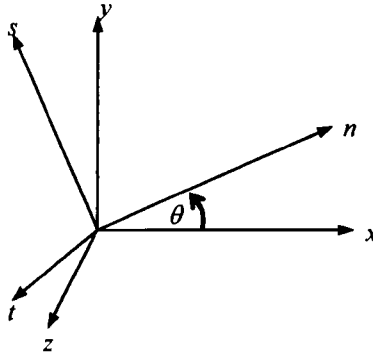


**Figure 3-7 – Angles Between Local and Crack Co-ordinate Systems Used To Calculate Direction Cosines**

Similarly the crack stresses are expressed as an assemblage of stresses from each crack.

$$\mathbf{s}^{cr} = [\mathbf{s}_1^{cr} \quad \mathbf{s}_2^{cr} \quad \dots \quad \mathbf{s}_n^{cr}]^T \quad \text{Equation 3-68}$$

where each stress term is defined as:

$$\mathbf{s}_i^{cr} = [\sigma_{nn,i}^{cr} \quad \sigma_{ns,i}^{cr} \quad \sigma_{st,i}^{cr}]^T \quad \text{Equation 3-69}$$

The relationship between the global stress vector and the crack stress vector is also made via the rotation matrix,  $\mathbf{N}$ .

$$\mathbf{s}^{cr} = \mathbf{N}^T \boldsymbol{\sigma} \quad \text{Equation 3-70}$$

The basic assumption is made that the crack stresses are a direct function of the crack strains.

$$\mathbf{s}^{cr} = f(\mathbf{e}^{cr}) \quad \text{Equation 3-71}$$

The above relationship is defined in the constitutive relationship as:

$$\mathbf{s}^{cr} = \mathbf{D}_{secant}^{cr} \mathbf{e}^{cr} \quad \text{Equation 3-72}$$

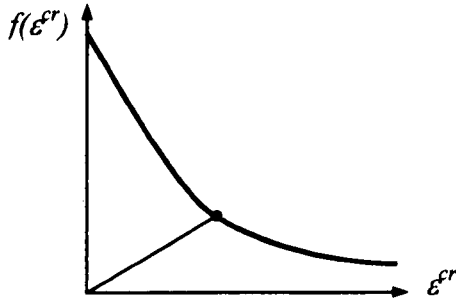
Which expands to:

$$\begin{bmatrix} \sigma_{nn}^{cr} \\ \sigma_{ns}^{cr} \\ \sigma_{st}^{cr} \end{bmatrix} = \begin{bmatrix} D_{secant}^I & 0 & 0 \\ 0 & G & 0 \\ 0 & 0 & G \end{bmatrix} \begin{bmatrix} \epsilon_{nn}^{cr} \\ \epsilon_{ns}^{cr} \\ \epsilon_{st}^{cr} \end{bmatrix} \quad \text{Equation 3-73}$$

where the subscripts,  $i$ , have been omitted for clarity.

The assumption that the coupling terms are zero implies that there is no interaction between the normal and shear behaviour on the crack. It can be argued that for pure mode-I failure the effects of shear and coupling terms are negligible. Indeed, the reason to omit coupling terms was because it was considered that the increased level of sophistication necessary was not out-weighted by a corresponding increase in accuracy and realism. However, it is also true that for more complex stress states coupling becomes more important. For example, the presence crack-dilatancy results in shear strains inducing normal strain. (It is interesting to note that the Total Strain Based Crack Model investigated later in this thesis extends the concept of coupling further by modelling the interaction between orthogonal cracks. However the effects produced are subtle and only become significant when modelling the effects of lateral cracking on compression behaviour). Ultimately the analyst must be aware of the simplifications made in the formulation and consider their possible effects on the analysis.

The mode-I secant modulus,  $D_{secant}^I$ , is obtained via the mode-I softening relationship (Figure 3-8) as follows:



$$D_{secant}^I = \min \begin{cases} D_{secant, previous}^I \\ \frac{f(\epsilon_{nn}^{cr})}{\epsilon_{nn}^{cr}} \end{cases} \quad \text{Equation 3-74}$$

Figure 3-8 – Mode-I Softening Relationship



If unloading is induced the current secant stiffness is frozen and remains so until the strain level exceeds the previously attained maximum value. As stated above, this results in complete recovery of the crack strain upon full unloading. This is conceptually equivalent to a complete closure of the crack. Also, reloading of a previously cracked element produces a suitably softer response than the initial loading. Options relating to the choice of softening relationship are covered in more detail later in this chapter.

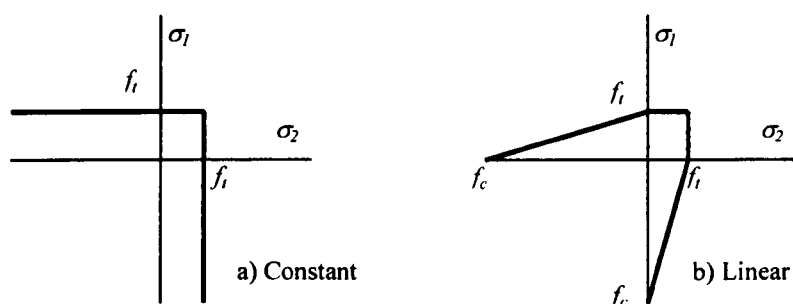


**Figure 3-9 – Two Options for Tension Failure Criterion**

The initiation of the first crack at a sample point is governed by the Rankine criterion. Both a traditional Rankine criterion with a constant material strength,  $f_t$ , and one where  $f_t$  reduces linearly with increasing lateral compressive stress are available (Figure 3-9). If the principal stress exceeds the material strength then a crack plane is formed normal to the principal stress direction. As this is a Fixed Crack Model the orientation of this crack remains constant throughout the subsequent stages of the analysis. In addition to the Rankine criterion the formation of additional cracks must satisfy the condition that the angle between the existing cracks and the principal stress exceeds the value of the *threshold angle*,  $\alpha_{TD}$  (Figure 3-10).

Due to this second constraint it is possible for the situation to arise where the principal stress temporarily exceeds the material strength.

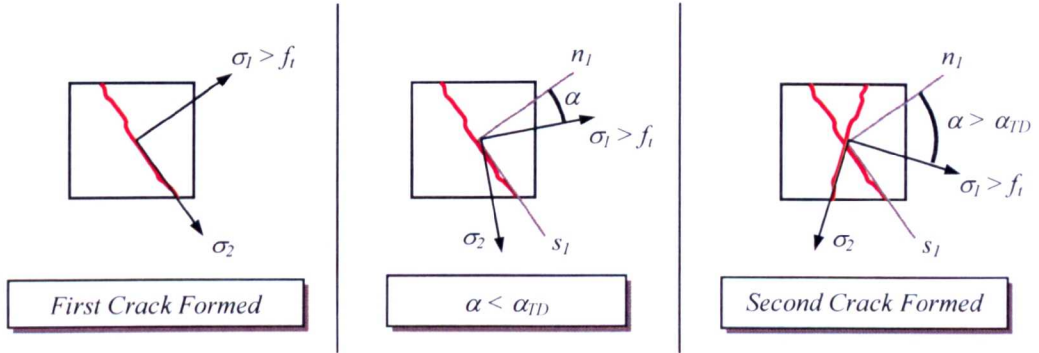


Figure 3-10 - Initial and Subsequent Crack Formation

### 3.2.2 Constitutive Equations

The derivation of the constitutive equations for cracked concrete starts from the strain decomposition expression (Equation 3-62).

$$\boldsymbol{\sigma} = \mathbf{D}(\boldsymbol{\varepsilon} - \boldsymbol{\varepsilon}^{cr}) \quad \text{Equation 3-75}$$

Substitution of Equation 3-63 leads to:

$$\boldsymbol{\sigma} = \mathbf{D}(\boldsymbol{\varepsilon} - \mathbf{N}\mathbf{e}^{cr}) \quad \text{Equation 3-76}$$

Substitution of the equation relating crack and global stress (Equation 3-70) and the crack stress and strains (Equation 3-72) leads to the following:

$$\boldsymbol{\sigma} = \mathbf{D}(\boldsymbol{\varepsilon} - \mathbf{N}[\mathbf{D}_{secant}^I]^{-1} \mathbf{N}^T \boldsymbol{\sigma}) \quad \text{Equation 3-77}$$

Which requires some algebraic manipulation to give the final relationship between total stress and total strain.

$$\boldsymbol{\sigma} = \left[ \mathbf{D} - \mathbf{D}\mathbf{N}[\mathbf{D}_{secant}^I + \mathbf{N}^T \mathbf{D}\mathbf{N}]^{-1} \mathbf{N}^T \mathbf{D} \right] \boldsymbol{\varepsilon} \quad \text{Equation 3-78}$$

It is common to express the reduction in normal and shear stiffness in terms of the scaling factors  $\mu$  and  $\beta$  respectively. The diagram below (Figure 3-11) shows how the sum of the elastic (uncracked concrete) and the inelastic (crack) material behaviour produces the combined cracked concrete response.

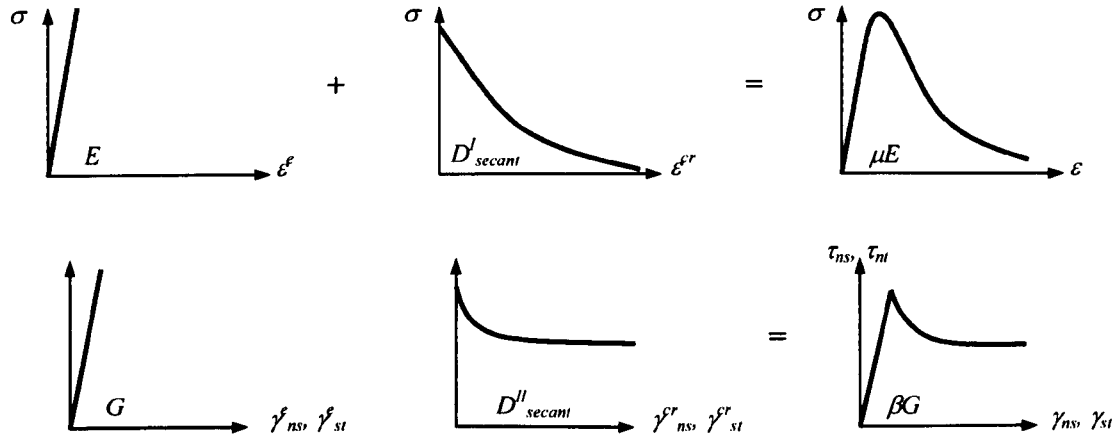


**Figure 3-11 - Equivalence of Traditional Crack Parameters**

The relationship is determined algebraically by considering the linear-elastic stiffness matrix. In this case the matrix for plane stress:

$$\mathbf{D} = \frac{E}{1-\nu^2} \begin{bmatrix} 1 & \nu & 0 \\ \nu & 1 & 0 \\ 0 & 0 & \frac{1}{2}(1-\nu) \end{bmatrix} \quad \text{Equation 3-79}$$

The assumption is made that the crack coordinate system is aligned with the global system. As a consequence the rotation matrix,  $\mathbf{N}$  reads:

$$\mathbf{N} = \begin{bmatrix} 1 & 0 & 0 \\ 0 & 0 & 1 \end{bmatrix}^T \quad \text{Equation 3-80}$$

Substituting the total stress-total strain relationship derived above (Equation 3-78) into Equation 3-80 above and then performing some algebraic manipulation produces:

$$\begin{bmatrix} \sigma_x \\ \sigma_{yx} \\ \sigma_{yz} \end{bmatrix} = \begin{bmatrix} \frac{\mu E}{1-\mu\nu^2} & \frac{\mu\nu E}{1-\mu\nu^2} & 0 \\ \frac{\mu\nu E}{1-\mu\nu^2} & \frac{\mu E}{1-\mu\nu^2} & 0 \\ 0 & 0 & \frac{\beta E}{2(1+\nu)} \end{bmatrix} \begin{bmatrix} \varepsilon_x \\ \varepsilon_{xy} \\ \varepsilon_{yz} \end{bmatrix} \quad \text{Equation 3-81}$$

where  $\mu$  and  $\beta$  are defined in terms of the secant stiffness moduli as:

$$D'_{secant} = \frac{\mu}{1-\mu} E \quad D''_{secant} = \frac{\beta}{1-\beta} G \quad \text{Equation 3-82}$$

### 3.2.3 Softening Models

Crack opening and softening is considered to be controlled by mode-I fracture energy,  $G_f$ . The advantage of this approach over less sophisticated models is detailed below.

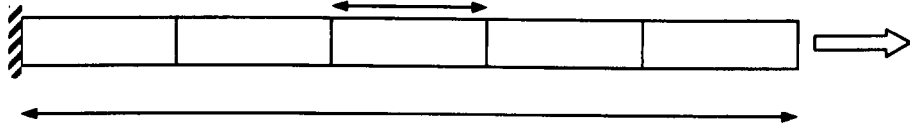


Figure 3-12 - 1D Bar Extension

Figure 3-12 shows a classic 1-D bar extension test. The length of the bar is  $l$  and, in this instance, has been discretised by 5 elements. The centre element has a slight imperfection shown by a small reduction in strength when compared to the surrounding elements. Under uniaxial loading the bar will initially behave elastically until the material strength is exceeded. At this stage cracking will initiate in the centre element and this will lead to strain localisation and elastic unloading of the other elements. Ultimately these other elements will return to zero strain whilst the cracked element will reach the strain  $\varepsilon_{nn,ult}^r$ .

Therefore, the extension of the bar,  $\Delta l$  is given by:

$$\Delta l = \varepsilon_{nn,ult}^{cr} h = \varepsilon_{nn,ult}^{cr} \frac{l}{n} \quad \text{Equation 3-83}$$

where  $n$  is the number of elements the bar is divided into. The average strain in the bar can therefore be calculated.

$$\varepsilon = \frac{\Delta l}{l} = \frac{\varepsilon_{nn,ult}^{cr} l}{nl} = \frac{\varepsilon_{nn,ult}^{cr}}{n} \quad \text{Equation 3-84}$$

Thus it is clear, that for a constant value of ultimate strain, as the level of discretisation increases the average strain in the bar decreases and the global structural response becomes more brittle. Figure 3-13 also shows that less energy is required to soften smaller elements and at some level of discretisation,  $\alpha$ , no additional energy is needed to soften the cracked element.

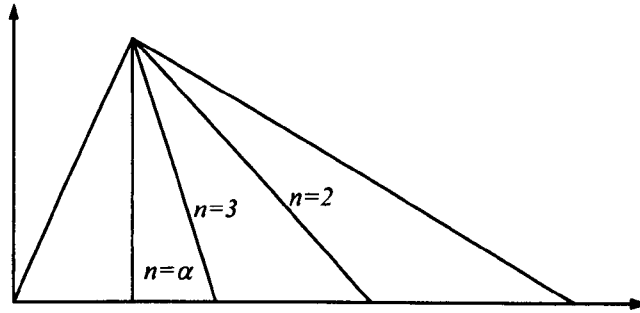


**Figure 3-13 - Effects Of Discretisation On Global Structural Response**

These potential problems can be avoided by defining  $\varepsilon_{nn,ult}^{cr}$  in terms of fracture energy,  $G_f$ . This parameter is defined as the amount of energy required to open a unit area of crack and is taken to be a material property. For an individual element the following relationship holds:

$$G_f^l = h \int_{\varepsilon_{nn}^{cr}=0}^{\varepsilon_{nn}^{cr}=\infty} \sigma_{nn}^{cr}(\varepsilon_{nn}^{cr}) d\varepsilon_{nn}^{cr} \quad \text{Equation 3-85}$$

where  $h$  is the ‘crack band width’ and is a measure of the equivalent crack length. The relationship is depicted graphically in Figure 3-14

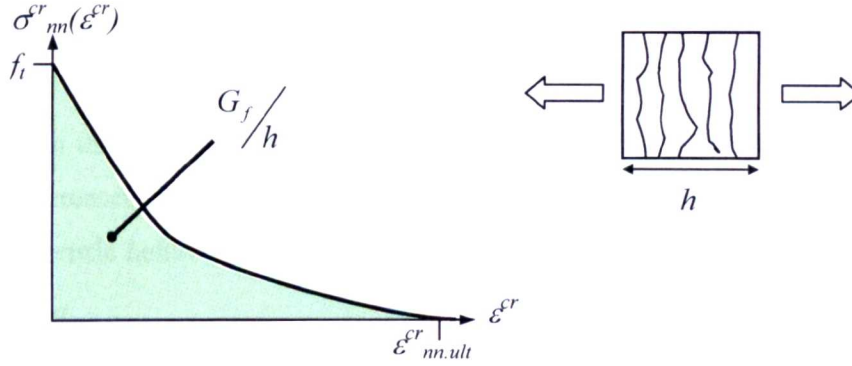


**Figure 3-14 - Fracture Energy**

Adopting this approach based on fracture energy ensures that mesh objectivity is retained during the failure process.

The relationship between crack stress,  $\sigma_{nn}^{cr}$ , and crack strain,  $\epsilon_{nn}^{cr}$  is given by the relationship in Equation 3-86. The function  $y()$ , represents the actual softening diagram chosen.

$$\sigma_{nn}^{cr} = f_t \cdot y\left(\frac{\epsilon_{nn}^{cr}}{\epsilon_{nn,ult}^{cr}}\right) \quad \text{Equation 3-86}$$

Substitution of Equation 3-86 into Equation 3-85 and then substituting the integration

variable,  $\epsilon_{nn}^{cr}$  for  $\chi = \frac{\epsilon_{nn}^{cr}}{\epsilon_{nn,ult}^{cr}}$  results in the following relationship:

$$G_f^I = h \cdot f_t \left( \int_{\chi=0}^{\chi=\infty} y(\chi) d\chi \right) \epsilon_{nn,ult}^{cr} \quad \text{Equation 3-87}$$

Ultimate crack strain is assumed to have some finite limit therefore can be expressed as:

$$\epsilon_{nn,ult}^{cr} = \frac{1}{\alpha} \frac{G_f^I}{h \cdot f_t} \quad \text{where, } \alpha = \int_{\chi=0}^{\chi=\infty} y(\chi) d\chi \quad \text{Equation 3-88}$$

However, this approach does impose some limits on the element size. For example, considering a material with a linear softening response (Figure 3-15), the Softening modulus,  $E_s$ , is given by:

$$E_s = \left[ \frac{2G_f}{hf_t^2} - \frac{1}{E} \right]^{-1} \quad \text{Equation 3-89}$$

It is clear from this relationship that as the size of the element increases the crack band width also increases. Hence the gradient of the softening slope gets steeper. At some critical value brittle behaviour will be produced and beyond which snap-back will occur.

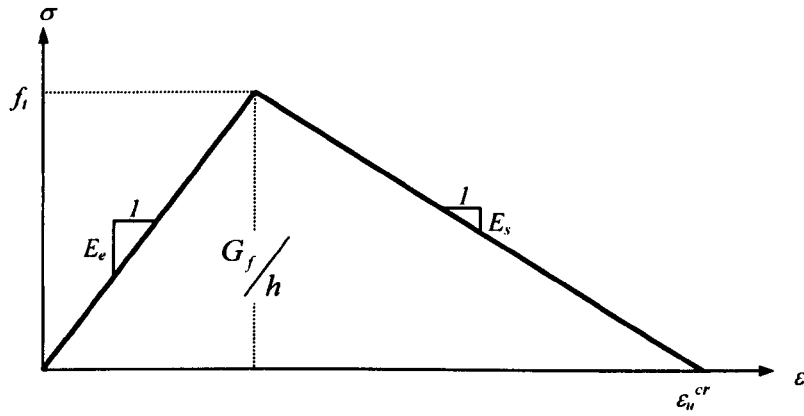
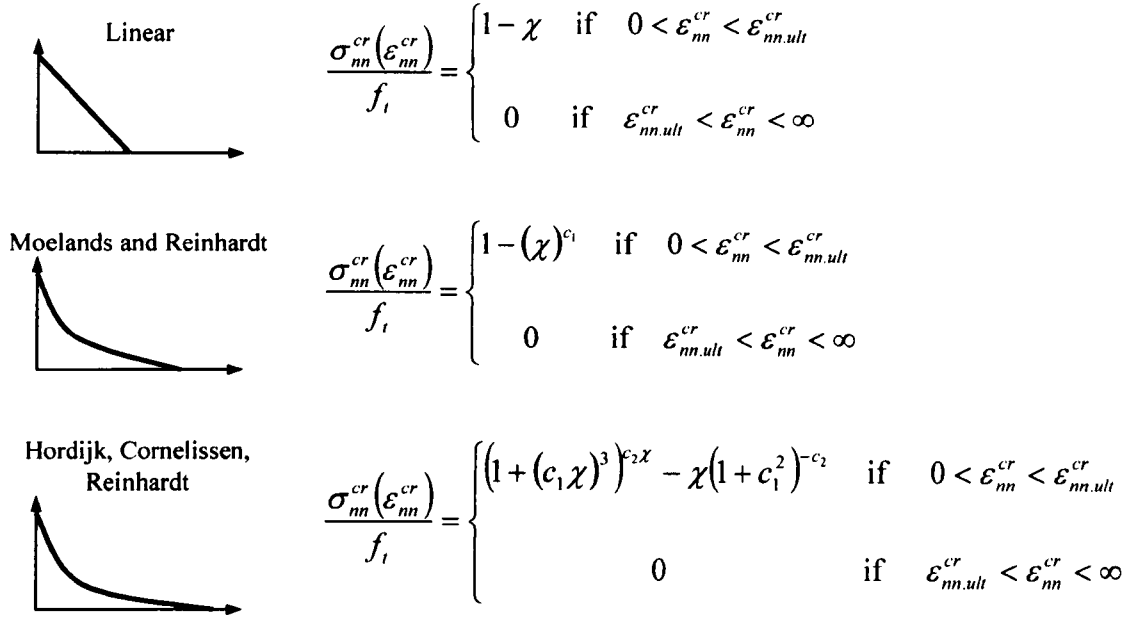


Figure 3-15 - Geometry of Material Stress-Strain Response Diagram

In order to avoid this the crack band width must not exceed the value given by:

$$h_{\max} = \frac{G_f E}{\alpha f_t^2 \frac{dy}{d\chi} \Big|_{\chi=0}} = \frac{2G_f E}{f_t^2} \quad \text{Equation 3-90}$$

Figure 3-16 below details the three energy based softening models available. Coefficients  $c_1$  and  $c_2$  are user defined and modify the curvature of the non-linear softening models.



**Figure 3-16 - Fracture Energy Based Softening Models**

In addition to these models two not based on fracture energy are presented. These being the brittle cracking model, where strength is reduced to zero upon cracking, and the multi-linear model, which allows the user to define the slope (Figure 3-17).



**Figure 3-17 - Non-Energy Based Softening Models**

### 3.2.4 Shear Stiffness Reduction

Three options are available to model the reduction of shear stiffness upon cracking. The simplest of which is full shear retention, i.e. the elastic modulus  $G$  is not reduced. The second is a constant reduction of the shear stiffness. This is defined via the relationship:

$$D_{\text{secant}}'' = \frac{\beta}{1 - \beta} G \quad \text{Equation 3-91}$$



where  $\beta$  is the so-called *shear reduction factor* and takes a value between 0 and 1.

Also available is an extension of this approach where the retention factor is defined as a function as follows:

$$\beta = \frac{1}{1 + 4447 \varepsilon_{nn}^{cr}} \tag{Equation 3-92}$$

This has the advantage that as the crack opens the shear resistance decreases and with a wide-open crack the shear resistance approaches zero (Figure 3-18).

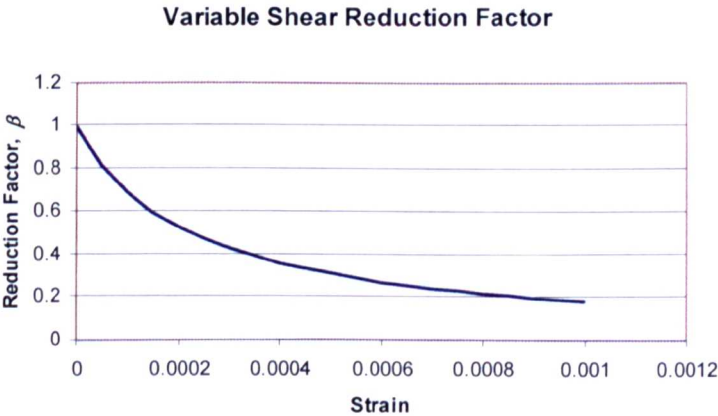


Figure 3-18 - Variable Shear Reduction Factor

### **3.3 Summary**

It can be seen from the above that both the Multi-Surface Plasticity Model and the Traditional Crack Model provide suitable constitutive frameworks with which the tensile fracturing behaviour of concrete can be modelled sufficiently accurately. The Plasticity Model assesses and updates the stress state in 3D stress space throughout. The yield conditions are defined as a surface in this space and a flow rule defines the evolution of the yield surface due to damage via cracking, crushing, etc. In contrast the Traditional Crack Model assesses the stress state as set of equivalent uniaxial cases. For each case the yield condition is defined via a maximum strength criterion and the subsequent evolution of the material due to cracking is simply defined via a 1D tensile stress-strain relationship. The combination of these equivalent uniaxial cases gives a realistic representation of an orthotropic material such as fractured concrete. In the following chapter these constitutive models will be used to analyse anchor pullout problems and their performance will be assessed.

## **CHAPTER 4**

### **2D and Preliminary 3D Modelling**

In this chapter the preliminary work on anchor modelling and analysis is presented. The first section covers 2D, plane-stress modelling of the RILEM anchor bolt problem. This problem was used as a benchmark with which to evaluate the performance of both the Multi-Surface Plasticity and Traditional Multiple Fixed Crack Models. Comparisons are also made with results produced by other researchers. In the second section a more realistic anchor bolt geometry is considered. In addition to plane-stress analysis, this problem was also analysed under axisymmetric conditions. The effects of lateral confinement are investigated as a precursor to edge effect investigation. A basic model for anchor expansion is also developed along with investigation and analysis of the failure mechanisms produced. In the final section the anchor problem is extended into three dimensions. Discussion of the added complexities of geometric model creation in 3D is presented. The effects of anchor position and edge distance are also investigated in brief.

All modelling was carried out using the finite element package DIANA v7.2 [TNO (1999)] on a 450MHz Sun Ultra10 with 576MB of physical ram.

#### **4.1 RILEM Benchmark Problem**

The first anchor problem to be analysed in this work was the RILEM round robin problem presented in Chapter 2. The original challenge had attracted 27 submissions with a great number of different numerical models and modelling approaches used. Therefore the problem represented an ideal benchmark with which to test the modelling features and abilities of both the Multiple Fixed Crack Model and the Multi-Surface Plasticity Models.

##### **4.1.1 Problem Details**

The invitation to the round robin analysis offered the choice of several variations on the basic problem geometry relating to the ratio of anchor depth to support spacing. The dimensions of the particular problem chosen for this study are shown in Figure 4-1 and

are the ones most commonly selected for investigation by contributors to the round robin analysis. The optional lateral confinement stiffness, as defined in the model specification, was set as zero.

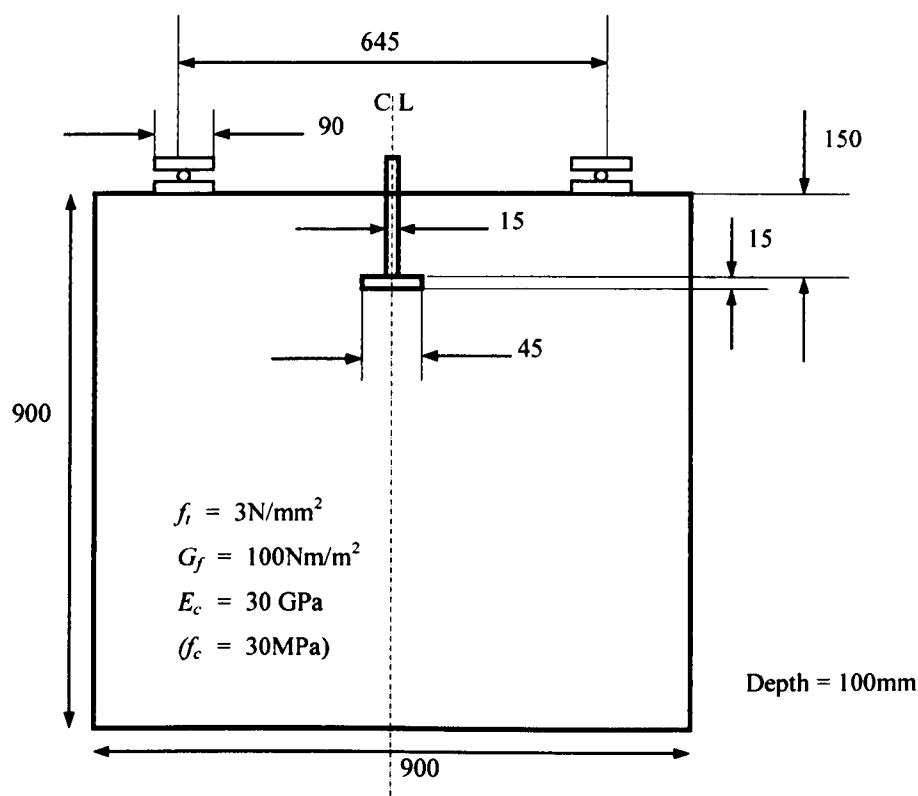


**Figure 4-1 - RILEM Problem Geometry and Material Properties**

The problem was analysed under plane stress conditions. Owing to the symmetry about the centre-line (CL) it was possible to analyse the problem by considering only one half of the structure. Of course, this negated the possibility of non-symmetric crack formation but this approach was followed by the majority of contributors to the round robin and thus allowed more direct comparisons to be made between their results and those produced here. By considering the action of the anchor a further simplification was made. Since the steel anchor was not bonded to the surrounding concrete the interaction between the two was assumed to be minimal therefore the primary action of the anchor was to transmit the pullout load to the concrete. This was simplified by removing the steel anchor from the model and applying the load directly to the concrete (as detailed in the diagram below).

The final simplification was to replace the loading platen with a single point restraint positioned at the platen centre.

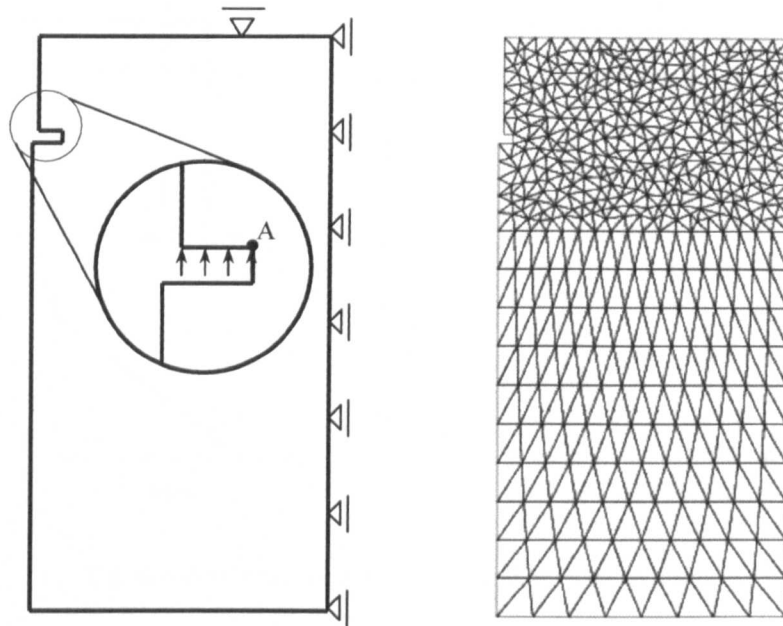


**Figure 4-2 – Boundary Conditions, Load Application and Finite Element Mesh for RILEM Problem**

The problem was then discretised by approximately 1000, 3-noded triangular elements. An unstructured mesh was chosen so as to avoid mesh alignment problems. Also, the discretisation was set to be finer in the zone likely to experience cracking and coarser for the intact zone (Figure 4-2).

This problem was analysed using both the Crack Model and the combined Rankine/Von Mises Plasticity Model (see Chapter 3 for details), (Figure 4-3). For the Crack Model the Rankine failure criterion with a constant tensile strength ( $f_t$ ) was used. A linear softening model governed post-crack tensile softening whilst shear was controlled by a constant shear retention factor ( $\beta$ ) of 0.03. Softening behaviour in the Plasticity Model was modelled via a Hordijk non-linear softening diagram. For both models the load as applied as a prescribed displacement acting on the top edge of the anchor notch.

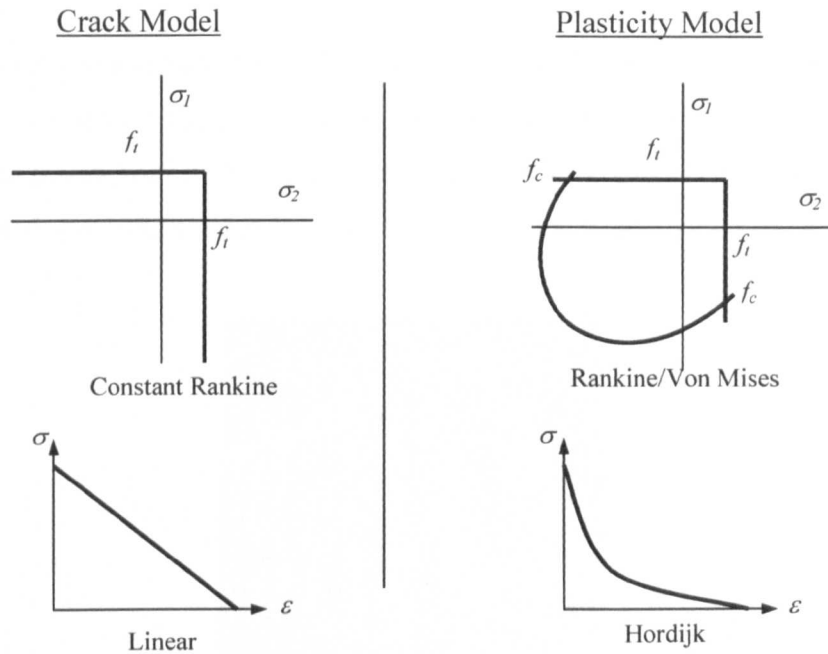


**Figure 4-3 - Failure and Tension Softening Models Used**

#### 4.1.2 RILEM Analysis Results

The displaced shapes for both analyses are very similar (Figure 4-4). In both cases a crack initiated at the anchor tip and progressed through the concrete towards the support point. The majority of the researchers involved in the round robin analyses reported similar behaviour and this showed that the support position had a very strong influence on the crack direction.

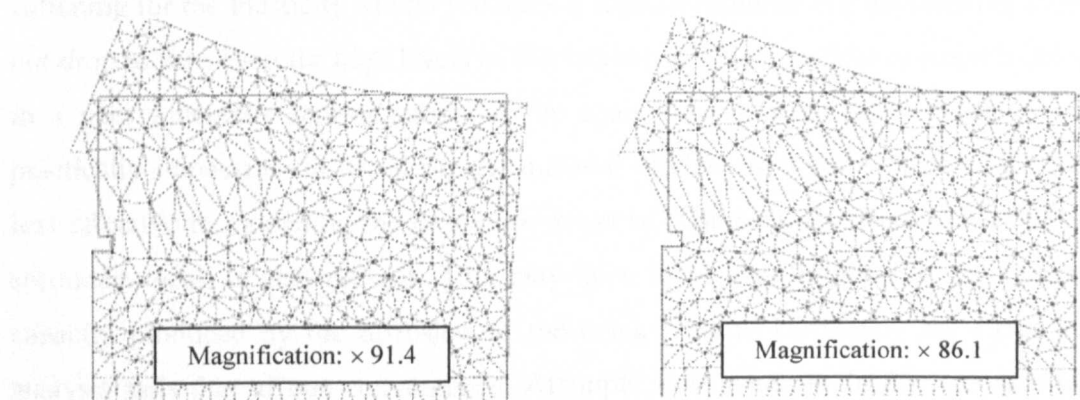


**Figure 4-4 - Displaced Shape a) Crack Model, b) Plasticity Model**

Comparison of the two results shows that the crack zone for the Plasticity Model is more localised than the more diffuse pattern seen for the crack model. This can be seen more clearly seen in the contour plot of effective plastic strain (Figure 4-5). The width of the crack stays relatively constant and is either 1 or 2 elements wide.

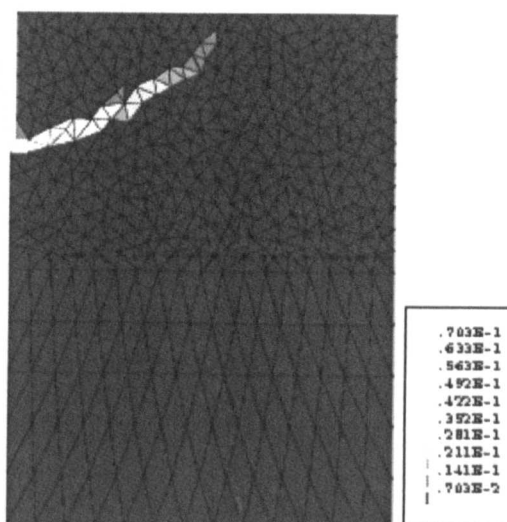


**Figure 4-5 - Effective Plastic Strain for RILEM Problem (Plasticity Model)**

The effects of the differing crack zones can be seen in the load-displacement plot (Figure 4-6). Initially both models exhibit the same linear-elastic response. In the subsequent stages of the analysis the diffuse cracking of the Crack Model allows the tensile forces to be spread over a larger area and thus resulting in a higher failure load. Post-peak softening for the Plasticity Model produces a smooth response but the resisting load does not drop to zero even for high levels of displacement. This is typical of stress locking due to a poor kinematic representation of the crack discontinuity (see Chapter 6) and is practically impossible to avoid for the material models used here. The Crack Model is less effective in modelling the post-peak response. The peak itself is well defined but a secondary peak is also present. This may be a local manifestation of the increase in capacity produced by the diffusion of the crack pattern. Ultimately the Crack Model analysis fails due to non-convergence. Attempts were made to further the analyses by reducing the analysis step size, increasing the maximum number of iterations permitted

and modifying the non-linear solution scheme. However none of these options proved particularly successful.

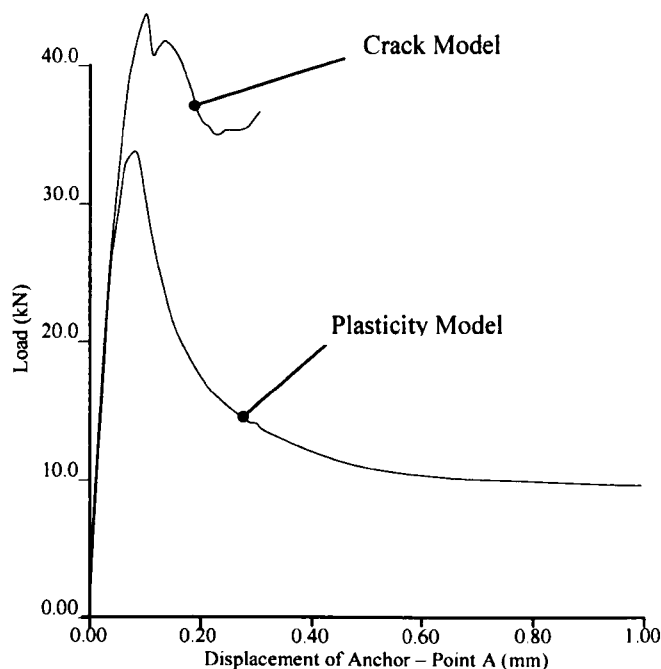


**Figure 4-6 - Load-Displacement Plots for RILEM Analysis Using Crack Model and Plasticity Model**

As there is a wide scatter of results, comparison of these load-displacement responses with those produced by contributors to the round robin analysis proved to be difficult, especially in the post peak response. However comparison of the peak load was possible. The mean peak load produced via analytical methods for the particular RILEM geometry considered here was 42.7kN (with a standard deviation of 9.7). This compares well with the peak load value of 41.5kN produced with the Crack Model here. The Plasticity Model produced a lower peak of 32.4kN, however, it is closer to the mean peak load of 34.5kN produced by experimental testing. It is not possible to say on this basis alone that the Plasticity Model is more accurate. Indeed one of the main conclusions from the round robin analysis was that although it was possible to analyse the problem with a reasonable degree of accuracy with the methods considered, differing choices in such factors as mesh discretisation, boundary conditions and material properties lead to a great heterogeneity in the results [di Tommaso and Manfronti (1993)]. However because the Plasticity Model



proved to be better capable of modelling post-peak behaviour and was more stable it was adopted for subsequent 2D analysis work.

**4.2 Expansion Anchor Modelling in 2D**

The anchor type considered in the RILEM round robin analysis was of the ‘cast-in place’ type and uses mechanical interlock in order to transmit pullout forces into the base material. The focus of this research work was expansion anchors in which the pullout forces are transmitted across a frictional bond between the anchor and concrete. This frictional bond is activated as a result of expansion forces applied by the anchor onto the face of the hole. However, in order to simplify the modelling of such an anchor it was assumed that the frictional bond was sufficiently strong so as not to allow any sliding and therefore the interface could be modelled as a fully bonded connection. Later detailed analysis of the interfacial behaviour between anchor and concrete showed this result to be reasonable (Chapter 8). The Rawl M12 SafetyPlus anchor was chosen as the basis of the geometry for the new problem as it is typical of anchors of this type. Details on the failure load of the anchor when positioned at various edge distances were available in the design guide [Rawl, (1997)] and provided a benchmark against which the analysis work could be measured.

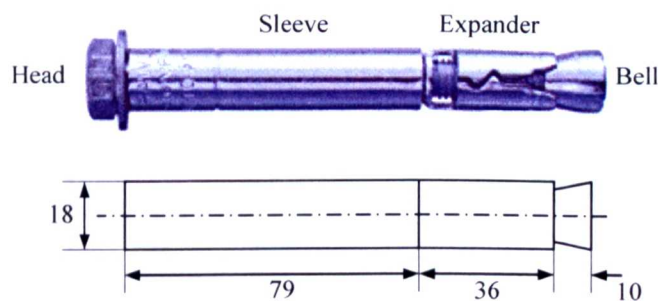


**Figure 4-7 - Rawl SafetyPlus Anchor and FE Model Geometry**

The geometry of the anchor problem illustrated in Figure 4-7 above shows how the anchor is split into a sleeve and expander section. The expander was fully bonded to the concrete over its full length whereas the sleeve remained completely unbonded. This treatment of the expander-concrete interface is rather simplistic as it did not account for the variation in shear strength over the length of this interface but it was taken as a reasonable initial approximation. The expansion bell is also shown although it had no significant influence on the analyses.

As mentioned earlier the position of the supports in the RILEM problem had a significant effect on the crack formation and hence structural response. The ratio of support span to anchor embedment depth had been chosen to be close to that specified in the EOTA (European Organisation for Technical Approvals) guidelines [EOTA (1997)] for tension test rigs. However it was appealing to investigate the nature of crack formation and propagation in cases where these factors were not significantly influenced by supports. It can also be argued that the test conditions specified in the EOTA guidelines are slightly artificial. The arrangement of the testing equipment is shown in Figure 4-8a. It can be seen that the testing machine is positioned on the concrete specimen and this induces compressive stresses at the support points hence influencing the crack formation. However, in the case of a fixture being suspended from a concrete ceiling by an anchor bolt the supports are remote from the anchor, therefore the crack formation is not influenced in this way.

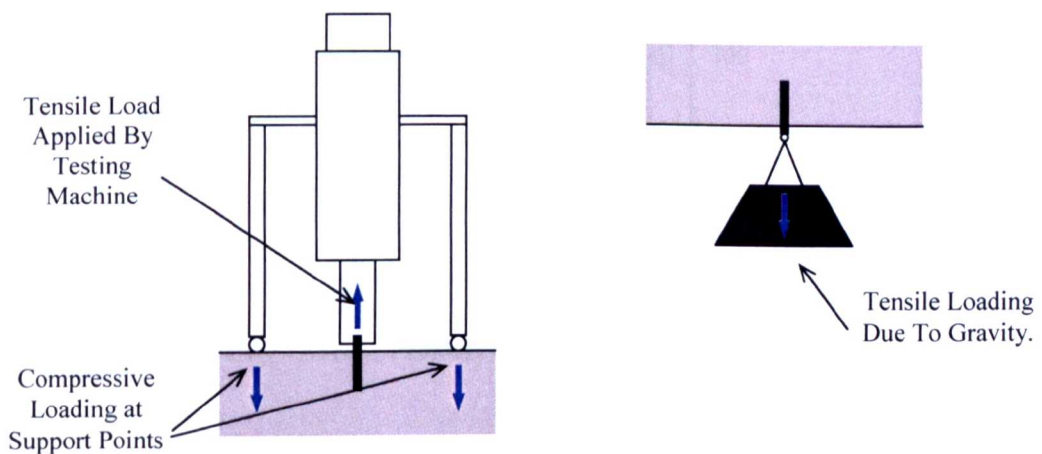


**Figure 4-8 - a) Anchor Testing Equipment, b) Fixture Suspended from Ceiling by Anchor Bolt**

#### 4.2.1 Plane Stress Modelling of Anchor Bolt

Although plane-stress modelling isn't a particularly suitable approach for the analysis of expansion anchor bolts as it doesn't take into account the important circumferential stresses, it did provide an ideal transitional stage between the plane-stress modelling of the RILEM problem and the subsequent axisymmetric modelling of the expansion anchor. When considering the boundary conditions, the concrete block was considered as being part of a larger structure (Figure 4-9). This resulted in horizontal displacement restraints on the right-hand boundary and vertical restraints on the bottom boundary. Horizontal restraints were also applied on the left-hand boundary to account for symmetry conditions.

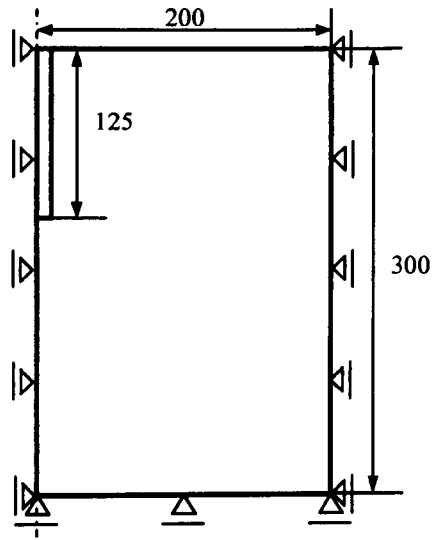
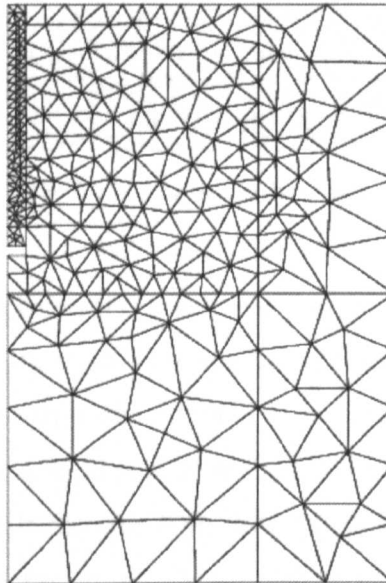


Figure 4-9 - Anchor Problem Boundary Conditions and Dimensions

A number of factors were considered when choosing the dimensions of the block. For the M12 SafetyPlus anchor the minimum recommended embedment is 105mm. A depth of 115mm was chosen for the problem thus the depth of the concrete block had to be 230mm or greater. A lesser depth would mean that the distance from the bottom of the expander to the base of the block was less than to the top. This would result in a tendency for the crack to propagate downwards as this path offers less resistance. A depth of 300mm was chosen. The width of the block was required to be wide enough to encompass the complete concrete failure cone. Rawl guidelines suggested that the full anchor capacity

was reached with an edge distance of 200mm. Therefore this was adopted as the block width. Loading was applied in the form of a prescribed displacement to the top surface (head) of the anchor bolt.

The problem was meshed using approximately 600, 3-noded plane stress triangular elements as before, with a higher level of discretisation around the anchor bolt (Figure 4-10). The combined Rankine von Mises Plasticity Model was used with material properties the same as those used for the round robin analysis.



**Figure 4-10 - Anchor Bolt Problem FE Mesh**

Computation of the problem was complete successfully however results showed that the crack intersected the right-hand boundary rather than reaching the top of the block (Figure 4-11). This result is an indication that without the influence of the supports on the top of the concrete block the natural angle that the crack assumes is much shallower.

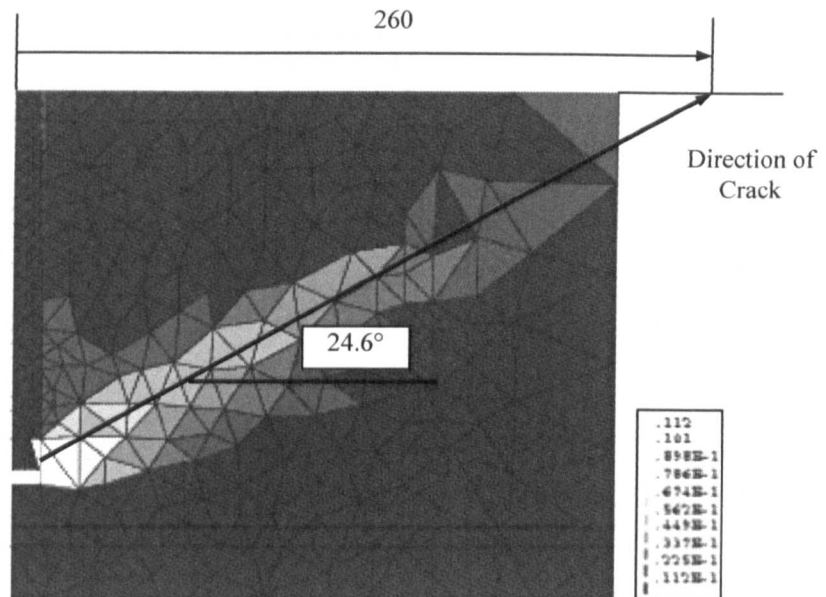


**Figure 4-11 - Effective Plastic Strain for Anchor Bolt Problem**

Figure 4-12 is the load-displacement graph for this analysis where displacement is measured at the anchor head (the position where the applied displacement was applied). It shows that the initial response from the problem is essentially linear-elastic followed by some softening behaviour and a local peak at around 28kN. This is the expected response and compares well with the behaviour seen with the round robin problem. However, instead of unloading, the response shows a short plateau section followed by a significant increase in the load resisted as the anchor displacement is increased.

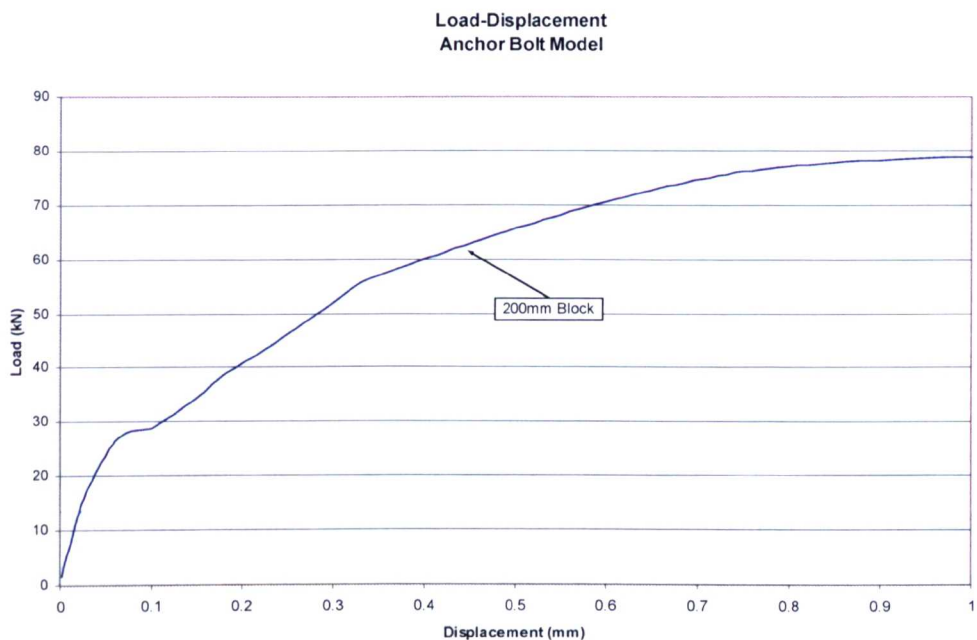


**Figure 4-12 - Load-Displacement Graph for Anchor Bolt Problem**

This behaviour is caused due to the influence of the boundary and may be illustrated by considering the stress state in the cone section of the concrete block (Figure 4-13). As the crack progresses through the structural action of the concrete the cone becomes comparable to that of a cantilever beam. The right-hand boundary provides the horizontal support whilst the intact concrete below provides vertical support. The pullout force causes the top of the ‘beam’ to go into compression and the bottom into tension. This compressive strut effectively suppresses the tensile stress state required to allow further cracking and reduction in the structure’s ability to sustain increased loading.



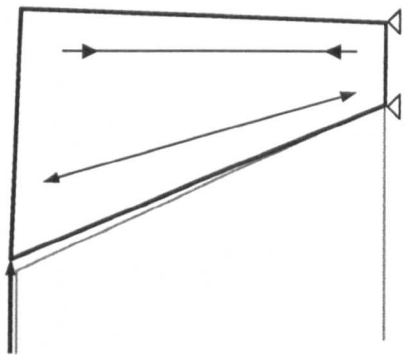


**Figure 4-13 - Failure Mechanism and Stress Paths**

The original geometry of the anchor problem was revised in two stages. Firstly the concrete block was widened to accommodate the shallower failure cone and thus produce a full concrete cone. By considering the crack angle produced the first anchor problem it was estimated that the required width of the block should be 300mm (Figure 4-11). Analysis of this wider geometry produced a crack with a shallower angle than before (Figure 4-14). The general direction of the crack showed a slight upward curve with an intersection with the boundary in the top right corner.

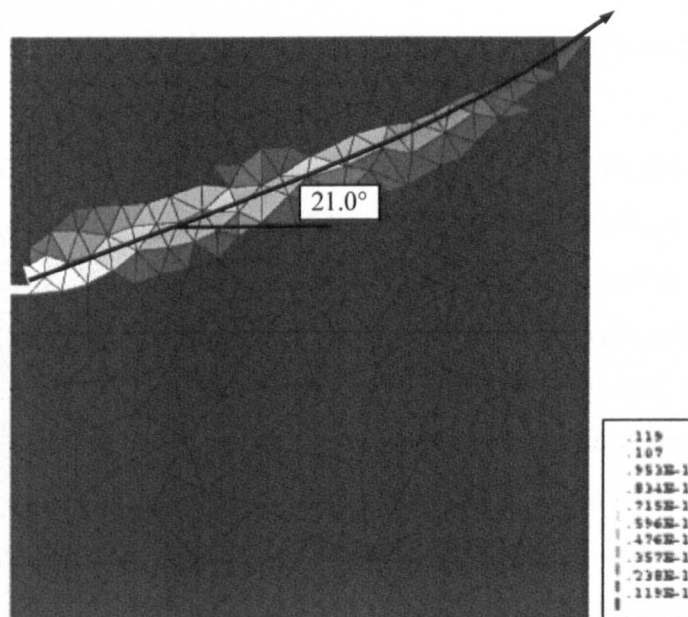


**Figure 4-14 - Effective Plastic Strain Plot for Wide Anchor Bolt Problem**



Comparison of the load-displacement response of the 300mm wide block with that of the 200mm block showed a very similar response although the 300mm block produced a softer response with less of an increase in sustained load as the displacement increases (Figure 4-15).

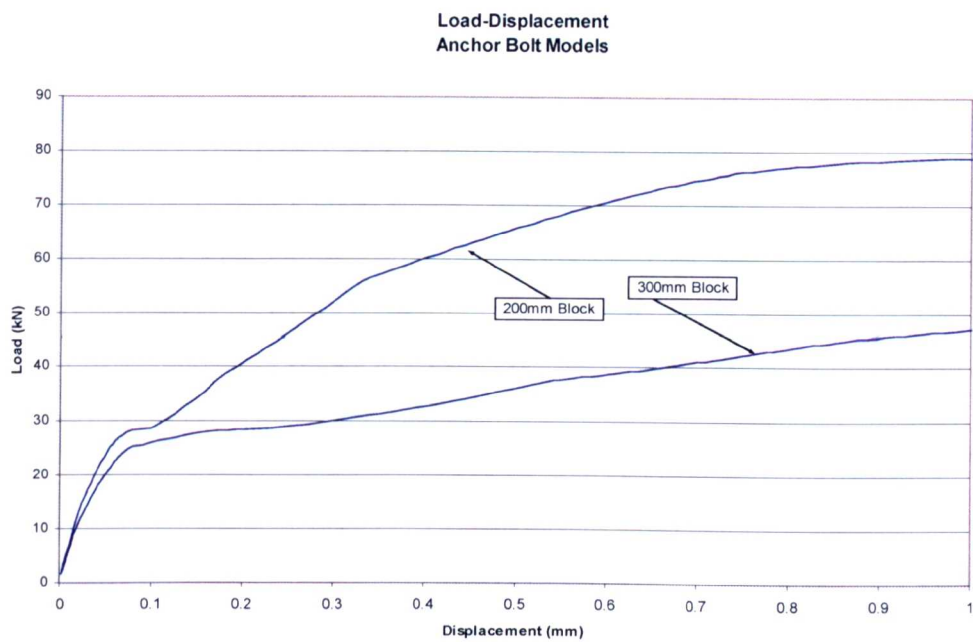


**Figure 4-15 - Load-Displacement Responses for 300mm and 200mm Wide Blocks**

The second revision to the anchor problem was to modify the right-hand boundary conditions. As stated previously, the constraint conditions specified on this boundary were designed to replicate the confinement effects of surrounding concrete. However, this allows the formation of the compressive strut that prevents the unloading of the problem. Simply removing the lateral restraint at the right-hand boundary and restraining the bottom boundary in the horizontal direction would eliminate this structural action. However, since it is quite possible to find some level of lateral confinement on a concrete member containing an anchor bolt it was decided to investigate the effects of differing levels of confinement on the anchor response. To do this a 10mm strip of fictitious material was attached along the right-hand edge of the problem and restrained in the horizontal direction as shown in Figure 4-16. Material properties were elastic with a

constant Poisson's ratio of 0.2 and choice of Young's modulus depending on the level of lateral confinement desired.

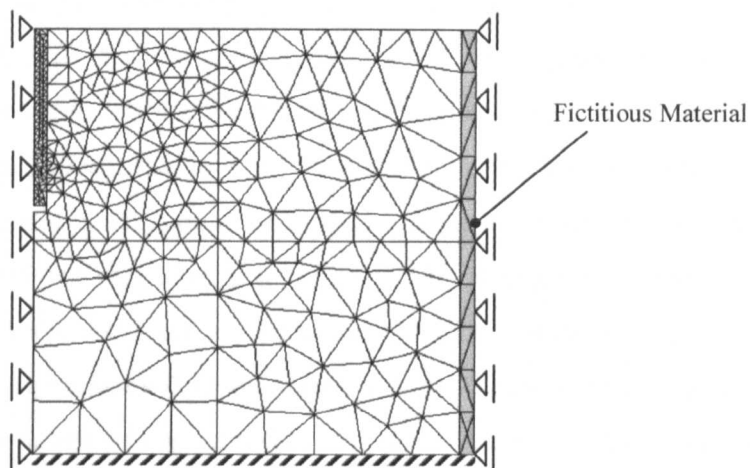


**Figure 4-16 – Placement of Fictitious Material to Create Variable Confinement Problem**

Various stiffnesses for the fictitious material were considered ranging from approximately zero up to a value equal to that of the elastic stiffness of concrete. The effects of differing confinement levels can be clearly seen in the displaced shaped produced (Figure 4-17) where there is significant lateral movement towards the top of the block when the specimen unrestrained.

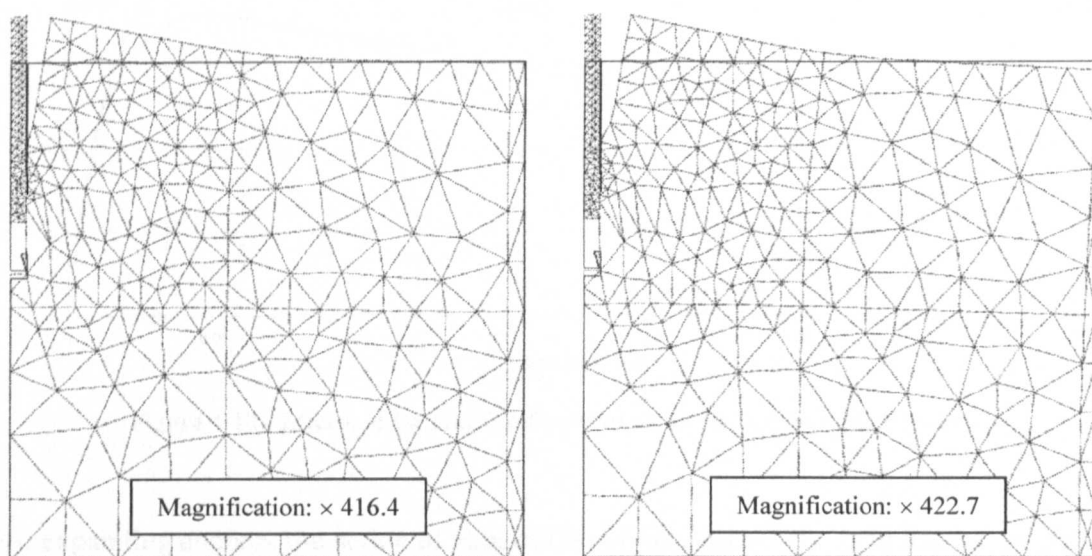


**Figure 4-17 - Displaced Shapes for High and Low Lateral Confinement**

Significantly the load-displacement graph shows that for the unconfined problem there is a well defined peak load followed by unloading. This confirms the hypothesis that lateral confinement is responsible for preventing the full development of the failure crack. The response also showed that for the unconfined problem the divergence from the linear-elastic response occurred for a lower applied displacement than with the confined problems. The study also showed that at a stiffness of 50% of that of concrete ( $1.5 \times 10^4 \text{ N/mm}^2$ ) there was sufficient confinement developed via the fictitious material to cause the problem to act in a manner very similar to a fully confined problem. Although a peak load was not produced for the confined problems there is a stage in the analysis where the rate of softening is high (area shown between dotted lines, Figure 4-18). It seems likely that if softening in these problems had continued the peak load would have been present in this zone. The significance of this is that, as expected, for higher levels of confinement the peak load is greater.

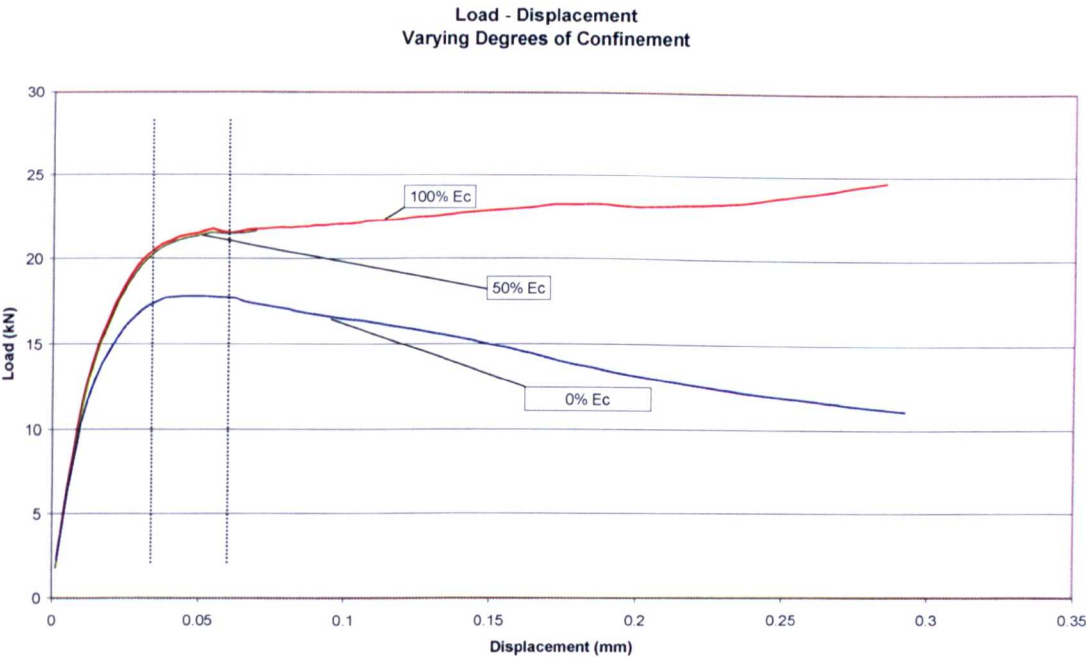


**Figure 4-18 - Effects of Lateral Confinement on Load-Displacement Response**

For expanding anchors the action of expansion not only causes the mobilisation of greater frictional bond strength along the anchor/concrete interface it also induces compressive

stresses in the surrounding concrete. In order to investigate this behaviour a conceptual model was required that simulated the expansion of the anchor. In reality the expansion of the anchor is performed in two stages (Figure 4-19). Firstly, after being inserted into the hole the anchor head is turned until a required torque has been reached. This causes the bell of the anchor to be drawn into the expander and thus cause the leaves of the expander to open. This not only produces a significant normal force on the anchor/concrete interface but it also causes the expander to key into the concrete. During the loading phase there is an increase in the expansion force proportional to the pullout load sustained by the anchor. This may induce further expansion and increase the keying effect.

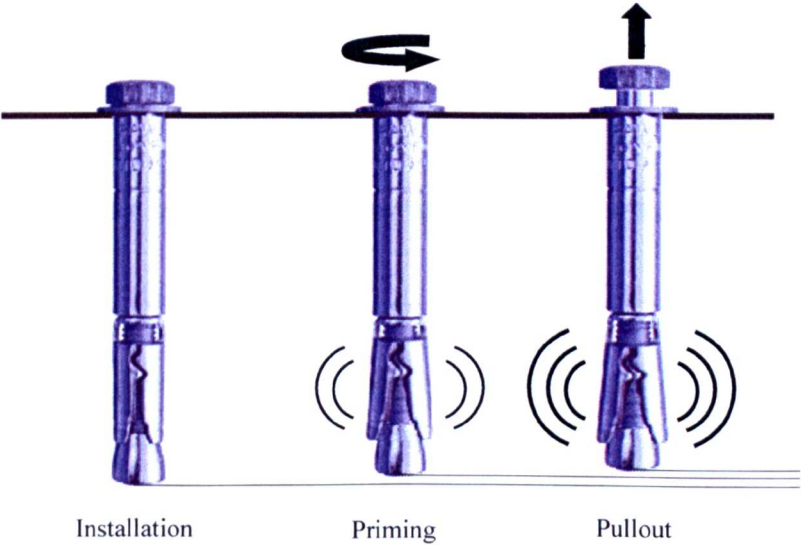


**Figure 4-19 - Expansion Stages of Anchor**

The method of achieving expansion of the anchor was via so-called ‘tied displacements’ whereby the displacement of defined slave nodes was a function of the displacement of a master node. In this way the lateral displacement of the expander was prescribed as a function of the total vertical displacement of the anchor head during pullout (Figure 4-20). The relationship was defined such that the anchor assumed a trapezoidal profile when expanded. In addition it was possible to model the expansion during priming simply by prescribing displacements to the expander. However due to a lack of data on the level of expansion produced by priming this secondary behaviour was omitted.



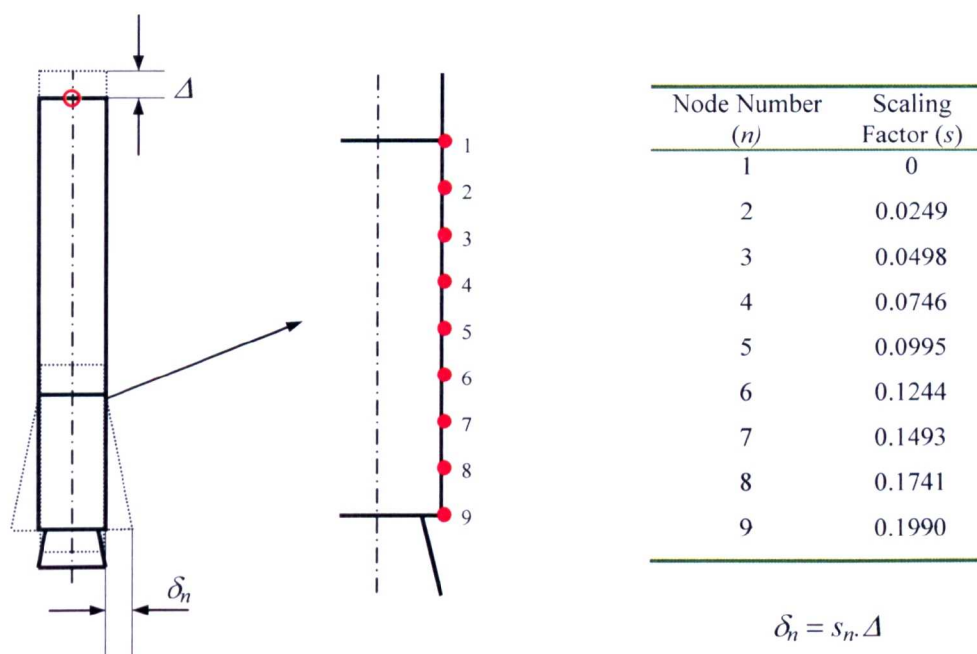


**Figure 4-20 - Tied Displacement Method for Anchor Expansion**

The tied displacement method was applied to the existing model. Analyses of the expanding anchor problem were carried out for conditions of both full and zero lateral confinement (Young's Modulus of the fictitious material set to 100%  $E_c$  and 0%  $E_c$  respectively). For the purposes of comparison the load-displacement responses for these analyses are plotted along with those from previous, non-expanding anchor analyses.

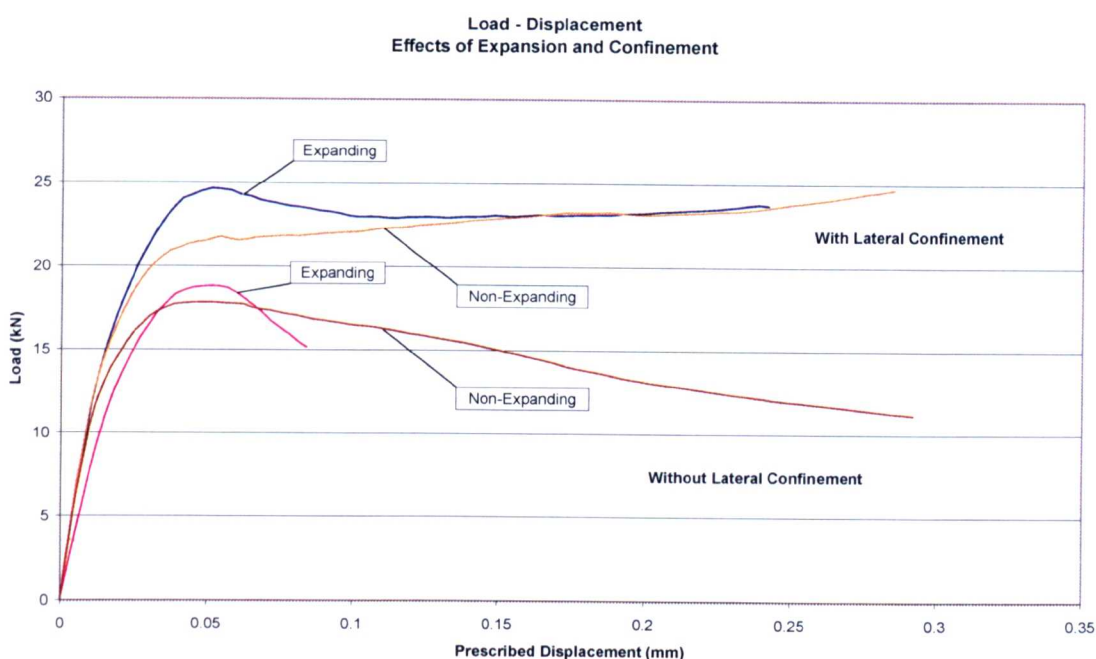


**Figure 4-21 - Effects of Anchor Expansion and Lateral Confinement**

It is immediately obvious from the graph above (Figure 4-21) that lateral confinement has a greater influence on the peak load than expansion. However, it must be noted that in reality expansion is the more significant aspect as its primary purpose is to create a sufficiently strong frictional interface between anchor and concrete to be able to sustain the applied tensile load. Insufficient strength of this interface would lead to slipping and ultimately failure of the anchor. Due to the complexity of modelling such a frictional interface this behaviour was not modelled in the current problem. In this study, in case of both with and without lateral confinement, the expansion problems soften later and reach higher peak loads than the non-expanding problems. The initial rate of post-peak softening is also greater. In the latter stages of the analyses there is a convergence of the responses of the confined problems suggesting that the effects of expansion are less influential in the post-peak phase. Whether this would be the case for the unconfined problems is unclear as the expanding problem failed due to non-convergence and could not be progressed further. Also apparent in the results is that the presence of lateral confinement enhances the effects of expansion. For the unconfined problem the addition

of expansion increased the peak load by 5.6% whereas for the confined problem the increase was 14.0%.

#### **4.2.2 Axisymmetric Modelling of Anchor Bolt**

Although plane-stress modelling provided useful results it is unable to model out of plane stresses and ultimately an unsuitable approach for modelling of anchor problems. In particular, hoop or ring stresses are of importance when considering much of the structural action related to anchor modelling. These stresses are produced as a result of radial straining about the anchor and act to provide a level of resistance or confinement to the problem (Figure 4-22).

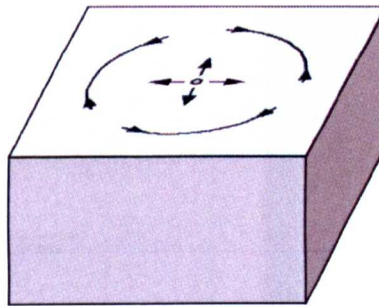


**Figure 4-22 – Diagram Showing Radial Expansion Stresses and Associated Circumferential Stresses**

Axisymmetric analysis allows this stress component to be included. It may also be argued that since both the shape of the failure surface and the geometry of the anchor itself as approximately symmetrical about their central axis that axisymmetric analysis is well suited to anchor pullout modelling.

The changes required to make the plane-stress problem suitable for axisymmetric analysis were firstly to remove the symmetry restraint along the left-hand edge. The geometry of the problem remained unchanged and although the finite element mesh remained the same the element type was changed. 3-noded, isoparametric, axisymmetric, ring elements of triangular cross-section were used. Once again these elements employed a linear integration rule with a single Gauss. Material properties and analysis method were the same as before.

It is immediately obvious that for a non-expanding anchor with no lateral confinement the load-displacement response produced by the axisymmetric problem is much stiffer than that produced by the plane stress problem (Figure 4-23a). The contour plot of effective plastic strain shows that the failure mechanism is via cracking local to the expander with little evidence of the formation of a concrete cone (Figure 4-24).

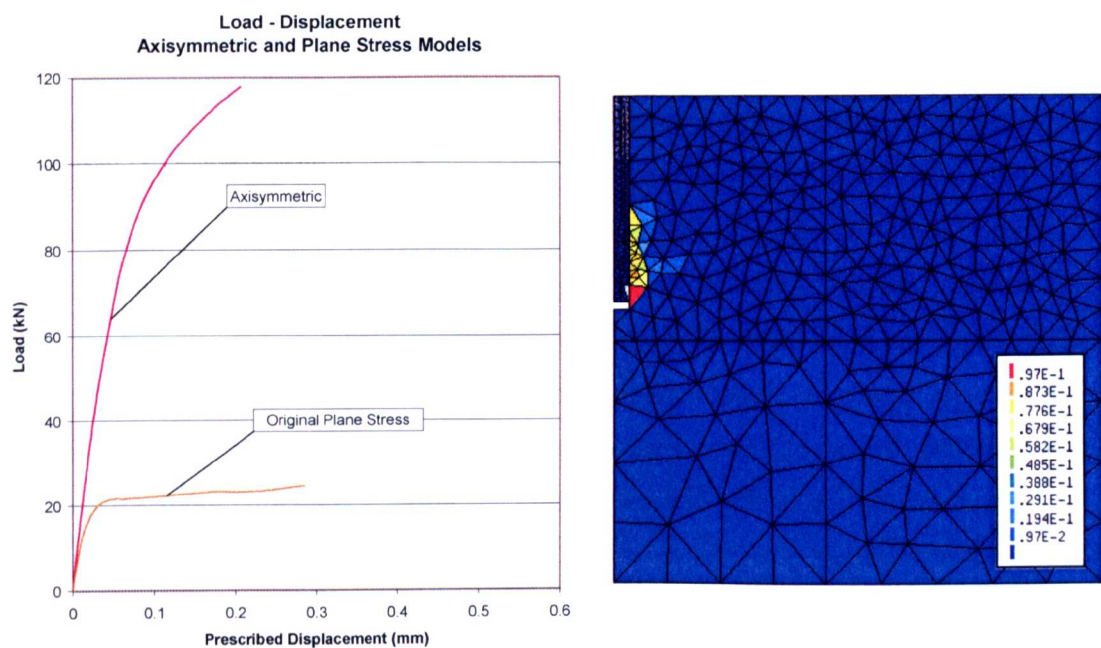


**Figure 4-23 - a) Load-Displacement Response and b) Plastic Strain Plot for Axisymmetric Anchor Bolt Problem**

An important point to note when comparing plane stress and axisymmetric problems is that although the two-dimensional geometry may be identical what is implied in a three-dimensional context can be quite different. The plane-stress problem considered here may be visualised in 3D as a flat slice concrete with a width, as specified, of 200mm (Figure 4-24). Within this the anchor spans the whole width. In contrast the concrete block for the axisymmetric problem is a cylinder of diameter 300mm. The anchor is an 18mm diameter cylinder sitting at the centre of the block.



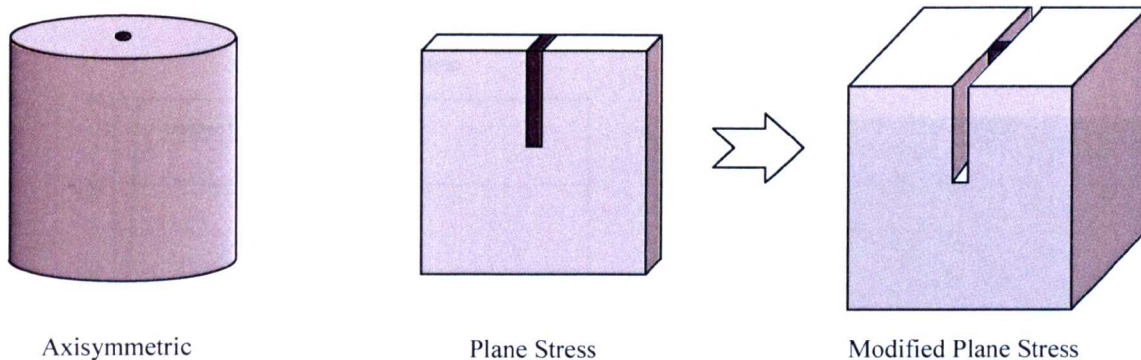


**Figure 4-24 - 3D Visualisation of 2D Problems**

In order to make a closer comparison of the axisymmetric and plane stress problems a modified version of the plane stress problem was analysed for which the concrete block thickness was set to 600mm and the anchor thickness 18mm (Figure 4-24). The effect of this was to provide a higher, and more realistic, level of horizontal confinement to the anchor. Essentially the increased thickness of the concrete leads to an increased stiffness for the concrete elements in the plane stress approximation. However, this modified problem still does not give as suitable a representation of the anchor problem as the axisymmetric model does since radial and circumferential effects are not captured.

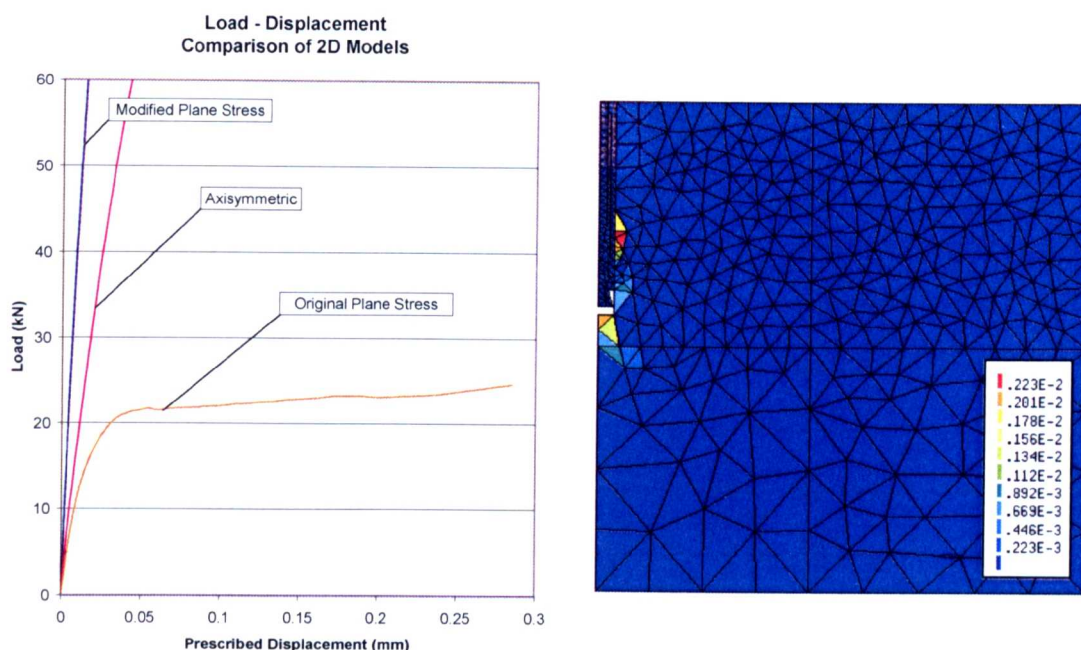


**Figure 4-25 – Load-Displacement Graph and Effective Plastic Strain for Modified Plane Stress Anchor Bolt Problem**

The plot of effective plastic strain for the modified plane stress problem (Figure 4-25b) shows a very similar failure mode to that produced by the axisymmetric problem with localised cracking around the expander. The load-displacement response reveals that this problem behaves in a much more stiff manner than the original plane stress problem (Figure 4-25a). It is also considerably stiffer than the axisymmetric analysis. Differences such as this are to be expected since although the geometries of the two problems are more equivalent the finite element idealisations used are still different. As will be shown later, the ring stresses in the axisymmetric problem play an important part in the response of the problem. Despite these differences the modified plane stress problem does support the findings from the axisymmetric problem.

As with the plane stress problem a simple study into the effects of expansion and confinement was performed. Two levels of lateral confinement were considered; full and none. Expansion was achieved via the tied displacements method.

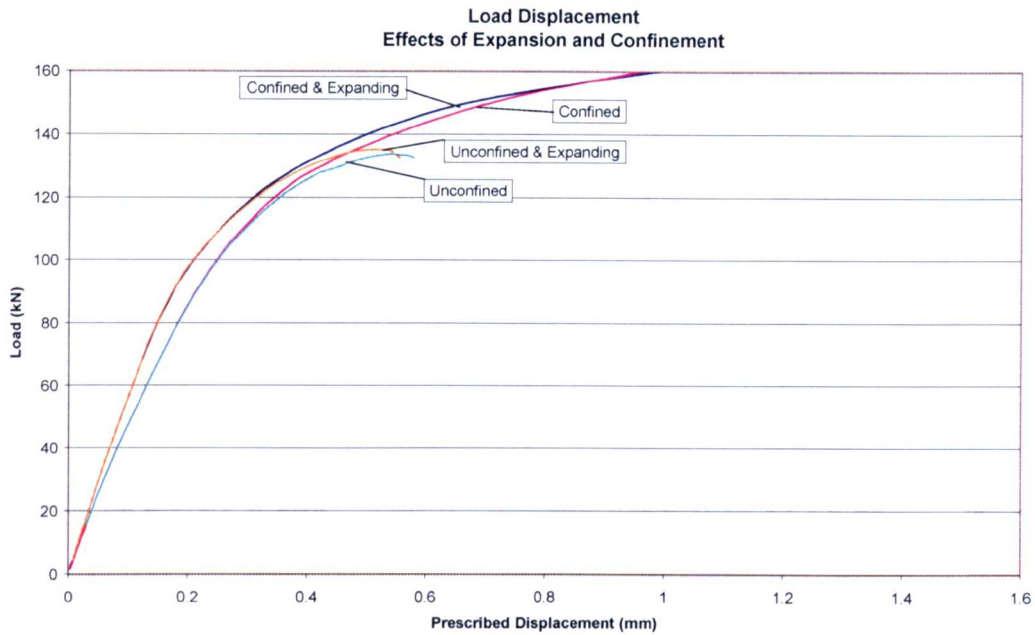


**Figure 4-26 - Effects of Lateral Confinement and Expansion on Axisymmetric Anchor Bolt Problem**

Unlike the results produced by the plane stress problem there is a clear difference in the initial linear elastic response of the expanding problems in comparison with the non-expanding ones (Figure 4-26). This result was verified via results of linear elastic analyses of these problems. The reasons for this difference are not very clear however a likely explanation can be found by considering the effects of the expansion. A problem was created where no pullout load was applied. Instead a loadcase was defined to induce the expansion of the anchor alone via prescribed displacements. The displaced shape produced by the analysis of this new problem shows that the anchor is drawn downwards (Figure 4-27) due to the Poisson's effect in the expander. If the anchor head had been restrained vertically a tensile force would have been induced in the anchor. For the pullout analyses considered above this is precisely the situation and therefore, at a given prescribed displacement, the resisting load as measured at the anchor head consists of two components. The first of these is from the resistance to pullout, as produced for non-expanding problems. The second component is a resistance to the tension in the anchor caused by expansion. Therefore the analyses of the expanding anchor problem always produced a larger load for a given displacement.

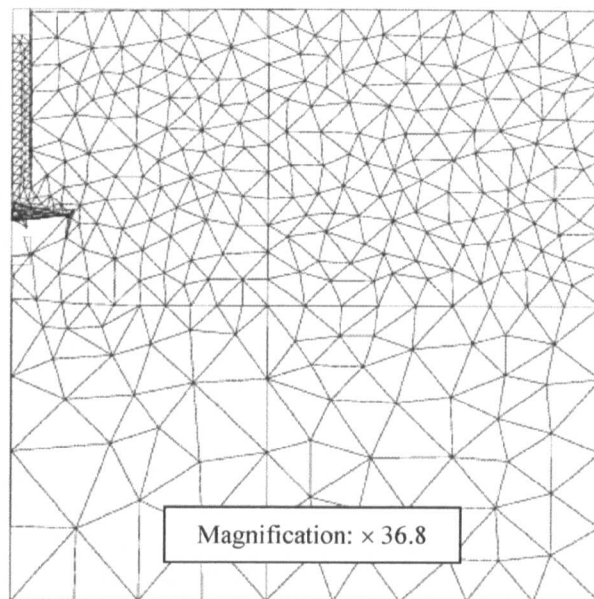


**Figure 4-27 - Displaced Shape Produced by Anchor Expansion Alone**

In the later stages of the analysis the effects of expansion become less apparent as the material around the expander softens and thus provides less resistance. The influence of lateral confinement on preventing the propagation of the crack become the dominant feature and it can be seen in the load-displacement plot that the responses of the two confined problems converge, as do those of the unconfined analyses. The plane stress problems also produced this latter type of behaviour.

For all the above axisymmetric analyses the failure mode that was produced was via a localised failure around the anchor expander rather than the expected concrete cone. Pukl et al reported similar results when analysing an expanding anchor under axisymmetric conditions [Pukl, et al (1994)]. However, in that case tensile stresses arising from the Poisson effect and very large compressive stress in the radial direction was the cause. For the analyses presented here the cause was investigated by considering the stress histories for various points along the expected concrete cone crack path (Figure 4-28).



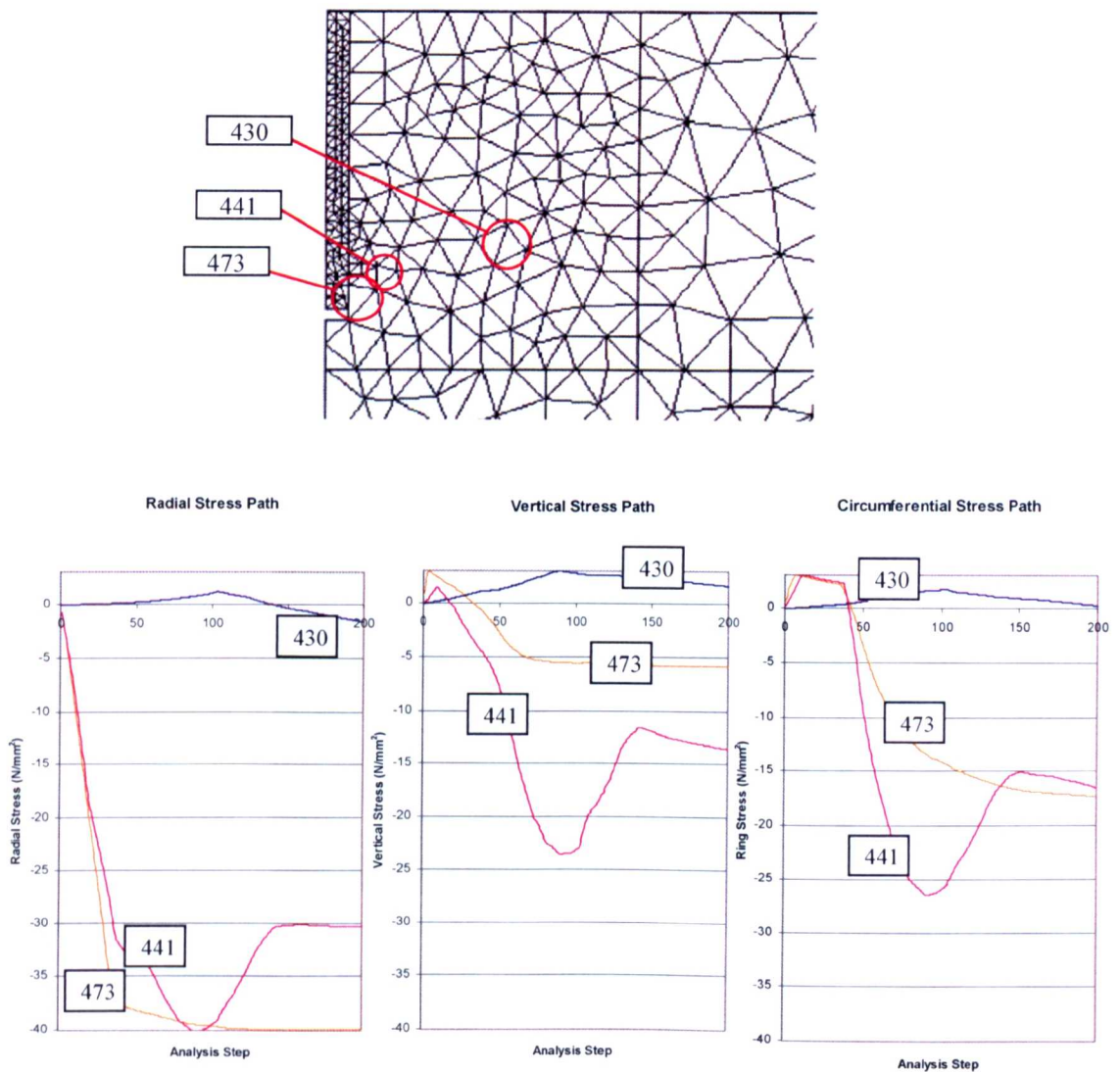


**Figure 4-28 - Stress Histories for Points Along Expected Crack Path for Axisymmetric Analysis of Expanding Anchor Problem with Full Lateral Confinement Using Rankine-Von Mises Model.**

It can be seen from these stress histories that the compressive stresses in the radial direction are dominant for the elements close to the expander (elements 441 & 473). This is to be expected because of the expansion process. The vertical stresses for these elements are initially tensile due to the pullout load, also as expected. In the circumferential direction the initial tensile stresses were predicted also due to the expansion of the anchor. However, what was interesting was that these elements close to the expander would come to a state of triaxial compression.

In order to give a better insight into the processes taking place the problem was reanalysed using a Plasticity Model with only a Rankine failure surface (i.e. unlimited compressive strength). The plot of effective plastic strain reveals the failure mode to be via concrete cone (Figure 4-29).

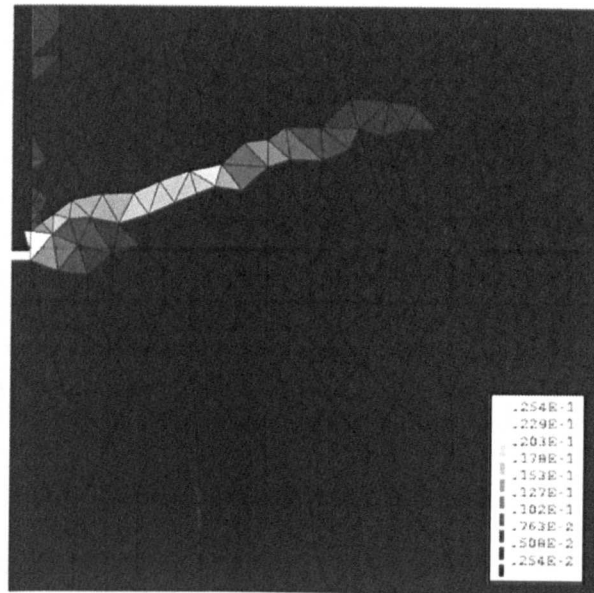


**Figure 4-29 - Effective Plastic Strain Plot for Axisymmetric Analysis of Anchor Pullout Problem with Expansion and Confinement, Performed Using Rankine Plasticity Model**

It can also be seen from this plot that there is some amount of plastic straining present close to the anchor as before but that this strain is lower than before and of a much lower magnitude than that of the concrete cone crack. This result also means that the adoption of the localised failure mode was due to compression behaviour as the two material models are identical in all other respects

The stress history plots for the Rankine-only analysis show some important differences from those of the combined Rankine-Von Mises (Figure 4-30). It can be seen that the stress states of all the points under consideration immediately went into compression. These compressive stresses continued to grow without bounds since there was no compression side to the failure surface. For the vertical stress the graph is fairly similar to

before except in that the history of element 441 shows it to continue to become more compressive whereas for the combined Rankine-Von Mises analysis this trend reversed around analysis step 100. The circumferential stresses are again predominantly tensile. However for this analysis the elements close to the expander remain in tension in this direction whereas two of the elements further away become subject to compression in the circumferential direction.

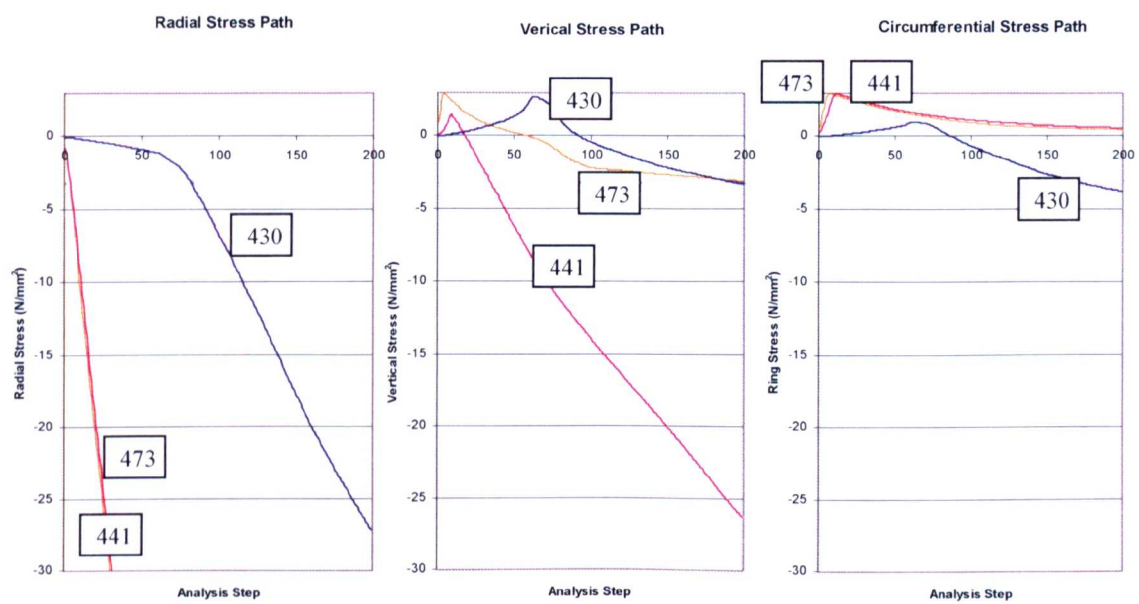


**Figure 4-30 - Stress Histories for Points Along Actual Crack Path for Axisymmetric Analysis of Expanding Anchor Problem with Full Lateral Confinement Using Rankine Only Model.**

For the combined Rankine-Von Mises Model stress histories of elements along the expected concrete cone crack path have been shown to fail in tension as expected so both concrete cone and local failure modes were active. However it is evident that the compressive failure of elements close to the expander caused the localised failure to become dominant. Since this a valid mode given the stress states present it raised the question of whether or not the expansion model itself was valid. In reality expansion of the anchor is a function of the tensile stress in the bolt. By instead prescribing expansion to be a function of the vertical displacement of the anchor head, spurious expansion could be induced by vertical straining of the concrete under loading (either elastic or crack

strains). Additionally, this approach was not able to account for the level of radial confinement the concrete provides to resist expansion. Indeed, this model for expansion assumed no resistance from the concrete. It must also be noted that the tied displacement method only dealt with the kinematics of anchor expansion and no account was taken of the frictional interface between anchor and concrete. What was required was a more accurate expansion model. However, it was decided to leave further research into expansion until edge effects had been tackled in three-dimensional models.



### **4.3 Anchor Modelling in 3D**

Although plane-stress and axisymmetric idealisations have their strengths (primarily their relatively low computation expense), the structural action involved in anchor pullout is fully three-dimensional. In particular, behaviour such as splitting failure associated with small edge distances cannot be captured in 2D analyses [Pukl et al (1994)]. The reasons for this can be seen when comparing axisymmetric and 3D approaches. Firstly, due to the nature of the axisymmetric approach, the anchor bolt is always considered to be in the middle of the concrete block. As such it is impossible to simulate the effects of the presence of a single, free edge. Also the axisymmetric model may be thought of as being made up of an assemblage of rings at different heights and of different radii. For each ring the radial, circumferential and vertical stresses are constant at every point around the ring. This approach precludes the possibility of phenomena such as discrete radial cracking and non-symmetric concrete cone failures. 3D modelling avoids these limitations since the stress state at each point in 3D space may be independently calculated. As one of the primary aims of this research was to investigate the relationship between anchor response and edge distance it was necessary to move to modelling the problem in 3D.

#### **4.3.1 Complexities Introduced by 3D Modelling**

Three-dimensional modelling increases the complexity of a number of different aspects, not least of which are the creation of the geometric model and the finite element mesh. Although the specification of the basic model geometry may be quite straightforward care must be taken as to how this geometry will affect the creation of the FE mesh. For example a common limitation of mesh generation software is that volumes that are to be discretised by regular, hexahedral elements must themselves be hexahedral. To aid model creation it is often desirable to divide the basic geometry of the problem into smaller, so-called macro elements. It must be noted that in this context the macro elements are only used to aid the meshing process and, for the analysis stage, the problem is treated as one unit. The advantage being that the FE discretisation may be more accurately defined at a local level. An extension of this concept was considered for the anchor model. A sub-model could be created that consisted of the anchor bolt sitting in a small block of concrete (Figure 4-31). The anchor geometry could be as detailed as necessary and a fine

FE mesh could be constructed in the concrete. This sub-model could then be installed into a much larger block of concrete in whatever position was required. This plan had the advantage that it ensured the modelling of the anchor remained the same between tests and that once the anchor model had been constructed the process of making models to test the anchor in different positions would be much quicker.

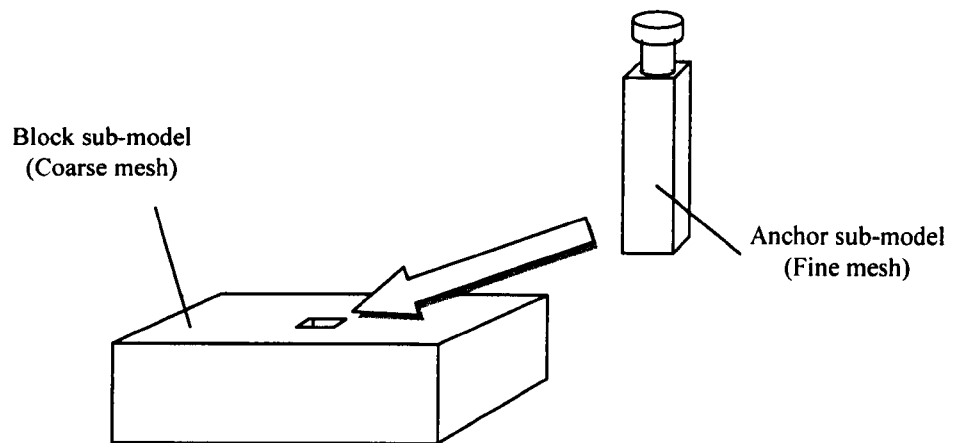


**Figure 4-31 - Sub-Model Concept for Creation of Geometric Model and Meshing Process**

The disadvantage of this approach was in making the connection between the anchor and block sub-models. For each node on the surface of the hole in the block there has to be an equivalent node in the same position on the anchor sub-model. Achieving this when using an unstructured tetrahedral mesh was practically impossible. However, three variations on this approach were used for subsequent model creation.

For modelling using unstructured tetrahedral meshes the entire geometry was specified as one model with the anchor in the centre position. To achieve different edge distances the outer corner points of the concrete block were translated into the appropriate positions prior to generating the FE mesh (Figure 4-32). Although this method did not retain the same mesh topology between models it did have the advantage of speed of model creation and the fact that the anchor position remained unchanged relative to the global coordinate system.

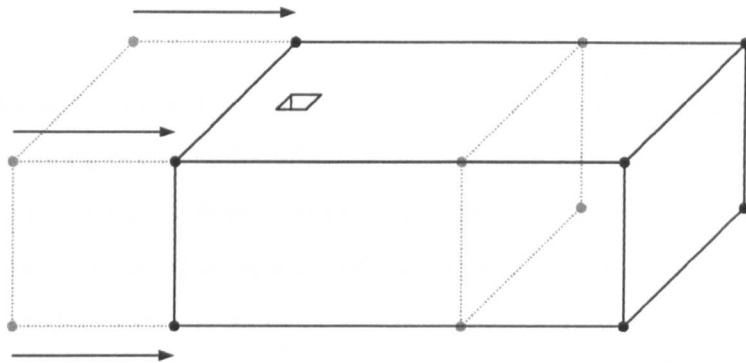


**Figure 4-32 - Translation of Concrete Block Outer Boundary to Modify Anchor Edge Distance**

Later analyses used hexahedral meshes and the regular nature of these allowed models for different anchor positions to be created by distorting the FE mesh. A computer program was written which took the filename of a reference FE mesh and the required anchor edge distances as input parameters. A translation of the node points surrounding the anchor was then performed to achieve this new edge position (Figure 4-33). An effect of this approach is that the finite element size becomes smaller on the sides close to the anchor (and larger on the other sides). This higher level of discretisation is obviously desirable in the zone where crack development has most effect on ultimate strength. In this method mesh topology remains constant, as does the anchor position in the global coordinate system.

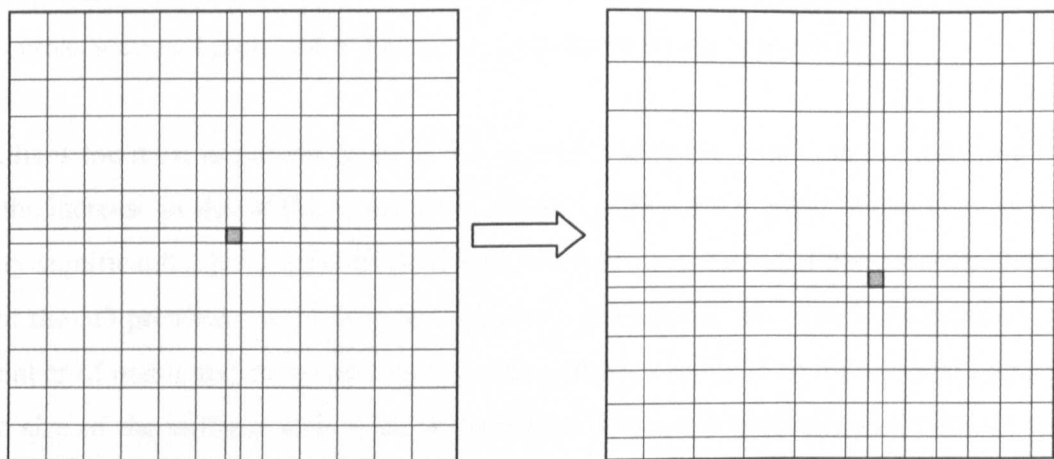


**Figure 4-33 - Mesh Distortion Method of Modifying Anchor Edge Distance**

The final model creation method was used for anchor models that contained interface elements to model the frictional interface between anchor and concrete (Chapter 8). Since the model geometry was relatively complex and included zero thickness elements it was necessary to write a piece of computer code to create the necessary anchor and interface finite element model. Input parameters for this program were a list of node points and corresponding coordinates for the nodes sitting on the surface of the hole in the concrete block. This ensured compatibility between the two sub-models. The FE mesh for the block itself was created, as before, using the chosen pre-processor. Block and anchor sub-models were then combined manually.

Judging the quality and suitability of the finite element mesh also becomes more difficult for 3D problems. An analyst will generally assess a mesh by eye prior to using it to ensure it meets their requirements. This becomes practically impossible for irregular, 3D meshes. The ability to freely rotate and view cross sections of the mesh in the pre-processor helps with the assessment of the mesh, particularly for areas of the problem where the analyst has specific requirements of the mesh. However the analyst also be guided by statistical evaluation. For example, most pre-processors can make an assessment of mesh quality based on factors such as aspect ratio, skew and warping of the elements. The challenge of visualisation also extends to post-processing and the interpretation of results. In this work this problem was mainly tackled through the use of 2D cross sectional plots and 3D graphing techniques where appropriate.

Perhaps the most important point to note when making the transition to modelling in 3D is the increase in size of the problem description. Firstly the number of elements increases very significantly. For a cube-like problem it would be expected, if there were  $n$  elements, that the 3D problem would have  $n^{3/2}$  elements. Associated with this is an increase in the number of nodes and integration points. These factors result in an exponential increase in the size of the stiffness matrix for the problem. There are mathematical methods within the FE framework of DIANA to improve the efficiency of the solution process, however

it is inevitable that 3D analyses will be significantly more computationally expensive than 2D analyses.

#### 4.4 Preliminary 3D Anchor Modelling

Initial creation of the 3D problem was based on the sub-model idea and made use of primitives within the chosen pre-processor for 3D work – GiD v6.1.2 [CIMNE (2000)]. Although it was relatively simple to create the desired geometry (Figure 4-34) the number of finite elements needed was in excess of four and a half thousand. This was despite requesting a large element size of the meshing algorithm. The reason for this was due to what may be thought of as the ‘discretisation gradient’. That is, the rate of change in element size from one zone to another. The detailed geometry of the anchor sub-model dictated the minimum element size and due to the discretisation gradient set by the meshing algorithm the larger element size defined by the user for the surrounding concrete was not attained. As a model geometry for more detailed and accurate analysis this mesh was satisfactory. However, due to the computational expense a less detailed geometry with fewer elements was required.

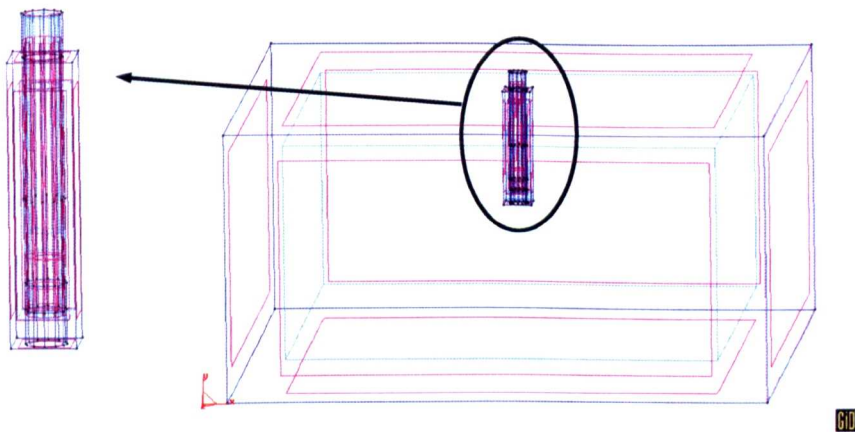
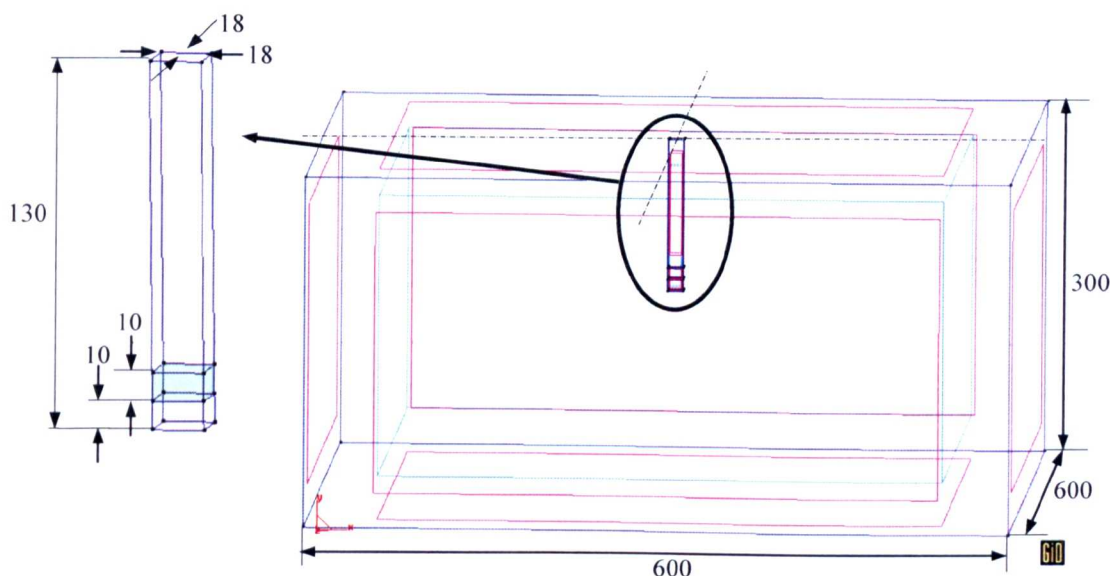


Figure 4-34 – Meshing Primitives for a) Anchor Sub-Model and, b) Complete Model

The anchor geometry was simplified (Figure 4-35) with the main changes being that only the expander section of the anchor was modelled (shown shaded) and that the cross-section was square rather than decagonal.



**Figure 4-35 – Primitives for Simplified 3D Anchor Problem**

Dimensions of the anchor are similar to those of the 2D problems although the length of the expander was decreased. The reason for this was that under expansion the lower part of the expander displaces most and it is this section that forms the strongest bond with the concrete. Therefore it was considered appropriate for a fully bonded interface, as modelled here, to only bond the lower part of the expander to the concrete. Meshing of this simplified problem required only 1500 elements. Undoubtedly this is a rather coarse discretisation but, as the subsequent analyses show, the results produced were accurate enough for the intended purpose and the decreased analysis time allowed more extensive studies to be performed within a reasonable timeframe.

One final obstacle presented by 3D modelling was that the Plasticity Model, which had been used previously for 2D expansion anchor modelling, was not available in the framework of DIANA. Instead DIANA's Multiple Fixed Crack Model (Chapter 3) was used for these analyses with a linear tension softening diagram and constant shear

retention (Figure 4-36). The steel of the anchor was modelled, as before, as a linear-elastic material.

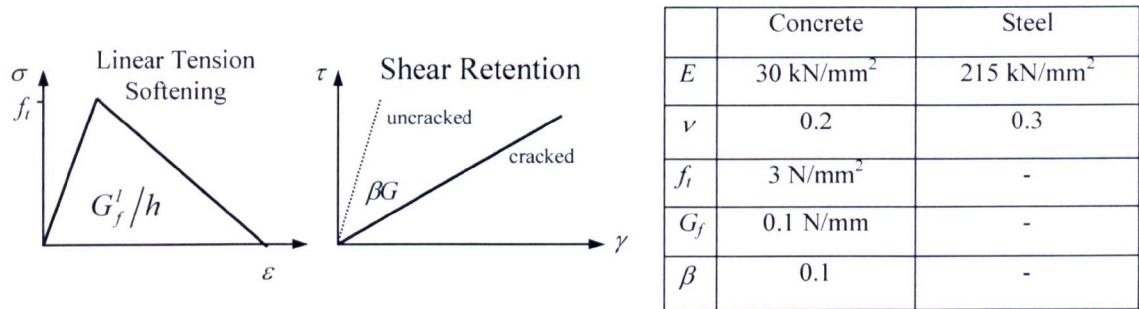


Figure 4-36 - Material Properties for 3D Anchor Problems

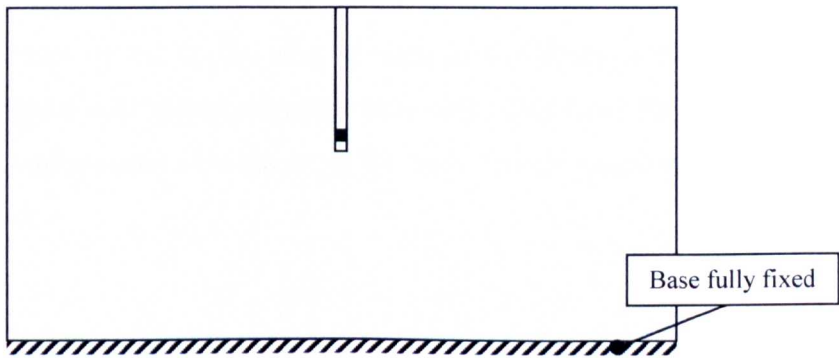
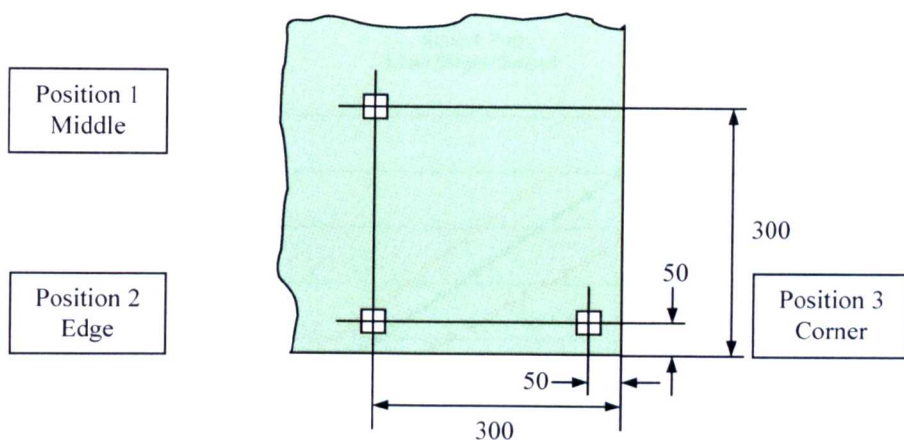


Figure 4-37 - Boundary Conditions

The base of the concrete was restrained in X, Y and Z directions (Figure 4-37) and a prescribed displacement applied to the top of the anchor bolt. A set of three anchor problems were constructed, each of which having the anchor located in a different position (Figure 4-38).





**Figure 4-38 – Anchor Bolt Positions**

Prior to the full non-linear analysis a linear analysis was performed. The load-displacement responses of the anchor bolt in each of the three positions are shown in Figure 4-40 and Figure 4-41. Displacements were measured from the top of the anchor bolt (Figure 4-39) whilst loads were taken as the total vertical reaction force on the base of the concrete block.

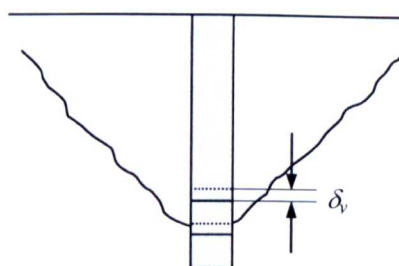


**Figure 4-39 – Anchor Displacement Measurement**

The results clearly show the effects of edge distance on the stiffness of the response. With the anchor in position 1, the middle of the concrete block, the behaviour of the problem is over 10% stiffer than when the anchor is in position 2, the side of the block. The response in position 2 is in turn stiffer (15.5%) than that produced when the anchor is located at the corner of the block, position 3.

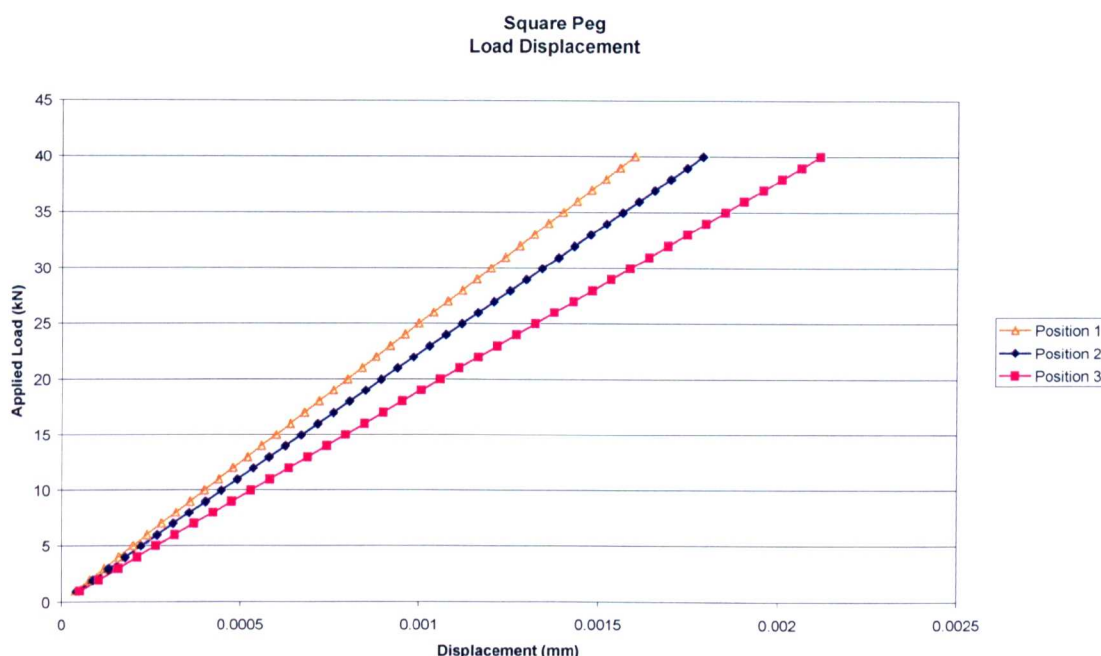


**Figure 4-40 - Effects of Anchor Position on Load-Displacement Response**

The effects of edge distance on the non-linear response were even more apparent (Figure 4-41). Compared with position 1 the resisted load at the yield point and subsequent peak load produced at position 2 are obviously lower. Moving the anchor to the corner further reduces both these characteristics. Unfortunately, for the edge and middle positions, the analyses failed before the peak loads were found. Attempts were made to progress the analyses further by using such methods as decreasing the load step, increasing the maximum number of iterations and using a line search algorithm. Despite these efforts the analyses failed due to non-convergence before a peak was found.

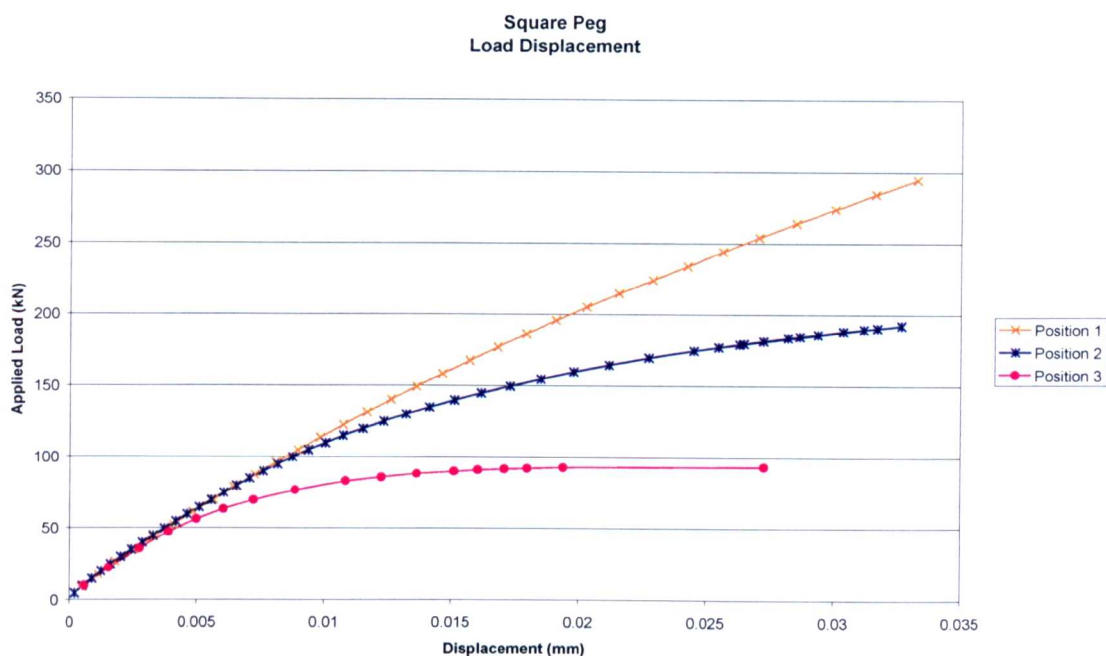


**Figure 4-41 - Effects of Anchor Position on Non-Linear Response**

The reasons for the edge effects are clearly illustrated by examining the contour plots of maximum principal stress, S1. Under loading a ‘stress bulb’ forms around the anchor. This is a localised zone of material which has in increased intensity of stress. The rest of the surrounding material remains largely unaffected by the anchor load. As can be seen in Figure 4-42, the stress bulb formed when the anchor is in the middle of the concrete block is approximately symmetrical and clear of the edges. (It is hoped that a finer mesh discretisation will produce a better defined shape). In contrast, the bulb formed with the anchor at the side of the block is truncated by the edge. This leads to a higher stress concentration and therefore the material failure occurs earlier in the loading process. The situation for position 3 is more severe (Figure 4-43) since the formation of the stress bulb is interrupted by 2 sides.

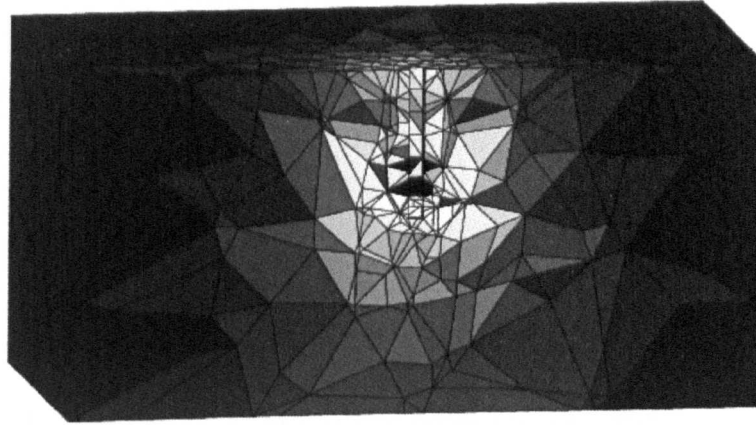


**Figure 4-42 – Principal Stress Contour Plot for Central Position (Vertical Cross-section Through Anchor)**

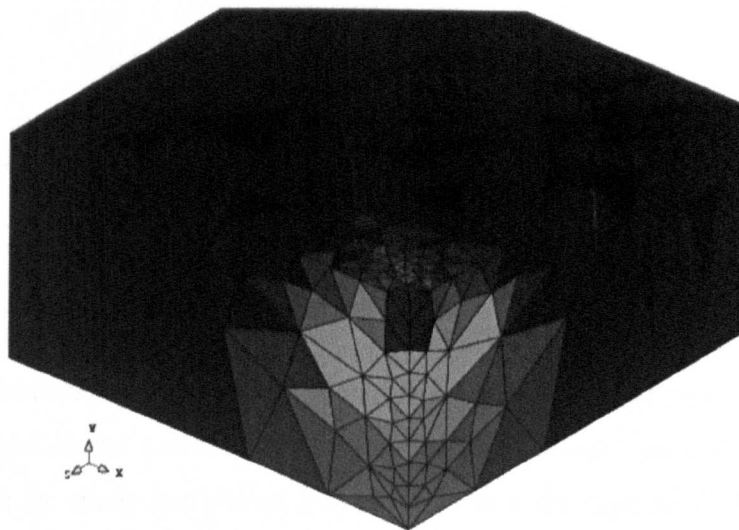


**Figure 4-43 - Principal Contour Plot for Corner Position**

Displaced shape plots proved to be of little value in determining the mode of failure since the unstructured mesh made it difficult to identify the magnitude and direction of the displacements. However, contour plots of crack strain were much more informative. Figure 4-44 shows the plot for midway through the loading of the anchor when located at the side of the block. The crack straining formed in an approximately conical shape around the anchor with a zone of much greater straining beginning to extend outwards from the anchor itself. A similar plot for anchor position 3 and at a later load step shows

the conical area to have expanded further. However, what is interesting is the pattern of higher straining is much more developed and better defined. The crack pattern is reminiscent of that found in concrete cone failure.

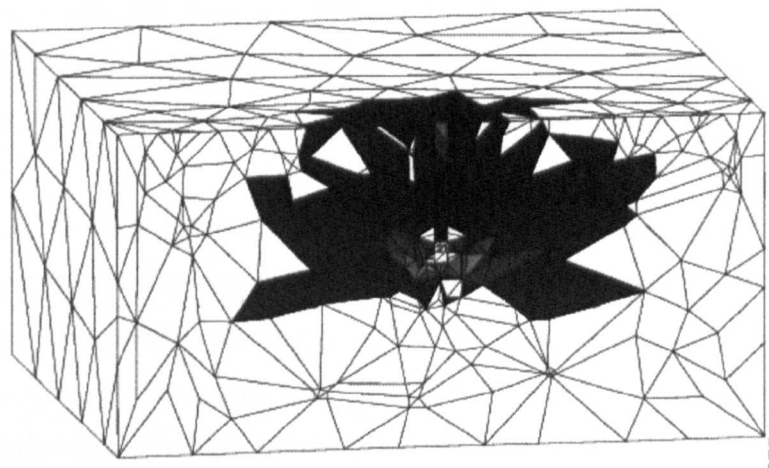


**Figure 4-44 - Crack Strain Contour Plot for Edge Position (Vertical Cross-section Through Anchor)**

As stated above, a feature of the load-displacement responses that was disappointing was the lack of a clearly defined peak load and subsequent post-peak response. To further explore this issue another more robust constitutive model was obtained. The Total Strain-Based Crack Model was a new constitutive model for concrete that had become available and experience by others had shown this new model to be superior in this respect to the Traditional Multiple Fixed Crack Model. A full description of the Total Strain Based Crack Model is presented in Chapter 5 and subsequent analyses made use of this model.

#### **4.5 Summary**

In this chapter a number of different anchor pullout problems have been examined and analysed. Firstly the Round Robin problem proposed by RILEM was tackled using both the Traditional Crack Model and the combined Rankine-Von Mises Plasticity Model. Both constitutive models produced realistic results in terms of failure mode and load-displacement response and both compared well with the results of contributors to the round robin. The Plasticity Model was selected for future 2D analysis work due to its ability to better trace the post-peak response of the problem.

For a realistic anchor bolt geometry the effects of lateral confinement were examined. In plane-stress analyses higher confinement levels lead to higher peak strength and also seemed to prevent post peak softening behaviour. A basic modelling technique for anchor expansion via tied displacements was also investigated. For plane-stress cases this resulted in a higher peak load but similar post-peak response. In the case of axisymmetric analyses neither expansion nor confinement levels had a significant effect on initial anchor behaviour although confined problems showed no definite peak load and did not soften before the analyses failed due to lack of convergence.

The complexities of 3D modelling were considered and proposals made on various techniques to generate FE meshes for arbitrary anchor positions within the concrete block. A basic edge/corner effect study was carried out and showed the reduction in initial stiffness associated with low edge distance. An alternative material model for concrete was also identified that could potentially overcome the problems of robustness and stress locking that, thus far, had prevented peak loads from being obtained.

## CHAPTER 5

### Total Strain Based Crack Model

#### 5.1 Introduction

This constitutive model, as proposed by Feenstra et al, was originally developed for the Norwegian joint industry project INDACS (Integrated Nonlinear Design and Analysis of Concrete Structures) [Feenstra, Rots, Arnesen, Teigen, Hoiseth (1998), Feenstra (1999)]. Its basis comes from the Modified Compression Field Theory as proposed by Vecchio and Collins [Vecchio and Collins (1986)]. Its primary aim was to provide a robust tool for the analysis of 3D reinforced concrete structures. Also of great importance was that the solutions found were accurate and take into account phenomena such as lateral stress effects in the description of the 3D stress state. The model has been implemented in DIANA version 7 [TNO (1999)] and has been extended to cater for a range of stress situations plane stress, axisymmetry, etc) and both fixed and rotating crack concepts are implemented.

Unlike more traditional crack models (e.g. [Rots and Blaauwendraad (1989)]) this approach is formulated in terms of total strain throughout rather than decomposing strain into elastic and crack parts. Proponents for crack decomposition argue that separating the total strain allows the researcher to consider each component separately and that this will lead to a more realistic description of the material. However, the Total Strain Based Crack Model provides a material model that is more detailed than the original Crack Model provided in DIANA in that it models compressive behaviour and lateral stress effects. The second advantage of strain decomposition is that the crack strain may be further decomposed into contributions from a number of individual cracks without requiring significant alteration to the model. This second point is not so relevant to the Total Strain Based Crack Model presented here as it models only a single crack. Of course, the issue of which class of crack model (rotating, fixed, multiple, etc) is most realistic and accurate is still widely debated [Ohmenhauser, et al (1998), Rots and Blaauwendraad (1989)] and has been covered previously in Chapter 2.

## 5.2 Theory

The Total Strain Based Crack Model is orthotropic in nature. The material behaviour on each of the principal or crack planes being assessed and updated independently. The exceptions to this rule are the cases where lateral effects are modelled. e.g. Poisson's effect, compressive strength reduction due to lateral cracking. An important point to note is that although this model is termed a 'single crack model' this refers to the fact that only a single crack exists per plane. Therefore, in conditions of triaxial tension it is possible for there to be a total of three, mutually perpendicular cracks present. The following description of the model follows that of Feenstra's report on its implementation [Feenstra (1999)] and related documents [Feenstra, Rots, Arensen (1998), TNO (1999)].

### 5.2.1 Basics

In the Total Strain Based (TSB) Crack Model the strain vector in the element coordinate system,  $\epsilon'_{xyz}$  is updated by the strain increment,  $\Delta\epsilon_{xyz}$ , as shown in .

$$\epsilon'_{xyz}{}^{t+1} = \epsilon'_{xyz} + \Delta\epsilon_{xyz} \quad \text{Equation 5-1}$$

Prior to crack initiation the stress-strain relationship is assessed in the principal strain directions,  $123$  (Figure 5-1). The principal strains and axes are calculated from the strain tensor for the element coordinate system,  $E_{xyz}$ . The diagonal terms of  $E_{123}$  (Equation 5-2) are the principal stresses whilst the rotation matrix  $\mathbf{R}$  holds the direction cosines that define the rotation from the element coordinate system into the principal system.

$$\mathbf{E}_{123} = \mathbf{R} \mathbf{E}_{xyz} \mathbf{R}^T \quad \text{Equation 5-2}$$

Tensile failure in the model is governed by the Rankine criterion. If the stress in the principal strain direction violates the maximum allowable stress a crack plane is formed perpendicular to this direction. In the case of the fixed crack formulation the crack directions,  $nst$ , are then frozen in this orientation. For the Rotating Crack Model the crack plane is continually updated to remain aligned with the principal plane.



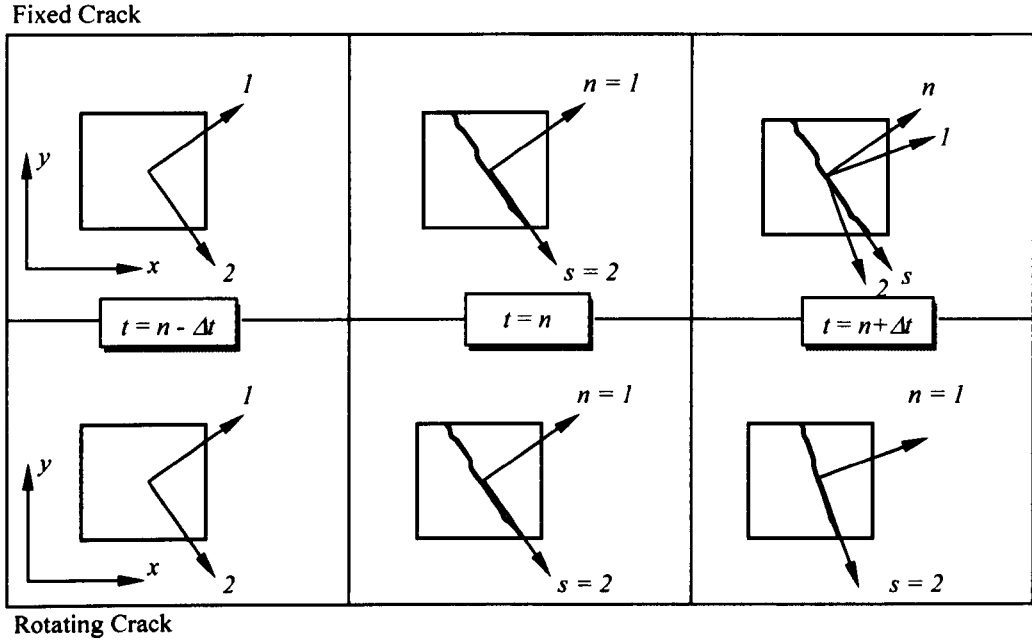


**Figure 5-1 – Crack Evolution for Rotating and Fixed Crack Systems**

The strain vector in the element co-ordinate system is transformed into the crack system by means of the strain transformation matrix, **T**.

$$\epsilon_{nst} = \mathbf{T} \epsilon_{xyz} \quad \text{Equation 5-3}$$

The nature of **T** is dependent on whether a rotating or fixed crack approach is employed. For the Rotating Crack Model, the components of **T** are obtained from the current rotation matrix **R**.

$$\mathbf{R} = \begin{bmatrix} c_{xn} & c_{xs} & c_{xt} \\ c_{yn} & c_{ys} & c_{yt} \\ c_{zn} & c_{zs} & c_{zt} \end{bmatrix} \quad \text{Equation 5-4}$$

where  $c_{xn} = \cos \theta_{xn}$ , the cosine between the  $x$  &  $n$  axes, etc (Figure 5-2).

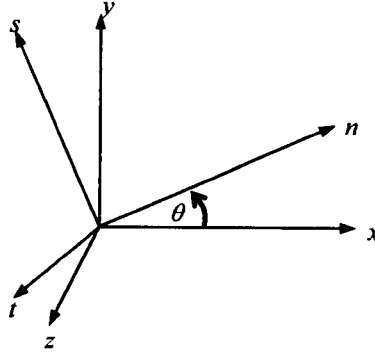


**Figure 5-2 - Angles Between Local and Crack Co-ordinate Systems Used To Calculate Direction Cosines**

For a general three-dimensional system the T matrix will be assembled as follows:

$$\mathbf{T} = \begin{bmatrix} c_{xn}^2 & c_{yn}^2 & c_{zn}^2 & c_{xn}c_{yn} & c_{yn}c_{zn} & c_{zn}c_{xn} \\ c_{xs}^2 & c_{ys}^2 & c_{zs}^2 & c_{xs}c_{ys} & c_{ys}c_{zs} & c_{zs}c_{xs} \\ c_{xt}^2 & c_{yt}^2 & c_{zt}^2 & c_{xt}c_{yt} & c_{yt}c_{zt} & c_{zt}c_{xt} \\ 2c_{xn}c_{xs} & 2c_{yn}c_{ys} & 2c_{zn}c_{zs} & c_{xn}c_{ys} + c_{yn}c_{xs} & c_{yn}c_{zs} + c_{zn}c_{ys} & c_{zn}c_{xs} + c_{xn}c_{zs} \\ 2c_{xs}c_{xt} & 2c_{ys}c_{yt} & 2c_{zs}c_{zt} & c_{xs}c_{yt} + c_{ys}c_{xt} & c_{ys}c_{zt} + c_{zs}c_{yt} & c_{zs}c_{xt} + c_{xs}c_{zt} \\ 2c_{xt}c_{xn} & 2c_{yt}c_{yn} & 2c_{zt}c_{zn} & c_{xt}c_{yn} + c_{yt}c_{xn} & c_{yt}c_{zn} + c_{zt}c_{yn} & c_{zt}c_{xn} + c_{xt}c_{zn} \end{bmatrix} \quad \text{Equation 5-5}$$

For the fixed crack formulation the rotation matrix calculated at the point when cracking of the element first occurred will be used in the construction of the transformation matrix.

The constitutive model is then formulated in the crack coordinate system.

$$\sigma_{nst} = \sigma(\epsilon_{nst}) \quad \text{Equation 5-6}$$

An updated stress vector in the element coordinate system is calculated by multiplying the stress vector in the crack coordinate system by  $\mathbf{T}^T$

(Noting that  $\mathbf{T}^T = \mathbf{T}^{-1}$ ).

$$\sigma_{xyz} = \mathbf{T}^T \sigma_{nst} \quad \text{Equation 5-7}$$

During the determination of the principal directions for the rotating crack formulation a check is made for so called ‘spurious rotation’ of the principal axes. Such a rotation is deemed spurious if it causes a sudden reordering of the principal axes. Reordering may drastically reduce the convergence rate and, since one of the primary aims of the Total Strain Based Crack Model is robustness the following procedure is employed in order to avoid such problems.

$${}^{t+\Delta t}\mathbf{R}^T {}^t\mathbf{R} = \begin{bmatrix} \cos \phi_{nn} & \cos \phi_{ns} & \cos \phi_{nt} \\ \cos \phi_{sn} & \cos \phi_{ss} & \cos \phi_{st} \\ \cos \phi_{tn} & \cos \phi_{ts} & \cos \phi_{tt} \end{bmatrix} \quad \text{Equation 5-8}$$

The rotation matrix for the last converged step  $t$  is denoted as,  ${}^t\mathbf{R}$ . The equivalent rotation matrix for current step is,  ${}^{t+\Delta t}\mathbf{R}$ . The relative rotation of the principal directions between the two steps (Figure 5-3) may be calculated by taking the product of the two rotation matrices (Equation 5-8). If the rotation between the two normal vectors,  ${}^t\mathbf{n}$  and  ${}^{t+\Delta t}\mathbf{n}$ , is found to be greater than  $45^\circ$  (i.e.  $\cos \phi_{nn} < 1/2\sqrt{2}$ ) the ordering of the axes is assumed to be erroneous and a correction is performed. The current normal vector,  ${}^{t+\Delta t}\mathbf{n}$  is swapped with the shear vector,  ${}^{t+\Delta t}\mathbf{s}$  if  $\cos \phi_{ns} \geq 1/2\sqrt{2}$ , or swapped with  ${}^{t+\Delta t}\mathbf{t}$  if  $\cos \phi_{nt} \geq 1/2\sqrt{2}$ . This effectively means that the vector closest to the orientation of the previous normal vector is chosen as the new normal vector. In order to maintain the right-handed configuration of the coordinate system the new shear vector (either  $\mathbf{s}$  or  $\mathbf{t}$  depending on which was swapped above) is calculated by taking the outer product of vectors  $\mathbf{n}$  and the unchanged shear direction. The corrected rotation matrix,  ${}^{t+\Delta t}\mathbf{R}$ , is then multiplied by the previous rotation matrix,  ${}^t\mathbf{R}$ , as before and the shear vector,  $\mathbf{s}$ , is subjected to the above procedure. Finally the process is repeated a third time for the vector,  $\mathbf{t}$ . The new rotation matrix,  ${}^{t+\Delta t}\mathbf{R}$ , can now be used in the creation of the transformation matrix,  $\mathbf{T}$  (Equation 5-5).

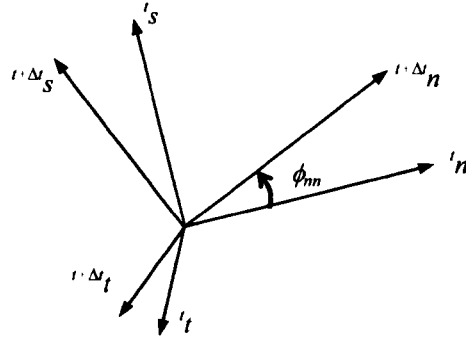


Figure 5-3 - Rotation of Principal Axes

### 5.2.2 Loading and Unloading

Tensile and compressive forces will lead to cracking and crushing of the material. The strain history is monitored via six internal damage variables collected in the vector  $\alpha$ .

$$\alpha = \begin{bmatrix} \alpha_1 \\ \dots \\ \alpha_{ncomp} \\ \alpha_{ncomp+1} \\ \dots \\ \alpha_{ncomp \times 2} \end{bmatrix} \quad \text{Equation 5-9}$$

The vector is shown here in its general form where  $ncomp$  is the total number of stress/strain components. For example, in a 3D solid structure the number of stress/strain components will be 6 whereas for axisymmetry only 4 components are considered. The components of  $\alpha$  are defined as follows:  $\alpha_1 \rightarrow \alpha_{ncomp}$  record the maximum level of strain (tension) encountered and  $\alpha_{nstr+1} \rightarrow \alpha_{ncomp \times 2}$  record the minimum level (compression). A condition of this model is that damage recovery is impossible. In other words, the absolute values of  $\alpha_1 \rightarrow \alpha_{ncomp \times 2}$  will either remain constant or increase due to further straining.

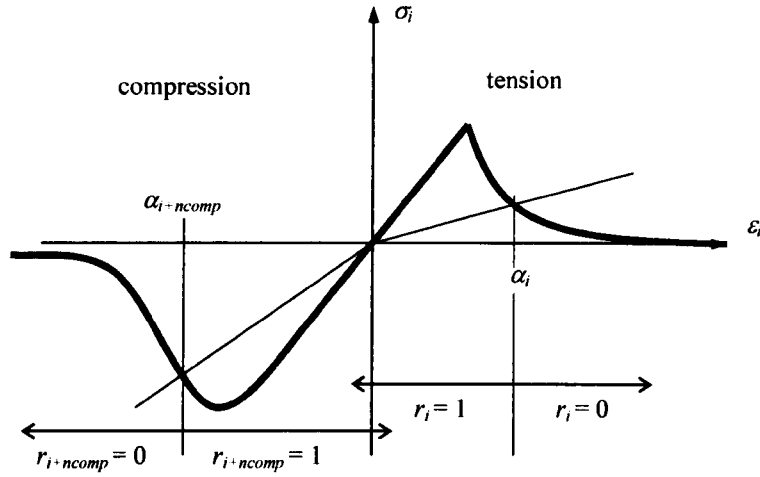


Figure 5-4 - Loading-Unloading Variables

Loading and unloading is controlled by six constraint variables collected in the vector  $\mathbf{r}$

$$\mathbf{r} = \begin{bmatrix} r_1 \\ \dots \\ r_{ncomp} \\ r_{ncomp+1} \\ \dots \\ r_{ncomp \times 2} \end{bmatrix} \quad r_n = \begin{cases} 0 & \text{if } \varepsilon_n > \alpha_n \\ 1 & \text{if } \varepsilon_n \leq \alpha_n \end{cases} \quad n = 1, \dots, ncomp$$

Equation 5-10

The operation of vectors  $\alpha$  and  $\mathbf{r}$  is illustrated in Figure 5-4 for stress-strain component  $i$ . If 'active' loading is defined as the condition whereby the strain component,  $\varepsilon_i$  exceeds the previous maximum as recorded by  $\alpha$  then it can be seen that in cases of active tension the value of  $r_i$  is set to 0. Active compressive loading results in  $r_{i+ncomp}$  being set to 0. Non-active loading is defined as the condition whereby  $\varepsilon_i$  does not exceed previous maximum. In this case unloading or reloading is occurring and the values of  $r_i$  and  $r_{i+ncomp}$  are set to 1. In the TSB Crack Model unloading and reloading is carried out along the secant path. Thus, on complete unloading of the element there will be no residual, unrecoverable strain.

The uniaxial stress-strain relationship in the direction  $i$  is defined as

$$\sigma_i = f_i(\alpha, \varepsilon_{nst}) g_i(\alpha, \varepsilon_{nst}) \quad \text{Equation 5-11}$$

The uniaxial strength function,  $f_i$  is not only dependent on the strain and the damage variable in the direction  $i$  but is also dependent on the values of these variables in the other directions. The second function,  $g_i$  is the loading-unloading function and acts as a scaling function on the uniaxial strength (Figure 5-5). In the current implementation it is defined as follows:

$$g_i = \begin{cases} 1 - \frac{\alpha_i - \varepsilon_i}{\alpha_i} & \text{if } \varepsilon_i > 0 \\ 1 - \frac{\alpha_{i+ncomp} - \varepsilon_i}{\alpha_{i+ncomp}} & \text{if } \varepsilon_i < 0 \end{cases} \quad \text{Equation 5-12}$$

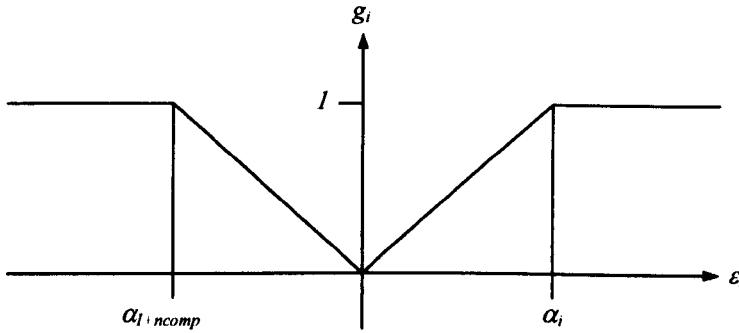


Figure 5-5 - Loading-unloading function

This leads to a secant unloading-reloading approach. It is noted that alternative behaviour could be modelled, e.g. elasto-plastic. This would be achieved by supplying a different loading-unloading function. However, at present there is no option to do this within the DIANA framework.

Updating of the internal variable  $\alpha$  is carried out via the expression

$$\alpha^{t+\Delta t} = \alpha^t + \mathbf{W} \Delta \varepsilon_{nst} \quad \text{Equation 5-13}$$

where the matrix  $\mathbf{W}$  is defined as

$$\mathbf{W} = \begin{bmatrix} w_1 & 0 & 0 \\ 0 & \ddots & 0 \\ 0 & 0 & w_{ncomp} \\ w_{ncomp+1} & 0 & 0 \\ 0 & \ddots & 0 \\ 0 & 0 & w_{ncomp \times 2} \end{bmatrix} \quad \text{where } \begin{aligned} w_{n,n} &= 1 - r_n & n &= 1 \rightarrow ncomp \\ w_{ncomp+n,n} &= 1 - r_n & n &= ncomp + 1 \rightarrow ncomp \times 2 \end{aligned}$$

$$\text{Equation 5-14}$$

### 5.2.3 Stiffness Matrices

A number of different incremental-iterative non-linear solution schemes may be used with the TSB Crack Model (Newton-Raphson, Secant, etc (Figure 5-6)). This requires that both secant and tangent stiffness matrices be formulated.

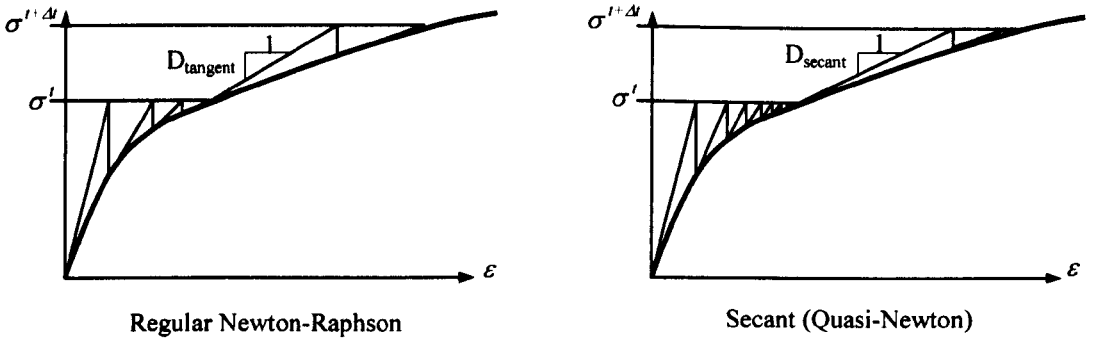


Figure 5-6 – Non-linear Solution Procedures

The derivation of the secant stiffness matrix is based on the concept of an orthotropic material with zero Poisson's Ratio. When expressed in the principal coordinate system this leads to a diagonal matrix.

$$\mathbf{D}_{\text{secant}} = \begin{bmatrix} E_1 & 0 & 0 & 0 & 0 & 0 \\ 0 & E_2 & 0 & 0 & 0 & 0 \\ 0 & 0 & E_3 & 0 & 0 & 0 \\ 0 & 0 & 0 & \frac{E_1 E_2}{E_1 + E_2} & 0 & 0 \\ 0 & 0 & 0 & 0 & \frac{E_2 E_3}{E_2 + E_3} & 0 \\ 0 & 0 & 0 & 0 & 0 & \frac{E_3 E_1}{E_3 + E_1} \end{bmatrix} \quad \text{Equation 5-15}$$

where  $E_i$  is the normal secant stiffness defined as:

$$E_i = \frac{f_i(\boldsymbol{\alpha}, \boldsymbol{\varepsilon}_{nst})}{\alpha_i} \quad \text{and} \quad E_i = \frac{f_i(\boldsymbol{\alpha}, \boldsymbol{\varepsilon}_{nst})}{\alpha_{i+ncomp}} \quad \text{Equation 5-16}$$

for the tensile and compressive regimes respectively.

In the crack coordinate system the tangent stiffness matrix decomposes into four sub-matrices as follows

$$\mathbf{D}_{\text{tangent}} = \begin{bmatrix} \mathbf{D}_{nn} & \mathbf{D}_{n\theta} \\ \mathbf{D}_{\theta n} & \mathbf{D}_{\theta\theta} \end{bmatrix} \quad \text{Equation 5-17}$$

$\mathbf{D}_{nn}$  holds the stiffness terms relating to normal strain whilst the  $\mathbf{D}_{\theta\theta}$  sub-matrix contains the shear components.  $\mathbf{D}_{n\theta}$  and  $\mathbf{D}_{\theta n}$  hold the coupling terms between shear and normal strain.

For the rotating crack concept these coupling terms will be equal to zero since the crack plane will remain aligned with the principal plane. Because the material is assumed to be orthotropic it is likely that the rotation of principal strain will differ from that of principal stress [Bazant (1983)]. As stated above, the plane of orthotropy (the crack plane) is co-rotated with the principal plane for strain. This will lead to the condition whereby the axes of principal stress will not coincide with those for principal strain (i.e. a lack of



coaxiality). The consequence of this is that the principal stress-strain curve cannot be used directly to relate stress and strain.

One solution to this problem is to include a set of transformations to map between the principal stress and strain axes in the formulation of the tangent stiffness matrix. A second solution is to enforce coaxiality. This can be done by first considering the change in principal strain direction caused by a small increment in shear strain (Figure 5-7).

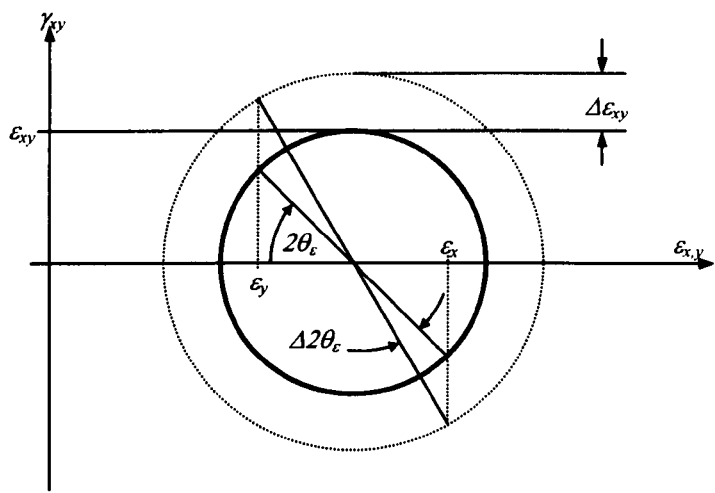


**Figure 5-7 - Principal Strain Rotation**

$$\Delta 2\theta_{\epsilon} = \frac{\Delta \epsilon_{xy}}{2(\epsilon_x + \epsilon_y)}$$

**Equation 5-18**

If  $|\Delta \epsilon_{xy}| \ll |\epsilon_x - \epsilon_y|$ .

A small increment in shear stress will produce a change in the principal stress direction as follows.

$$\Delta 2\theta_{\sigma} = \frac{\Delta \sigma_{xy}}{(\sigma_x + \sigma_y)}$$

**Equation 5-19**

If  $|\Delta\sigma_{xy}| \ll |\sigma_x - \sigma_y|$ . For coaxiality  $\theta_\varepsilon = \theta_\sigma$ . By combining Equation 5-18 and Equation 5-19 we can arrive at:

$$\frac{\sigma_{xy}}{\varepsilon_{xy}} = \frac{(\sigma_x - \sigma_y)}{2(\varepsilon_x - \varepsilon_y)} = G_{xy} \quad \text{Equation 5-20}$$

Hence, the  $\mathbf{D}_{\theta\theta}$  sub-matrix may be assembled as follows

$$\mathbf{D}_{\theta\theta} = \begin{bmatrix} \frac{(\sigma_1 - \sigma_2)}{2(\varepsilon_1 - \varepsilon_2)} & 0 & 0 \\ 0 & \frac{(\sigma_2 - \sigma_3)}{2(\varepsilon_2 - \varepsilon_3)} & 0 \\ 0 & 0 & \frac{(\sigma_3 - \sigma_1)}{2(\varepsilon_3 - \varepsilon_1)} \end{bmatrix} \quad \text{Equation 5-21}$$

This method has the advantage over the first solution in that it is much easier to calculate and therefore less expensive computationally.

For the fixed crack formulation the sub-matrix  $\mathbf{D}_{n\theta}$  is set equal to zero as it is assumed that normal stress components are not dependant on shear stresses. However, shear stress is assumed to be influenced by normal stress and therefore the  $\mathbf{D}_{\theta n}$  reads as follows

$$\mathbf{D}_{\theta n} = \begin{bmatrix} \frac{\partial \sigma_{ns}}{\partial \varepsilon_{nn}} & \frac{\partial \sigma_{ns}}{\partial \varepsilon_{ss}} & \frac{\partial \sigma_{ns}}{\partial \varepsilon_{tt}} \\ \frac{\partial \sigma_{st}}{\partial \varepsilon_{nn}} & \frac{\partial \sigma_{st}}{\partial \varepsilon_{ss}} & \frac{\partial \sigma_{st}}{\partial \varepsilon_{tt}} \\ \frac{\partial \sigma_{tn}}{\partial \varepsilon_{nn}} & \frac{\partial \sigma_{tn}}{\partial \varepsilon_{ss}} & \frac{\partial \sigma_{tn}}{\partial \varepsilon_{tt}} \end{bmatrix} \quad \text{Equation 5-22}$$

Also for the fixed crack formulation the shear component sub-matrix is given by

$$\mathbf{D}_{\theta\theta} = \begin{bmatrix} \frac{\partial \sigma_{ns}}{\partial \gamma_{ns}} & 0 & 0 \\ 0 & \frac{\partial \sigma_{st}}{\partial \gamma_{st}} & 0 \\ 0 & 0 & \frac{\partial \sigma_{tn}}{\partial \gamma_{tn}} \end{bmatrix} \quad \text{Equation 5-23}$$

In both the fixed and rotating crack systems the normal stiffness terms are expressed as

$$\mathbf{D}_{nn} = \begin{bmatrix} \frac{\partial \sigma_{nn}}{\partial \epsilon_{nn}} & \frac{\partial \sigma_{nn}}{\partial \epsilon_{ss}} & \frac{\partial \sigma_{nn}}{\partial \epsilon_{tt}} \\ \frac{\partial \sigma_{ss}}{\partial \epsilon_{nn}} & \frac{\partial \sigma_{ss}}{\partial \epsilon_{ss}} & \frac{\partial \sigma_{ss}}{\partial \epsilon_{tt}} \\ \frac{\partial \sigma_{tt}}{\partial \epsilon_{nn}} & \frac{\partial \sigma_{tt}}{\partial \epsilon_{ss}} & \frac{\partial \sigma_{tt}}{\partial \epsilon_{tt}} \end{bmatrix} \quad \text{Equation 5-24}$$

Off diagonal terms are not set to zero since the lateral strain effects are accounted for in the calculation of principal stresses.

The partial differential terms found in the stiffness matrix may be calculated by first differentiating the stress-strain relationship (Equation 5-11) with respect to principal strain,  $\epsilon_{nst}$  and noting that the differential of the internal variable,  $\alpha$  with respect to the principal strain vector,  $\epsilon_{nst}$  is given by the matrix  $\mathbf{W}$  (Equation 5-14).

$$\frac{\partial \sigma_{ii}}{\partial \epsilon_{nst}} = g_{ii}(\alpha, \epsilon_{nst}) \left\{ \mathbf{W}^T \frac{\partial f_{ii}}{\partial \alpha} + \frac{\partial f_{ii}}{\partial \epsilon_{nst}} \right\} + f_{ii}(\alpha, \epsilon_{nst}) \left\{ \mathbf{W}^T \frac{\partial g_{ii}}{\partial \alpha} + \frac{\partial g_{ii}}{\partial \epsilon_{nst}} \right\} \quad \text{Equation 5-25}$$

This expression may be expanded as follows:

$$\begin{aligned}
 \mathbf{D}_{nst} = & \begin{bmatrix} (m_1 r_1 + (1 - m_1) r_4) E_1 & 0 & 0 \\ 0 & (m_2 r_2 + (1 - m_2) r_5) E_2 & 0 \\ 0 & 0 & (m_3 r_3 + (1 - m_3) r_6) E_3 \end{bmatrix} \\
 + & \begin{bmatrix} g_1 & 0 & 0 \\ 0 & g_2 & 0 \\ 0 & 0 & g_3 \end{bmatrix} \begin{bmatrix} \frac{\partial f_1}{\partial \varepsilon_1} & \frac{\partial f_1}{\partial \varepsilon_2} & \frac{\partial f_1}{\partial \varepsilon_3} \\ \frac{\partial f_2}{\partial \varepsilon_1} & \frac{\partial f_2}{\partial \varepsilon_2} & \frac{\partial f_2}{\partial \varepsilon_3} \\ \frac{\partial f_3}{\partial \varepsilon_1} & \frac{\partial f_3}{\partial \varepsilon_2} & \frac{\partial f_3}{\partial \varepsilon_3} \end{bmatrix} \\
 + & \begin{bmatrix} g_1 & 0 & 0 \\ 0 & g_2 & 0 \\ 0 & 0 & g_3 \end{bmatrix} \begin{bmatrix} \frac{\partial f_1}{\partial \alpha_1} & \frac{\partial f_1}{\partial \alpha_2} & \dots & \frac{\partial f_1}{\partial \alpha_3} \\ \frac{\partial f_2}{\partial \alpha_1} & \frac{\partial f_2}{\partial \alpha_2} & \dots & \frac{\partial f_2}{\partial \alpha_3} \\ \frac{\partial f_3}{\partial \alpha_1} & \frac{\partial f_3}{\partial \alpha_2} & \dots & \frac{\partial f_3}{\partial \alpha_3} \end{bmatrix} \begin{bmatrix} 1 - r_1 & 0 & 0 \\ 0 & 1 - r_2 & 0 \\ 0 & 0 & 1 - r_3 \\ 1 - r_4 & 0 & 0 \\ 0 & 1 - r_5 & 0 \\ 0 & 0 & 1 - r_6 \end{bmatrix}
 \end{aligned}
 \tag{Equation 5-26}$$

Secant stiffness terms are defined as before (Equation 5-16).

The status variable,  $m_i$  is used to flag the stress state as being either compressive or tensile and is defined as

$$m_i = \begin{cases} 1 & \text{if } \varepsilon_i > 0 \\ 0 & \text{if } \varepsilon_i \leq 0 \end{cases}
 \tag{Equation 5-27}$$

The operation of the tangent stiffness formula can best be described by writing out one of the stiffness terms in full.

$$\frac{\partial \sigma_i}{\partial \varepsilon_i} = (m_i r_i + (1 - m_i) r_{i+ncomp}) E_i + g_i \left( (1 - r_i) \frac{\partial f_i}{\partial \alpha_i} + (1 - r_{i+ncomp}) \frac{\partial f_i}{\partial \alpha_{i+ncomp}} \right)
 \tag{Equation 5-28}$$

Firstly, considering a tensile condition:  $m_i = 1$ ,  $r_{i+ncomp} = 1$ . This causes the equation to reduce to

$$\frac{\partial \sigma_i}{\partial \varepsilon_i} = r_i E_i + g_i (1 - r_i) \frac{\partial f_i}{\partial \alpha_i} \quad \text{Equation 5-29}$$

This further reduces depending on whether or not an active tensile loading state is present.

$$\frac{\partial \sigma_i}{\partial \varepsilon_i} = \begin{cases} \frac{\partial f_i}{\partial \alpha_i} & \text{for active loading} \\ E_i & \text{for non - active loading / unloading} \end{cases} \quad \text{Equation 5-30}$$

Following a similar approach for compressive strain states the stiffness term reduces to

$$\frac{\partial \sigma_i}{\partial \varepsilon_i} = \begin{cases} \frac{\partial f_i}{\partial \alpha_{i+ncomp}} & \text{for active loading} \\ E_i & \text{for non - active loading / unloading} \end{cases} \quad \text{Equation 5-31}$$

This process reveals that due the way in which the tangent stiffness matrix is formulated it elegantly reduces to provide either a tangent or secant stiffness where needed. Because the internal status variables  $r_i$  and  $m_i$  are set to binary values it ensures that the terms they act on are either present or vanish completely from the overall equation. This undoubtedly adds to the robustness and accuracy of the model.

Calculation of the partial differentials in the tangent stiffness formulation is performed via a finite difference scheme.

$$\frac{\partial f_i}{\partial \varepsilon_j} = \frac{f_i(\mathbf{a}, \varepsilon_{nst} + h \mathbf{e}_j) - f_i(\mathbf{a}, \varepsilon_{nst})}{h} \quad \text{Equation 5-32}$$

and

$$\frac{\partial f_i}{\partial \alpha_j} = \frac{f_i(\mathbf{a} + h \mathbf{a}_j, \varepsilon_{nst}) - f_i(\mathbf{a}, \varepsilon_{nst})}{h} \quad \text{Equation 5-33}$$

where the components of vectors  $\mathbf{e}$  and  $\mathbf{a}$  are equal to zero except for the  $j^{th}$  component. The step size,  $h$  is given as  $tol.\varepsilon_j$  and  $tol.\alpha_j$  respectively, where  $tol$  is the square root of the machine precision. In the current implementation of the model  $tol$  is set to  $1 \times 10^{-16}$  thus assuming a machine precision of  $1 \times 10^{-32}$ . Considering this assumption, it does seem slightly conservative considering that most modern computers adhere to the IEEE floating point standard allowing a precision of  $1 \times 10^{-53}$  [Vandenberghe (2002)]. It may be that this value as chosen in order to reduce loss of precision due to round off errors in the calculation of the above equations. In any case the use of a finite difference approach does yield several advantages, the primary one being that the complex step of deriving the algebraic derivatives of the uniaxial strength function need not be done. It must also be noted that the more complex the derivate, the more prone it is to rounding errors when calculating its value. Therefore, there may be little gain in accuracy or computation time in using the algebraic derivative.

#### **5.2.4 Poisson's Effects**

Due to the Poisson's effect uniaxial tension and compression will lead to lateral displacement. If this displacement is constrained a passive lateral confinement will be produced. It has been noted that experimental research data reveals an increase in Poisson's ratio from an elastic value of 0.15 up to approximately 0.5 in the failure zone of concrete under compressive loading [Feenstra et al, (1998)]. Therefore it is obvious that this phenomena is important in the modelling of concrete in three-dimensions. The Poisson's Effect is handled in a linear-elastic fashion in the TSB Crack Model through the use of the equivalent uniaxial strain concept.

The constitutive equation for an elastic material in a 3D stress-strain state is given by:

$$\sigma_{nst} = \frac{E}{(1+\nu)(1-2\nu)} \begin{bmatrix} 1-\nu & \nu & \nu & 0 & 0 & 0 \\ \nu & 1-\nu & \nu & 0 & 0 & 0 \\ \nu & \nu & 1-\nu & 0 & 0 & 0 \\ 0 & 0 & 0 & \frac{1-2\nu}{2} & 0 & 0 \\ 0 & 0 & 0 & 0 & \frac{1-2\nu}{2} & 0 \\ 0 & 0 & 0 & 0 & 0 & \frac{1-2\nu}{2} \end{bmatrix} \epsilon_{nst} \quad \text{Equation 5-34}$$

This may be rearranged as follows

$$\sigma_{nst} = \begin{bmatrix} E & 0 & 0 & 0 & 0 & 0 \\ 0 & E & 0 & 0 & 0 & 0 \\ 0 & 0 & E & 0 & 0 & 0 \\ 0 & 0 & 0 & \frac{E}{2(1+\nu)} & 0 & 0 \\ 0 & 0 & 0 & 0 & \frac{E}{2(1+\nu)} & 0 \\ 0 & 0 & 0 & 0 & 0 & \frac{E}{2(1+\nu)} \end{bmatrix} \begin{bmatrix} \frac{1-\nu}{(1+\nu)(1-2\nu)} & \frac{\nu}{(1+\nu)(1-2\nu)} & \frac{\nu}{(1+\nu)(1-2\nu)} & 0 & 0 & 0 \\ \frac{\nu}{(1+\nu)(1-2\nu)} & \frac{1-\nu}{(1+\nu)(1-2\nu)} & \frac{\nu}{(1+\nu)(1-2\nu)} & 0 & 0 & 0 \\ \frac{\nu}{(1+\nu)(1-2\nu)} & \frac{\nu}{(1+\nu)(1-2\nu)} & \frac{1-\nu}{(1+\nu)(1-2\nu)} & 0 & 0 & 0 \\ \frac{\nu}{(1+\nu)(1-2\nu)} & \frac{\nu}{(1+\nu)(1-2\nu)} & \frac{\nu}{(1+\nu)(1-2\nu)} & 0 & 0 & 0 \\ 0 & 0 & 0 & 1 & 0 & 0 \\ 0 & 0 & 0 & 0 & 1 & 0 \\ 0 & 0 & 0 & 0 & 0 & 1 \end{bmatrix} \epsilon_{nst} \quad \text{Equation 5-35}$$

Noting that  $\frac{E}{2(1+\nu)}$  is the elastic shear modulus Equation 5-35 may be expressed in the compact form

$$\sigma_{nst} = E \tilde{\epsilon}_{nst} \quad \text{Equation 5-36}$$

where  $\tilde{\epsilon}_{nst}$  is known as the equivalent uniaxial strain vector and is defined by

$$\begin{bmatrix} \tilde{\epsilon}_{nn} \\ \tilde{\epsilon}_{ss} \\ \tilde{\epsilon}_{tt} \\ \tilde{\epsilon}_{ns} \\ \tilde{\epsilon}_{st} \\ \tilde{\epsilon}_{m} \end{bmatrix} = \begin{bmatrix} \frac{1-\nu}{(1+\nu)(1-2\nu)} & \frac{\nu}{(1+\nu)(1-2\nu)} & \frac{\nu}{(1+\nu)(1-2\nu)} & 0 & 0 & 0 \\ \frac{\nu}{(1+\nu)(1-2\nu)} & \frac{1-\nu}{(1+\nu)(1-2\nu)} & \frac{\nu}{(1+\nu)(1-2\nu)} & 0 & 0 & 0 \\ \frac{\nu}{(1+\nu)(1-2\nu)} & \frac{\nu}{(1+\nu)(1-2\nu)} & \frac{1-\nu}{(1+\nu)(1-2\nu)} & 0 & 0 & 0 \\ \frac{0}{(1+\nu)(1-2\nu)} & \frac{0}{(1+\nu)(1-2\nu)} & \frac{0}{(1+\nu)(1-2\nu)} & 1 & 0 & 0 \\ 0 & 0 & 0 & 0 & 1 & 0 \\ 0 & 0 & 0 & 0 & 0 & 1 \end{bmatrix} \begin{bmatrix} \epsilon_{nn} \\ \epsilon_{ss} \\ \epsilon_{tt} \\ \epsilon_{ns} \\ \epsilon_{st} \\ \epsilon_m \end{bmatrix}$$

Equation 5-37

or

$$\tilde{\epsilon}_{nst} = \mathbf{P} \epsilon_{nst}$$

Equation 5-38

where  $\mathbf{P}$  is known as the expansion matrix.

These lateral expansion effects can be accounted for in a manner that is transparent to the computational flow of the existing finite element framework by substituting  $\tilde{\epsilon}_{nst}$  for  $\epsilon_{nst}$  in the calculation of crack stress vector in the principal coordinate system (Equation 5-6). The tangent sub-matrix  $\mathbf{D}_{nst}$  must also be modified as follows:

$$\mathbf{D}_{nst} = \frac{\partial \sigma_{nst}}{\partial \epsilon_{nst}} = \frac{\partial \sigma_{nst}}{\partial \tilde{\epsilon}_{nst}} \mathbf{P} \quad \text{Equation 5-39}$$

Derivations of the equivalent elastic strain may be found for other stress-strain states by starting with the appropriate linear-elastic constitutive relationship and following the above procedure.



5.2.5 Tensile and Compressive Behaviour

Tensile failure in the model is governed by the Rankine criterion. Post peak behaviour may be modelled via one of the tension softening response curves. Four models based on fracture energy are provided [Reinhardt (1984), Cornelissen, Hordijk, Reinhardt (1986), Hordijk (1991)] along with elastic, elastic-perfectly plastic and brittle models (Figure 5-8).

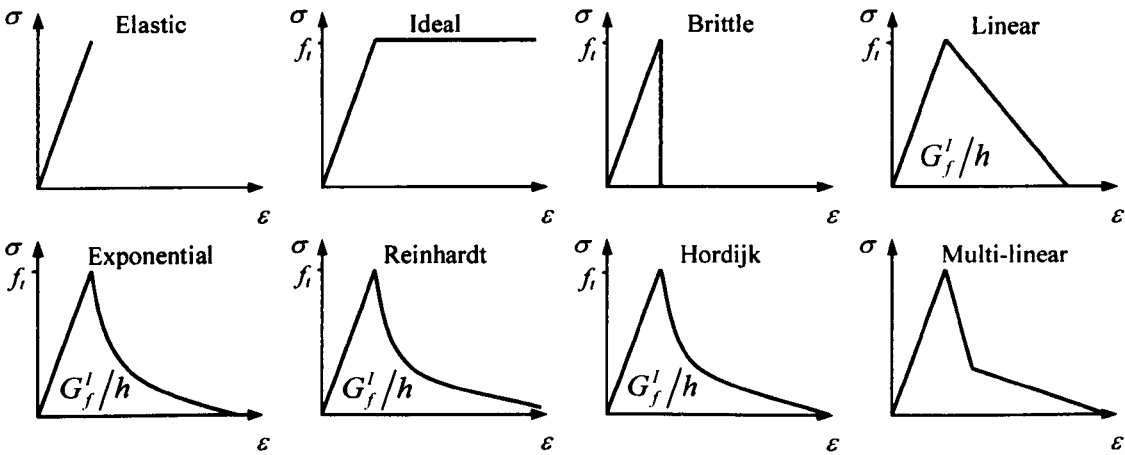
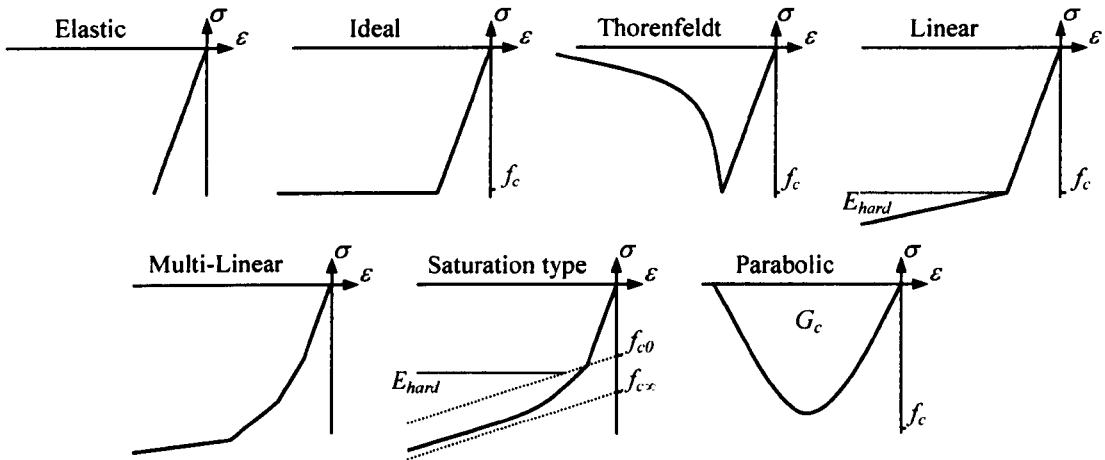


Figure 5-8 – Predefined Material Response Curves for Tension

In a similar way basic compressive behaviour is governed by one of a number of predefined stress-strain functions provided (Figure 5-9).

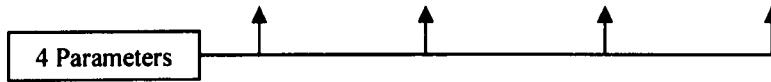


**Figure 5-9 - Predefined Material Response Curves for Compression**

### 5.2.6 Lateral Confinement Effects

For concrete it has been found that its behaviour is pressure dependent. Both strength and ductility increase with increasing isotropic stress that may arise from lateral confinement. In the Total Strain Based Crack Model the increase in strength is modelled by a Hsieh-Ting-Chen [Hsieh, Ting and Chen (1982)] four-parameter failure surface the equation for which is shown below.

$$f = 2.0108 \frac{J_2}{f_{cc}^2} + 0.9714 \frac{\sqrt{J_2}}{f_{cc}} + 9.1412 \frac{f_{cl}}{f_{cc}} + 0.2312 \frac{I_1}{f_{cc}} - 1 = 0 \quad \text{Equation 5-40}$$



where the stress invariants  $J_2$  and  $I_1$  are calculated from the principal concrete stresses.  $f_{cc}$  is the maximum concrete compressive strength and  $f_{cl}$  is the maximum principal stress.

The linear elastic stress vector  $\sigma_c$  is multiplied by a scaling factor,  $s$  such that Equation 5-40 holds. The compressive failure stress of the concrete is then given by multiplying the minimum principal stress by the scaling factor.

Figure 5-10 shows the effect the above method has on the stress-strain response of concrete under lateral compression. The limiting case is that of the full triaxial stress condition where the failure surface cannot be reached and a linear stress-strain relationship is produced.

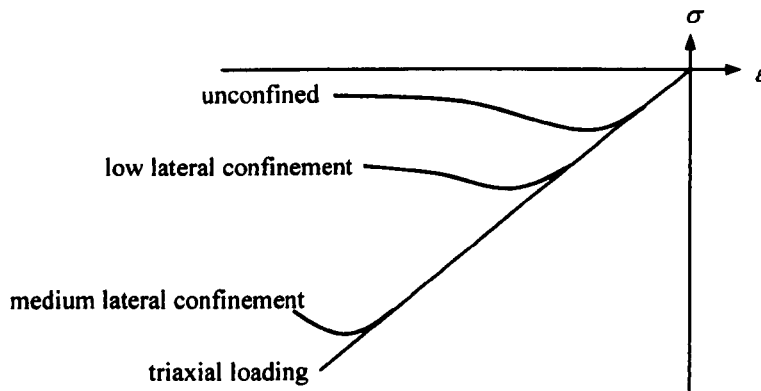


Figure 5-10 - Influence of Lateral Confinement on Compressive Stress-Strain Curve

### 5.2.7 Compression Softening Effects

Experimental research carried out by many research groups has shown that concrete will reveal a reduced compressive strength if significant tensile strains perpendicular to the direction of principal compressive stress are present. In their review of experimental and analytical research into this phenomenon Vecchio and Collins [Vecchio and Collins (1993)] proposed two models for this compression softening. Model A gave a reduction in both material strength and the associated strain level whereas Model B modified only the strength (Figure 5-11). When compared with experimental results, Model A gave a significantly better correlation coefficient as compared with Model B (0.861 v 0.682), however it is Model B that is employed in the Total Strain Based Crack Model. In the absence of further explanation of this choice it is assumed that Model B is either simpler to implement or is in some way more compatible with the framework of the Crack Model.

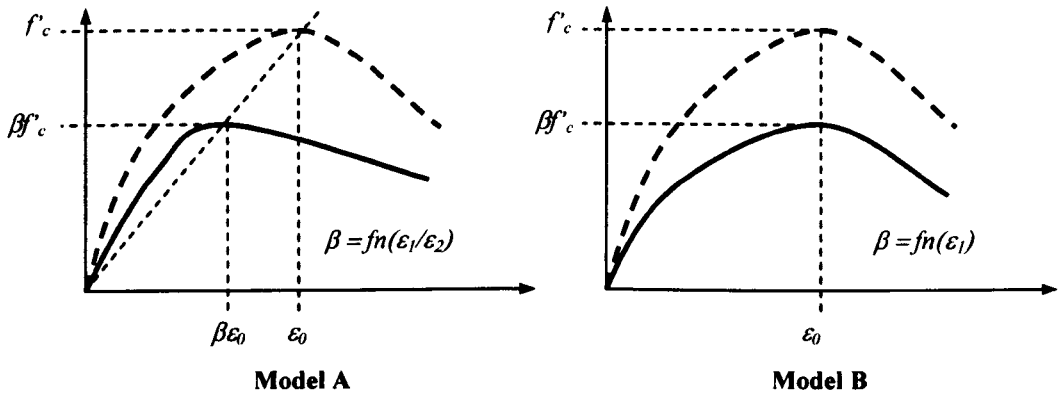


Figure 5-11 - Compression Softening Models [Vecchio and Collins (1993)]

The approach used is to apply a reduction factor  $\beta_{ocr}$ , to the compressive strength,  $f_p$  (Figure 5-12). This is defined as:

$$\beta_{ocr} = \frac{1}{1 + K_c} \leq 1 \quad \text{Equation 5-41}$$

where

$$K_c = 0.27 \left( \frac{\alpha_{lat}}{\epsilon_0} - 0.37 \right) \quad \text{Equation 5-42}$$

and

$$\alpha_{lat} = \sqrt{\alpha_{l,1}^2 + \alpha_{l,2}^2}$$

**Equation 5-43**

$\epsilon_0$  is defined as the strain in the concrete at peak stress. Equation 5-43 provides a measure of average lateral damage (strain) and is a function of the tensile damage factors,  $\alpha_{l,1}$ ,  $\alpha_{l,2}$ , in the directions perpendicular to the compressive force.

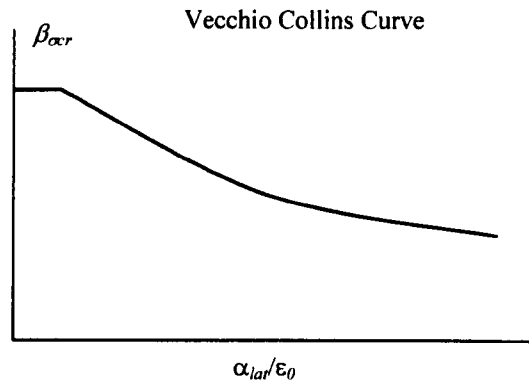


**Figure 5-12 - Reduction Factor Due to Lateral Cracking [Vecchio and Collins (1993)]**

5.2.8 Shear Behaviour

Upon cracking of concrete shear stresses may still be transmitted via aggregate interlock [Hofstetter and Mang (1995), Vecchio and Collins (1986)](Figure 5-13). However there will be a reduction in the shear stiffness.

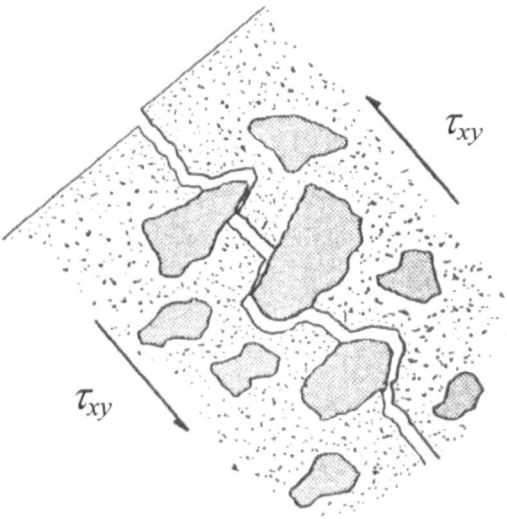


Figure 5-13 - Aggregate Interlock

In the context of smeared crack models it has become common practice to represent this reduction by means of a shear retention factor,  $\beta$  [Rots, et al (1985)]. Various formulations for the calculation have been developed however the present model provides only a constant shear retention (Figure 5-14). For this a suitable value of  $\beta$  is chosen as a material parameter and upon cracking the shear stiffness  $G$ , is calculated as follows:

$$G_{cr} = \beta G \quad \text{where} \quad 0 \leq \beta \leq 1$$

Equation 5-44

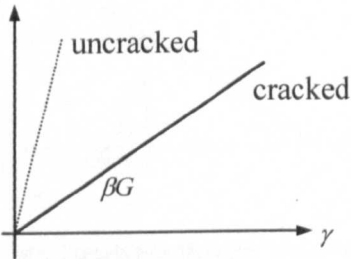


Figure 5-14 - Shear Retention Model

### 5.2.9 Post-processing

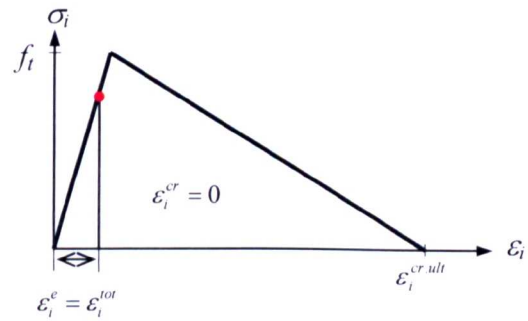
Since the TSB Crack Model is formulated in terms of total strain throughout, in order to obtain values of crack strain equivalent to those of the Traditional Crack Model a decomposition of the total strain is performed in the post-processing stage. This is achieved by subtracting the elastic stiffness, based on the initial Young’s modulus, from the total strain.

$$\epsilon_i^{cr} = \epsilon_i^{tot} - \epsilon_i^e$$

$$\epsilon_i^{cr} = \epsilon_i^{tot} - E\sigma_i$$

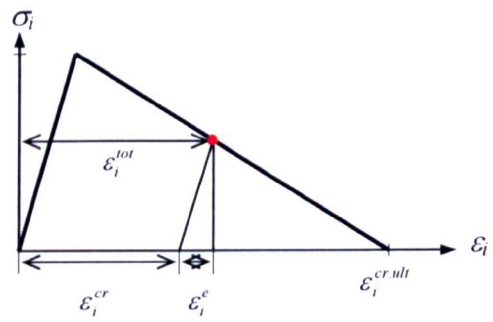
**Equation 5-45**

Thus for the initial, linear-elastic material response  $\epsilon_i^e = \epsilon_i^{tot}$  hence the crack strain is zero.



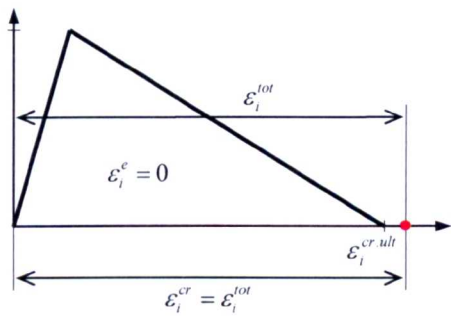
**Equation 5-46 - Strain Decomposition for Initial Linear-Elastic Stage**

For the post-peak, softening region the above decomposition results in both elastic and crack components of strain.



**Equation 5-47 - Strain Decomposition for Post-Peak Softening Stage**

It is interesting to note that for this region, as the total strain increases, the portion attributed to elastic straining decreases and the crack component increases. This is in agreement with the actual material behaviour since the concrete in the intact zone will elastically unload as the crack opens.



**Equation 5-48 - Strain Decomposition for Strains Greater than Ultimate Crack Strain**

Finally, when the total strain meets and exceeds the ultimate crack strain,  $\epsilon_i^{cr,ult}$  the elastic component becomes zero and  $\epsilon_i^{cr} = \epsilon_i^{tot}$ .



5.3 Benchmarking of Model

In order to understand how the Total Strain Based Crack Model behaved in practice and how the individual features contributed to the overall material response a number of benchmark studies were undertaken.

For the initial tests a single element, 3D model was created as shown below (Figure 5-15). The rotating formulation of the TSB Crack Model was used with exponential tension softening.

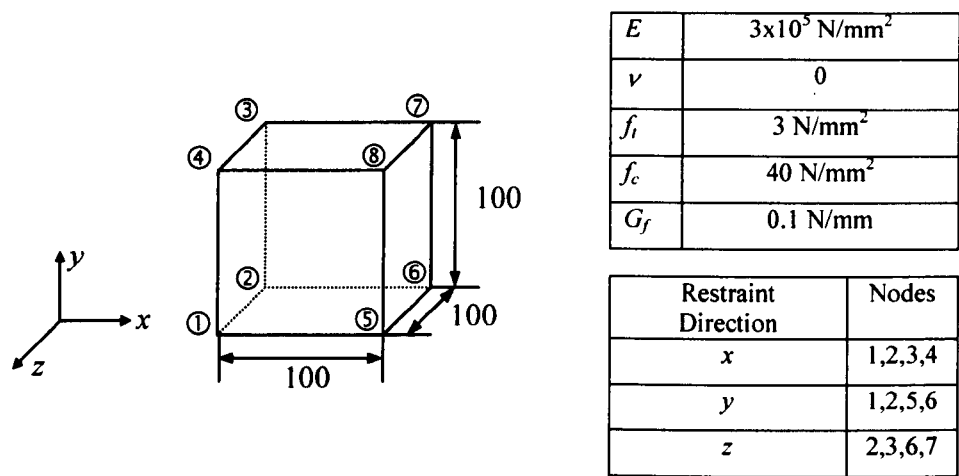


Figure 5-15 - Initial Benchmark Model

5.3.1 Biaxial Loading-Unloading Response

The first test in this series consisted of two prescribed displacements being applied to the block simultaneously. The first was applied to the right-hand face (nodes 5,6,7,8) in the positive x-direction. The second was applied to the top face (nodes 3,4,7,8) in the positive y-direction. The ratio of the magnitude of the x displacement to the y displacement can be expressed as:

$$\Delta x = s.\Delta y$$

Equation 5-49

where s is a scaling factor in the range 0 to 1.

The model was tested with various values of s and the associated responses are shown in Figure 5-16.

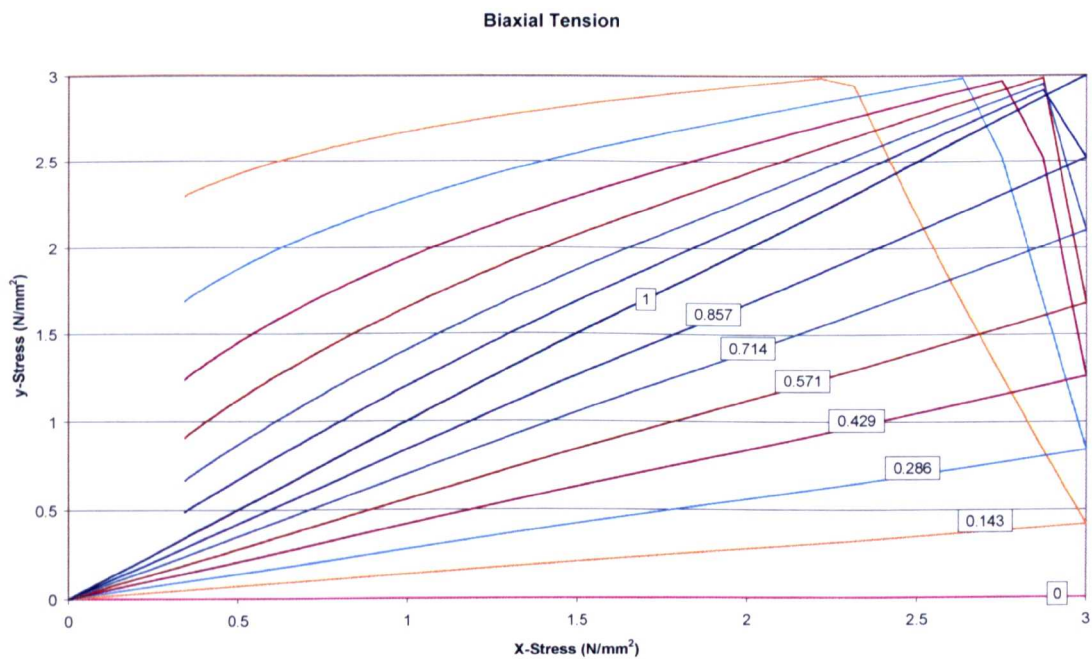
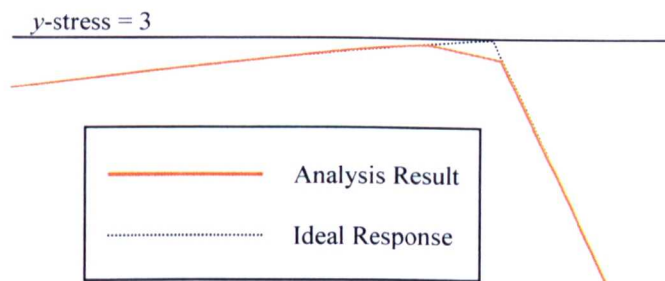


Figure 5-16 - Biaxial Tension Test of Single Element

With a value of  $s=0$  the test is effectively a uniaxial extension test. The response shows the value of stress in the x-direction increasing up to the material strength of 3 N/mm<sup>2</sup> followed by a reduction in stress level associated with material softening. In this case the value of stress in the y-direction remains zero. With values of  $s>0$  the y-stress component

is non-zero. Its value rises until it reaches the tensile limit and then reduces due to softening. It can be seen that the softening slope is a curve due to the exponential softening model used in these analyses. It is clear that the term ‘single crack model’ in this context refers to the fact that it is possible to have a single crack on each of the mutually orthogonal crack planes. In this case, due to the choice of loading, the global, principal and crack planes are aligned and remain so during the analysis. A second important point illustrated by these responses is that the tensile loading-unloading behaviour in given crack direction is independent of stress level and material state in the other crack directions. This also underlines the orthotropic nature of this material model. It is noted that for most of the analyses the  $y$ -stress does not actually reach the tensile stress of the material (Figure 5-16). This occurs because the chosen displacement step size was such that no analysis step exactly coincided with the point where the stress in the  $y$  direction reached  $3 \text{ N/mm}^2$ . With exceedingly small displacement steps this peak could have been reached and the responses would have been the same as the ideal model response (Figure 5-17).



**Figure 5-17 - Comparison of Analysis Result and Ideal Model Response**

In the second set of tests a number of different displacement histories were examined. For the first case the block was subjected to uniaxial extension followed by a return to the original length and finally a re-extension. The stress-strain response shown below (Figure 5-18) reveals an initial linear-elastic response up to the yield strength of the material followed by a period of softening. As the model is unloaded in the second stage of the analysis the response follows the secant unloading path as expected and on reaching the

original length there is a zero stress state. Finally, the reloading response of the structure follows the secant path.

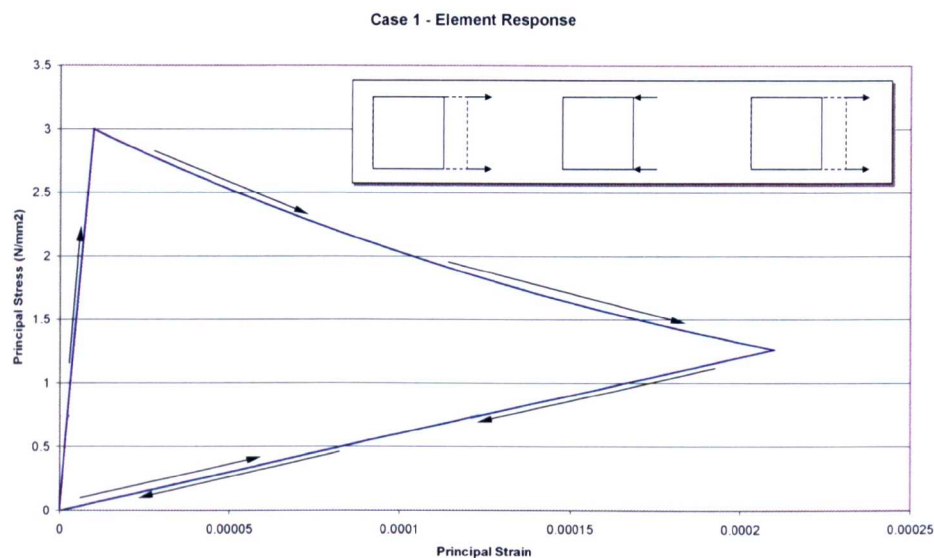
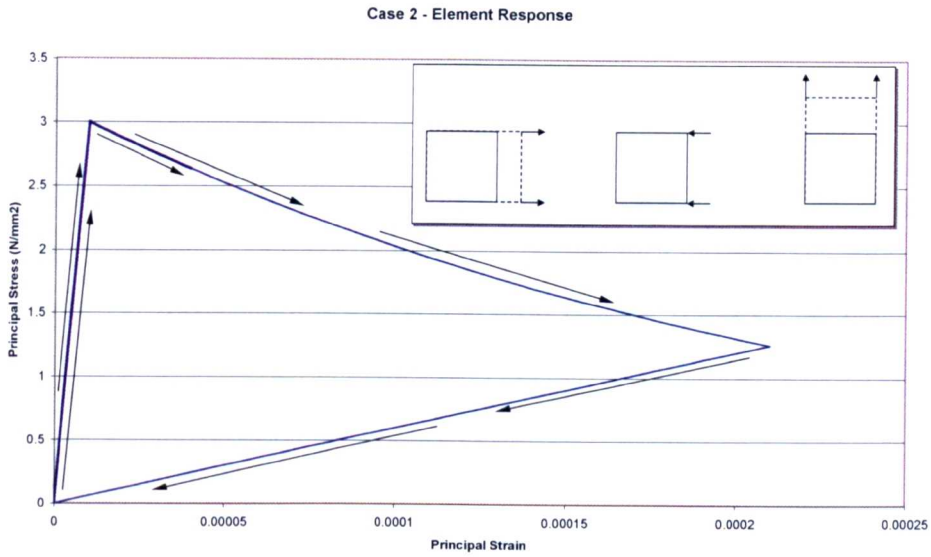


Figure 5-18 - Case 1 Response

The second case differs from the first in that the displacement in the final stage is applied in the y-direction. Although the internal damage variables,  $\alpha$ , are directional, this test was devised in order to determine how these variables were updated upon full unloading of the initial crack and reloading in a perpendicular direction. In particular whether the primary crack plane would rotate to align itself with the new principal plane. The response shown in Figure 5-19 shows the same elastic loading, softening and secant unloading as seen in the previous case. However, in the third stage, instead of reloading along the secant path as the previous test had done, the structural response follows the linear elastic path up to the material limit and then follows the softening slope. This implies that the history variables for the crack formed in stage 1 were not used. This result was unexpected as a rotation of the crack plane to the new principal plane was anticipated.





**Figure 5-19 - Case 2 Response**

Although the theory of the TSB Crack Model was clear the precise implementation of the model in this respect was not as clearly documented. Therefore three possible reasons for this behaviour were proposed.

1. Although unlikely, it was thought possible that the strain history variables had been reset to their initial values since the model had been returned to its initial state before the loading was applied in the third stage.
2. The rotating formulation of the TSB Crack Model was used therefore the crack planes are constantly updated so as to remain aligned with the principal planes. In this analysis, due to the choice of loading, both the primary crack direction and the direction of maximum principal strain were both collinear with the global direction,  $x$ . The loading in the third stage of the analysis was in the  $y$ -direction, perpendicular to the previous loading. This direction was also likely to be collinear with the secondary crack direction,  $s$ . It was thought possible that the model recognised this occurrence and therefore calculated the response in terms of the undamaged crack plane,  $s$  rather than the damaged plane,  $n$ .

3. The third reason was that ordering of the principal planes was being modified by the procedure detailed in section 5.2.1 that detects spurious rotation of such planes.

The first option was easily tested by only partially unloading the model in stage 2 of the analysis. This was done and the results are shown in Figure 5-20. Following the maximum principal stress-strain response it is clear that the linear-elastic loading path is followed again in the third stage of the analysis therefore disproving the first theory.

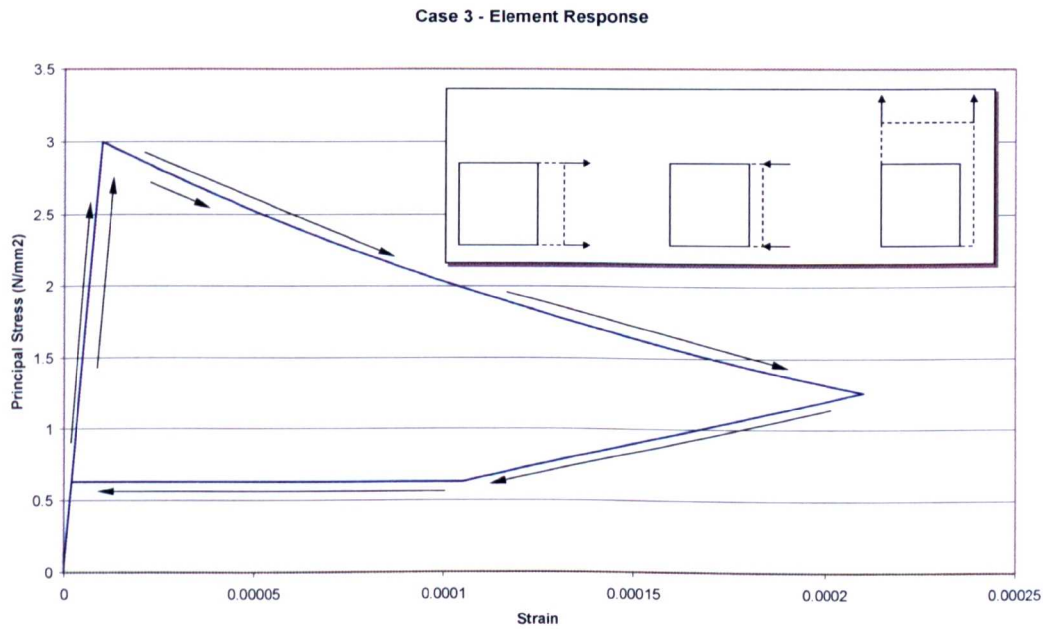


**Figure 5-20 - Case 3 Response**

The second theory was tested by applying a displacement in the third stage in such a way as not to produce a principal plane that coincided with a current crack plane. This was done by applying a displacement in the  $xy$ -direction to the upper, right edge of the structure (nodes 7 and 8). As can be seen for the response in Figure 5-21, the loading, softening and unloading behaviour was exactly the same as that produced in case 2. However, in the third stage of the analysis a different stiffness is apparent. This is much stiffer than the secant stiffness that was expected but it is softer than the initial elastic stiffness found in stage 1 of the analysis. On investigating this further it was found that

the new stiffness was exactly the same as that produced if the model is only loaded in the  $xy$ -direction (i.e. stages 1 and 2 of the analysis are skipped). Therefore it was clear that the Total Strain Based Crack Model was not assigning the previously damaged crack plane,  $n$  to be aligned to the updated principal plane but instead assigning one of the undamaged crack planes ( $s$  or  $t$ ). Furthermore, this test ruled out the second theory proposed.

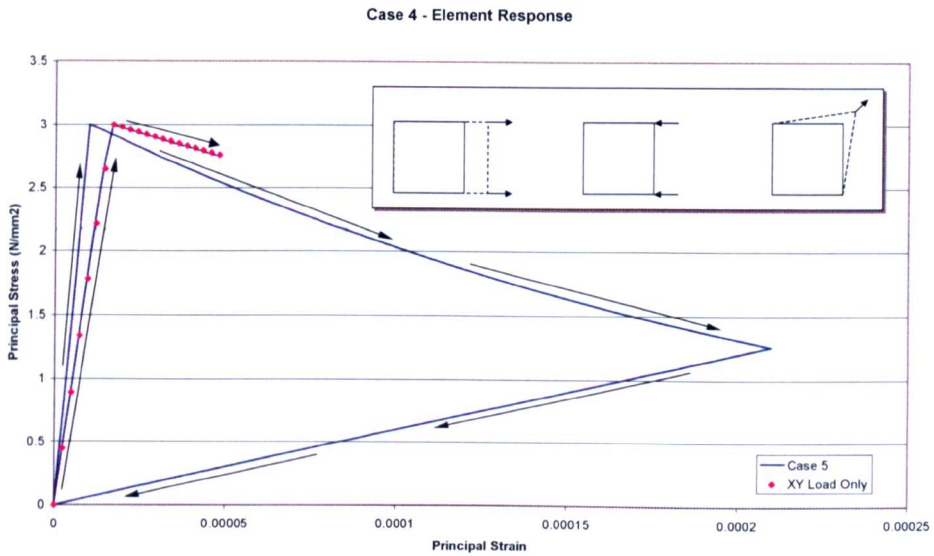


**Figure 5-21 - Case 4 Response**

The third theory was investigated by first looking at the orientation and rotation of the principal planes during the course of analysis cases 2 to 4 (Figure 5-22). For all three cases the maximum principal plane remains aligned with the  $xx$ -plane for stages 1 and 2 of the analyses. In stage 3 there is an instantaneous jump to a new orientation. For cases 2 and 3 the jump is  $90^\circ$  and a  $48.31^\circ$  jump for case 4. The routine that corrects for spurious rotations of the principal planes is invoked if the rotation between two updates is greater than  $45^\circ$ . Therefore the routine comes into effect in cases being considered and the stage 3 loading is considered to form a crack on a previously undamaged crack plane.

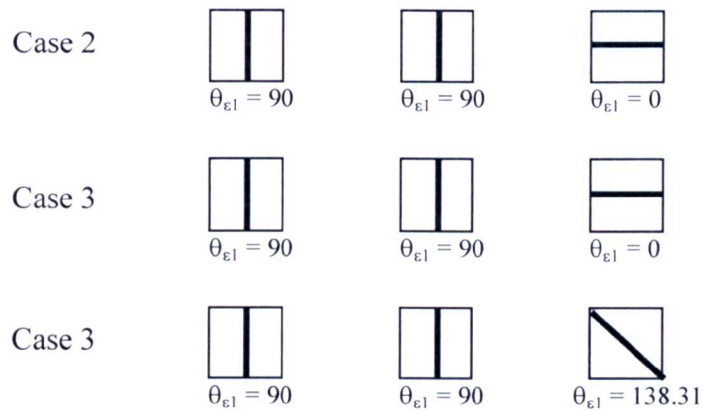


**Figure 5-22 - Rotation of Principal Plane**

To avoid activating the correction routine the principal plane must rotate gradually into its new orientation. This was achieved by only partially unloading the element in stage 2 of the analysis and then applying the  $xy$  displacement as before. The stress-strain response is shown in Figure 5-23.

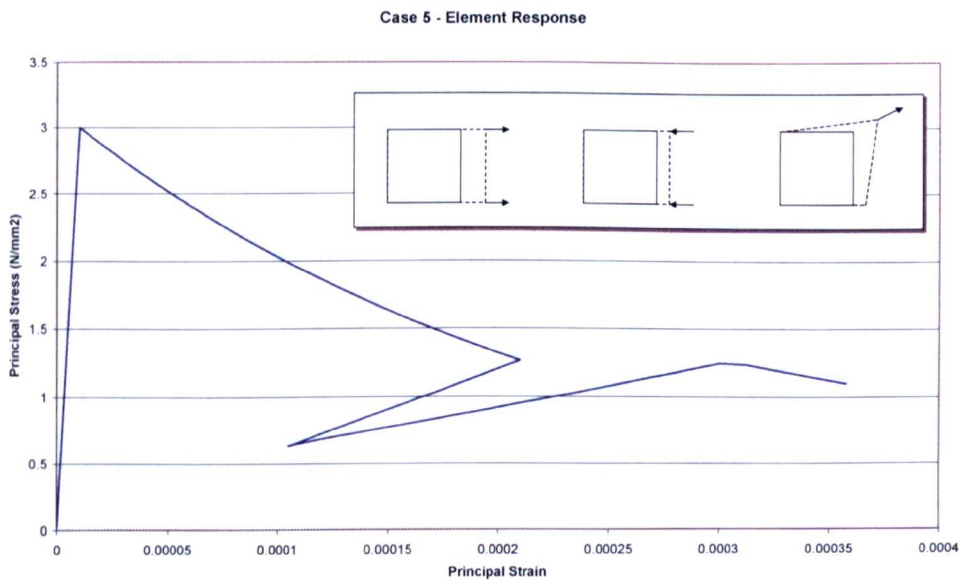


**Figure 5-23 - Case 5 Response**

It can be clearly seen that the reloading response does not use the initial elastic stiffness but instead uses the secant stiffness. Looking at the history of the principal plane (Figure



5-24) confirms that, in the third stage of the analysis, there is a gradual rotation rather than a sudden jump.

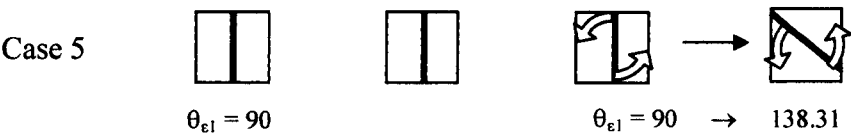


Figure 5-24 - Case 5, Rotation of Principal Plane

It is true to say that the above analyses represent the extreme cases and are perhaps not realistic in terms of the structural behaviour found in larger structures. However they do illustrate how a simple check, such as the one for spurious rotation of the principal axes, can lead to unexpected results.

### 5.3.2 Ghavamian Uniaxial Load Reversal Test

The MECA project was initiated in 2000 by Electricité de France to investigate the suitability of a number of 3D constitutive models in the analysis of concrete fracture. The first set of results was published in 2003 and details a number of benchmark tests [Ghavamian, Carol (2003)]. The first of these is a uniaxial tension-compression test with load reversals. The geometry and material properties of which is detailed in Figure 5-25.

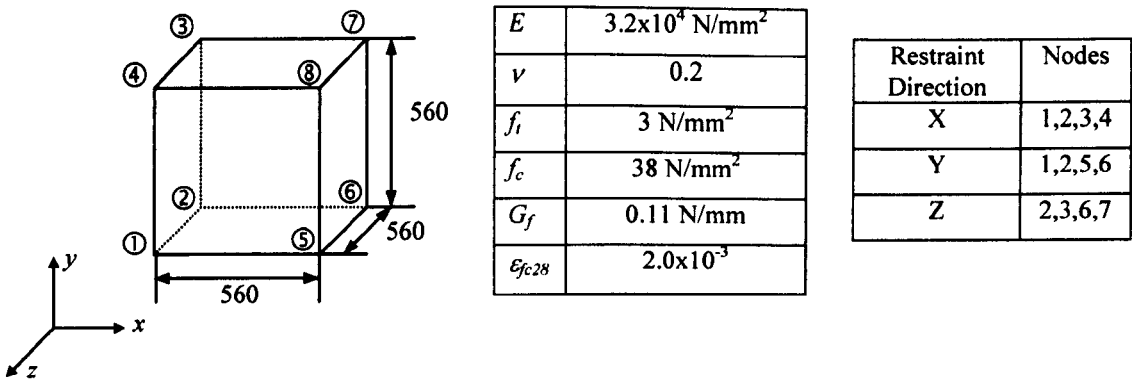
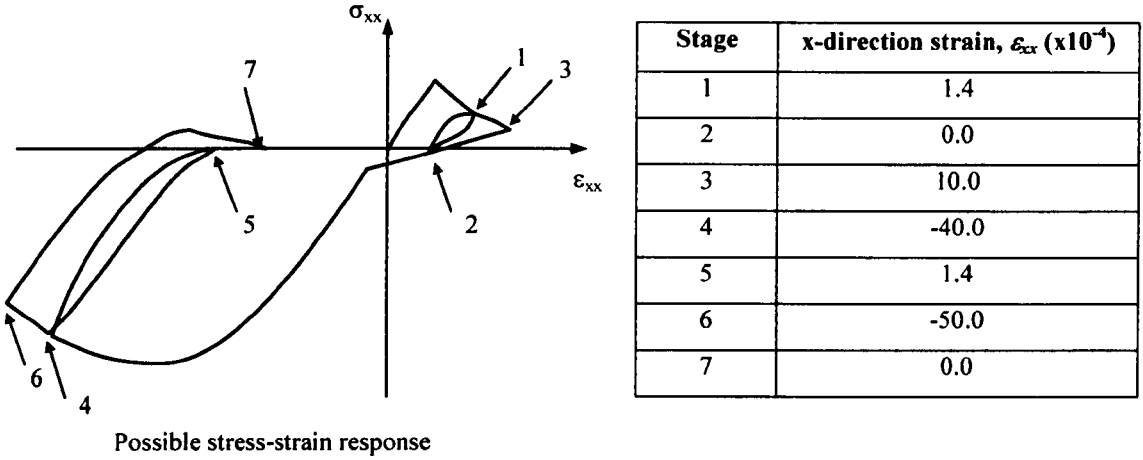


Figure 5-25 - Ghavamian Uniaxial Load Reversal Test Geometry and Original Material Parameters

During the course of the analysis the model is subjected to a complex strain history as shown in Figure 5-26.



**Figure 5-26 - Strain History (after Ghavamian (2003))**

One possible flaw with this model is the choice of value for  $G_f$ . Although a value of 0.11 N/mm is realistic for concrete, problems are encountered for this benchmark due to the size of the finite element. Assuming a linear softening response the ultimate strain for the model can be calculated as follows:

$$\epsilon_{ult} = \frac{2G_f}{f_t h} = 0.9 \times 10^{-4}$$

Equation 5-50

where  $h$  is the crack band width and is taken to be the length of the diagonal of one of the element's faces (Figure 5-27).

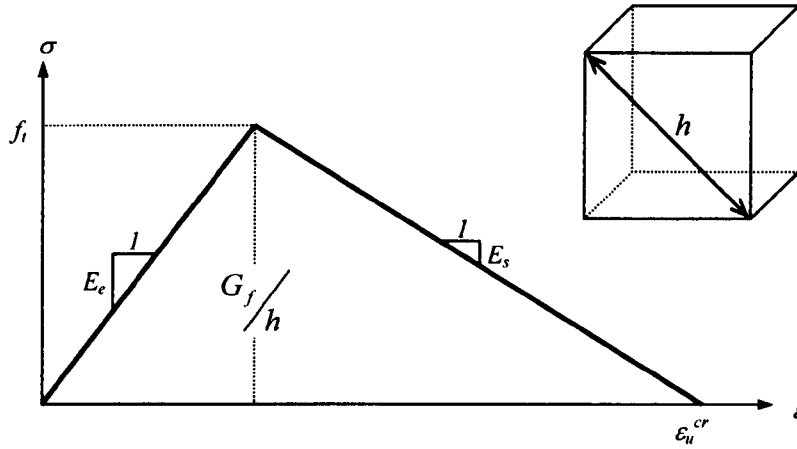


**Figure 5-27 - Determination of Ultimate Crack Strain by Consideration of Element Stress-Strain Diagram and Fracture Energy**

It is obvious from this calculation that it is not possible for the model to achieve the strain level prescribed in stage 3 of the analysis ( $10.0 \times 10^{-4}$ ). By rearranging the above equation the required  $G_f$  can be calculated.

$$G_{f.req} = \frac{\epsilon_{ult} f_t h}{2} = 1.188 \quad \text{Equation 5-51}$$

This revised value of  $G_f$  was used in the subsequent analyses. As before, the rotating formulation of the TSB Crack Model was used although for a uniaxial test such as this the fixed crack formulation would have given identical results. For the tensile regime an exponential softening curve was used. For the compressive regime a parabolic hardening/softening relationship was chosen. The determination of the value of compressive fracture energy,  $G_c$ , associated with this relationship was not simple. There is much discussion as to what value of  $G_c$  is representative for concrete. A value of between  $2\text{N/mm}^2$  and  $8\text{N/mm}^2$  seems to be acceptable. However, the large size of the finite element again caused problems. In order to achieve results that were comparable to those produced by other researches a value of  $G_c$  of between  $20\text{N/mm}$  and  $80\text{N/mm}$  was required. As with the value of tensile fracture energy, this value is an order of magnitude greater than normally used.

The analyses were performed using a Newton-Raphson iteration scheme. Each analysis consisted of 252 steps each of which required rarely more than 4 iterations to complete and never more than 8. Results of the analyses are shown below.

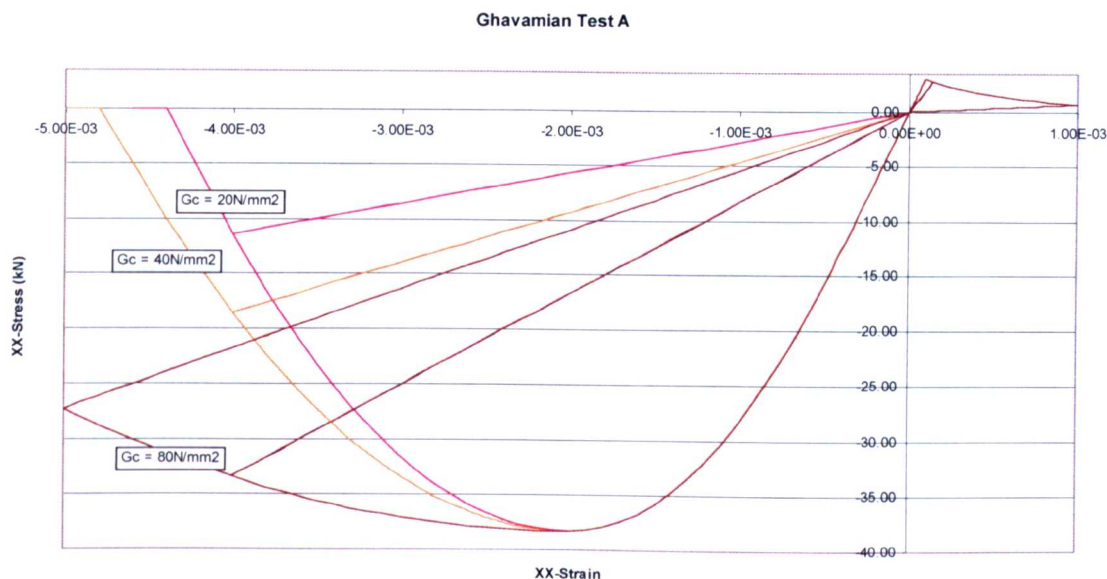


**Figure 5-28 - Ghavamian Uniaxial Load Reversal Test Results**

In stages 1, 2 and 3 of the analysis a tensile strain with a value greater than the elastic limit is applied. This strain is then removed and, in the third stage, a larger tensile strain applied. From the response shown in Figure 5-28 it can be seen that the model exhibits the correct, initial elastic strain response up to the material tensile strength. The response then follows the softening slope. As seen before, unloading and reloading follows the secant path with a zero stress state being produced where strain is zero. In stage 4 the prescribed strain becomes compressive. The response curve again follows the secant path back to the origin as the tensile strain is removed. As the strain state becomes compressive the model once again assumes an initial elastic stiffness. This shows the transition between tension and compression has been correctly identified. It also highlights the fact that, for a given crack plane, tensile and compressive damage are independent. In the fifth stage the strain once again becomes tensile and model unloads along the secant path again until reaching the origin. It then follows the secant path for the tensile regime up to the prescribed strain level. In the penultimate load reversal the

response correctly traversed between the tensile and compressive regimes, following the secant paths until the strain level reaches the previous maximum. The response then continues along the parabolic, softening path. The final stage sees the model returned to a zero strain state with the response curve following the secant path back to the origin.

The obvious difference between the three analyses is their compressive response. For the two lower values of  $G_c$  the element loses all strength before the maximum specified strain value of  $-50.0 \times 10^{-4}$  is reached.

This test highlights the robustness of the Total Strain Based Crack Model. The various load reversals were all achieved without any numerical difficulties. Transition between tension and compression was correctly detected, as was the transition between active and non-active loading.

### 5.3.3 Willam Anisotropy Test

Proposed by Willam, Pramono and Sture in 1987 [Willam et al (1987)], the following model has become a classic test for testing anisotropic models and was also used in the MECA Project. The geometry and material properties of the model are very similar to those previously considered (Figure 5-29). Loading is applied in 2 stages. The first being prescribed strain increments with the components  $\varepsilon_{xx}$ ,  $\varepsilon_{yy}$  and  $\varepsilon_{xy}$  taking the ratio, 1:- $\nu$ :0. The  $\varepsilon_{yy}$  component being chosen so as to prevent stresses forming in the  $y$ -direction due to the Poisson's effect. Stage 1 is ended when  $\sigma_{xx}=f_t$ . For stage 2 the strain increments take the ratio, 1:1.5:1. This is designed to cause a state of biaxial tension with a rotation of the principal strain axes. Although the test may seem rather artificial when considered as a stand-alone model, such a stress history may be experienced by elements forming part of a larger structure. In analyses where cracking is present, elements often experience both changes in load pattern and principal plane rotation even if the external loading remains monotonous. See Chapter 6 for further investigation.

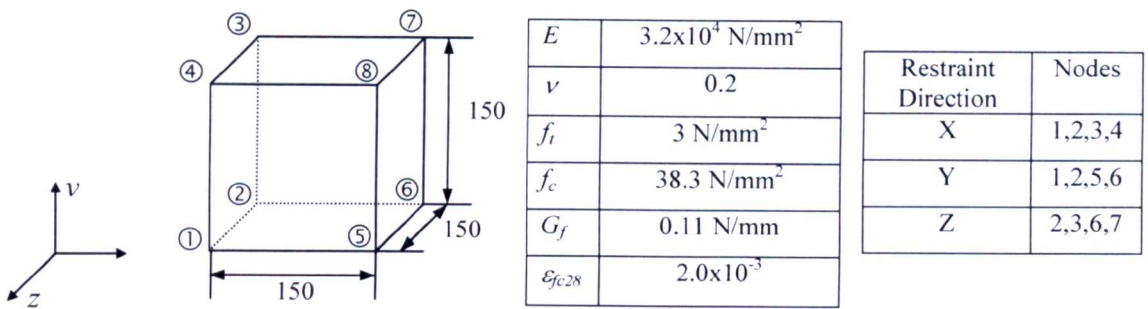


Figure 5-29 - Willam Test

As before the analysis was carried out using the rotating formulation of the TSB Crack Model with exponential tension softening.

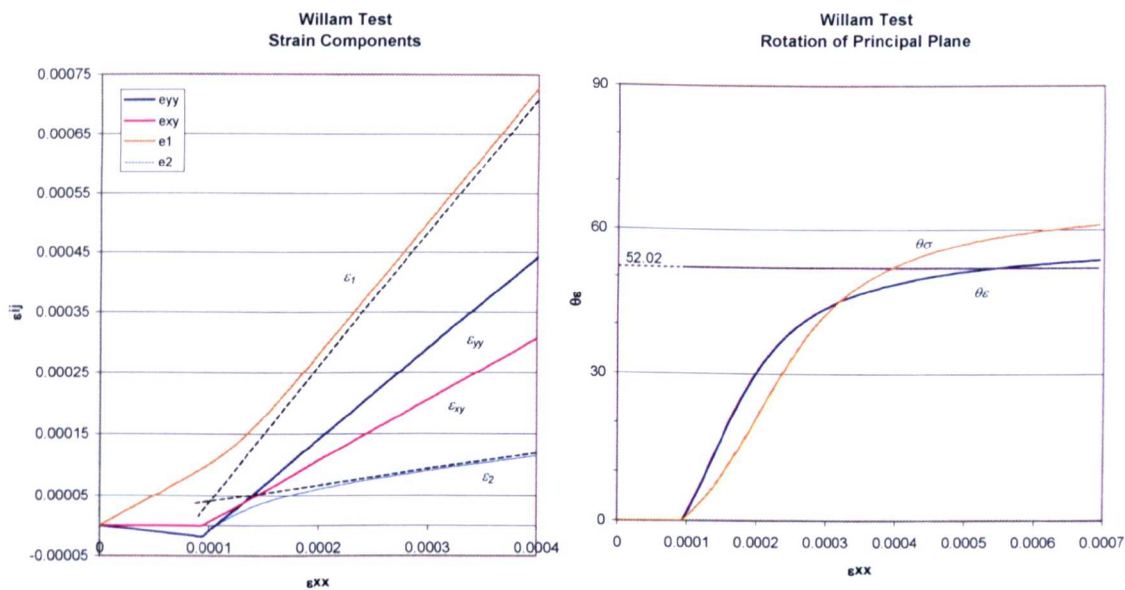


Figure 5-30 - a) Stress Components, b) Principal Plane Rotations

Figure 5-30(a) above shows the prescribed strains  $\epsilon_{yy}$  and  $\epsilon_{xy}$  plotted against the third prescribed strain,  $\epsilon_{xx}$ . Strain in the  $x$ -direction increases at a constant rate during this test and has been used as a form of ‘time variable’ in many of the subsequent graphs. Figure 5-30(b) shows the rotation of both the principal stress and strain during the course of the

analysis. From standard calculations of principal strain it can be found that ideally the principal strain should approach 52.02 degrees as the analysis time tends to infinity. The graph shows a small over-rotation of approximately 1.5 degrees. This small inaccuracy comes from the formulation of the TSB Crack Model although its exact causes could only be discovered by detailed investigation of the model formulation and implementation.

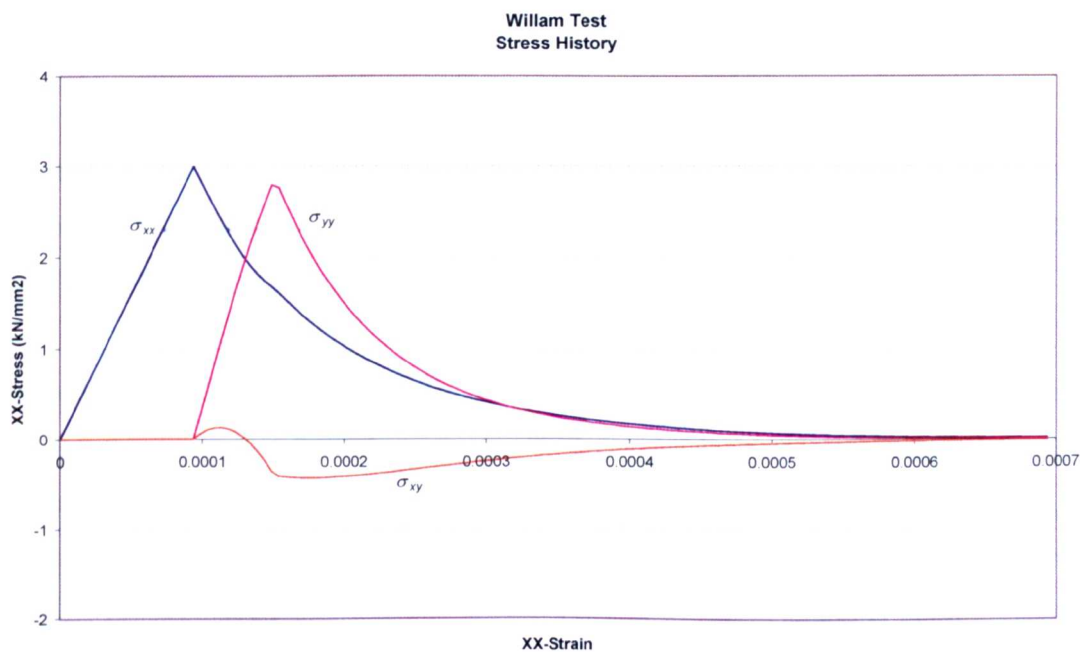


Figure 5-31 - Stress Histories

The stress histories for the 3 components of stress are plotted in Figure 5-31. Stress in the  $x$ -direction increases with the initial elastic stiffness until reaching the material tensile capacity as expected. There then follows a softening slope with the stress approaching zero at a strain of approximately 0.0006. As prescribed, the  $y$ -stress increases at a greater rate than the  $x$ -stress. The peak stress is slightly less than the material strength,  $f_t$  since the principal plane has rotated by this stage in the analysis and hence the stress vector  $\sigma_{yy}$  is no longer colinear with a principal direction. A softening slope follows and again the stress tends to zero at strains beyond 0.0006. The shear stress history is rather more interesting. After an initial positive value a so-called shear inversion is present with the stress approaching zero as the strain reaches 0.0006.

As part of the MECA project Ghavamian *et al* compiled a list of trends associated with anisotropic models based on the results and observations of other researchers [Ghavamian et al (2003)]. The first of these was that anisotropic models such as microplane and multi-crack models might show a small plateau or second peak in the middle of the descending part of the  $\sigma_{xx}$  response curve. Such a feature is caused by a second crack being formed or microplane becoming active as the principal plane rotates away from the orientation of the initial crack/micro plane. The structural response then has contributions from the existing, damaged plane and a new, undamaged plane. This can result in an apparent increase in structural stiffness and hence a plateau or second peak in the  $\sigma_{xx}$  response. This behaviour is not present in the rotating formulation of the Total Strain Based Crack Model since crack plane is co-rotated with the principal strain plane.

The second trend notes that the peak value of  $\sigma_{yy}$  might exceed the current value of  $\sigma_{xx}$ . Figure 5-31 shows that this occurs for the TSB Crack Model. The phenomenon is caused due to the fact that this is an anisotropic model and an additional, independent crack plane forms perpendicular to the existing one. At the point where  $\sigma_{yy}$  exceeds  $\sigma_{xx}$  the rotation angle of the secondary crack plane,  $s$ , with respect to the  $yy$ -plane is approximately 10 degrees and the shear stress is small. Therefore  $\sigma_{yy} \approx \sigma_s$  and so it is reasonable that  $\sigma_{yy}$  exceed  $\sigma_{xx}$ .



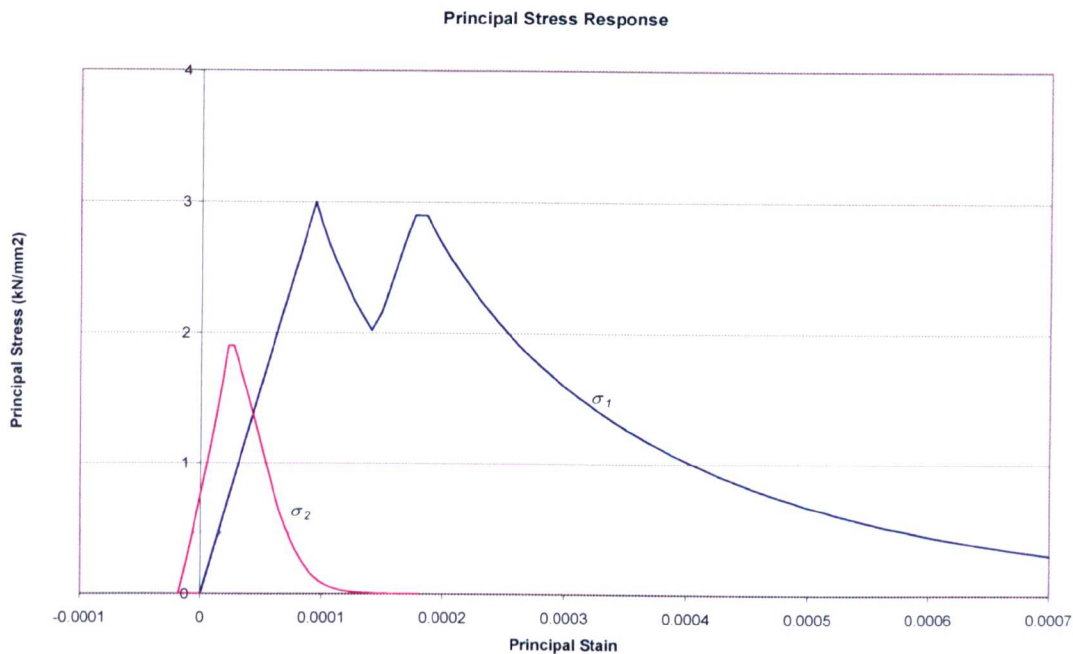


**Figure 5-32 - Principal Stress Response**

The anisotropic nature of the model is also illustrated in the principal stress response (Figure 5-32). There is a distinct second peak on the plot of maximum principal stress. This is due to the fact that the crack and principal planes are aligned and initially the stress on the first crack plane,  $n$ , is the major stress. As the crack opens the strength capacity of the plane decreases. Simultaneously stress on the second crack plane,  $s$ , is increasing and, at some point, exceeds that of the first plane. Thus becoming the major principal stress. However, it must be noted that this graph can be somewhat misleading as although the principal stress directions are swapped, the principal strain directions remain unchanged. Therefore beyond this point the direction of the measured variables do not coincide.

The initial positive shear stress followed by a shear inversion is also common for anisotropic models. The reasons for this behaviour are related to the rotation of the principal planes. It must be remembered that global shear stress is not calculated directly in the Total Strain Based Crack Model, instead the stress state is formulated in the crack coordinate system and transformed back to the global coordinate system. Of course, for

the rotating crack formulation of the model the crack and principal directions are co-linear. In the initial part of stage 2 of the analysis there is a steady and rapid rotation of the principal planes. At the same time  $\sigma_1$  is reducing as  $\sigma_2$  is increasing. These two events produce the initial peak then reduction in  $\sigma_{xy}$ . The transition from positive to negative shear stress coincides with second plane becoming the plane of maximum principal stress. As the stress on this new maximum principal stress plane continues to increase so too does the shear stress. In the later stages of the analysis, when the rotation of the principal plane is relatively slow, the softening on the two crack planes leads to a reduction in the shear stress. This stress tends to zero as the strain reaches 0.0006.

The above observations underline the anisotropic nature of the Total Strain Based Crack Model. Subtle differences are also highlighted between the behaviour of the rotating formulation of the model and those produced by more traditional anisotropic models. The test also shows the suitability of the model in situations where the stress-strain state is complex and non-monotonic.

#### **5.4 Summary**

In this chapter the Total Strain Based Crack Model has been presented as a suitable constitutive model for the analysis of fracturing concrete. Like Traditional Crack Models, it assesses the stress state as a set of three uniaxial cases oriented in mutually perpendicular directions. Both tensile and compressive failures are provided for. Additionally lateral effects from confinement, compression softening and the Poisson's Effect are also considered. Unlike the Traditional Crack Model, it is formulated in terms of total strain throughout without decomposition into elastic and inelastic components. Both Rotating and Fixed Crack formulations are available.

The Rotating Crack formulation in particular was thoroughly tested via a set of benchmark problems including the Ghavamian and Willam Tests. Its behaviour in terms of multiple crack initiation in conditions of rotating principal stress was examined in detail. The robustness of the model for complex, non-monotonic loading was also highlighted.

## **CHAPTER 6**

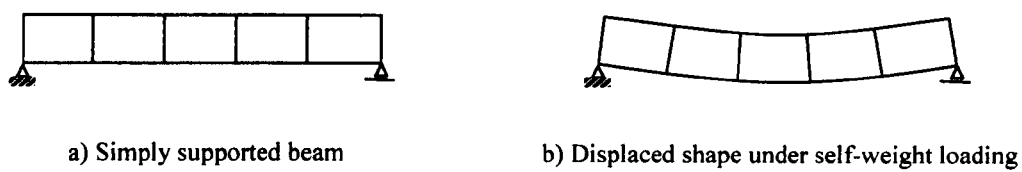
### **Investigation of the Causes and Effects of Stress Locking**

This chapter focuses on the phenomenon known as stress locking. This is a form of behaviour that causes finite element models to produce overly stiff responses. In this context, stress locking refers not only to the more familiar shear and volumetric locking found in linear elastic analyses but also encompasses other sources of spurious stress accumulation found in non-linear analyses. Whereas the benchmark studies of the previous chapter concentrated on features and behaviour particular to the Total Strain Based Crack Model, the field of stress locking is of relevance to Crack Models in general and, in some cases, is also applicable to continuum softening models as a whole.

Four different sources of stress locking are illustrated and explained in turn. The causes of each type of the spurious stress accumulation are investigated and solutions to avoid such problems are presented. The chapter concludes by detailing and discussing the choice of finite element, constitutive model and associated parameters that were used for subsequent analyses.

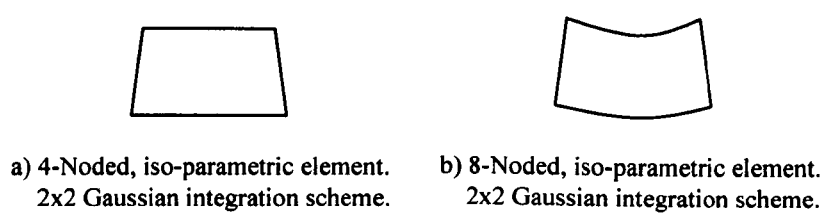
**6.1 Traditional Stress Locking**

The term ‘stress locking’ is most commonly used in the context of a spurious build up of stress within a finite element due to an inability of the chosen element type to accurately model the required displacement field. The simplest example of this is ‘shear locking’.



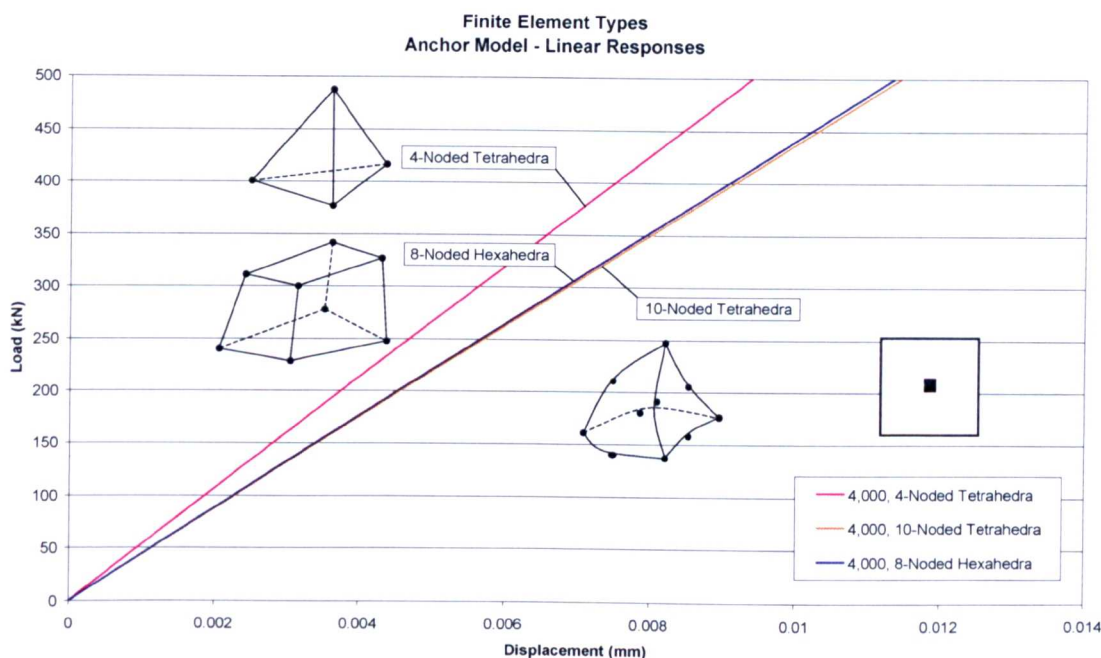
**Figure 6-1 - Simple Beam Bending Problem**

Figure 6-1a shows a simply supported beam in its initial configuration, discretised by five quadrilateral elements. Figure 6-1b shows the expected displaced shape when the beam is subject to self-weight loading.



**Figure 6-2 - Displaced shapes for linear and quadratic elements**

If attention is focused on the centre element it can be seen that the choice of finite element type is important to the structural response (Figure 6-2). At this position the element is subjected almost exclusively to bending, the top of the element in compression, the bottom in tension and shear stress is at its minimum. Both elements respond with a shortening of the top face and an extension of the bottom. However, the linear element is unable to model the curvature of these faces and, as a result, an erroneous shear stress is introduced. This stress is often referred to as ‘parasitic shear’. Also, the energy required to shear the element in this way is greater than that to cause bending therefore the response will appear overly stiff.



**Figure 6-3 – Structural Responses for Finite Element Types**

Figure 6-3 shows the linear responses produced when analysing the 3D anchor problem detailed in Section 4.4 (anchor in centre of block) using a variety of element types (Figure 6-4). It is clear from the graph that the 4-noded, linear, tetrahedral elements produced the stiffest response. The response given by the 10-noded, quadratic, tetrahedral elements is significantly softer since they don't suffer from shear locking. However, this increased accuracy comes at a price. Whereas the 4-noded tetrahedra commonly use a 1-point integration scheme, 10-noded elements use at least a 4-point scheme. This fact coupled with the increased number of degrees of freedom and the added complexity of the higher order shape functions, means that such quadratic elements are much more computationally expensive than their linear equivalents. However, one point to note is that due to their superior kinematics it may be possible to use fewer quadratic elements than linear elements for a given problem.

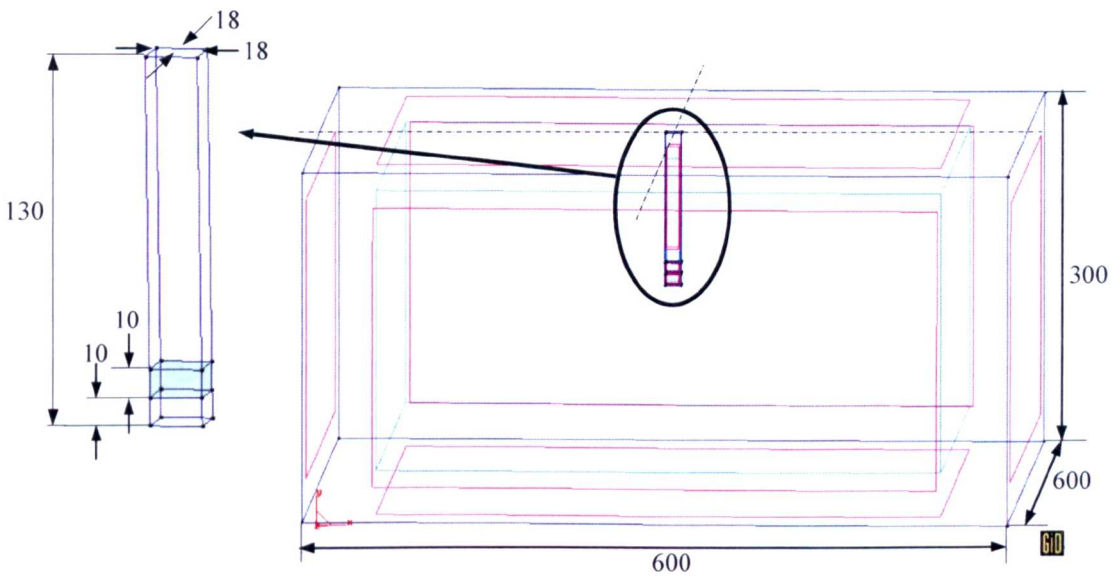


**Figure 6-4 - 3D Anchor Pullout Problem Geometry - Anchor in Centre Position**

A number of other solutions are available to reduce the effects of such stress locking. The simplest of which is to increase the discretisation level. By doing so the displaced shape will give a closer approximation of the bending shape seen in reality. Therefore the amount of parasitic stress will be less. Another option is to select a more complex linear element type. In the present case the response produced by an 8-noded hexahedra element was found to be very close to that of the 10-noded tetrahedra. However this is not a general rule as the performance of a given element is related to the structural action produced in the structure.

## 6.2 Stress Locking Due To Local Crack Misalignment

Traditional stress locking is a phenomenon found in finite element analysis as a whole, however stress locking caused by crack misalignment at a local level is peculiar to crack models. The problem arises when the principal stresses at the Gauss point level rotate away from the orientation of the crack (Figure 6-5). The term ‘misalignment’ is used because in reality, if a finite volume of concrete were considered during the initial stages of cracking, many microscopic cracks would be present. Each of these micro-cracks would be roughly aligned perpendicular to the maximum principal stress. At this point, if the principal direction were to change these micro-cracks would be likely to close and new cracks form perpendicular to the new principal direction. However, for fixed crack FE models the crack orientation remains static upon crack initiation

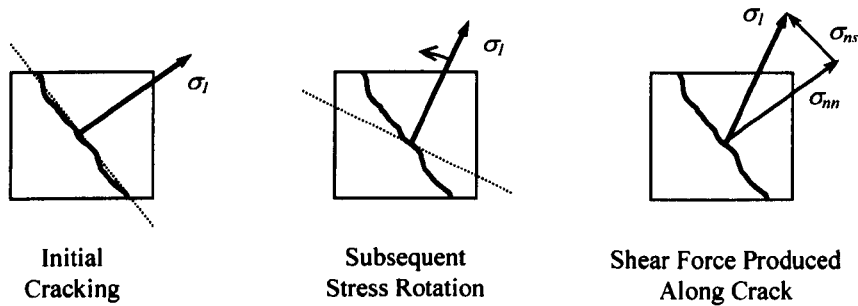


**Figure 6-5 – Shear Stresses Induced by Principal Stress Rotation**

Figure 6-5 above shows that upon rotation the principal stress is resisted both by a crack normal stress,  $\sigma_{nn}$ , and by a shear stress along the crack,  $\sigma_{ns}$ . Obviously, as the angle between the crack normal and principal direction increases so too does the magnitude of the shear stress. The limiting case being when the principal stress is perpendicular to the crack normal and the applied load is resisted by shear alone. Since softening is usually governed by the crack normal stress it is possible for very significant shear stresses to build without any associated degradation of the material. The severity of this shear stress accumulation is dependent on the laws governing crack initiation and evolution.

In the case of a fully developed crack the behaviour in reality again differs from that which the Fixed Crack Model provides. If the principal direction were to rotate at this



point in the analysis it is likely that an additional crack would form. Once again aligned perpendicular to the principal plane. For the Single Fixed Crack Model this is not possible.

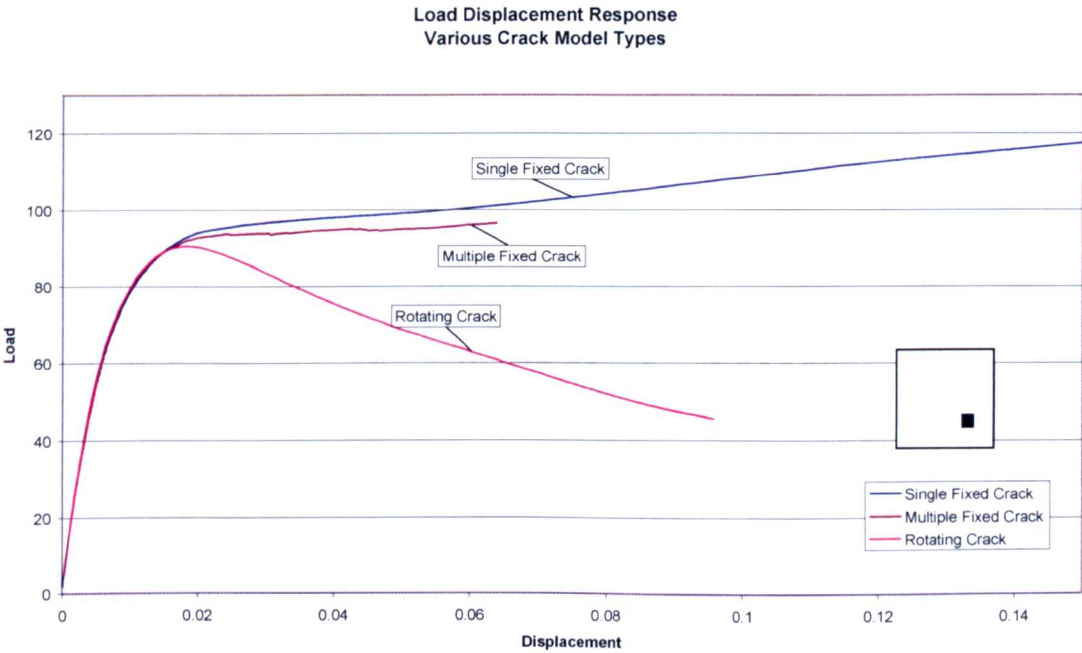
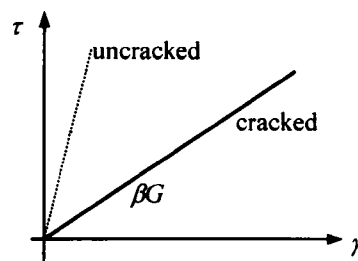


Figure 6-6 - Comparison of Structural Responses for Different Crack Models

Figure 6-6 above shows a comparison of the three types of smeared crack models when used to analyse the anchor model with the anchor in corner position. The implementation of the Multiple Fixed Crack Model is that of the Traditional Crack Model. Single and Rotating Crack Models are implemented in the Total Strain Based Crack Model.

It can be seen that the responses of the two Fixed Crack Models are very similar. The Multiple Fixed Crack Model seems to produce a slightly softer response after the main softening takes place. It was conjectured that this was due to the fact that additional cracks may form when the angle between the principal stress and the crack normal exceeds a given threshold value. It was therefore less likely that the magnitude of these spurious shear stresses would reach as high a level as in the Single Crack Model before another crack was formed.

Initially the response of the Rotating Crack Model is identical to that of the Fixed Crack Models. However, the softening response is quite different. For this model there is a well-defined peak load followed by significant unloading. The analysis failed due to non-convergence before complete unloading took place. Obviously, since the Rotating Crack Model rotates the crack so as to remain aligned with the principal plane, no spurious build up of shear stresses is developed. However, for Fixed Crack Models lowering the shear retention factor,  $\beta$ , can lessen the severity of the shear stress accumulation.



**Figure 6-7 - Shear Retention Model**

In the TSB Crack Model the post crack shear stiffness is modelled via a constant shear retention model (Figure 6-7). This model is obviously only applicable when used with the fixed crack approach. For previous analyses the shear retention factor,  $\beta$  was set to 0.03. Subsequently, a range of lower values was considered including 0 (i.e. zero shear stiffness upon fracture). These analyses were carried out using the previous anchor problem with the anchor in the corner position. The results are shown in Figure 6-8 along with results produced by the Rotating Crack Model.

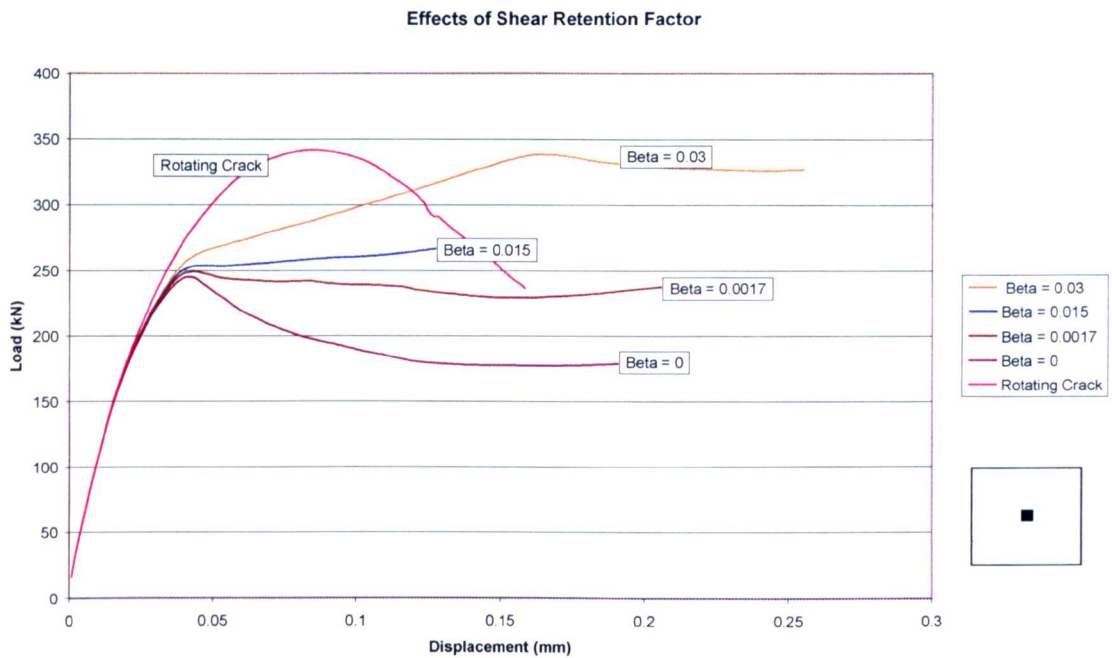


**Figure 6-8 - Effects of Shear Retention on Load-Displacement Response**

As with the previous anchor position, the Rotating Crack Model produced a well defined peak load and subsequent unloading of the problem. Initial yielding of the fixed crack analyses was similar however the responses after this were markedly different. It is quite clear that reducing the shear retention factor reduces the problem's post crack stiffness. With a retention factor of less than 0.0017 a peak load becomes apparent however after the initial unloading the responses reach a plateau and, in fact, begin reloading slightly. This is the case even for the model with no post-cracking shear strength. Similar results have also been reported by Rots and Blaauwendraad [Rots and Blaauwendraad (1989)].



**Figure 6-9 - Maximum Principal Stress**

(Light shades show high stress)

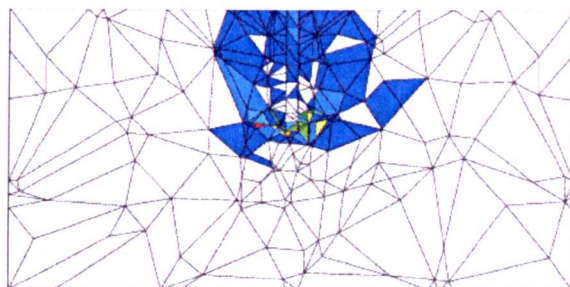


**Figure 6-10 - Crack Strain**

(Dark shades show high strain)

Figure 6-9 above shows a contour plot of Maximum Principal Stress,  $\sigma_1$ , for the anchor problem when analysed with the fixed crack formulation of the TSB Crack Model and a Shear Retention Factor of zero. The plot was produced for an analysis step soon after peak load. Figure 6-10 is the corresponding plot of Crack Strain for the primary crack. It can be seen from these contour plots that in the zones where crack strain is highest the largest values of principal stress can also be found. This appears contrary to expected material behaviour since, as the crack opens, the element's stiffness should decrease. For this reason it is unusual for the cracked elements to be carrying a higher load than the surrounding, undamaged ones.

Both of the above results suggest an additional source of stress locking. Further evidence is apparent in the evolution of principal stress. Several elements along the length of the crack were selected and the maximum principal stress history for each is plotted in Figure 6-11. The prescribed tensile strength for the concrete was  $3 \text{ N/mm}^2$  and it can be clearly seen that on reaching this limit the gradient of the stress paths alters dramatically as the elements soften. Most of the elements show a period of unloading following this point but several elements begin reloading and exceed the maximum tensile stress.



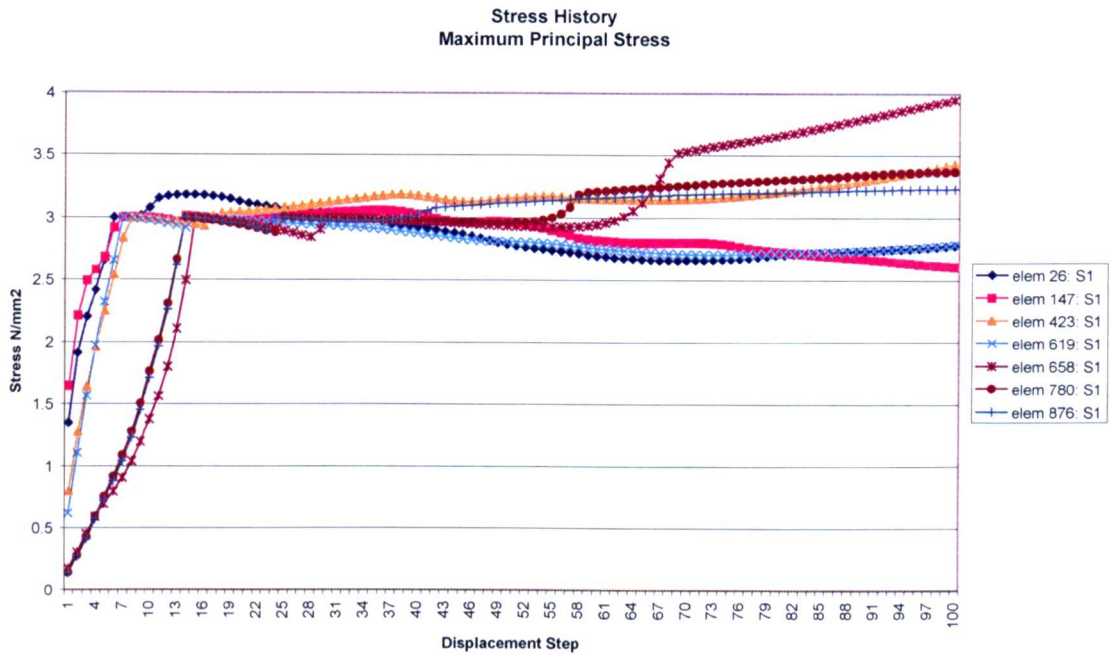


**Figure 6-11 - Principal Stress History of Elements Along Crack**

The reason for this behaviour is, as before, due to a spurious stress accumulation as a consequence of crack misalignment. In crack models stresses are assessed in the direction normal to the crack plane. For the fixed crack formulation the principal plane may deviate from that of the crack (Figure 6-12). In this situation the maximum principal stress,  $\sigma_I$  may exceed the tensile strength of the material,  $f_t$  but the resolution of the principal stresses onto the crack plane,  $\sigma_{In}$ , may be less than or equal to  $f_t$ .

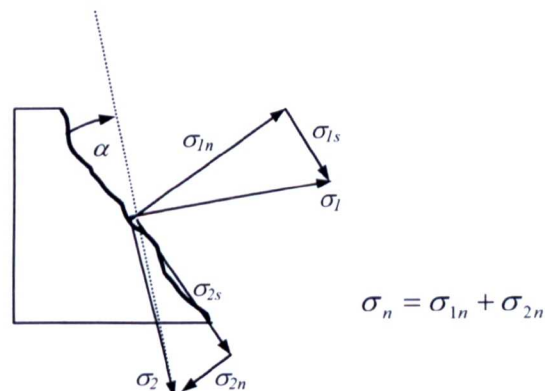


**Figure 6-12 - Resolution of Principal Stresses Leading to Nonalignment of Principal Plane and Crack**

Whilst the mechanism that leads to this form of stress locking is relatively simple and its effects are quite apparent from both the global and element level responses, finding definitive proof that this is the phenomenon that is producing these results is rather more challenging.

In the pre-cracking phase of the analysis the responses are as expected. Figure 6-13 is a plot of principal stress versus principal strain for the elements selected above. Their response approximately corresponds to that of the linear-elastic behaviour defined by Young’s Modulus thus confirming that the locking process is associated with non-linear behaviour.

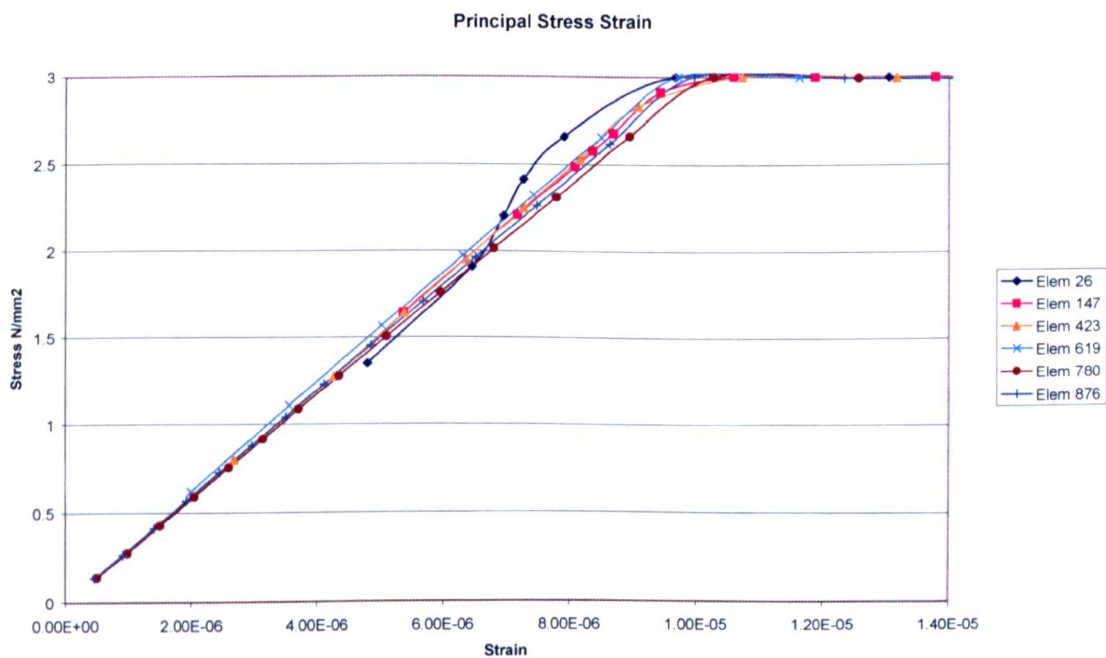


**Figure 6-13 - Principal Stress vs Principal Strain Response for Elements Along Crack**

By dividing the values of principal stress by the corresponding principal strain an ‘effective’ Young’s Modulus was produced. This value gives an indication of the stiffness of the element considered. Figure 6-14 shows a plot of these ‘effective’ Young’s Moduli versus global displacement of the problem. Each of the curves shows an exponential decrease in ‘effective’ Young’s Modulus post yield. This is in agreement with the exponential softening model used in this analysis and hence proves that, in terms of the

relationship between stress and strain, the softening of the elements is occurring correctly and therefore not responsible for the spurious stresses.

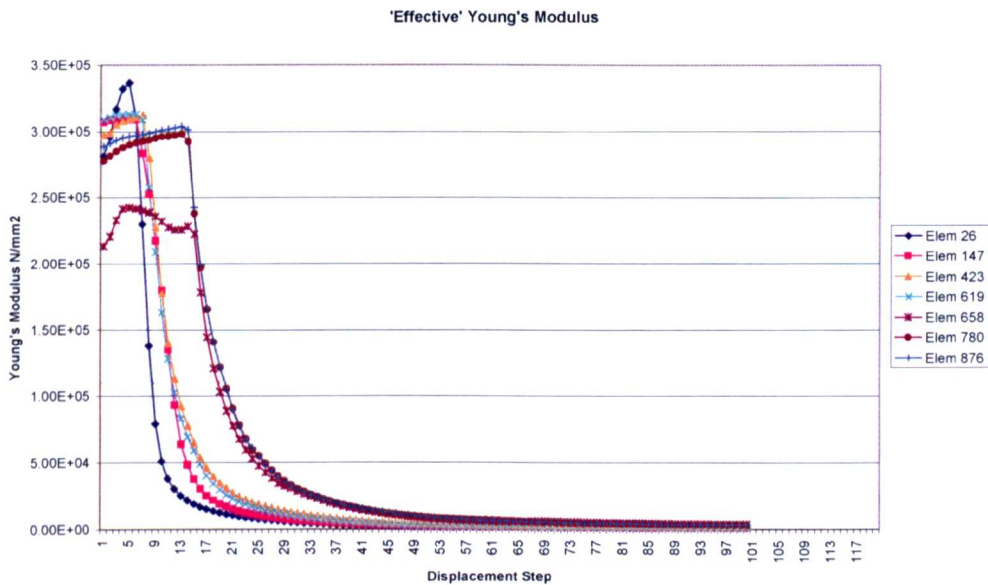
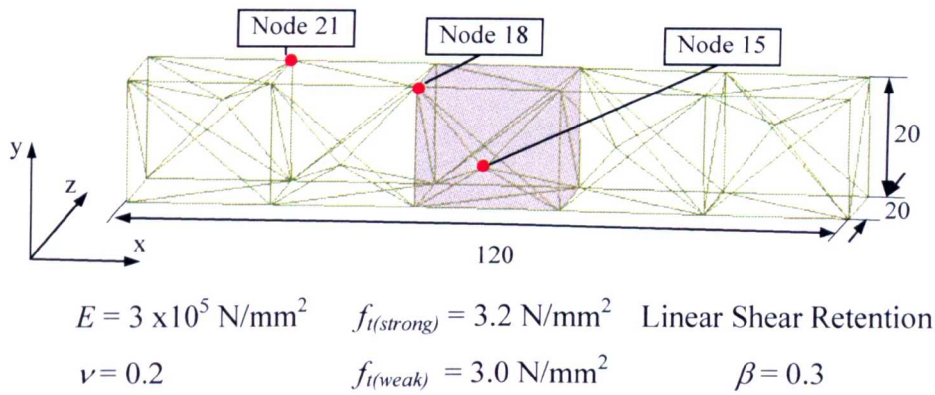


Figure 6-14 - 'Effective' Young's Moduli for Crack Elements

None of the above proves that the form of stress locking discussed is responsible for the behaviour illustrated. In order to confirm this a series of simpler benchmark problems were analysed with the focus being on stress evolution. With these the structural behaviour was better understood and therefore the interpretation of the results was easier. Two post-processing programs were also developed in Matlab v4.2 [Math Works Inc. (1995)] to aid the understanding of the results. The first plotted stress history data for a chosen point in the form of a three-dimensional line graph. The second plotted the orientation of the principal plane for each analysis step based on the direction cosines of the maximum principal stress vector.

### 6.2.1 1D Bar Problem



**Figure 6-15 - 1D Bar Problem**

The first problem examined was a 3D interpretation of the classic 1D bar (Figure 6-15). The bar was fully fixed at the left hand end and a horizontal displacement was prescribed for the free end to produce a uniform tensile stress state in the problem. Because of its uniaxial nature no rotation of the principal planes occurs therefore misalignment of the crack should not occur. Material properties were as shown above with the middle section of the bar having a slightly lower tensile strength than the surrounding concrete. This was done to promote cracking and strain localisation in the centre of the bar. The problem was analysed using the fixed crack version of the TSB Crack Model with a Rankine failure criteria and linear tension softening. Linear shear retention was also employed with a retention factor of 0.3.

On completion of the analysis three nodes were selected for inspection. Node 15, in the centre of the cracked zone, node 18, on the corner of the zone, and node 21, in the uncracked zone. Stress histories for this data are shown in the form of three dimensional line graphs in Figure 6-16. As an aid to interpretation the stress history plots shown below have a drop shadow plotted on the  $\sigma_1$ - $\sigma_2$  plane.



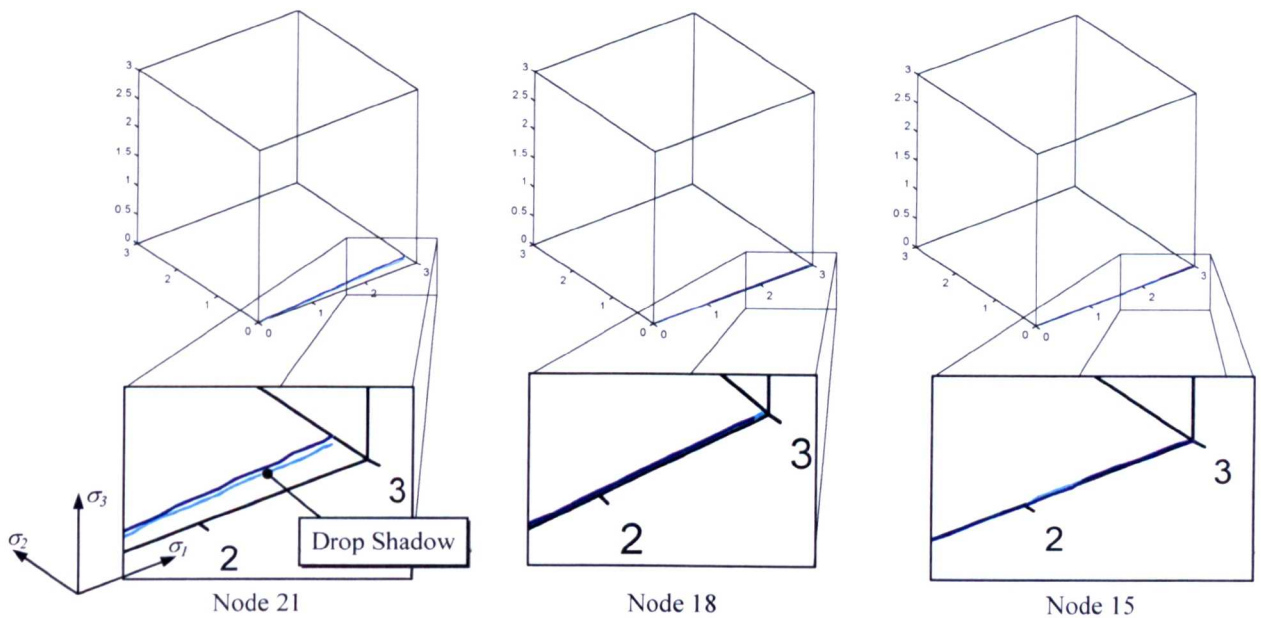


**Figure 6-16 - 1D Bar Stress History Plots**

Looking at the plots for nodes 15 and 18 first, it can be seen that the path of the stress history travels exclusively along the  $\sigma_1$  axis thus meaning that the node was subject to uniaxial tension. As expected the stresses do not exceed the tensile strength of the weaker material. Although not apparent from the diagrams the stress paths during the softening phase returns along the same paths as the loading phase. The history for node 21 differs for the others in that it deviates very slightly from the  $\sigma_1$  direction. This feature is due to the fact the fully fixed end prevents straining due to the Poisson's Effect thus resulting in a stress build up. Similar plots were produced for the global axis system. These were found to be identical to the principal stress plots with  $x=\sigma_1$ ,  $y=\sigma_2$ ,  $z=\sigma_3$ .

Plots were made showing the orientation of the principal plane for each step of the analysis. Figure 6-17 below shows these for the three most important stages of the analysis.

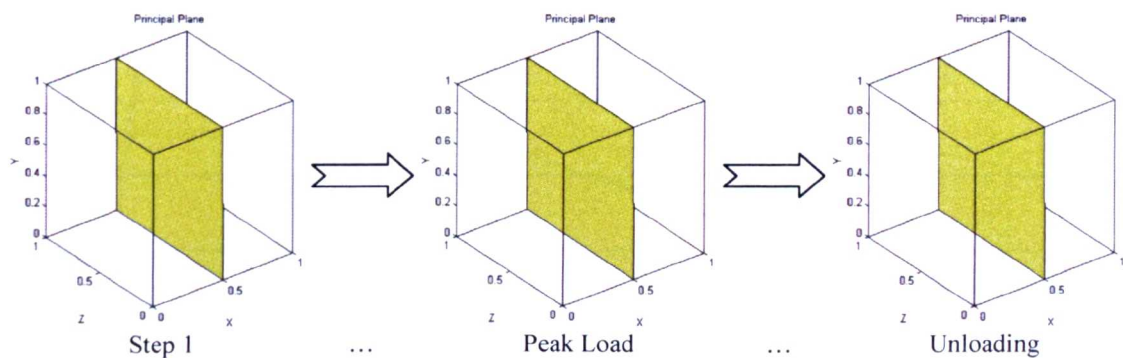


**Figure 6-17 - 1D Bar Principal Plane History (Node 15, Centre)**

It can be seen from these plots that the orientation of the principal plane remained perpendicular to the direction of the applied external load throughout the analysis. Although only the data for node 15 is shown here the plots for nodes 18 and 21 were virtually identical.

It can be seen from the load-displacement response (Figure 6-18) that there is no evidence of reloading due to stress locking. This is as expected since the orientation of the principal plane remains fixed throughout the analysis hence coplanar with the crack and so  $\sigma_I = \sigma_n$ .

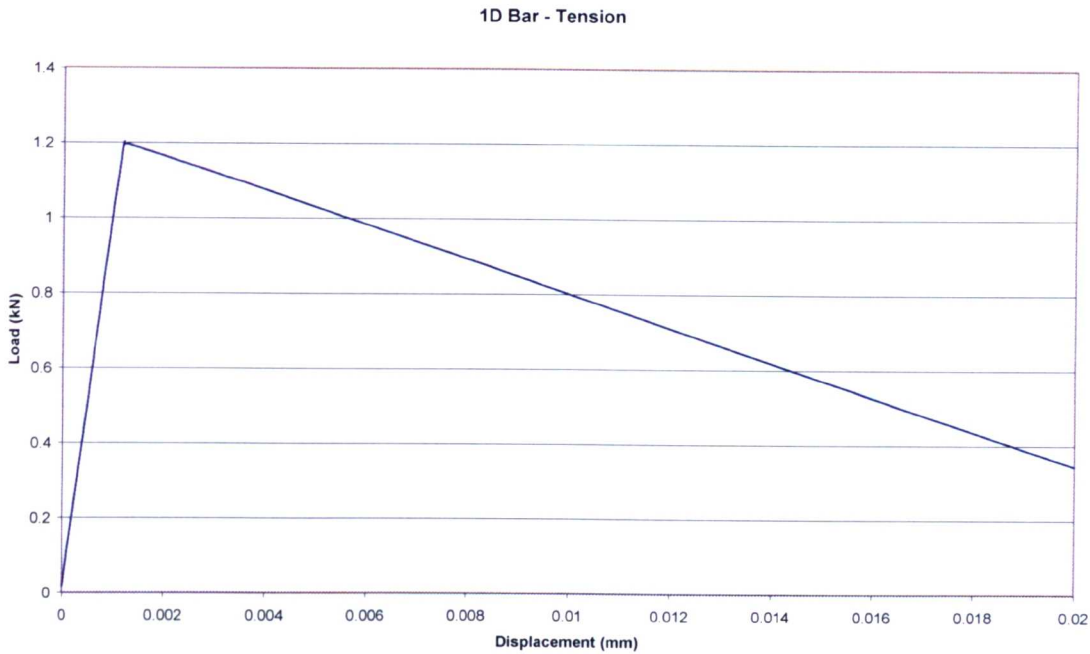


Figure 6-18 - 1D Bar Global Load-Displacement Response

### 6.2.2 Three Point Notched Beam Bending Problem

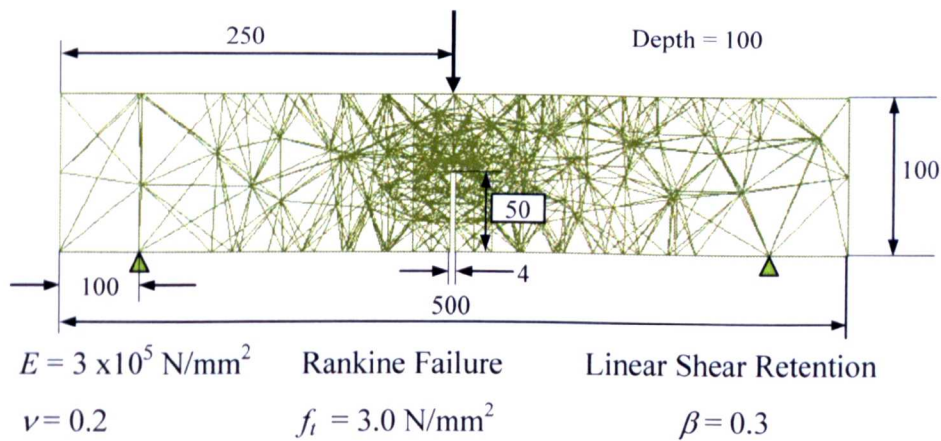
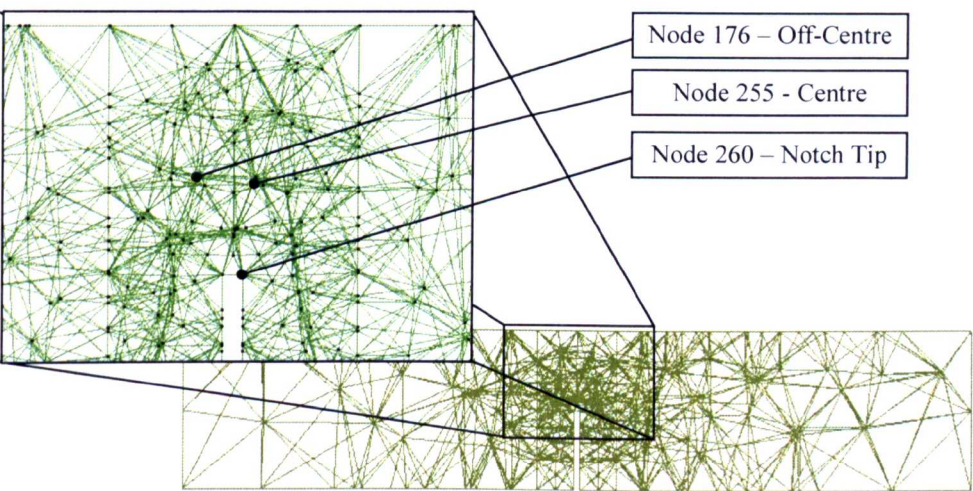


Figure 6-19 - 3 Point Bending Problem

The second benchmark problem that was examined was a notched beam subjected to three point bending (Figure 6-19). This produced a more complex stress state than the 1D bar problem and introduced the possibility of some rotation of the principal planes. As shown, the problem was supported in  $x$  and  $y$  directions at two supports on the base. A prescribed displacement was then applied to the middle of the beam. The problem was

discretised by 4-noded, tetrahedral elements, each with a single integration point. Initially the fixed crack formulation of the TSB Crack Model was used with a Rankine failure criterion, linear tension softening and linear shear retention as before.



**Figure 6-20 - Nodes Examined**

Again, several nodes were selected for examination (Figure 6-20). Node 260 was situated at the notch tip where the crack initiated and nodes 176 and 255 were positioned some distance away from this but still within the crack zone.

The plot for node 260 (notch-tip) shows that it is initially subject to triaxial tension (Figure 6-21). As the analysis progresses the stress state changes to combined tension and compression.



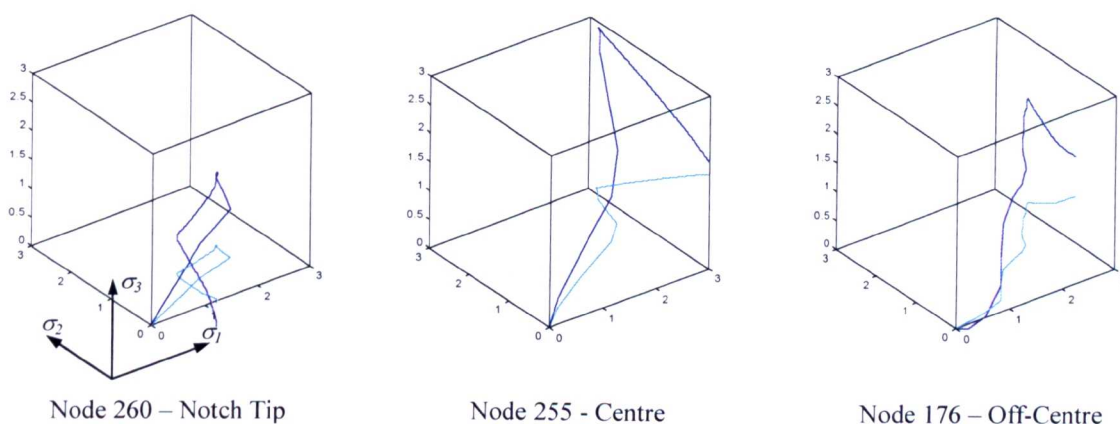


**Figure 6-21 - Three Point Bending Principal Stress History Plots**

Examination of the global stress history for node 260 (Figure 6-22) reveals that there is unloading in the  $x$ ,  $y$  and  $z$  directions. This is probably due to softening, due to cracking, of the elements associated with this node.

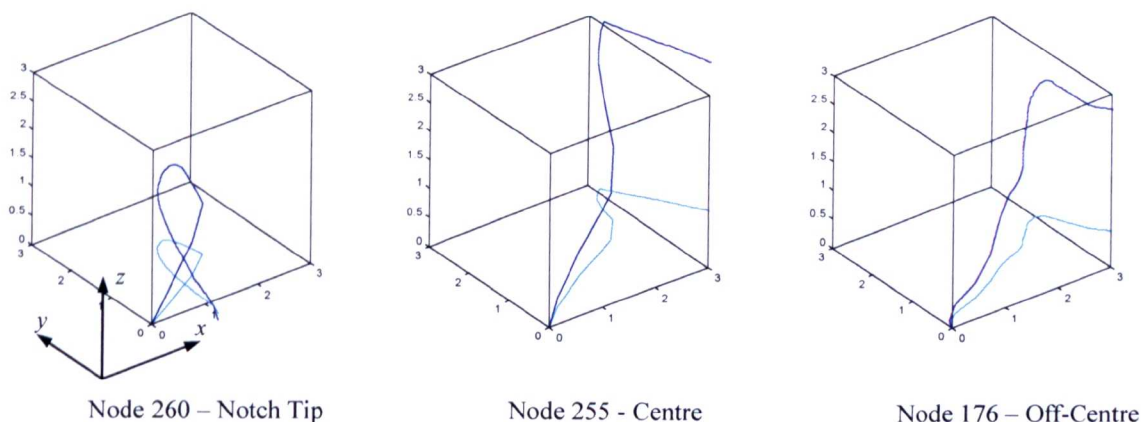
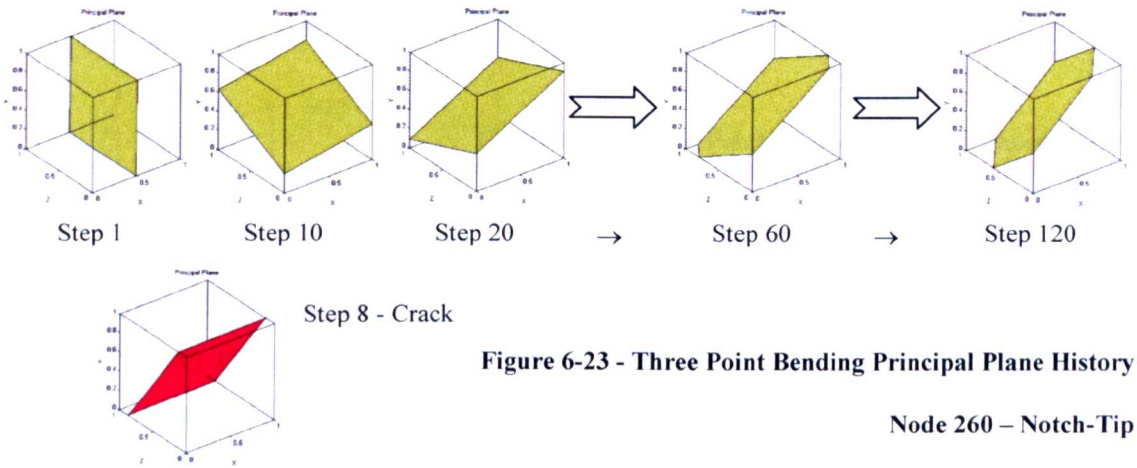


**Figure 6-22 - Three Point Bending Global Stress History Plots**

The behaviour of nodes 176 and 255 in the principal coordinate system is markedly different from that of node 260. Both initially go into triaxial tension, however  $\sigma_1$  exceeds the material strength of  $3 \text{ N/mm}^2$ . The direction of the stress paths changes at this point. Again, this is likely to be due to the associated elements softening. However, during the course of the analysis the value of the maximum principal stress continues to increase.

For a three point bending test it is primarily the stresses in the  $x$ -direction that drive the fracture and softening process. The global stress history plots for these two nodes show that it is  $\sigma_1$  that is responsible for the excessive principal stress.



Plots of the orientation of the principal plane show that its position varies wildly for at least the first 20 steps of this 120-step analysis (Figure 6-23). This is despite selecting a suitably small displacement increment. Beyond step 20 the rate of change becomes more gradual. The initial orientation of the principal plane is perpendicular to the  $x$ -direction as expected. However, the principal plane rotates away from this orientation prior to the formation of the crack, which is estimated to form in step 8. This is only an estimate since the stress data reported was a volume-averaged value and hence takes contributions from each element associated with the given node. The crack is assumed to form when this average stress exceeds the tensile strength of the concrete. The principal plane then continues to rotate giving rise to a situation where stresses can build and lead to locked-in stress. However, in this instance the orientation the principal plane takes when it settles is close enough to that of the crack plane so as not to produce any significant stress locking.

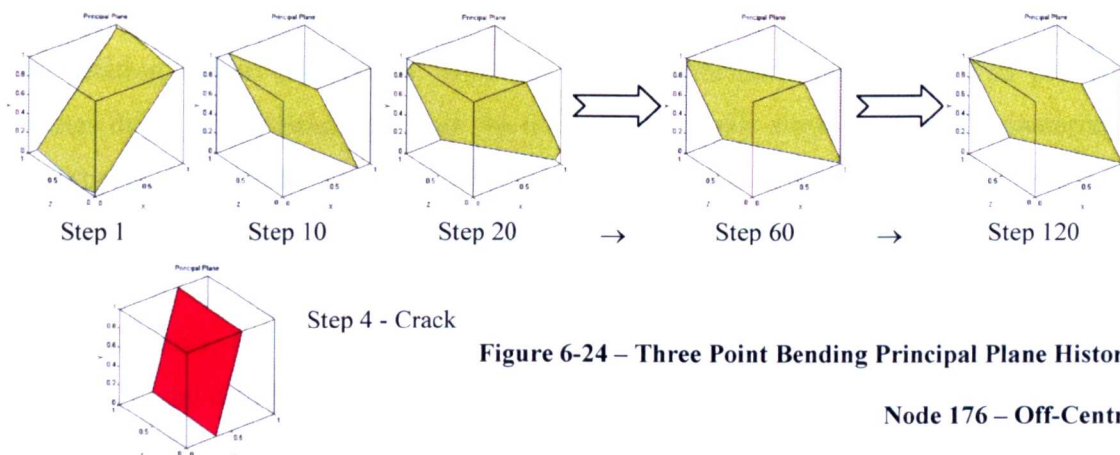


**Figure 6-24 – Three Point Bending Principal Plane History**

**Node 176 – Off-Centre**

As with node 260 (notch-tip) the orientation of the principal plane associated with node 176 (off-centre) changes vary rapidly during the initial stages of the analysis (Figure 6-24). However, the orientation it assumes by step 20 remains relatively constant throughout the rest of the analysis. Again, the crack is estimated to form early in the analysis. In this case the orientation was very different from the subsequent, stable orientation and therefore produced stress locking and caused the principal stress to exceed the tensile limit of the material. Similar examination of node 255 (centre) showed a comparable rotation of the principal plane and significant difference between the orientation of the principal and crack planes.

The analysis was repeated using the Rotating Crack Model instead of the fixed crack formulation. The stress history plots for the chosen nodes are shown in Figure 6-25.

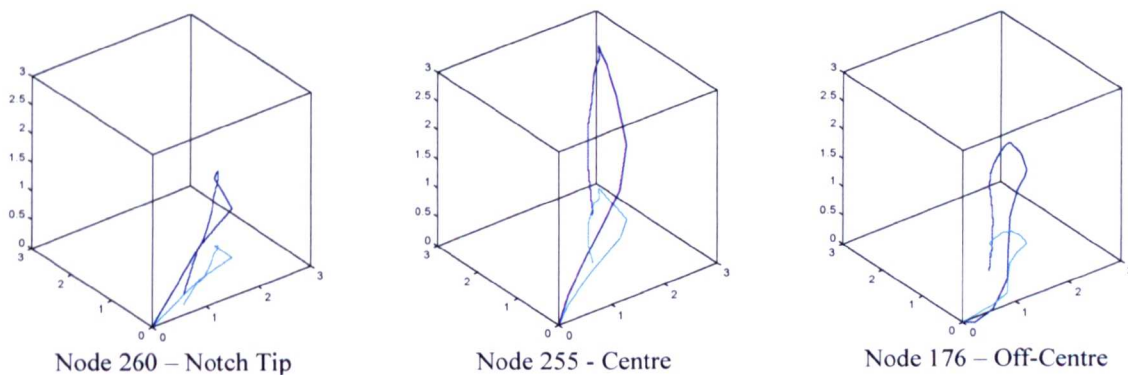


**Figure 6-25 - Three Point Bending Stress History Plots. ROTATING Crack Model**

The rotation of the crack plane with that of the principal plane means that principal stresses drive the material response. As a result the tensile stress limit of the material is not exceeded, as can be clearly seen from the above plots. This model is also free from problems of spurious build up of shear stress.

As stated above, the data being used in the investigation of stress history was volume averaged, nodal data. That is, a weighted average calculated for each node point based on the value of stress existing in each of the elements that share the node under consideration. For 3D analyses with an unstructured tetrahedral mesh it is not uncommon for as many as sixteen elements to share a common node. For this reason it is quite possible for the details of the material behaviour and its relationship to the chosen constitutive model to be lost in the averaging procedure. Using Gauss point data gives a much clearer indication of processes involved, as it is these values that are used in the constitutive model itself. A postprocessor was written to transform global Gauss point data into the principal co-ordinate system by means of the Jacobian method [Press (1993)].

In the analysis above node 255 (centre) showed stresses significantly in excess of the material limit. The Gauss point data for the elements sharing node 255, i.e. those contributing to the volume averaged nodal values, was collected. From this data, four individual Gauss points were selected for more detailed examination. It is worth remembering at this point that, for the particular tetrahedral element used in these analyses, there is only a single Gauss point.



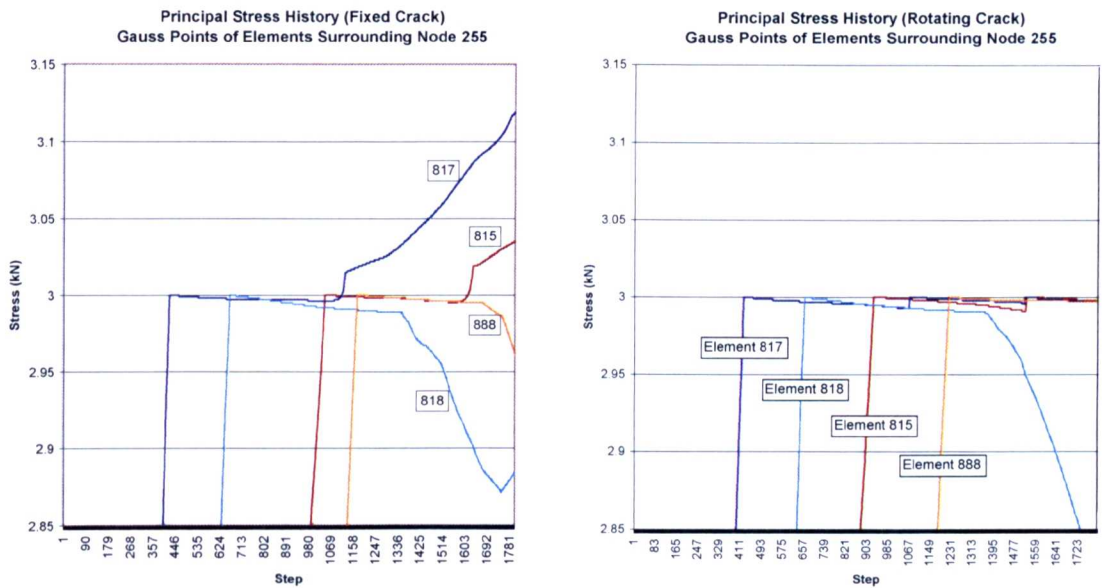


**Figure 6-26 - Principal Stress History. a) Fixed Crack Model, b) Rotating Crack Model**

Figure 6-26a above shows the history of maximum principal stress for the chosen Gauss points. It can be clearly seen that for the points of elements 815 and 817 the principal stress exceeds the concrete strength whereas points 818 and 888 show a softening behaviour. Figure 6-26b shows the equivalent principal stress history for the analysis using the Rotating Crack Model. In this case none of the chosen points exceed the concrete strength. Indeed, none of the points associated with node 255 exceed the 3N/mm limit.

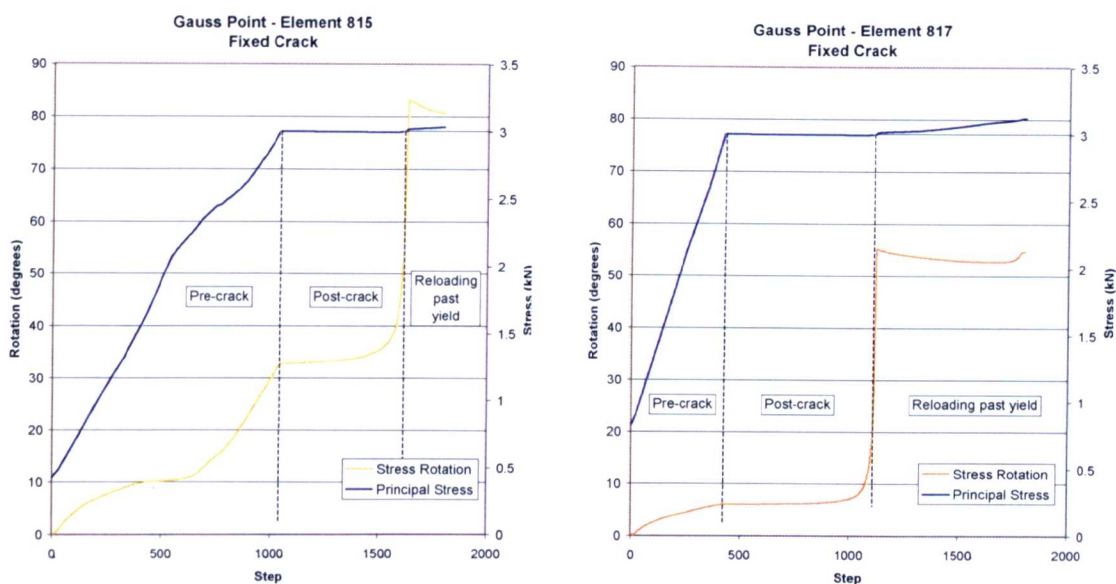
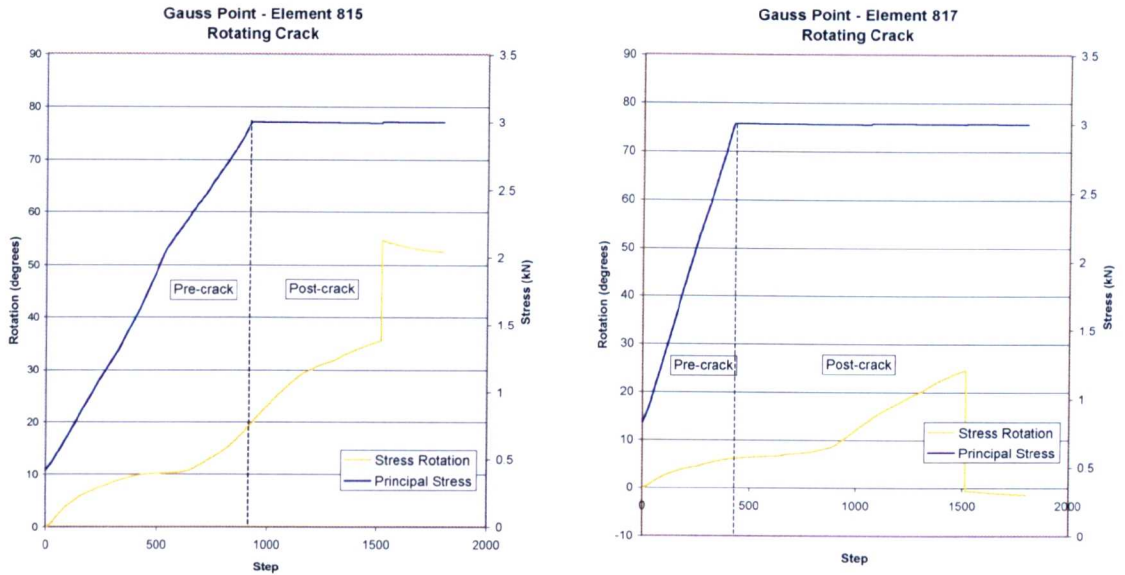


Figure 6-27 - Gauss Point History (Fixed Crack). a) Element 815, b) Element 817

Figure 6-27 above shows both the principal stress history and the rotation of the principal plane for the two points found to exceed the tensile limit of the concrete. This rotation is taken as the included angle between the principal stress vector in step 1 and the current principal stress vector. In this way it captures the rotations in each of the three planes. In both plots there are three distinct phases. Firstly, an initial ‘pre-crack’ period where the principal stress levels remain below the concrete tensile strength. On reaching the tensile limit of the concrete the crack plane is formed in an orientation co-planar with the current principal plane. As a fixed crack analysis was used to produce the above results any further rotation of the principal plane may lead to stress locking. As can be seen from the graphs, there is a period where the principal plane remains in a static position. However, at the end of this period there is a significant rotation and an associated increase in principal stress past the material limit.



**Figure 6-28 - Gauss Point History (Rotating Crack). a) Element 815, b) Element 817**

The equivalent history plots for the rotating crack analysis are shown in Figure 6-28. What is significant is that for both points there is a significant rotation of the principal plane in the post-crack phase of the analysis and yet no build up of excess stress. It was also observed that for the fixed crack results there was a noticeable change in the rotation behaviour of the principal plane associated with the onset of cracking. For the Rotating Crack Model the principal plane rotates freely without being affected by the crack initiation.

Figure 6-29 shows history plots for the Gauss points associated with elements 818 and 888. Neither of these points showed excessive stress levels. However, it is interesting to note that the Gauss point for element 818 shows a small but continuous rotation in the principal plane in the post-crack phase. It is likely that the rotation was small enough so as not to cause significant stress locking. The additional effect of the material softening process also helps to prevent this problem. In contrast, the Gauss point for element 888 shows a very significant amount of rotation in the pre-crack phase but the principal plane remains static once the crack has formed.

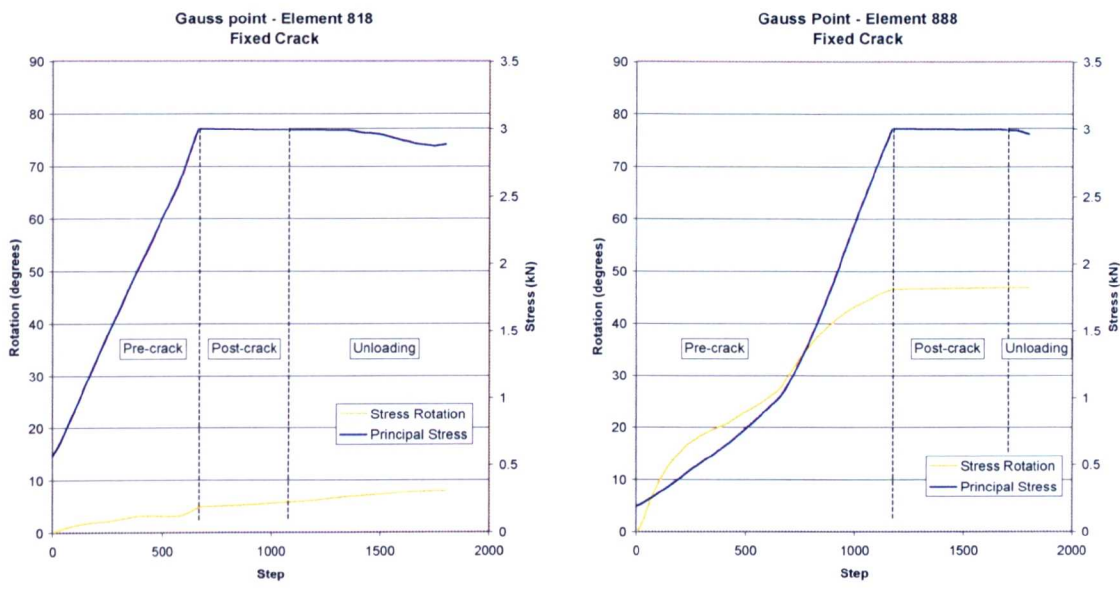


Figure 6-29 - Gauss Point History (Fixed Crack). a) Element 818, b) Element 888

Once again the history plots for the same nodes from the rotating crack analysis shows no excessive principal stresses even with significant rotation of the principal planes in the post-crack section of the analysis (Figure 6-30). For Element 818’s Gauss point there is also some softening of the material present.

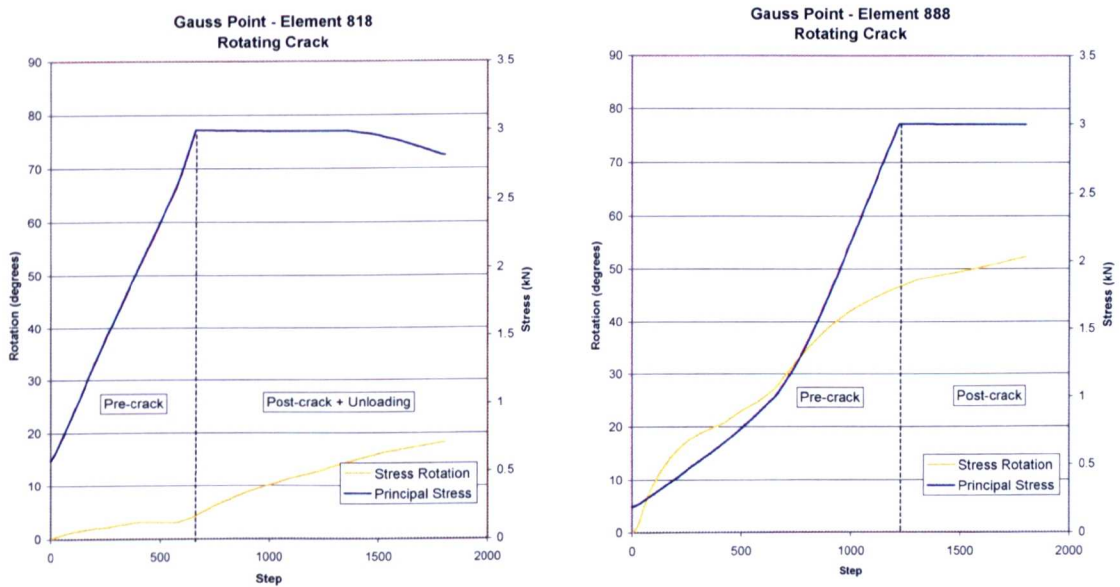


Figure 6-30 - Gauss Point History (Rotating Crack). a) Element 818, b) Element 888

The above studies serve both to illustrate the presence of stress locking due to crack misalignment at the Gauss point level but also to show how the use a Rotating Crack Model avoids this phenomenon. Relative merits of the different forms of crack model have already been discussed in Chapter 2 however in situations where a rotation of the principal plane is likely during the course of the analysis both fixed crack formulations (single and multiple) prove unsuitable.



**6.3 Stress Locking Due To Poor Kinematic Representation of Crack Discontinuity**

A third, more subtle form of spurious stress accumulation may also be present in smeared crack analyses. As with traditional stress locking this form of locking is caused by an inability of the finite elements to provide the kinematics necessary to represent the strain field. In this case it is the highly localised field produced by the presence of a crack that is the source of the difficulties [Jirásek, Zimmermann (1998)]. The effects of this phenomenon can be observed in the load-displacement response of the 3-point bending problem presented above. The problem was discretised by 4 noded tetrahedra and the rotating crack formulation of the Total Strain Based Crack Model was used. The response is shown below (Figure 6-31).

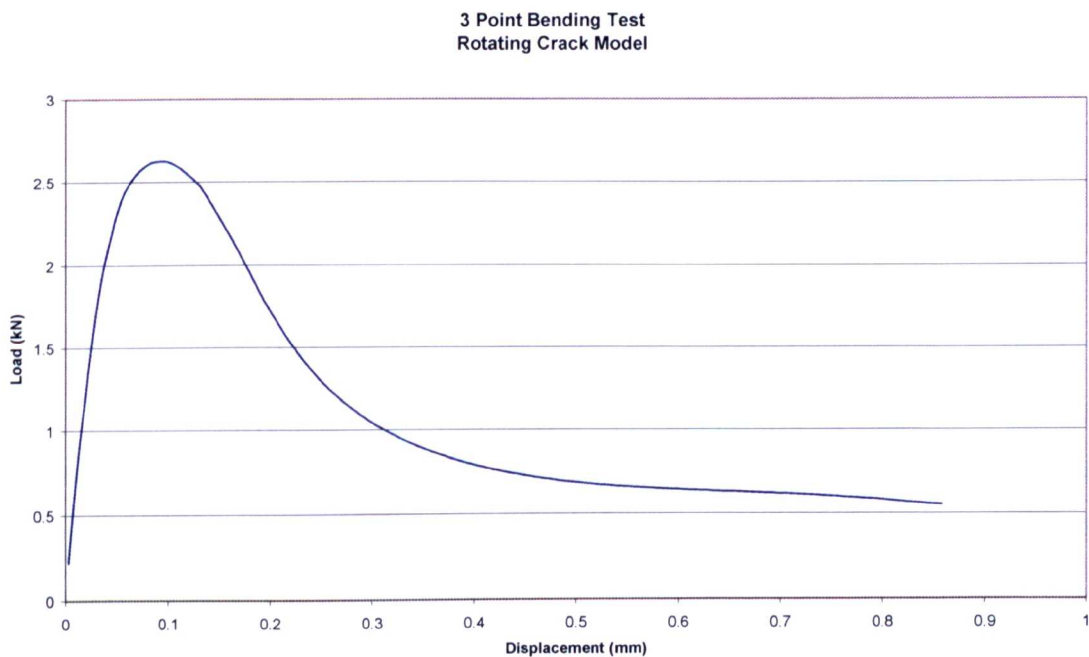


**Figure 6-31 - 3 Point Bending Test Response (RC Model)**

It is clear from the graph that the analysis is free from stress locking due to crack misalignment since there is a clearly defined peak load and an extensive period of post-peak softening. It would be expected that at a sufficiently large level of displacement the problem should break completely and the resisting force should be zero. However, it can be seen that the rate of softening slows greatly in the latter stages of the analysis. Jirásek and Zimmermann report a roughly constant plateau with higher residual load resistance of

almost 25% of the peak load when analysing a similar specimen using the Traditional Rotating Crack Model. The following illustration of the problem follows that of Jirásek and Zimmermann's work.

The mechanism for this type of spurious stress accumulation can best be illustrated by considering a 2D problem subject to uniaxial tensile loading (Figure 6-32a). As the load level increases so too does the intensity of uniform strain present in the structure. When peak load is reached a crack will form perpendicular to the direction of applied stress. The strains will localise to the cracking elements whilst the intact elements will unload elastically.

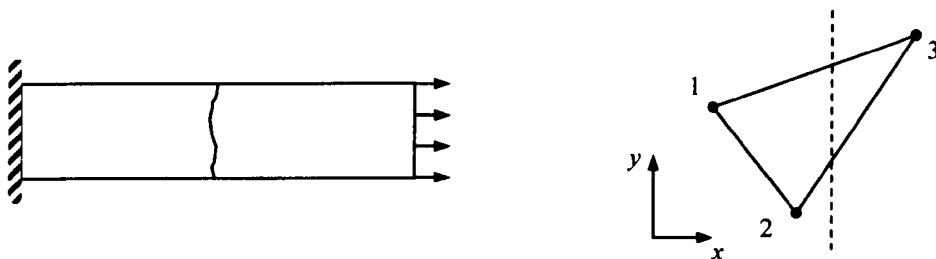


Figure 6-32 - a) Uniaxially Loaded Problem, b) Cracking Element

If the structure is discretised by constant strain triangle elements a single element within the crack zone can be examined (Figure 6-32b). The coordinate system is aligned so that the  $x$ -axis is perpendicular to the crack. The standard relationship between strain,  $\epsilon$  and nodal displacements,  $\delta$  can be written as:

$$\epsilon = B\delta \quad \text{Equation 6-1}$$

where  $B$  is the strain matrix:

$$B = \frac{1}{2A} \begin{bmatrix} y_2 - y_3 & 0 & y_3 - y_1 & 0 & y_1 - y_2 & 0 \\ 0 & x_3 - x_2 & 0 & x_1 - x_3 & 0 & x_2 - x_1 \\ x_3 - x_2 & y_2 - y_3 & x_1 - x_3 & y_3 - y_1 & x_2 - x_1 & y_1 - y_2 \end{bmatrix}$$

$$\text{Equation 6-2}$$

where  $A$  is the element area and  $x_n$  and  $y_n$  are the nodal coordinates in the  $x$  and  $y$  directions respectively.

For the purposes of this investigation it is more helpful to express the element strain in terms of relative nodal displacements. The standard form is reformulated as follows:

$$\begin{bmatrix} u_2 - u_1 \\ v_2 - v_1 \\ u_3 - u_1 \\ v_3 - v_1 \end{bmatrix} = \begin{bmatrix} -1 & 0 & 1 & 0 & 0 & 0 \\ 0 & -1 & 0 & 1 & 0 & 0 \\ -1 & 0 & 0 & 0 & 1 & 0 \\ 0 & -1 & 0 & 0 & 0 & 1 \end{bmatrix} \begin{bmatrix} u_1 \\ v_1 \\ u_2 \\ v_2 \\ u_3 \\ v_3 \end{bmatrix} \quad \text{Equation 6-3}$$

$$\bar{\delta} = Q\delta \quad \text{Equation 6-4}$$

In this way node 1 is taken as the reference node and nodal displacements are calculated relative to this point. Equation 6-4 is then pre-multiplied by  $Q^T$

$$Q^T \bar{\delta} = Q^T Q \delta \quad \text{Equation 6-5}$$

Rearrange

$$\delta = \underbrace{(Q^T Q)^{-1}}_{\bar{Q}} Q^T \bar{\delta} = \bar{Q} \bar{\delta} \quad \text{Equation 6-6}$$

Substituting into Equation 6-1 gives

$$\varepsilon = \underbrace{BQ}_{\bar{B}} \bar{\delta} = \bar{B} \bar{\delta} \quad \text{Equation 6-7}$$

Prior to the formation of the crack in the element the relative displacements are given by:

$$u_i - u_j = \frac{\sigma_x}{E} (x_i - x_j) \quad \text{and} \quad v_i - v_j = -\frac{\nu \sigma_x}{E} (y_i - y_j) \quad \text{Equation 6-8}$$



Substituting these equations into Equation 6-7 yields the expected expressions for strain:

$$\varepsilon_x = \frac{\sigma_x}{E}; \quad \varepsilon_y = \frac{\nu\sigma_x}{E} \quad \text{and} \quad \gamma_{xy} = 0 \quad \text{Equation 6-9}$$

When cracking initiates the equations for the relative displacements  $u_2-u_1$ ,  $v_2-v_1$  and  $v_3-v_1$  remain unchanged. However, the equation for  $u_3-u_1$  must be modified with the addition of the crack opening,  $w_c$ , the effects of which are smeared over the element.

$$u_3 - u_1 = \frac{\sigma_x}{E}(x_3 - x_1) + w_c \quad \text{Equation 6-10}$$

The relative displacement equations for the cracked state can be substituted into Equation 6-7 as before. The resulting equation can be rearranged so as to highlight the contributions from the elastic and crack components. Note, although this form of strain decomposition is more in line with the formulation of traditional crack models it is equally valid in relation to the Total Strain Based Crack Model since the components of total strain implicitly contain components from elastic and inelastic strains.

$$\begin{bmatrix} \varepsilon_x \\ \varepsilon_y \\ \gamma_{xy} \end{bmatrix} = \begin{bmatrix} 1 \\ -\nu \\ 0 \end{bmatrix} \frac{\sigma_x}{E} + \begin{bmatrix} y_1 - y_2 \\ 0 \\ x_2 - x_1 \end{bmatrix} \frac{w_c}{2A} \quad \text{Equation 6-11}$$

For the current configuration and orientation of the crack the crack opening should only contribute on the strain in the  $x$  direction, however it is clear that it also produces a contribution to the shear strain as follows:

$$\gamma_{xy} = \frac{(x_2 - x_1)}{2A} w_c \quad \text{Equation 6-12}$$

The value of Equation 6-12 will only be equal to zero when  $(x_1-x_2) = 0$ . In other words, when the face 1-2 is parallel to the crack. For all other cases a spurious shear stress will be developed within the element. It is important to note that it is the finite element

interpolation and not the material model that produces this effect. Therefore any material model that provides anisotropic softening is potentially at risk from this phenomenon. An additional effect of this spurious shear stress is that it will cause a rotation in the principal axes for the element thus causing them to be out of alignment with the global principal directions. The limit of this rotation may be calculated as follows:

$$\theta' = \lim_{w_c \rightarrow \infty} \frac{1}{2} \arctan \frac{\gamma_{xy}}{\epsilon_x - \epsilon_y} = \frac{1}{2} \arctan \frac{x_2 - x_1}{y_2 - y_1} \quad \text{Equation 6-13}$$

Geometrically this equates to half the included angle between the normal to the crack and the normal to the element side that is not intersected by the crack (Figure 6-33).

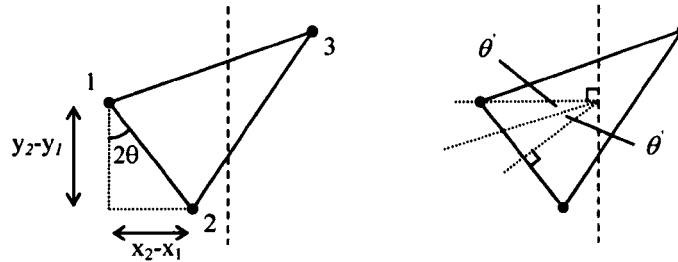


**Figure 6-33 - Deviation Angle From Principal Direction**

It is clear to see that the angle of deviation from the true principal direction can be quite significant and is related to the geometry of the element.

In the latter stages of the analysis the crack will be large and correspond to the presence of a wide-open crack. In reality the portions of the element on either side of the crack would move apart freely as two rigid bodies. No stress transfer would occur between the two. For the finite element method the strain state across the crack is entirely comprised of the smeared crack strain. For the current example the principal strains can be calculated from the global strains given by Equation 6-11.

$$\epsilon_1 = (\cos \theta')^2 \epsilon_x + (\sin \theta')^2 \epsilon_y + \cos \theta' \sin \theta' \gamma_{xy} = \left[ (\cos \theta')^2 (y_1 - y_2) + \cos \theta' \sin \theta' (x_2 - x_1) \right] \frac{w_c}{2A} \quad \text{Equation 6-14}$$

$$\varepsilon_2 = (\sin \theta')^2 \varepsilon_x + (\cos \theta')^2 \varepsilon_y + \cos \theta' \sin \theta' \gamma_{xy} = \left[ (\sin \theta')^2 (y_1 - y_2) + \cos \theta' \sin \theta' (x_2 - x_1) \right] \frac{w_c}{2A}$$

**Equation 6-15**

By rearranging Equation 6-13 the following expression can be obtained:

$$(x_2 - x_1) = (y_1 - y_2) \tan 2\theta' = (y_1 - y_2) \frac{2 \cos \theta' \sin \theta'}{\cos^2 \theta' - \sin^2 \theta'} \quad \text{Equation 6-16}$$

Substituting this into the above equations for principal strain gives:

$$\varepsilon_1 = (y_1 - y_2) \frac{(\cos \theta')^2}{(\cos^2 \theta' - \sin^2 \theta')} \frac{w_c}{2A} \quad \text{Equation 6-17}$$

$$\varepsilon_2 = -(y_1 - y_2) \frac{(\sin \theta')^2}{(\cos^2 \theta' - \sin^2 \theta')} \frac{w_c}{2A} = -\frac{(\sin \theta')^2}{(\cos \theta')^2} \varepsilon_1 \quad \text{Equation 6-18}$$

Clearly both principal strains grow proportionally as the crack opening increases, the primary principal strain being positive whilst the secondary principal strain is negative. In the case of the Total Strain Based Crack Model the element will eventually soften in the secondary principal direction only if an appropriate compression-softening model has been specified. In terms of principal stresses the following relationships can be derived:

$$\sigma_1 = 0; \quad \sigma_2 = -\frac{E w_c}{2A} (y_1 - y_2) \frac{(\sin \theta')^2}{(\cos^2 \theta' - \sin^2 \theta')} \quad \text{Equation 6-19}$$

These principal stresses may then be transformed back into the global coordinate system to produce the following:

$$\sigma_x = (\cos \theta')^2 \sigma_1 + (\sin \theta')^2 \sigma_2 = -\frac{y_1 - y_2}{2A} \frac{(\sin \theta')^4}{(\cos^2 \theta' - \sin^2 \theta')^2} E w_c \quad \text{Equation 6-20}$$

$$\sigma_y = (\sin \theta')^2 \sigma_1 + (\cos \theta')^2 \sigma_2 = -\frac{y_1 - y_2}{2A} \frac{(\cos \theta')^2 (\sin \theta')^2}{(\cos \theta')^2 - (\sin \theta')^2} Ew_c \quad \text{Equation 6-21}$$

$$\gamma_{xy} = \cos \theta' \sin \theta' (\sigma_1 - \sigma_2) = -\frac{y_1 - y_2}{2A} \frac{\cos \theta' (\sin \theta')^3}{(\cos \theta')^2 - (\sin \theta')^2} Ew_c \quad \text{Equation 6-22}$$

It is important to note that all three stresses are non-zero and are proportional to the crack opening. Therefore, for a wide-open crack there may be a significant transfer of stresses across the crack. This is obviously contrary to the behaviour of a crack in reality.

The stress transfer across an open crack is illustrated in the following example of a typical finite element model discretised by equilateral, constant strain triangles and subject to loading in the  $x$  direction so as to cause cracking as shown (Figure 6-34).

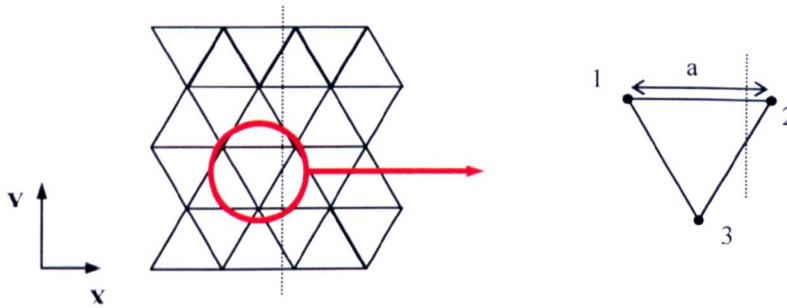


Figure 6-34 – Typical FE Mesh Structure

Considering a single elements and using the equations derived above the rotation of the principal axes,  $\theta'$ , is  $15^\circ$  and hence the principal stresses for a wide-open crack are;  $\sigma_1=0$  and  $\sigma_2=-0.07735Ew_c/a$ . Corresponding stresses in the global coordinate system are;  $\sigma_x=-0.00518Ew_c/a$ ,  $\sigma_y=-0.07216Ew_c/a$ , and  $\gamma_{xy}=0.01934Ew_c/a$ .

Nodal forces may be calculated using the standard finite element formula:

$$\mathbf{f} = \int \mathbf{B}^T \boldsymbol{\sigma} dA = \mathbf{A} \mathbf{B}^T \boldsymbol{\sigma} \quad \text{Equation 6-23}$$

where  $\mathbf{f}$  is the nodal force vector.

$$\begin{aligned} \mathbf{f} &= [f_{1x} \quad f_{1y} \quad f_{2x} \quad f_{2y} \quad f_{3x} \quad f_{3y}]^T \\ &= [7.1 \quad -26.4 \quad -9.7 \quad 36.1 \quad 2.6 \quad -9.7]^T \times 10^{-3} Ew_c \end{aligned} \quad \text{Equation 6-24}$$

The spurious stress transfer across the open crack can be calculated by applying the nodal forces calculated for the single element above, mirroring the element in the horizontal and vertical axes as necessary. The resulting forces are shown in Figure 6-35 (the common multiplier,  $\times 10^{-3} Ew_c$ , has been dropped for clarity).

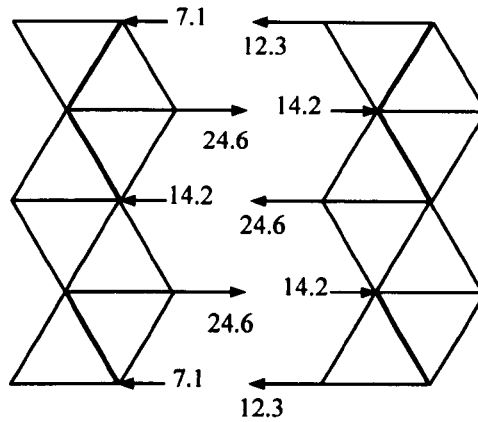


**Figure 6-35 - Spurious Stress Transfer Across Crack**

Globally the line of cracked elements acts as a cohesive layer the magnitude of which is proportional to the opening of the crack. This explains the source of the residual strength seen in the load-displacement response of the 3-point bending problem. As stated above, in the absence of a compression-softening model these forces may grow seemingly without limit. However, the tension forces present induce tensile stresses in the surrounding elements thus causing them to crack and soften. Although this secondary

cracking leads to further softening in the structure it is undesirable as it is contrary to the aim of crack modelling to develop a localised strain field representative of a crack.

Although the above example consists of triangular elements the same stress-locking phenomenon is produced in quadrilateral elements if the crack is not aligned parallel with the element's sides. Similarly, locking will occur in three-dimensional tetrahedral and hexahedral elements if the crack plane is not parallel to an element side. Higher order elements provide more complex kinematics and as such are able to relax these spurious stresses by adjusting the displacement field. However the very nature of these types of elements inevitably leads to increased computational expense whilst not completely overcoming the problem of spurious stress accumulation.

There are three possible ways to prevent this form of stress-locking. The first way is to align the finite element mesh such that the mesh lines lie parallel to the crack lines. However this requires *a priori* knowledge of the crack direction. By running a 'first guess' problem and updating this as necessary this information could be obtained. However this process is intrinsically slow for all but relatively simple problems and impractical for three-dimensional modelling. It also means that the original mesh topology is lost therefore comparisons between different load cases are less straightforward.

A second option is to adopt a Damage-type model. In the isotropic formulation of this material model softening applies equally in all directions and is governed by the damage parameter  $\alpha$  [Mazars, Pijaudier-Cabot (1998), Oliver, et al (1990)]. At a sufficiently high level of strain the value of  $\alpha$  will be zero. Therefore the element will have no stiffness be incapable of generating spurious stresses. A hybrid model proposed by Jirásek and Zimmermann initially models cracking via the standard Rotating Crack formulation [Jirásek and Zimmermann (1998)]. Once a sufficient level of strain has been developed there is a transition to a Damage-type model where the stiffness matrix, as produced by the Crack Model, is scaled by a damage variable. This ensures the anisotropic nature of the material is preserved until the loss of stiffness is complete. However, as pointed out

by Rots and Blaauwendraad, this does mean that on ultimate failure of the element the stiffness perpendicular to the crack is lost [Rots and Blaauwendraad (1989)]. This is obviously at odds with material behaviour in reality.

The third option to prevent these spurious stresses is to use a finite element that incorporates embedded discontinuities [Wells et al (2001), Alfaiate et al (2001)]. These discontinuities are often added by extending the displacement interpolation functions locally by the addition of an extra nodal degree of freedom at existing nodes. However, the element still retains the same order of interpolation as the standard element from which it is derived. Such enhanced elements are a fairly recent development however their potential for the future looks promising.

#### 6.4 Stress locking Due To Finite Element Displacement Compatibility

This fourth and final form of stress locking occurs because of the requirement in finite element analysis for displacement compatibility at the node points [Rots and Blaauwendraad (1989)]. The problem may be illustrated by means of this following simple example.

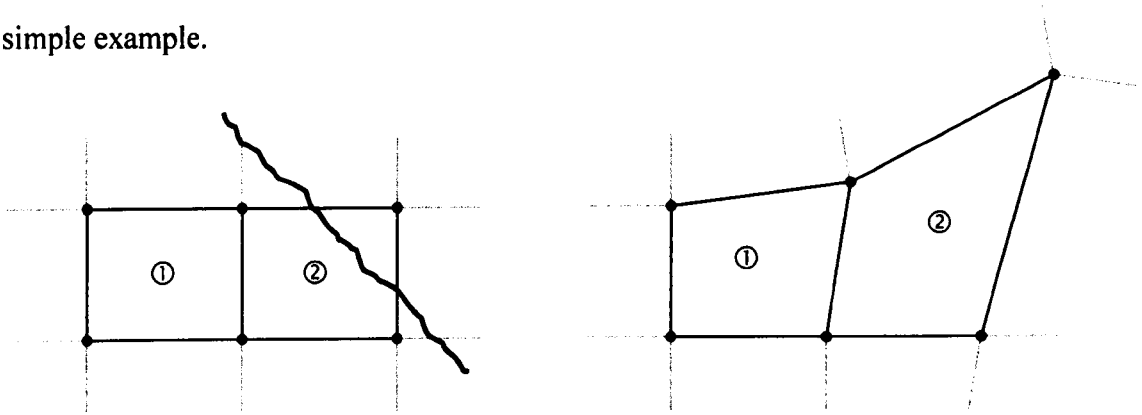


**Figure 6-36 - Smeared Crack Inducing Stress In Surrounding Elements**

The diagram on the left in Figure 6-36 shows an undeformed mesh and focuses on two elements which form part of a larger structure. A crack forms such that its path crosses element 2 but not element 1. For smeared softening models the effects of the crack opening are modeled by distributing an equivalent strain across the whole element. In this case element 2 deforms as shown in Figure 6-36b. However, as a consequence of displacement compatibility element 1 will also undergo straining. This is obviously in disagreement with the behavior seen in reality. As the crack continues to open the induced strains in element 1 will lead to a spurious stress build up. This process will result in an overly stiff global structural response. If these locked in stresses exceed the material strength cracking will occur in element 1 also. This is also undesirable since it results in a diffuse crack zone rather than localization. Although the elements chosen are 4-noded quadrilaterals the following argument is equally valid for other element types.

The preventative measures discussed above for stress locking due to poor kinematic representation of the crack discontinuity are equally applicable to the current stress locking problem and carry with them the same disadvantages.



### **6.5 Summary and Choice of Model and Parameters**

During the course of this investigation into stress locking a number of different sources have been identified. This information then influenced the choice of geometric model, constitutive model and the associated parameters used for subsequent analysis work. Since the primary aim of this research was to model the failure mechanism of anchor bolts it was vital that a failure load could be identified. For this reason the Rotating Crack Model was selected so as to prevent the spurious stress accumulation caused by crack misalignment and so allow softening of the problem in the post peak regime. The Isotropic Damage Model was also considered as an alternative choice of constitutive model. As stated above, this would have avoided the problems associated with poor kinematic representation of the crack and limitations due to the displacement compatibility requirement. However, it was considered that the modelling of material anisotropy was important and so the Isotropic Damage Model was not used.

Initially modelling was carried out using 4-noded tetrahedral elements with a single point integration scheme for compatibility with previous analysis and also because the unstructured mesh produced avoided mesh alignment problems. Later analysis adopted 8-noded hexahedral elements with a  $2 \times 2 \times 2$  integration scheme as they had shown to be less prone to traditional stress locking (Section 6.1). A regular mesh was used and partially aligned with the expected crack direction so as to address the sources of locking due to the smeared representation of the crack.

In conclusion, it is important to be aware of these sources of spurious stress accumulation. Although there may be no way to eliminate them from an analysis their effects can be reduced to an acceptable level if appropriate choices are made when selecting the components for the numerical modelling.

## CHAPTER 7

### Influence of Edge Effects

In Chapter 4 preliminary attempts were made to study the effects of edge distance on anchor performance. Although softer structural responses were produced when the anchor neared the edge and corners of the concrete block the full structural responses and associated failure mechanisms were not identified due to modelling difficulties. In this chapter the Total Strain Based Crack Model is used with parameters and options chosen to avoid these problems. The study was extended to examine the structural response of the model for the anchor in a wide range of positions. Various aspects were observed such as stress distribution and crack pattern. The so-called ‘Edge Reductions Factors’ were also calculated and compared to design guide values. Finally, problems revealed via a mesh sensitivity study are investigated and solutions proposed.

#### 7.1 Expansion Anchor Failure Modes

As discussed previously, when considering anchors subject to tensile loading a number of failure mechanisms are possible (Figure 7-1) [Rawlplug (1999b), Hilti (2001)]. In cases where the frictional bond strength between the anchor and surrounding concrete is exceeded, the anchor will simply pull out leaving the concrete intact.

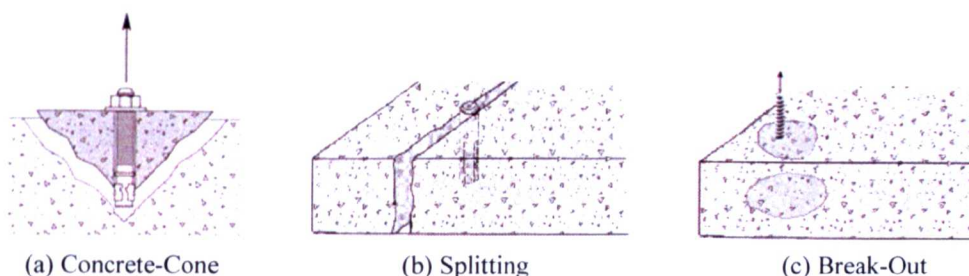


**Figure 7-1 - Anchor Failure Modes**

With a sufficiently high contact strength the anchor will be able to effectively transmit loads into the base material. In such circumstances both the failure mode and the ultimate failure load are influenced by edge effects. Given a sufficient distance from the free

edges of the base material a concrete-cone failure is likely. With a decreasing edge distance, the ultimate load capacity will be lower and the associated failure mode may be via splitting, breakout or a combination of the above.

7.2 Middle/Edge/Corner Models Revisited

The finite element models analysed towards the end of Chapter 4 were re-examined taking into account the findings of the investigation into stress locking as follows (Figure 7-2). The rotating formulation of the Total Strain Based Crack Model [Feenstra (1999)] was used with exponential softening for post-peak behaviour in the tensile regime. In compression, concrete behaviour was prescribed as linear elastic since the expected failure modes of the anchor were tensile driven. The base of the concrete was fixed in all directions and prescribed displacements were applied to the top of the expander to simulate pullout.

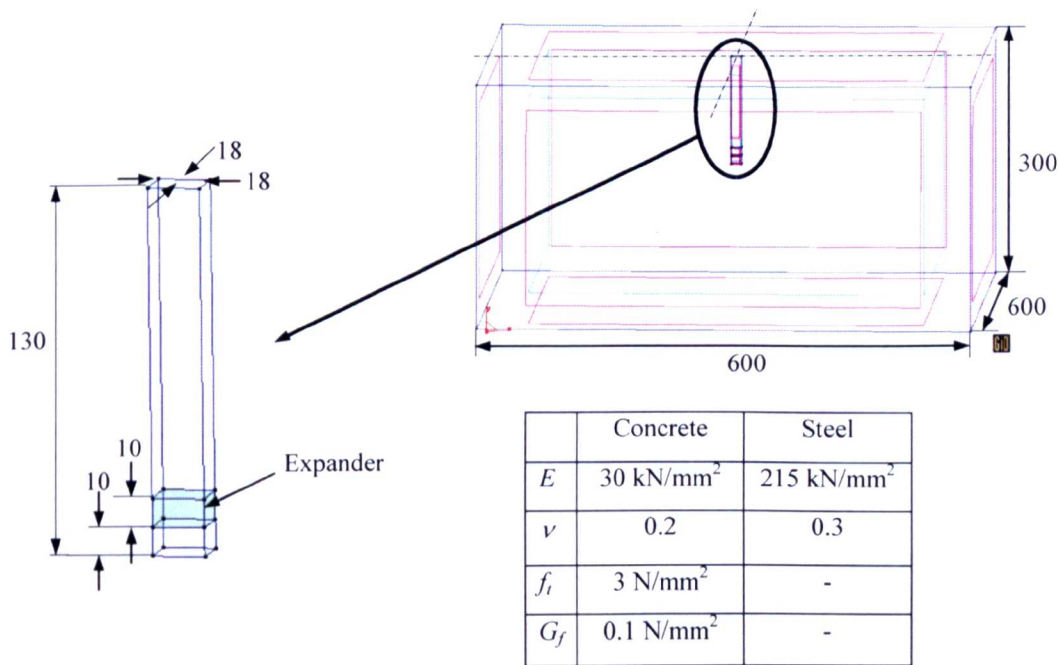
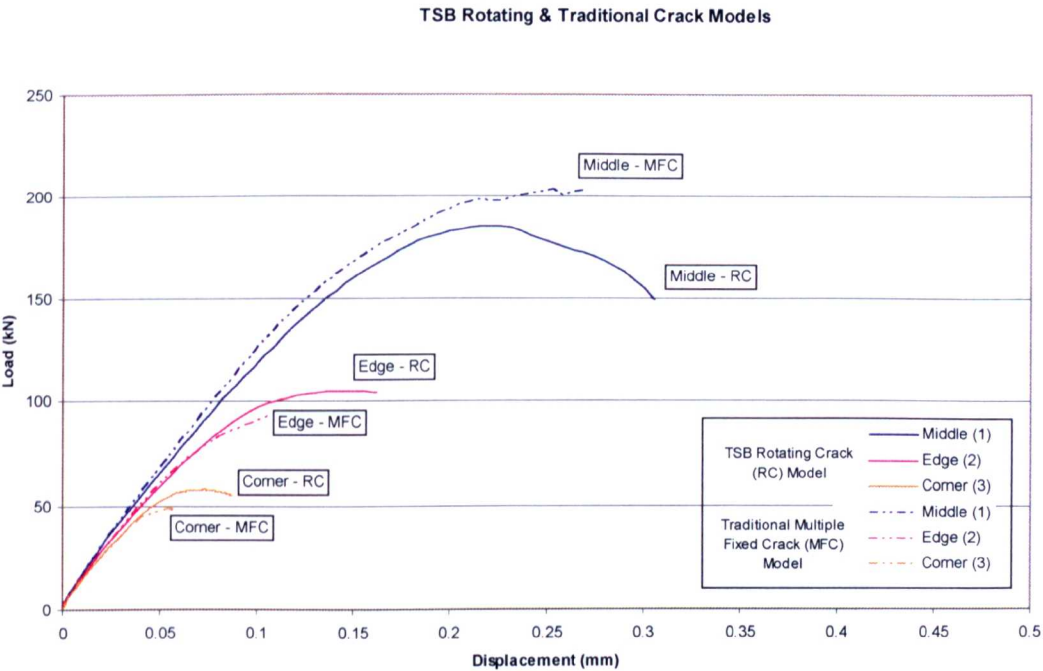


Figure 7-2 - 3D Anchor Pullout Problem Geometry - Anchor in Centre Position

Comparing the load-displacement results produced by both material models for the middle position (Figure 7-3) shows that the Rotating Crack Model gives a generally softer response whereas for the corner and edge positions its response is slightly stiffer. It is possible that the multiple crack nature of the Traditional Crack Model lead to the softer response pre-peak in these cases. However, it is in the post-peak regime that the Rotating Crack Model suffers less from stress locking due to crack misalignment and in all three

cases found the peak load. Unfortunately lack of convergence in the non-linear solution process prevented a more complete trace of the post-peak response to be obtained for the edge and corner models. Lowering the tolerance, from a maximum relative energy variation of  $1 \times 10^{-4}$  to  $1 \times 10^{-3}$ , and allowing continuation after nonconvergence allowed the analysis to bridge this zone of instability. However this resulted in a prominent jump in the load-displacement response and so cannot be trusted as a valid solution. It is unfortunate neither of the material models were able to analyse the edge and corner models further. It would have been interesting to discover whether models analysed with the Rotating Crack Model continued to produce softening whilst those analysed with the Traditional Multiple Fixed Crack Model produced increasing stress locking and hence higher sustained loads.



**Figure 7-3 - Comparison of TSB Rotating Crack Model and Traditional Multiple Fixed Crack Model**

Use of the TSB Rotating Crack Model produced much clearer indications of failure modes for the models. Firstly, considering the model with the anchor in the middle of the block, the post-peak contour plot of crack strain shows a definite cone failure (Figure 7-4).

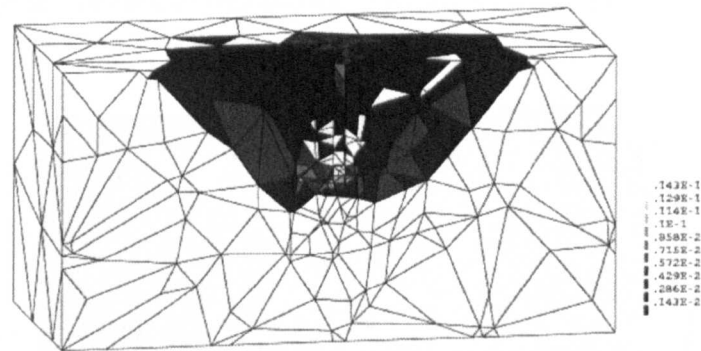


**Figure 7-4 - Crack Strain for Middle Position. Cross-Section through Anchor**

The darker areas are associated with small crack strains such as those of microcracks whereas the lighter areas represent more fully developed cracks. Significant cracks can be seen extending outwards and upwards from the anchor. Also of interest is the radial crack developing in the top surface of the concrete block. It can be seen from the displaced shape (Figure 7-5) that during the pullout process there is significant vertical deformation of the top surface of the concrete. Due to this the surface is subjected to tensile stress in the  $xz$  plane which leads to the formation of these radial cracks.

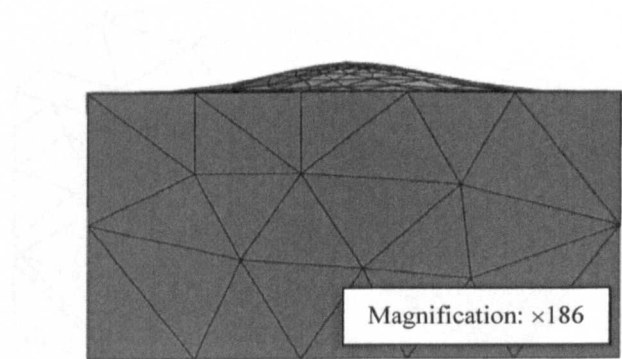


**Figure 7-5 - Displaced Shape for Middle Position**



Examination of the maximum principal stresses reveals no problems of tensile stresses exceeding the material strength (Figure 7-6). Comparing with the plot of crack strain it can be seen that principal stresses are lower in cracked elements and higher stresses can be found in elements close to the crack tip. This shows more realistic modelling of concrete behaviour as opposed to that produced by the Traditional Crack Model.

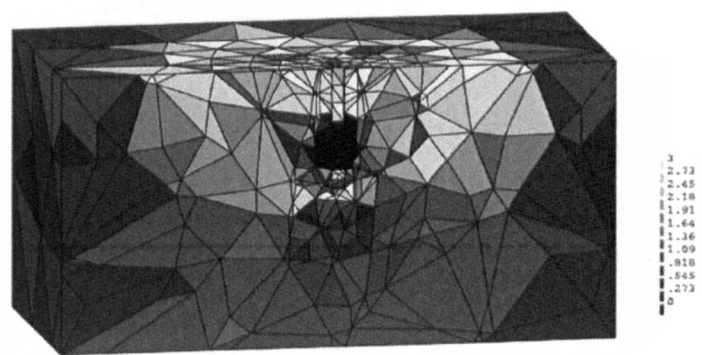


**Figure 7-6 - Maximum Principal Stress for Middle Position. Cross-Section through Anchor**

The crack pattern for the edge model clearly shows the effect of the free edge on the failure mode (Figure 7-7). Once again the crack extends from the anchor upwards and outwards however its angle almost horizontal towards the free edge. Away from the edge the angle of the crack is much steeper than for the middle position model.

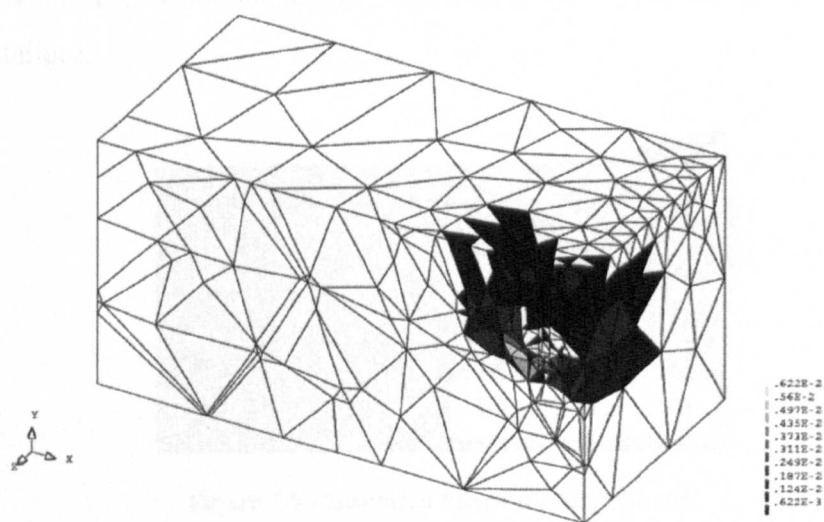


**Figure 7-7 - Crack Strain for Edge Position. Cross-Section through Anchor**

The contour plot of maximum principal stress shows the ‘stress bulb’ severely truncated by the free edge (Figure 7-8). Once again there is no evidence of spuriously high tensile stresses in the model.

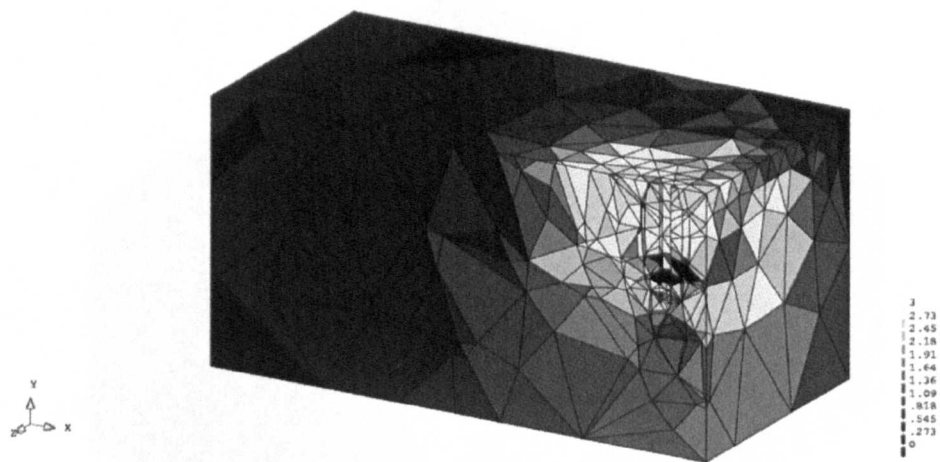


**Figure 7-8 - Maximum Principal Stress for Edge Position. Cross-Section through Anchor**

In this case the displaced shape (Figure 7-9) is very illuminating in classifying the failure mode. The figure shows the model in elevation and in addition to the vertical displacement of the top surface of the block there is a horizontal displacement of the vertical face closest to the anchor. In such a case the failure would be identified as a break-out failure.

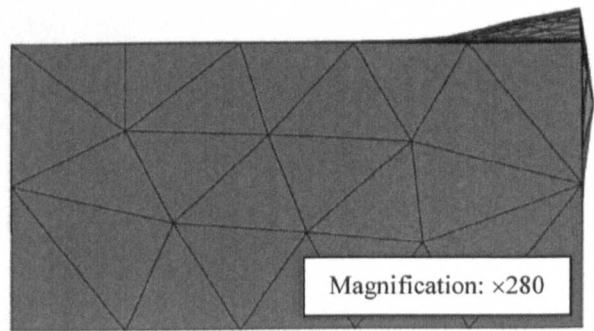


**Figure 7-9 - Displaced Shape for Edge Model**



The corner model produced a similar response, however in this case two free edges in close proximity to the anchor have the effect of lowering the anchor capacity. The maximum principal stress plot (Figure 7-10), produced for a stage of the analysis just past the peak load, shows a very similar pattern to that produced for the Traditional Crack Model.

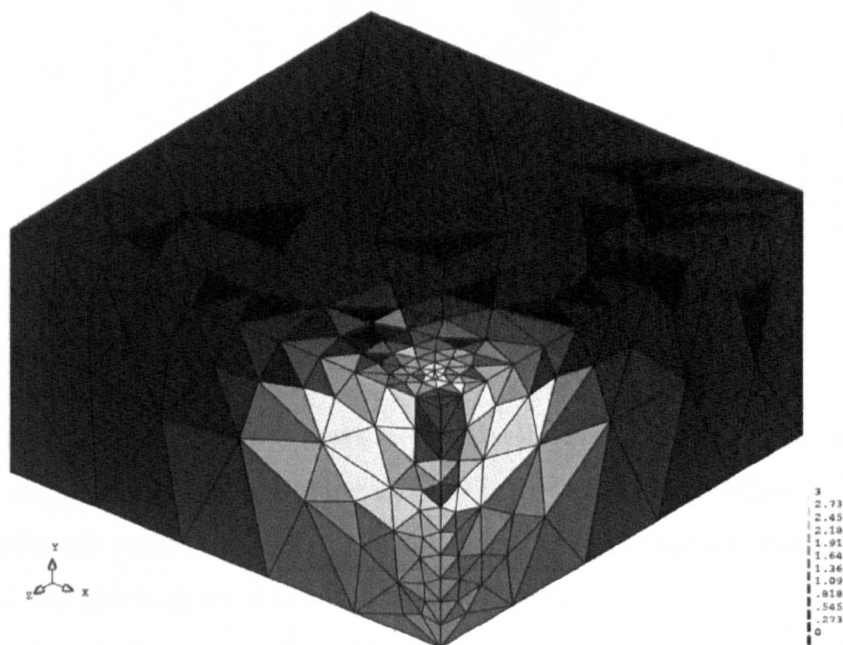
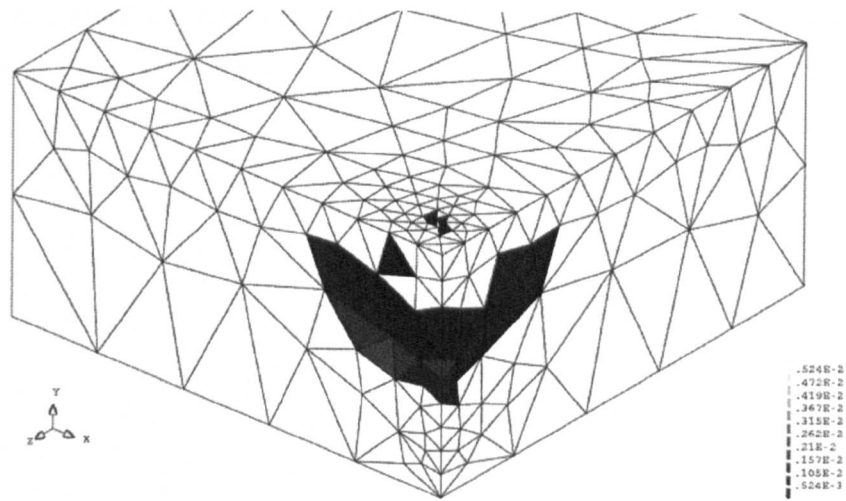


Figure 7-10 - Maximum Principal Stress for Corner Model

The constraint of the free edges serves to concentrate the stress in a highly localised zone towards the corner of the block. It is this stress concentration which leads to the anchor failure at a lower load.



**Figure 7-11 - Crack Strain for Corner Position**

The associated crack strain plot shows a very well defined horizontal crack that has extended to meet the vertical face of the block (Figure 7-11). The displaced shape shows a rotation of the top section of the block's corner hence the expected failure mode is via a separation of this part from the main block (Figure 7-12).

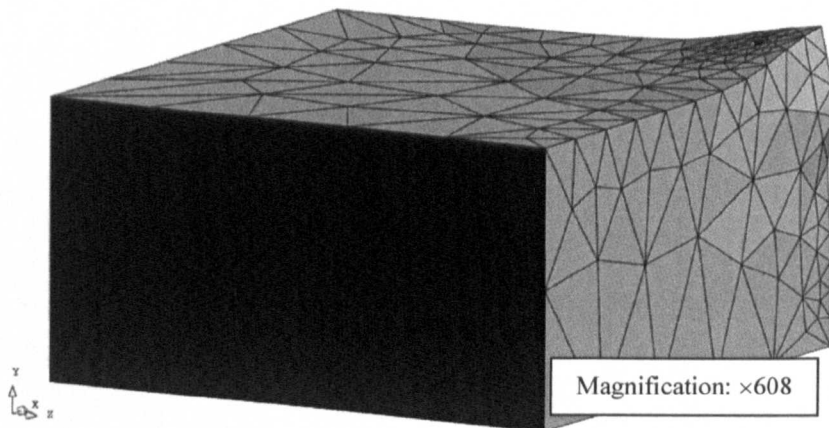


**Figure 7-12 - Displaced Shape for Corner Position**

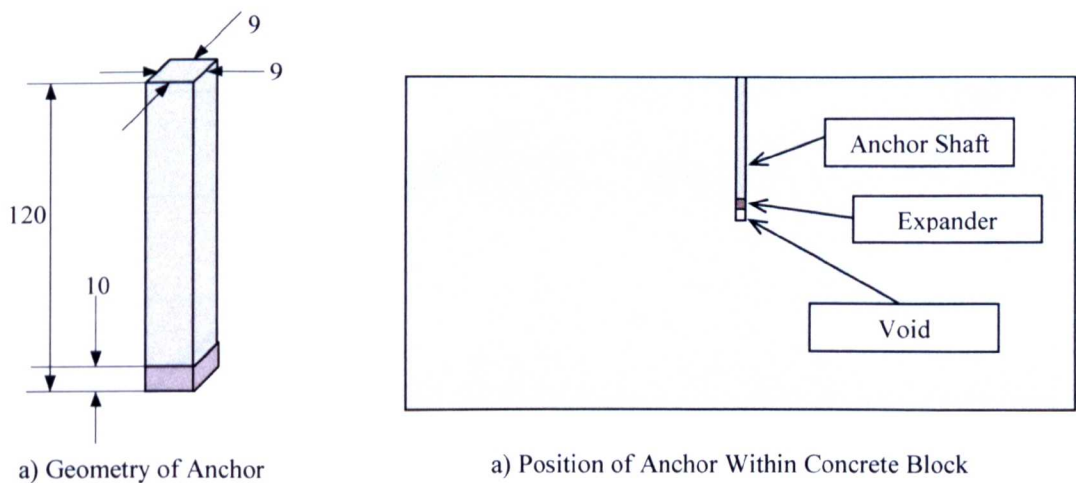
The above analyses show the improvements in the quality of the results produced by the Total Strain Based Crack Model with the rotating crack formulation compared with the Traditional Multiple Fixed Crack Model. In all cases the peak load was found and plots

of crack strain showed a much less diffuse crack pattern. Failure modes were also very apparent from the analysis results.

7.3 Detailed Edge Effect Study

Following the basic middle/edge/corner study carried out earlier a more extensive edge effect study was undertaken. The aim of which was to model in more detail the behaviour of decreasing tensile failure associated with decreasing edge distance. The Rawl Fixings Design Guide [Rawlplug (1997)] presents this data in tables in the form of Edge Reduction Factors. These are essentially scaling factors which are applied to the maximum tensile failure load for a given anchor in order to find its tensile capacity for a given edge distance.

The geometric sub-model for the anchor that was used previously was altered slightly to better represent an M12 RAWL SafetyPlus anchor (Figure 7-13) [Rawlplug (1997)].



	Concrete	Steel
$E$	$3 \times 10^4 \text{ N/mm}^2$	$2.1 \times 10^7 \text{ N/mm}^2$
$\nu$	0.2	0.2
$f_t$	$3 \text{ N/mm}^2$	-
$G_f$	$0.1 \text{ N/mm}$	-

Figure 7-13 - M12 Anchor Model Problem

As before, the assumption was made that in operation the lower part of the anchor expander would be largely responsible for the transfer of contact and tensile stresses. As

such, only the bottom 10mm of the expander was modelled and this was fully bonded to the surrounding concrete. The rest of the anchor was omitted from the geometric model. By selecting a square cross-section with sides of 9mm the contact area of the expander section (shown in grey) was  $360\text{mm}^2$ . This compares well with the  $377\text{mm}^2$  area assumed for the M12 anchor bolt. Material properties were as shown above and again the Rotating Crack Model was used with exponential tension softening and elastic response in compression. The anchor sub model was placed at seven different edge distances in turn corresponding to those listed in the design guide. The complete models were then discretised by approximately 1500, 4-noded, linear tetrahedra. Figure 7-14 shows the load-displacement responses for the different analyses with the edge distances labelled.

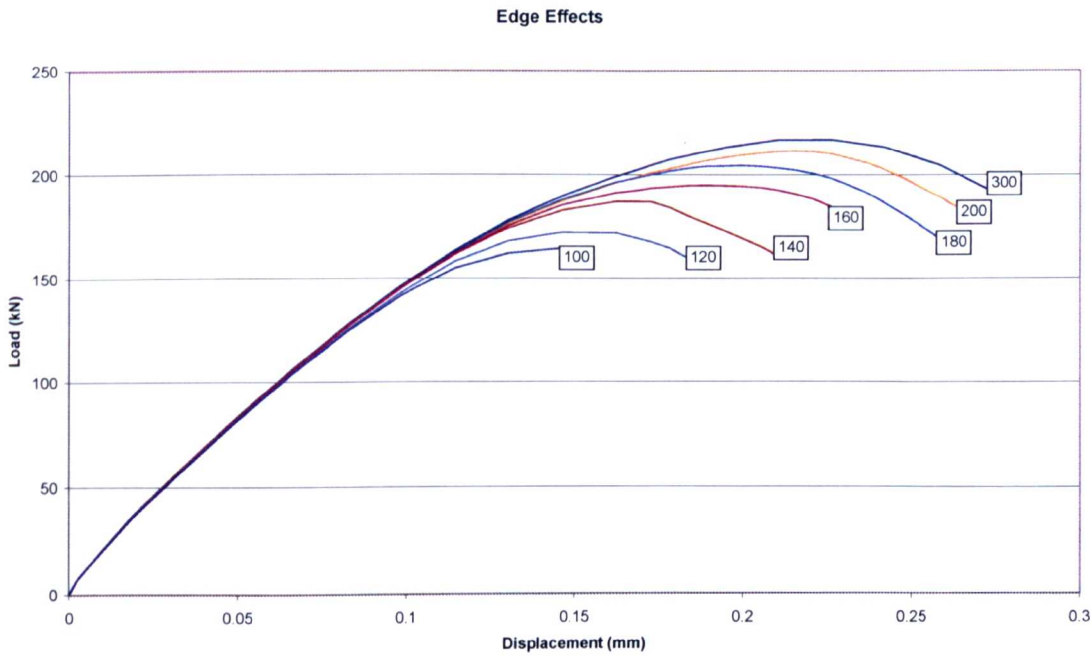


**Figure 7-14 - Effects of Edge Distance on Peak Load**

Initially all of the analyses show a similar linear response. This is to be expected as previous analyses had shown that the influence of the edge become more apparent as the loading increases. The closer an anchor is to the edge the earlier its response begins to soften and the corresponding peak load is also lower. As with previous anchor bolt analysis using the Rotating Crack Model the peak loads are well defined and there is post peak softening behaviour (although this is limited for the 100mm edge distance analysis).

The common cause for the termination of these analyses was non-convergence. However, as the main focus of this series of analyses was to determine the peak loads and failure modes, attempts to further the analyses were only carried out as far as to ensure the true peak load had been found rather than some local maximum.

The Rawl design data indicated that at an edge distance of 200mm full tensile capacity of the anchor bolt could be achieved hence, when calculating reduction factors for this study, the maximum load resisted by the anchor with a 200mm edge distance was taken as the reference value. However, it can be seen from the graph above (Figure 7-14) that the peak load at 300mm edge distance is noticeably higher than that at 200mm. There are a number of possible reasons for this difference between the design data and the numerical results produced here. The most obvious one was that the geometry of the model was too crude to reproduce the required behaviour. Although the geometry is indeed basic the results presented below show that the edge effect phenomenon was modelled very accurately. A second possibility is that the figures in the design guide are conservative and subject to some form of safety factor [Rawl (1997), Fuchs (2001), Czarnecki, et al (1993)]. Without further information this hypothesis cannot be confirmed.

The fact that the value for a 300mm edge distance was much greater than that produced for 200mm also raised the issue as to what was the true maximum tensile load for the modelled anchor. The dimensions of the concrete block sub-model had been chosen based on experience gained from previous 2D modelling. This had shown that the crack formation for an anchor in the middle position would be completely contained within a block of this size. The middle model above had shown this to also be valid for 3D analyses. Before this current study the data in the Rawl Design Guide appeared to support this as well.

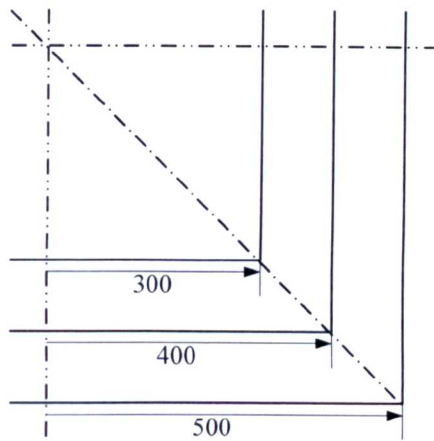


**Figure 7-15 - Block Sub-Model Modifications To Increase Edge Distance**

In order to determine the true peak load the concrete block sub model was first altered to make it 800mm and then 1000mm square (Edge distances of 400 and 500mm respectively (Figure 7-15)). The depth of the block was kept constant at 300mm. The results of the analyses are shown in Figure 7-16.

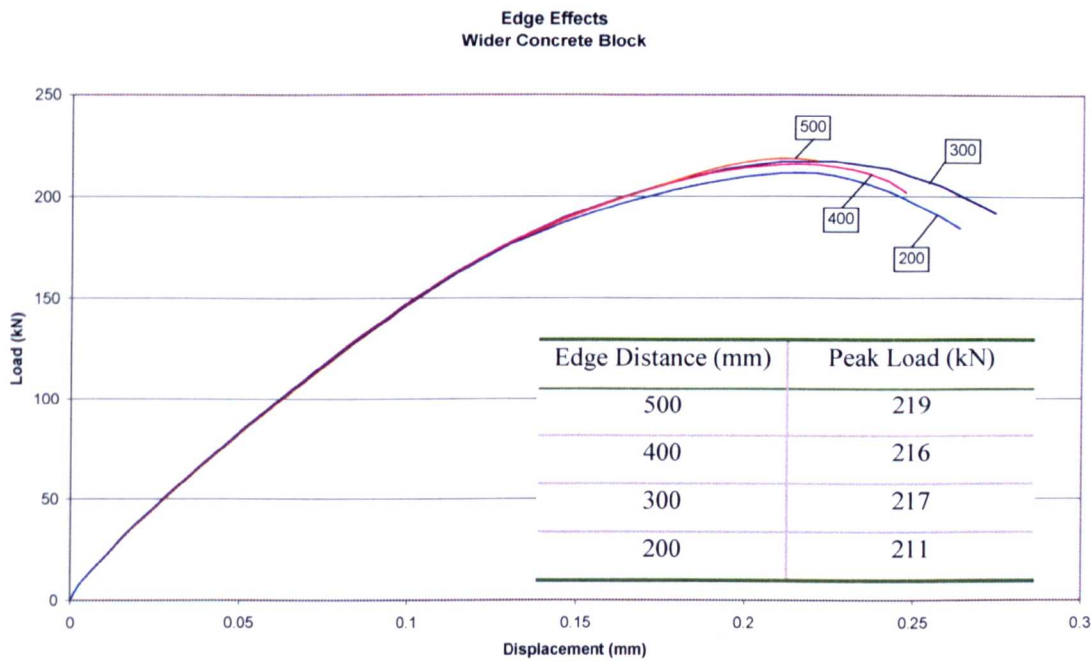


**Figure 7-16 - Determination of True Tensile Capacity**

The analyses show a 0.5% decrease in peak strength for the anchor at 400mm edge distance. At 500mm edge distance there is a 0.7% increase in peak strength. For each of these models a new FE mesh was generated and although the element type and size remained the same, the mesh topology was different. Therefore it is not surprising that there are differences in the results of the analyses. However, since the magnitude of these differences is small it can be concluded that there is no significant difference in ultimate capacity for anchors placed with an edge distance in excess of 300mm.

The Edge Reduction Factors mentioned above are a common method used by anchor bolt manufacturers to express in their design guides the lowering in tensile capacity due to decreased edge distance. This reduction factor is calculated as:

$$\text{ReductionFactor}_n = \frac{\text{Peak Load}_n}{\text{Ref.Load}} \quad \text{Equation 7-1}$$

where  $n$  is the edge distance. In common with the edge reduction factors in the design guide, the *Reference Load* was taken as the peak load resisted by the anchor when it is 200mm away from the free edge.



Reduction factors for the numerical analyses were plotted along side those provided by Rawlplug and trend lines were fitted to the results (Figure 7-17).

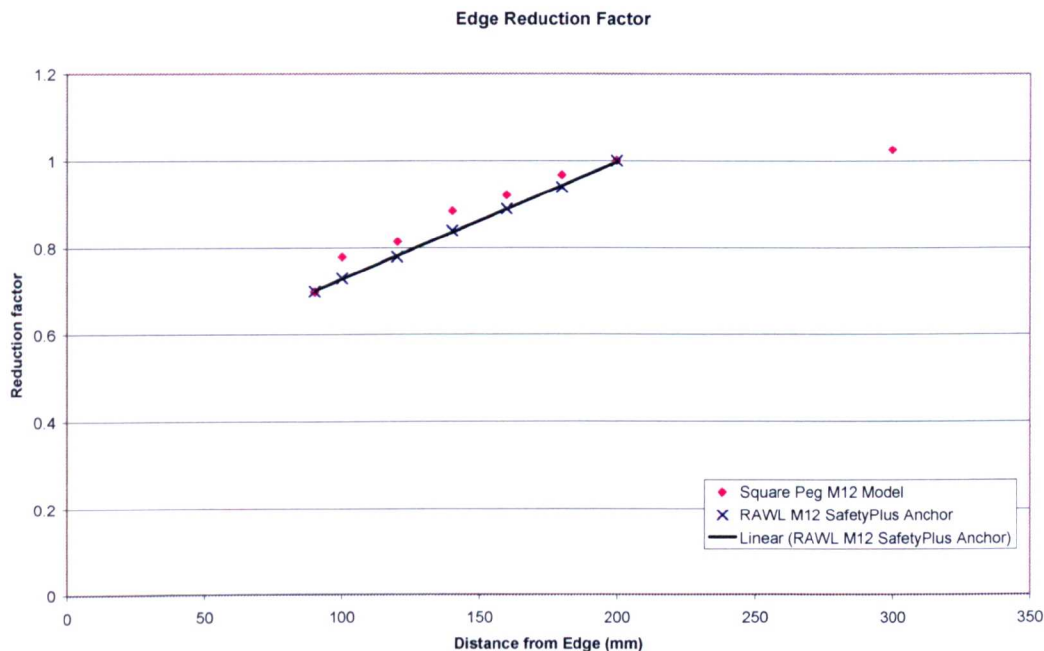


**Figure 7-17 - Edge Reduction Factors (M12 Anchor)**  
**(Reference Load @ 200mm Edge Distance)**

The graph shows a good correlation between the design guide reduction factors and those calculated from the numerical analyses. The design guide indicates an approximately linear decrease in strength from 200mm edge distance down to 90mm. The calculated values follow this trend but generally exceed those from the guide. The reason for this may be either that the design guide provides conservative values or that the results from the analysis are inaccurate. Another possibility is that the choice of reference load used in the calculation of the reduction factors is incorrect. Indeed, when the ultimate load for a 300mm edge distance is chosen as the reference load and the reduction factors recalculated, the result is a tighter scatter around the design guide reduction factors (Figure 7-18).

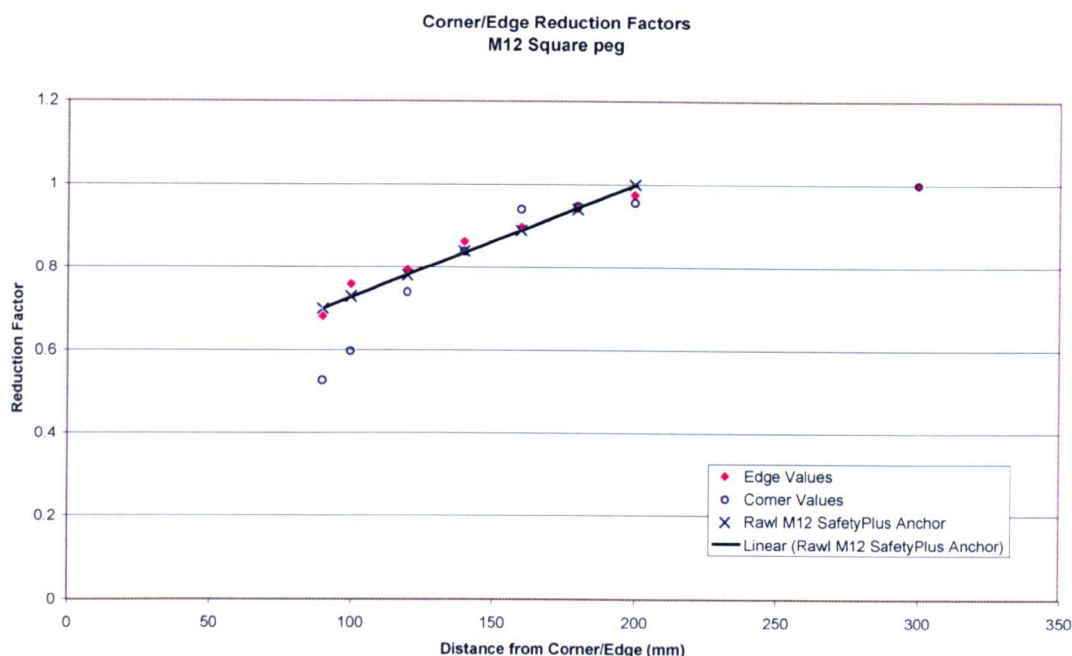


**Figure 7-18 – Alternative Calculation of Edge & Corner Reduction Factors**  
**(Reference Load @ 300mm edge distance)**

The above figure (Figure 7-18) also shows the strength reduction factors obtained by analysing the anchor in numerous positions as it approaches the corner of the block. Between 300 and 140mm edge distance the strength reduction is very similar to that when a single edge is approached. With edge distances below 140mm the trend for the corner approach diverges and shows a much larger reduction than that of the edge approach.

Extending the concept of edge reduction factors a whole area may be mapped out and the corresponding reduction factors calculated. The 600x600mm concrete sub-model was split up in this way (Figure 7-19). By utilising symmetry conditions and by using a linear interpolation scheme the number of points that needed to be analysed was reduced from 225 down to 24, of which 15 had been analysed in the previous edge and corner studies.

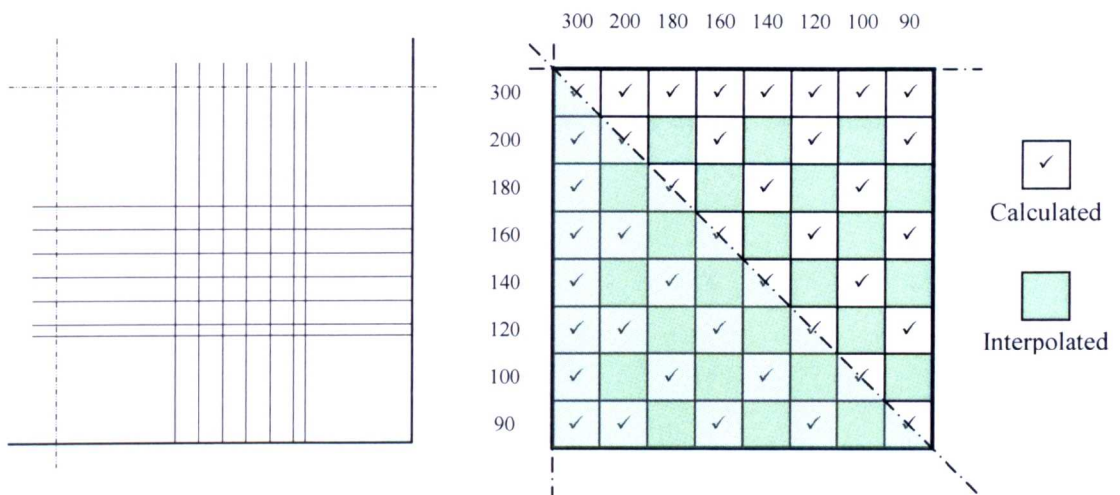


**Figure 7-19 - Sample Points and Reduction Factor Calculation**

The calculated reduction factors are displayed in the form of a contour plot in Figure 7-20.

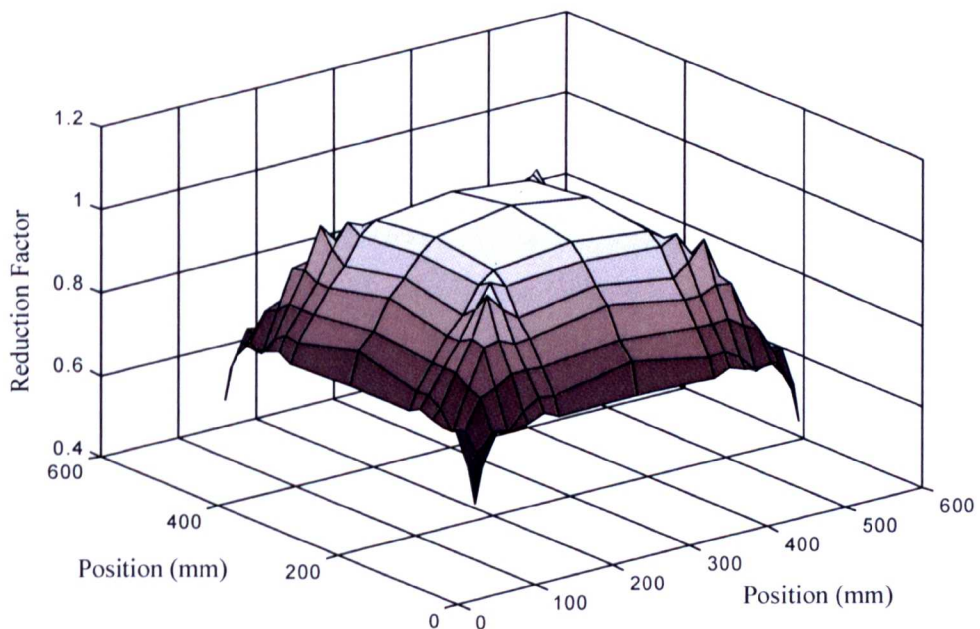


**Figure 7-20 - Reduction Factors for M12 Anchor in 600x600 Block**

It is quite clear from the plot that when an anchor position approaches two edges that the strength reduced much more rapidly than when only one edge is providing an influence. For example, when the anchor is in the position  $x=300$ ,  $y=90$ , the strength reduction factor is 0.71. However, when the anchor is in the corner with position  $x=90$ ,  $y=90$ , the reduction factor becomes 0.55.

**7.4 Investigation Into Mesh Sensitivity**

A sensitivity study was performed in order to determine the effects of mesh discretisation on the behaviour of the model. The model with the anchor in the middle position was selected as a representative example geometry. This was then discretised by 4-noded tetrahedra as before. Five different FE meshes were generated by the pre-processor, GiD, with the total number of elements ranging from 1513 to 5264 (Figure 7-21).

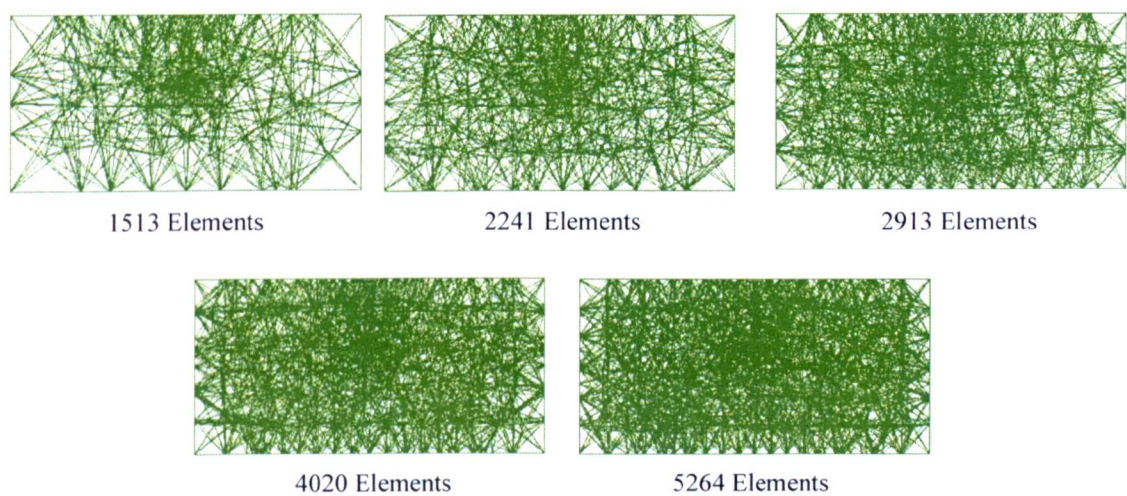


**Figure 7-21 - Different Mesh Discretisations**

The linear-elastic load-displacement responses for these meshes (Figure 7-22) show an unexpectedly wide scatter in the initial stiffness of the model. Instead of showing a general softening of the model with higher discretisation, leading to a convergence of results, these analyses show both stiffer and softer results increasing discretisation. The results for 4020 and 5264 elements do seem to coincide but, in light of the other results, this was deemed to be a numerical artefact rather than an indication of convergence.



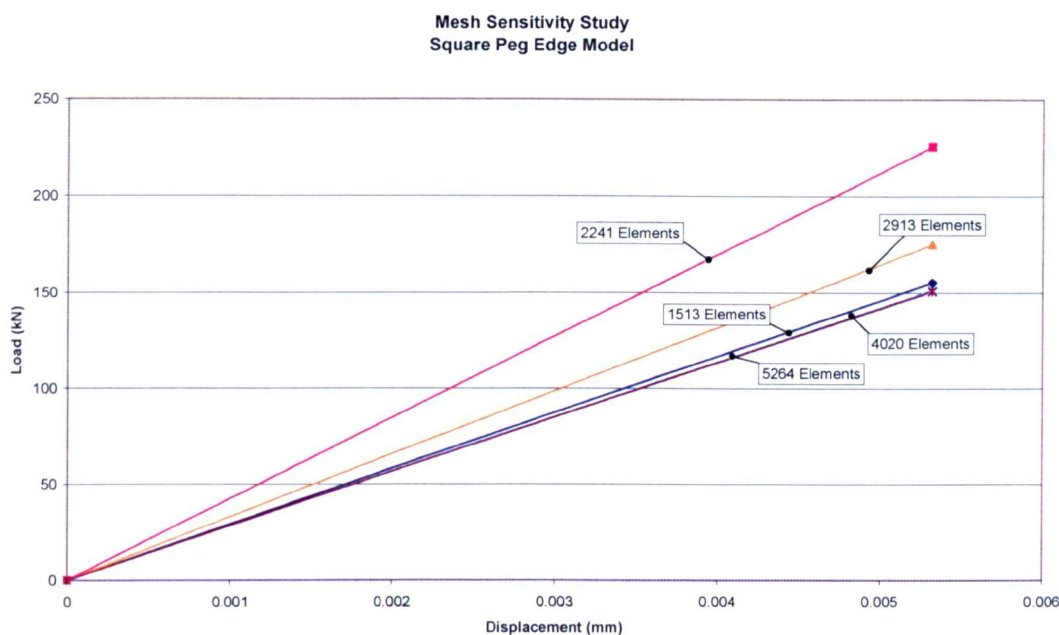


**Figure 7-22 - Linear Elastic Responses of Mesh Sensitivity Analyses**

What the results did show was a strong sensitivity to the arrangement of the F.E. mesh around the anchor expander. In examining the individual meshes more closely, it became apparent that although the overall discretisation of the models differed, the number of elements forming the anchor remained the same i.e. seventeen elements (Figure 7-23). Hence the number of nodes on the anchor-concrete interface remained the same. Furthermore the number of concrete elements in contact with the anchor remained similar. Therefore the increase in the level of discretisation at a global level did not translate to a corresponding increase at the local level around the anchor.

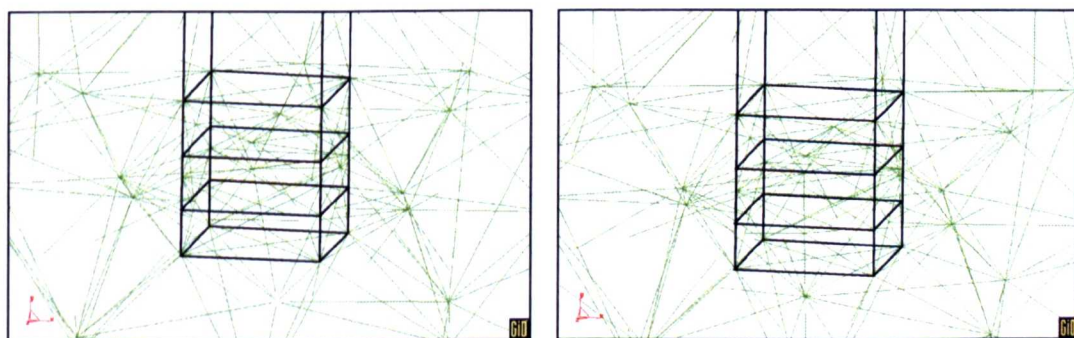


**Figure 7-23 - - Comparison of 1513 and 5264 Element Meshes**

The problem was obviously due to the operation of the mesh generation algorithm in GiD. Explicitly setting a suitably high level of discretisation for the anchor bolt resulted in an unreasonably high number of elements for the concrete block. This was despite specifying a course mesh in this volume. GiD was unable to produce the desired rate of change of element size between the anchor and outer boundary of the block. Before proposing a solution to this problem the opportunity was taken to investigate further the implications of having a very limited number of nodes to transfer the load between steel and concrete whilst at the same time reducing the concrete element size.

In its simplest and most extreme case this form of situation can be represented by a triangle loaded at one corner as shown (Figure 7-24).

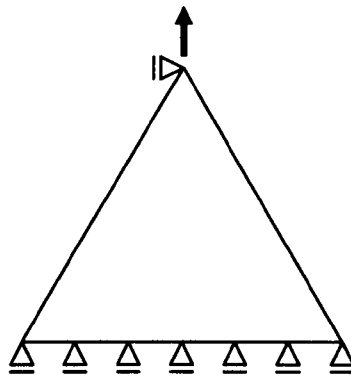


**Figure 7-24 – Simple Load Area/Discretisation Model**

A linear elastic material was chosen for the model with a Poisson's Ratio of zero. The model was then discretised by 3-noded triangular elements employing a single point Gaussian integration scheme. Several discretisation levels were examined for between a single element and 9990 elements. The load-displacement graph ( Figure 7-25) shows a wide range of responses. The stiffness of the model consistently decreases with decreased element size however, plotting load against number of elements shows that although the solution is seeming to converge the process is very slow.

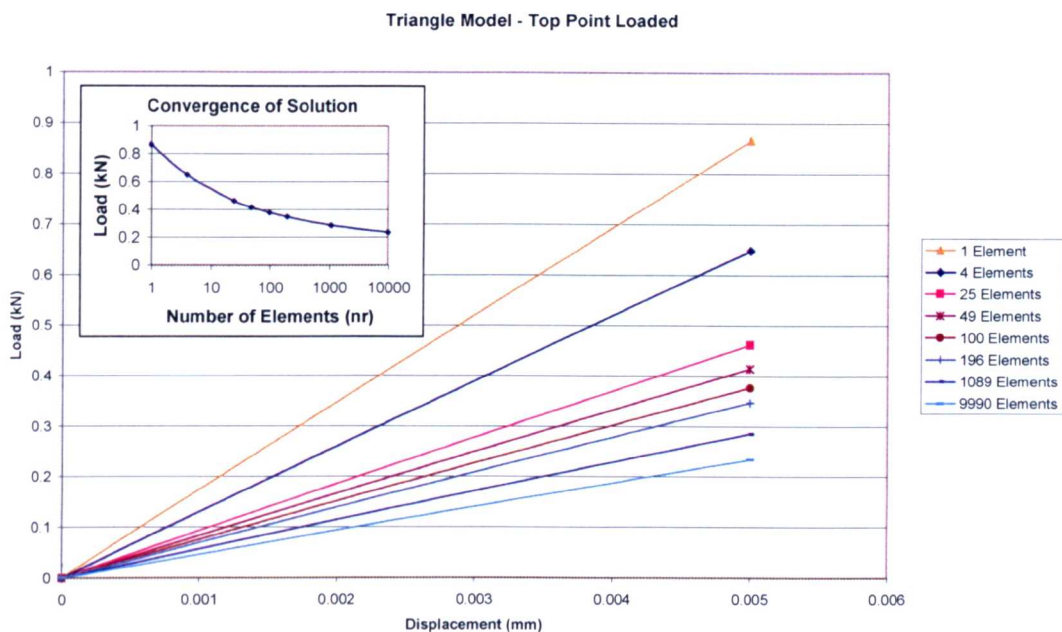


**Figure 7-25 - Triangle Model - Single Load Point**

To overcome the problem of coarse discretisation of the anchor-concrete interface it was necessary to apply more manual control over the meshing process. This opportunity was taken to move to a regular mesh of 8-noded hexahedra (brick) elements using a 2x2x2 Gaussian integration scheme. In the chapter on stress locking it had been shown that these elements were better able to model the displacement field required in anchor pullout models although they had not been used earlier due to their increased computational expense. The area of the anchor-concrete interface was also increased to cover the full expander length. This not only avoided problems of stress singularities but this geometry was also necessary for the detailed analysis of the expander-concrete interface presented in the following chapter.



## **7.5 Summary**

In this chapter the influence of edge effects has been studied in detail. The Total Strain Based Crack Model proved to be a suitably robust constitutive model for analysing these pullout problems. The results were accurate in terms of both the failure modes produced and the relative reduction in strength due to reducing edge distance and compared well with anchor design guide figures. A mesh discretisation study highlighted the problems of having a small number of elements in the load transfer zone between anchor bolt and concrete.

## **CHAPTER 8**

### **Modelling of Anchor Expansion Effects**

In this chapter various aspects of anchor expansion are examined. First of all the mechanics of the anchor are explained. This includes a discussion of the means by which pullout load is transferred to the surrounding concrete and the structural interaction which is set up. Two main components are identified in order to analyse this behaviour. Firstly, a model for anchor-concrete interface that takes into account its pressure dependent frictional behaviour. Secondly, a method by which to simulate anchor expansion in a realistic manner. To satisfy the first requirement the Coulomb Plasticity Model is presented and applied to structural interface elements. Several options are considered for the second requirement including kinematic restrains (as used in Chapter 4), prescribed displacements and full contact models. The chapter concludes by discussing the remaining modelling difficulties and solutions available.

#### **8.1 Material Behaviour Associated With Anchor Expansion**

The primary means by which expanding anchors transmit pullout loads to the surrounding concrete is via a frictional interface. Therefore, in simple terms, the greater the expansion force generated by the anchor, the higher the frictional resistance to the pullout. This behaviour is complicated by the fact that concrete will crack and crush when its strength is exceeded.

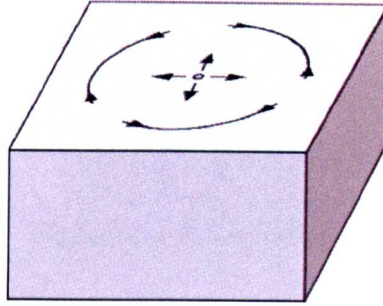


**Figure 8-1 – Radial Expansion Stresses and Associated Circumferential Stresses**

Radial expansion forces will give rise to tensile circumferential stresses in the concrete as it strains to accommodate the expansion (Figure 8-1). If sufficiently high, these stresses will lead to radial cracking. The magnitude of the stresses may be calculated by approximating the problem as a thick-walled cylinder subject to uniform internal pressure [Timoshenko, (1934)].

$$\sigma_c = -\frac{a^2 b^2 (p_o - p_i)}{b^2 - a^2} \cdot \frac{1}{r^2} + \frac{p_i a^2 - p_o b^2}{b^2 - a^2} \quad \text{Equation 8-1}$$

where  $a$  and  $b$  are the internal and external radii,  $p_i$  and  $p_o$  are the internal and external pressures and  $r$  is the radius at which the stress is being considered. As can be seen from Equation 8-1 the intensity of the circumferential stress obeys an inverse square law. Therefore the stress level drops rapidly as the distance from the hole increases and hence radial cracking due to expansion is a localised effect. It is also dependent on the level of confinement provided by the body of concrete and from confining pressures arising from applied loads.

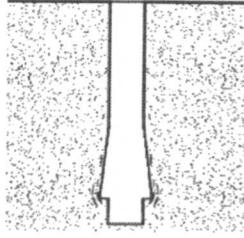


**Figure 8-2 - Keying Effect**

Another important effect of the expansion on the concrete is to induce crushing. Very high compressive stresses are generated at the tip of the expander leaf. Once again, treating the problem as a thick-walled cylinder (Equation 8-2), it can be seen that the inverse square law applies again thus leading to a localised effect. The resulting crushing leads to the so-called keying effect. Here the deformation of the concrete allows the anchor to transmit a portion of the pullout load into the substrate via direct normal forces rather than purely shear (Figure 8-2). The full importance of this keying action is not understood at this time. It is obviously dependent on the concrete compressive strength and the magnitude of the pullout force. Difficulties in modelling this behaviour are discussed later in this chapter.

$$\sigma_r = \frac{a^2 b^2 (p_o - p_i)}{b^2 - a^2} \cdot \frac{1}{r^2} + \frac{p_i a^2 - p_o b^2}{b^2 - a^2}$$

**Equation 8-2**

## 8.2 Structural Interface Elements

The Total Strain Based Crack Model allows the modelling of both compressive and tensile failure. However, the pressure dependent, frictional behaviour of the anchor-concrete interface must be modelled separately. When modelling such interfaces structural interface elements may be used (Figure 8-3). These define interfacial behaviour in terms of the relation between the tractions, normal and shear to the interface plane, and corresponding displacements. Because of their formulation it is permissible for interfaces to have zero thickness thus allowing them to be inserted into existing models without altering the existing geometric dimensions. Both a nodal lumping scheme and numerically integrated formulations are supported for these elements [Bittencourt (1993)]. The latter was chosen to maintain consistency with the integration schemes of the existing finite elements. Briefly the formulation of numerically integrated interface elements is as follows:

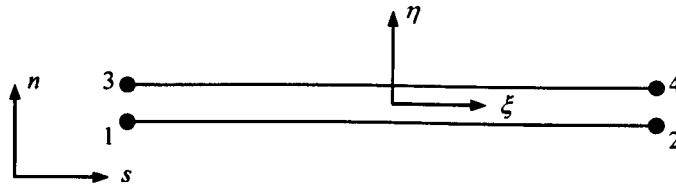


Figure 8-3 - 4-noded Line Interface Element

The nodal displacement vector,  $\mathbf{v}$ , is defined as:

$$\mathbf{v} = [v_n^1 v_n^2 v_n^3 v_n^4 v_s^1 v_s^2 v_s^3 v_s^4]^T \quad \text{Equation 8-3}$$

where the subscripts denote the direction of the displacement (normal or tangential to the interface) and the superscripts give the node number. The continuous displacement field vector,  $\mathbf{u}$ , is defined for the upper and lower sides of the interface as:

$$\mathbf{u} = [u_n^u u_n^l u_s^u u_s^l]^T \quad \text{Equation 8-4}$$

Subscripts, as before, denote the direction. Superscripts denote upper or lower side. This vector is obtained by multiplying the nodal displacement vector by the matrix of interpolation polynomials, **H**:

$$\mathbf{H} = \begin{bmatrix} \mathbf{n} & 0 & 0 & 0 \\ 0 & \mathbf{n} & 0 & 0 \\ 0 & 0 & \mathbf{n} & 0 \\ 0 & 0 & 0 & \mathbf{n} \end{bmatrix} \quad \text{Equation 8-5}$$

where  $\mathbf{n} = [N_{1-3}, N_{2-4}]$  and  $N_{a-b}$  is the interpolation function related to node pair  $a$  and  $b$ .

The matrix, **L**, relates the continuous displacement field vector to the relative displacement vector,  $\Delta \mathbf{u}$  as follows:

$$\Delta \mathbf{u} = \mathbf{L} \mathbf{u} \quad \text{Equation 8-6}$$

where **L** is defined as:

$$\mathbf{L} = \begin{bmatrix} -1 & +1 & 0 & 0 \\ 0 & 0 & -1 & +1 \end{bmatrix} \quad \text{Equation 8-7}$$

The relationship between relative displacements and nodal displacements may be written in full to obtain the **B** matrix:

$$\Delta \mathbf{u} = \mathbf{L} \mathbf{H} \mathbf{v} = \mathbf{B} \mathbf{v} \quad \text{Equation 8-8}$$

For example, for the 4-noded line interface considered here the **B** matrix expands as:

$$\mathbf{B} = \begin{bmatrix} -\mathbf{n} & \mathbf{n} & 0 & 0 \\ 0 & 0 & -\mathbf{n} & \mathbf{n} \end{bmatrix} = \begin{bmatrix} -N_{1-3} & -N_{2-4} & N_{1-3} & N_{2-4} & 0 & 0 & 0 & 0 \\ 0 & 0 & 0 & 0 & -N_{1-3} & -N_{2-4} & N_{1-3} & N_{2-4} \end{bmatrix}$$

$$\quad \text{Equation 8-9}$$

Normal and tangential tractions for the element may be calculated from relative displacements via the constitutive relationship as follows:

$$\mathbf{t} = \begin{bmatrix} t_n \\ t_t \end{bmatrix} = \mathbf{D}\Delta\mathbf{u} = \begin{bmatrix} d_n & 0 \\ 0 & d_t \end{bmatrix} \begin{bmatrix} \Delta u_n \\ \Delta u_t \end{bmatrix} \quad \text{Equation 8-10}$$

where  $\mathbf{D}$  is the material matrix defined by a suitable material model.

In order to calculate the equivalent nodal forces,  $\mathbf{f}$ , the element stiffness matrix,  $\mathbf{K}$ , must be formed. This is accomplished by integrating over the iso-parametric coordinates according to:

$$\mathbf{K} = \int_{\xi=-1}^{\xi=1} \int_{\eta=-1}^{\eta=1} \mathbf{B}^T \mathbf{D} \mathbf{B} \det J d\eta d\xi \quad \text{Equation 8-11}$$

In the case of the line interface element considered here the interpolation functions  $N_i$  are independent of  $\eta$  hence Equation 8-11 may be rewritten as:

$$\mathbf{K} = b \int_{\xi=-1}^{\xi=1} \mathbf{B}^T \mathbf{D} \mathbf{B} \frac{\partial x}{\partial \xi} d\xi \quad \text{Equation 8-12}$$

where  $b$  is the element thickness as defined for plane stress and plane strain modelling.

A similar approach to the above may be followed in order to derive the equations defining elements of higher order and for planar interface elements.

As mentioned above, the material matrix,  $\mathbf{D}$ , is defined via a suitable material model for the interface. Two such models considered were the Bond Slip Model for reinforcement and, the more general, Coulomb Friction Models. On first inspection the problem of the pullout of a cylindrical anchor embedded from a hole in a concrete block may seem analogous to that of a reinforcing bar being pulled out of a concrete block there is a key difference in the treatment of forces normal to the interface. In the case of reinforcement model found in DIANA the shear capacity of the steel-concrete interface is considered to be independent of the normal force thus making it insufficient for the modelling of

expansion anchors. The Coulomb Friction model, however, does consider pressure dependent behaviour.

The formulation process for the Coulomb Friction Model follows closely that of the Mohr-Coulomb Plasticity Model for continuum elements [TNO (1999)]. Equations for the yield surface,  $F$ , and plastic potential surface,  $Q$ , are shown below with both the friction angle,  $\phi$  and the initial cohesion,  $c$ , being a function of the hardening parameter,  $\kappa$ .

$$F = \sqrt{t_t^2 + t_n^2} \tan \phi(\kappa) - c(\kappa) = 0 \quad \text{Equation 8-13}$$

$$Q = \sqrt{t_t^2 + t_n^2} \tan \psi \quad \text{Equation 8-14}$$

The variable  $\psi$ , is the dilatancy angle. For all analyses this was set equal to  $\phi$ , thus leading to associative plasticity. For a 2D stress space this results in the familiar initial failure surface (Figure 8-4).

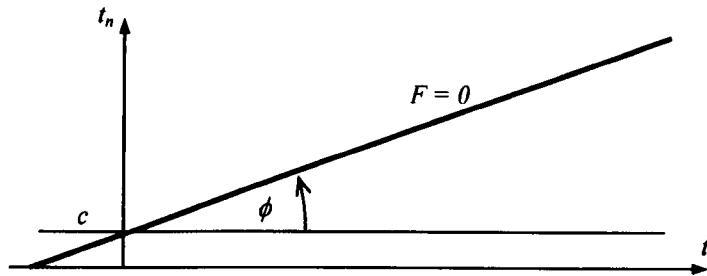


**Figure 8-4 - Coulomb Friction Initial Failure Surface**

The model provides a number of additional features. Firstly, user-defined hardening diagrams may be prescribed for both cohesion and friction angle. Also, a tension cut-off criteria may be set whereby the normal traction is set to zero and the shear behaviour altered when a prescribed tensile traction is reached. Default behaviour is for zero shear strength retention upon meeting this criterion. Alternatives are constant shear retention and shear retention according to an aggregate interlock model. Neither of these additional



features were engaged in the modelling of the anchor-concrete interface owing to insufficient information on the non-linear behaviour of the anchor-concrete interface.

### 8.3 Sensitivity Studies on Coulomb Friction Interface

A series of sensitivity studies were performed to assess the performance of structural interface elements combined with the Coulomb Friction Model. The benchmark model used throughout was a cube of sides 10mm (Figure 8-5). The model consisted of two elements. The first formed the cube itself and was an 8-noded iso-parametric brick element employing a 2x2x2 Gaussian integration scheme. The second element was a 4+4 noded quadrilateral planar interface element situated on the base of the cube. The plane of the interface was aligned with the bottom surface of the cube and the bottom surface of the interface constrained in all three axes. The interface was given zero thickness (although, for clarity, a thickness is shown in the figure below). For these analyses a 3x3 Newton-Cotes integration scheme was used for the interface element. This scheme was chosen because it has integration points situated at the node points and therefore is able to pick up the extreme values expected at these positions in this problem.

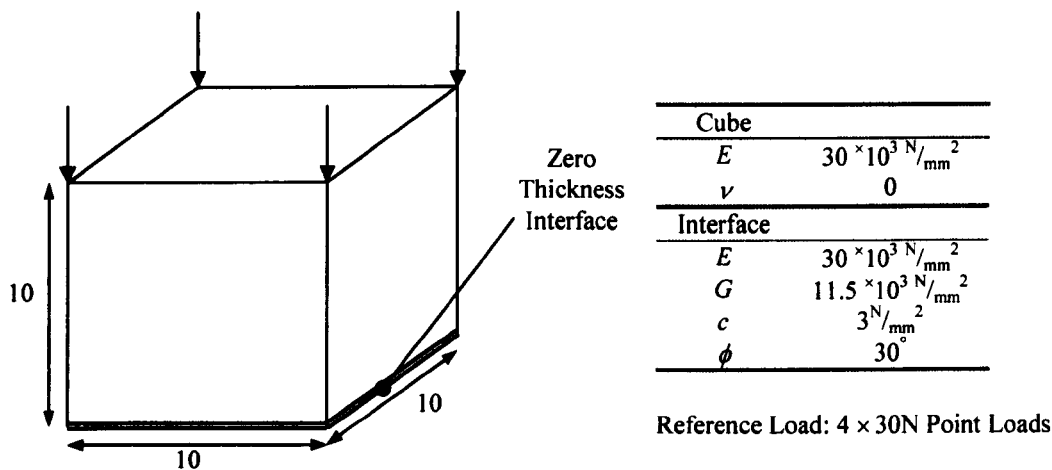


**Figure 8-5 - Cube Benchmark Model For Frictional Interface and Associated Reference Values for Material Properties**

The cube itself was treated as a linear elastic material, its properties remaining constant throughout the tests. Reference values are shown for the interface material parameters

and vertical loading applied to the top of the cube. In each of the analyses a displacement was prescribed for the left-hand surface of the cube element and the resulting reaction force in the  $x$ -direction was recorded on the bottom nodes of the interface.

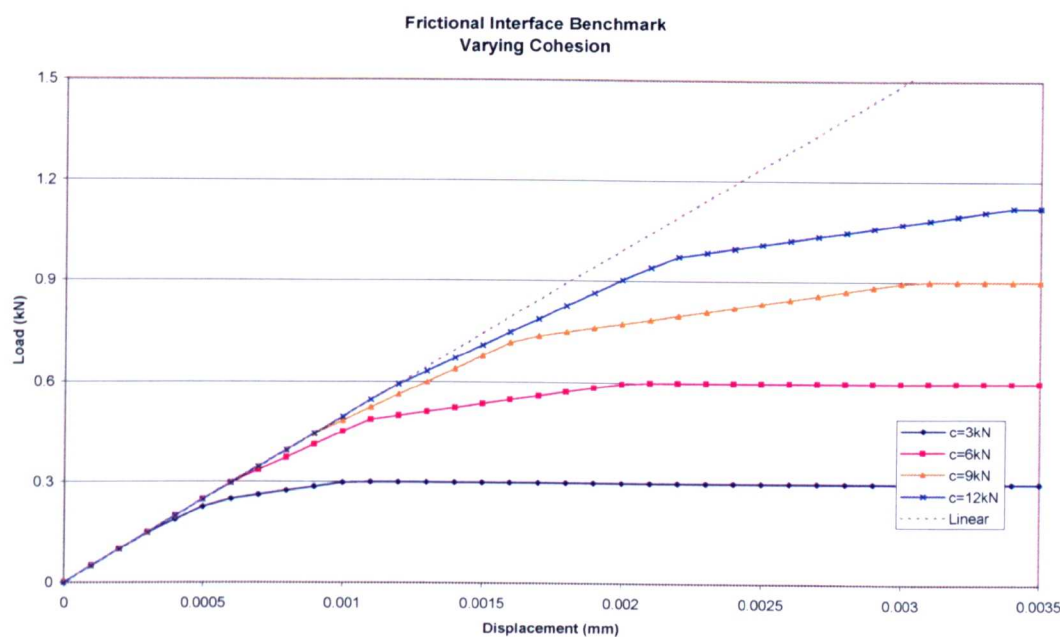
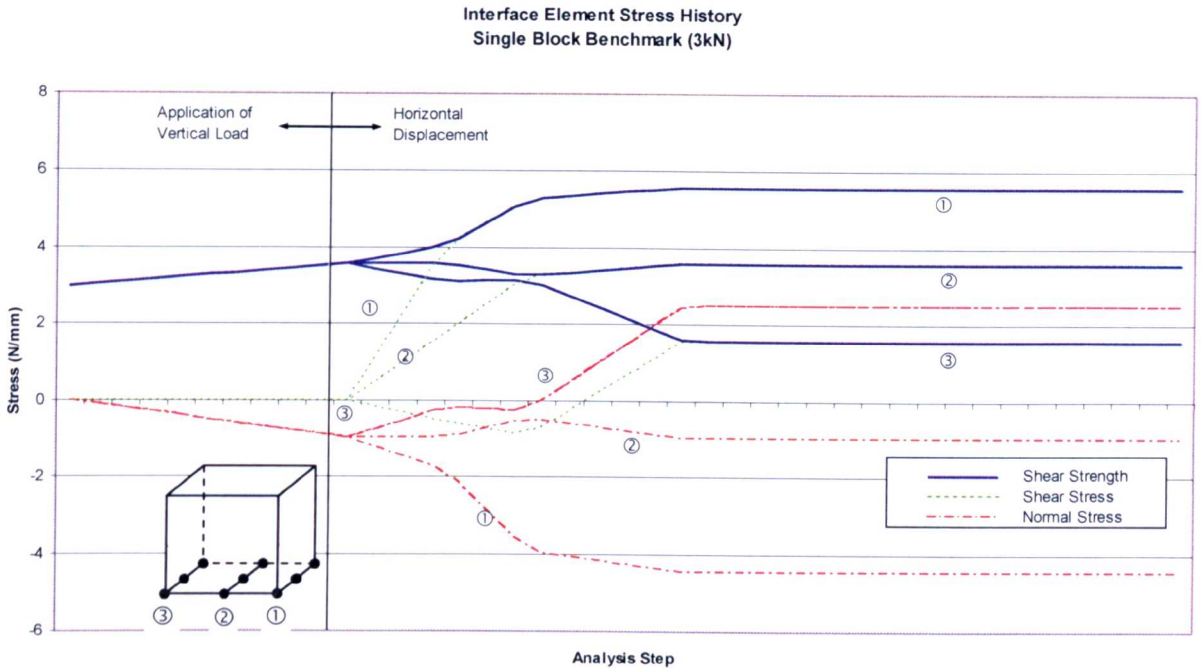


Figure 8-6 - Cube Benchmark, Effects of Varying Cohesion

The figure above shows the effects of varying the initial cohesion value,  $c$ , on the interface whilst keeping the other parameters at their reference value (Figure 8-6). As expected, increasing  $c$  increases the strength of the interface and hence the point at which the load-displacement response deviates from linear elastic behaviour. What was unexpected was that failure of the interface wasn't at one discrete point followed by perfectly plastic behaviour. Instead the stiffness of the interface degraded in clearly defined steps. By examining the stress history of each integration point the reason for this was discovered.



The strength of the interface at each integration point was calculated by obtaining the normal stress for the given point and applying the Mohr-Coulomb equation (Equation 8-15). A graph was then produced of stress and strength history (Figure 8-7). Shear stress in the  $z$ -direction has been omitted as it is zero throughout.

$$f_s = \sigma_n \tan \phi + c \quad \text{Equation 8-15}$$

From the graph the two stages of the analysis can be clearly seen. Initially the vertical compressive loading is applied and is associated with a uniform rise in normal stress at all of the integration points and a corresponding increase in shear strength from the initial cohesion value. There was no increase in shear stress during this stage as the Poisson's Ratio of the cube was zero and Poisson effects are not part of the interface element formulation. Following the compressive load was the application of the horizontal displacement of the cube. Position 1 shows an increasing compressive stress and hence strength whereas positions 2 and 3 show the opposite response. This behaviour may be explained by the fact that the interface elements are not subject to pure shear. The bottom

face of the elements is fully fixed and horizontal displacements are applied to a line of nodes on the top surface (Figure 8-8). This condition alone would produce pure shear. However the addition of the prescribed displacements on the top of the cube element act to induce a bending component and so tensile forces are created in the interface.

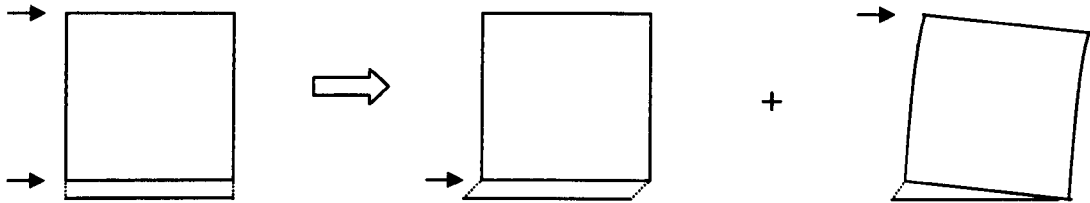


**Figure 8-8 – Structural Action on Base Due to Components of Load**

Position 1 shows an increasing shear stress that eventually reaches the shear strength. Subsequently the strength and strength plots become collinear, satisfying the condition prescribed by the yield surface equation (Equation 8-13). Positions 2 and 3 show a decrease in normal stress due to the bending effects and associated decrease in shear strength. Once again the shear stress increases until it meets the strength of the interface and then the plots become collinear. The important point in respect to the load-displacement histories (Figure 8-6) is that due to the non-uniform stress state on the base of the cube, and hence in the interface element, integration points reported material failure at different stages in the analysis and hence the multilinear load-displacement response.

A similar progressive failure was apparent in the studies of normal force and of friction angle (Figure 8-9). In the case of the normal force study the total vertical compressive loading was increased in 0.1kN increments from 0 to 0.3kN in successive analyses. The results showed the expected  $0.1 \times \tan 30^\circ$  kN increase in failure load for each increment in normal force. For studies into varying friction angle,  $\phi$ , values from  $0^\circ$  to  $60^\circ$  were used. Again the results also showed a change in the failure load as predicted by Equation 8-15.

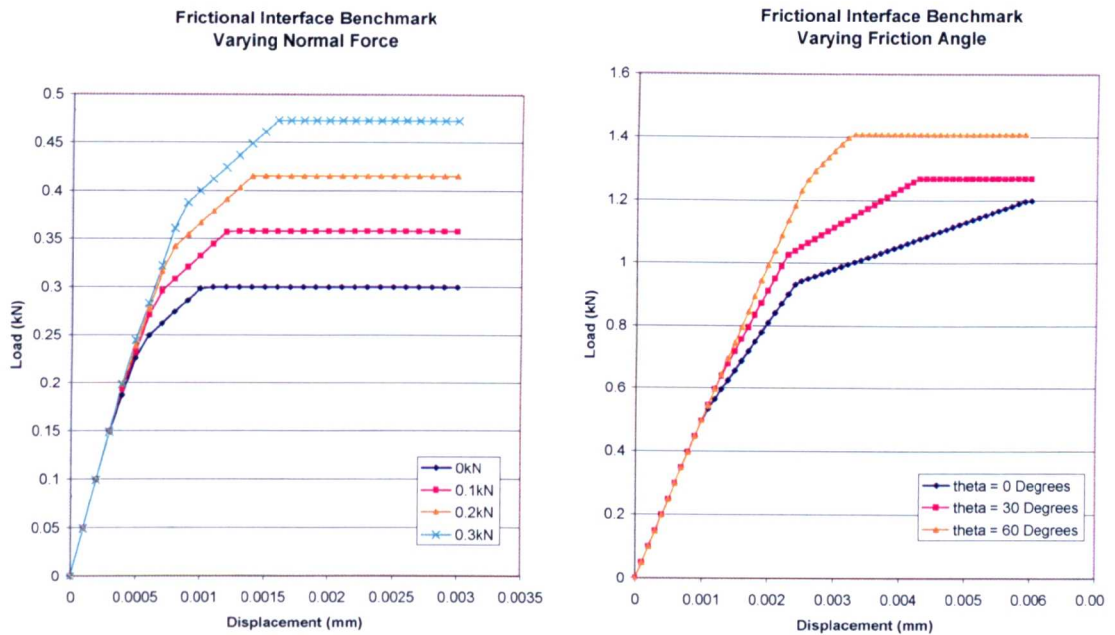


**Figure 8-9 - Cube Benchmark, a) Varying Normal Force, b) Varying Friction Angle**

The final sensitivity study was concerned with the effects of the stiffness moduli set for the interface. The normal and shear moduli chosen for the preceding analyses were chosen to be similar to those of the cube itself so conceptually the cube and interface were the same material (although differing characteristics of the behaviour of that material were simulated by the two different constitutive models). Figure 8-10 below shows the load displacement response for a number of different interface stiffnesses and interface types. The load-displacement response for the model with no interface element is also shown as a baseline result. The response for a very stiff, linear elastic interface (Young’s Modulus of  $3 \times 10^{20}$ ) appears collinear with that of the model with no interface. However, the load-displacement response for a linear-elastic interface, with the value of Young’s Modulus set to the reference value of  $30 \times 10^3 \text{ N/mm}^2$ , was significantly softer. It may be considered that as an element’s thickness decreases, its resistance to shear would increase. However, due to the formulation of the interface element the resistance is independent of the thickness. This is the behaviour shown in the graph.

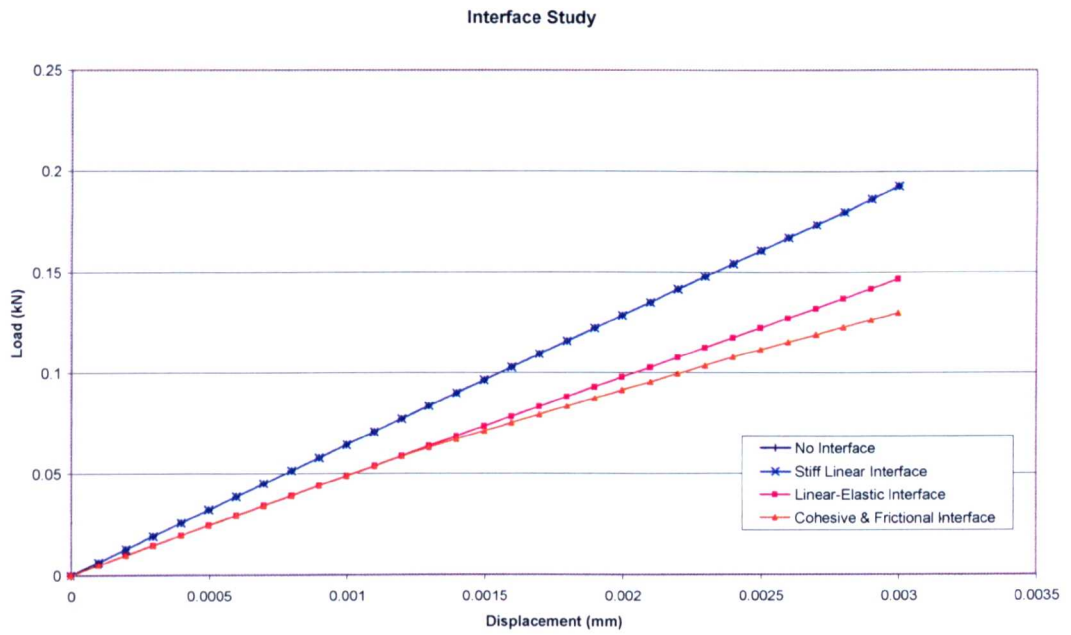


**Figure 8-10 - Cube Benchmark, Effects of Varying Interface Stiffness**



8.4 2D Modelling of Anchor Bolt with Frictional Interface

A 2D, plane-stress model using 4-noded quadrilaterals was constructed following the geometry of the brick element model considered in Chapter 7. As with previous 2D modelling of anchors one half of the model was analysed owing to symmetry conditions. In the interface between steel anchor and concrete four 2-noded line interface elements were placed with initial stiffnesses equal to that of concrete. The reference values for cohesion and friction angle were again 3 N/mm<sup>2</sup> and 30° respectively. Again, a Newton-Cotes integration scheme was used this time with three integration points. A uniform expansion pressure was applied to the anchor as shown in Figure 8-11. Where expansion pressures are quoted, they refer to the sum value of this distributed load. The anchor was unrestrained along this boundary to allow free expansion. It is noted that the magnitude of the expansion pressure and its uniformity were estimated choices however, in the absence of more detailed information on the true nature of expansion forces at this stage, these values were deemed acceptable for the investigation performed here. The concrete was once again modelled via the rotating crack formulation of the Total Strain Based Crack Model (parameters as chosen in Chapter 7).

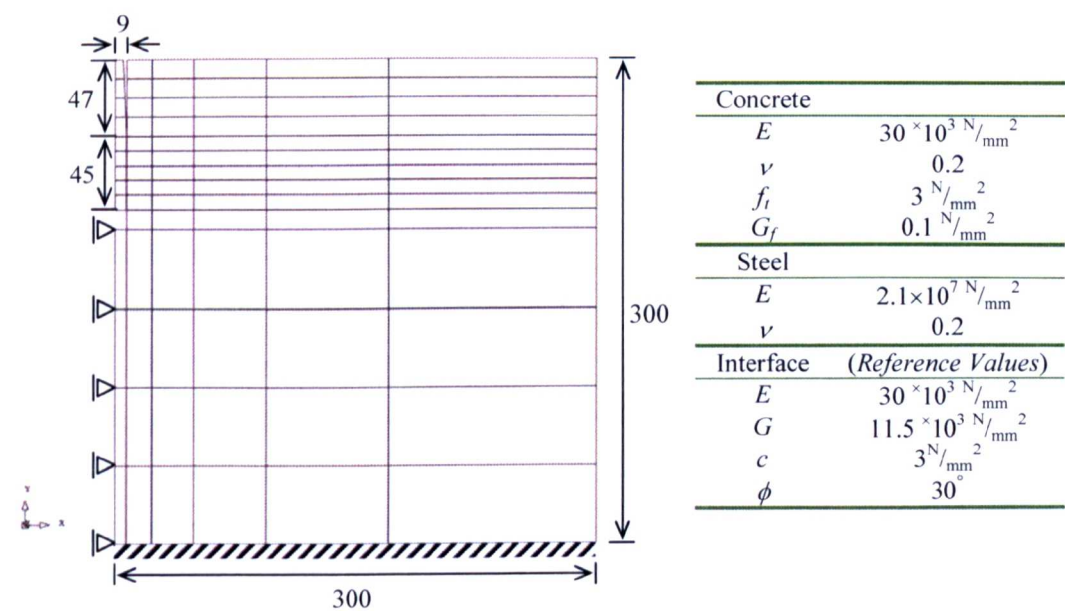
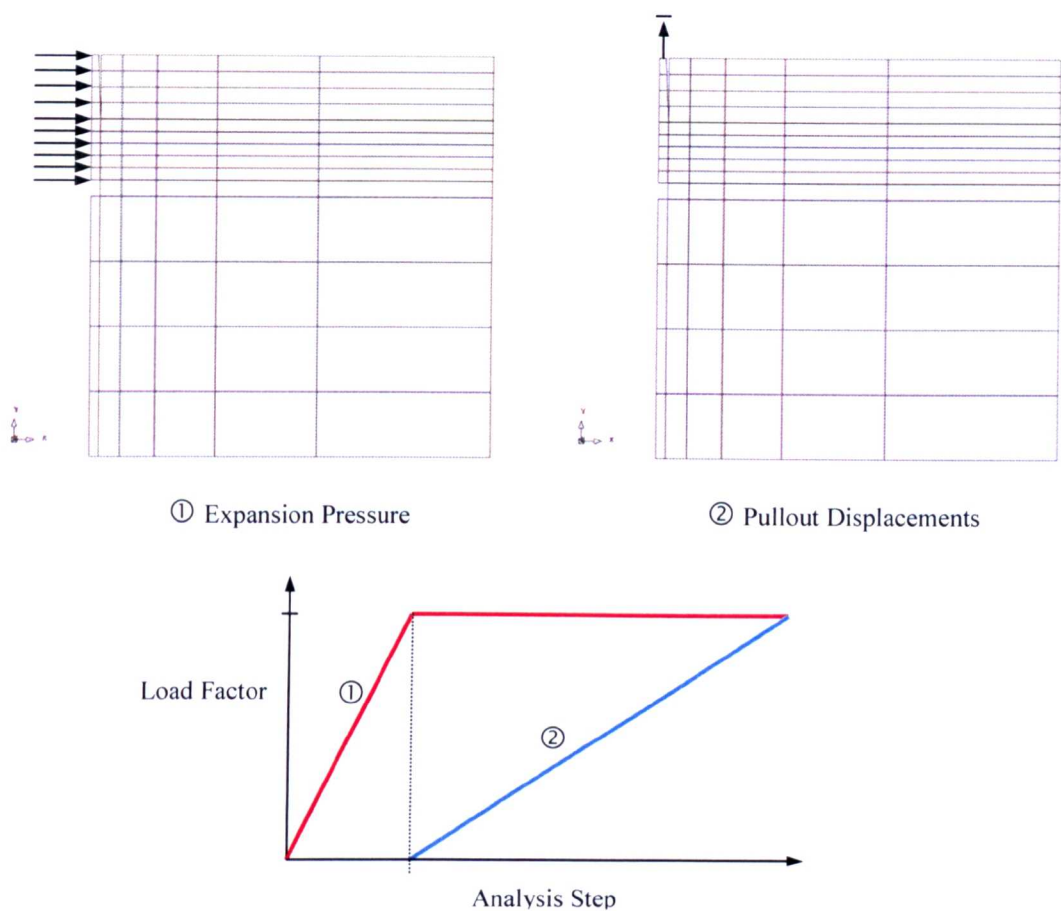


Figure 8-11 - 2D Expansion Anchor Problem Geometry and Material Properties



**Figure 8-12 - 2D Expanding Anchor Problem Showing The Two Loadcases and Loading History**

For the first set of analyses in this study a range of different expansion forces were considered from no force up to 600N total force whilst the other parameters remained at their reference value. This force was applied incrementally in the first stage of the analysis. The expansion force was then frozen at the desired level and pullout was simulated by application of displacements to the anchor head (Figure 8-12). The graph of load-displacement responses below (Figure 8-13) also includes the response from the model when the anchor and concrete are fully bonded and no interface elements are present. For that particular analysis no expansion pressure was applied.



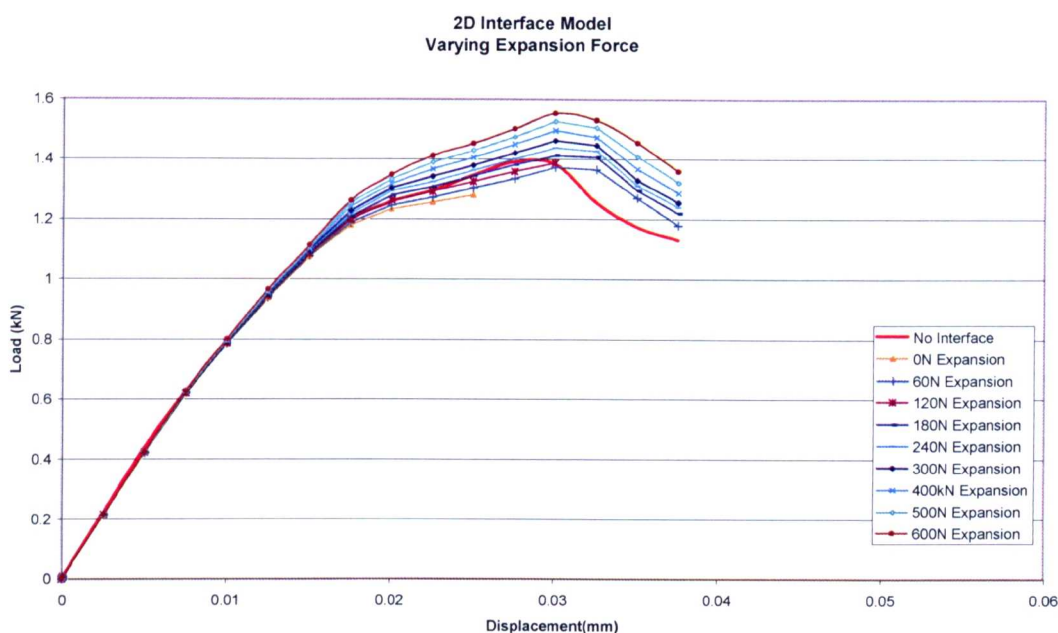


**Figure 8-13 - 2D Anchor Interface Model, Varying Expansion Pressure**

The most obvious features of the graph are that all analyses follow the same linear-elastic response and that the higher the level of expansion force the higher the peak load resisted. It is also clear that with expansion forces lower than 180N the anchor has a lower load carrying capacity than the fully bonded model. Of the analyses with these lower expansion levels both the 120N and ‘no expansion’ runs terminated due to non-convergence prior to the end of the analysis. The stress histories at various Gauss points (Figure 8-14) reveal more information of the causes of these failures (Figure 8-15, Figure 8-16 & Figure 8-17).

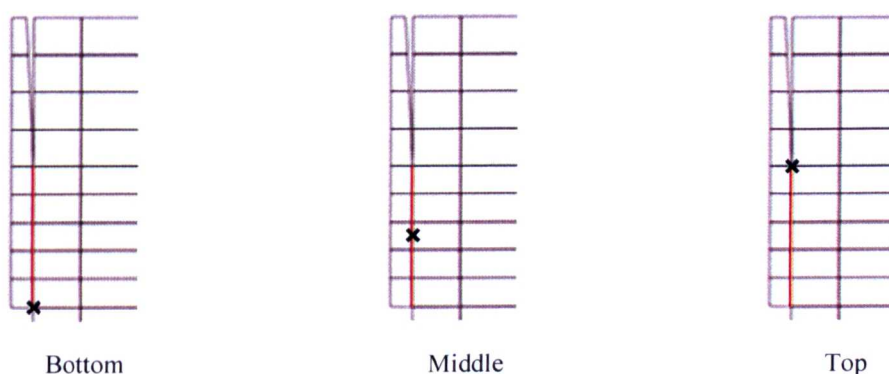


**Figure 8-14 - Position of Gauss Points Examined**

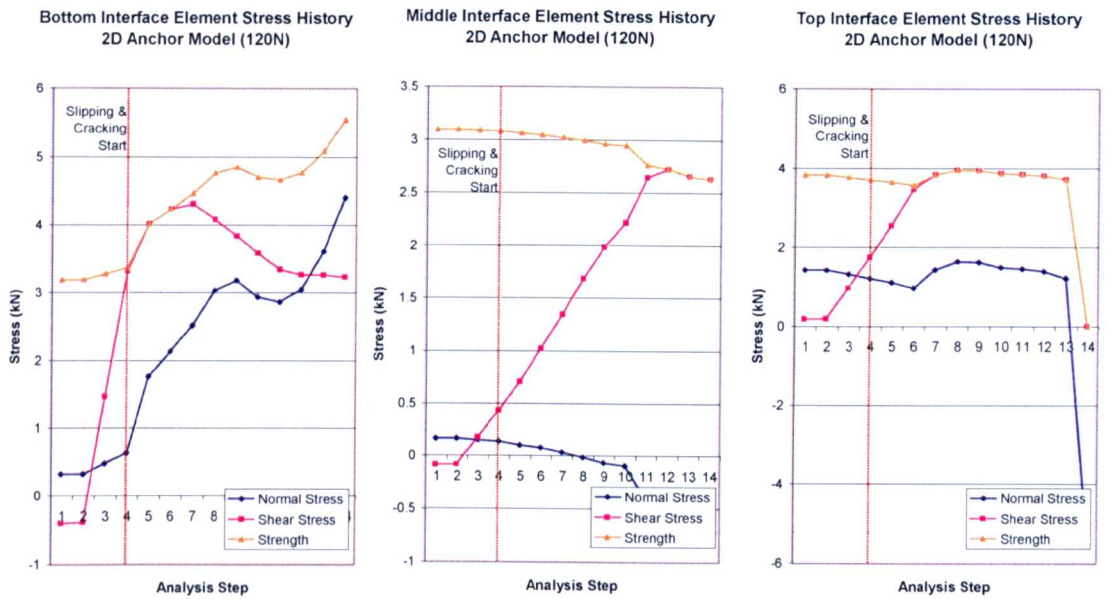


Figure 8-15 - Interface Stress Histories, 120N Expansion

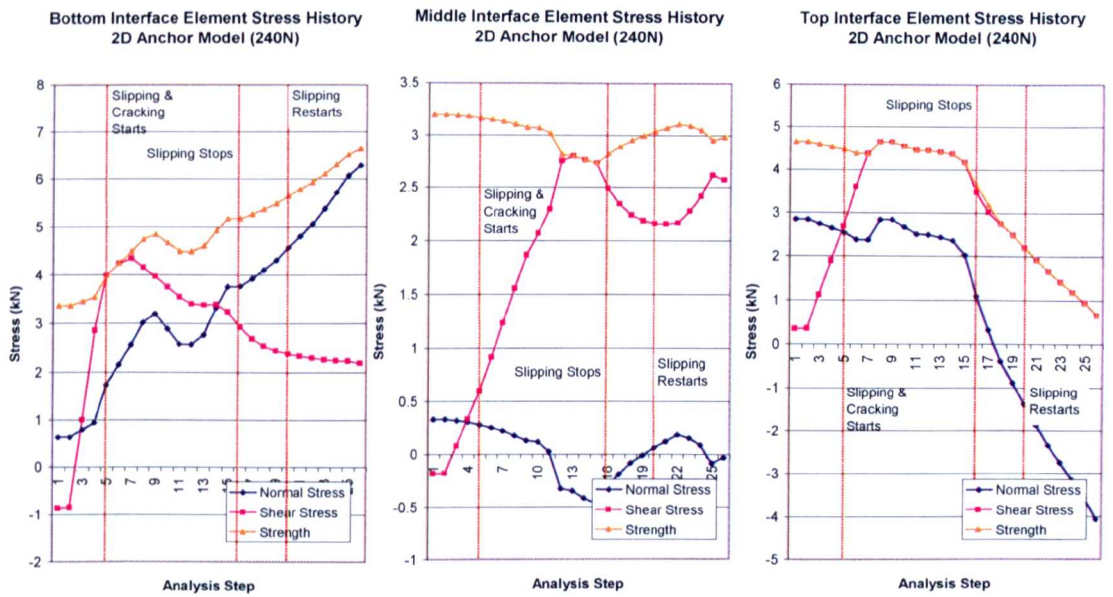
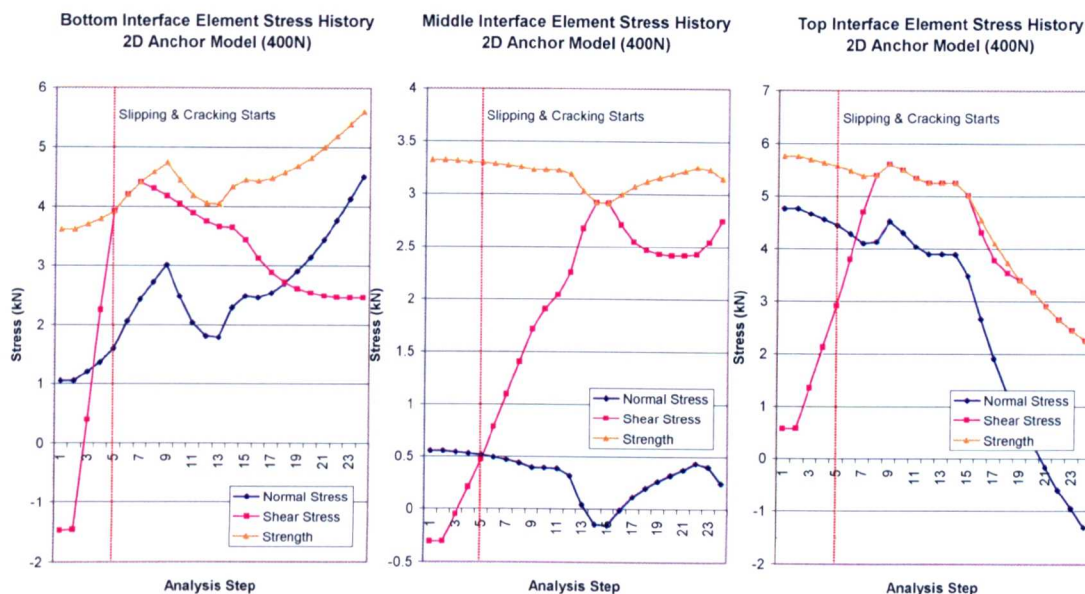


Figure 8-16 - Interface Stress Histories, 240N Expansion



**Figure 8-17 - Interface Stress Histories, 400N Expansion**

The normal stress, shear stress and interface strength histories shown above are for the analyses with 120N (Figure 8-15), 240N (Figure 8-16) and 400N (Figure 8-17) expansion force respectively. For each set histories are given for the bottom most integration point on the interface, the middle one and the top one. Also shown on the graphs are details of what point in the history slipping and cracking started or stopped. This information refers to the global response of the model rather than to the particular integration point being considered.

In broad terms the behaviour of each of the analyses is similar although the magnitude of the stresses differ. In all cases sliding and cracking behaviour both commence at a pullout load of 7.6N. It can be seen from the load-displacement graph (Figure 8-13) that beyond this point the responses for the different expansion levels diverge from both the linear-elastic response and from each other. In all cases the bottom integration point is where the slipping is reported first. The histories for each of the three levels of expansion show this point to experience the most rapid increase in shear stress upon the application of the pullout load. This result is unsurprising given that there is a tensile stress concentration in the concrete elements at the bottom of the anchor-concrete interface that gives rise to the

initiation of cracking. Across the interface this stress will be manifest as a vertical shear stress.

Another behaviour in common with the histories is that the bottom integration point stopped slipping after a few load steps and sliding started at the top integration point. The reasons for this are not clear however one likely reason is that two processes control the behaviour. Firstly the cracking at the base of the anchor acts to relax the shear stresses on the lower part of the anchor. Whilst, at the same time, displacement of the concrete block causes the hole the anchor is in to widen. The upper section showing the greatest displacement. This leads to a drop in the normal force across the interface hence decrease in shear capacity.

Returning to the load-displacement graph (Figure 8-13) it can be seen that of the analyses considered only the 120N one terminated before reaching the peak load. Analysis failure was via non-convergence and on the final step it was reported that all integration points were sliding, there were 20 active cracks and 3 closing cracks. In comparison, for the same pullout displacement step, the 240N analysis had 22 active cracks, 2 closing cracks and all points except the one close to the bottom of the interface were sliding. The differences are small but it is thought that this single point which resisted slipping is key to shifting the balance from a sliding failure to that of a concrete failure. In the case of the 120N expansion analysis once the interface is sliding at all points it acts as a perfectly plastic material. Essentially there are two degraded, non-linear materials present along the stress path from anchor head to concrete base. Finding a solution then becomes a difficult process as not only has the capacity to resist further pullout loading been lost, but there is no means by which to resist closure of the existing cracks. It is therefore unsurprising that convergence problems were encountered.

In the post-peak regime the analysis for the 240N expansion model showed a period where sliding of the interface stopped completely. This is associated with a large drop in resisted load. The status output reports 2 additional active cracks for this analysis step and 3 additional unloading cracks. This suggests crack localisation and an unloading of

concrete elements close to the interface and as a result there is a drop in shear stress (Figure 8-16). Later in the analysis the shear stresses again reach the strength of the interface but by this stage cracking is the dominant failure mechanism. Towards the end of the analysis only the top of the interface is still reported as slipping. However, this is due to the separation of concrete and anchor as the hole widens. The stress history graph for the top integration point shows that there is a very pronounced increase in the rate of decline of the normal force. The increase in rate is because of the strain localisation which increases the rate of failure of the structure and hence the opening of the hole. The same behaviour is also present in the 400N expansion analysis.

The behaviour of the 400N expansion analysis differs slightly from that of the 240N analysis. This is to be expected since the expansion force is great enough to ensure a failure in the concrete. However the increased level of the force will alter the stress state within the model and hence lead to a different solution. Globally the most obvious difference is the increased ultimate capacity of the anchor. Cracking of the concrete and slipping of the interface both initiate at the same stage in the analysis as for the previous analysis. At no point does the sliding of the interface stop completely but from the stress history plots it can be seen that in the post-peak regime sliding does halt at some integration points. In fact, for the later stages of the analysis the bottom half of the interface is able to resist the shear stresses present.

What the above analyses illustrate is that there is a complex interaction between the non-linear behaviours of concrete and interface. Furthermore, the combination of the two materials can lead to numerical difficulties in the solution process and ultimately non-convergence. Identification of the physical failure mechanism suggested by the analyses is not readily achieved by traditional means of examining stress or strain contours, load-displacement response or displaced shape. However, sliding being reported at all points in cases of non-convergence is a strong indicator of a sliding failure and may be backed up by stress history data.



A study of the effects of varying levels of cohesion,  $c$ , was also carried out. For these analyses the expansion force was set to zero whilst all other parameters remained at their reference value. The load-displacement responses show that for no cohesion and for a cohesion of 3 N/mm<sup>2</sup> the interface fails in sliding before reaching peak load (Figure 8-18). Cohesion levels above this produce responses that follow the response of the model with no interface very closely. Therefore it may be concluded that, unlike the cube model, increased cohesion does not lead to a significant increase in failure load. Instead the model switches from a sliding failure to a concrete failure. Also of note is the fact that the interface stiffness was set to the lower value more comparable to that of concrete rather than the higher value considered in some of the cube sensitivity studies. The resulting difference in load-displacement response from the ‘no interface’ model is slight. Therefore the overall stiffness of the anchor model may be considered to be relatively insensitive to the interface stiffness.

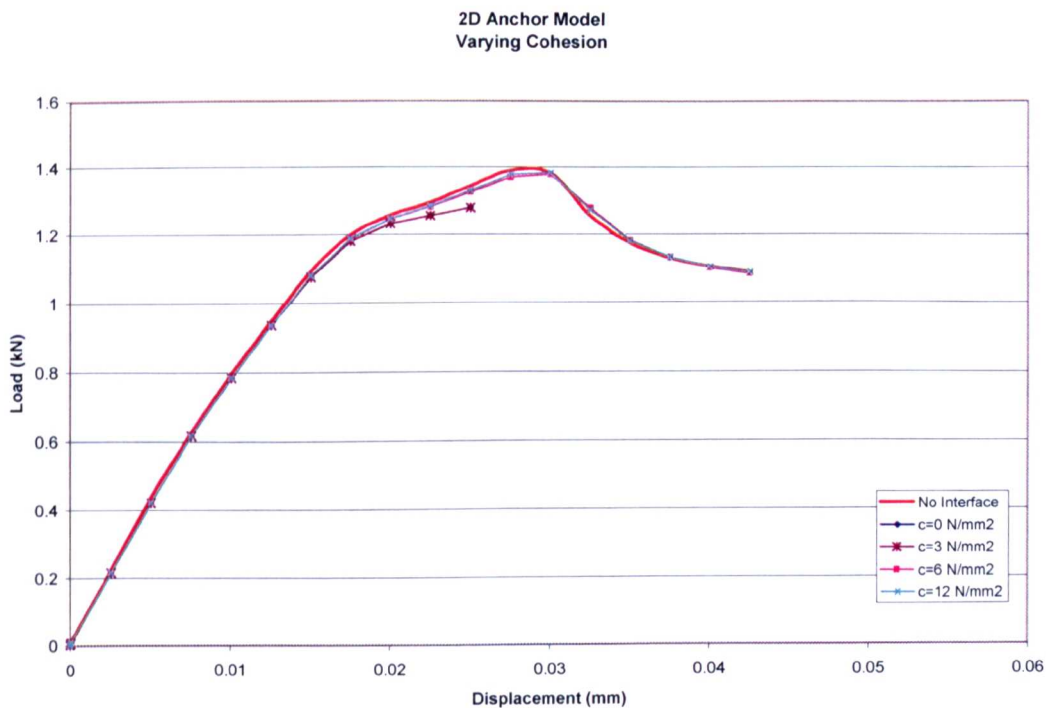


**Figure 8-18 - 2D Anchor Interface Model, Varying Cohesion**

A study of the effects of friction angle,  $\phi$ , also showed that no significant increase in failure stress was gained by increasing its value (Figure 8-19). As with cohesion, the effect was the switch the failure mechanism to a concrete failure rather than a sliding one.

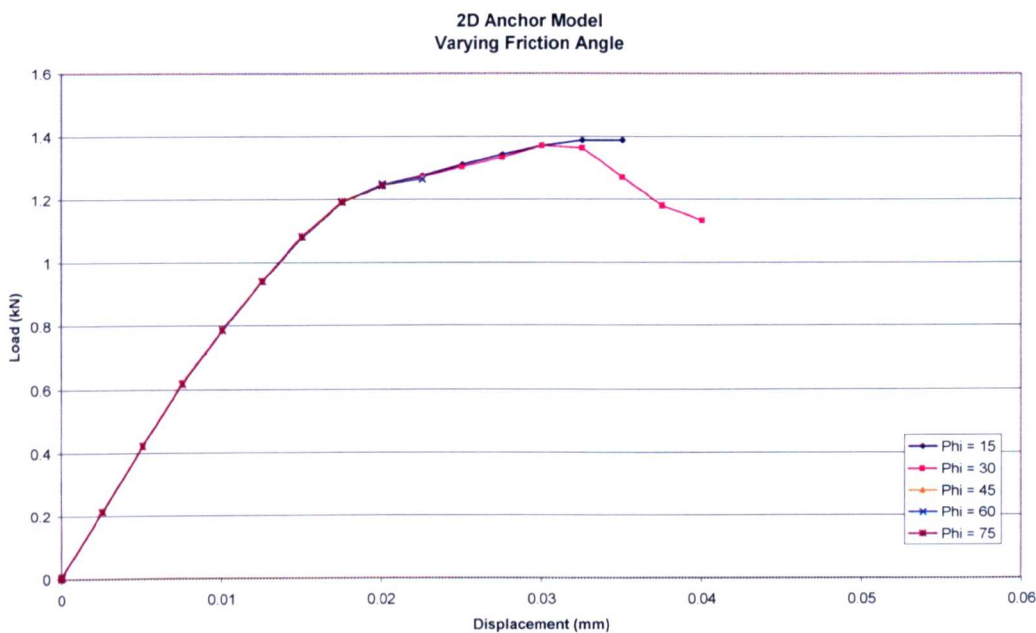
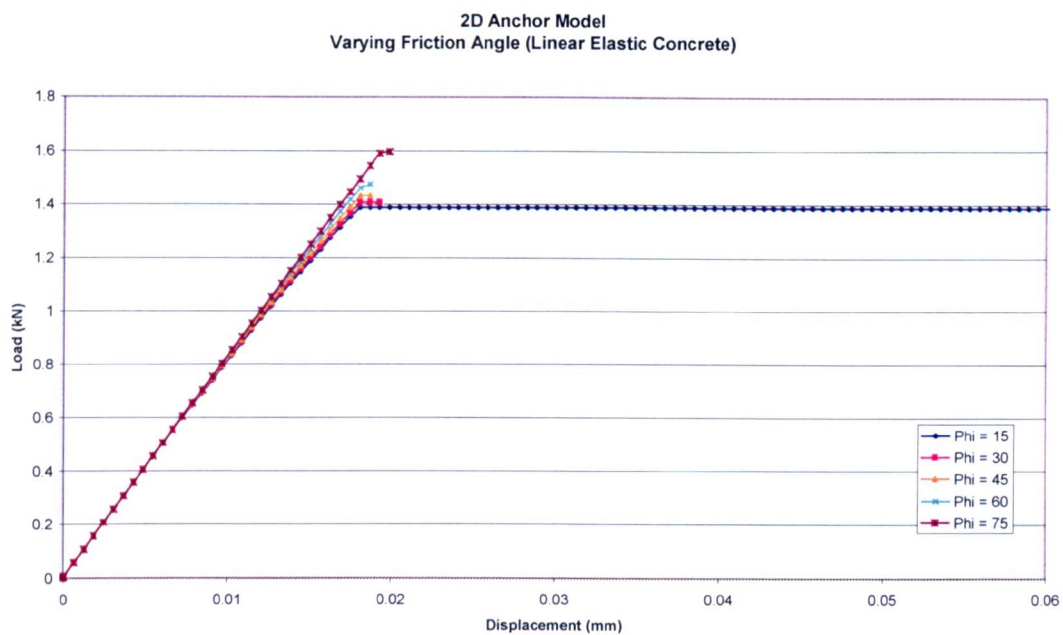


Figure 8-19 - 2D Anchor Interface Model, Effects of Varying Friction Angle

Out of interest the study of friction angle was repeated but with the concrete set as a linear-elastic material. This ensured that the failure mechanism was via interface sliding and the resulting load-displacement response shows the expected increase in failure load associated with increased friction angle (Figure 8-20).



**Figure 8-20 - 2D Anchor Interface Model, Varying Friction Angle With Linear-Elastic Concrete**



8.5 3D Modelling Of Anchor Bolt With Frictional Interface

The previous 3D anchor model with the square anchor and regular mesh was adapted to incorporate interface elements between anchor and concrete. In this instance 8-noded planar interface elements were used with a 2x2 Gaussian integration scheme. The form of the anchor itself was also modified by splitting it into 4 separate units (Figure 8-21). This way each section acted much like a leaf in the actual anchor design and each of these leaves could be expanded freely.

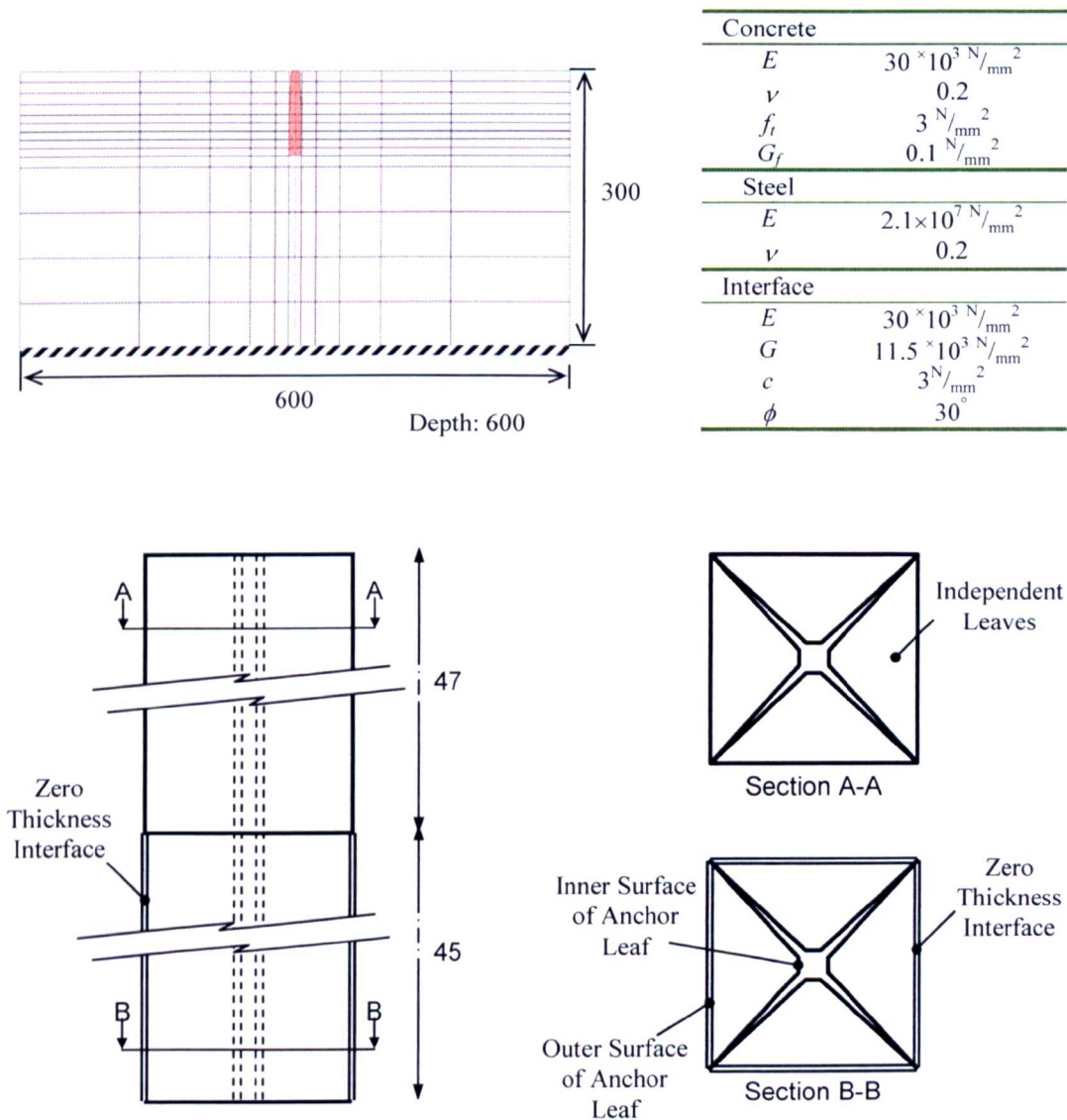
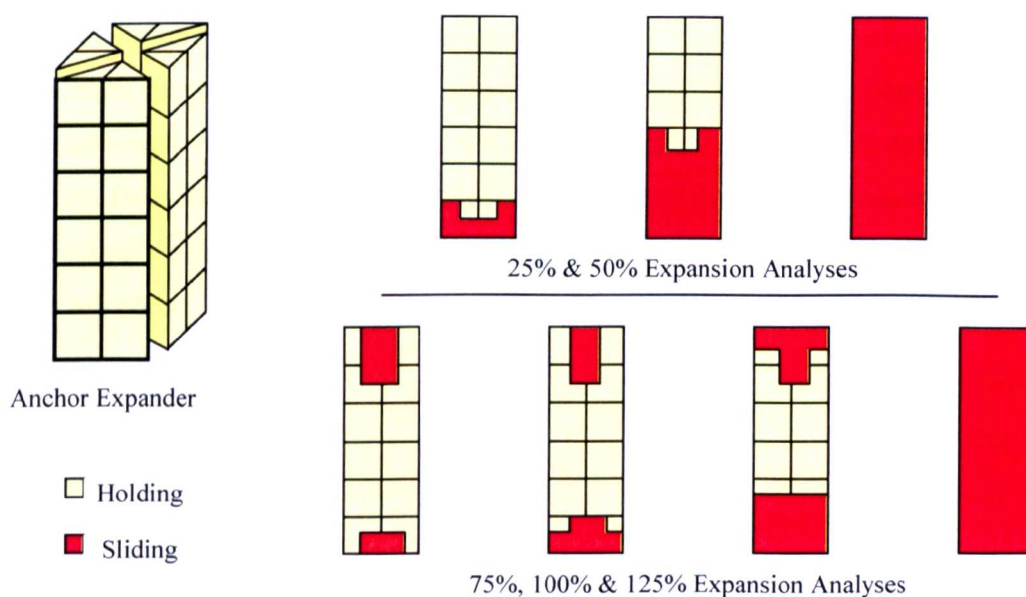


Figure 8-21 – 3D Anchor Problem with Details of Modified Square Anchor

As with the previous 2D model, the expansion forces were applied to the outer surface of the anchor (i.e. directly onto the interface elements) whilst the pullout displacements were applied to the anchor head. Calculations based on anchor installation guidelines [Rawl Fixings (1997)] showed that an expansion force 355kN/mm around the circumference would give a reasonable approximation of the initial expansion level. Details of these calculations are presented later in this chapter. Six analyses were performed with expansion force ranging from 0% to 125% of the required expansion. Also in common with the 2D anchor model, this expansion force was applied uniformly over the contact area. The analyses were performed in 2 stages. Firstly the expansion force was applied followed by the pullout loading (pullout was further split into a slow stage and a normal stage for computational reasons). However, all analyses terminated in the initial stages of pullout, at a displacement of between  $6 \times 10^{-5}$  and  $8 \times 10^{-5}$  mm, due to non-convergence.



**Figure 8-22 - Evolution of Sliding Surface**

The diagrams above (Figure 8-22) show the evolution of the sliding surface for one face of the anchor expander however, being that the model is symmetrical, all four faced showed a similar evolution. The convention ‘inner’ and ‘outer’ is used to refer to Gauss points towards the edge or middle of the expander face respectively. Analyses showed

that the sliding behaviour differed between models with up to 50% of the expansion force applied and those with higher expansion levels. For the lower levels of expansion sliding initiated in the lower part of the expander during pullout. As the analyses progressed the sliding zone extended upwards until the whole face was reported to be sliding and the analysis terminated. For the higher levels of expansion there is also a sliding zone formed at the top of the expander surface which extends downwards during the course of the pullout to meet the sliding zone evolving from the bottom.

The stress histories provide more detail of the sliding failure. Figure 8-23 is for 100% expansion. Calculated shear strength is shown as before along side horizontal and vertical shear stresses. In addition the magnitude of the resultant shear is also plotted. Gauss point 5000-3, at the bottom of the expander, was one of the first points to slide. It can be seen that, although the expansion of the anchor increased the shear strength, the resultant shear just prior to pullout is 22% of the capacity of the interface. Both horizontal and vertical shear stresses are responsible in equal measure. Gauss point 5024-1 is towards the middle of the expander and is an outer point. It shows a similar behaviour to that of the previous point although in this case the resultant shear prior to pullout is 48% of the shear capacity. Here the vertical shear stress is approximately zero but horizontal shear is high. For both points pullout causes a rise in vertical stress that eventually exceeds the capacity of the interface.

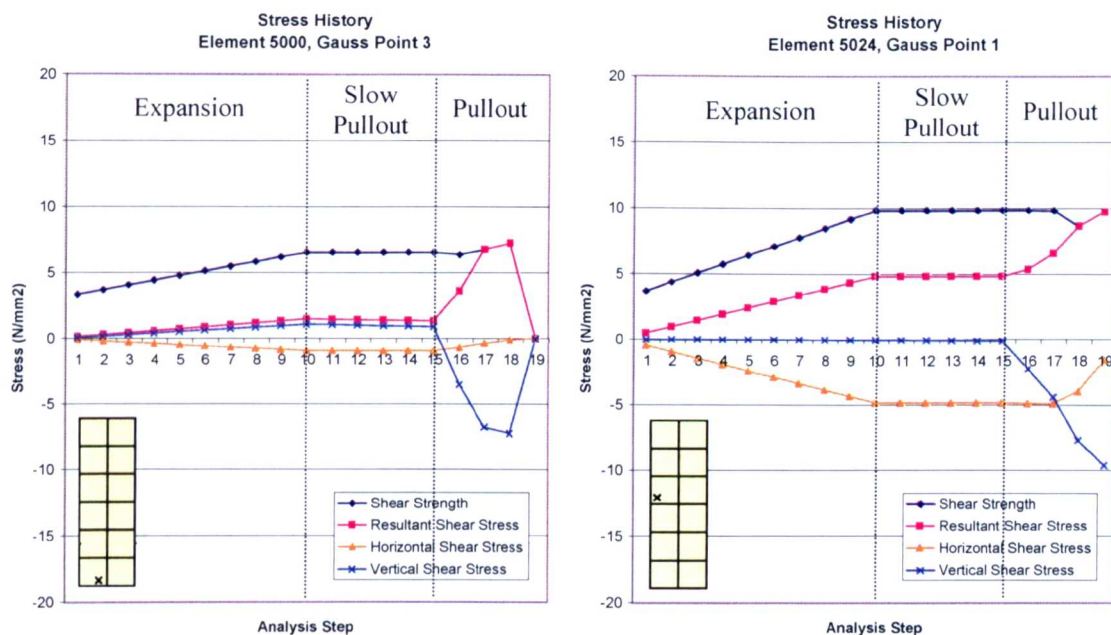


**Figure 8-23 - Stress Histories for Interface Gauss Points 5008-3 and 5024-1 [100% Expansion]**

The stress history response for 25% expansion shows a very similar pattern (Figure 8-24). The magnitude of the stresses is obviously lower in the expansion phase but there is still a significant reduction in available shear capacity caused by shear stresses generated during expansion. Additional analyses with much higher expansion levels showed that although the shear strength was increased, the available capacity for pullout was always diminished by these shear stresses generated by expansion. The limiting case was found when expansion levels were high enough to initiate radial cracking in the concrete and this exacerbated the shear stress problem to the extent that the interface failed in shear during expansion.



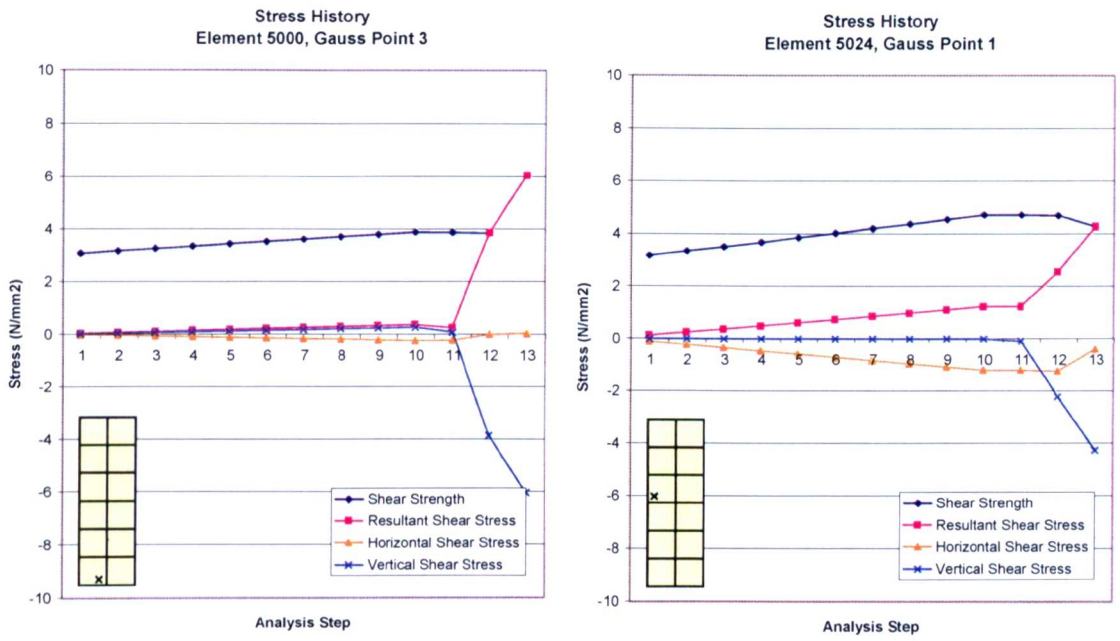


**Figure 8-24 - Stress Histories for Interface Gauss Points 5000-3 and 5024-1 [25% Expansion]**

A linear-elastic analysis for the expansion stage was performed and stress profiles were created for both the inside and outside lines of Gauss points (Figure 8-25). What is initially obvious when comparing the two graphs is that the shear strength is almost two and a half times higher for the outside Gauss points. This is related to an increased normal stress and is due to the fact that the corners of the hole in the concrete are stiffer relative to the sides of the hole. There is also an increase in the normal force at both the top and bottom of the expander. The causes of this are investigated below. The vertical stress level was relatively low and took the form of an s-curve. This is a result of the Poisson effect. Expansion of the anchor causes a contraction in the axial direction. The vertical displacement at the middle of the expander is zero hence positive shear stresses above this point and negative stresses below. In both profiles the horizontal shear is the predominant contributor to the resultant shear stress. The ratio of shear strength to resultant shear is between 2:1 to 3:1 for the two profiles although it is clear that this ratio is significantly lower for the 3<sup>rd</sup> Gauss point from the bottom on the inner profile. This corresponds to point 5008-3 which analyses showed to be one of the first points to begin sliding. From this it can be said that as long as the materials remain within the elastic

range during expansion, higher levels of expansion pressure will result in a greater available shear capacity. However, the fact remains that a high horizontal shear stress is undesirable as it acts to reduce the available capacity thus necessitating a higher expansion pressure. Also, as will be shown, these stresses are a product of approximations made when modelling the anchor geometry and not related to the real behaviour of the anchor.

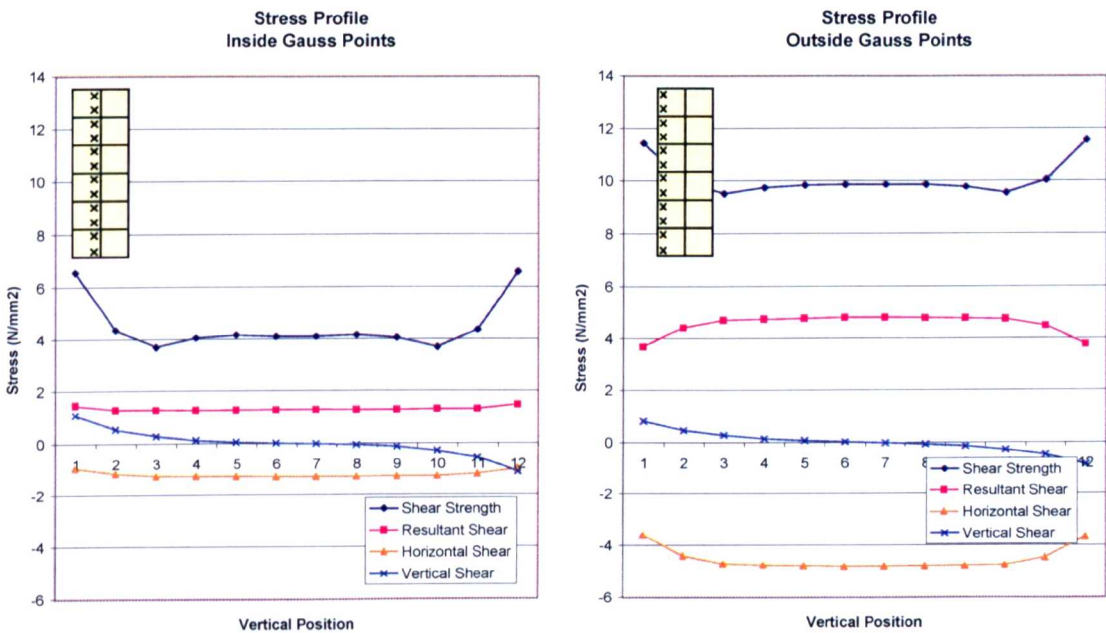


Figure 8-25 - Stress Profiles on Interface for Expansion

Similar stress profiles were created for a linear-elastic analysis of the model when subjected to  $1\times10^{-2}$ mm pullout displacement of the anchor head (Figure 8-26). In this case no expansion pressure was applied. What is immediately clear from the plots is that for several of the inner points and all of the outer points, the resultant shear exceeds the shear capacity of the interface. This is not surprising for an unexpanded anchor. As expected the major contributor to the resultant shear is vertical shear stress.

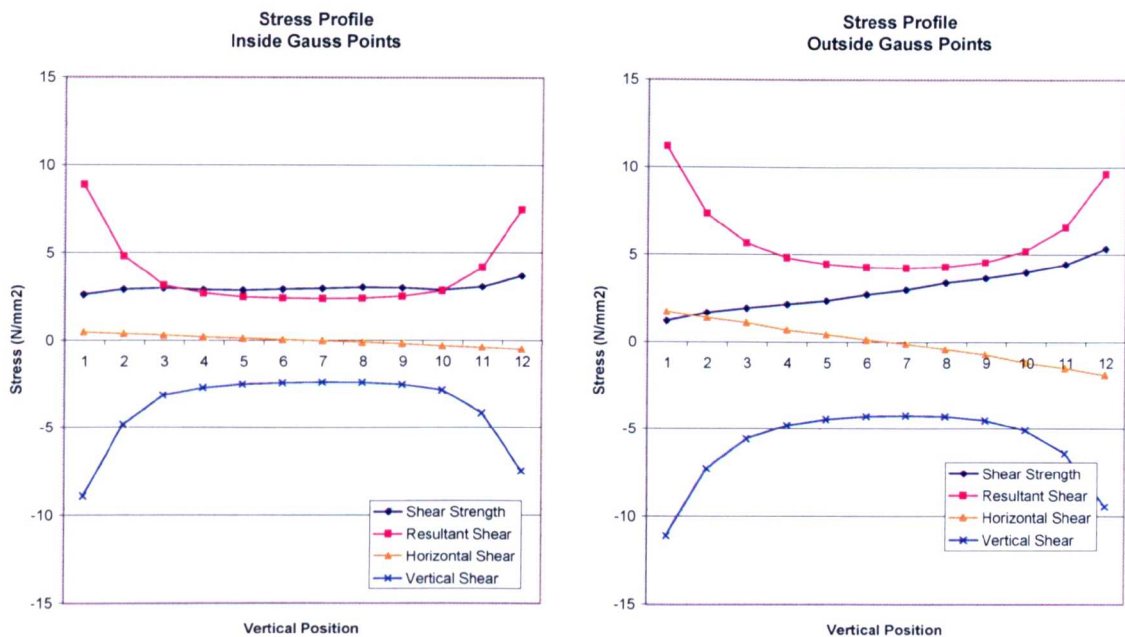


Figure 8-26 - Stress Profiles On interface for Pullout

The nonuniformity of the normal stresses (hence shear strength) was examined by means of simpler expansion models (Figure 8-27 - Figure 8-29). The complexity of these model ranged from simple uniaxial compression (Figure 8-27) to an anchor-like problem (Figure 8-29). These models were 3D but were only one element thick in the z-direction. This was to further simplify the model. A steel section representing the expander was placed at the left of the models and was connected to the concrete block via the same quadrilateral interface elements used above. As with the 3D anchor model, expansion stresses were applied at the outer surface of the expander, directly onto the interface.

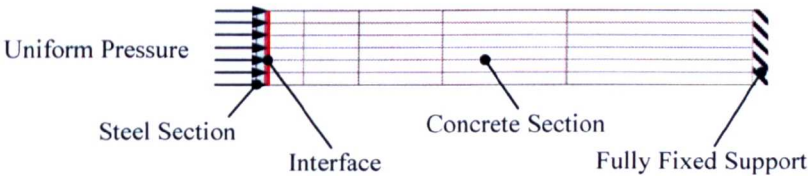
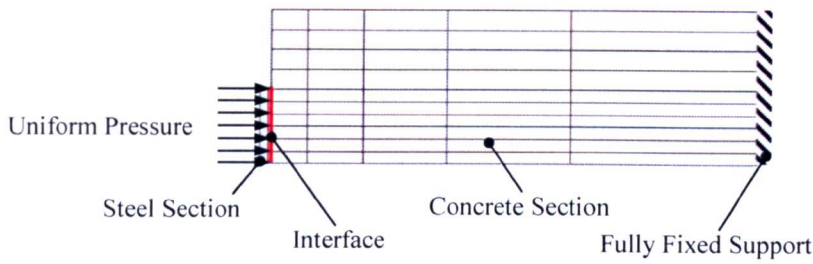
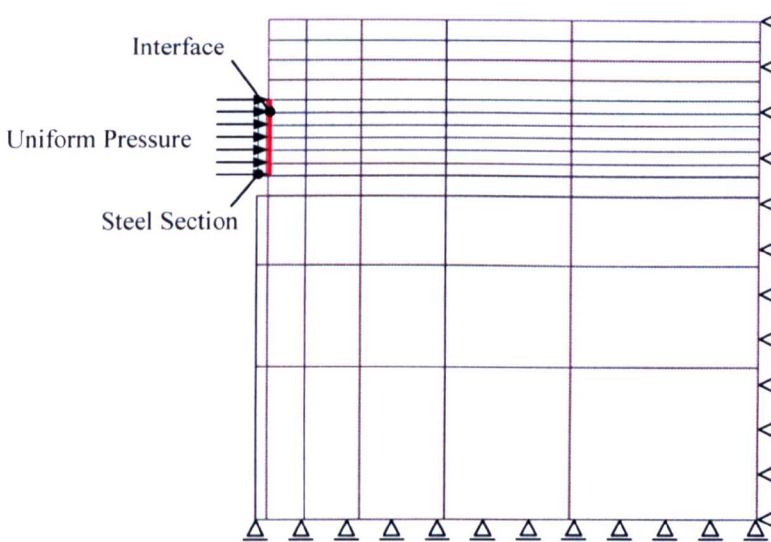


Figure 8-27 - Simple Expansion Problem 1 - Uniform Uniaxial Compression



**Figure 8-28 - Simple Expansion Problem 2 - Interface Only Partially Covers Left-Hand Face**



**Figure 8-29 – Simple Expansion Problem 3 – ‘2D’ Anchor Problem Geometry But Differing Boundary Conditions**

The stress profiles show that for the first model there is a uniform distribution of normal stress (Figure 8-30). With the addition of the concrete above the expander in the second model the profile becomes mainly linear with a sharp increase in stress at the upper Gauss points. Likewise the addition of the material below the anchor leads to a similar jump in normal stress at the bottom of the interface and the resulting profile becomes very similar to that seen for the 3D anchor model above.



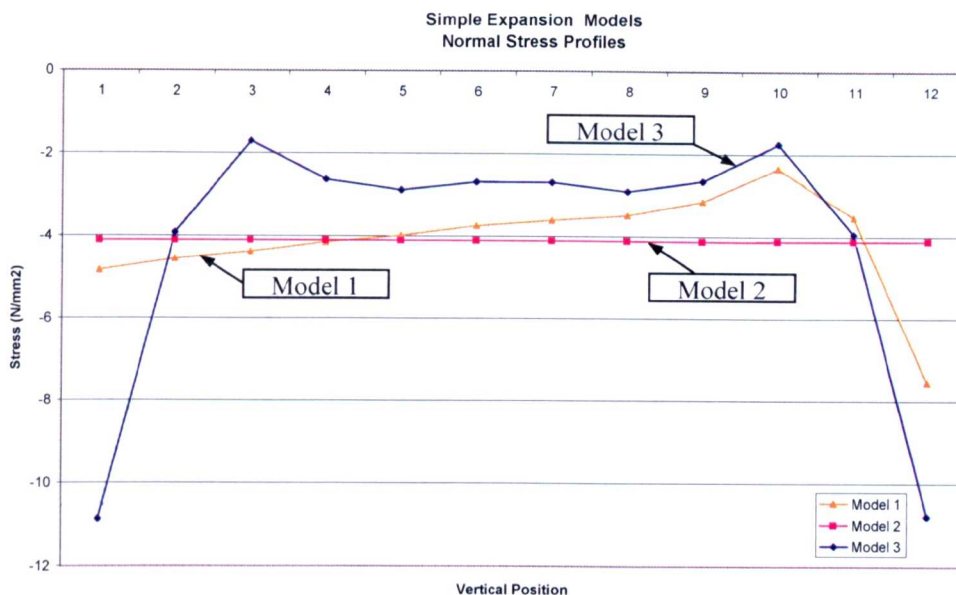


**Figure 8-30 - Normal Stress Profiles on Interface for Simple Expansion Models**

The origin of the high horizontal shear stresses seen in the 3D anchor model can be explained by considering the relative displacements of the inner and outer nodes of the interface elements (Figure 8-31a). It is clear that both the inner and outer nodes at the middle of each side move in the same direction however this is not the case for the corner nodes. Because the anchor was constructed as four separate leaf units, and because the outer nodes of the anchor are the inner nodes of the interface, the displacement of these corner points is either in the  $x$  or  $z$ -direction exclusively. However, the corner point for a given interface element is shared with the adjacent element and also with the corner of the hole in the concrete. Therefore the displacement of this point has components in both  $x$  and  $z$ -directions. This means that there is a relative horizontal displacement in each element and hence a shear stress developed. The influence of this relative displacement is greatest for the outer Gauss points and this is reflected in the higher horizontal shear stress reported at these points (Figure 8-25).

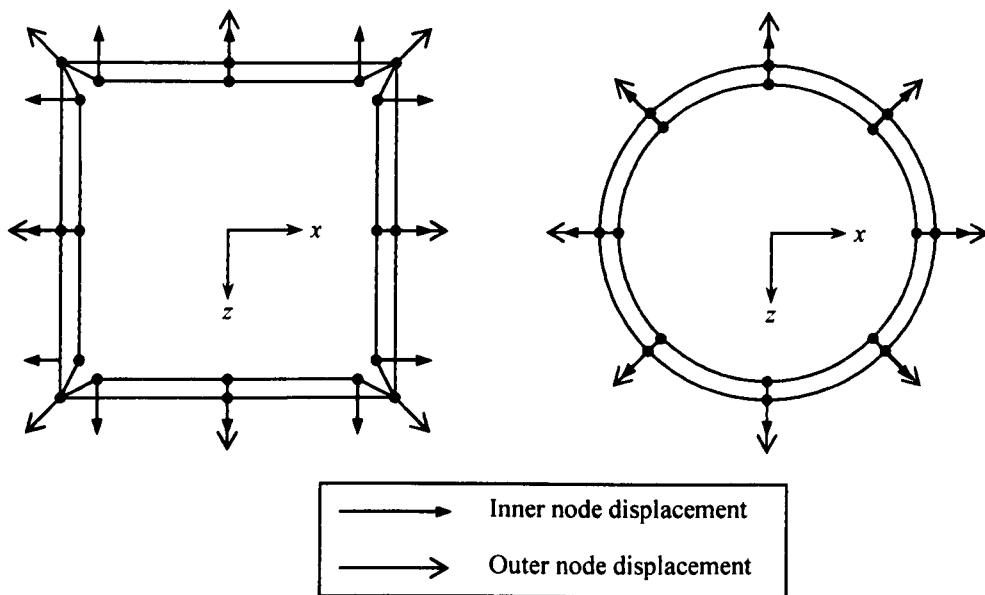


**Figure 8-31 - Displacement of Inner & Outer Interface Nodes for Square & Circular Anchor Cross Sections**

In reality the cross-section of the anchor bolt in plan is circular (Figure 8-31b). In this situation it is apparent that the relative displacements are very significantly lower. It is therefore clear that the presence of these high horizontal shear stresses is predominantly as a result of the geometric design of the model and the manner in which expansion loading is applied rather than the expected behaviour of an expanding anchor bolt. In order to reduce these effects it is necessary to make efforts to align the displacement vectors for the inner and outer nodes at the corner points.

The first method attempted to reduce the horizontal shear was to consider alternative loading patterns by which to apply the expansion load. Figure 8-32 below shows the three basic loading patterns considered. As before the loads were applied to the nodes forming the outer surface of the expander/inner surface of the interface element. Patterns 1 and 2 are essentially a decomposition of the loading pattern used previously. Pattern 3 applies forces at the corner points horizontally across the plane of the interface in order to apply the necessary horizontal displacement component to these nodes.

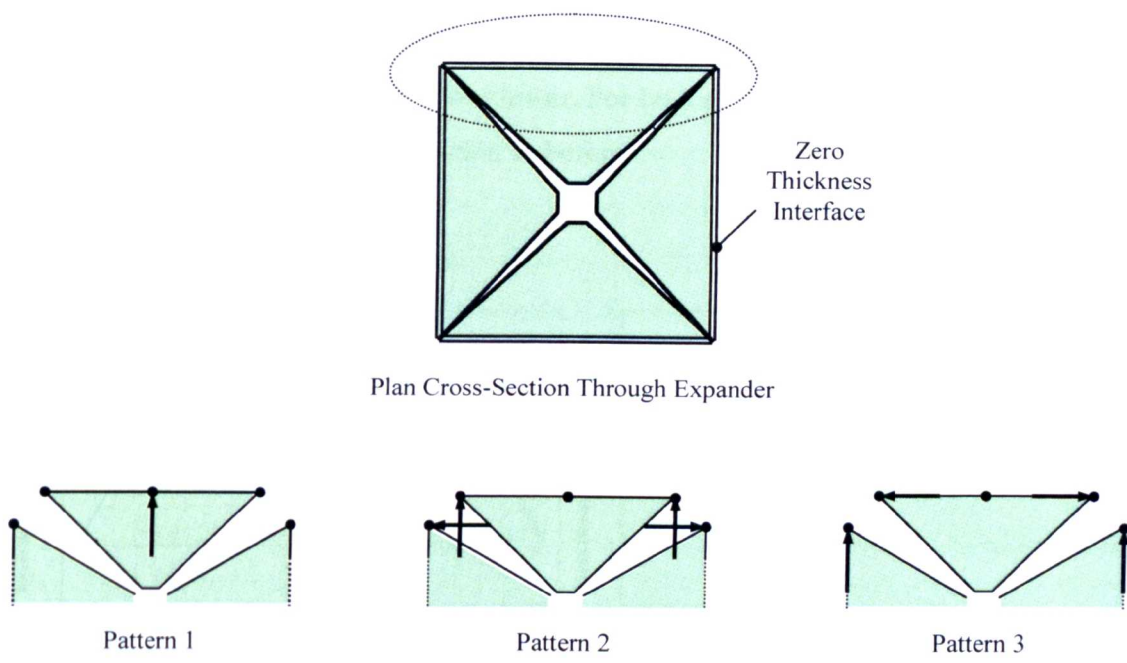


Figure 8-32 - Basic Loading Patterns for Expansion

Linear-elastic analyses were performed for each of the loading patterns with a suitable reference load and stress profiles created (Figure 8-33, Figure 8-34 & Figure 8-35).

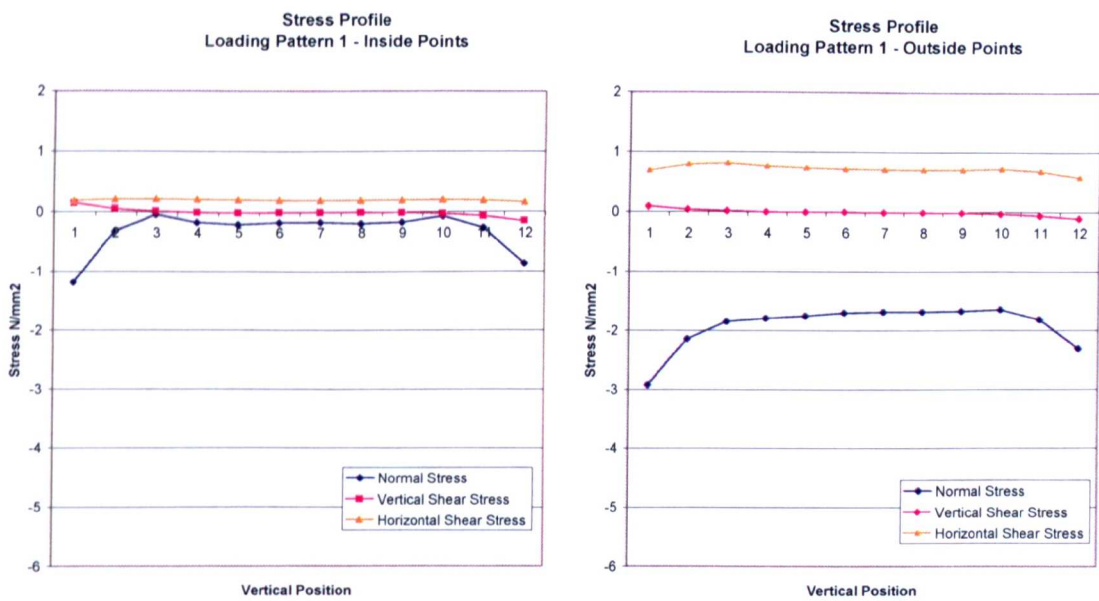


Figure 8-33 - Pattern 1: Interface Stress Profiles

From the profiles it can be seen that the effects of loading patterns 1 and 2 are very similar. Loading just the middle nodes does lead to a smaller horizontal shear stress but the corresponding normal stress is also lower. For both patterns the vertical shear stress is low and follows the s-curve distribution as before.

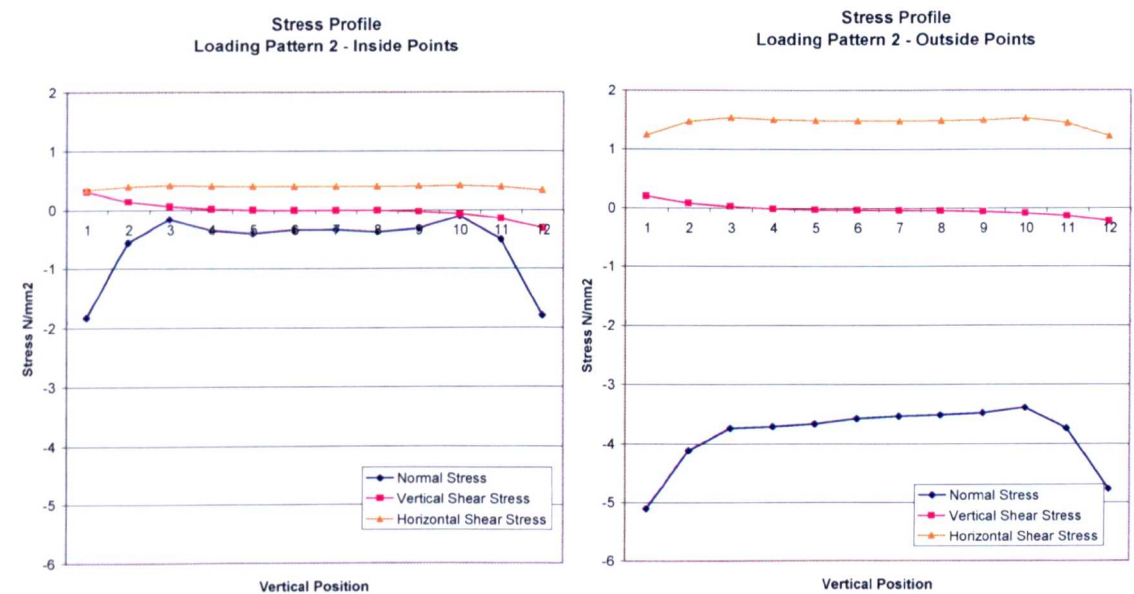


Figure 8-34 - Pattern 2: Interface Stress Profiles

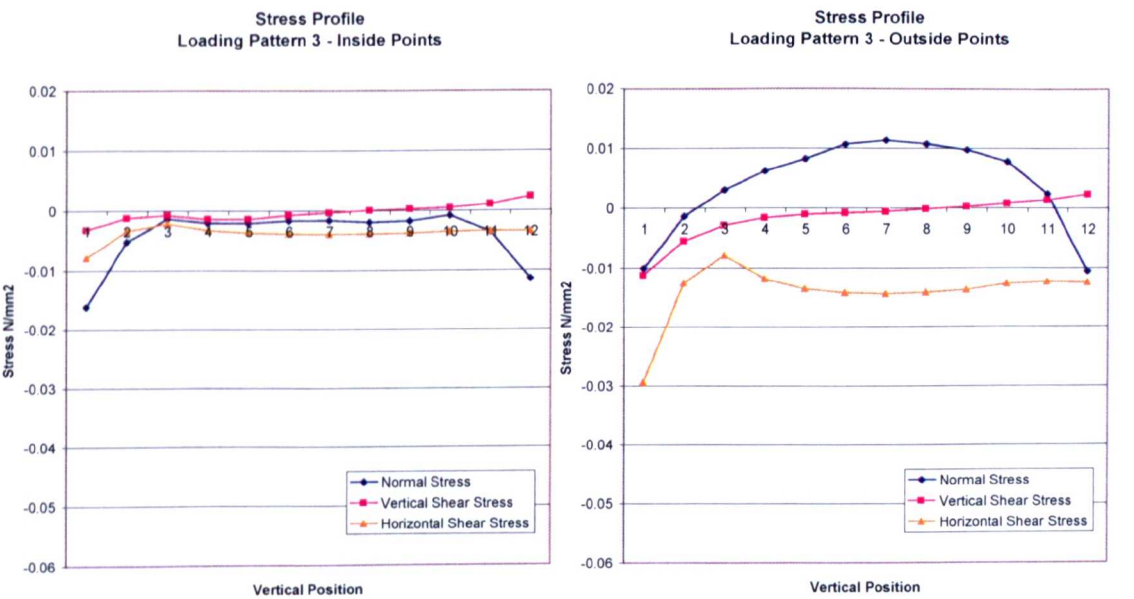


Figure 8-35 - Pattern 3: Interface Stress Profiles

The stresses produced for pattern 3 are around 100 times lower than those for the other analyses. This is expected given that the forces applied act directly to stretch the anchor leaves as well as to press them against the concrete. For the inside Gauss points the horizontal shear stress is higher than the normal stress. However its sign is opposite to that of previous profiles. This is also the case for the outer points although the normal stress is tensile for the majority of the interface. Also significant is the fact that the s-curve for the vertical shear stress is the inverse of previous profiles.

Using these properties of Profile 3, a linear combination of it and the first profile was produced. Appropriate scaling factors were applied so as to minimise the horizontal and vertical shears and give an expansion pressure equivalent to that of the previous 100% expansion analysis (Figure 8-36). The plot shows that the available shear capacity is much improved.

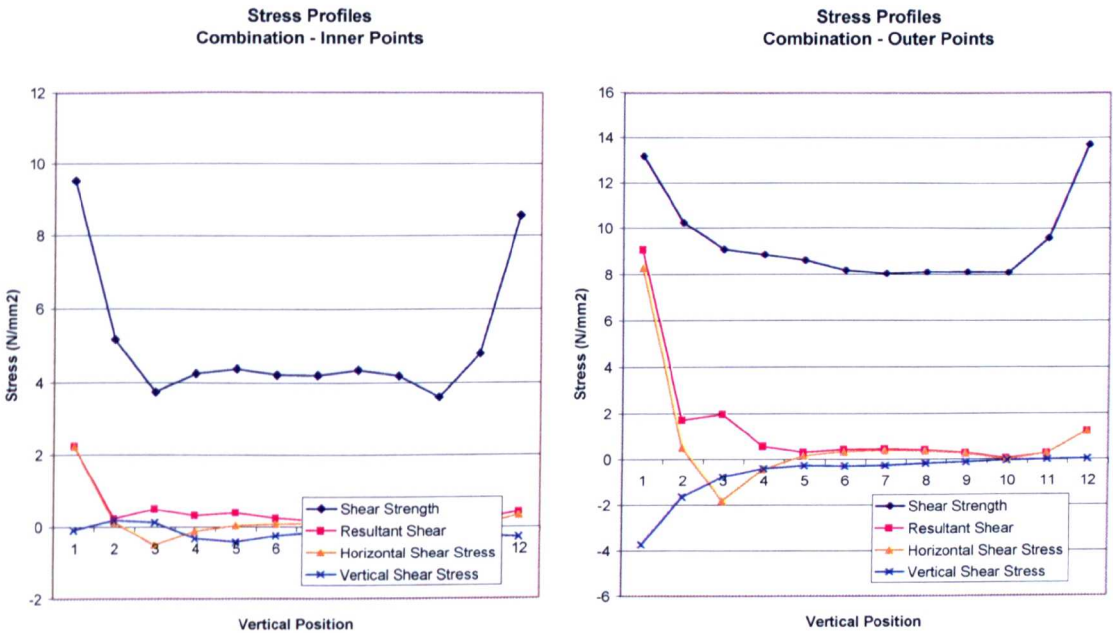


Figure 8-36 - Combination Loading: Interface Stress Profiles



As with the previous analyses with full initial expansion, the model terminated during the early stages of pullout. The evolution of the sliding surface was slightly different in that sliding started from the bottom of the expander and spread upwards (Figure 8-37).

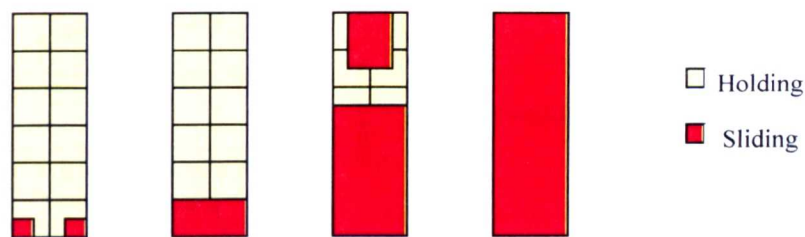
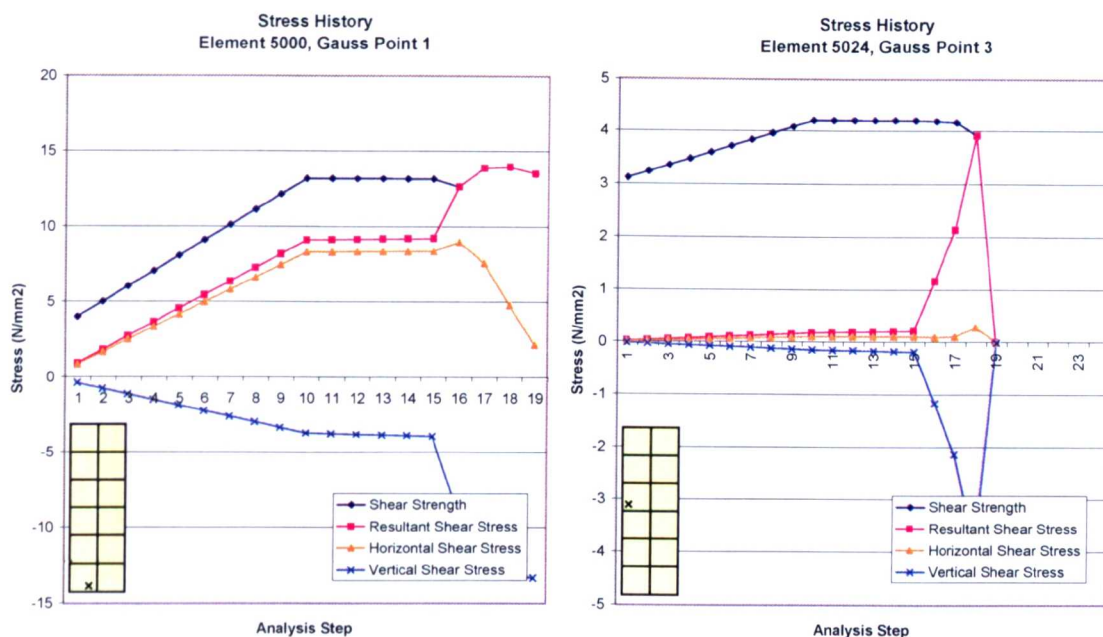


Figure 8-37 - Evolution of Sliding Surface

The stress history graph for Gauss point 5008-1 (Figure 8-38a), the first points to slide, shows a 1.4:1 ratio of shear strength to resultant shear stress once expansion is complete. This is still much lower than was desired but was predicted by the linear elastic stress profile (Figure 8-36). The high horizontal stress reported at this point suggested that sliding failure was likely. For Gauss point 5024-3 (Figure 8-38b) the ratio is much better (25:1) and that both vertical and horizontal shear stresses are very small. A similar response was seen for most of the other Gauss points.



**Figure 8-38 - Stress Histories for Interface Gauss Points 5008-1 and 5024-3**

As shown above, failure was due to sliding caused by pullout forces. The level of expansion pressure was increased by a factor of 4 in order to discover whether the interface would hold and a concrete cracking failure be invoked.

The analysis progressed over twice as far as before but was still a long way off the pullout displacement of 0.2mm reported at peak load for previous analyses without the frictional interface. However, some interesting behaviour was observed. From mid-way through the expansion phase cracking began to occur in the model. It formed radially around the lower part of the expander. Also, in the later stages of the expansion, sliding began to occur (Figure 8-39). Since this was not predicted by the initial linear-elastic stress profiles, it must be a non-linear effect, possibly caused by secondary horizontal cracking of the concrete elements connected to the interface.

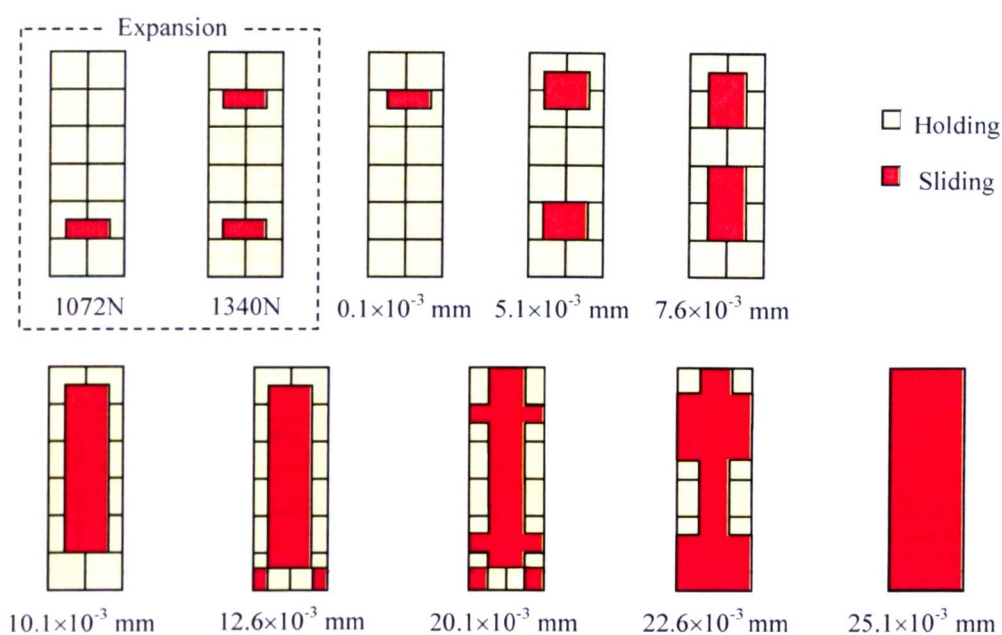


**Figure 8-39 - Evolution of Sliding Surface. Higher Expansion Force**

The stress histories for this analysis also show these non-linear effects caused by concrete cracking (Figure 8-40). Although the plot for Gauss point 5000-1 has a very similar form to that of the previous analysis, the plot for point 5024-3 is quite different. It shows high horizontal stresses and significant vertical stresses forming during the expansion phase. Sliding at other points would cause a redistribution of stresses hence leading to the stress state shown here.



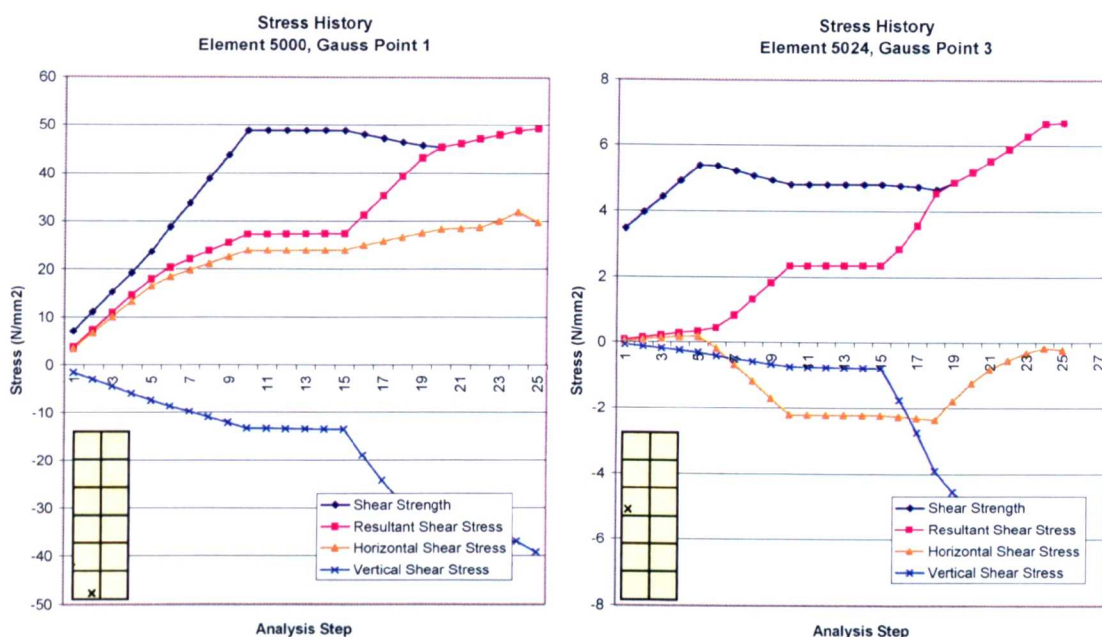


**Figure 8-40 - Stress Histories for Interface Gauss Points 5008-1 and 5024-3. Higher Expansion Force**

Combining load patterns in the above analyses did produce better results in terms of a greater available shear capacity once expansion was complete however significant horizontal shear forces remained in areas of the expander surface. Increasing the expansion pressure did help to increase capacity but also caused cracking to occur which, in turn, initiated sliding. A possible remedy would be to make efforts to reduce the horizontal stresses in the problem areas. This could be achieved by further splitting the basic loading patterns into load cases that considered only one ring of forces at a time. This would then allow for greater flexibility in combining the loads and hence greater scope to adjust the shear stress profiles. However, in the discussion above it was shown that misalignment of the displacement vectors was the primary cause of spurious shear stress and that the square cross-section of the anchor problem made alignment difficult. Therefore, before applying such procedures, it was decided that the effects on the stress profiles of using an expander geometry that more closely matched that of a circular anchor bolt should be investigated. It was thought that this would, by design, reduce the horizontal shear stresses.

### 8.6 3D Octagonal Anchor Bolt Geometry

The anchor geometry was modified to form an octagonal cross section (Figure 8-41). This shape was selected since not only did it meet the requirement of being closer to the true cross-sectional shape but also the changes required were minimal and many of the node and element numbers remained consistent between this and the previous model. It was also decided to make the anchor solid rather than having separate leaf elements. Although this meant that much of the force applied to cause expansion pressures in the interface was required to also expand the solid steel bolt, the advantage was that no additional loads needed to be applied to the ‘corner’ nodes to ensure their displacement vectors were aligned.

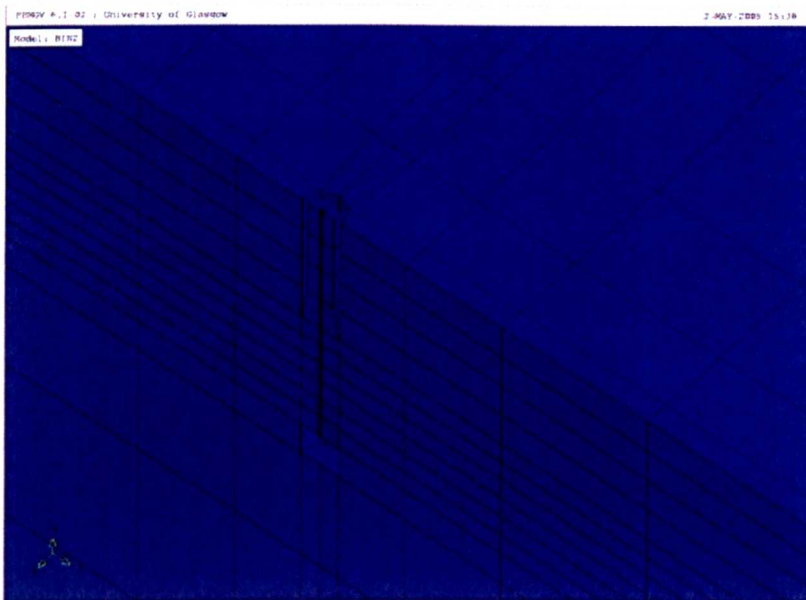


**Figure 8-41 – Finite Element Mesh for Octagonal Anchor Model (Cross Section Through Anchor)**

As suggested above, the loading on the octagonal anchor was first split up into seven load cases - one for each ring of nodes. By using the theory of superposition the resulting stress profiles from linear-elastic analyses of the load cases were then combined and scaled to produce the desired normal stress profile. Because of the mesh topography there was still a difference in the stress profiles of the ‘inner’ and ‘outer’ Gauss points. In order to resolve this the new nodal loadings were split into two new load cases – one for the ‘middle’ nodes and one for the ‘edge’ nodes.

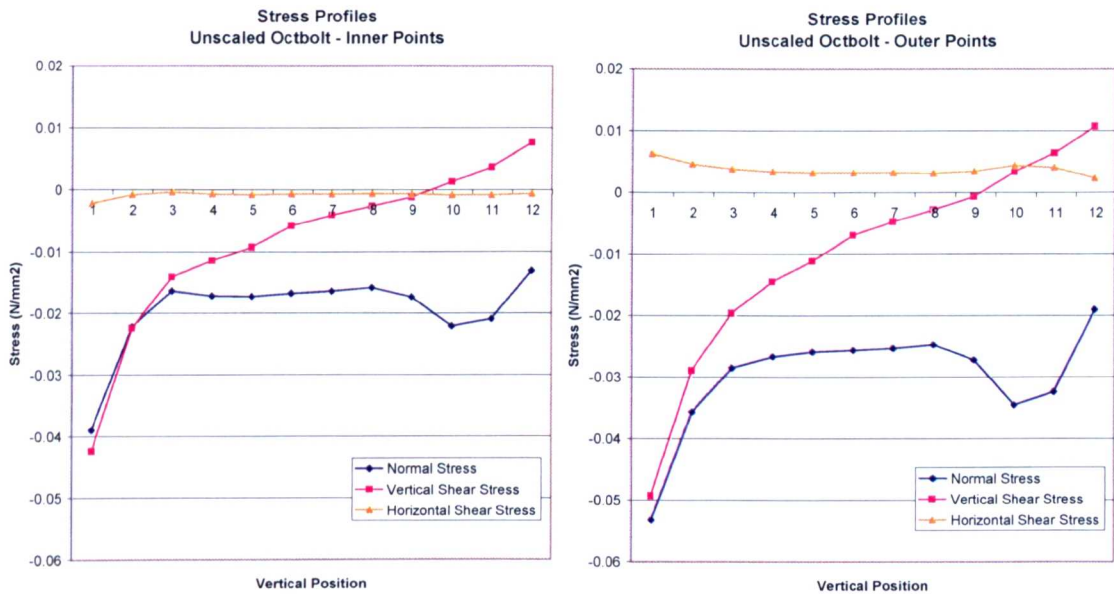


**Figure 8-42 - Unscaled Octagonal Bolt Interface Stress Profiles**

From the initial unscaled loadcases (Figure 8-42) it is immediately obvious that the horizontal shear stresses are very much lower than for the previous square anchor model. However, the Poisson's effect leads to higher vertical stresses.

By using the theory of superposition the seven ring loadcases were scaled to produce the profiles below (Figure 8-43). Scaling was performed on a trial and error basis with the target being to produce an approximately uniform normal stress profile. The complexity of the interaction of these loadcases made it unrealistic to find an ideal combination therefore the profiles above were accepted as being adequate. The argument for the increase in normal stress towards the bottom of the expander being that in reality, due to the mechanics of the expansion process, higher normal forces are to be found in this location.

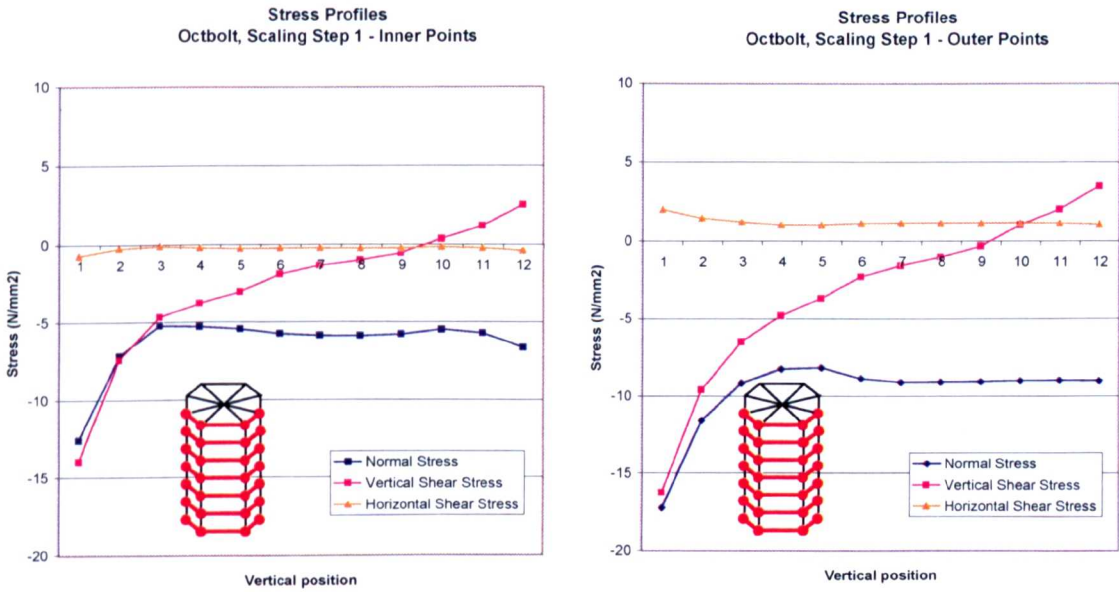
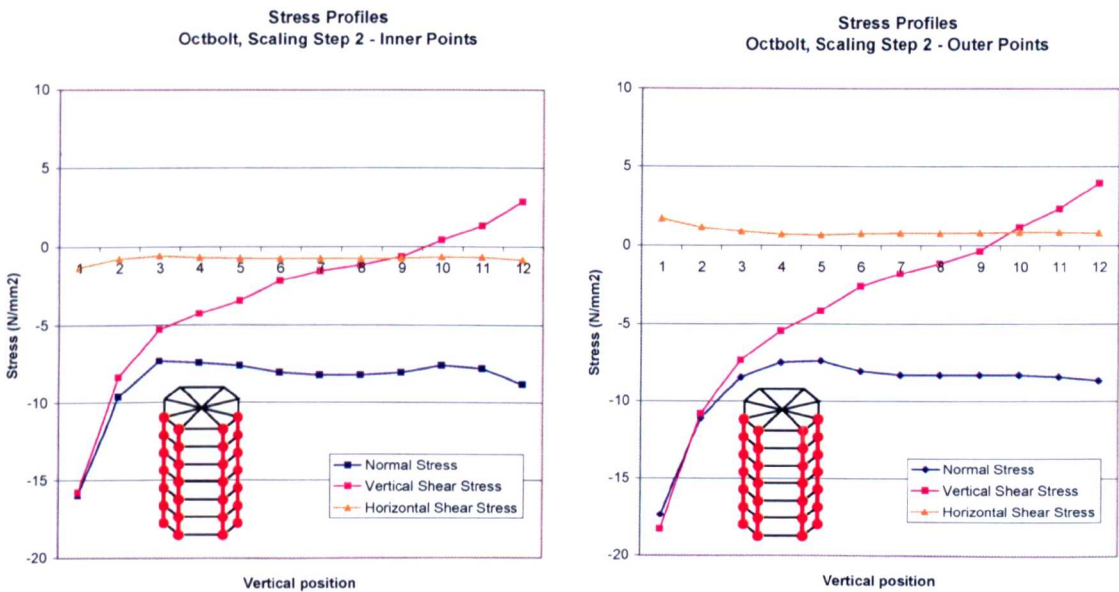


Figure 8-43 - Octagonal Bolt, Scaling Step 1 Interface Stress Profiles



The final step was to use the two loadcases for ‘middle’ and ‘corner’ nodes to attempt to align the stress profiles for inner and outer Gauss points (Figure 8-44). The result was rather successful but the high vertical shear stress approaches or exceeds the normal stress at several locations. Whilst it is true that the Poisson Effect is an inherent aspect of the material behaviour of steel, by comparing the finite element model with the actual anchor expander it may be argued that the effect is not applicable in this case.



**Figure 8-44 - Octagonal Bolt, Scaling Step 2 Interface Stress Profiles**

For the real anchor expansion is achieved via the action of the expander mechanism (Figure 8-45). Anchor leaves are hinged at the top and free to rotate. Tension applied to the bolt itself will cause axial straining in both the bolt and the bell hence radial straining due to the Poisson effect. However, these components are not in contact with the concrete and so have a negligible on the anchor-concrete interface. The leaves are mainly subject to radial compressive stresses and therefore axial and circumferential straining via the Poisson effect will be present. These effects will be concentrated towards the bottom of the leaves where the bell applies the expansion force. The overall displacement due to the straining will be small and localised hence the surrounding interface elements will only report a corresponding small, localised shear stress.

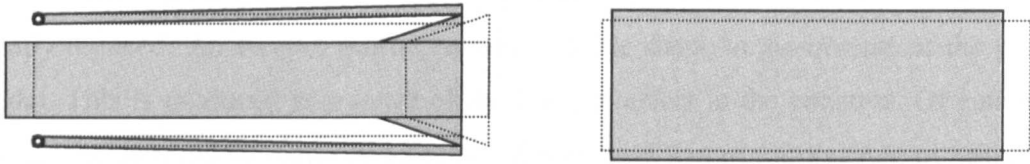


**Figure 8-45 - Real Anchor and FE Anchor Bolt Expansion**

In comparison, the current finite element model expands approximately uniformly over the length of the expander hence the axial displacement due to the Poisson effect is much greater. Adopting a displacement profile more like that of the real anchor would help reduce this effect and was attempted later on. However, unlike the real mechanism, modelling the expander as a solid block does not allow the free expansion of the outer surface without an associated Poisson effect. Also, in order to achieve a proper localisation of the stresses in the expander tip a much higher discretisation of the anchor and surrounding material is required. Limitations of computer hardware made this an impractical proposition. Therefore a more efficient approach to avoid these unrealistically high shear forces was to set Poisson's ratio for the anchor material to be zero.

The stress profiles below (Figure 8-46) show that a zero Poisson's ratio for the anchor had very little effect on normal or horizontal stresses but that the vertical shear stress was greatly reduced. An s-curve profile remains but the shape is the inverse of the previous model. This is produced as a result of the Poisson effect in the concrete. Of course, this vertical stress could be removed by setting the Poisson's ratio for concrete to zero but this would be unrealistic. It would also be possible to select a value of Poisson's ratio for steel that would allow the axial displacement of expander and concrete to be equal hence avoid vertical shear. This was deemed an unnecessary complication given that vertical shear stress was now acceptably small.

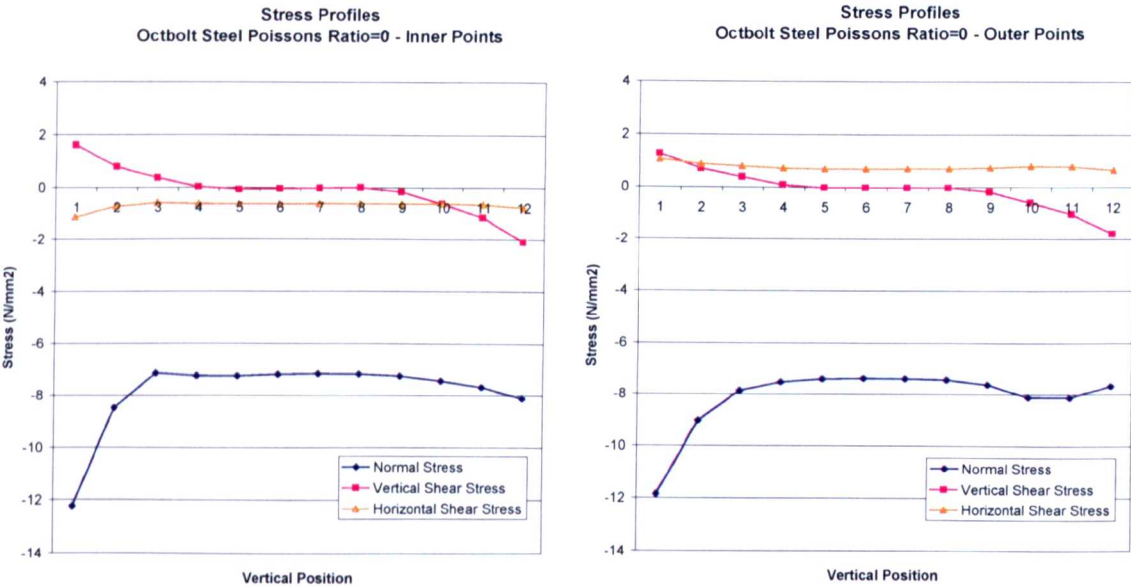
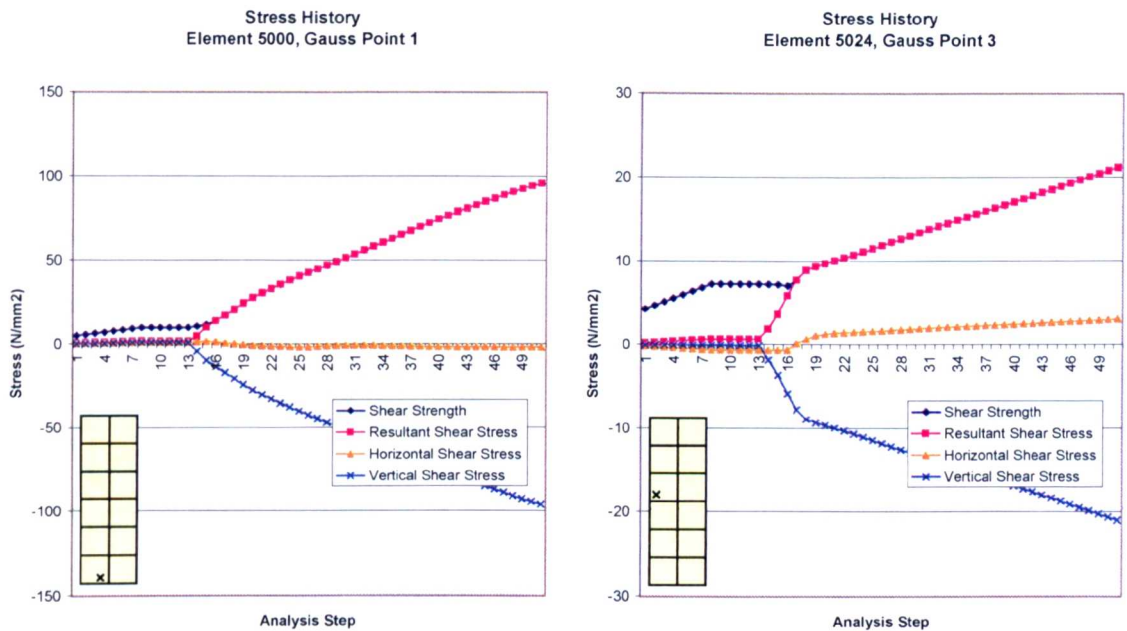


Figure 8-46 - Octagonal Bolt (Poisson's Ratio for Steel=0), Interface Stress Profiles

Analysis of this new anchor model produced much improved results in terms of removing the unrealistic vertical shear stresses. With 100% of the initial expansion pressure there was still a failure of the interface due to sliding during the early stages of pullout. However, the horizontal and vertical shear stresses remained low in the expansion stage and thus the available shear strength to resist sliding was higher (Figure 8-47). Both stress histories show that vertical stresses due to pullout are by far the largest contributor to resultant stress and that the horizontal stresses present are also generated in the pullout phase.





**Figure 8-47 - Stress Histories for Interface Gauss Point 5000-1 and 5024-3**

In light of these results the analysis was rerun with the expansion pressure increased by a factor of ten. Although this level of expansion was well above the initial priming level it was considered feasible for pullout conditions. Unlike previous analyses with higher expansion pressures, no sliding occurred in the expansion phase. However some radial cracking did start at an expansion pressure of  $14.88 \text{ N/mm}^2$  and progress almost continuously throughout the analysis (Figure 8-48). Although the exact location of these cracks is difficult to determine, contour plots of crack strain show them to be situated around the expander. This is expected behaviour as calculated by the equations for a thick-walled cylinder (Equation 8-1). Only during the transition from expansion to pullout was there any significant crack closure. Although, for such a change of the stress state in the concrete, this isn't unexpected.

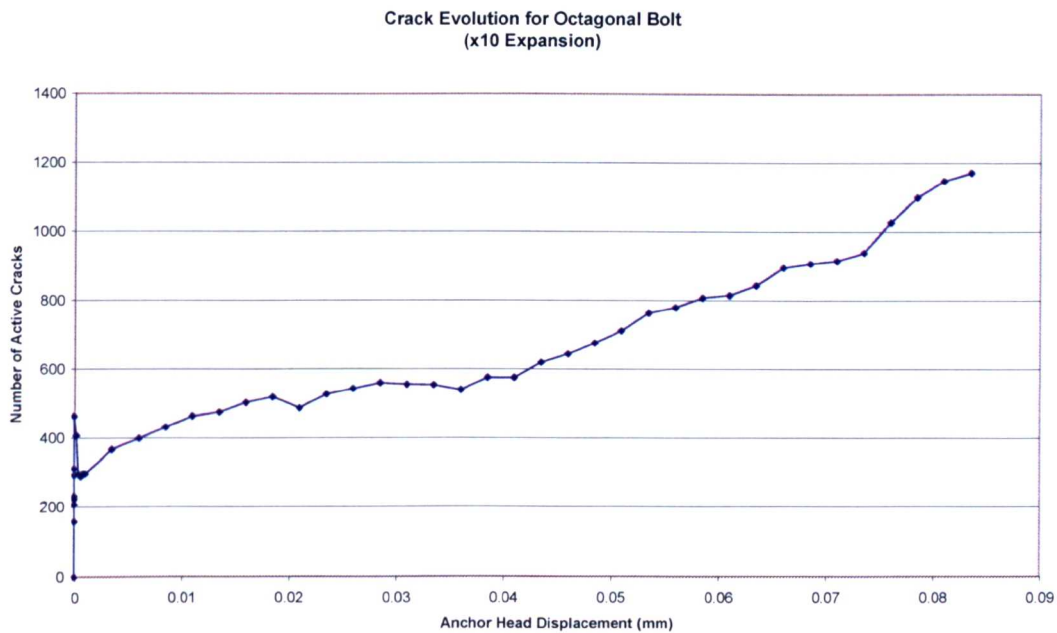


**Figure 8-48 - Evolution of Concrete Cracking for Octagonal Anchor Model (x10 Expansion)**

Due to the higher shear strength and the more uniform stress profile, the evolution of the sliding surface is much more progressive than before (Figure 8-49).

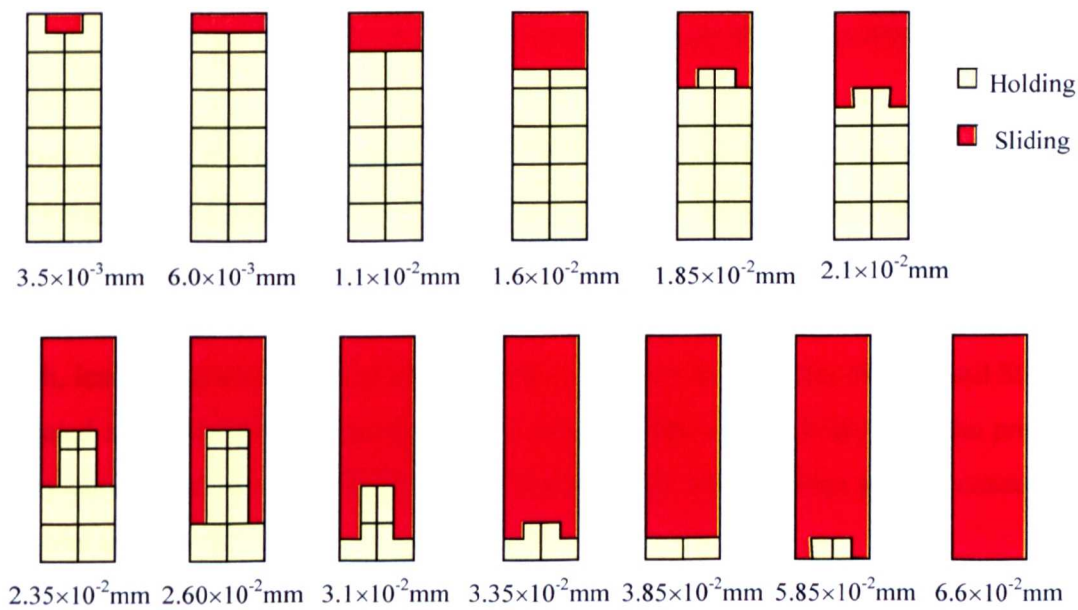


**Figure 8-49 - Evolution of Sliding Surface for Octagonal Bolt, x10 Expansion Force**

The two main features of the evolution are that sliding begins from the top of the expander and progresses down its length and that the outer points slide before the inner ones. The first feature is expected due to the fact that the combination of expansion and pullout loads results in the upper Gauss points having the lowest resistance to shear. The fact that the outer points slide first can be explained by looking at the stress profiles for pullout (Figure 8-26). Here it can be seen that the resultant shear is larger for the outer points.

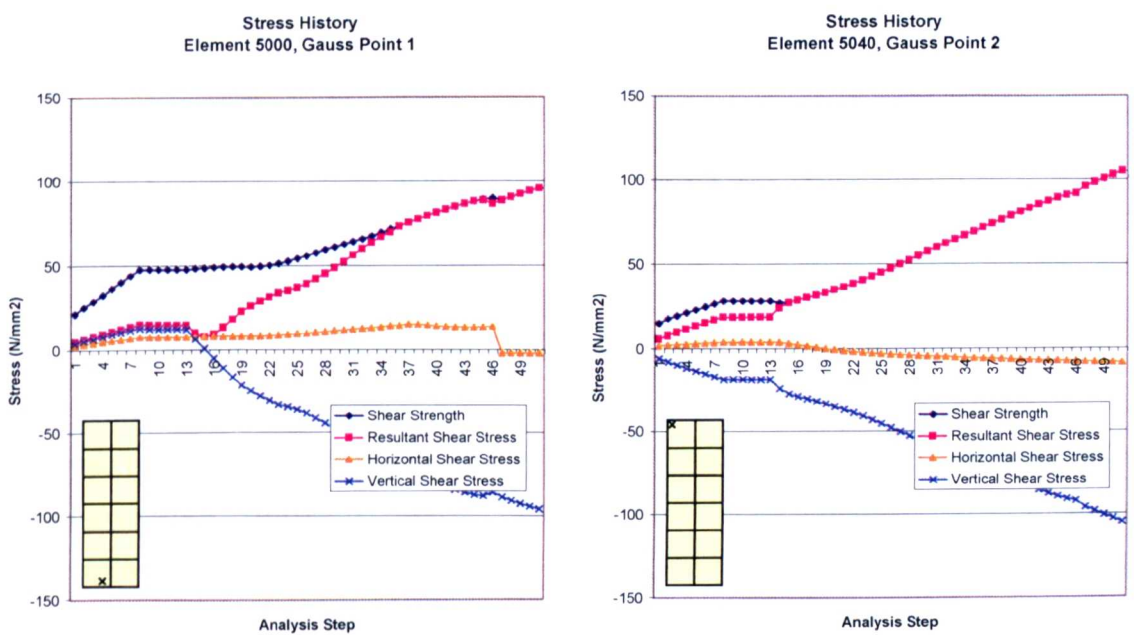
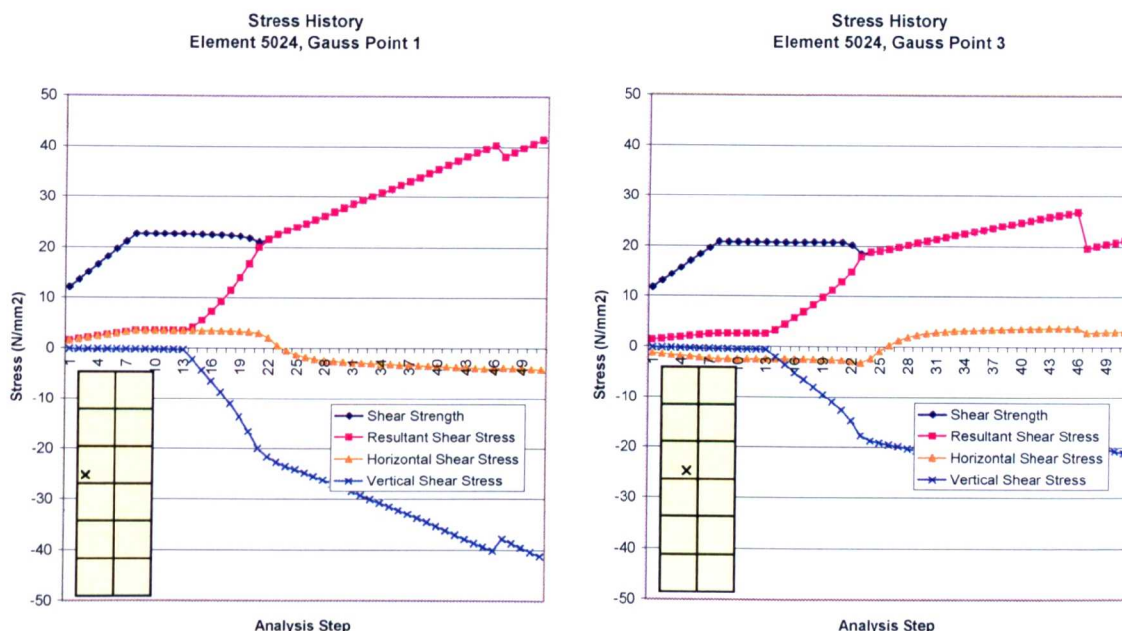


Figure 8-50 - Stress Histories for Interface Gauss Points 5000-3 and 50040-2

The stress profiles reveal more detail (Figure 8-50 & Figure 8-51). It can be see that for Gauss points 5000-1 and 5040-2, at the bottom and top of the expander respectively, that vertical shear stress due to the Poisson effect in the concrete is the reduces the available shear capacity slightly. For the top point this, combined with the lower total shear strength, leads to an early sliding failure during pullout. Gauss points 5024-1 and 5024-3 are located at mid-height on the outer and inner positions respectively. Here the profiles are very similar but the more rapid rise in vertical shear stress during pullout causes the outer point to fail first.





**Figure 8-51 - Stress Histories for Interface Gauss Points 5024-1 and 5024-3**

For these responses there is a long period of sliding before the analysis terminated due to non-convergence. This is because the parameters set for the Coulomb interface model were defined such as to allow the interface to behave perfectly plastically beyond the frictional strength of the interface. As stated previously, without further information on the nature of the anchor-concrete interface during sliding failure, it is difficult to judge whether or not this behaviour is realistic. However, one indicator that it may indeed be incorrect is found in the load-displacement response (Figure 8-52). The graph shows the response for the current octagonal bolt model with the frictional interface and an expansion pressure equal to ten times the initial priming pressure and also the response for a similar octagonal bolt model but without the expansion pressure and with a fully bonded interface. The two responses are initially very similar despite the differences mentioned. This confirms that for a sufficiently high expansion force the anchor-concrete interface acts as though it was fully bonded. Also marked on the graph is the point at which all Gauss points were reported as sliding. It can be seen that even beyond this point the tensile force resisted by the anchor increases. This is incorrect behaviour as the load should either remain constant or decrease. Further investigation would be required in

order to determine the reasons for this result but, again, this would be better approached with information on the actual response of sliding anchors. Instead this shortcoming is acknowledged and behaviour of the anchor when sliding at all points is judged accordingly.

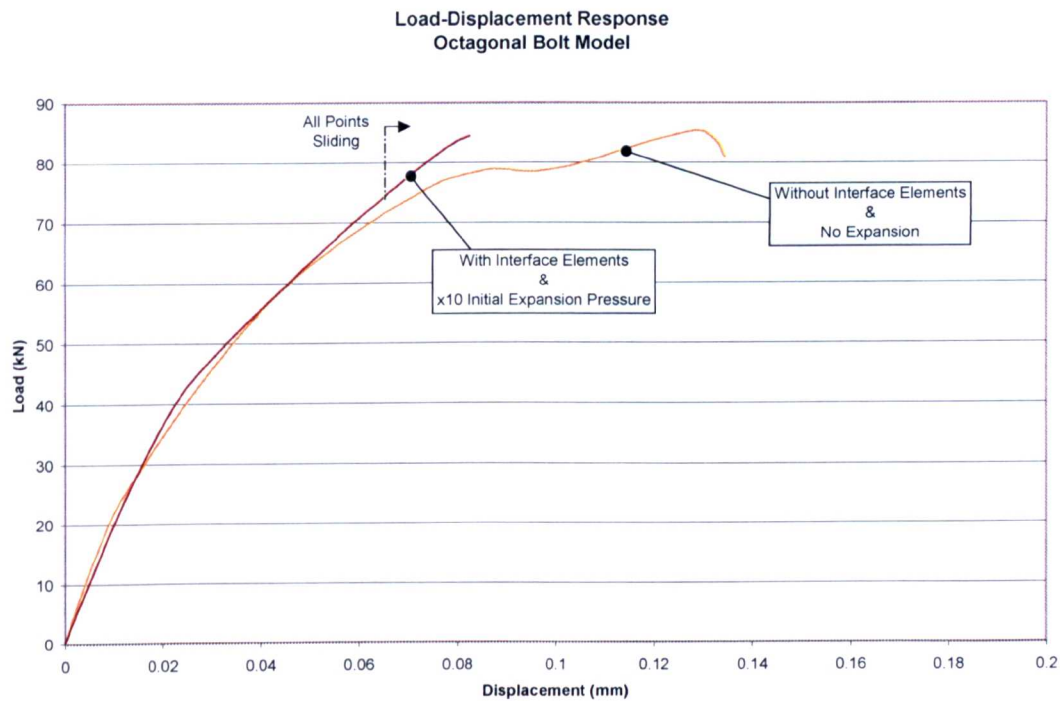


**Figure 8-52 - Load-Displacement Response for Octagonal Bolt Models**

The octagonal bolt model with the higher expansion pressure produced the most extensive cracking of any of the expansion models analysed so far. The contour plot below shows crack strain on the left and maximum principal strain on the right for a cross-section through the middle of the model (Figure 8-53).

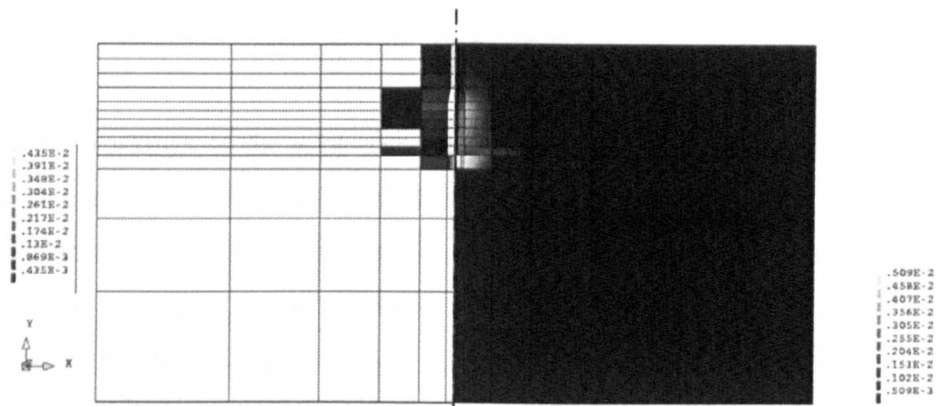


**Figure 8-53 – Octagonal Bolt (x10 Expansion), Crack Strain & Principal Strain**

The plot shows both radial cracking around the anchor caused by expansion pressures but there is also a crack below the anchor which is the beginnings of a concrete cone failure. It therefore seemed promising that, with a suitable expansion force, a concrete cone failure could be achieved rather than a sliding one.

It has been shown that the current octagonal anchor model produced the desired level of expansion without any significant detrimental shear forces arising from the approximate nature of the anchor geometry or the modelling of the expansion. Also, via superposition it was possible to mould the normal force profile into the desired form. Up until this stage the desired profile had a roughly uniform expansion pressure however, in the absence of specific knowledge of the true stress profile for an expansion anchor, this profile had been an arbitrary choice. In order to arrive at a more realistic profile it was necessary to consider alternative methods for modelling the kinematics of the anchor expansion.

### **8.7 Kinematic Model For Anchor Expansion**

The combination of structural interface elements and the Coulomb Friction Model satisfy the requirement for a material model with which to simulate the anchor-concrete interaction. The second requirement for modelling expanding anchors is a suitable kinematic model of the expansion itself. Before proposing suggestions it is worth re-examining the mechanics of the anchor in more detail.

In essence the workings of the expander mechanism are simple. If it is assumed that the expansion sleeve is restrained in the axial direction but free in the radial direction then a vertical displacement of the bell will result in an opening of the expander leaves. Such a displacement of the bell is caused either by the vertical displacement of the anchor head or a rotation of the head so as to induce the displacement via the threaded connection between bell and bolt. In this arrangement, if interfaces within the anchor bolt are assumed frictionless, the relationship between bolt head displacement (axial or rotational) and expansion is linear (assuming minimal deformation of the steel). However, in reality the concrete provides resistance against expansion. Thus the relationship between anchor head displacement and expansion additionally becomes a function of radial confinement and, since concrete is a non-linear material, this is a non-linear relationship. A second complication is that slippage of the expansion sleeve or vertical displacements in the concrete will lead to a vertical displacement of the anchor head with no associated increase in expansion. In fact, such a displacement may lead to a decrease in expansion. Ideally a kinematic model for anchor expansion must be able to capture all of the above behaviour.

Previous modelling of anchor expansion had employed the concept of tied displacements or kinematic restraints (Chapter 4) with some limited success. The main weakness of the method was in prescribing the radial displacements of the leaves to be a function of the axial displacement of the anchor head. Situations such as rigid body displacement of the anchor due to sliding or displacement of the concrete resulted in a spurious expansion of the anchor. Additionally, this approach is not able to account for the level of radial confinement the concrete provides to resist expansion. Indeed, the previous modelling



using tied displacements had assumed no resistance from the concrete. However, it was proposed that many of these shortcomings could be overcome by basing expansion on some relative displacement of the anchor bolt rather than the absolute displacement of the head as used previously.

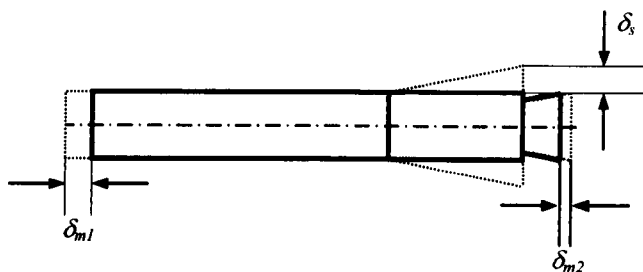


**Figure 8-54 - Kinematic Restraints Based On Relative Displacement**

A relative displacement, rather than an absolute one, may be achieved by defining the displacement of the slave nodes to be a function of a pair of master nodes.

$$\delta_s = C_{m1} \delta_{m1} - C_{m2} \delta_{m2} \quad \text{Equation 8-16}$$

where  $\delta_s$  is the displacement of the slave node,  $\delta_{m1}$  and  $\delta_{m2}$  are the displacements of the master nodes and  $C_{m1}$  and  $C_{m2}$  are the corresponding weighting factors applied to the master node displacements. The obvious choice of master nodes is the centre of the anchor head and the centre of the bottom of the bell (Figure 8-54). In this way any rigid body translations of the anchor would not result in expansion. However, this method is still insensitive to confining pressures. The extreme case being encountered where confinement prevents expansion and thus tensile loading of the anchor would lead to straining of the bolt. This tied-displacement model would still predict an expansion due to the relative displacement of the anchor head relative to the bell.

The most rigorous way of simulating anchor expansion is to explicitly model each of the anchor bolt components and their interaction. This requires the use of a contact model. The stability and robustness of the DIANA framework was such that an alternative

framework was required for such an analysis. ADINA v8.1 [ADINA (1998)] provided an appropriate contact model with the ability to apply a Coulomb friction law to the contact surface. The drawbacks were that the version of the software available only allowed for 2D analysis and the material model for concrete was plasticity based rather than of the smeared crack type. This second point meant that modelling of the concrete would not benefit from features such as material orthotropy or from the experience gained in investigating the behaviour of the Total Strain Based Crack Model. A compromise solution was to use contact modelling in ADINA to provide an insight into the contact stress profile created between expander and concrete. This was done using the Coulomb Friction Model for the contact interface but a linear-elastic model for both steel and concrete. The aim was then to replicate this stress profile in the octagonal bolt model in DIANA using the superposition method as above. This approach meant that the interface behaviour could not evolve during the course of the analysis as a result of the action of the expander mechanism. For example, an increasing expansion pressure could not be created due to tensile stresses in the anchor during pullout. Instead the profile would act as a snapshot of one particular stage in the expansion process. The most logical choice was to select the stress state relating to the priming of the anchor when it is initially installed. The priming process requires the anchor head to be turned until a specific torque is achieved. This induces an expansion force in the expander and hence mobilises an initial frictional shear resistance in the anchor-concrete interface.

The first stage in the process was to relate the torque moment as specified in the anchor installation guide to the corresponding tensile force created in the bolt of the anchor. For there to be any resistance to turning, the head of the bolt and components below (washer, plate, etc) must be in contact with each other and the top of the concrete (Figure 8-55).

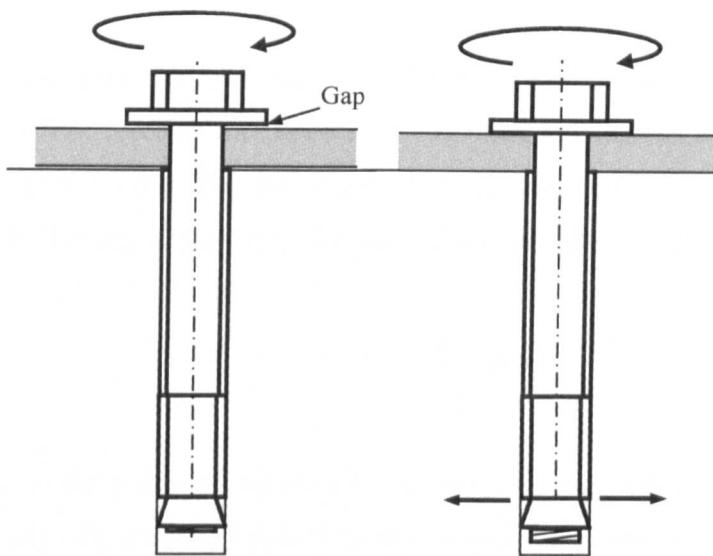


Figure 8-55 - a) Unresisted Turning b) Resistance to Torque

The initial tight fit of the anchor in the hole prevents slipping as the subsequent turning causes the bell to press against the leaves hence inducing an expansion pressure. At this stage the turning force applied to the bolt head must be resisted by circumferential shear stresses on the expander-concrete contact (Figure 8-56a).

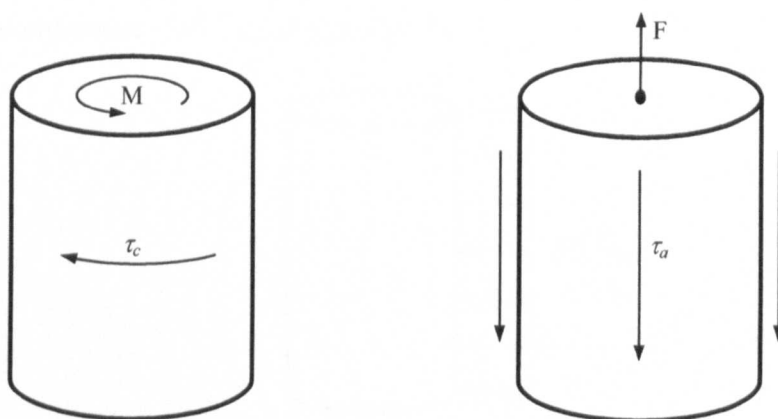


Figure 8-56 - Interface Shear Stresses Induced By a) Torque, and b) Tension

The magnitude of this stress is calculated as:

$$\tau_c = \frac{M}{r_{\text{expander}} A}$$

Equation 8-17

where  $M$  is the applied torque,  $r_{expander}$  is the radius of the expander and  $A$  is the expander surface area. The force of the bell on the expander also causes axial shear stress on the interface (Figure 8-56b). The translation of torque into vertical force occurs on the thread of the bolt-bell contact. Knowing the pitch of the thread the force is calculated thus:

$$F = \frac{M}{r_{thread}} \tan \theta$$

Equation 8-18

where  $r_{thread}$  is the radius of the thread ring and  $\theta$  is the pitch of the thread. Axial shear force is simply calculated as force  $F$  divided by expander area,  $A$ .

The combination of these two shear stresses gives the resultant shear stress on the interface. The observation was made that the anchor must mobilise sufficient shear resistance to prevent the anchor from turning during priming. Therefore it was possible to determine the required normal stress via the Coulomb friction relationship. In the case of the M12 SafetyPlus anchor the specified torque for priming is 80Nm [Rawl Fixings (1997)]. This equates to a normal stress of  $7.44 \text{ N/mm}^2$  or, as expressed as a force per mm around the circumference,  $335 \text{ N/mm}$  (Figure 8-57).

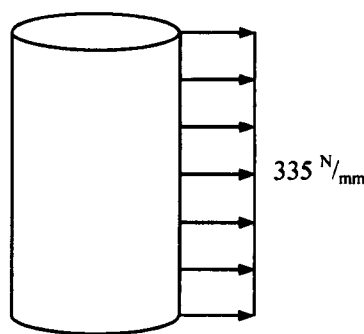


**Figure 8-57 - Expansion Pressure Derived From Priming Torque**

8.8 Contact Modelling of Anchor Mechanism

The ADINA contact model was constructed in 2D using a combination of linear, 4-noded, plane-stress elements and quadratic, 3-noded, line contact elements. The higher order used for the interface allowed for a more detailed reporting of the stress state and also provided better compatibility with the stress output from DIANA’s interface elements. The diagram below shows the position of the Gauss points in DIANA and points in ADINA where the contact variables are reported (Figure 8-58).

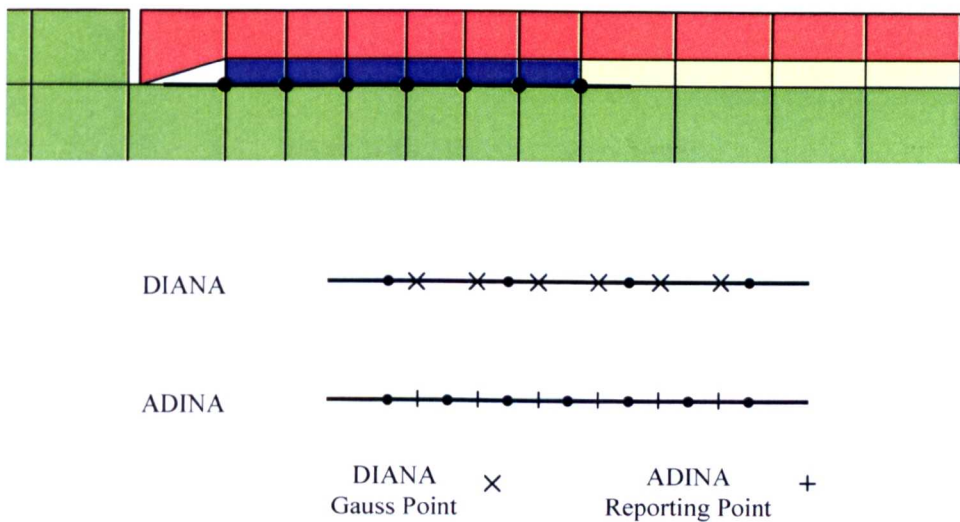
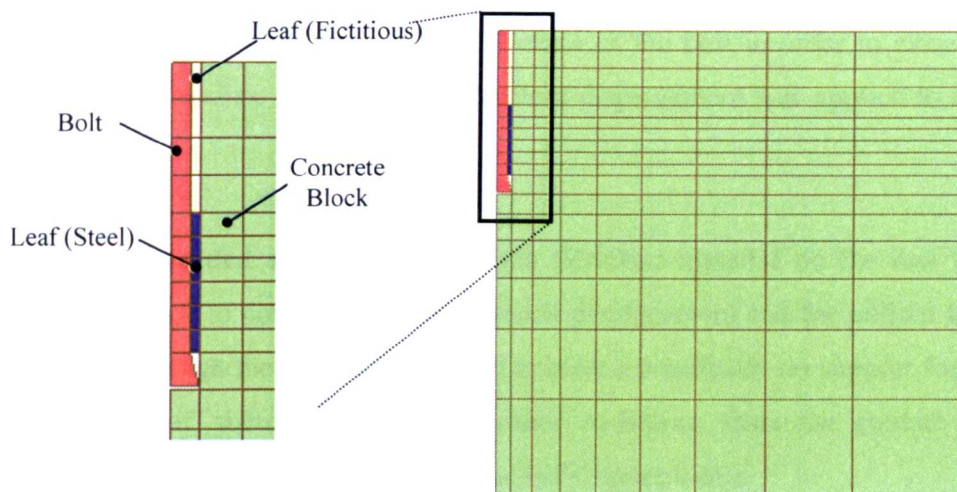


Figure 8-58 - Comparison of Reporting Points for DIANA & ADINA Interfaces

Outwardly the FE mesh for the ADINA model looked almost identical to the previous 2D pullout model with the sliding interface. The key difference was that the model was made up of 3 independent bodies; the bolt, the leaf and the concrete block (Figure 8-59).



**Figure 8-59 - ADINA Contact Model**

The diagram shows that the leaf body is separated into a steel section representing the leaf itself and a section of fictitious material above. This was done for computational reasons. The intention was for the leaf to be free of boundary constraints and only subject to external forces applied to it via contacts with the bolt and concrete. However, the software was unable to allow for this. Instead a section of fictitious material with a very low stiffness was used to connect the leaf to a fully fixed boundary at the top of the body. In practice this has a negligible effect on the leaf behaviour. Other boundary constraints were as before with a symmetry constraint on the left edge and the base of the block being fully fixed. Contact elements were placed along the right-hand edge of the bolt, both vertical surfaces of the steel part of the leaf and along the vertical surface of the hole in the concrete. Initially a very small gap (0.01mm) was left between the each of the 3 bodies since having the surfaces in contact from the start of the analyses produced convergence problems. Finally, care was taken to ensure the angle of the bell at the bottom of the bolt matched that of the real anchor.

All materials were modelled as being linear-elastic for reasons stated above. However, the contact elements along the steel-concrete contact made use of a Coulomb friction model. The initial cohesion and friction angle values were set to match those of the Coulomb interface model used in DIANA. The steel-steel contact between leaf and bolt



was assumed to be frictionless. Loading was performed in two stages. Firstly a horizontal displacement was applied to the left-hand surface of the bolt in order to close the gaps between the three bodies. Subsequently a pullout displacement was applied to the top of the bolt.

The analyses proceeded as expected with the fictitious material on the leaf providing negligible resistance to both the initial horizontal displacement and the pullout thereafter. Interestingly, although the fictitious material provided practically no support for the steel portion of the leaf, there was sufficient shear resistance from the contact with the concrete to prevent any vertical sliding of the leaf (Figure 8-60)

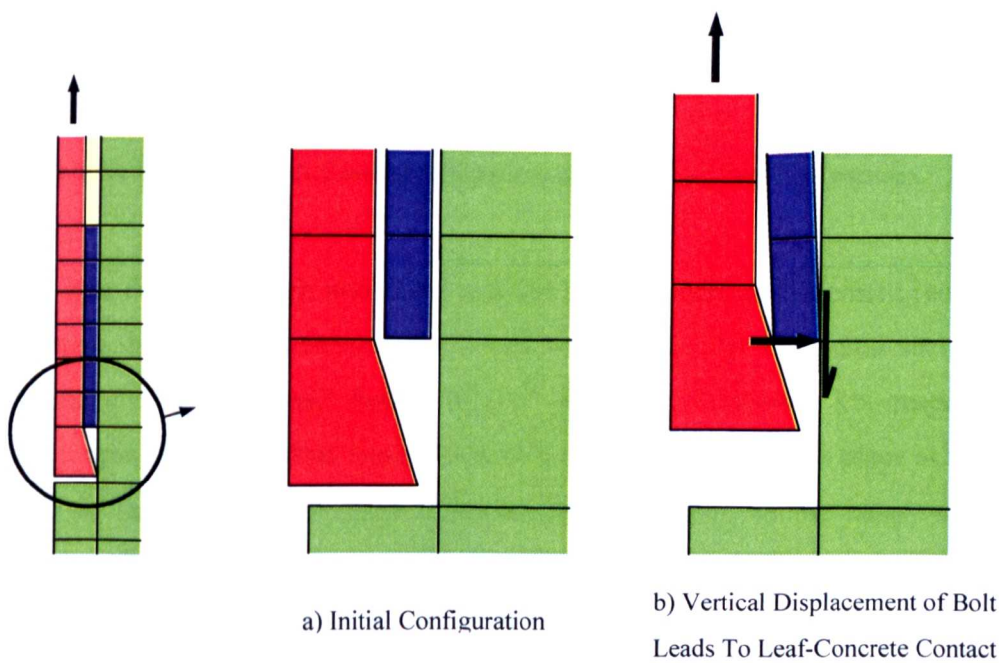


**Figure 8-60 - Displacement of Anchor Components Leading to Mobilisation of Frictional Resistance**

The aim of the analysis was to produce a total expansion force that was equal to that caused by priming the anchor. The graphs below show the horizontal displacements for the leaf and concrete and also the profile of normal tractions produced when this desired expansion level was attained (Figure 8-61).



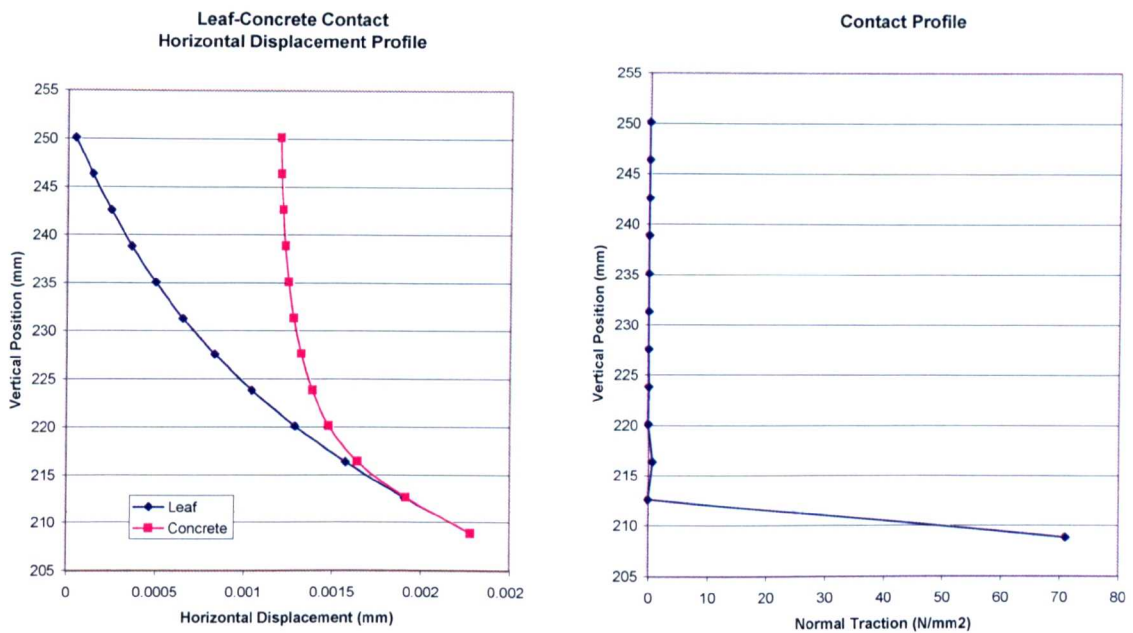


**Figure 8-61 - a) Leaf & Concrete Displacement, b) Contact Surface Traction**

As can be seen from the graph above the amount of horizontal displacement required in order to create the desired expansion force was very small. The associated anchor head displacement and pullout load was  $1.00 \times 10^{-2}$  mm and  $1.14 \times 10^{-2}$  kN respectively. Therefore, judging by the pullout load, it can be seen that priming takes place at the very lowest end of the load-displacement response for the anchor, in the zone where the overall structural response is indistinguishable from the linear-elastic response. Thus the use of linear-elastic material types can be considered valid.

One point of concern was that only a single pair of contact elements actually made contact thus raising questions as to the true extent of the surface contact. To investigate this further a second model was analysed with 20 contact elements on each side of the leaf-concrete interface. This compares with 6 on the previous model. This again resulted in a single point of contact and almost identical leaf and concrete horizontal displacement profiles. For an anchor head displacement of  $1.00 \times 10^{-2}$  mm, the normal traction profile differed in that the peak traction at the contact point was now almost  $300 \text{ N/mm}^2$ . This was expected due to the reduced contact area. It was considered that further refinements in the

discretisation of the contact surfaces would produce an ever-smaller contact area and a singularity in the stress profile. Of course, in reality this would not be the case. However, although the leaf may initially make contact at one point at the bottom, the high compressive stress created will cause highly localised crushing of the concrete. This is the beginning of the keying effect mentioned previously and will lead to a larger contact area. However, in order to model such small-scale behaviour a very fine mesh would be required in conjunction with a suitable material model for the crushing of concrete. Such refinements were deemed to be outside the scope of this contact analysis. In particular they would present problems in mapping the stress profile back to the DIANA model. Instead the current contact model mesh was retained.

The mapping of the stress profile from the ADINA contact analysis back onto the DIANA interface model was carried out by splitting the expansion loading on the anchor expander in DIANA into 14 separate load cases (7 vertical positions and separate cases for ‘inner’ and ‘outer’ nodes). Once again, by using the theory of superposition it was possible to scale and combine these loadcases such that the required result was achieved. The process of determining the correct scaling factors is detailed below.

The stress profiles created by each of the loadcases were recorded in vectors  $\mathbf{r}_1$  to  $\mathbf{r}_{14}$  (Figure 8-62).

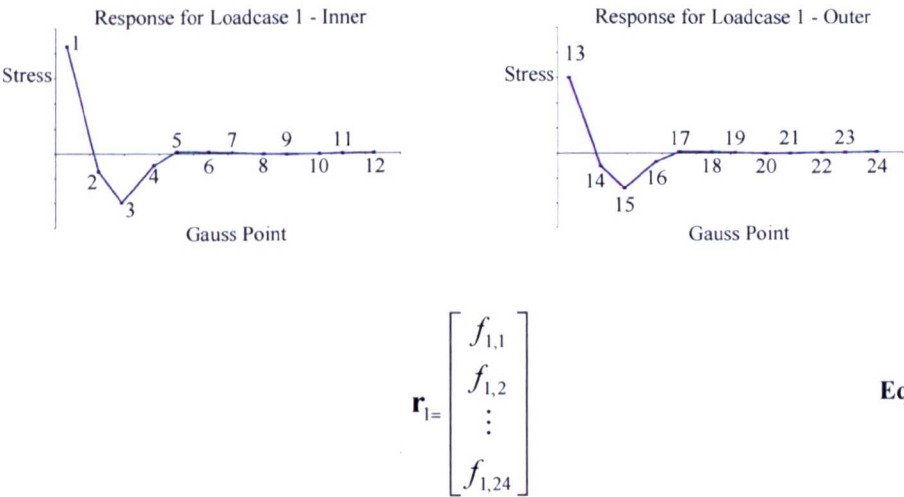


**Figure 8-62 - Storage of Stress Response Data in Response Vector, r**

and stored in the response matrix, **R**.

$$\mathbf{R} = [\mathbf{r}_1 \quad \mathbf{r}_2 \quad \cdots \quad \mathbf{r}_{14}] \quad \text{Equation 8-20}$$

The target profile, as provided by ADINA, was stored in the vector **T**.

$$\mathbf{T} = \begin{bmatrix} t_1 \\ t_2 \\ \vdots \\ t_{24} \end{bmatrix} \quad \text{Equation 8-21}$$

In order to achieve the target profile the 14 loadcases must be multiplied by scaling factors,  $c_n$ , stored in the vector, **C**.

$$\mathbf{C} = \begin{bmatrix} c_1 \\ c_2 \\ \vdots \\ c_{14} \end{bmatrix} \quad \text{Equation 8-22}$$

Leading to simply:

$$\mathbf{RC} = \mathbf{T} \quad \text{Equation 8-23}$$

However, since the response matrix is not symmetrical it is not possible to solve for **C** by inverting **R**. Instead, the equation was solved by pre-multiplying both sides by  $\mathbf{R}^T$ .

$$\begin{aligned} (\mathbf{R}^T \mathbf{R}) \mathbf{C} &= \mathbf{R}^T \mathbf{T} \\ \overline{\mathbf{R}} \mathbf{C} &= \mathbf{R}^T \mathbf{T} \\ \mathbf{C} &= \overline{\mathbf{R}}^T (\mathbf{R}^T \mathbf{T}) \end{aligned} \quad \text{Equation 8-24}$$

The scaling coefficients were applied to the DIANA model and a linear-elastic analysis performed in order to check the stress profiles on the interface (Figure 8-63). It can be seen that the fit to the ADINA profile is very good. The small differences seen are due to the fact that the ADINA reporting points and DIANA Gauss points were not located at the same positions. Therefore linear interpolation was used to derive suitable target stresses. Also, the system of equations solved above is over defined in that there are more equations than unknowns. Therefore the solution produced is a form of average that best fits the target points. Although the target was defined only in terms of normal stresses it can be seen from the graph below that the vertical stress profile produced in DIANA very closely matches that of the ADINA model. This result acts to confirm the equivalence of the contact and interface models under these conditions.

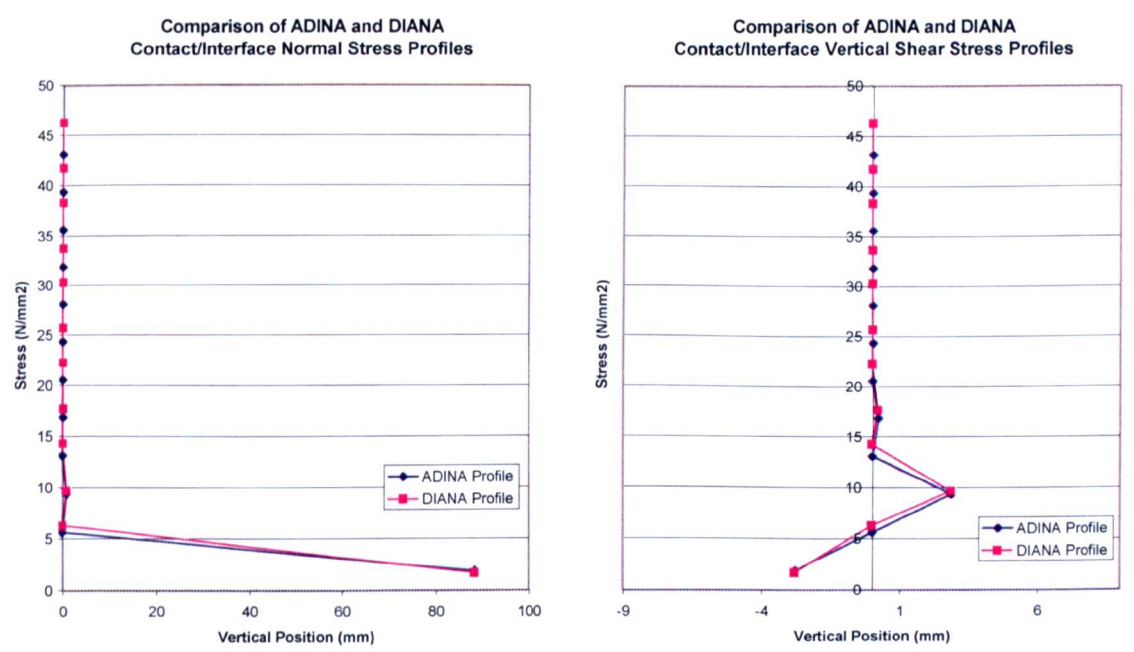
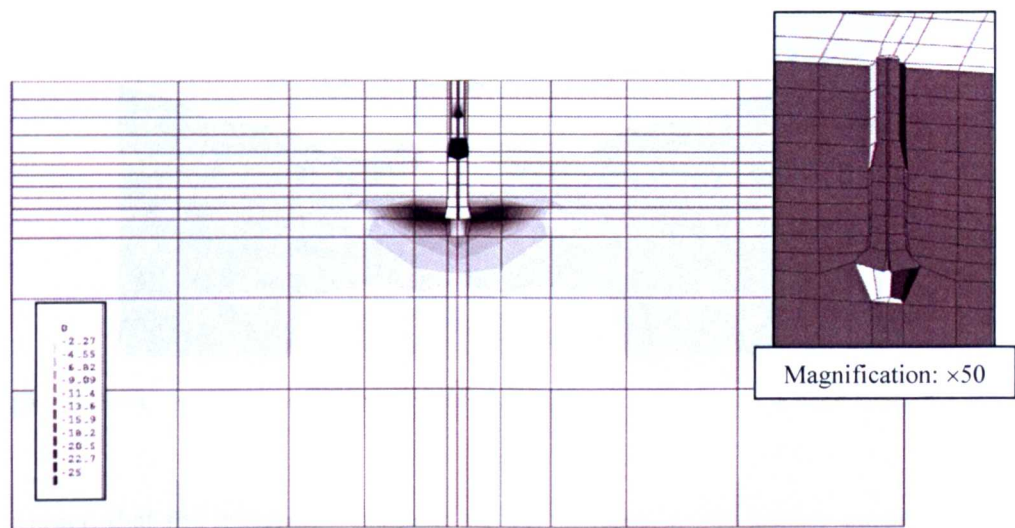


Figure 8-63 - Comparison of ADINA and DIANA Interface Stress Profiles



A full non-linear analysis of the expansion stage was then performed. Convergence of the solution process via the Newton-Raphson scheme was good and required only 15 load steps in order to apply the necessary load.



**Figure 8-64 - Minimum Principal Stress Contour Plot for Primed Anchor and Displaced Shape of Primed Anchor (insert)**

Figure 8-64 shows a contour plot for the minimum principal (compressive) stresses for the fully expanded anchor. It shows the higher compressive stresses are localised around the bottom of the expander as expected. There is also a lack of symmetry of the compressive stress zone about the horizontal axis. This is due to the fact that because of the geometry, the concrete below the hole is stiffer and therefore attracts more stress. There may also be a slight effect of mesh bias. The insert shows the displaced shape of the anchor in more detail. It can be seen that the outer profile of the expander roughly follows the parabolic shape seen in the ADINA contact analysis.

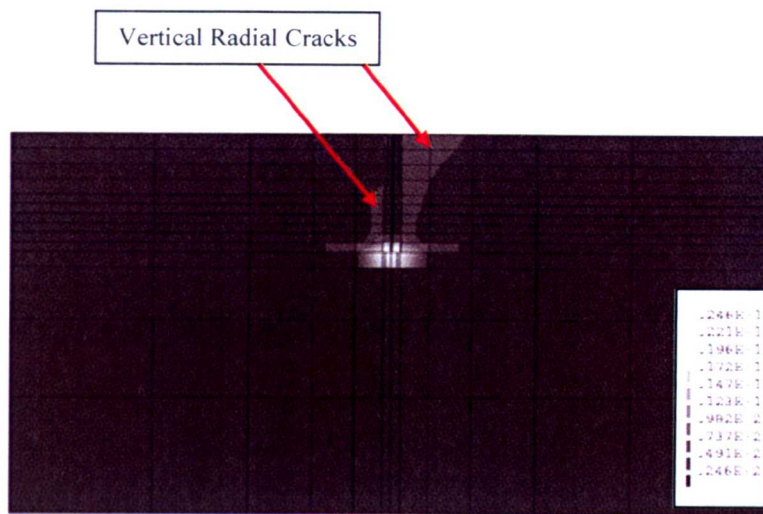


**Figure 8-65 – Cross-Sectional Contour Plot of Maximum Principal Strain for Primed Anchor**

It was noted that the expansion process during priming of the anchor caused significant tensile stresses. These were generated in the circumferential direction and result in radial cracks as seen in Figure 8-65. This is realistic to expect that priming of the real anchor would cause similar minor cracking.

The next stage of the analysis is pullout of the anchor. In reality tensile stresses applied to the head of the anchor cause further expansion pressures. However, this numerical model did not simulate this behaviour. Instead the pullout analysis was run with a range of different initial expansion pressures between one and ten times the priming pressure applied before the pullout itself. In each case the expansion loadcase was performed without any problems with convergence. However, from the first step of the pullout loadcase, non-convergence problems arose in the solution process. Initially a Newton-Raphson scheme was used with a maximum of 50 iterations allowed and the tolerance based on internal energy set to  $1 \times 10^{-4}$ . To begin with the convergence process continued slowly but steadily. However, at some point the process began to oscillate (recognised by a repeating pattern of out of balance energy states). Eventual failure occurred when the maximum number of iterations was reached. No reason for this behaviour was apparent but certainly it is not unexpected for the transition from one loading regime to a very different one to cause significant changes in the stress state and hence lead to difficulties

in converging on an equilibrium state. In order to overcome this difficulty the displacement step size for the pullout loadcase was reduced by a factor of five to a value of  $5.00 \times 10^{-4}$  mm. The solution scheme was changed to a Quasi-Newton Method (also known as the Secant Method). Generally convergence is slower with this method than the full Newton-Raphson scheme so the maximum number of iterations was increased to 100. With these changes the analyses converged although the solution time was much greater than that of the previous expansion analyses.

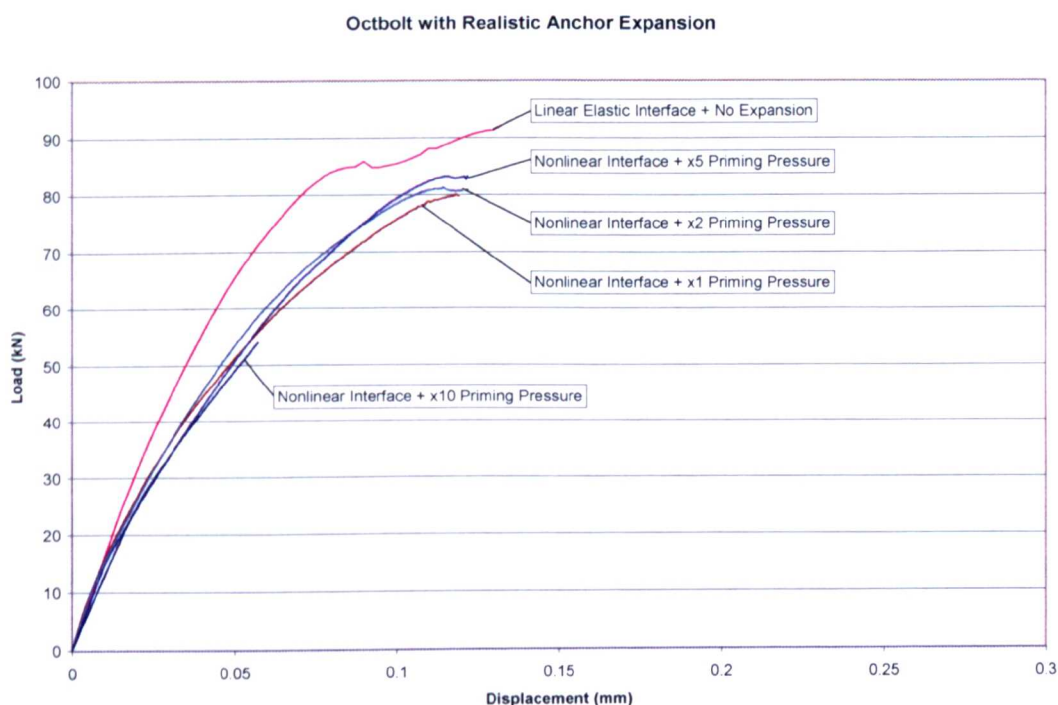


**Figure 8-66 - Load Displacement Response of Octagonal Anchor Bolt with Varying Levels of Expansion Pressure Based on Contact Analysis Expansion Stress Profile**

As it can be seen for the load-displacement graph above (Figure 8-66) that the analysis with an initial expansion pressure of 10 times the priming pressure terminated before reaching peak load. This was again due to non-convergence and attempts to further the analysis failed.



For all the expansion levels considered for the above analyses there was slipping reported at the majority of the Gauss points right from the first step of the pullout loadcase. This was to be expected since the normal stress across the interface at these points was approximately zero after expansion. By the second step all but the bottom Gauss points were reported to be slipping. This state remained until the analyses terminated due to non-convergence. Therefore the failure cannot be attributed to a sliding failure.

The load-displacement graph also shows very similar responses for the different expansion levels with the greater expansion levels producing slightly higher peak loads. However, all responses are softer than that of the linear elastic interface result. This is because the smaller load transfer zone between the anchor expander and the concrete resulted in a higher concentration of tensile stress and hence lead to increased softening of the concrete as compared to the linear-elastic interface model with load transfer over the whole depth of the expander. This effect is less influential on the ultimate load as once the crack has travelled some distance from the anchor the effect of the smaller load transfer zone is not as great.

It is interesting to note that in the initial stages of pullout increasing expansion pressure is associated with decreasing stiffness (Figure 8-67). This may be because the higher levels of expansion create larger radial cracks and hence lower levels of confining pressure. It is also worth noting that detailed observations such as the ones above are only made possible by the use of numerical modelling.

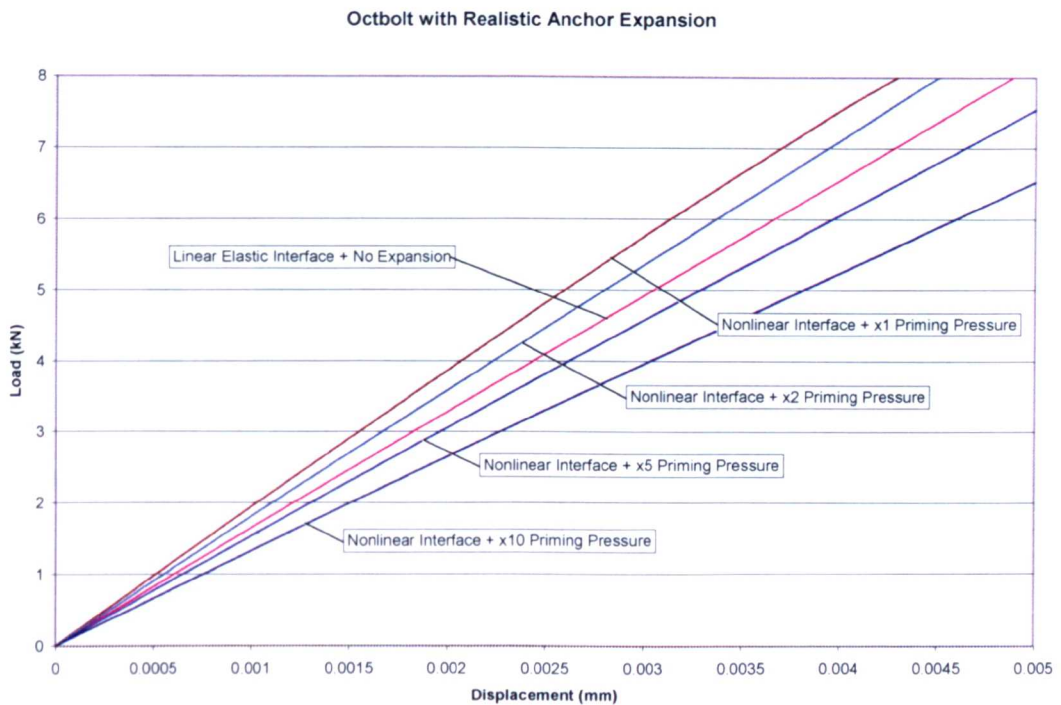


**Figure 8-67 - Load-Displacement Responses for Varying Levels of Expansion Pressure (Initial Pullout)**

The contour plot of maximum principal stress shows that the failure mode for the anchor bolt would have been via concrete cone failure (Figure 8-68). Both initial cone formation and major radial cracks are present. This behaviour is common amongst all the initial expansion pressures considered.

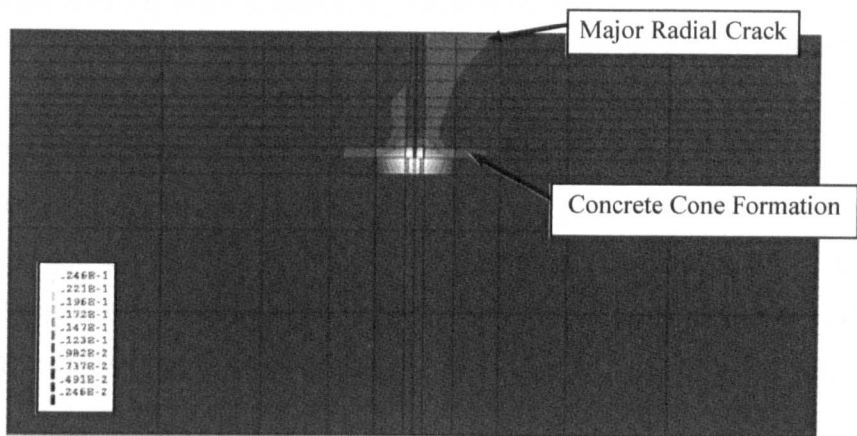


**Figure 8-68 - Maximum Principal Strain at Peak Load for Octagonal Bolt with x5 Expansion Pressure**

**8.9 Edge Effect Study with Expanding Anchor Model**

The purpose of the expansion of the anchor is to generate enough frictional resistance across the anchor-concrete interface in order to resist the pullout force. To resist this expansion force the concrete block must provide sufficient radial confinement. However, the close proximity of a free edge results in less effective confinement and hence affects the expansion anchor behaviour. Possible outcomes considered included splitting or breakout failure on the free side during expansion, lower initial stiffness of the anchor during pullout or lower failure load for the anchor during pullout (Figure 8-69).

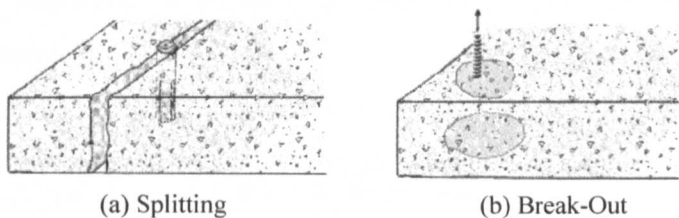
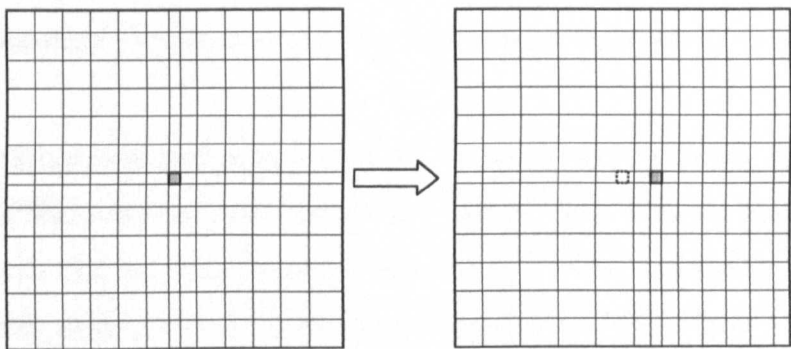


**Figure 8-69 - Possible Failure Modes due to Expansion of Anchor**

Initially the study considered 4 different edge distances (300mm, 200mm, 180mm, 140mm and 100mm) and a constant expansion force of  $\times 5$  the priming expansion level. This level of expansion was chosen as the expansion force during pullout is higher than the priming level and analyses using this value had produced good results. The mesh distortion method detailed in Chapter 4 was used to create the required finite element meshes (Figure 8-70). This had the advantages that it was fast, preserved the mesh topology and also provided smaller element sizes in the most critical areas of the model.



The analyses were run as before with the same selection of step size, solution method and maximum number of iterations. However it was found that once again convergence problems were encountered in the pullout phase of the analysis. In some cases a further reduction of the step size succeeded in progressing the analysis further but for the 200mm edge distance analysis failure occurred on the first step of pullout. The 180mm analysis terminated on the second step and the 100mm analysis terminated at just under 25% of the peak load. In all cases the bottom ring of Gauss points on the interface were not reported as sliding therefore a sliding failure of the interface can be ruled out. Also, in none of the cases was there significant cracking of the concrete so breakout or splitting failures did not take place.

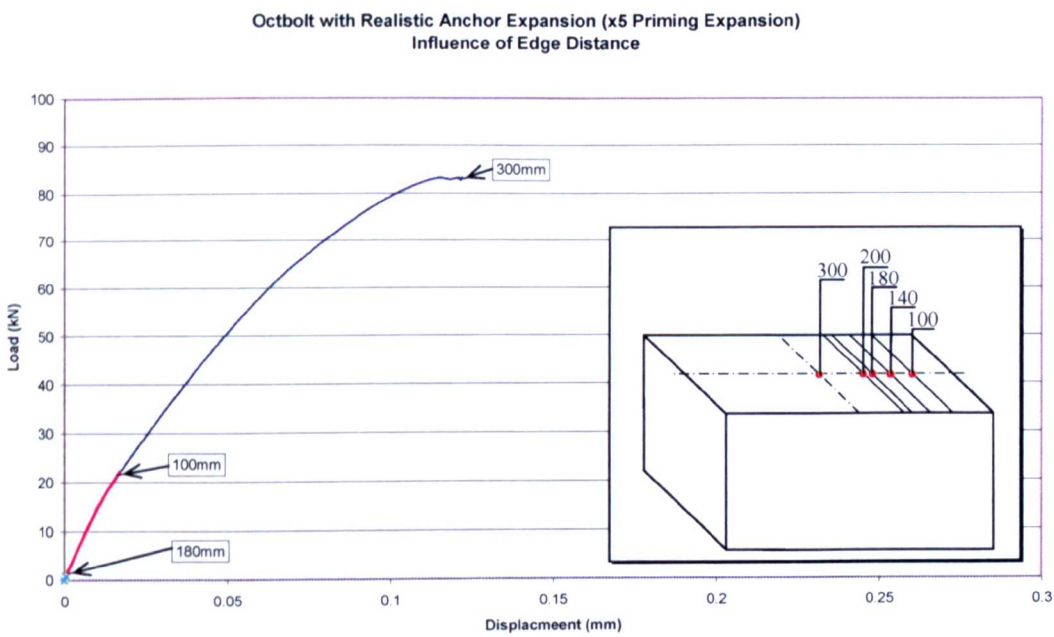


**Figure 8-71 - Load-Displacement Response for Expanding Anchor Placed at Various Edge Distances**

From the load-displacement responses produced it can be seen that there is no apparent difference in stiffness between the 100mm and 300mm edge distance analyses (Figure 8-71). This shows that the expansion behaviour was insensitive to the edge distance. For the previous edge effect study in Chapter 7 no divergence of the 100mm response from the 300mm one was noticed until the applied tensile load was in excess of 50% of the

failure load. It is expected that if the analysis for 100mm edge distance presented here had progressed further a similar behaviour would have been seen.

It is unfortunate that numerical difficulties made the above study inconclusive. In addition to examining the effects of the given expansion pressure on anchors at different edge distances it would also have been interesting to look at how different levels of expansion affect these responses. In particular a study could have been performed whereby for each edge distance the expansion pressure was continuously increased until it lead to failure. In this way it could be determined if higher expansion pressures are permissible for large edge distances and for low edge distance cases the pressure should be limited to a lower level.

The exact cause of the lack of convergence of the solution remains unknown and without more detailed information on the internal states within the FE program it is difficult to investigate further. However the Total Strain Based Crack Model had proven to be a stable and robust constitutive model for other applications. It is possible that the interface model is rather less robust and this may have lead to the problems encountered. Another possibility is suggested by the oscillation in the values of out-of-balance energy reported at the end of each iteration. This may be due to an interaction between the cracking and sliding processes. An increase in crack opening will relax the normal stresses across the anchor-concrete interface. However, this action will promote an increase in sliding. Sliding, in turn, will serve to reduce the tensile stresses across the crack plane and thus arrest the cracking process. Of course, if the cracking process does not progress, the normal stresses across the anchor-concrete interface remain high, tensile stresses across the crack plane increase and the series of events above is repeated. A circular dependency such as this will lead to the type of oscillations seen in the reported out-of-balance energies. It is possible that there are other options in terms of solution method, step size, etc that would overcome such problems and lead to a more stable (although perhaps slower) analysis.

### 8.10 Summary

In this chapter the modelling aspects of an expanding anchor were examined. The properties of the anchor-concrete interface were modelled using structural interface elements with a Coulomb Friction Model defining the relationship between normal and shear tractions and displacements. Sensitivity studies were performed on both single block and 2D anchor pullout problems. Attention was paid to the stress histories of the interface elements in order to give a more detailed understanding of the factors concerned. 3D anchor problems were then analysed. Problems of spurious shear stresses were identified. Firstly, nonalignment of the nodal displacement vectors of the inner surface of the interface elements with respect to the outer ones lead to high, horizontal shear stresses. Alternative expansion loading patterns to reduce this misalignment helped but it was found that using an anchor cross-section that was closer to being circular provided a more effective solution to this problem. Secondly, unexpectedly high vertical shear stresses attributed to the Poisson's effect in the expander were found. Radial expansion of the leaves led to a shortening of these sections in the vertical direction. This effect was addressed by reducing the Poisson's Ratio to zero for the expander. The stress profile for expansion stresses across the interface was manipulated by decomposing the expansion loading pattern into a number of individual loadcases. Linear-elastic analyses of each of these in turn produced a set of profiles that were combined using the theory of superposition. However, in order to determine the appropriate target stress profile more detailed modelling of the expansion kinematics was required.

Various modelling techniques for the kinematic modelling of anchor expansion were considered. The tied-displacement method used in Chapter 4 was rejected as it was shown that expansion of the anchor was governed by a relationship between tensile stress in the bolt and expansion stress on the expander rather than between bolt displacement and expansion displacement. Instead, modelling the expansion mechanism as a contact problem was deemed the most satisfactory solution. However, it was not practical to perform such an analysis in the current modelling framework given limitations that this framework presented. An alternative method of obtaining the correct contact stress profile via contact modelling using an alternative framework and superimposing those



stresses on the current problem was adopted. The contact problem consisted of individual bodies representing the bolt, leaves and concrete block. The stress profile resulting from the analysis of the problem was successfully mapped into the existing, non-contact model by means of the super-position method mentioned above. A lack of robustness in the FE program lead to convergence problems which prevented a study into the combined effects of edge distance and expansion level from being performed. However, with the anchor located in the centre of the block very satisfactory results were produced. An increase in stiffness and peak load associated with increasing expansion levels was shown. Also, the crack patterns produced were realistic, showing the expected radial and concrete cone cracks.

## CHAPTER 9

### Sequentially Linear Orthotropic Fracture Model

In the previous chapter attempts were made to model the pullout of an expanding anchor. Non-linear models were used for both the concrete fracture/crushing and for the anchor-concrete interface. Applied loading was non-proportional, comprising of an expansion case followed by the pullout case. Convergence problems prevented a full and complete analysis from initial linear behaviour, through to peak load and ending with post-peak, from being produced. Reductions in displacement step size and increases in maximum number of iteration helped to some extent in furthering the analysis but failed short of the peak load. Various non-linear solution procedures were used (Full Newton-Raphson, Modified Newton-Raphson, Arc-Length, Secant [Crisfield (1991)]) but a suitably robust technique to analyse the problem was not found.

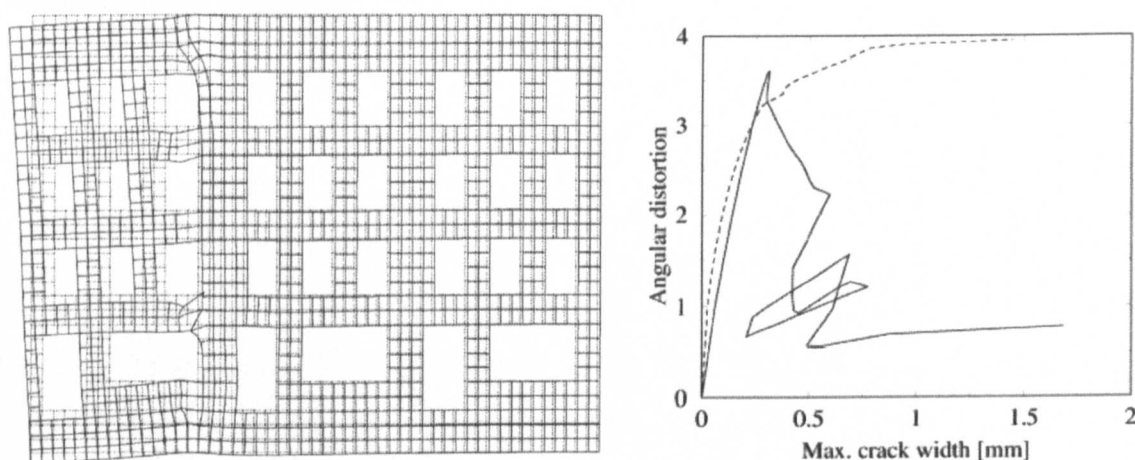


**Figure 9-1 – a) Displaced Shape of Masonry Façade Subjected to Differential Settlement, b) Angular Distortion vs Maximum Crack Width [Rots (2001)]**

Rots encountered similar problems in attempting to trace the displacement response of a large-scale masonry façade subject to differential settlement (Figure 9-1a) [Rots (2001)]. In this case the large scale of the structure meant that there was a large capacity for the storage of elastic energy. This, coupled with the low fracture energy of the masonry, lead

to a very brittle response. Four prominent snap-backs were produced as the crack jumped discontinuously from window to window (Figure 9-1b). Tracing this highly non-linear response proved to be a challenge. Both tangent stiffness and arc-length solution schemes failed when used with the Traditional Cracks Model, Rankine Plasticity Model (Chapter 3) or Total Strain Based Crack Model (Chapter 5). Only with a Discrete Crack Model and fine control using the arc-length method was it possible to partially trace the response. However this required a significant amount of work in selecting suitable parameters for the analysis and failed to detect all 4 snaps.

These are just two example of how a structural analysis may fail to produce the desired result in spite of the fact that there is nothing inherently wrong in the geometric model, constitutive model or the non-linear solution scheme employed. This chapter investigates so-called sequentially linear analysis techniques as a possible alternative to current non-linear analyses for concrete cracking problems. A basic model and associated results are presented. The model is then extended to cater for orthotropic material behaviour associated with crack planes.

## 9.1 Background

In the present case of anchor pullout it was thought that the main factor that contributed to the numerical failure was the fact that there were two possible failure modes (sliding and cracking) and that a circular dependence could arise between the two. In other models the cause of the numerical failure may be due to a convoluted load-displacement response as a result of the problem's geometry, its material behaviour or a combination of the two. Snap-through and snap-back behaviours [Crisfield (1991)] in particular require great care if a fully converged solution and complete structural response is to be obtained. If current analysis techniques fail the common approach to overcome such numerical difficulties is to propose an enhancement. Such enhancements tend to add complexities to the modelling framework so that particular behaviours are handled more effectively. However, an alternative approach is to seek a more simplistic model that is inherently free from the difficulties presented but one that is capable of capturing the complex behaviour that is of interest.

In this study so-called sequentially linear techniques were investigated. These make use of a series of linear-elastic analyses, after each of which the state of the problem is assessed and updated based on a set of failure criteria. One such example of this is lattice modelling [Vervuurt, van Mier, Schlangen (1993), Schlangen, Vervuurt, van Vliet, van Mier (1999)]. Here the structure is represented by a network of beam elements. A linear analysis is performed and the most critical beam identified based on an appropriate criterion (maximum tensile strength, bending capacity, etc). This beam is then removed and the whole procedure is repeated. The difficulties presented in this form of analysis include the determination of suitable material properties for the beam elements, choice of lattice structure (regular, irregular, etc) and achieving mesh objectivity. However the primary advantage of the technique is that because the analysis is sequentially linear there is no need for iterations and non-linear solution schemes. It follows that problems of divergence, lack of convergence and spurious behaviour are completely avoided.

Inspired by these benefits of lattice modelling, research has been carried out in an attempt to bring such advantages to F.E. continuum modelling [Rots (2001), Rots & Invernizzi

(2003)]. The advantage of this being that continuum modelling is more familiar ground and thus parameters such as material properties are more readily defined. The procedure employed is, in many ways, similar to that of van Mier's approach to lattice modelling (Figure 9-2).

The applied external load may take the form of an actual load or an applied displacement. It remains constants throughout the analysis, i.e. no load/displacement stepping is performed – the full and final load is applied from the start. Identification of the critical element is performed by finding the element whose principal stress to failure stress ratio is greatest. This is essentially an expression of the Rankine failure criterion used previously. Dividing the principal stress by the failure stress, for this element, provides a scaling factor that is applied to the global load and displacement vectors to obtain corresponding vectors relating to failure of this element. The next step of the procedure is to reduce the Young's modulus and failure stress for the element. The important point to note is that it is a reduction of these values that is performed, thus introducing softening behaviour, rather than simply a removal of the critical element. The reductions are carried out in a step-wise manner according a softening diagram (Figure 9-2(e)). Theoretically any suitable softening diagram may be chosen but in the case of Rots work a linear diagram was selected.

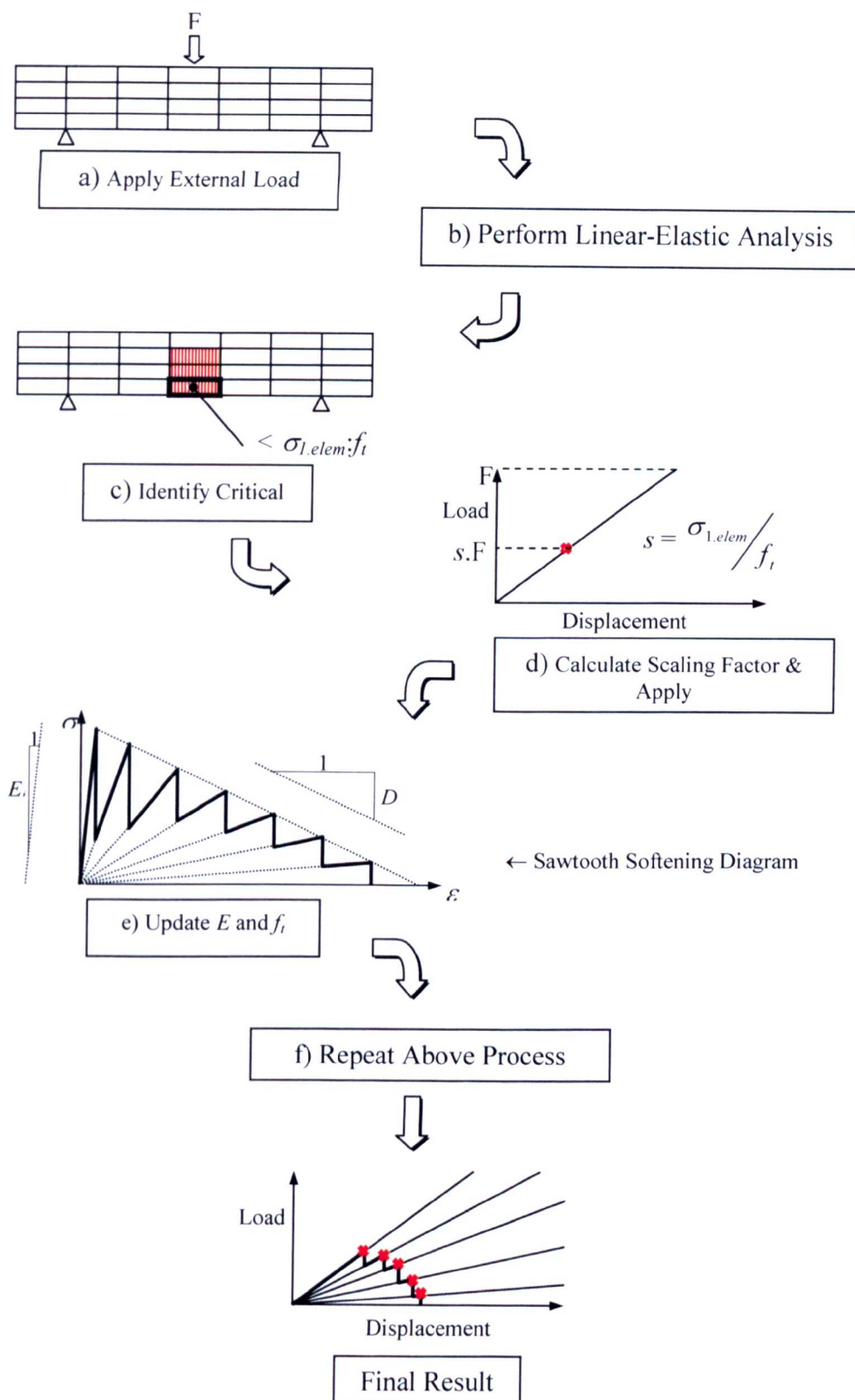


Figure 9-2 - Sawtooth Softening Model, Analysis Procedure as Presented by Rots (2001)

The softening diagram is derived from a parent curve, e.g. linear or exponential softening. For a linear parent curve, when an element is found to be critical the updated Young's modulus,  $E_i$ , is calculated as:

$$E_i = \frac{E_{i-1}}{a}, \text{ for } i = 1 \text{ to } n \quad \text{Equation 9-1}$$

where  $i$  is the current softening stage,  $n$  is the number of reductions allowed and  $a$  is the reduction factor (e.g. if  $a=2$  then the Young's modulus is halved at each stage).

The associated reduced failure strength,  $f_{t,i}$ , is calculated thus:

$$f_{t,i} = \varepsilon_{ult} E_i \frac{D}{E_i + D} \quad \text{Equation 9-2}$$

where  $\varepsilon_{ult}$  is the ultimate crack strain and  $D$  is the slope of the descending branch of the parent curve. Once the number of reductions allowed for the element is reached it is effectively removed from the problem. For convenience this is achieved by setting the Young's modulus to a very low value.

A number of variations on the above step-wise softening procedure have been proposed with the aim to improve softening behaviour and to attain mesh objectivity. However the essence of the method remains very much unchanged [Rots & Invernizzi (2003)].



**9.2 Implementation Of Sequentially Linear Model**

The work presented here is an initial study into the applicability the sequentially linear analysis technique in the finite element modelling of anchor pullout. This was carried out making use of the FE package DIANA as the modelling framework although any FE package able to solve linear elastic problems may be suitable. The DIANA source code was not available in order to make the necessary changes directly to the workings of the program but it was still possible to create the SL Model as a wrapper program that used DIANA as it analysis engine (Figure 9-3). Once again, this approach can be applied to any suitable FE package. The drawback of this approach was that the only practical way to modify the material properties of selected elements due to softening was to assign different material types to each of the elements within the problem. State variables for each element would also need to be stored within the wrapper program so that identification of the critical element was done on the basis of the updated material parameters. Although possible, this was deemed unwieldy and impractical as it required extensive changes to be made to existing input files. Instead, softening behaviour was omitted but the idea retained for future addition to the software.

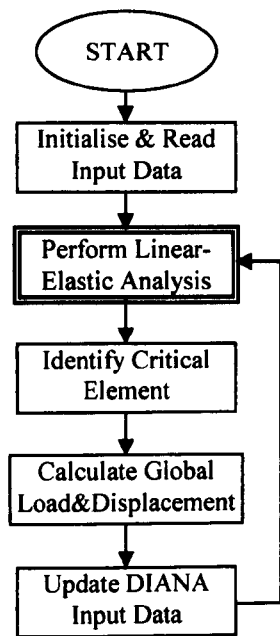


**Figure 9-3 - Interaction of Sequentially Linear Model and Chosen Finite Element Package**

Full source code is reproduced in Appendix I but details of each section and its implementation are discussed here.

### 9.2.1 Initialise & Read Input Data

Opting for straight element ‘removal’ instead of softening allowed the DIANA input files to remain practically identical therefore previous anchor problems could be reanalysed immediately using this new method. The only change was the addition of an element type for the damaged element (Figure 9-4). For this implementation of the SL Model only damage of the concrete was considered. This is in line with previous anchor pullout analyses. It was also assumed that all concrete had a tensile failure strength of  $3\text{ N/mm}^2$ .

Material Type	Young’s Modulus	Poisson’s Ratio
Steel	$2.10\times10^7$	0.2
Concrete	$3.00\times10^4$	0.2
Damaged Concrete	$1.00\times10^{-7}$	0.0

Figure 9-4 - Material Properties for Pullout Analysis

The DIANA input file is copied and the original remains unchanged throughout the analysis. It is the duplicate that is updated to account for changes in material assignments due to damage. The analysis also required a secondary data file with information specific to the Sequentially Linear analysis. A typical data file looks as follows:

```

RESTART      0
CRITERION    4
MAXSTEPS     500
CELEMS       1-716 721-1280 1297-1856
TOTALELEM    1856
NGAUSS       1
  
```

The RESTART variable allows the analysis to be continued from a previous state rather than from an undamaged state. In practice this means using the updated input data file

rather than the initial one. CRITERION is the selection of failure rule. MAXSTEPS is simply the maximum number of steps that will be performed. As there is no automated procedure for identifying which finite elements are concrete and hence available for cracking, CELEMS and TOTALELEM manually define this. Finally, NGAUSS defines how many Gauss points there are per element so that the correct amount of data is read from the analysis output file. In the above case only 1 set of stress data is required. For 2 or more Gauss points the data for each point is read and then averaged to give the average stress state of the element.

### **9.2.2 Perform Linear-Elastic Analysis**

This step was simply a matter of calling the chosen FEA program to perform the analysis. In this case DIANA was used and hence the call was:

```
system("diana datafile.dat commandfile.com")
```

where datafile.dat was the DIANA input file prepared above and commandfile.com was the analysis command file consisting of:

```
*FILOS
INITIA
*INPUT
*LINSTA
*POST
SELECT
  NODES ALL /
END SELECT
OUTPUT NEUTRA ASCII FI="ldisp"
  DISPLA
  FORCE REACTION
END OUTPUT
OUTPUT TABULA FI="lstress"
  STRESS TOTAL CAUCHY LOCAL INTPNT
END OUTPUT
*END
```

Mostly this file initiates and performs the linear analysis. However, the post-processing section is of interest. Displacements and reaction forces are requested so that a load-displacement diagram can be created later. Also the Cauchy stresses in the local coordinate system are requested in the form of a table for each integration point. For a 4 Gauss point element the format of this table is:

Element 1	Gauss Point 1	$\sigma_x$	$\sigma_y$	$\sigma_z$	$\sigma_{xy}$	$\sigma_{yz}$	$\sigma_{xz}$
Element 1	Gauss Point 2	$\sigma_x$	$\sigma_y$	$\sigma_z$	$\sigma_{xy}$	$\sigma_{yz}$	$\sigma_{xz}$
Element 1	Gauss Point 3	$\sigma_x$	$\sigma_y$	$\sigma_z$	$\sigma_{xy}$	$\sigma_{yz}$	$\sigma_{xz}$
Element 1	Gauss Point 4	$\sigma_x$	$\sigma_y$	$\sigma_z$	$\sigma_{xy}$	$\sigma_{yz}$	$\sigma_{xz}$

### 9.2.3 Identify Critical Element

The process of identifying the most critical element was performed by examining each concrete element in turn. The local stress state for each integration point belonging to the current element was read in from the results table. An average stress was calculated for the element if more than one Gauss point existed and the principal stresses calculated. These principal stresses were then tested against the chosen failure rule. The most critical element was the one meeting the failure criterion and whose ratio of maximum principal stress to tensile strength was greatest.

A number of different rules for defining element failure were considered. Although the Rankine criterion detailed above is an excellent rule by which to detect cracking, the complete removal of the cracked element does not recognise the fact that, in reality, orthogonal to the crack plane the material appears almost undamaged. Removal of the element would not allow loads to be transmitted across this plane. Therefore a second rule was proposed whereby elements would only be deemed to have failed if both the maximum principal stress exceeded the tensile failure strength and one of the other principal stresses was also tensile. For convenience this is referred to as the ‘biaxial rule’ and the previous one referred to as the ‘uniaxial rule’ (Figure 9-5).

$(\sigma_1 > f_t)$	-	Uniaxial Rule
$(\sigma_1 > f_t) \text{ AND } ((\sigma_2 > 0) \text{ OR } (\sigma_3 > 0))$	-	Biaxial Rule

**Figure 9-5 - Element Failure Rules**

In pseudo code the identification of the critical element reads as follows:

```

open(resultsfile.tb)
for elem_loop = 1 to num_conc_elems
  current_elem = conc_elems[elem_loop]
  read(elem_num)

  while elem_num != current_elem
    read(elem_num)
  endwhile

  for gauss_loop=1 to num_of_gauss_points
    read(sigma_x, sigma_y, sigma_z, sigma_xy, sigma_yz, sigma_xz)
    add_to_tensor()
  next gauss_loop

  stress_tensor / num_of_gauss_points
  find-principal-stresses()

  if criterion = "uniaxial" then
    if sigma_1 > ft then
      if sigma_1 / ft > current_max then
        current_max = sigma_1 / ft
        critical_elem = current elem
      endif
    endif
  endif

  if criterion = "biaxial" then
    if (sigma_1 > ft) AND ((sigma_2 > 0) OR (sigma_3 > 0)) then
      if sigma_1 / ft > current_max then
        current_max = sigma_1 / ft
      endif
    endif
  endif

```

```

        critical_elem = current_elem
    endif
endif
endif

next_elem_loop
close(resultsfile.tb)

```

#### 9.2.4 Calculate Global Load and Displacement

Once the critical element was identified the applied displacement and associated load were scaled back according to the ratio of maximum principal stress to tensile failure stress. A scaling factor was calculated as  $f_t / \sigma_1$  for the critical element and stored in an output file.

In post processing this was then applied to the load and displacement results.

#### 9.2.5 Update DIANA Input Data

The material assignments in the working data file were parsed and updated to reflect the updated material type for the failed element. For example, if the critical element was number 50, the data for the current step might read:

```

MATERIALS
717-720 1281-1296          / 1
1-716 721-1280 1297-1856  / 2

```

Once updated it would read:

```

MATERIALS
717-720 1281-1296          / 1
1-49 51-716 721-1280 1297-1856 / 2
50                          / 3

```

where 1, 2 and 3 are the material types for steel, concrete and damaged concrete respectively.

The next step of the Sequentially Linear analysis would then be performed as before by calling the DIANA with the updated file as input.



**9.3 2D Anchor Modelling – Coarse Mesh**

This first problem to be analysed was the 2D plane-stress anchor problem that was used previously in the study of the anchor-concrete interface in Chapter 8 (Figure 9-6). The basic geometry and boundary conditions remained the same but the problem was remeshed with 3-noded, linear, plane-stress elements. The reason for the triangular elements as opposed to the quadrilaterals used in previous analyses was that early versions of the Sequentially Linear code could only assess elements with a single Gauss point. The later 3D extension of the code added the ability to handle multiple Gauss points. The interface elements between anchor and concrete were not included in this problem, as they had no purpose in a linear analysis, and instead the anchor was fully bonded to the surrounding concrete. Analyses were performed for both the uniaxial and biaxial removal rules. In both cases there were no problems attaining solutions and the analyses stopped when either the maximum displacement or analysis step had been reached.

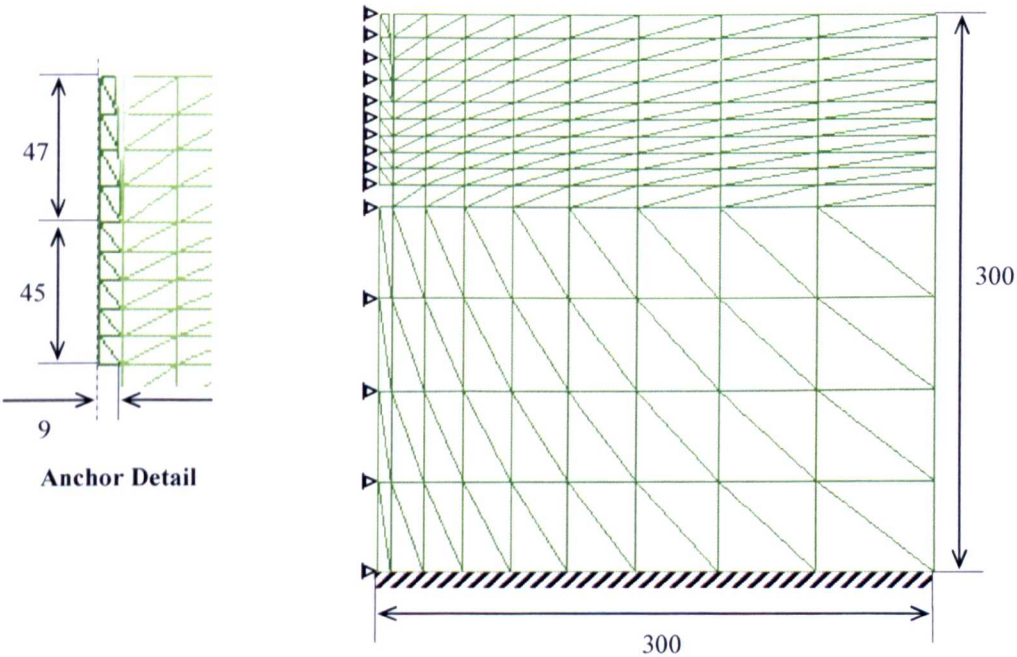


**Figure 9-6 - 2D Plane Stress Anchor Problem**

For comparison the same problem was also analysed twice using the rotating crack formulation of the Total Strain Based Crack Model. Firstly using with an exponential

softening behaviour and subsequently with a brittle behaviour. The softening analysis was taken to be the reference solution. The brittle analysis was equivalent to the sequentially linear analysis using the uniaxial rule in that both used the Rankine criterion to identify cracking elements and effectively removed them. The difference lay in the fact that for the TSB Crack Model the analysis was progressed via stepwise increments of displacement followed by an iterative procedure to obtain a solution that satisfied static equilibrium. In this case both TSB analyses failed due to non-convergence.

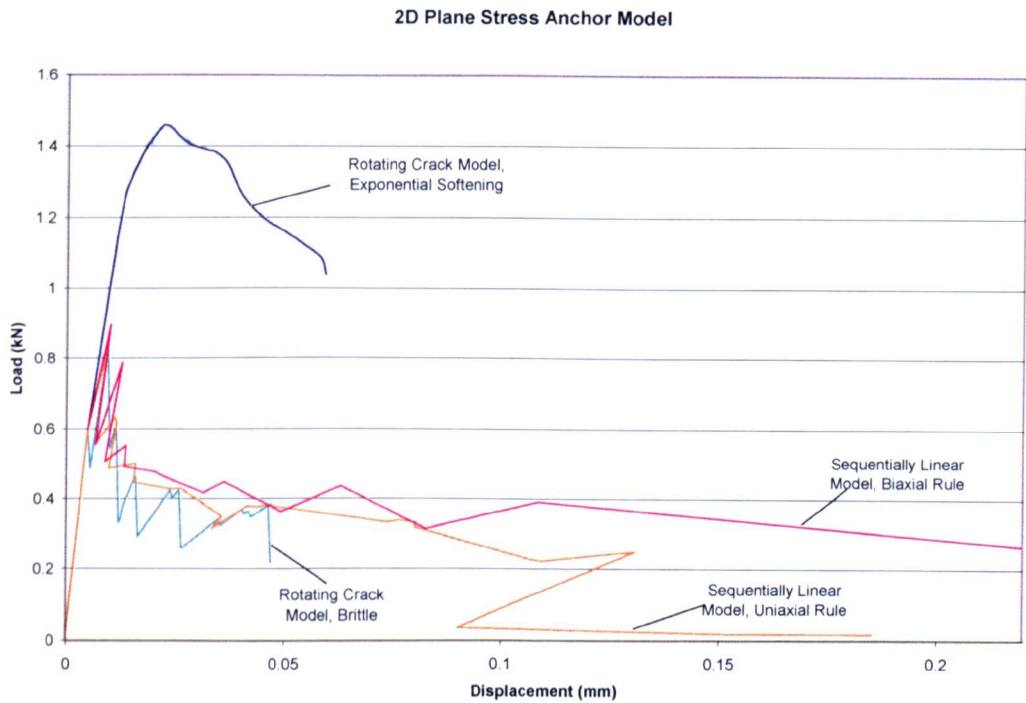
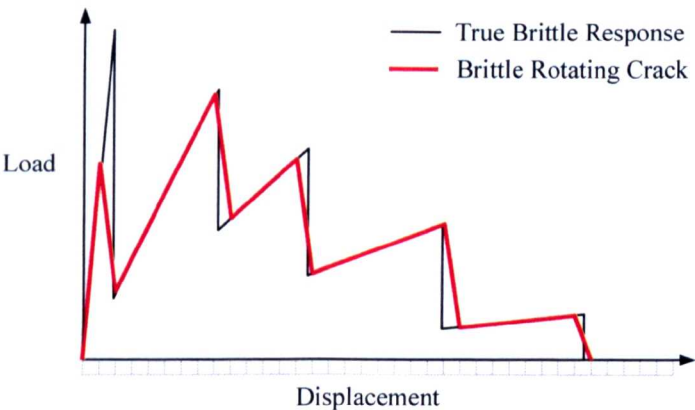


**Figure 9-7 - Load Displacement Response for 2D Plane Stress Problem (Coarse Mesh)**

From the load-displacement plot above (Figure 9-7) it is immediately obvious that the response of the TSB analysis with exponential softening is very different to that of the other analyses. The primary reason for this is that the brittle models take no account of fracture energy and therefore the true non-linear behaviour of the material cannot be modelled. This leads to mesh-inobjective results and therefore an inability to produce the correct load-displacement response. The solution to this shortcoming is to introduce a softening procedure as detailed above. However, since this was deemed impractical, at

this stage, it is more useful to make comparisons between the Sequentially Linear Model and the brittle Rotating Crack Model.

All three brittle models predicted similar peak loads. As expected, the uniaxial rule produced the results most like those of the brittle Rotating Crack Model as their failure criteria were most alike. It can be argued that, of the two, the Sequentially Linear Model is the more accurate in that it seeks the failure points for each element individually and calculates the associated global load and displacement values. In contrast, the brittle Rotating Crack Model, in this case, has the anchor displacement dictated by the displacement stepping scheme and is required to calculate the associated load by satisfying equilibrium. Therefore it is quite likely for the point of crack initiation to be missed and instead the displacement step relates to a subsequent point in the response where crack opening and stress redistribution has taken place.



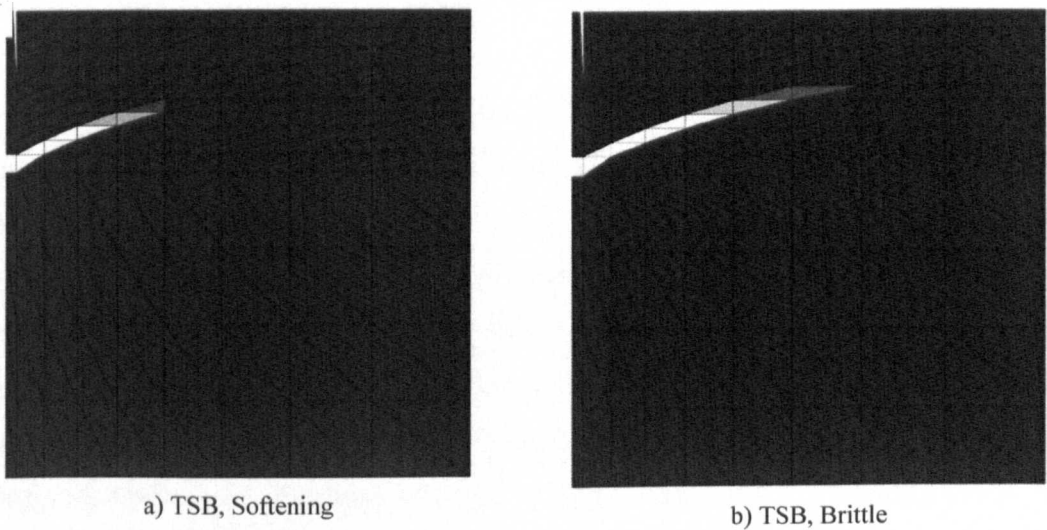
**Figure 9-8 - Brittle Rotating Crack Response**

Figure 9-8 above highlights the possible inaccuracies in the response produced by the brittle rotating crack model. Obviously accuracy is greatly increased if the size of the displacement step is set to some suitably small value. The ‘True Brittle Response’ can be thought of as the response produced with a step size approaching zero. In the above figure the displacement step size for the Brittle Rotating Crack is shown in grey below the axis. In this case 31 steps are used (plus an indeterminate number of internal iterations) but a satisfactory result has not been produced. In comparison the Sequentially

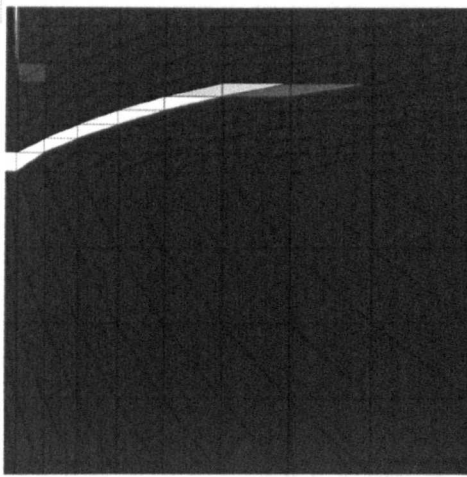


Linear Model is able to reproduce the correct load-displacement response in only 6 steps. However, it must be noted that brittle models are particularly sensitive to problems of insufficiently small step size. Because of their progressive crack opening, it is not so critical to catch the crack initiation in softening models hence they suffer less from this problem. Also, it will be shown that the advantage of fewer steps for the Sequentially Linear Model does not scale well for meshes with greater numbers of elements.

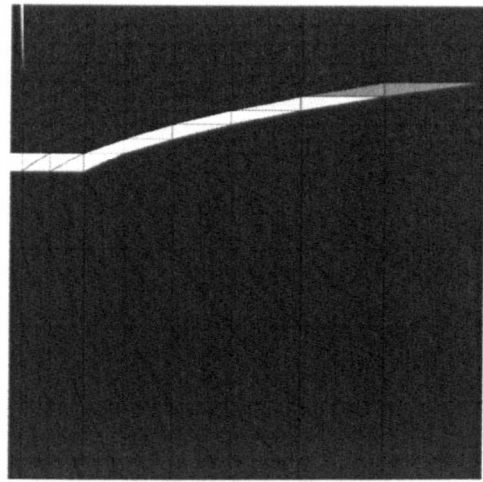
Returning to the load-displacement diagram for the anchor analysis (Figure 9-8) it can be seen that although similar the biaxial rule produces a higher peak load and overall stiffer response. This was expected since the rule requires two separate criteria to be met. Reasons for the difference in the response can also be seen in the contour plots for principal strain (Figure 9-9 & Figure 9-10).



**Figure 9-9 - Principal Strain Plots for TSB Crack Model Analyses of 2D Plane Stress Anchor Pullout Problem (Coarse Mesh)**



c) Sequentially Linear, Uniaxial



d) Sequentially Linear, Biaxial

**Figure 9-10 - Principal Strain Plots Sequentially Linear Analyses of 2D Plane Stress Anchor Pullout Problem (Coarse Mesh)**

It can be seen that both TSB Crack models and the Sequentially Linear Model using the uniaxial rule all predict the same failure pattern. The Sequentially Linear Model using the biaxial rule produces a horizontal crack initially before an inclined crack forms. This is because of the compression strut that forms between the base of the anchor and edge of the concrete block (Figure 9-11). This zone of compressive stress means that the biaxial tensile stress criterion cannot be satisfied. Therefore the crack is deflected downwards resulting in a failure mode which requires more energy to develop. It was also observed that for all four models that there is noticeable mesh bias. This is a common problem for coarse meshes and the fine, irregular mesh used in the following section exhibits this phenomenon much less.

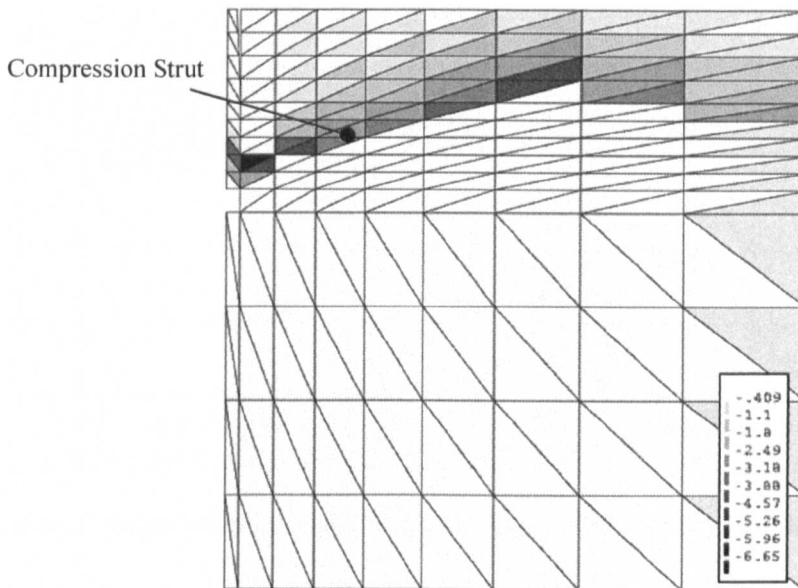


**Figure 9-11 - Contour Plot of Minimum Principal Stress ( $\sigma_2$ ) for Plane Stress Pullout Analysis Using Sequentially Linear Model with Biaxial Rule**

The principal strain plots also shows that although the Sequentially Linear Model using the uniaxial rule did not produce the correct load-displacement response (for reasons outlined above) it did correctly produce the failure mode (Figure 9-12). In fact it traces it more completely than the TSB Crack models and does do more quickly and robustly. For comparison; the Rotating TSB Crack Model with tension softening required 127 steps, the brittle TSB Crack Model required 99 steps and the Sequentially Linear Model required 28.

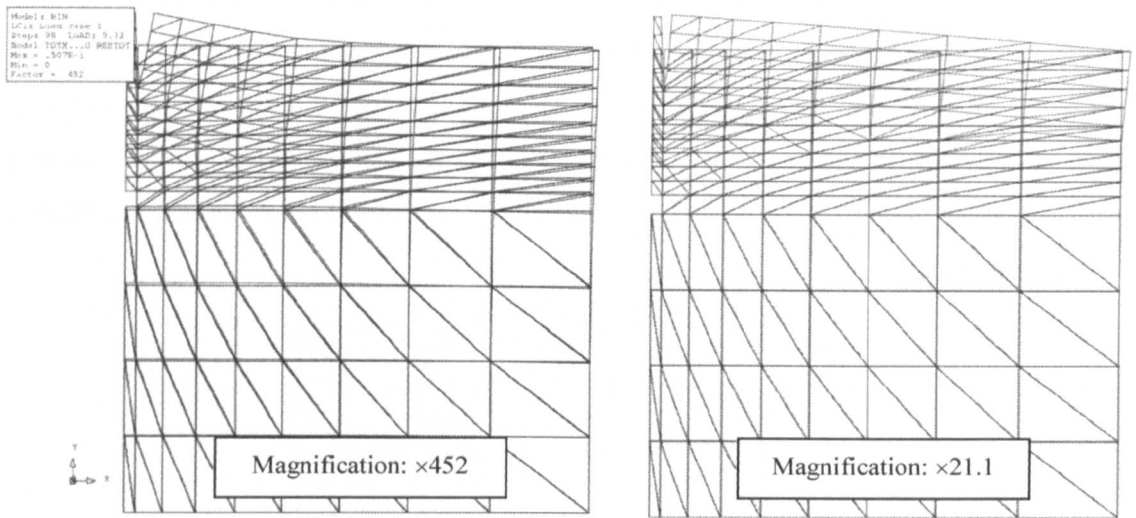


**Figure 9-12 - Displaced Shapes, a) TSB Crack Model (Softening), b) SL Model (Uniaxial)**

Displaced shapes for the ends of each analysis show that, for the uniaxial SL model, the more advanced crack and greater strain localisation mean that the concrete below the crack is largely undisturbed. For the TSB Crack Model with tension softening this is not the case.



#### 9.4 2D Anchor Modelling – Fine Mesh

Following the success of the analyses of this coarse mesh, a finer mesh was produced with a more unstructured arrangement of elements (Figure 9-13). Finer meshes generally give rise to more accurate solutions but, in the case of brittle material models, they also produce better softening behaviour at a structural level. This is due to the more progressive nature of the failure.

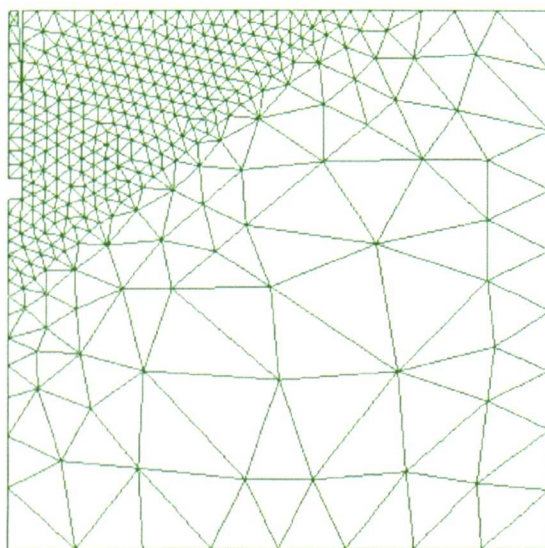


**Figure 9-13 - Fine Mesh for 2D Plane Stress Anchor Pullout Problem**

The new mesh was analysed using the Rotating Crack and SL Models as before. The load-displacement responses for these show a number of interesting features (Figure 9-14). Firstly the brittle models further under-predict the peak failure load as compared with the coarser mesh. This is a consequence of inobjectivity with respect to mesh refinement. The smaller elements lead to a sharper stress peak at the tip of the crack band and hence an earlier failure. This is a common problem exhibited by models not accounting for fracture energy. Secondly, the Biaxial SL Model shows a response that is wildly different from that of the other models. Once again this is due to the alternative failure rule causing the problem to adopt a slightly different failure mode – one requiring more energy to progress the crack. Beyond this, the response is not very informative except that confirms that the Biaxial rule does not produce the correct material behaviour for concrete. The response of the SL Model using the uniaxial failure rule is more

encouraging. It can be seen that it exhibits a post-peak softening response much like that of the Rotating Crack Model with tension softening. The response is also very similar to that of the brittle Rotating Crack model. In this case the Uniaxial SL Model required 71 analysis steps as compared with 57 for the brittle Rotating Crack model. However, because the analysis progressed further and no account is taken of internal iterations within the TSB Crack model, the SL Model can again be considered more computationally efficient and robust. In comparison, the TSB Crack Model with softening required 270 steps. Although it is quite possible that this number could be reduced it would require some amount of time to find the optimum number of steps whereas the SL Model automatically uses the number of steps required

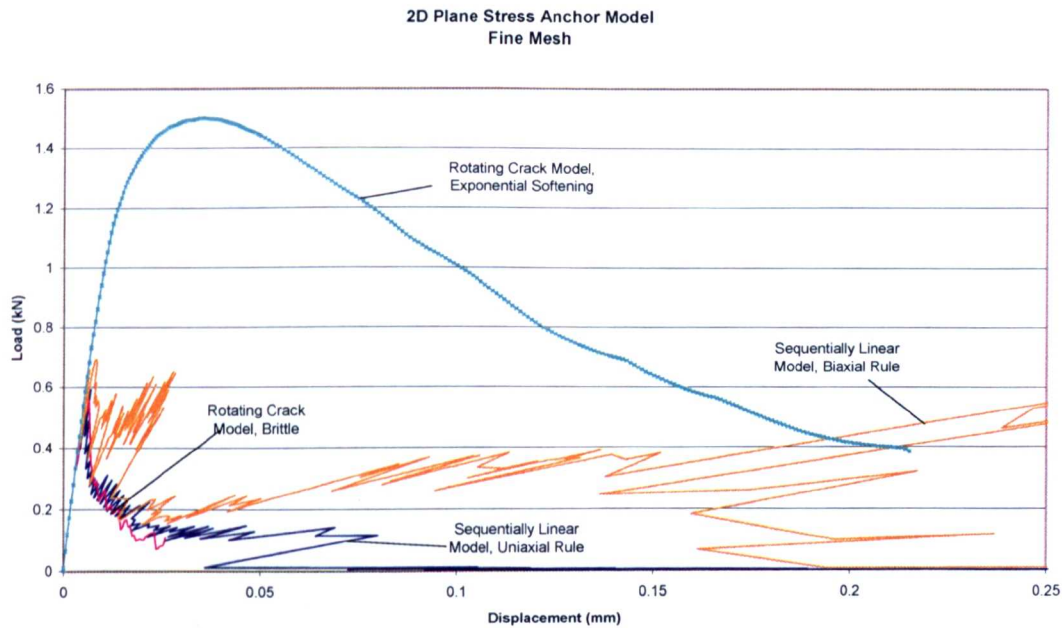


**Figure 9-14 - Load Displacement Response for 2D Plane Stress Problem (Fine Mesh)**

The crack patterns, as highlighted in the principal strain plots (Figure 9-15), are slightly different for each model. At first it appears that the biaxial rule for the Sequentially Linear Model produces a pattern that is greatly different from the others. However crack patterns were derived from the principal strain plots by drawing a line through the centroid of each element exhibiting high principal strain. By overlaying these cracks patterns on a common diagram (Figure 9-16) it can be seen that, after the initial

downward deviation, the crack follows a rather similar path to the others. Unlike the results produced by the coarser mesh, the crack for the Uniaxial SL Model differs slightly from that of the brittle Rotating Crack Model. The reasons for this most likely lie with the shortcomings in the Rotating Crack Model of the fixed step size.

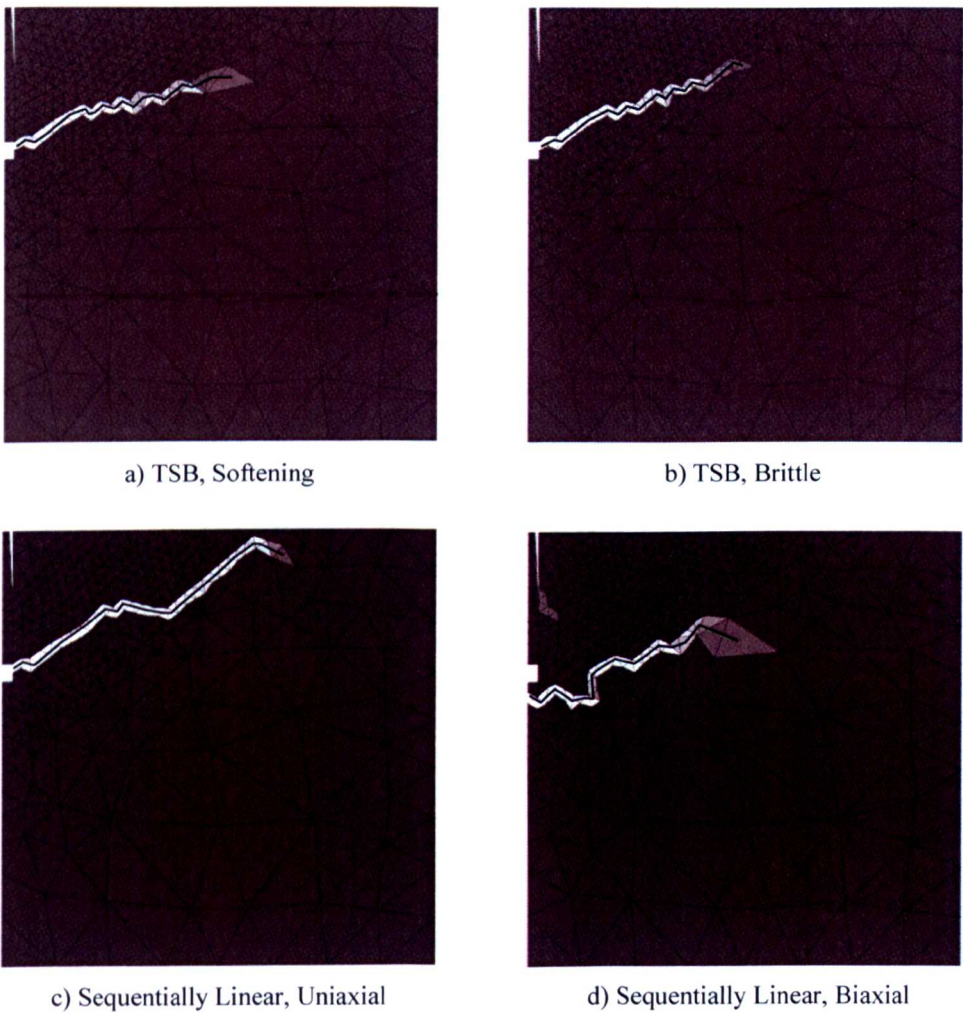


**Figure 9-15 - Principal Strain Contour Plots for Fine 2D Mesh**

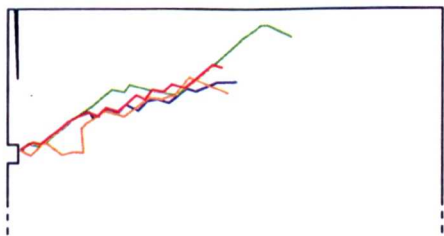


**Figure 9-16 - Crack Patterns Derived From Principal Strains**



The Uniaxial SL Model does show an interesting behaviour where the crack almost meets the free surface at the top of the concrete block. Because the structural actions taking place is essentially bending in this zone the single remaining element between the crack tip and free surface is unable to capture this behaviour (Figure 9-17). In this case compressive stresses are dominant and hence the element is unable to fail. Because of this the crack is deflected as can be seen in the contour plot. However, if the orientation of the element was different it is possible that tensile stresses would be dominant and the crack would indeed extend to the free surface. Overall it is concluded that the Sequentially Linear Model using the uniaxial rule for failure accurately produces the correct failure mode and load-displacement response within the limitations of a brittle model.

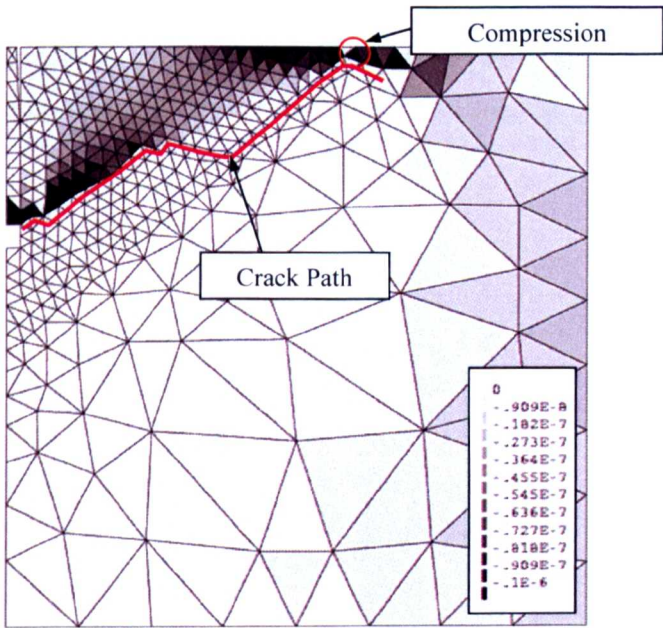


**Figure 9-17 - Contour Plot of Minimum Principal Stress ( $\sigma_2$ ) for Plane Stress Pullout Analysis Using Sequentially Linear Model with Uniaxial Rule**

The displaced shapes below illustrate well the failure mechanism taking place (Figure 9-18). In particular the shape for the Sequentially Linear Model with the uniaxial failure rule shows the classic concrete cone failure.

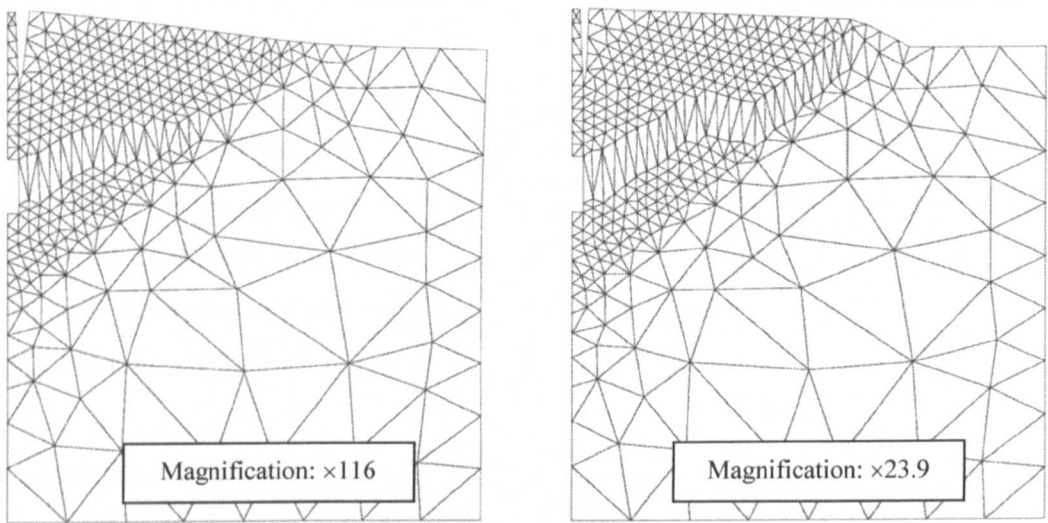


**Figure 9-18 - Displaced Shapes, a) TSB Crack Model (Softening), b) SL Model (Uniaxial)**

### **9.5 3D Anchor Modelling**

The logical extension for this modelling framework was to further develop it to support three-dimensional modelling. This was very straightforward since the majority of the complexities of the 3D modelling were handled by the underlying FE framework. The opportunity was taken to introduce directionality to the ‘cracks’ formed in the Sequentially Linear Model. Therefore, the principal stress would be assessed not only on its magnitude but also its direction. The material would then have its stiffness removed in the appropriate direction. This compares with the previous model where element stiffness was removed in all directions upon cracking. Crack directionality was possible via the use of an orthotropic elastic material type (i.e. Young’s Modulus defined independently for each of the element’s local planes). With this it was possible to individually define the elastic material properties in each of the element’s local axes.

The rules for introducing a plane of orthotropy (a crack) to an element consisted of two parts. Firstly a ‘failure rule’ by which to determine the most critical element and secondly a ‘crack formation rule’ which determined which plane or planes were to be ‘softened’. Three combinations of failure and crack formation rule were examined and are detailed below. One limitation of the model was that the crack planes could only be formed normal to the element local axes. This was imposed because having arbitrary crack planes would have involved having different materials defined for each element. As with the softening behaviour this was deemed unwieldy. Again, however, future developments may implement both of these features.

The failure rules are as follows:

1. The first rule was the same as the uniaxial one used previously and simply found the element with the highest Maximum Principal Stress to Element Tensile Stress ratio.

```
if criterion = "multiple uniaxial" then
  if sigma_1 > ft then
    if sigma_1 / ft > current_max then
      current_max = sigma_1 / ft
      critical_elem = current elem
    endif
  endif
endif
```

2. The second rule added the additional constraint that only a single crack plane could form per element.

```
if criterion = "single uniaxial" then
  if (sigma_1 > ft) AND (material_type = "virgin concrete") then
    if sigma_1 / ft > current_max then
      current_max = sigma_1 / ft
      critical_elem = current elem
    endif
  endif
endif
```

It should be noted that the biaxial failure rule previously used in the isotropic models was not considered at all for directional cracking as its purpose had been to account for the directional nature of cracks in the isotropic model. This requirement was now redundant.



The crack formation rules for the orthotropic model were:

- A. Choose the local axis plane whose normal is aligned most closely to the principal stress vector as the crack plane.

```
plane = 1
if abs(c_y) > abs(c_x) then
    if abs(c_z) > abs(c_y) then plane = 3 else plane = 2
else
    if abs(c_z) > abs(c_x) then plane = 3
endif
```

where  $c_x$ ,  $c_y$  and  $c_z$  are the direction cosines for the maximum principal stress with respect to the local axes  $x$ ,  $y$  &  $z$  respectively. These cosines were produced as part of the Jacobian solution method used to find the principal stresses.

- B. If the normal to a local axis plane is within  $60^\circ$  of the principal stress vector then the plane is cracked. Note: This may result in more than one crack plane.

```
plane = 1
if abs(c_x) >= 0.5 then plane = 1

if abs(c_y) >= 0.5 then
    if (plane = 0) then plane = 2
    if (plane = 1) then plane = 4
endif

if abs(c_z) >= 0.5 then
    if (plane = 0) plane = 3
    if (plane = 1) plane = 6
    if (plane = 2) plane = 5
    if (plane = 4) plane = 7
endif
```

In the above pseudo code the values of the variable plane refer to:

Value	1	2	3	4	5	6	7
Plane	yz	xz	xy	yx & xz	xz & xy	yz & xy	xy, yz, xz

The rationale behind the second crack rule was that because the cracks were restricted to form in the direction of the element local axes it was quite possible for a crack to be misaligned by up to 45° according to rule A thus leading to significant stress locking. Rule B attempts to avoid this by forming multiple cracks if the maximum principal stress vector lies within certain bounds between element axes. This is illustrated for a 2D case in Figure 9-19 and shows the 3 distinct zones.

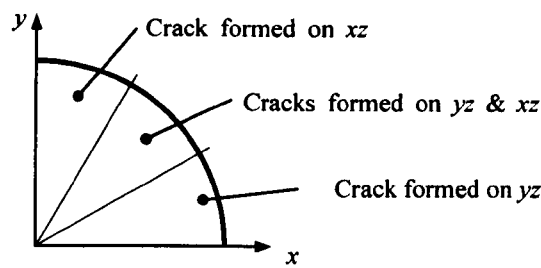
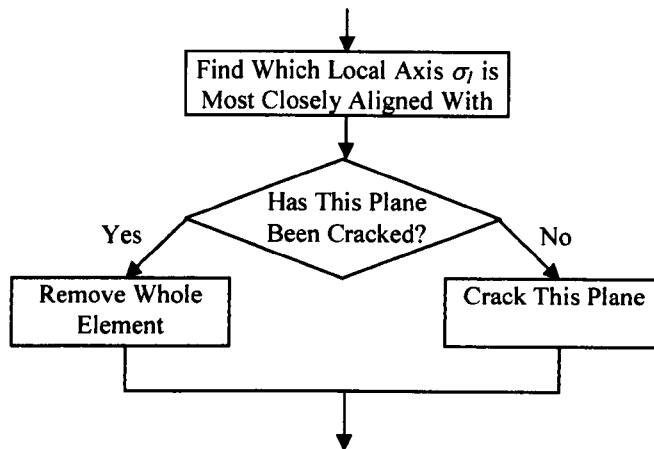


Figure 9-19 - Rule B Crack Plane Orientation Determination

The failure and crack formation rules were combined in three different combinations:

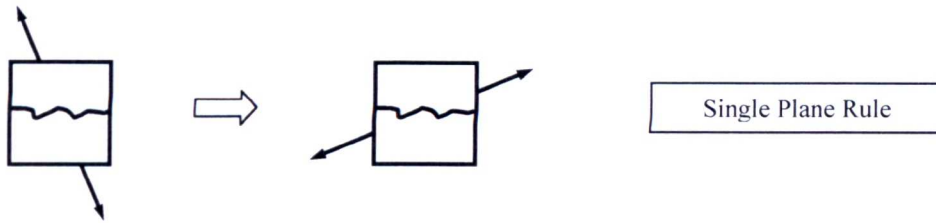
Combined Rule Name	Failure Rule	Crack Formation Rule
Single Plane (SP)	2	A
Multiple Plane A (MP-A)	1	A
Multiple Plane B (MP-B)	1	B

For the Multiple Plane B rule, also with a view to avoid stress locking due to crack misalignment, the treatment of a critical element differs depending on whether or not the potential crack plane has previously been cracked (Figure 9-20). Virgin planes are simply cracked whereas, if a crack exists, the whole element is ‘removed’.

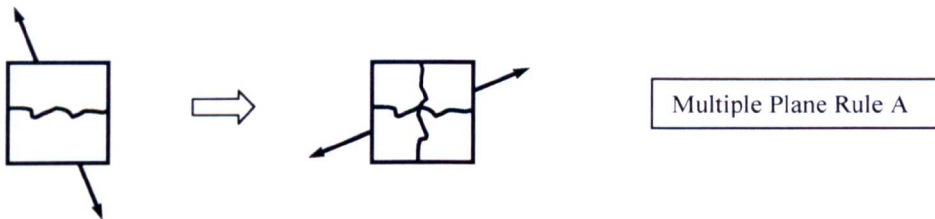


**Figure 9-20 – Multiple Plane B Rule – Stress Locking Detection and Treatment**

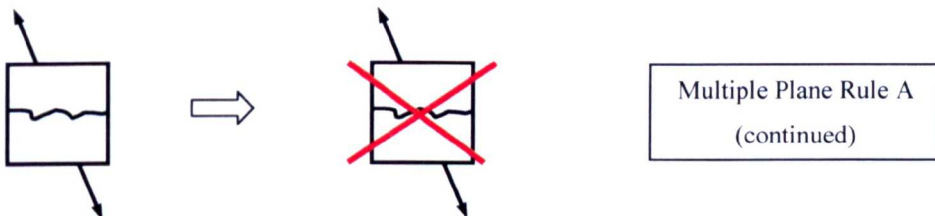
In contrast, for the Single Plane rule the condition that the critical element must be uncracked means that no element removal is possible even if the principal stress exceeds the failure strength on subsequent steps. Figure 9-21 below shows pictorially what happens when the maximum principal stress exceeds the tensile failure strength of the concrete. The initial orientation of the stress vector is  $35^\circ$  to the vertical and it subsequently rotates by  $90^\circ$ .



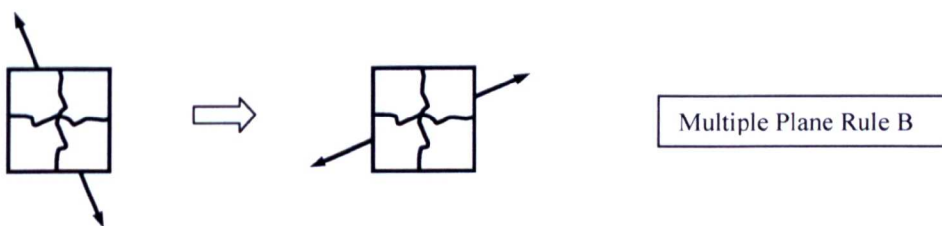
Crack initiates on element local plane closest to principal plane. No further cracks can develop even when maximum principal stress vector rotates.



Crack initiates on element local plane closest to principal plane. If principal plane rotates such that another element plane is more closely aligned, an additional crack forms.



If, on a subsequent step the same plane is identified as critical the whole element is 'removed'.



Cracks form on all planes orientated within  $60^\circ$  of the principal plane.

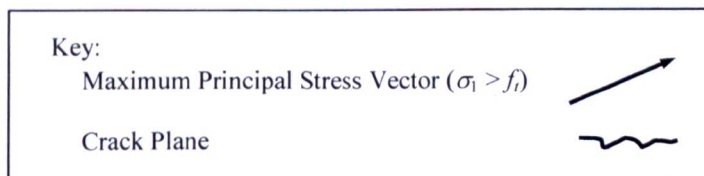


**Figure 9-21 - Pictorial Representation of Cracking Process for the Rules Defined**

The first problem to be analysed was the 3D anchor pullout previously analysed for the edge effect study in Chapter 7 (Figure 9-22).

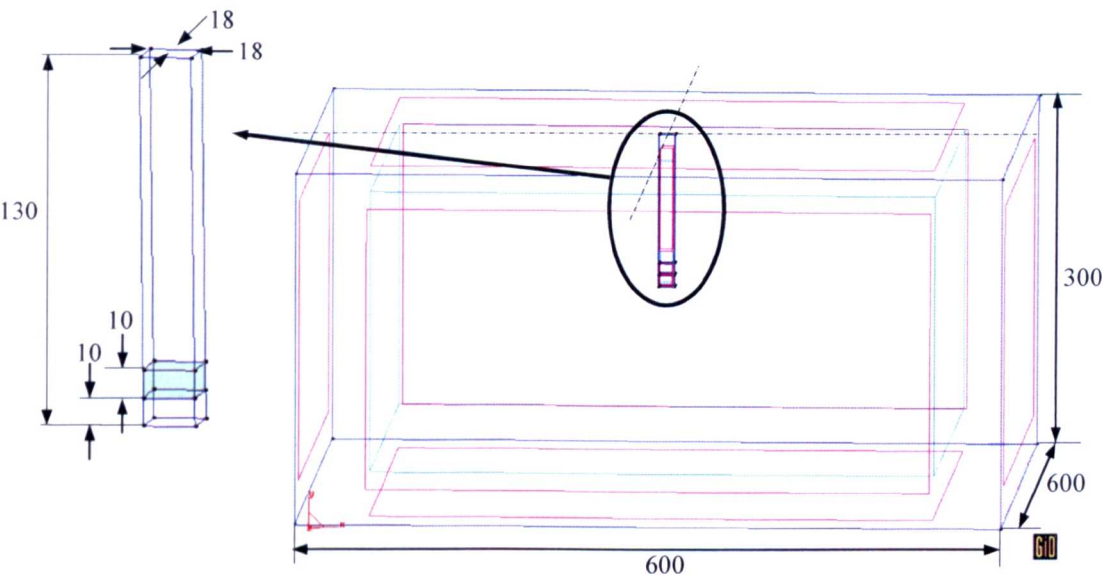
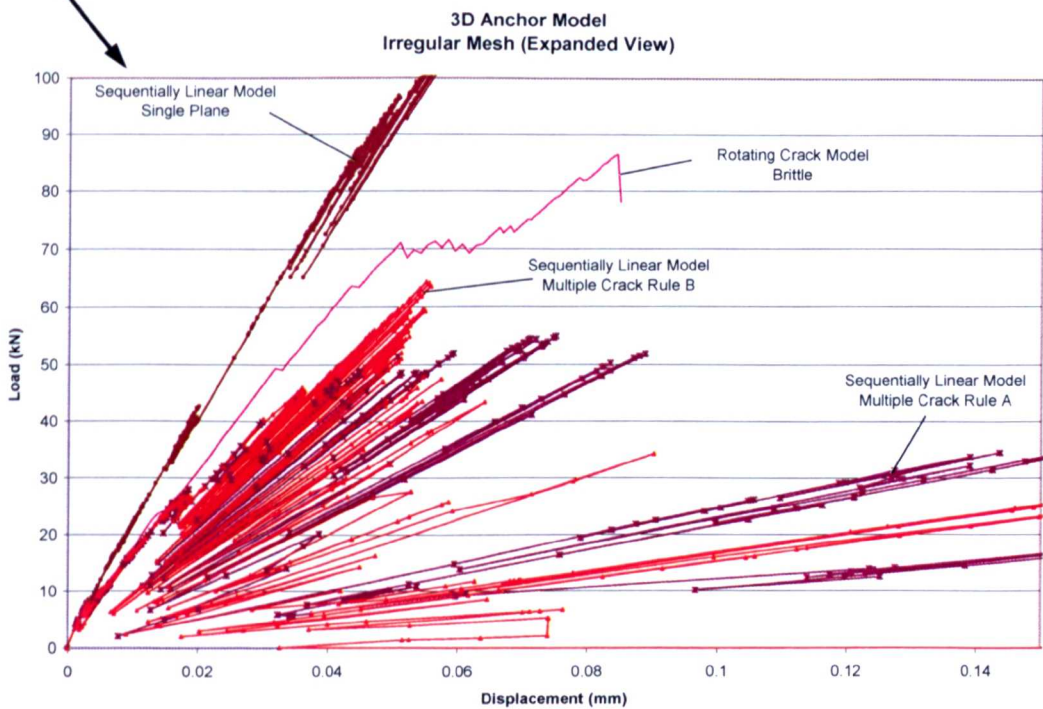
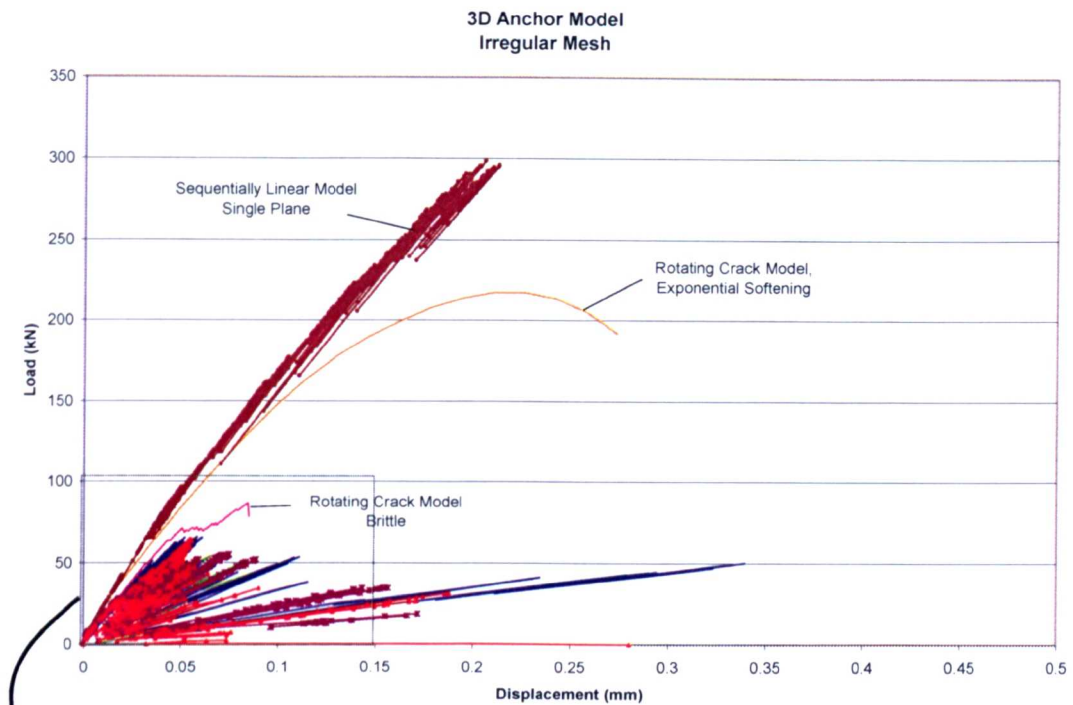


**Figure 9-22 - 3D Anchor Pullout Problem Geometry**

The anchor was located in the middle of the concrete block. Discretisation was performed using 4-noded, linear, iso-parametric tetrahedra. The base of the concrete block was fixed in all directions and prescribed displacements were applied to the top of the anchor expander. Analyses were performed using both the brittle and softening rotating crack models, uniaxial and biaxial isotropic SL models and all three orthotropic SL models. The resulting load-displacement responses are shown in Figure 9-23 and Figure 9-24.

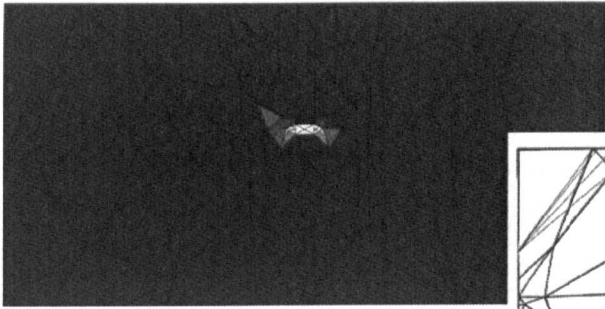


From Figure 9-23 above it can be seen immediately that the Single Plane rule for the SL Model gave an almost linear response and failed to model the global reduction in stiffness of the problem as cracking progressed. This is unsurprising given that previous studies had shown a significant rotation in the principal stresses during the course of an analysis and therefore the fixed nature of the crack formed in this model leads to a large amount of stress locking and hence overly stiff response.

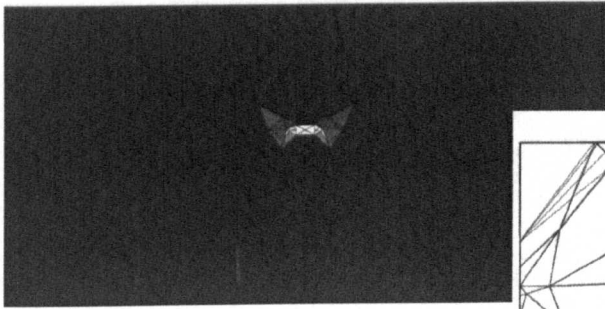
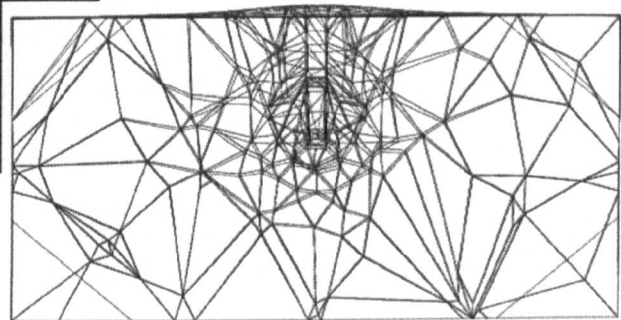
The responses for the other models are shown in more detail in Figure 9-24. The sawtooth nature of the responses from the Sequentially Linear models makes it difficult to interpret the graph. However it is clear that none of these responses are particularly close to that of the Brittle Rotating Crack model.

Looking at the principal strain contour plots and displaced shapes for the analyses (Figure 9-25) the reasons for the differences in the load-displacement responses become more apparent. The failure mode for both the Rotating Crack Model with tension softening and with brittle behaviour was the classic concrete cone as expected. Of the Sequentially Linear models only the Single Plane rule produced this failure model. Both the isotropic Uniaxial rule and the Multiple Plane Rule A gave very localised failures around the anchor expander where effectively the anchor was pulled out of the hole. This similarity is due to the fact that both models use the same rule for identifying a cracking element. The fact that the second model has directional cracks doesn't play a significant role since either additional cracks were developed to further degrade the element or else the same plane was selected for failure more than once hence resulting in the element being removed. For the Multiple Plane Rule B the lack of this element removal scheme to avoid stress locking lead to a rather unusual failure mode whereby the concrete below the anchor has been cracked and softened.

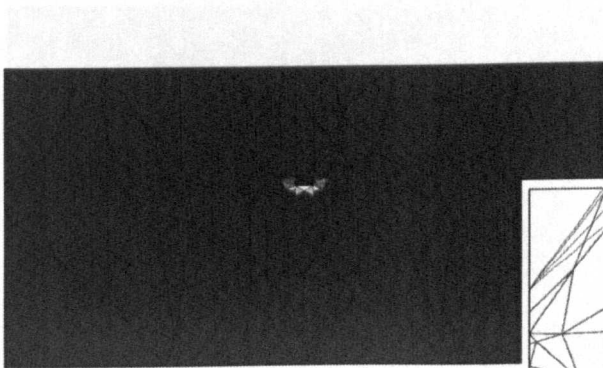
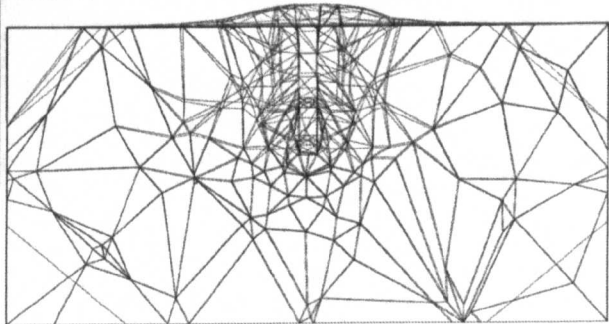




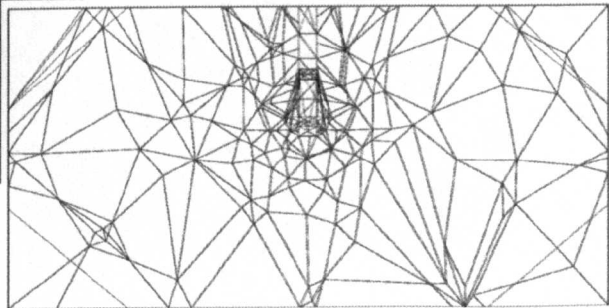
a) Softening Rotating Crack Model

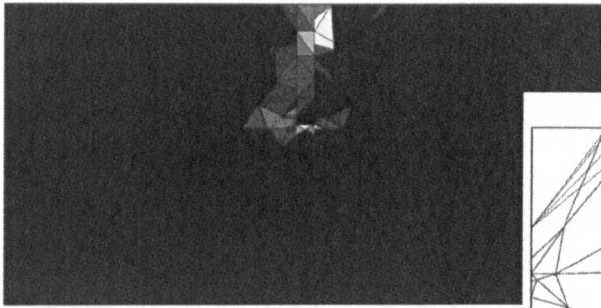


b) Brittle Rotating Crack Model

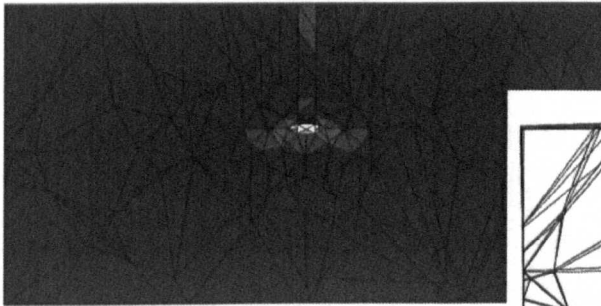
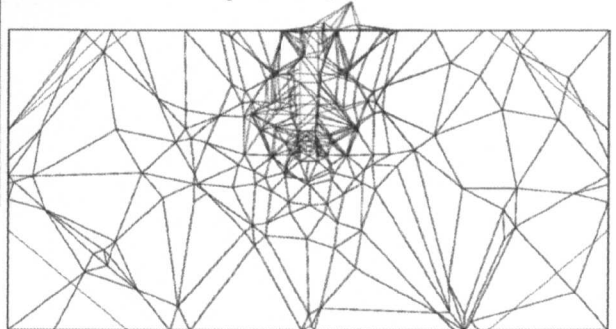


c) Sequentially Linear Model –  
Isotropic Crack, Uniaxial Failure Rule

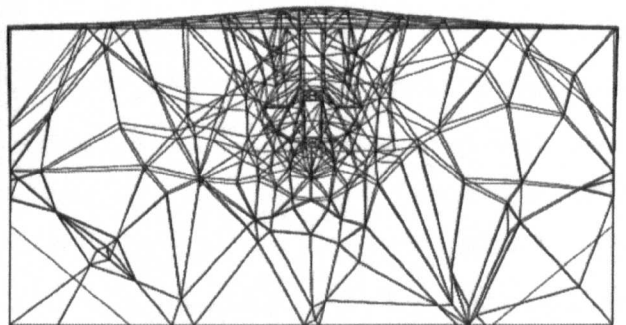




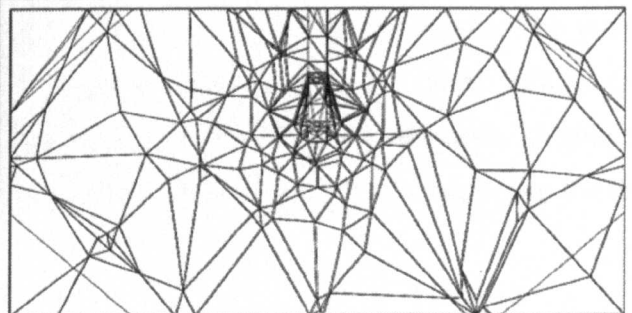
d) Sequentially Linear Model –  
Isotropic Crack, Biaxial Failure Rule



e) Sequentially Linear Model –  
Single Plane



f) Sequentially Linear model –  
Multiple Plane A



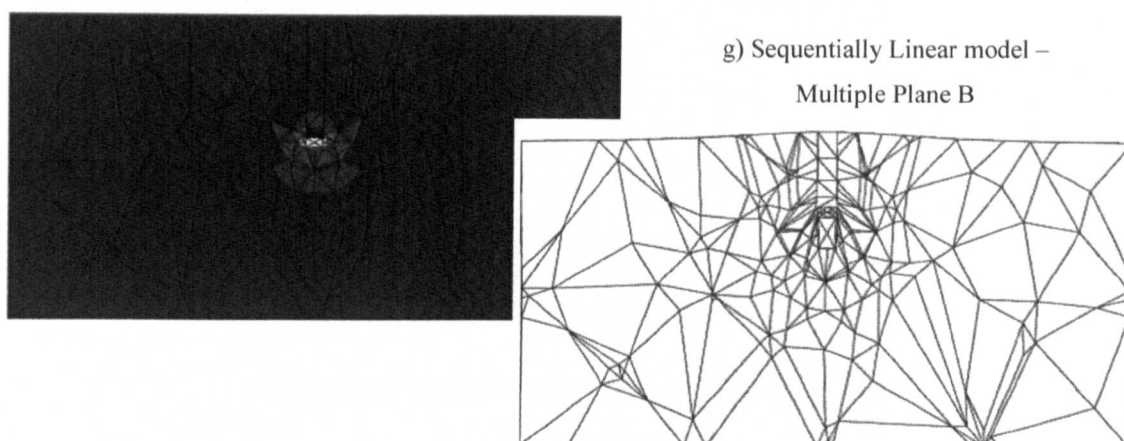


**Figure 9-25 - Principal Strain & Displaced Shapes for 3D Pullout Analyses (Irregular Mesh)**

The results from the Sequentially Linear models were poorer than expected when compared with the similarity between SL and Rotating Crack results for the 2D problem. There were a number of possible reasons for this. Firstly, findings from 2D analyses indicate that the coarseness of the mesh has a significant effect. 2D results showed that a finer mesh results in much better behaviour. However, the scalability of the Sequentially Linear Model becomes an issue. For 2D analyses there was a clear advantage for the model in terms of computation time. However, by virtue of the fact that each cracking element is processed in turn, a greater number of elements along the crack path leads to a corresponding increase in analyses time. This is very apparent in the transition from 2D to 3D meshes. The fixed load stepping scheme of the TSB Rotating Crack Model becomes an advantage in that a number of cracks on many elements can be processed in one step compared with the ‘single crack per step’ nature of the SL model. The table below (Figure 9-26) illustrates the greater number of steps required for the SL Model. As such time constraints prevented finer meshes from being analysed. However, although the model does not present speed advantages in this case it still remains attractive for its numerical stability.

Model	Number of Steps
Rotating Crack Model, Softening	27
Rotating Crack Model, Brittle	98
SL Model, Uniaxial Rule	215
SL Model, Biaxial Rule	472
SL Model, Single Fixed Crack	1000*
SL Model, Multiple Orthogonal Cracks	466

\*Analysis terminated when maximum number of steps was reached

**Figure 9-26 - Number of Analysis Step for Each Analysis**

The second possible reason for the poor results was the unstructured nature of the finite element mesh. The addition of crack directionality was intended to provide an improved description of crack behaviour and hence produce more accurate results. However the limitation that cracks could only form aligned to the element's local axes meant that there could be a significant discrepancy between the required crack direction and the one formed by the model. An unstructured mesh therefore results in a somewhat unpredictable array of crack orientations. It was thought that a better result would be produced by using a regular mesh with some alignment of the element axes to the expected crack directions.

9.6 3D Anchor Modelling – Regular Mesh

The 3D regular mesh used for previously in Chapter 8 for anchor modelling was deemed more suitable and was analysed using both TSB models and all three SL models that have directional cracking (Figure 9-27).

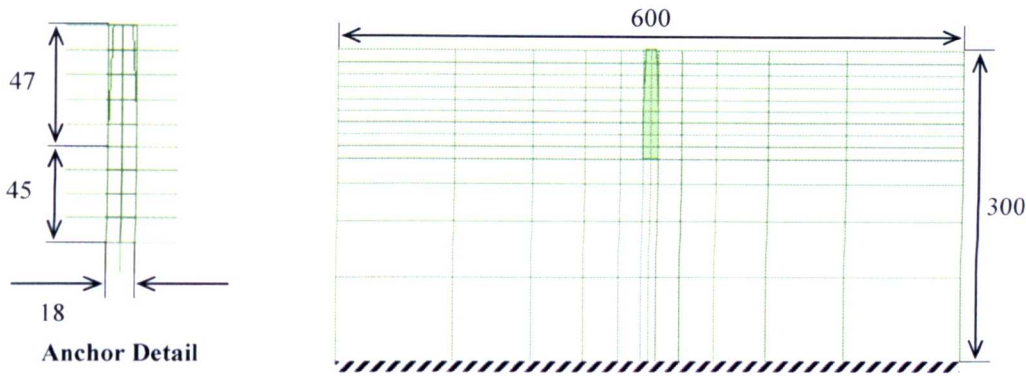


Figure 9-27 – Cross-Sectional Elevation Of 3D Anchor Problem (Regular Mesh)

The resulting load-displacement responses were considerably better than with the irregular mesh (Figure 9-28).

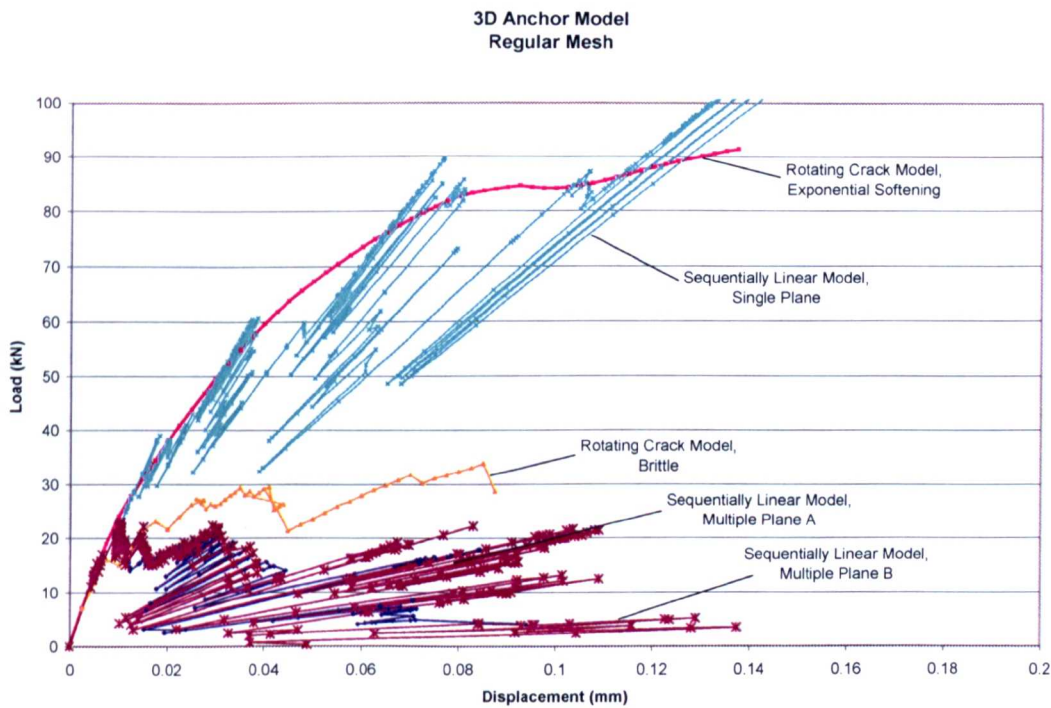


Figure 9-28 - Load-Displacement Response for 3D Problem (Regular Mesh)

The response of the Sequentially Linear Model with the Single Plane rule follows the response of the Softening Rotating Crack Model reasonably well for a brittle model. Both the SL models with Multiple Plane Rules also produce a better response than before. However again the mode of failure produced is via a localised fracturing of the concrete surrounding the anchor expander. All other models produced the expected concrete cone failure. For the Single Plane, Sequentially Linear Model there was a very strong mesh bias present. This is expected given the limited number of orientations available for the crack and the alignment of the elements. Associated principal strain plots and displaced shapes are presented in Figure 9-29.

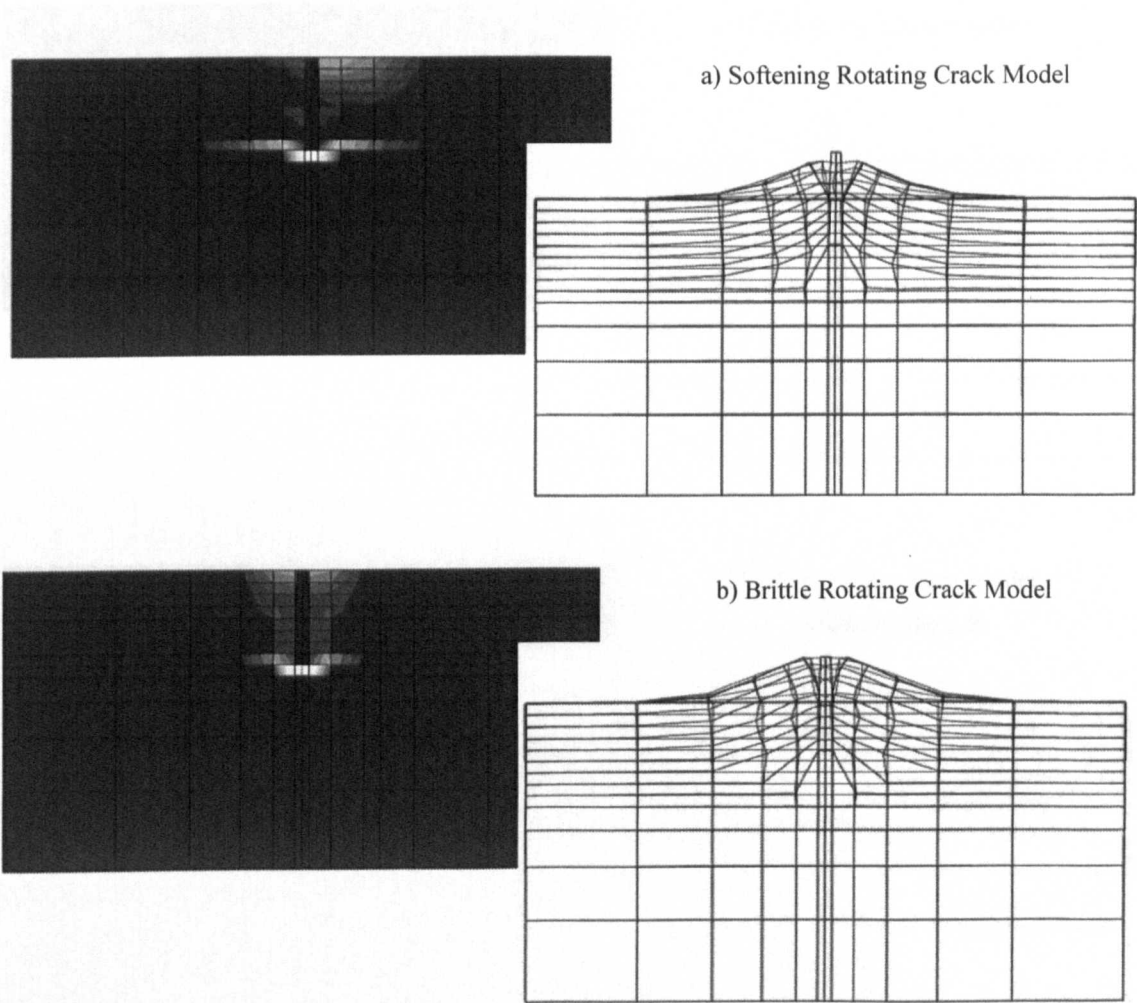
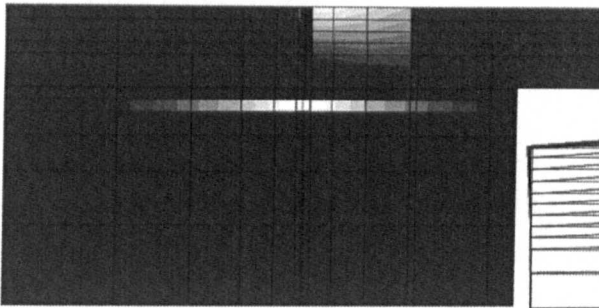
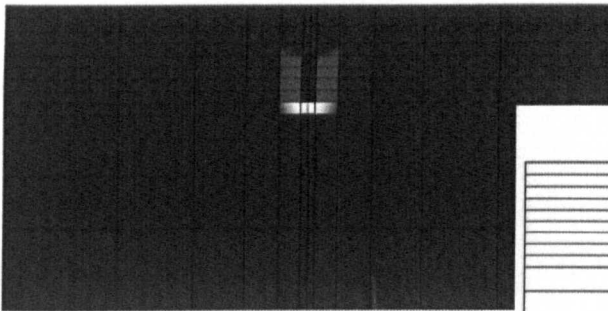
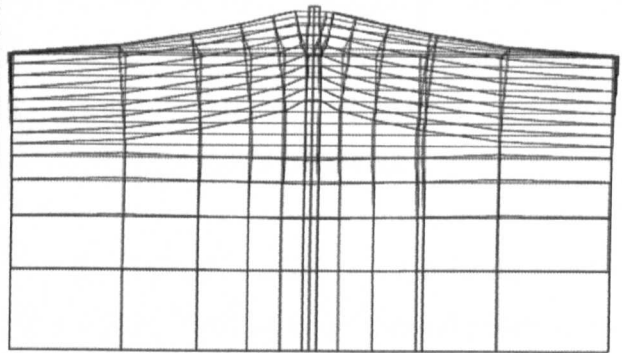


Figure 9-29: Principal Strain Plots and Displaced Shapes for the Softening Rotating Crack Model and the Brittle Rotating Crack Model

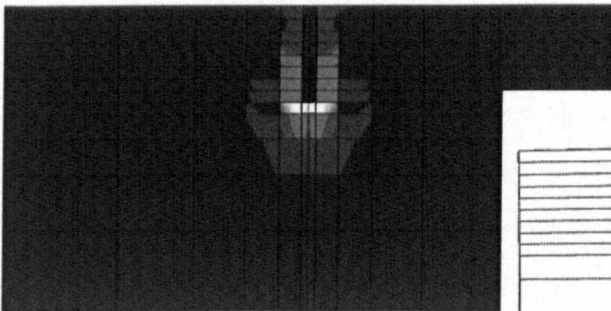
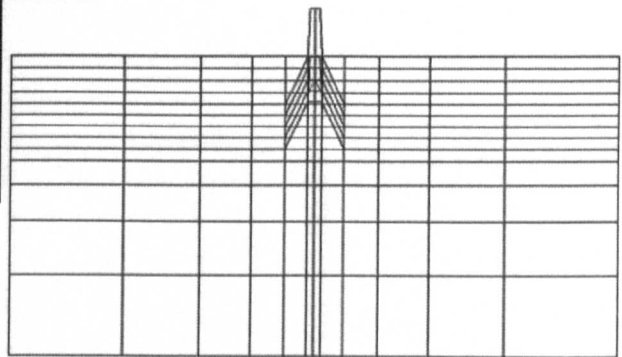




c) Sequentially Linear Model –  
Single Plane



c) Sequentially Linear Model –  
Multiple Plane A



c) Sequentially Linear Model –  
Multiple Plane B

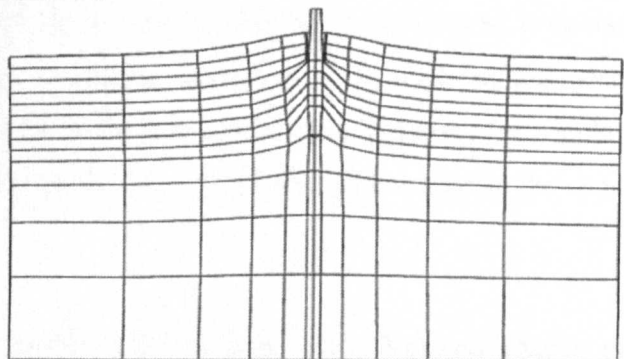


**Figure 9-29 - Principal Strain & Displaced Shapes for 3D Pullout Analyses (Regular Mesh)**



**9.7 Edge Effect Study**

A study into the effects of edge distance on pullout behaviour was undertaken with the primary aim to discover if the various failure rules for the Sequentially Linear Model could correctly capture the anchor behaviour. As with the analyses of the regular mesh in the previous section, only the orthotropic Sequentially Linear models were used along with the Rotating Crack models with both softening and brittle behaviour.

The previous 3D, concrete block was used for the edge effect study. Four different anchor positions were considered starting from 300mm from the free edge (central position) to 100mm from the edge (Figure 9-30).

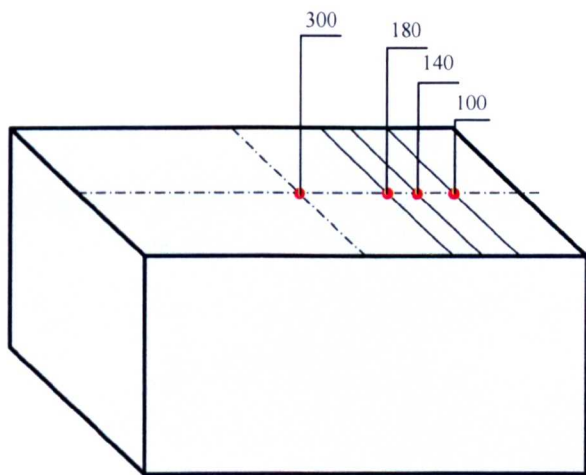


**Figure 9-30 - Anchor Positions for Edge Effect Study**

Once again the base of the block was fully fixed and pullout of the anchor performed by applying prescribed displacements to the top of the anchor. Both regular and irregular meshes were used for the study to allow comparisons to be drawn. By applying the mesh distortion technique (detailed in Chapter 4) to the regular mesh used above, the regular FE meshes for this study were generated. For the irregular meshes, those used in the edge effect study of Chapter 7 were reused.

A full set of plots for maximum principal strain contours and displaced shapes is presented in Appendix II. Load-displacement graphs are presented below (Figure 9-31 - Figure 9-34).

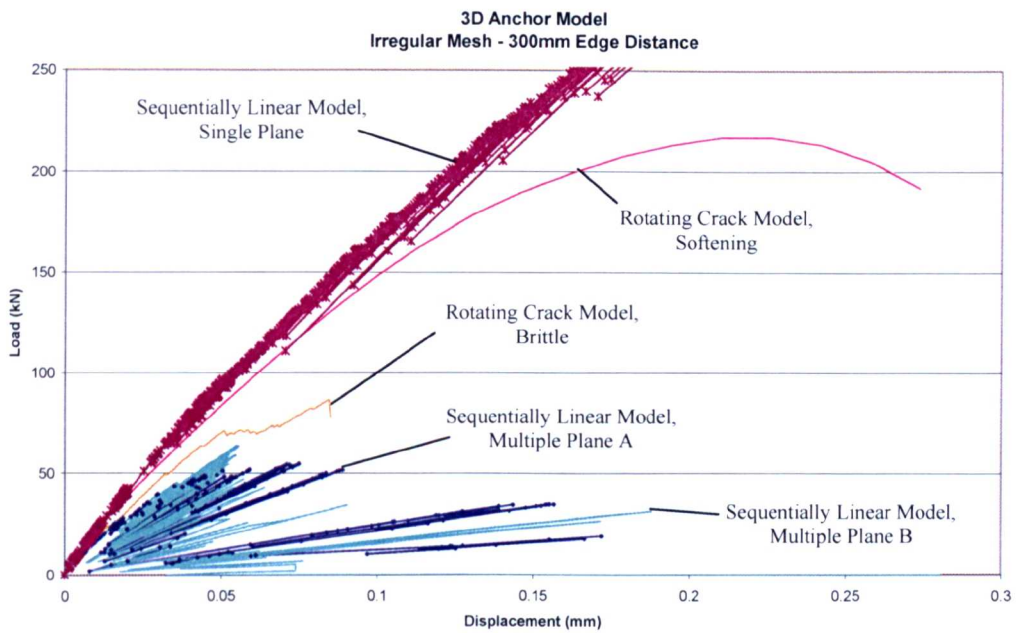


**Figure 9-31 - Load Displacement Graph for Pullout of Anchor at 300mm Edge Distance Using SL Models and an Irregular Mesh**

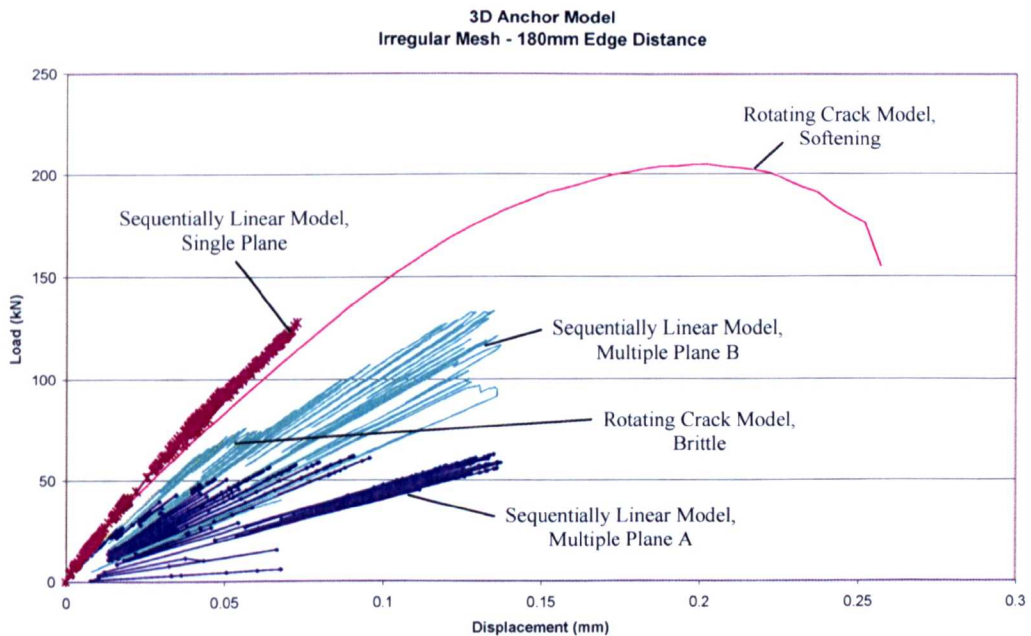


**Figure 9-32 - Load Displacement Graph for Pullout of Anchor at 180mm Edge Distance Using SL Models and an Irregular Mesh**

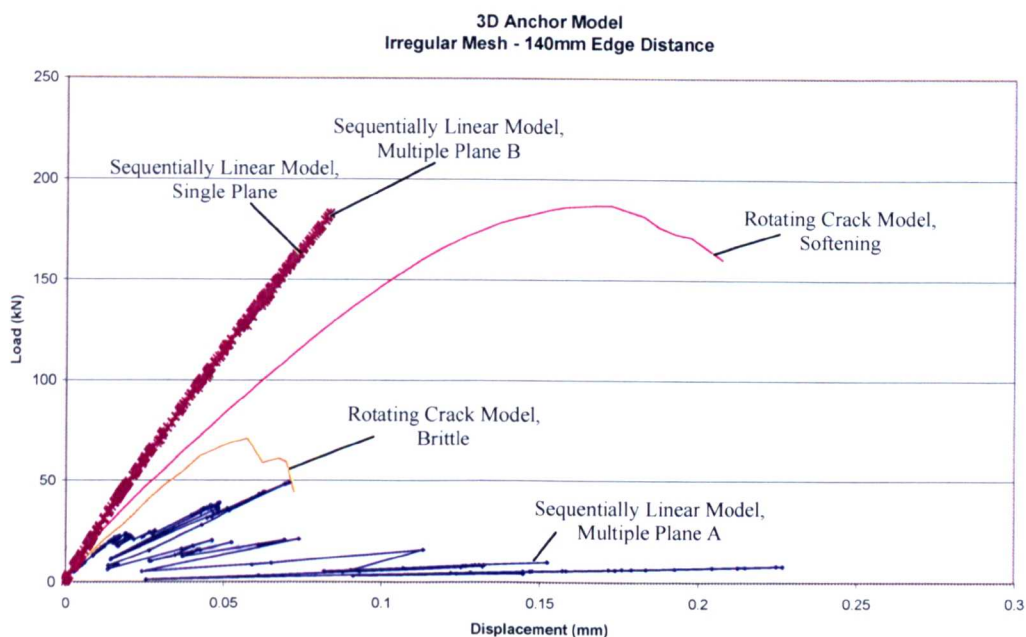


**Figure 9-33 - Load Displacement Graph for Pullout of Anchor at 140mm Edge Distance Using SL Models and an Irregular Mesh**

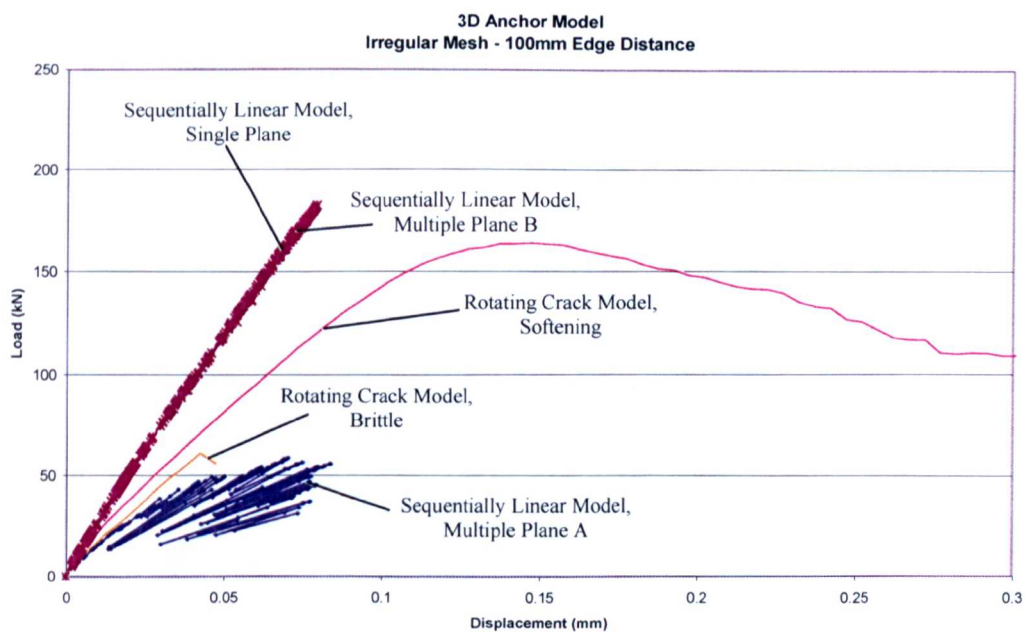


**Figure 9-34 - Load Displacement Graph for Pullout of Anchor at 100mm Edge Distance Using SL Models and an Irregular Mesh**

As before, the result from the Rotating Crack Model using exponential post-peak softening was taken as the reference solution. It can be seen from the load-displacement graphs above that with decreasing edge distance both the peak load and associated anchor displacement decrease. For the other models a general decrease in stiffness was noticed for decreasing edge distance. It is immediately obvious that once more the Sequentially Linear Model using the Single Plane rule for cracking does not give a softening response as the analysis progressed and instead seems to retain the initial linear-elastic stiffness. Figure 9-36 below states the failure mode for each analysis. It can be seen that for the Sequentially Linear models the Single Plane rule produces the same failure mode as the Rotating Crack Model with softening most often yet still produces this overly stiff response (Figure 9-35).

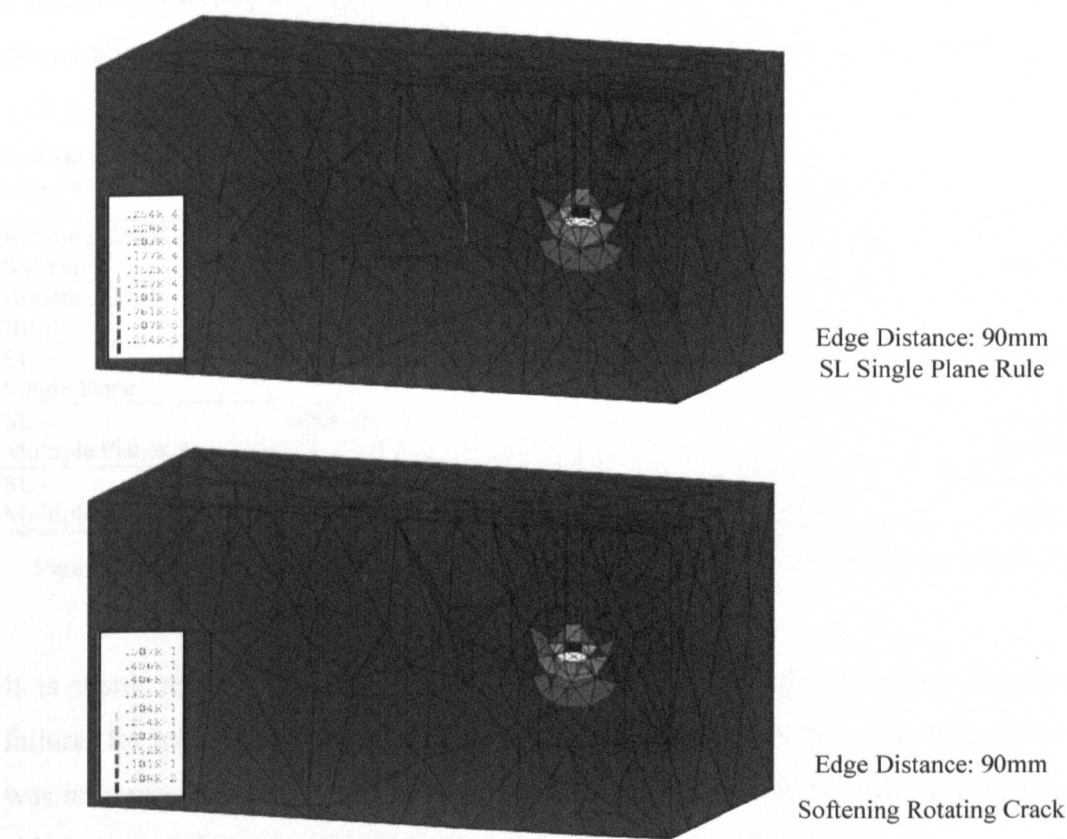


**Figure 9-35 - Comparison of Maximum Principal Strain Contour Plots for Post Peak Regime**

Multiple Plane Rule A produces load-displacement responses that appear more like the Brittle Rotating Crack Model but generally does not produce similar failure modes. It is

interesting to note that the Multiple Plane rule which allows many cracks to be formed at once (Rule B) gives similar responses to Rule A for 300 and 180mm edge distance but for lower distances it produces responses that are barely distinguishable from the Single Plane rule. The overly stiff response of the Single Plane rule had previously been attributed to stress locking due to the fact that the crack plane formed may be a significant angle away from the correct crack plane orientation and that no further planes could be formed to relieve this stress. This type of behaviour was not expected with the Multiple Plane Rule B because it did allow for additional cracks to form. However, one attribute that separates these rules from the Multiple Plane Rule A was that neither allow for the removal of an element if a previously cracked plane is reselected as being the most critical. Therefore it is likely that it is this feature that allows the Rule A analyses to produce a softening response. It also indicates that the restriction of only forming crack planes aligned with the local axis planes leads to unrealistic material behaviour.

**Irregular Mesh Analyses**

	300	180	140	100
Rotating Crack – Softening	Concrete Cone	Concrete Cone	Concrete Cone	Cracking Below Anchor
Rotating Crack – Brittle	Concrete Cone	Concrete Cone	Concrete Cone	Concrete Cone
SL – Single Plane	Concrete Cone	Concrete Cone	Cracking Below Anchor	Cracking Below Anchor
SL – Multiple Planes A	Pull Out	Pull Out	Concrete Cone	Cracking Below Anchor
SL – Multiple Planes B	Cracking Below Anchor	Concrete Cone	Cracking Below Anchor	Cracking Below Anchor

**Figure 9-36 - Failure Modes for Irregular Mesh with Differing Edge Distances and Model Types**

It is worth noting that, although the Rotating Crack Models produced concrete cone failures for most combinations of edge distance and softening type, the shape of the cone was influenced by the free edge. The figure below shows how the crack on the free edge side is at a much lower angle than that on the other side (Figure 9-37).

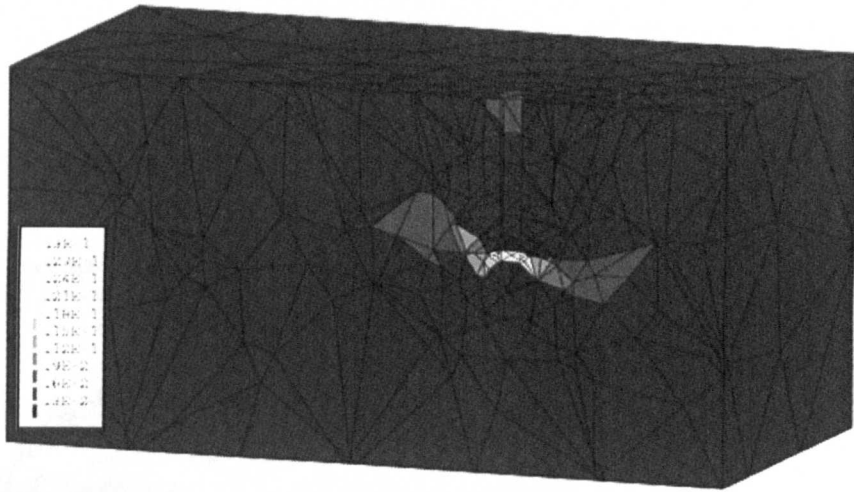


**Figure 9-37 - Maximum Principal Strain Contour Plot for Rotating Crack Model  
(Exponential Softening) at 180mm Edge Distance. Cross-section through Anchor**

The edge effect study was repeated for regular FE meshes. As before, a full set of plots for maximum principal strain contours and displaced shapes is presented in Appendix II and the corresponding load-displacement graphs are shown below (Figure 9-38 - Figure 9-41).



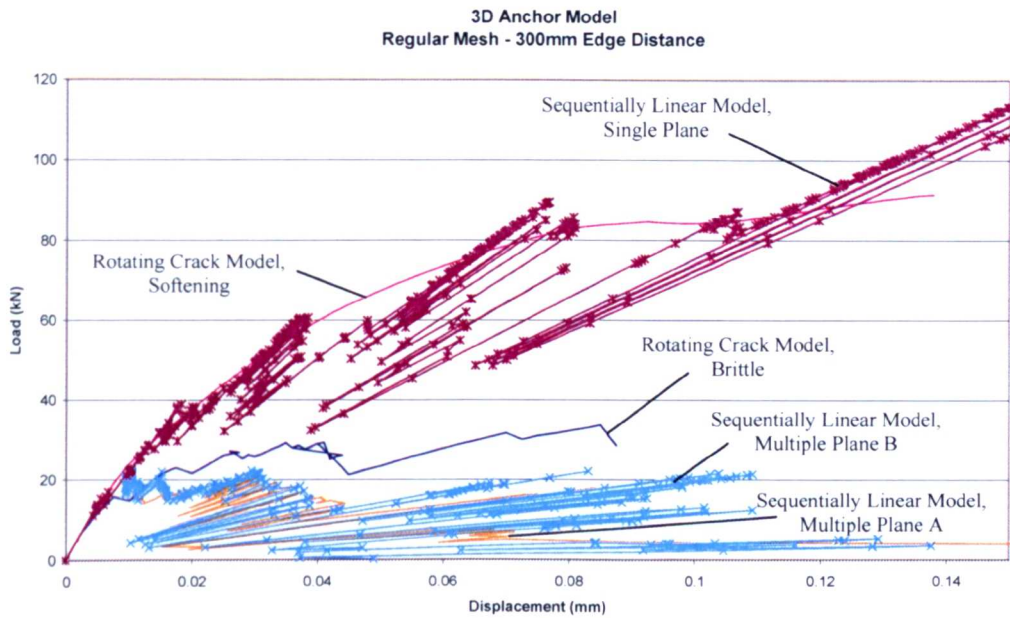


**Figure 9-38 - Load Displacement Graph for Pullout of Anchor at 300mm Edge Distance Using SL Models and a Regular Mesh**

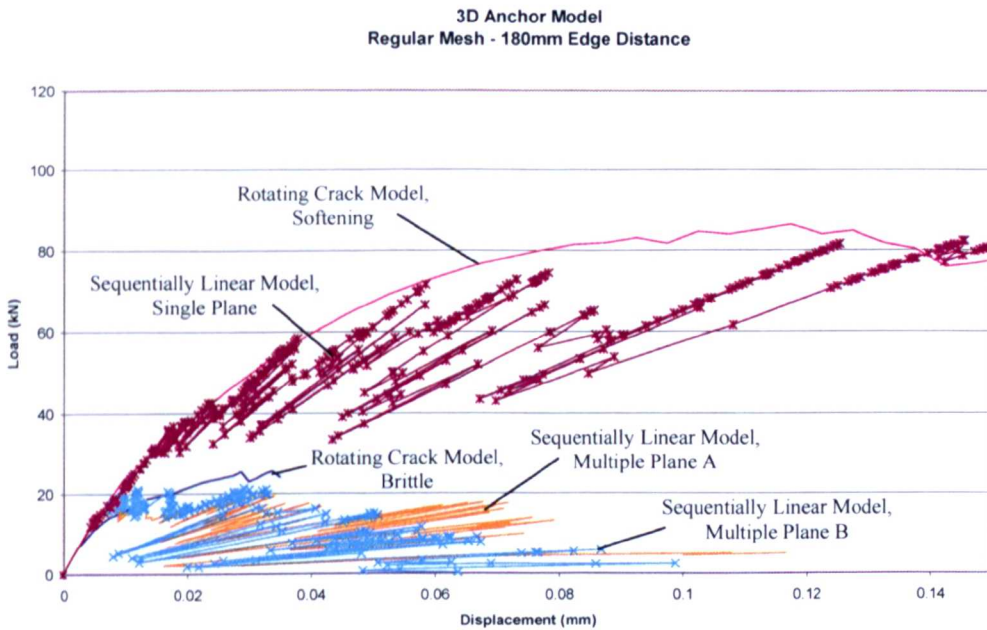


**Figure 9-39 - Load Displacement Graph for Pullout of Anchor at 180mm Edge Distance Using SL Models and a Regular Mesh**



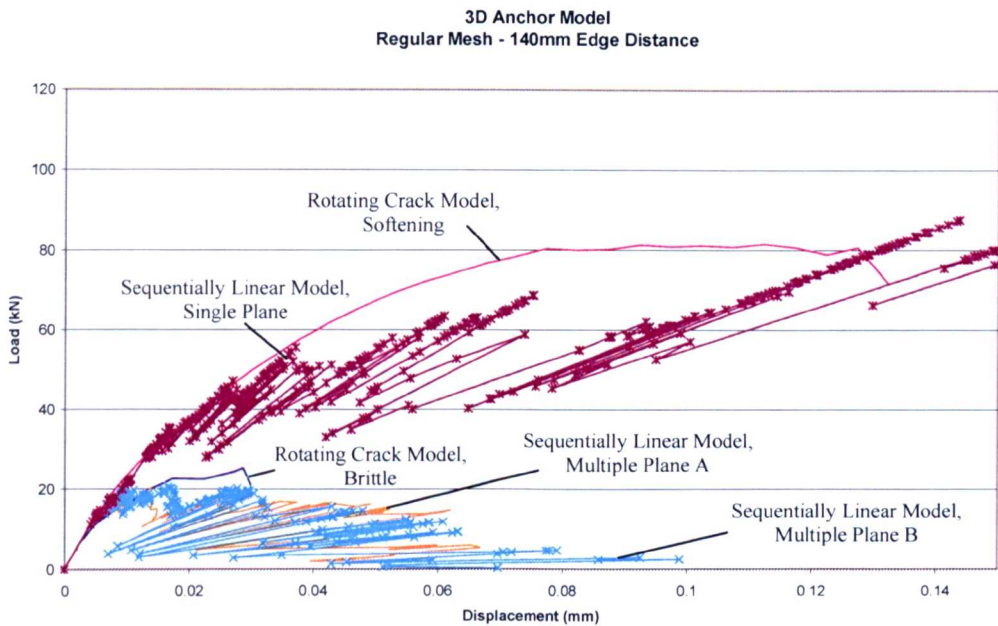


**Figure 9-40 - Load Displacement Graph for Pullout of Anchor at 140mm Edge Distance Using SL Models and a Regular Mesh**

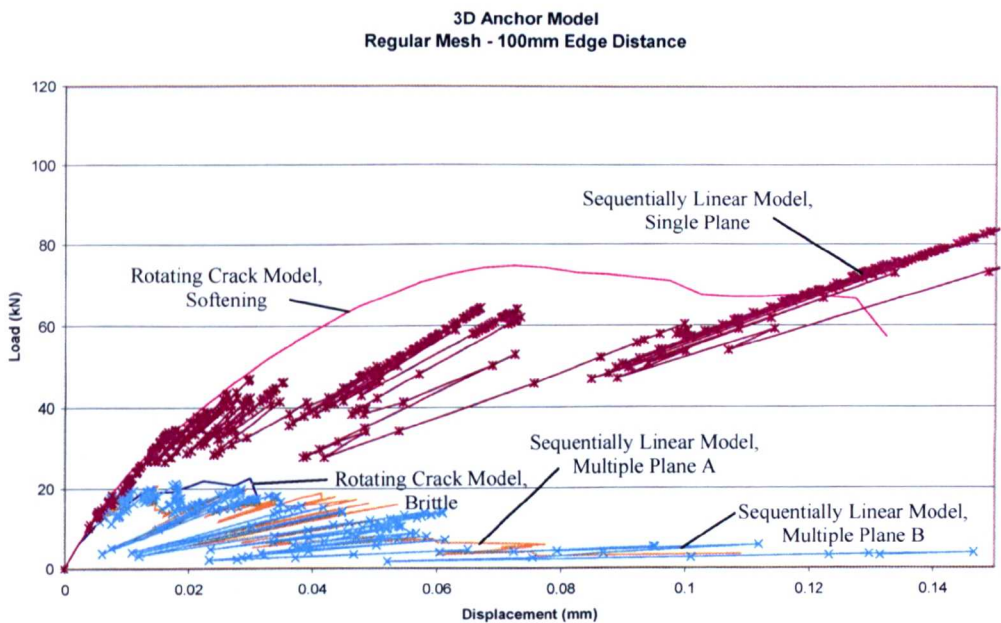


**Figure 9-41 - Load Displacement Graph for Pullout of Anchor at 100mm Edge Distance Using SL Models and a Regular Mesh**

It can be seen in the load-displacement graphs above that, for the regular mesh analyses, many of the features seen in the irregular mesh analyses are present. However, one

difference that is immediately apparent is the softening behaviour exhibited by the Sequentially Linear Model using the Single Plane rule. For 300 and 180mm edge distances the load-displacement responses from this model are quite similar to that of the Rotating Crack Model with exponential softening. However, for lower edge distances the match is less close after the 0.03mm of anchor pullout. This is because the failure mode for these analyses was via localised cracking below the anchor bolt instead of the concrete cone failure predicted by the Rotating Crack Model (Figure 9-43). Another point worth noting is that the angle of the concrete cone formed for the 300mm and 180mm edge distance problems was  $0^{\circ}$  (Figure 9-42). Therefore the term ‘cone’ is used very loosely. As mentioned before, the restriction of only being able to form cracks on element local axis planes restricts the rotation of the crack and hence a cone shape does not form.

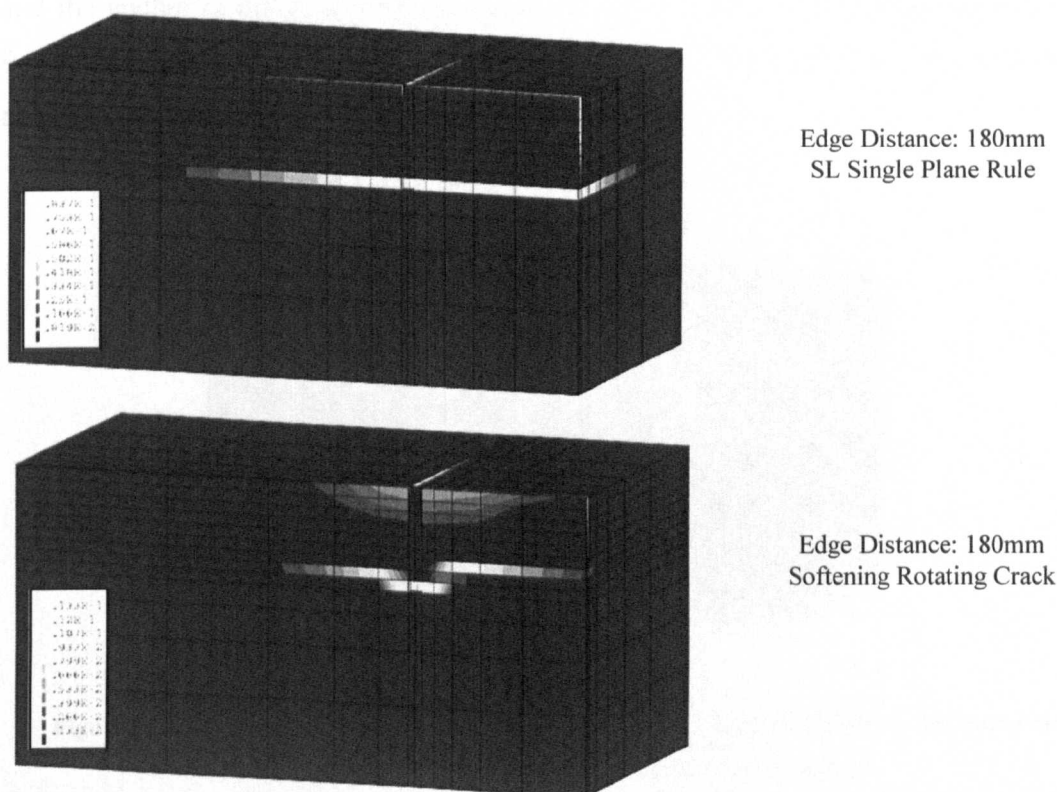


**Figure 9-42 - Comparison of Maximum Principal Strain Contour Plots for Post Peak Regime**

Regular Mesh Analyses

	300	180	140	100
Rotating Crack – Softening	Concrete Cone	Concrete Cone	Concrete Cone	<i>Concrete Cone</i>
Rotating Crack – Brittle	Concrete Cone	Concrete Cone	Concrete Cone	Concrete Cone
SL – Single Plane	Concrete Cone	Concrete Cone	<i>Concrete Cone</i>	<i>Concrete Cone</i>
SL – Multiple Plane A	Pull Out	Pull Out	<i>Pull Out</i>	<i>Pull Out</i>
SL – Multiple Plane B	Cracking Below Anchor	<i>Pull Out</i>	<i>Pull Out</i>	<i>Pull Out</i>

Figure 9-43 - Failure Modes for Regular Mesh with Differing Edge Distances and Model Types (entries shown in italics denote differing behaviour from irregular analysis)

For the regular mesh analyses the results of the two Multiple Plane rules are more similar. Except for the centre position (300mm edge distance) the predicted failure modes are the same and are pull out failures. For this failure mode the concrete around the anchor fails and the anchor is pulled out of the block leaving it mainly intact (Figure 9-44 - Figure 9-45). Because of this localised failure it can be seen that the load-displacement responses are rather insensitive to the edge distance.

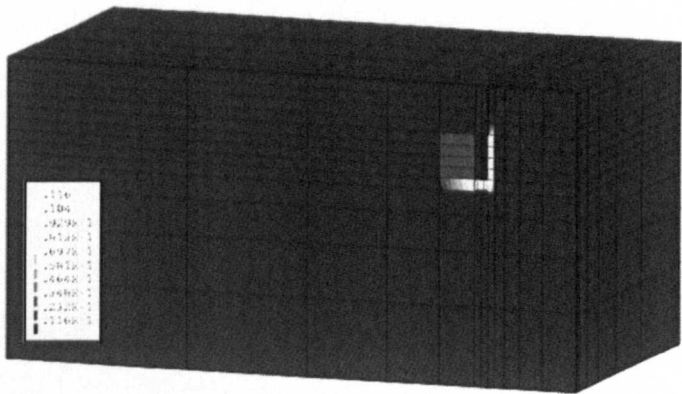
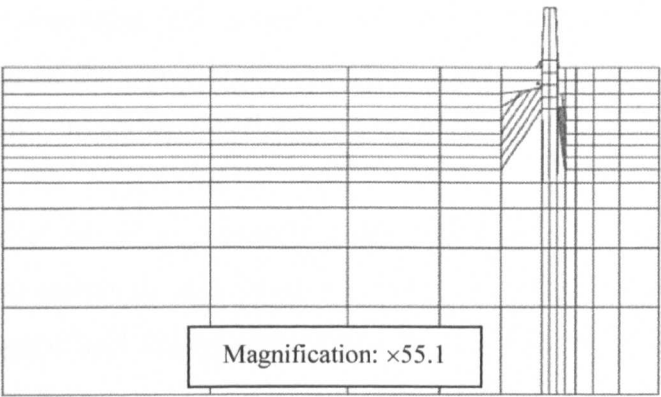


Figure 9-44 - Maximum Principal Strain for 100mm Edge Distance Problem Analyses Using Sequentially Linear Model with Multiple Plane Rule B



**Figure 9-45 - Displaced Shape Plot for 100mm Edge Distance Problem Analyses Using Sequentially Linear Model with Multiple Plane Rule B**

## 9.8 Summary and Conclusions

The study above highlights the potential of the Sequentially Linear technique. Its simplicity, in terms of the solution process, and stability are its key features. Even with this relatively basic implementation excellent results were produced for 2D anchor pullout analysis. The correct failure modes and load-displacement responses were produced and done so in a computationally efficient way. For 3D analyses the Sequentially Linear technique showed great promise. In many cases it gave the correct failure mode and good load-displacement response when the appropriate failure rule was used. However the limitations of crack orientation limit its accuracy and give rise to problems of mesh orientation. Also, and perhaps more importantly, low mesh density has a significant detrimental effect on the accuracy. None of the Failure Rules considered here gave a particularly satisfactory result.

Implementation of the model as a wrapper around an existing code was a useful technique as almost no changes were required to existing problems in order to apply SL analysis. Indeed, this is an approach that could be used with any suitable linear FE code. However it does present limitations when enhancing the SL model. The current model suffers from lack of mesh objectivity due to it not considering material softening and fracture energy. This could be solved by adding the regularised softening model proposed by Rots and Invernizzi. However, the softening model would be more suited to reside within the material library of the FE code rather than externally. The same is also true of the enhancements to the orthotropic crack feature that would allow cracks to form on planes other than those normal to the local element axes. Having the freedom to form cracks in arbitrary directions would also allow implementations of fixed, multiple fixed and rotating crack models to be developed and tested.

One remaining issue with Sequentially Linear models is their speed. It has been shown above that for relatively simple 2D problems the SL approach can greatly out-perform current non-linear models. The added advantage is that it automatically uses the optimum number of analysis steps to arrive at the solutions. In the case of 3D problems there was no speed advantage. This was due to the fact that a greater number of elements were

required to be cracked in order for the cracked surface to develop. This is a problem that is exacerbated by the introduction of material softening since several steps are required to fully crack (i.e. 'remove') an element. A number of options to speed up the analysis are possible. The most simplistic of which would be to process more than one element every step. Perhaps the four most critical elements could be softened in a given step. For problems with a degree of symmetry this would be an attractive solution as it is very likely that, upon processing one element, its symmetrical counterparts will come up for processing sequentially. If it could be assumed that the failure mode would remain identical then processing batches of four elements, for instance, would give a fourfold increase in speed. However, this assumption may not be correct and the approach could lead to a loss of accuracy.

An alternative approach to improving speed has been proposed by Rots and Invernizzi. This recognises that, for each step in the analysis, only a single stiffness term is altered. Therefore the solver routine may be altered so that the previous decomposition is updated and reused rather than recalculated every time.

Finally, there is work on going to develop interface elements for the Sequentially Linear model. The addition of these along with the other features proposed would lead to a very robust modelling framework with which the accurate analysis of expansion anchors could be performed. The Sequentially Linear Model itself does not place any restrictions on the type of approach to expansion modelling. Therefore, any of the techniques discussed in Chapter 9 could be used.

## **CHAPTER 10**

### **Summary and Recommendation for Future Work**

#### **10.1 Summary**

It has been shown that demands for higher performance, greater reliability and more flexibility have intensified research into anchor bolts. This research advances on several fronts - the design of new anchor technologies, the development of structural design methods and building codes and also research into the behaviour of anchors under complex loading conditions. For all these areas it has been shown that numerical modelling is an increasingly important tool; its strength being its ability to provide a unique insight into the structural processes involved in the load transfer from anchor to concrete from installation to ultimate failure. Historically numerical modelling of anchors has been focussed mostly on cast-in place anchors whose load transfer is via mechanical interlock. However, more recently work has been done on analysing anchors with more complex load transfer mechanisms such as bonded anchors and expansion anchors. It is the latter that has been the subject of the work presented here.

In order to effectively model anchor bolts it is necessary to have a suitably robust and accurate material model for concrete. Such a model must simulate the cracking behaviour most often associated with the tensile failure of anchors. Both the Traditional Crack Model and the Multi-Surface Plasticity Model were considered in this work and used in the analysis of the RILEM round robin anchor pullout problem. The results produced by both models were very satisfactory and compared well with those of other researchers in terms of peak load, failure mode and load-displacement response. However, the Traditional Crack Model showed an inability to fully trace the post-peak response due to significant stress locking. This was caused by misalignment of the crack planes as the principal planes rotated during the course of the analysis. This problem was also apparent in later 3D modelling of anchor pullout using this material model. The Total Strain Based Crack Model was chosen as an alternative as its rotating crack implementation was free from stress-locking due to crack misalignment. The formulation of the TSB Model



resulted in it being robust and extensive benchmarking showed it to be both accurate and reliable.

The phenomenon of stress locking itself was also investigated in detail and shown to be of great significance in anchor modelling. The effects of ‘traditional stress locking’, arising from the inability of a given element type to accurately model the required displacement field, can be mitigated by choosing a higher order element. It has also been shown that a more complex element type of the same order can reduce these effects. For anchor pullout problems it was proposed that 4-noded quadrilaterals and 8-noded brick elements are suitable for 2 and 3D analyses respectively. Problems associated with crack misalignment are peculiar to orthotropic softening models and, in the case of Crack Models, can only be reduced by selecting a Rotating Crack formulation. It is recommended that this be done even in cases of monotonic loading as rotation of the principal stress planes may still occur due to redistribution of stresses upon cracking. It was also shown that the concept of smeared cracks within FE modelling can lead to stress-locking either because of the requirement for displacement compatibility at the node points or because a poor kinematic representation of the crack discontinuity. Such problems may be avoided if the crack is modelled discretely using either DEM or a Discrete Crack Model, or by using a finite element incorporating embedded displacement discontinuities. Within this work standard finite elements were used however in latter models the finite element mesh was partially aligned with the expected crack trajectory to lessen the effects of this locking. The results produced were satisfactory although some degree of mesh bias was present in the crack formation. Overall it was concluded that awareness of these sources of spurious stress accumulation is very important. However, if appropriate choices are made when selecting the components for the numerical modelling their effects can be reduced to an acceptable level.

The study of the effects of low edge distance on the behaviour of anchor bolts was also a key feature of the presented work. This was investigated most thoroughly when considering an anchor bolt with a perfect bond between itself and the surrounding concrete. Analysis of this problem showed that even with a rather coarse, unstructured

mesh of tetrahedral elements the reduction in strength associated with reducing edge distance was accurately reproduced. This reduction compared very well with values presented in the design guide for the anchor under consideration. Also, the change in failure mode as the influence of the free edge increases was demonstrated. The study was extended to cover many positions for the anchor within the concrete block and a 3D surface was created to illustrate the associated strength reductions. The study showed the applicability of FE modelling of anchor bolts as a design tool for new anchor designs and for analysing proposed anchorage systems.

Modelling aspects of anchor expansion were examined in detail. The two necessary components identified were a suitable interface model for the anchor-concrete interface and a kinematic model to simulate the relationship between pullout force and expansion force. A Coulomb Friction Model applied to zero thickness structural interface elements was proposed for the modelling of the interface. This proved to be successful in that it gave a good representation of the pressure dependent, frictional interface present between the anchor expander and surrounding concrete. However, with the introduction of this interface it was apparent that its behaviour was very sensitive to the way the expansion forces were applied and also the geometry of the expander itself. In order to achieve the desired expansion force profile on the interface it was necessary to adopt an anchor geometry that was octagonal in plan cross-section and use a superposition process to 'tune' the application of expansion force such that the correct profile was achieved. It is noted that the correct profile can be achieved without such tuning if a contact analysis is performed rather than using a fully continuum-based approach and interface elements. In fact, this is what was done to obtain the correct profile initially. The individual components of the anchor expander were modelled explicitly as free bodies able to interact with one another as the expander was activated. For pragmatic reasons this contact analysis was performed in 2D using a different FE package from the main analysis. Ideally a single package should be used thus allowing the contact profile to evolve naturally as a result in changing pullout force and cracking of concrete. It was discovered that beyond the initial contact stages, the contact stress profile scaled linearly with pullout force. Therefore it was possible to apply a range of expansion pressures to

the full 3D model by scaling the expansion loadcase and show that increased expansion force leads to an increased stiffness in the load-displacement response of the anchor. Convergence problems prevented more detailed studies from being performed, in particular the influence of expansion pressure on anchors with low edge distance. This also demonstrated the difficulties of having two non-linear material models on the load path for the problem and underlined the need for robustness in each component of the analysis framework.

Problems of convergence when analysing expansion behaviour lead to the investigation of alternative modelling methods. So called ‘Sequentially Linear’ techniques comprise of a series of linear-elastic analyses, after each of which the most critical element is chosen, via a predetermined failure rule, and removed from the problem. This method was implemented in the framework of the Finite Element Method and a number of failure rules were proposed and analysed. Very satisfactory results were produced in terms of load-displacement response and crack pattern when analysing a 2D anchor pullout model with a Rankine-based failure rule. However, the results were mesh inobjective owing to the lack of an appropriate post-peak softening model based on fracture energy. For 3D analyses an orthotropic model was proposed whereby a crack was modelled by reducing the stiffness in an appropriate direction to zero. Although a number of different failure rules were proposed for this orthotropic model none resulted in particularly satisfactory results. This was mainly due to the fact that the orientations of the crack plane were limited to the local planes of the element being fractured. The effect was made worse by the relatively coarse mesh used. This aside, the model did show strength and stiffness reductions in the anchor as the edge distance decreased. In many cases the correct failure mode was also identified. Due to its nature the stability of the model was assured. And because of its simplistic nature it outperformed non-linear models in terms of speed for problems where the crack pattern is confined to a relatively small number of elements. Sequentially Linear analysis is a modelling technique that shows a great deal of potential.

Overall this work has identified and investigated the important aspects of the modelling of expansion anchors. Areas such as choice of modelling framework, selection of

appropriate constitutive models and associated parameters and simplification of the problem and its implication have been addressed. Each factor has been discussed in detail and recommendations given. The particular problem of interest was the influence of edge effects on the pullout behaviour of anchor bolts and this has been analysed successfully. Various methods for the simulation of the expansion mechanism have also been demonstrated. Finally an alternative FE modelling technique was developed and was demonstrated to be robust and capable of modelling anchor pullout problems. Overall the most successful set-up examined for the analysis of anchor pullout was the Rotating Crack formulation of the Total Strain Based Crack Model. When used with a structured finite element mesh of 8-noded brick elements the values of peak load produced were in reasonable agreement with design guide figures. Accurate crack patterns and failure modes were also captured.

## **10.2 Recommendations for Future Work**

There are a number of possible directions for research leading on from the work presented here. In terms of the detailed modelling of expanding anchors the current study exposed weaknesses associated with the robustness of the interface element model within the chosen framework. It is quite possible that this has been addressed in later versions of the software. However, there is no reason why other modelling frameworks could not be explored. These may be commercial, academic or developed by the researcher. The Total Strain Based Crack Model was noted for its robustness but it is likely that similar Rotating Crack Models are adequate for the purposes of anchor analysis. It was also noted that FE models including a displacement discontinuity embedded in the displacement field for the finite element itself [Jirasek (1998), Alfaiate, Wells, Sluys, de Borst (2001)] show great potential. They model the fracturing processes within concrete without many of the problems of stress locking associated with the smeared crack approach. Such methods are also being formulated for the modelling of interfaces. It would be interesting to see how these methods perform for the modelling of anchor bolts.

In the modelling of the expansion process itself there are a number of potential areas of research. Firstly the concept of linking the expansion force to the tensile force within the bolt is an attractive prospect. This would be achieved in a similar way to the tied-displacement method investigated in this work. The tension in the bolt would be assessed by summing the reaction forces at the anchor head and appropriate scaling factors used to derive the correct expansion forces for each position on the expander. The scaling factors themselves would be calculated by considering the relationship between pullout force and expansion profile found via the ADINA contact modelling. A small amount of additional computer code would be required to implement this approach. The advantage of this concept is that it recognises the expansion process as being a force-driven one rather than displacement-driven. A vertical displacement of the anchor head does not necessarily lead to a proportional radial displacement of the expander since the level of confinement provided by the concrete to resist such displacements varies throughout the pullout process. However, an increased tension in the bolt always leads to a proportional increase

in expansion force (assuming elastic properties for steel) and it is this relationship on which this method is based.

A more complex but more accurate way to model the expansion is by considering it as a contact problem and modelling it as such. This was successfully done for a 2D, plane stress problem in this work however the extension into 3D is important. Of greater importance is the inclusion of the contact modelling within the full pullout analysis rather than as a method to obtain a suitable steel-concrete contact stress profile for a subsequent, non-contact analysis. It is certain in the case of low edge distance that the expansion process of the anchor will be affected and that this has implications on peak load, load-displacement response and perhaps also the failure mode.

For the Sequentially Linear Model the first area of research should be to rewrite the model within a suitable FE framework. This may either be an existing FE framework capable of 3D linear-elastic analysis or a code developed by the researcher. By doing so features such as arbitrary crack orientations and material softening can be easily incorporated. The option of developing a new FE framework instead of using an existing one has the disadvantage of the initial groundwork required but may yield benefits when considering options to optimise the solver used for the model. The rewritten code should be developed to include both the so-called ‘sawtooth’ material softening as proposed by Rots and Invernizzi [Rots & Invernizzi (2003)] and also the orthogonal crack model based on an orthotropic material description as proposed in this work. With the benefit of having access to the source code of the FE framework the extension to include arbitrary crack directions should be implemented. The robustness of this model has been proven and it would be satisfying to see this coupled with accurate material modelling.

As with all computational work it is expected that advances in computer technology will allow for ever-increasing detail and complexity to be considered when analysing problems. The current modelling approaches capture the important aspects of the structural behaviour of anchor bolts. However the increased power of more modern computers will enable finer meshes to be used and geometries more closely following the

actual anchor bolts to be specified. It is expected that these improvements will bring greater accuracy and fidelity. It is also hoped that such advances will also allow computational modelling of expanding anchors become a realistic tool for structural designers and provide rapid and accurate analyses of complex anchorage systems.



## Appendix A

### Source Code for Sequentially Linear Wrapper Program

```
/* Sequentially Linear Wrapper 2.0
 *
 * DIANA frontend for SL analysis
 *
 */

#include <stdio.h>
#include <stdlib.h>
#include <string.h>
#include <math.h>
#include "jacobi_eigs.h"

#define MAXSTEPS    40
#define MINELEM     19
#define MAXELEM     591
#define FTCONC      3
#define MAXRANGE    10

typedef struct {
    int      number;
    int      direction;
    int      material;
} critical;

void readsl(char* datafile, int* criterion, int* maxsteps, int *restart, int elemrange[],
int *totelems, int *ngauss);
void parseelems(int elemrange[], char line[]);
int numberofelems(int elemrange[]);
critical findcritical(int criterion,int elemrange[], int mactable[], int ngauss);
int checkrange(int current_elem, int elemrange[]);
void readinput(char *datafile, critical critelem, int *mactable, int criterion);
void updatematerial(int elem, char *line);
void checklen(char *tmpline);
void addtotensor(double stensor[4][4], double svect[7]);
void findprincipal(double stensor[4][4], double eigvect[4][4], double eigval[4][4]);
void SortValues(double eigval[4][4], double eigvect[4][4]);
void swap(double x[4][4], double y[4][4], int index1, int index2);
int getdirection(double eigvect[4][4], int criterion);
int findnewmat(critical critelem, int *mactable, int criterion);
```

```

int main(int argc, char *argv[])
{
    char  datafile[256], comfile[256], command[256];
    int    criterion=0, maxsteps=0, restart=0, elemrange[MAXRANGE*2] = {0};
    int     totelems, ngauss=8, *mattable;
    int  step=1, range, loop;
    critical  critelem;

    critelem.number = 1;

    if (argc == 3) {
        strcpy(datafile, argv[1]);
        strcpy(comfile, argv[2]);
    } else {
        printf("Syntax: sl [dianafile] [commandfile]\n");
        return 0;
    }

    readsl(datafile, &criterion, &maxsteps, &restart, elemrange, &totelems, &ngauss);
    if (restart == 1) printf("\nRestarting Analysis\n");
    printf("Failure Criterion:    %d\n", criterion);
    printf("Number of Analysis Steps: %d\n", maxsteps);

    if (restart != 1) {
        remove("sl.dat");
        remove("output.txt");
        sprintf(command, "cp %s sl.dat", datafile);
        system(command);
    }
    sprintf(datafile, "sl.dat");
    sprintf(command, "diana %s %s", datafile, comfile);

    /* Create and initialise material table */
    mattable = (int *)malloc((totelems+1) * sizeof(int));
    range = 0;
    while ((elemrange[range] != 0) && (range < MAXRANGE)) {
        for (loop=elemrange[range]; loop<=elemrange[range+10]; loop++) {
            mattable[loop] = 2;
        }
        range++;
    }
    printf("Material Table Initialised\n");

    while((critelem.number !=0) && (step <= maxsteps)) {
        system(command);
        critelem = findcritical(criterion, elemrange, mattable, ngauss);
        readinput(datafile, critelem, mattable, criterion);
        printf("\nAnalysis Step %d\n", step);
        printf("Element %d is critical\n", critelem.number);
        printf("New Material: %d\n\n", mattable[critelem.number]);
        step++;
    }
    free(mattable);
    return 0;
}

```

```

void readsl(char* datafile, int* criterion, int* maxsteps, int *restart, int elemrange[],
int* totelems, int* ngauss)
{
    int    value;
    char    line[120], word[10], slfile[256], *p;
    FILE    *file;

    strcpy(slfile, datafile);
    p = strstr(slfile, ".");
    sprintf(p, ".sl");

    file = fopen(slfile, "r");
    if (file == NULL) {
        printf("Failed to open sl file: %s\n", slfile);
        exit(0);
    }

    while (fgets(line, 100, file) != NULL) {
        sscanf(line, "%s%d", word, &value);
        if (strcmp(word, "CRITERION", 9) == 0) *criterion = value;
        if (strcmp(word, "MAXSTEPS", 8) == 0) *maxsteps = value;
        if (strcmp(word, "RESTART", 7) == 0) *restart = value;
        if (strcmp(word, "CELEMS", 6) == 0) parseelems(elemrange, line);
        if (strcmp(word, "TOTALEM", 9) == 0) *totelems = value;
        if (strcmp(word, "NGAUSS", 6) == 0) *ngauss = value;
    }

    fclose(file);
}

```

```

void parseelems(int elemrange[], char line[])
{
    int    range=0;
    char    *p, *q;

    p = strtok(line, " \t");
    while ((p = strtok(NULL, " \t")) != NULL) && (range < MAXRANGE)) {
        if ((q = strpbrk(p, "-")) == NULL) {
            /* Single number entry */
            elemrange[range] = atoi(p);
            elemrange[range+10] = atoi(p);
        } else {
            /* Range entry */
            *q++ = 0;
            elemrange[range] = atoi(p);
            elemrange[range+10] = atoi(q);
        }
        range++;
    }
}

```

```

int numberofelems(int elemrange[])
{
    int range=0, nelems=0;

    while (elemrange[range] != 0) {
        nelems += ((elemrange[range+10] - elemrange[range]) + 1);
    }

    return nelems;
}

```

```

critical findercritical(int criterion, int elemrange[], int mattable[], int ngauss)
{
    int    current_elem=elemrange[0], range=0, end = 0, loop, loop2;
    int    found_elem, intpnt;
    double svect[7];
    double stensor[4][4] = {{0,0,0,0},{0,0,0,0},{0,0,0,0},{0,0,0,0}};
    double eigvect[4][4], eigval[4][4];
    double max_s1=FTCONC, load=0.0;
    char    line[120], resultsfile[15];
    FILE    *results, *out;
    critical    critelem, testelem;

    critelem.number = 0;

    sprintf(resultsfile, "lstress.tb");

    results = fopen(resultsfile, "r");
    if (results == NULL) {
        printf("Failed to open results file %s\n", resultsfile);
        return critelem;
    }

    if (fgets(line, 100, results) == NULL) {
        printf ("Failed to get line from input file\n");
        exit(0);
    }

    while ((fgets(line, 100, results) != NULL) && (end != 1)){
        fflush(stdout);
        sscanf(line, "%d", &found_elem);

        /* Read in the local stress components and form average stress tensor */
        if (current_elem == found_elem) {
            sscanf(line, "%d%d%lf%lf%lf%lf%lf", &found_elem, &intpnt,
                &stensor[1][1], &stensor[2][2], &stensor[3][3],
                &stensor[1][2], &stensor[2][3], &stensor[3][1]);
            stensor[2][1] = stensor[1][2];
            stensor[3][2] = stensor[2][3];
            stensor[1][3] = stensor[3][1];

            if (ngauss > 1) {
                for (loop=2; loop<=ngauss; loop++) {
                    do {
                        fgets(line, 100, results);
                        sscanf(line, "%d", &intpnt);
                    } while (intpnt != loop);
                    sscanf(line, "%d%lf%lf%lf%lf%lf%lf",
                        &intpnt, &svect[1], &svect[2], &svect[3], &svect[4], &svect[5],
&svect[6]);

                    addtotensor(stensor, svect);
                }

                for (loop=1; loop<=4; loop++) {
                    for (loop2=1; loop2<=4; loop2++) {
                        stensor[loop][loop2] = stensor[loop][loop2] / ngauss;
                    }
                }

                findprincipal(stensor, eigvect, eigval);
                if (checkrange(current_elem, elemrange) == 1) {

                    if (eigval[1][1] >= max_s1) {
                        printf("Principal Stress for element %d is: %lf\n", current_elem,
eigval[1][1]);
                    }

                    /* Multiple Fixed Crack (uniaxial - single crack initiation) */
                    if (criterion == 1) {
                        if (eigval[1][1] > max_s1) {
                            max_s1 = eigval[1][1];

```

```

        critelem.number = current_elem;
        critelem.direction = getdirection(eigvect, criterion);
        critelem.material = findnewmat(critelem, matable, criterion);
        load = eigval[1][1] / FTCONC;
    }
}

/* Multiple Fixed Crack (Biaxial - single crack initiation) */
if (criterion == 2) {
    if (eigval[1][1] > max_sl && ((eigval[2][2] > 0) || (eigval[3][3] > 0))) {
        max_sl = eigval[1][1];
        critelem.number = current_elem;
        critelem.direction = getdirection(eigvect, criterion);
        critelem.material = findnewmat(critelem, matable, criterion);
        load = eigval[1][1] / FTCONC;
    }
}

/* Single Fixed Crack Model */
if (criterion == 3) {
    if ((eigval[1][1] > max_sl) && (matable[current_elem] == 2)) {
        max_sl = eigval[1][1];
        critelem.number = current_elem;
        critelem.direction = getdirection(eigvect, criterion);
        critelem.material = findnewmat(critelem, matable, criterion);
        load = eigval[1][1] / FTCONC;
    }
}

/* Multiple Fixed Crack (uniaxial - Multiple Crack Initiation) */
if (criterion == 4) {
    if (eigval[1][1] > max_sl) {
        testelem.number = current_elem;
        testelem.direction = getdirection(eigvect, criterion);
        testelem.material = findnewmat(testelem, matable, criterion);
        if (testelem.material != matable[testelem.number]) {
            critelem = testelem;
            load = eigval[1][1] / FTCONC;
            max_sl = eigval[1][1];
        }
    }
}

/* Other Failure Criteria Would Go Here */

}
current_elem++;
if (current_elem > elemrange[range+10]) {
    range++;
    current_elem = elemrange[range];
    if (current_elem == 0) end = 1;
}
}

fclose(results);
printf("\nLoad Factor:  %lf\n", load);

out = fopen("output.txt", "a");
fprintf(out, "Load Factor:  %lf\n", load);
fclose(out);

return critelem;
}

```

```

int checkrange(int current_elem, int elemrange[])
{
    int range = 0, check = 0;

    while (elemrange[range] != 0) {
        if ((current_elem >= elemrange[range]) && (current_elem <= elemrange[range+10]))
            check = 1;
        range++;
    }
    return check;
}

void readinput(char *datafile, critical critelem, int *mattable, int criterion)
{
    int status=0, new_material;
    char line[100];
    FILE *data, *temp;

    data = fopen(datafile, "r");
    if (data == NULL) {
        printf("Failed to open DIANA datafile file\n");
        exit(0);
    }

    temp = fopen("sl.tmp", "w");
    if (temp == NULL) {
        printf("Failed to open temporary file %s\n", "sl.tmp");
        exit(0);
    }

    while (fgets(line, 100, data) != NULL) {
        switch (status) {

            case 0:
                if (strncmp("MATERIALS", line, 9) == 0) status = 1;
                break;

            case 1:
                if (strncmp("/", line, 1) == 0) {
                    updatematerial(critelem.number, line);
                } else {
                    if (strncmp("\n", line, 1) == 0) {
                        status = 2;

                        new_material = critelem.material;
                        fprintf(temp, "/ %d / %d\n", critelem.number, new_material);
                        mattable[critelem.number] = new_material;
                    }
                }
                break;

            case 2:
                /* Do nothing. We're past the Material data */
                break;
        }
        fprintf(temp, "%s", line);
    }

    fclose(data);
    fclose(temp);
    remove(datafile);
    rename("sl.tmp", datafile);
}

```

```

void updatematerial(int elem, char *line)
{
    int    listend=0, start, end, r1, r2;
    char  *p, *q, tmp[100], tmp2[10];

    sprintf(tmp, "/ ");

    p = strtok(line, " ");
    while ((p = strtok(NULL, " ")) != NULL) && (listend == 0) {
        tmp[0] = '\0';
        if (strcmp("/", p, 1) == 0) {
            listend = 1;
            sprintf(tmp, "/ %s", p+2);
        } else {
            /* Do stuff here to parse the material list */
            if ((q = strchr(p, "-")) == NULL) {
                /* Single number entry */
                start = atoi(p);
                if (start != elem) sprintf(tmp, "%s ", p);
            } else {
                /* Range entry */
                p[strlen(p, "-")] = '\0';
                strcpy(tmp2, p);
                start = atoi(tmp2);
                end = atoi((q+1));
                if ((start < elem) && (end > elem)) {
                    r1 = elem - 1;
                    r2 = elem + 1;
                    if ((start != r1) && (end != r2)) {
                        sprintf(tmp, "%d-%d %d-%d ", start, r1, r2, end);
                    } else {
                        if ((start == r1) && (end == r2)) {
                            sprintf(tmp, "%d %d ", start, end);
                        } else {
                            if (start == r1) sprintf(tmp, "%d %d-%d ", start, r2, end);
                            if (end == r2) sprintf(tmp, "%d-%d %d ", start, r1, end);
                        }
                    }
                }
            }
        }
        if (start == elem) start++;
        if (end == elem) end--;
        if (start != end) {
            sprintf(tmp, "%d-%d ", start, end);
        } else {
            sprintf(tmp, "%d ", start);
        }
    }
    strcat(tmp, tmp2);
}
checklen(tmp);
sprintf(line, tmp);
}

```



```
void checklen(char *tmpline)
```

```
{
    int    done=0;
    char   *p, *q, tmp[100];

    if (strlen(tmpline) > 60) {
        strcpy(tmp, tmpline);

        p = tmpline+30;    q = tmp+30;

        while (*p != '\0') {
            if ((*p == ' ') && (done != 1)) {
                sprintf(q, " / 2\n/ ");
                q = q + 9;
                done = 1;
            } else {
                *q = *p;
                q++;
            }
            p++;
        }
        // q++;
        *q = '\0';

        strcpy(tmpline, tmp);
    }
}
```

```
void addtotensor(double stensor[4][4], double svect[7])
```

```
{
    /* Construct Stress Tensor */
    stensor[1][1]+=svect[1]; stensor[1][2]+=svect[4]; stensor[1][3]+=svect[6];
    stensor[2][1]+=svect[4]; stensor[2][2]+=svect[2]; stensor[2][3]+=svect[5];
    stensor[3][1]+=svect[6]; stensor[3][2]+=svect[5]; stensor[3][3]+=svect[3];
}
```

```
void findprincipal(double stensor[4][4], double eigvect[4][4], double eigval[4][4])
```

```
{
    double tolerance = 0.0000000000001;

    jacob_i_eigs(3, stensor, eigvect, eigval, tolerance);
    SortValues(eigval, eigvect);

    /* Print the eigenvector associated with the maximum eigenvalue */
    /* printf("%12.3e, %12.3e, %12.3e, ", eigvect[1][1], eigvect[2][1], eigvect[3][1]);
*/
}
```

```
void SortValues(double eigval[4][4], double eigvect[4][4])
```

```
{
    if (eigval[2][2]<eigval[3][3]) swap(eigval, eigvect, 2, 3);
    if (eigval[1][1]<eigval[2][2]) swap(eigval, eigvect, 1, 2);
}
```

```

void swap(double x[4][4], double y[4][4], int index1, int index2)
{
    double tmpvals[4];
    int loop;

    /* Swap values on diagonal of x */
    tmpvals[1] = x[index1][index1];
    x[index1][index1] = x[index2][index2];
    x[index2][index2] = tmpvals[1];

    /* Swap columns on y */
    for (loop=1; loop<=3; loop++) {
        tmpvals[loop] = y[loop][index1];
    }
    for (loop=1; loop<=3; loop++) {
        y[loop][index1] = y[loop][index2];
    }
    for (loop=1; loop<=3; loop++) {
        y[loop][index2] = tmpvals[loop];
    }
}

int getdirection(double eigvect[4][4], int criterion)
{
    int direction;

    if (criterion !=4) {
        direction = 1;
        if (fabs(eigvect[2][1]) > fabs(eigvect[1][1])) {
            if (fabs(eigvect[3][1]) > fabs(eigvect[2][1])) {
                direction = 3;
            } else {
                direction = 2;
            }
        } else {
            if (fabs(eigvect[3][1]) > fabs(eigvect[1][1])) {
                direction = 3;
            }
        }
    } else {
        direction =0;
        //printf("cos x: %lf direction: %d\n", eigvect[1][1], direction);
        if (fabs(eigvect[1][1]) >= 0.5) direction = 1;
        //printf("cos y: %lf direction: %d\n", eigvect[2][1], direction);
        if (fabs(eigvect[2][1]) >= 0.5) {
            if (direction == 0) direction = 2;
            if (direction == 1) direction = 4;
        }
        //printf("cos y: %lf direction: %d\n", eigvect[3][1], direction);
        if (fabs(eigvect[3][1]) >= 0.5) {
            if (direction == 0) direction = 3;
            if (direction == 1) direction = 6;
            if (direction == 2) direction = 5;
            if (direction == 4) direction = 7;
        }
        if (direction == 0) {
            printf("Error: Direction equals zero!\n");
        }
    }

    return direction;
}

```

```

int findnewmat(critical critelem, int *mattable, int criterion)
{
    int new_material = 2;

    switch (mattable[critelem.number]) {
        case 2: /* Virgin Concrete */
            if (critelem.direction == 1) new_material = 5;
            if (critelem.direction == 2) new_material = 6;
            if (critelem.direction == 3) new_material = 7;
            if (critelem.direction == 4) new_material = 8;
            if (critelem.direction == 5) new_material = 9;
            if (critelem.direction == 6) new_material = 10;
            if (critelem.direction == 7) new_material = 4;
            break;

        case 5: /* Softened in X */
            if (critelem.direction == 1) {
                if (criterion == 4) {
                    new_material = 5;
                } else {
                    new_material = 4;
                }
            }
            if (critelem.direction == 2) new_material = 8;
            if (critelem.direction == 3) new_material = 10;
            if (critelem.direction == 4) new_material = 8;
            if (critelem.direction == 5) new_material = 4;
            if (critelem.direction == 6) new_material = 10;
            if (critelem.direction == 7) new_material = 4;
            break;

        case 6: /* Softened in Y */
            if (critelem.direction == 1) new_material = 8;
            if (critelem.direction == 2) {
                if (criterion == 4) {
                    new_material = 6;
                } else {
                    new_material = 4;
                }
            }
            if (critelem.direction == 3) new_material = 9;
            if (critelem.direction == 4) new_material = 8;
            if (critelem.direction == 5) new_material = 9;
            if (critelem.direction == 6) new_material = 4;
            if (critelem.direction == 7) new_material = 4;
            break;

        case 7: /* Softened in Z */
            if (critelem.direction == 1) new_material = 10;
            if (critelem.direction == 2) new_material = 9;
            if (critelem.direction == 3) {
                if (criterion == 4) {
                    new_material = 7;
                } else {
                    new_material = 4;
                }
            }
            if (critelem.direction == 4) new_material = 4;
            if (critelem.direction == 5) new_material = 9;
            if (critelem.direction == 6) new_material = 10;
            if (critelem.direction == 7) new_material = 4;
            break;

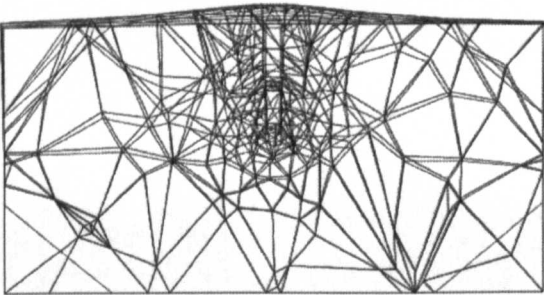
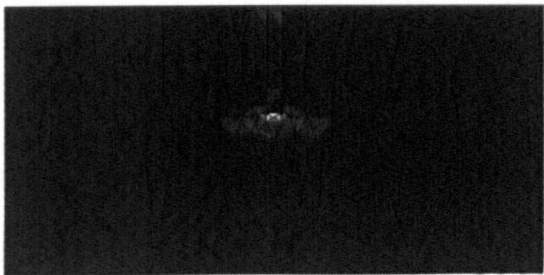
        case 8: /* Softened in X & Y */
        case 9: /* Softened in Y & Z */
        case 10: /* Softened in Z & X */
            new_material = 4;
            break;
    }
    return new_material;
}

```

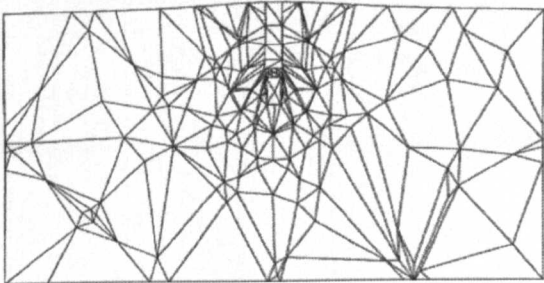
# Appendix B

## Sequentially Linear Analysis Diagrams

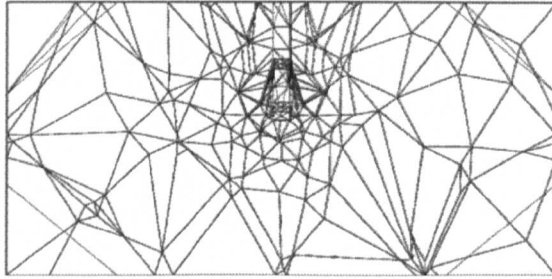
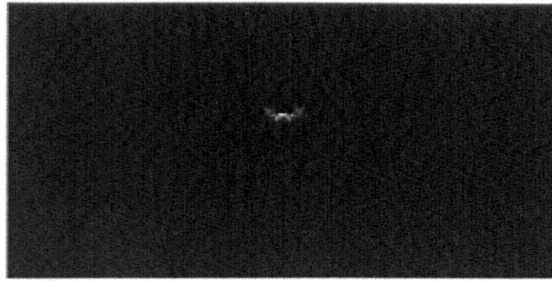
### Section 1 – Irregular Meshes



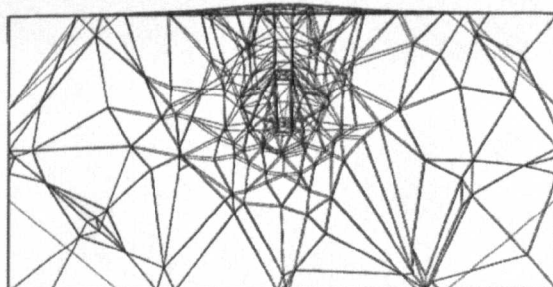
Edge Distance: 300mm, Single Plane Rule



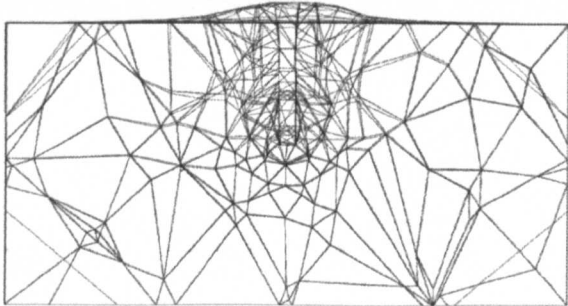
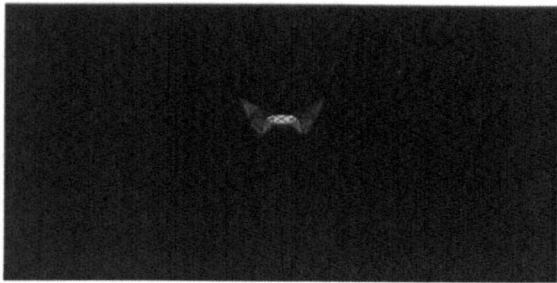
Edge Distance: 300mm, Multiple Plane Rule B



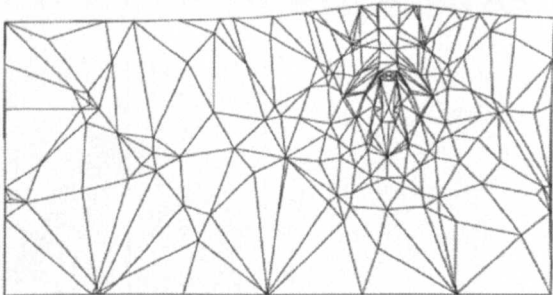
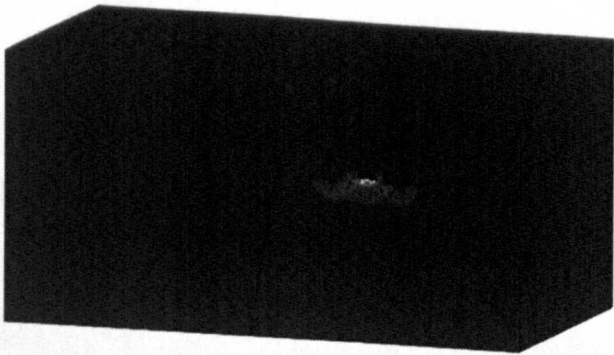
**Edge Distance: 300mm, Multiple Plane Rule A**



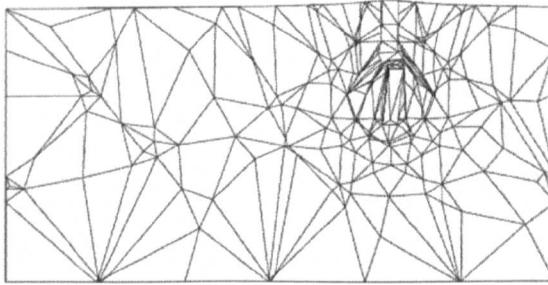
**Edge Distance: 300mm, Rotating Crack - Softening**



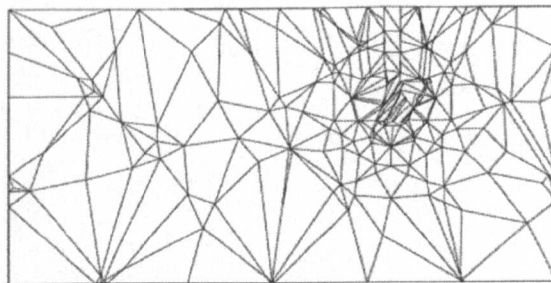
**Edge Distance: 300mm, Rotating Crack – Brittle**



**Edge Distance 180mm, Single Plane Rule**

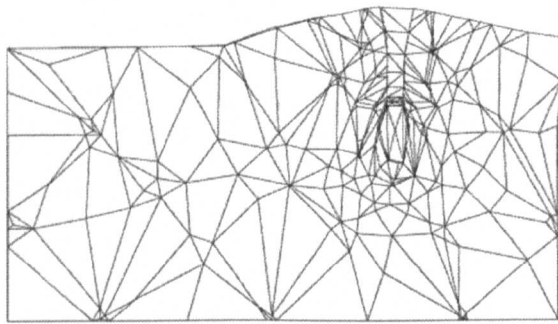


**Edge Distance 180mm, Multiple Plane Rule B**

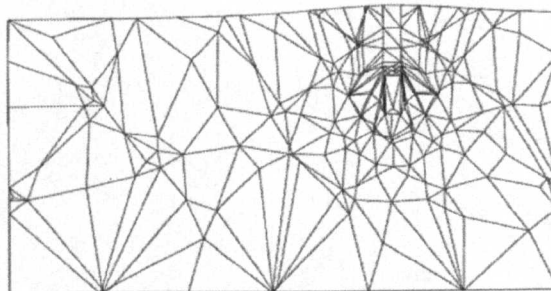
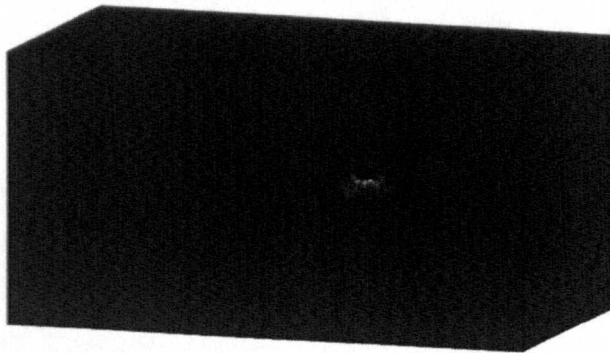


**Edge Distance 180mm, Multiple Plane Rule A**

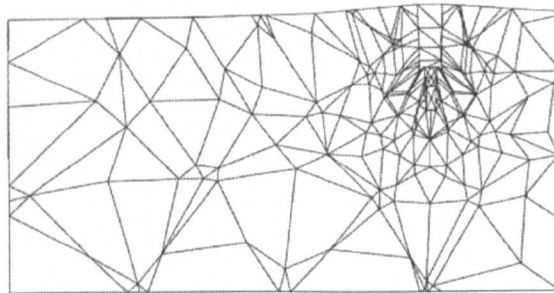
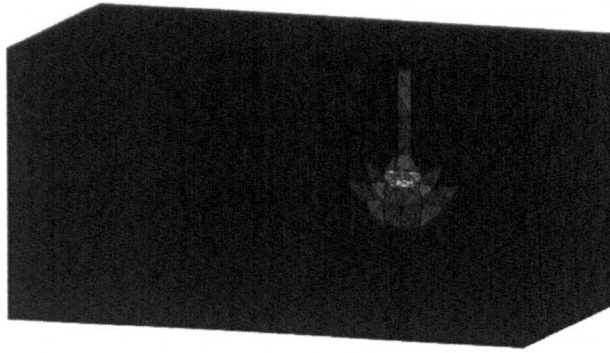




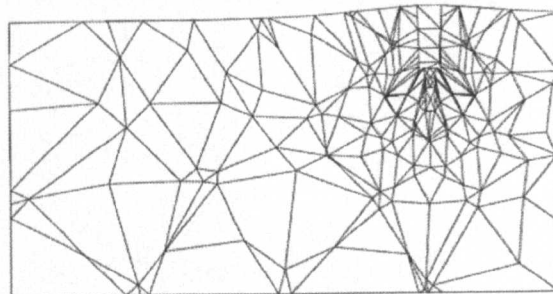
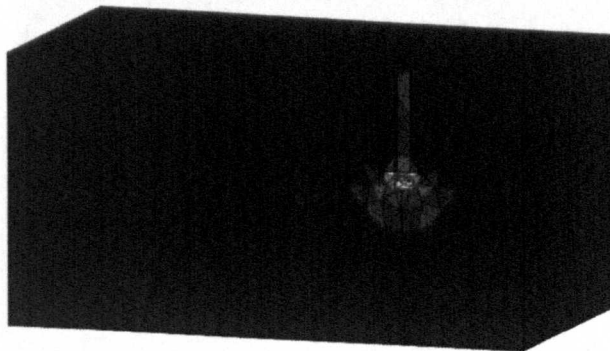
**Edge Distance 180mm, Rotating Crack – Softening**



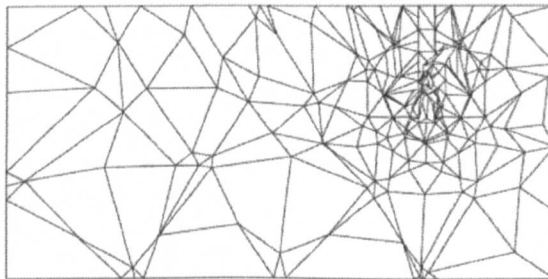
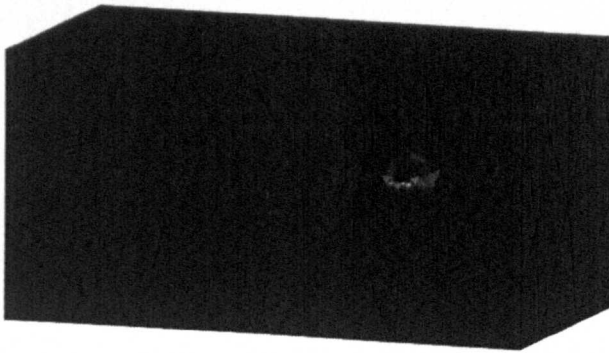
**Edge Distance 180mm, Rotating Crack - Brittle**



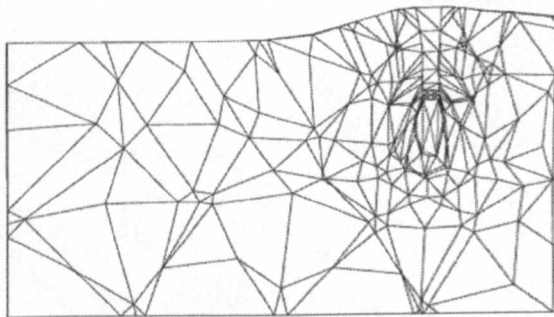
**Edge Distance 140mm, Single Plane Rule**



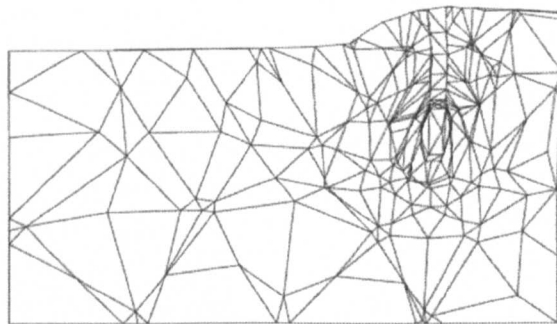
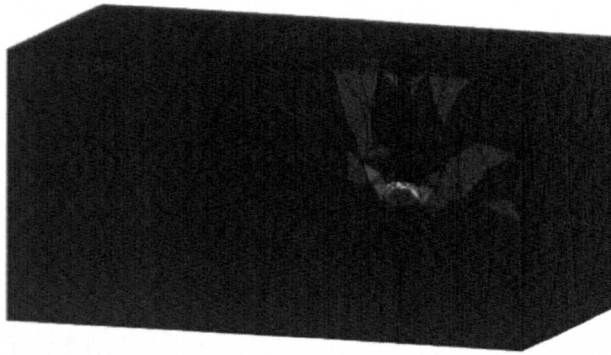
**Edge Distance 140mm, Multiple Plane Rule B**



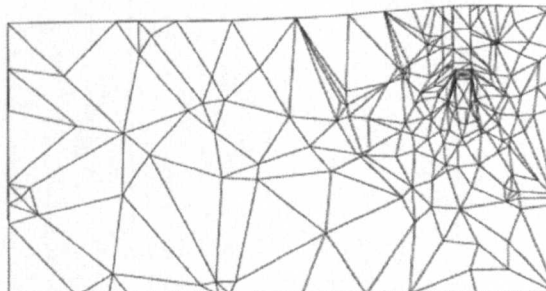
**Edge Distance 140mm, Multiple Plane Rule A**



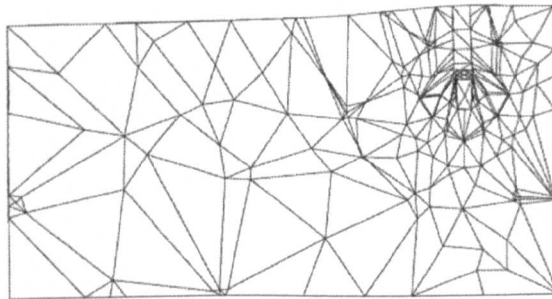
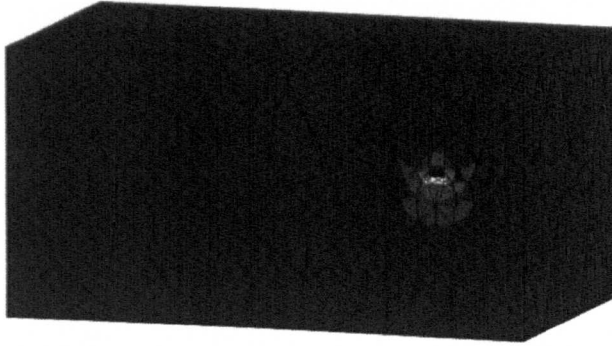
**Edge Distance 140mm, Rotating Crack - Softening**



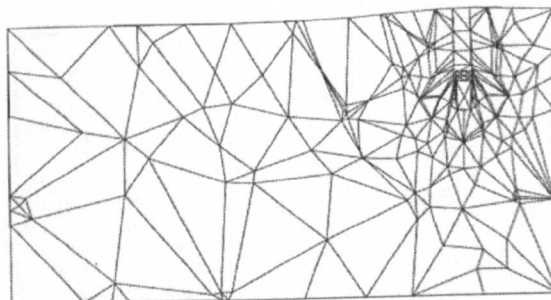
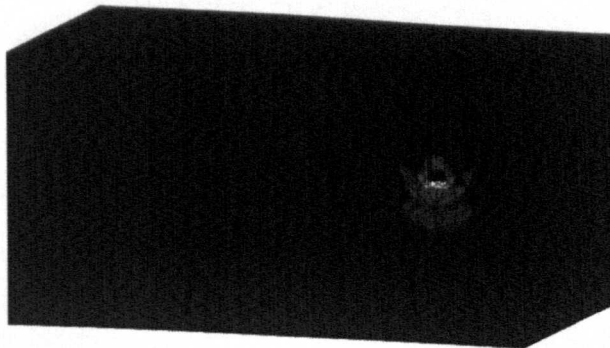
**Edge Distance 140mm, Rotating Crack – Brittle**



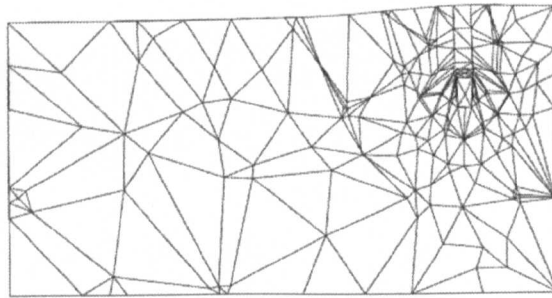
**Edge Distance 100mm, Single Plane Rule**



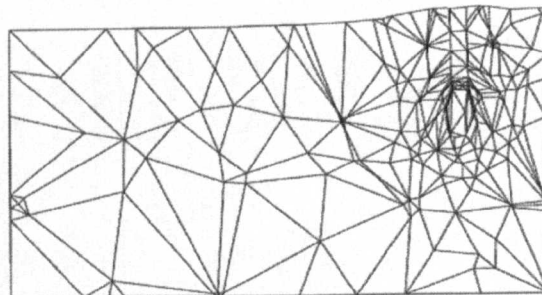
**Edge Distance 100mm, Multiple Plane Rule B**



**Edge Distance 100mm, Multiple Plane Rule A**

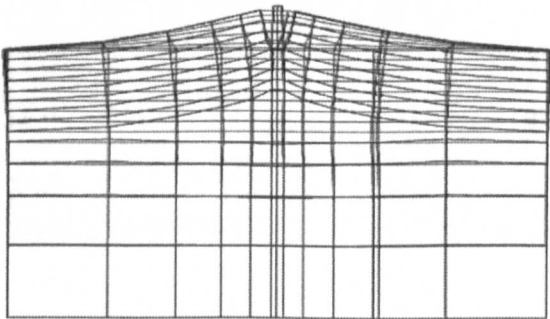
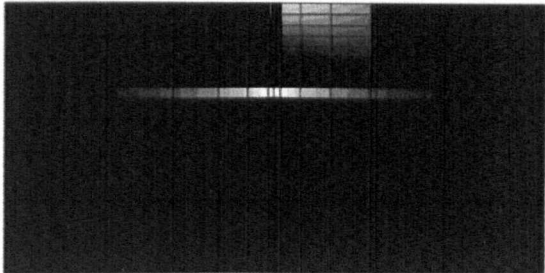


**Edge Distance 100mm, Rotating Crack – Softening**

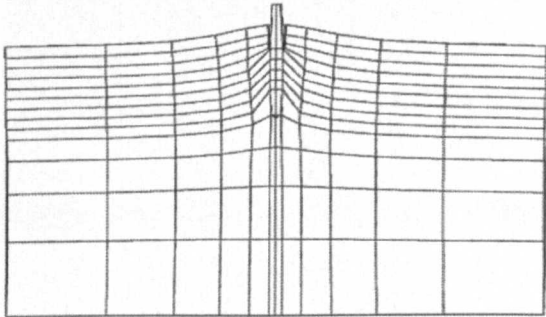
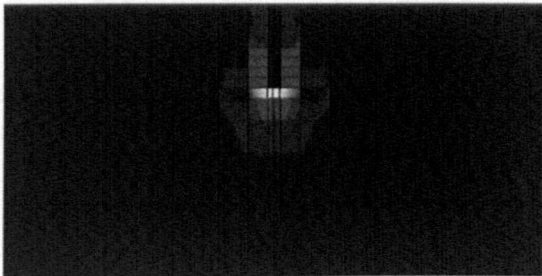


**Edge Distance 100mm, Rotating Crack - Brittle**

**Section 2 – Regular Meshes**

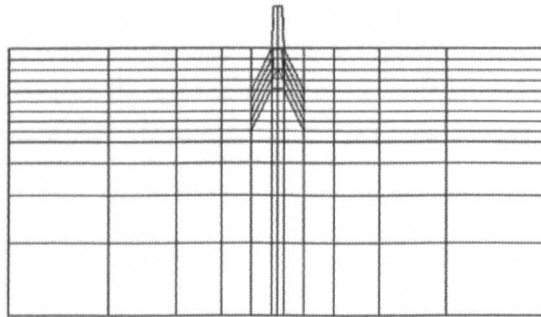
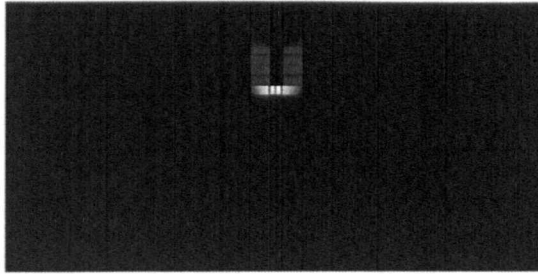


**Edge Distance: 300mm, Single Plane Rule**

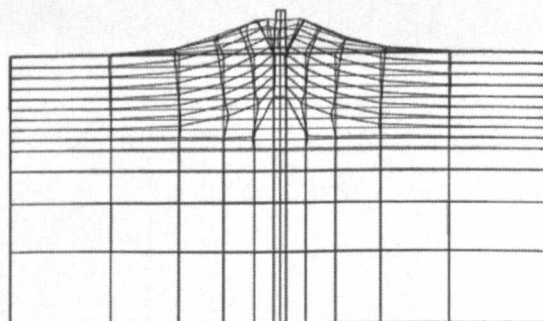
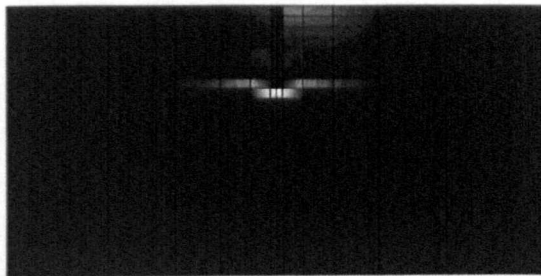


**Edge Distance: 300mm, Multiple Plane Rule B**

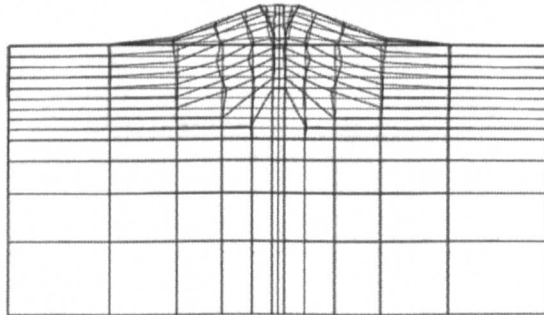
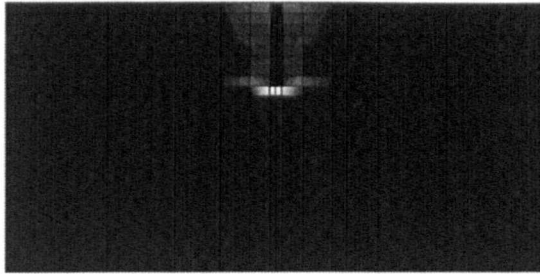




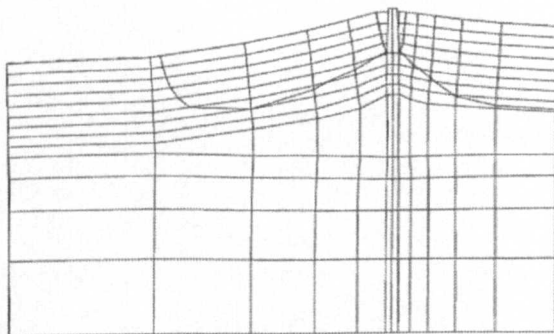
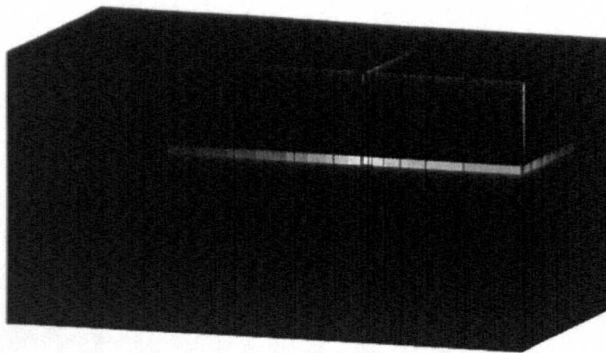
**Edge Distance: 300mm, Multiple Plane Rule A**



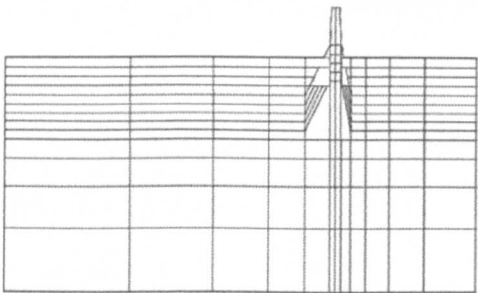
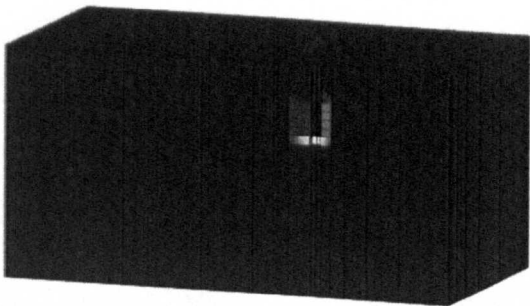
**Edge Distance: 300mm, Rotating Crack - Softening**



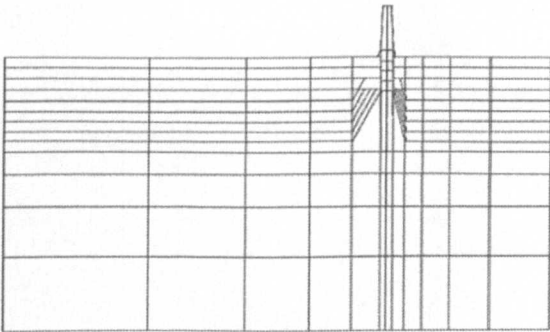
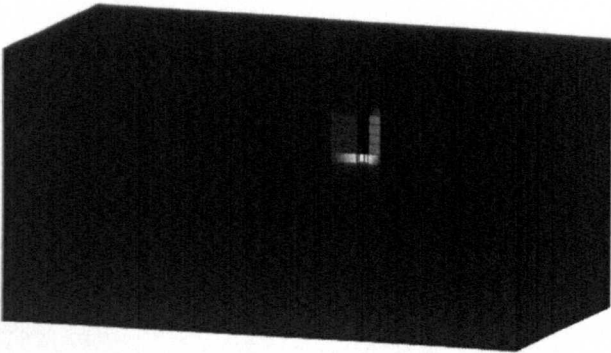
**Edge Distance: 300mm, Rotating Crack – Brittle**



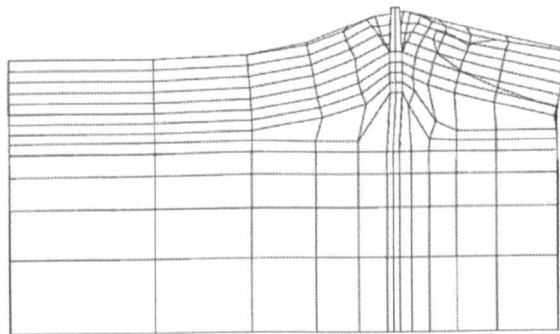
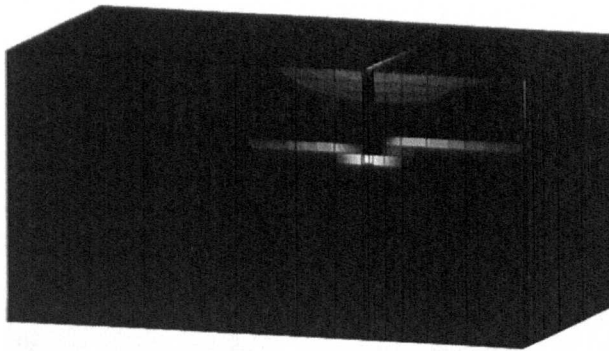
**Edge Distance 180mm, Single Plane Rule**



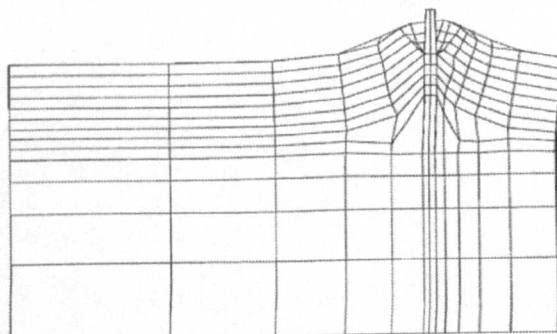
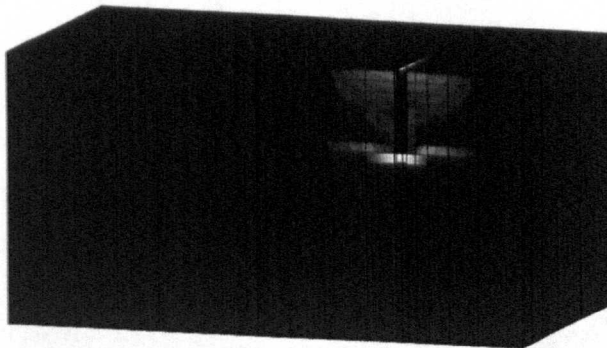
**Edge Distance 180mm, Multiple Plane Rule B**



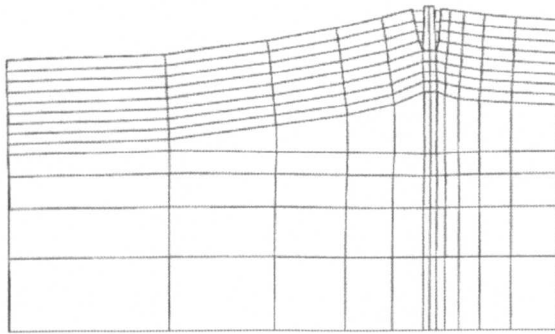
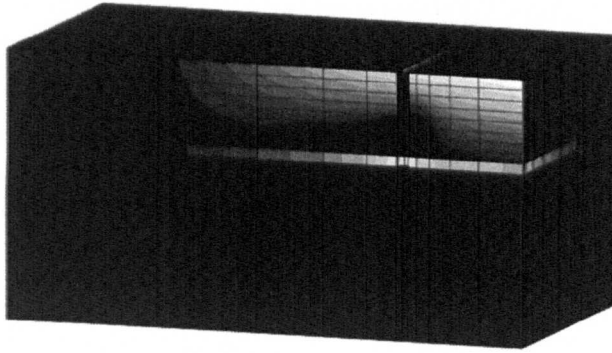
**Edge Distance 180mm, Multiple Plane Rule A**



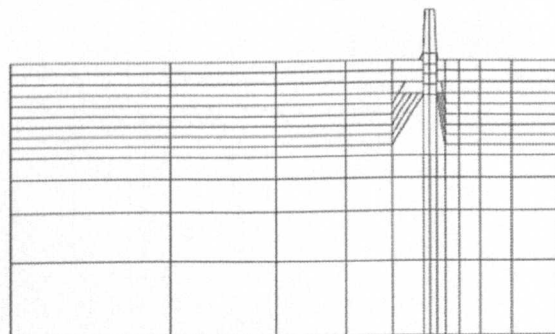
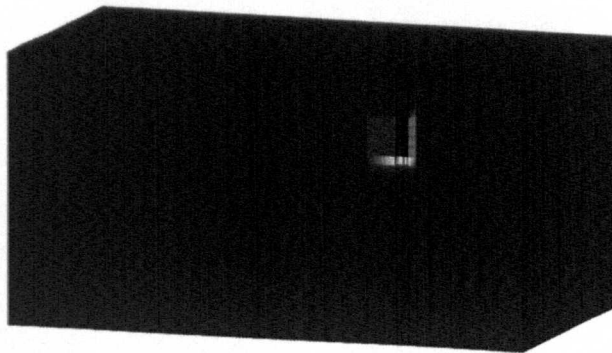
**Edge Distance 180mm, Rotating Crack – Softening**



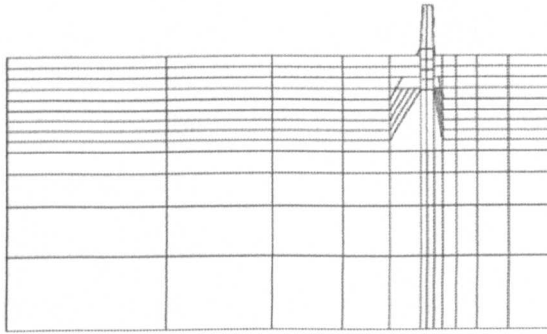
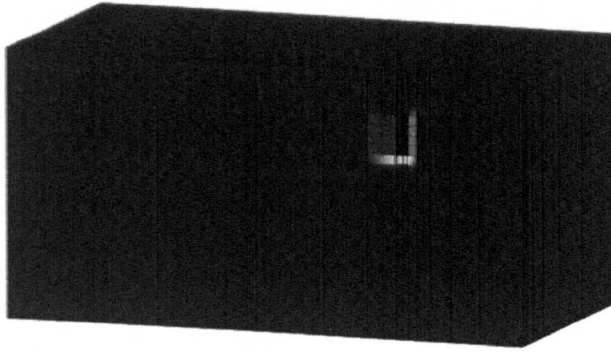
**Edge Distance 180mm, Rotating Crack - Brittle**



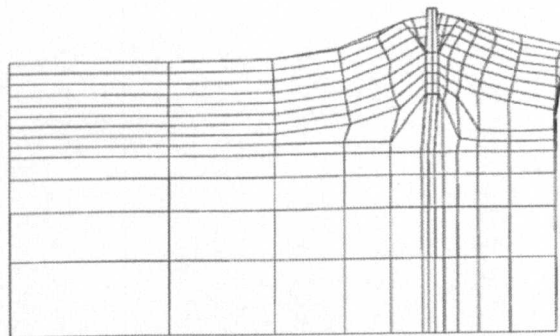
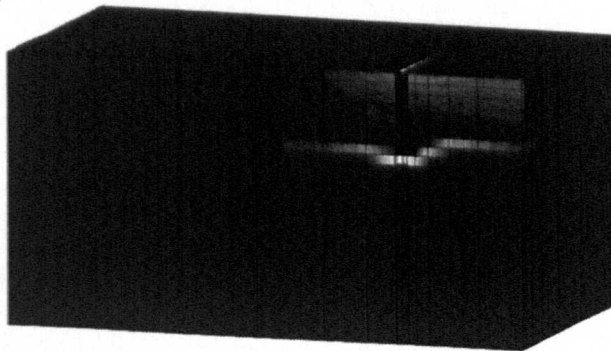
**Edge Distance 140mm, Single Plane Rule**



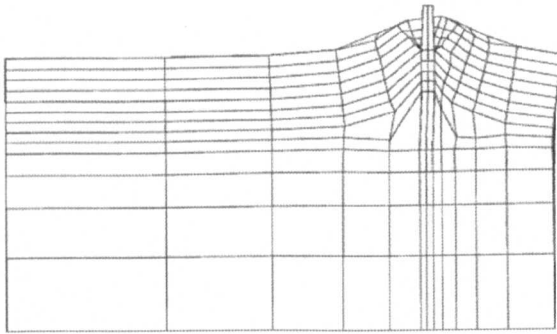
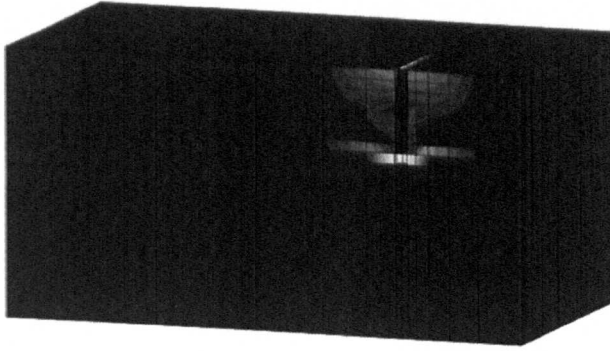
**Edge Distance 140mm, Multiple Plane Rule B**



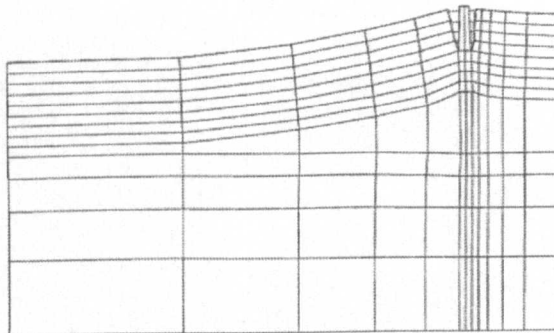
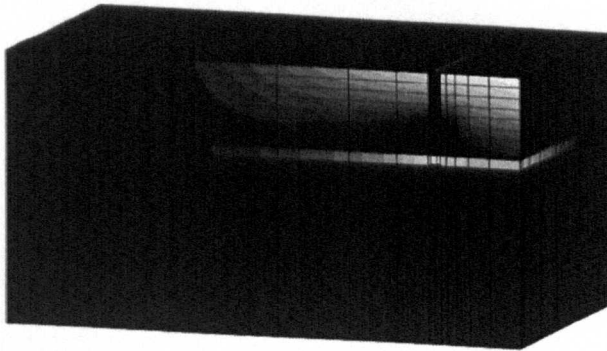
**Edge Distance 140mm, Multiple Plane Rule A**



**Edge Distance 140mm, Rotating Crack - Softening**

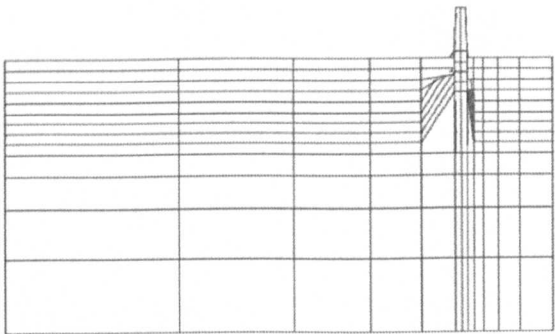
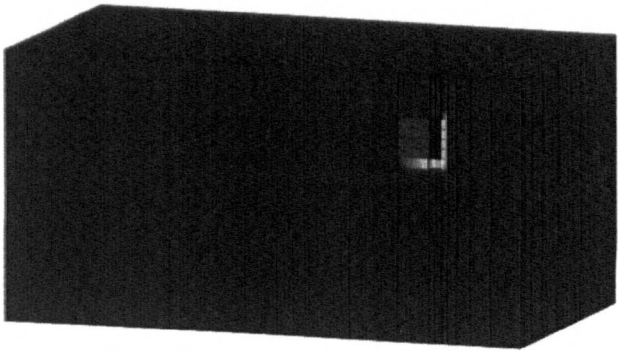


**Edge Distance 140mm, Rotating Crack – Brittle**

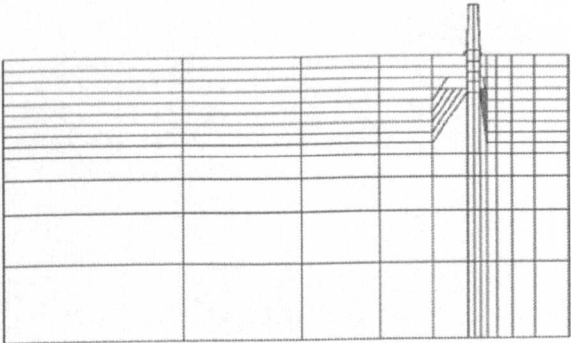
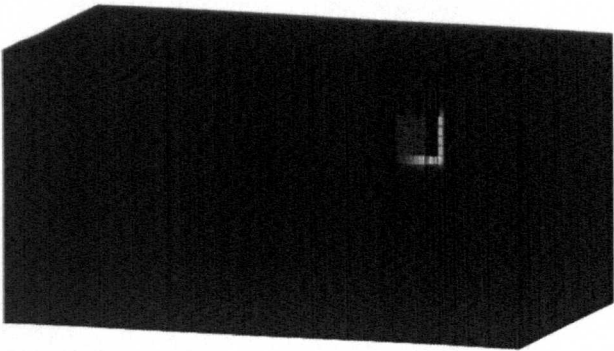


**Edge Distance 100mm, Single Plane Rule**

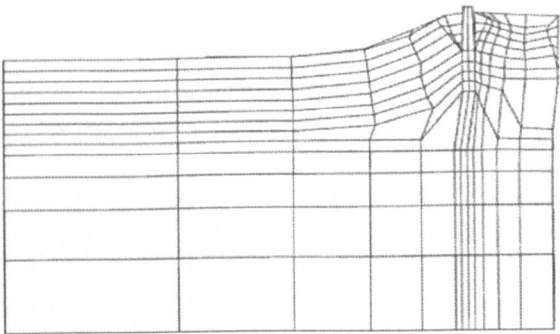
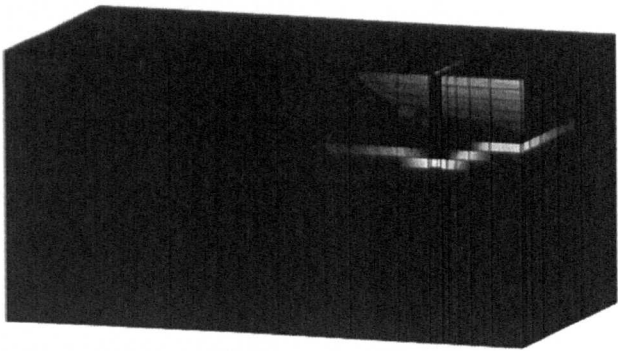




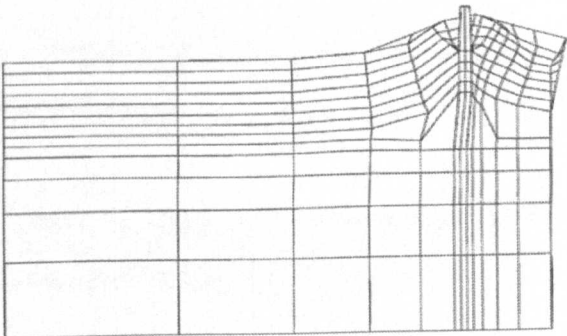
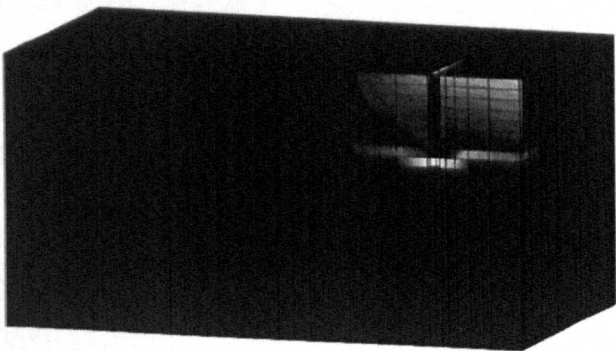
**Edge Distance 100mm, Multiple Plane Rule B**



**Edge Distance 100mm, Multiple Plane Rule A**



**Edge Distance 100mm, Rotating Crack – Softening**



**Edge Distance 100mm, Rotating Crack - Brittle**

## **Appendix C**

### **References and Bibliography**

ADINA R&D Inc. (1998) ADINA Reference Manual. Online ed.

Alfaiate, J., Wells, G.N., Sluys, L.J. (2001) Strong embedded discontinuities for simulating fracture in quasi-brittle materials. FRAMCOS 2001

Applequist, J. (1998) Tensors in a nutshell [online]

Asmus, J., Ozbolt, J. (2001) Numerical and experimental investigations of the splitting failure mode of fastenings. Eligehausen, R. (ed), Connections between steel and concrete. France:RILEM Publications s.a.r.l. 625-636

Baltay, P., Gjelsvik, A. (1989) "Coefficient of friction for steel on concrete at high normal stress", ASCE Journal of Materials in Engineering, 2 (1). 46-49

Bazant, Z.P. (1983) "Comment on orthotropic models for concrete and geomaterials". ASCE Journal of Engineering Mechanics, 109 (3). 849-865

Bazant, Z.P. (1984) "Size effect in blunt fracture: concrete, rock, metal". ASCE Journal of Engineering Mechanics, 110 (4). 518-535

Bazant, Z.P., Oh, B.H. (1985) "Microplane model for progressive fracture of concrete and rock". ASCE journal of Engineering Mechanics, 111 (4). 556-583

Bazant, Z.P., Lin, F. (1988) "Nonlocal smeared cracking model for concrete fracture". ASCE Journal of Structural Engineering, 114 (11). 2493-2510

Bazant, Z.P., Ozbolt, J. (1990) "Nonlocal microplane model for fracture, damage and size effect structures". ASCE Journal of Engineering Mechanics, 116 (?). 2485-2505

Bazant, Z.P., Tabbara, M.R., Pijaudier-Cabot, G. (1990) Random particle model for fracture of aggregate or fibre composites. ASCE Journal of Engineering Mechanics, 166 (2). 1689-1705

Bazant, Z.P., Jirasek, M. (1994) Damage nonlocality due to microcrack interactions: Statistical determination of crack influence function. In: Bazant, Z.P., Bittnar, M., Jirasek, M., Mazars, J. (eds.), Fracture and damage in quasibrittle structures. U.K.: E & FN Spon. 3-17

Bazant, Z.P. (2002) "Concrete fracture models: testing and practice". Engineering Fracture Mechanics, 69. 165-205

Bicanic, N. (1992) Time independent material nonlinearities. In: Hinton, E. (ed), NAFEMS Introduction to non-linear finite element analysis.

Bicanic, N., Pearce, C.J.

Bittencourt, T.N. (1993) Computer simulation of linear and nonlinear crack propagation in cementitious materials [online]. Cornell University, USA. Available from: [www.lmc.ep.usp.br/people/tbitten/gmec/teses/tese-TNB.pdf](http://www.lmc.ep.usp.br/people/tbitten/gmec/teses/tese-TNB.pdf) [Accessed January 2005]

Boussa, H., Mounajed, G., Mesureur, B., Heck, J.V. (2001) Three dimensional modelling of an anchorage to concrete using metal anchor bolts. Eligehausen, R. (ed), Connections between steel and concrete. France:RILEM Publications s.a.r.l. 637-646

Bruckner, M., Eligehausen, R., Ozbolt, J. (2001) Influence of bending compressive stress on the concrete cone capacity. Eligehausen, R. (ed), Connections between steel and concrete. France:RILEM Publications s.a.r.l. 647-657

Cannon, R.W. (1995) Straight talk about anchorage to concrete - Part 1. ACI Structural Journal, 92 (5). 580-586

Cannon, R.W. (1995) Straight talk about anchorage to concrete - Part 2. ACI Structural Journal, 92 (6). 724-734

Cervenka, V., Cervenka, J., Pukl, R. (2001) Atena - an advanced tool for engineering analysis of connections. Eligehausen, R. (ed), Connections between steel and concrete. France:RILEM Publications s.a.r.l. 658-667

CIMNE (2000) GiD reference manual. Online ed. from: <http://gid.cimne.upc.es/support> [Accessed: 21<sup>st</sup> September, 2005] Barcelona, Spain:International Centre for numerical Methods in Engineering.

Cook, R.,D. (1981) Concepts and applications of finite element analysis John Wiley & Sons.

Cook, R.A., Collins, D.M., Klingner, R.E., Polyzois, D. (1992) "Load-deflection behaviour of cast-in-place and retrofit concrete anchors". ACI Structural Journal, 89 (6). 639-649

Cook, R.A., Konz, R.C. (2001) Anchoring with bonded fasteners. Eligehausen, R. (ed), Connections between steel and concrete. France:RILEM Publications s.a.r.l. 361-370

Cotterell, B. (2002) "The past, present, and future of fracture mechanics". Engineering Fracture Mechanics, 69. 533-553

Cornelissen, H. A. W., Hordijk, D. A., And Reinhardt, H. W. (1986) Experimental determination of crack softening characteristics of normalweight and lightweight concrete. Heron 31, 2. The Netherlands.

Crisfield, M.,A. (1991) Non-linear finite element analysis of solids and structures 1st ed. Chichester, U.K.:John Wiley & Sons Ltd.

Czarnecki, R.M., Manrique, M.A., Samaddar, S,K, (1993) "Ultimate load capacities of expansion anchor bolts". Journal of Energy Engineering, 119 (2). 139-158

de Borst, R. (2002) "Fracture in quasi-brittle materials: a review of continuum damage-based approaches". Engineering Fracture Mechanics, 69. 95-112

de Borst, R., Carmeliet, J., Pamin, J., Sluys, L.J. (1994) New horizons in computer analysis of damage and fracture in quasi-brittle materials. In: Bazant, Z.P., Bittnar, M., Jirasek, M., Mazars, J. (eds)., Fracture and damage in quasibrittle structures. U.K.: E & FN Spon. 359-372

de Borst, R., Geers, M.G.D., Kuhl, E., Peerlings, R.H.J. (1998) Enhanced damage models for concrete fracture. In: de Borst, R., Bicanic. N., Mang, H., Meschke, G. (eds)., Computational modelling of concrete structures (euro-c 1998). Rotterdam, The Netherlands: A.A.Balkema. 231-248

de Borst, R., Nauta, P. (1985) "Non-orthogonal cracks in smeared finite element model". 35-46

di Tommaso, A., Manfroni, O. (1993) Comparison of finite element concrete models simulating pull-out tests. Rossmannith, H.P. (ed), Fracture and damage of concrete and rock (fdcr-2). U.K.: E & FN Spon. 548-558

Elfgren, L. (1998) Round robin analysis and testing of anchor bolts in concrete structures Research Report. Lulea university of Technology, Sweden.

Eligehausen, R., Balogh, T. (1995) "Behaviour of fasteners loaded in tension in cracked reinforced concrete". ACI Structural Journal, 92 (3). 365-379

Eligehausen, R., Hofacker, I., Lettow, S. (2001) Fastening techniques - current status and future trends. Eligehausen, R. (ed), Connections between steel and concrete. France:RILEM Publications s.a.r.l. 11-27

EOTA (European Organisation for Technical Approvals) (1997) Guidelines for european technical approval of metal anchors for use in concrete. Watford, UK:British Board of Agreement.

Feenstra, P.H. (1993) Computational aspects of biaxial stress in plane and reinforced concrete. PhD Thesis. Delft University of Technology, The Netherlands

Feenstra, P.H. (1999) Total strain-based crack models - Implementation document. TNO Report 99-MIT-NM-R/0004.

Feenstra, P.H., de Borst, R. (1995) "A composite plasticity model for concrete". International Journal of Solids and Structures, 33 (5). 707-730

Feenstra, P.H., Rots, J.G., Arnesen, A., Teigen, J.G., Hoiseth, K.V. (1998) A 3D constitutive model for concrete based on a co-rotational concept. In: de Borst, R., Bicanic, N., Mang, H., Meschke, G. (eds), Computational modelling of concrete structures (euro-c 1998). Rotterdam, The Netherlands: A.A.Balkema. 13-22

Fuchs, W. (2001) Evolution of fastening design methods in europe. Eligehausen, R. (ed), Connections between steel and concrete. France:RILEM Publications s.a.r.l. 45-60

Fuchs, W., Eligehausen, R., Breen, J. (1995) "Concrete capacity design (CCD) approach for fastening to concrete". ACI Structural Journal, 92 (1). 73-94



Guillermo, E. (1998) "Finite element analysis of failure response behaviour of anchor bolts in concrete". Nuclear Engineering and Design, 179. 245-252

Hofmann, J, Ozbolt, J., Eligehausen, R. (2001) Behaviour and design of fastenings with headed anchors at the edge under arbitrary loading direction. Eligehausen, R. (ed), Connections between steel and concrete. France:RILEM Publications s.a.r.l. 678-688

Han, D.J., Chen, W.F. (1987) "Constitutive modelling analysis of concrete structures". ASCE Journal of Engineering Mechanics, 113 (4) 577-593

Hillerborg, A., Modeer, M., Petersson, P.E. (1976) "Analysis of crack formation and crack growth in concrete by means of fracture mechanics and finite elements". Cement and Concrete Research, 6. 773-782

Hilti (2002) Fastening technology manual [online]. Principality of Liechtenstein:Hilti Corporation. Available from: [www.hilti.com](http://www.hilti.com) [Accessed April 2002]

Hofmann, J., Eligehausen, R., Ozbolt, J. (2001) Behaviour and design of fastenings with headed anchors at the edge under tension and shear load. FRAMCOS 2001 941-947

Hsieh, S.S., Ting, E.C., Chen, W.F. (1982) "A plasticity model for concrete" International Journal of Solids and Structures, 18 (3). 181-197

Hordijk, D. A. (1991) Local Approach to Fatigue of Concrete. PhD Thesis. Delft University of Technology, The Netherlands

James, G. (1994) Modern Engineering Mathematics. 3rd ed. Suffolk, UK:Addison Wesley.

Jirasek, M., Zimmermann, T. (1998) "Rotating crack model with transition to scalar damage". ASCE Journal of Engineering Mechanics 124 (3) 277-284

Jirasek, M., Zimmermann, T. (1998) "Analysis of rotating crack model". ASCE Journal of Engineering Mechanics, 124 (8). 842-851

Kankam, C.K. (1997) "Relationship of bond stress, steel stress and slip in reinforced concrete". ASCE Journal of Structural Engineering, 123 (1). 79-85

Karihaloo, B.L., (1993) Testing of anchor bolts in plane stress and axisymmetric geometries. Rossmanith, H.P. (ed), Fracture and damage of concrete and rock (fder-2). U.K.: E & FN Spon. 588-597

Kelly, A., Pohl, I. (1998) A book on C 4th ed. Massachusetts, USA: Addison Wesley.

Kim, S., Yu, C., Yoon, Y. (2004) "Sleeve-type expansion anchor behaviour in cracked and uncracked concrete". Nuclear Engineering and Design, 228. 273-281

Klingner, R.E. (2001) Probabilistic calibration of design methods. Eligehausen, R. (ed), Connections between steel and concrete. France: RILEM Publications s.a.r.l. 61-71

Kwak, H.G., Filipou, F.C. (1990) Finite element analysis of reinforced concrete structures under monotonic loads. Report No. UCB/SEMM-90/14, University of California, Berkeley, USA

Latenser, K. (2001) Development of common uniform regulations in Europe for the assessment of metal anchors. Eligehausen, R. (ed), Connections between steel and concrete. France: RILEM Publications s.a.r.l. 150-157

Lertsrisakulrat, T., Watanabe, K., Matsuo, M., Niwa, J. Localized fracture length and fracture energy of concrete in compression.

Li, L. (2001) Load bearing capacity of torque controlled expansion anchors Eligehausen, R. (ed), Connections between steel and concrete. France:RILEM Publications s.a.r.l. 170-177

Li, Y., Zimmermann, T. (1993) Simulation of concrete cracking: A numerical evaluation of the rotating crack model. Rossmann, H.P. (ed), Fracture and damage of concrete and rock (fcd-2). U.K.: E & FN Spon. 95-106

Li, Y.J., Eligehausen, R. (2001) Numerical analysis of group effect in bonded anchors with different bond strengths. Eligehausen, R. (ed), Connections between steel and concrete. France:RILEM Publications s.a.r.l. 699-706

Li, Y.J., Eligehausen, R., Ozbolt, J., Lehr, B. (2002) "Numerical analysis of quadruple fastenings with bonded anchors". ACI Structural Journal, 99 (2). 149-156

Li, Y.J., Eligehausen, R., Lehr, B., Ozbolt, J. (2001) Fracture analysis of quadruple fastenings with bonded anchors. FRAMCOS 2001 991-997

Lu, P.F., Vaziri, R. (1997) "The equivalence of stress- and strain-based plasticity theories". Computational Methods in Applied Mechanics and Engineering, 147. 125-138

Lundgren, K., Gylltoft, K. (2000) "A model for the bond between concrete and reinforcement". Magazine of Concrete Research, 52 (1) 53-63

Lura, P., Plizzari, G.A., Riva, P. (2001) Splitting-crack propagation in pullout tests. FRAMCOS 2001

Mar.A. (amar@wildefea.co.uk) (23 July 2003). Crack Strains. E-mail to Watson.D.S. (dwatson@civil.gla.ac.uk)

Mark, P. (1998) Numerical simulation of cracking in concrete during tensile loading. In: de Borst, R., Bicanic, N., Mang, H., Meschke, G. (eds), Computational modelling of concrete structures (euro-c 1998). Rotterdam, The Netherlands: A.A.Balkema. 119-125

Math Works Inc. (1995) The Student Edition of Matlab: version 4: user's guide 1<sup>st</sup> ed. New York, USA: Prentice-Hall Inc.

Mazars, J., Pijaudier-Cabot, G. (1989) "Continuum damage theory - Application to concrete". ASCE Journal of Engineering Mechanics, 115 (2). 345-365

Melcher, J.J., Karmazinova, M. (2001) The analysis of fastener strength using the limit state approach. Eligehausen, R. (ed), Connections between steel and concrete. France: RILEM Publications s.a.r.l. 212-219

Nienstedt, J., Mattner, R. (2001) "Three-dimensional modelling of anchoring systems in concrete", In: de Borst, R., Mazars, J., Pijaudier-Cabot, G., van Mier, J.G.M. (eds), Fracture Mechanics of Concrete Structures. Netherlands: A.A.Balkema. 1021-1026.

Nienstedt, J., Mattner, R., Nestler, U., Song, C. (2001) Simulation of fastening systems utilizing chemical and mechanical anchors. Eligehausen, R. (ed), Connections between steel and concrete. France: RILEM Publications s.a.r.l. 708-716

Nienstedt, J., Mattner, R., Wiesbaum, J. (1999) Constitutive modelling of concrete in numerical simulations of anchoring technology. Structural Engineering in the 21st Century 211-214

Obata, M., Inoue, M., Goto, Y. (1998) "The failure mechanism and the pull-out strength of a bond-type anchor near a free edge". Mechanics of Materials, 28. 113-122

Ohlsson, U., Elfgrén, L. (1993) Test of the load-bearing capacity of anchor bolts. Rossmanith, H.P. (ed), Fracture and damage of concrete and rock (fdcr-2). U.K.: E & FN Spon. 579-587

Ohmenhauser, F., Weihe, S., Kroplin, B. (1998) Classification and algorithmic implementation of smeared crack models. In: de Borst, R., Bicanic, N., Mang, H., Meschke, G. (eds), Computational modelling of concrete structures (euro-c 1998). Rotterdam, The Netherlands: A.A.Balkema. 173-182

Oliver, J., Cervera, M., Oller, S., Lubliner, J. (1990) Isotropic damage models and smeared crack analysis of concrete. In: Bicanic, N., Mang, H. (eds), Computer Aided Analysis and Design of Concrete Structures. Swansea, U.K.: Pineridge Press. 945-957

Ozbolt, J. (2001) Smeared fracture FE - analysis of reinforced concrete structures - theory and examples. Eligehausen, R. (ed), Connections between steel and concrete. France:RILEM Publications s.a.r.l. 609-623

Ozbolt, J., Eligehausen, R. (1993) Fastening elements in concrete structures - numerical simulations. Rossmanith, H.P. (ed), Fracture and damage of concrete and rock (fdcr-2). U.K.: E & FN Spon. 527-547

Ozbolt, J., Eligehausen, R. (1994) Scaling laws in concrete structures. In: Bazant, Z.P., Bittnar, M., Jirasek, M., Mazars, J. (eds), Fracture and damage in quasibrittle structures. U.K.: E & FN Spon. 311-318

Ozbolt, J., Eligehausen, R. (1995) "Model of reinforced concrete by the non-local microplane model". Nuclear Engineering and Design, 156. 249-257

Ozbolt, J., Eligehausen, R., Reinhardt, H.W. (1999) "Size effect on the cone pull-out load". International Journal of Fracture, 95. 391-404

Ozbolt, J., Hofmann, J., Eligehausen, R. (2001) *Headed stud anchor - cyclic loading and creep-cracking interaction of concrete*. Eligehausen, R. (ed), *Connections between steel and concrete*. France:RILEM Publications s.a.r.l. 717-728

Ozbolt, J., Li, Y., Kozar, I. (2001) "Microplane model for concrete with relaxed kinematic constraint". *International Journal of Solids and Structures*, 38. 2683-2711

Penick, T. (2000) *Properties of matrices* [online]. Austin, Texas, USA:TEI Controls. Available from: [www.teicontrols.com/notes/MatricesM340L/Matrices.pdf](http://www.teicontrols.com/notes/MatricesM340L/Matrices.pdf) [Accessed 4th June 2005]

Pivonka, P., Lackner, R., Mang, H.A. (2004) "Concrete subject to triaxial stress states: Application to pull-out analyses". *ASCE Journal of Engineering Mechanics*, 130 (12). 1486-1498

Prat, P.C., Gens, A. (1994) Microplane formulations for quasibrittle materials with anisotropy and damage. In: Bazant, Z.P., Bittnar, M., Jirasek, M., Mazars, J. (eds), *Fracture and damage in quasibrittle structures*. U.K.: E & FN Spon. 67-74

Press, W.H., Flannery, B.P., Tevkolsky, S.A., Vetterling, W.T. (1993) *Numerical recipes in C: The art of scientific computing* Cambridge University Press.

Pukl, R., Ozbolt, J., Eligehausen, R. (1998) Load-bearing behaviour of bonded anchors - Nonlinear simulation. In: de Borst, R., Bicanic. N., Mang, H., Meschke, G. (eds), *Computational modelling of concrete structures (euro-c 1998)*. Rotterdam, The Netherlands: A.A.Balkema. 849-853

Pukl, R., Ozbolt, J., Schlottke, B.M., Eligehausen, R. (1994) Computer simulation of steel expansion anchors embedded into small concrete members. In: Mang, H., Bicanic. N., de Borst, R. (eds), *Computational modelling of concrete structures (euro-c 1994)*. Swansea, U.K.: Pineridge Press Limited. 915-924

Rawl Fixings (1997) Specification & design guide. Glasgow, UK: The Rawlplug Company Ltd.

Rawlplug (1999) Design recommendations. [online]. Glasgow, UK: The Rawlplug Company Ltd. Available from: [www.rawlplug.com/manual/226.html](http://www.rawlplug.com/manual/226.html) [Accessed 15th November 1999]

Rawlplug (1999) Mechanical and adhesive anchors [online]. Glasgow, UK: The Rawlplug Company Ltd. Available from: [www.rawlplug.com/manual/22.2.html](http://www.rawlplug.com/manual/22.2.html) [Accessed 15th November 1999]

Reinhardt, H. W. (1984) Fracture mechanics of an elastic softening material like concrete. Heron 29. The Netherlands

Rodriguez, M., Zhang, Y., Lotez, D., Graves, H.L., Klingner, R.E. (1997) "Dynamic behaviour of anchors in cracked and uncracked concrete: a progress report". Nuclear Engineering and Design, 168 23-34

Rots, J.G. (2001) "Sequentially linear continuum model for concrete fracture", In: de Borst, R., Mazars, J., Pijaudier-Cabot, G., van Mier, J.G.M. (eds), Fracture Mechanics of Concrete Structures. The Netherlands: A.A. Balkema. 831-839

Rots, J.G. (2001) Sequentially linear continuum model for concrete fracture. FRAMCOS 2001 831-839

Rots, J.G., Blaauwendraad, J. (1989) Crack models for concrete: Discrete or smeared? Fixed, multi-directional or rotating? Heron 34. The Netherlands :



Rots, J.G., Invernizzi, S. (2003) Keynote Paper: Regularized saw-tooth softening. In: Bicanic, N., de Borst, R., Mang, H., Meschke, G. (eds), Computational modelling of concrete structures (euro-c 2003). The Netherlands.: Swets & Zeitlinger. 599-617

Rots, J.G., Nauta, P., Kusters, G., M., A., Blaauwendraad, J. (1985) Smeared crack approach and fracture localization in concrete. Heron 30. The Netherlands :

Salari, M.R., Spacone, E. (2000) "Finite element formulations of one-dimensional elements with bond-slip". Engineering Structures, 23. 815-826

Scarpas, A., Blaauwendraad, J. (1993) Nonlocal plasticity softening model for brittle materials. Rossmann, H.P. (ed), Fracture and damage of concrete and rock (fdcr-2). U.K.: E & FN Spon. 44-53

Schlangen, E., Vervuurt, A., van Vliet, M.R.A., van Mier, J.G.M. (1999) Numerical materials science of concrete using lattice analysis [online]. The Netherlands: DIANA Analysis. Available from: [www.diana.nl/](http://www.diana.nl/) [Accessed May 2000]

Shirvani, M., Klingner, R.E., Graves, H.L. (2001) Behaviour of tensile anchors in concrete: Statistical analysis and design recommendations. Elgehausen, R. (ed), Connections between steel and concrete. France:RILEM Publications s.a.r.l. 261-271

Simone, A., Wells, G.N., Sluys, L.J. (2001) A novel technique for modelling interfaces in reinforced brittle materials. FRAMCOS 2001 841-846

Stark, J.W.B., Hordijk, D.A. (2001) Where structural steel and concrete meet. Elgehausen, R. (ed), Connections between steel and concrete. France:RILEM Publications s.a.r.l. 1-10

Stirling, C.G. (2004) Algorithmic and modelling aspects of the discontinuous behaviour of structural masonry. PhD Thesis. University of Glasgow, U.K.

Timoshenko, S. (1934) Theory of Elasticity 1st ed. USA:McGraw-Hill Book Company Inc.

TNO Building and Construction Research (1999) DIANA user's manual. Online ed. Delft, The Netherlands:TNO Building and Construction Research.

Tran, T.X., Dorfmann, A., Rhie, Y.B. (1998) Micromechanical modeling of cracking and damage of concrete structures. In: de Borst, R., Bicanic. N., Mang, H., Meschke, G. (eds)., Computational modelling of concrete structures (euro-c 1998). Rotterdam, The Netherlands: A.A.Balkema. 61-69

Uchida, Y., Rokugo, K., Koyanagi, W. (1993) Numerical analysis of anchor bolts embedded in concrete plates. Rossmanith, H.P. (ed), Fracture and damage of concrete and rock (fdcr-2). U.K.: E & FN Spon. 598-607

Vecchio, F.J., Collins, M.P. (1986) "The modified compression field theory for reinforced concrete elements subject to shear". ACI Journal, 83 (22). 219-231

Vecchio, F.J., Collins, M.P. (1993) "Compression Response of Cracked Reinforced Concrete". ASCE Journal of Structural Engineering, 119 (12). 3590-3611

Vervuurt, A.H.J.M., van Mier, J.G.M., Schlangen, E. (1993) Pull-out of steel anchors embedded in concrete. Rossmanith, H.P. (ed), Fracture and damage of concrete and rock (fdcr-2). U.K.: E & FN Spon. 569-577

Wall, L., Christiansesn, T., Orwant, J. (2000) Programming Perl 3rd ed. Sebastopol, CA, USA:O'Reilly & Associates.

Wang, J., Navi, P., Huet, C. (1993) Finite element analysis of anchor bolt pull-out based on fracture mechanics. Rossmanith, H.P. (ed), Fracture and damage of concrete and rock (fdcr-2). U.K.: E & FN Spon. 559-567

Wang, J., Navi, P., Huet, C. (1993) Application of fracture mechanics to the study of crack propagation in concrete structures using a granular microcracked model. Rossmanith, H.P. (ed), Fracture and damage of concrete and rock (fdcr-2). U.K.: E & FN Spon. 176-185

Waszczyszyn, Z. (1989) Computational methods and plasticity. Report No. LR-583, Delft University of Technology, The Netherlands.

Weihe, S., Kroplin, B., de Borst, R. (1998) "Classification of smeared crack models based on material and structural properties". International Journal of Structures, 35 (12). 1289-1308

Willam, K., Pramono, E., Sture, S. (1987) Fundamental issues of smeared crack models. Shah, S., Swartz, S. (eds), Proc. SEM-RILEM International Conference on Fracture of Concrete and Rock, SEM, Bethel, Conn., 192-207

(1999) ABAQUS/Answers [online] Pawtucket, RI, USA:Hibbitt, Karlsson & Sorensen, Inc. Available from: [www.hks.com/reference/epaper/r\\_a99-02.pdf](http://www.hks.com/reference/epaper/r_a99-02.pdf) [Accessed 26th October 2004]

(2002) IEEE floating point numbers [online]. University of California, L.A., CA, USA. Available from: [www.seas.ucla.edu/ee103u/](http://www.seas.ucla.edu/ee103u/) [Accessed June 2002]

No date Evolution of fixings [online]. Glasgow, UK:The Rawlplug Company Ltd. Available from: [www.artex-rawlplug.co.uk](http://www.artex-rawlplug.co.uk) [Accessed 11th June 2005]

No date Joint model [online]. Cast 3M Solver. Available from: [www-cast3m.cea.fr/cast3m/html/Pegon/elemjoint.pdf](http://www-cast3m.cea.fr/cast3m/html/Pegon/elemjoint.pdf) [Accessed January 2005]

Friction coefficient bolted joints [online]. Available from: [www.roymech.co.uk/Useful\\_Tables/Tribology/co\\_of\\_frict.htm](http://www.roymech.co.uk/Useful_Tables/Tribology/co_of_frict.htm) [Accessed 26th October 2004]